Nanoscale Structure and Assembly at Solid-Fluid Interfaces

Volume II: Assembly in Hybrid and Biological Systems

Edited by Xiang Yang Liu and James J. De Yoreo

NANOSCALE STRUCTURE AND ASSEMBLY AT SOLID–FLUID INTERFACES

VOLUME II

Assembly in Hybrid and Biological Systems

Nanostructure Science and Technology

Series Editor: David J. Lockwood, FRSC
National Research Council of Canada
Ottawa, Ontario, Canada

Current volumes in this series:

Alternative Lithography: Unleashing the Potentials of Nanotechnology
Edited by Olivia M. Sotomayor Torres

Introduction to Nanoscale Science and Technology
Edited by Massimiliano Di Ventra, Stephane Evoy and James R. Heflin

Nanoparticles: Building Blocks for Nanotechnology
Edited by Vincent Rotello

Nanoscale Structure and Assembly at Solid–Fluid Interfaces (two-volume set)
Vol I: Interfacial Structures versus Dynamics
Vol II: Assembly in Hybrid and Biological Systems
Edited by Xiang Yang Liu and James J. De Yoreo

Nanostructured Catalysts
Edited by Susannah L. Scott, Cathleen M. Crudden, and Christopher W. Jones

Nanotechnology in Catalysis (two-volume set)
Edited by Bing Zhou, Sophie Hermans and Gabor A. Somorjai

Polyoxometalate Chemistry for Nano-Composite Design
Edited by Toshihiro Yamase and Michael T. Pope

Self-Assembled   Nanostructures
Jin Z. Zhang, Zhong-lin Wang, Jun Liu, Shaowei Chen and Gang-yu Liu

Semiconductor Nanocrystals: From Basic Principles to Applications
Edited by Alexander L. Efros, David J. Lockwood and Leonid Tsybeskov

NANOSCALE STRUCTURE AND ASSEMBLY AT SOLID–FLUID INTERFACES

VOLUME II

Assembly in Hybrid and Biological Systems

edited by

Xiang Yan Liu

Department of Physics
National University of Singapore
Singapore

James J. De Yoreo

Department of Chemistry and Materials Science
Lawrence Livermore National Laboratory
USA

Created in the United States of America

Table of Contents

Volume II
Assembly in Hybrid and Biological Systems

This page intentionally left blank

Nanoscale structure and assembly at solid–fluid interfaces

Series of Two Volumes

Editors:

Xiang Yang Liu

Department of Physics, National University of Singapore, Singapore

&

James J. De Yoreo

Department of Chemistry and Materials Science, Lawrence Livermore National Laboratory, USA

Foreword

Preface

VOLUME I: SOLID–FLUID INTERFACIAL STRUCTURE AND MOLECULAR SELF-ASSEMBLY AT THE NANO- AND MICRO-SCALE

List of contributors

Foreword

An old joke states that physicists apply good techniques to poorly characterized substances, while chemists work with good substances making use of poor techniques. Nowadays, biologists and biochemists also work with materials poorly characterized because of their complexity. Nevertheless, emerging now and reflected in this book is an era in which high-level techniques are applied to chemically well-controlled substances. The authors provide an excellent collection of fascinating stories on what happens at interfaces between crystalline materials and solutions. Scanning atomic force, tunneling, and vertical interferometric microscopies, modern optics, grazing X-ray diffraction, and molecular dynamic simulations in ionic systems are the major tools that the authors have applied and that have revealed the processes and interactions that people only dreamed of tackling half a century ago. The authors pay attention to the essential "know-how" of all these techniques. Certainly, such a book would not have been possible 20 or even 10 years ago.

This collection of articles reflects the breakthroughs that are happening in understanding surface pheonomena in chemically complex systems—crystals and other solid surfaces—in contact with mainly aqueous solutions containing ions of major components and additives to be adsorbed—from Mg^{2+} to protein ions, to viruses and antibodies. The last couple of decades brought about significant progress in understanding "tailor-made impurities" on the stereo-chemical level. This book reflects further steps towards more detailed quantitative physico-chemical insights. Inorganic crystal growth, dissolution, adsorption, nucleation in connection with specific crystal surface structures are the major subjects of the articles collected in Volume I. Visualization of structural details of viruses, protein crystals and formation of the latter, properties of "soft" biologically related objects and surfaces, like membranes, protein molecules immobilized for analyses, probing their structure and properties, and processes in formation of emulsion droplets provide a second group of objects and phenomena. This group is covered in Volume II. Here, too, crystal growth and adsorption are the key physico-chemical issues.

The demands to monitor environment, to create new nanoelectronics, and to bring more rationale to the endless ocean of exciting but still spotty findings in biology and medicine provide long-term and strong driving forces to move from art to science in all these areas. Yes, the general framework of crystal growth and surface science is now reaching its maturity. Unfortunately, existence of this framework does not yet mean quantitative predictive power, especially for the chemically complex systems, that are in our hands. We still have a long way to go to achieve the aimed spirit through precise quantitative knowledge from physics to chemistry and—which is a much more difficult task—to biology. This book provides a timely step in that direction.

On a more specific note, this book reflects the revival of an interest in crystal growth from solutions. It was boosted about two decades ago by needs to obtain crystals for non-

linear optics, in particular, for laser induced nuclear fusion (an effort in which one of the editors—J.J. De Yoreo—was successfully involved). Another strong incentive was, and is, growth of crystals either built of biological macromolecules or through biomineralization. These are extreme examples of crystallization in systems that are very complex chemically. Hydrothermal crystallization of zeolites and similar purely inorganic systems already exhibit significant complexity. The much larger diameter of biomacromolecules (from several to hundreds of nm) as compared both to conventional ions and to the range of molecular forces, adds additional degree of freedom to the system. Even a moderate change in conventional ionic solution composition, pH and temperature noticeably alters the surface of a biomacromolecule controlling crystallization of these species. Consequently, such a change means, in fact, that other species are to be crystallized. The several polymorphic modifications into which the majority of protein molecules crystallize under different conditions represents a convincing illustration. Thus biomacromolecular crystallization still depends on screening and serendipity. Bringing scientific rationale to this big and hot area is a challenge.

The reader may easily identify the papers dealing with each of the problems listed above so that the only thing that remains to be mentioned is that the authors of the papers are excellent experts in the field. I hope that the editors, X.Y. Liu and J.J. De Yoreo, active and highly recognized contributors to the effort aimed at merging physics, chemistry and biology on a rationale basis, will earn a big credit from our scientific community for having compiled this book.

A.A. Chernov
June 2003, Huntsville, AL

Preface

The initiative and motivation for this book arose from the constructive discussion of one of the editors with Dr. David Lockwood, who visited Singapore in 2001. One of the key questions raised, which ultimately led to this book, was how the structure of the solid–fluid interface could exert a direct impact on the formation of nano structures/phases. Of course, as more sparkling ideas were adopted from our fellow colleagues, who constructively contributed to the various chapters, the scope has been spun off far beyond this point. Nevertheless, this remains as the theme of this book.

All of us have read about the vast potential inherent in nanotechnology and the exciting impact it has in changing our lifestyle in the 21st century. One of the basic issues confronting us is how to fabricate devices or materials on the nano scale. What is the basic physics governing the formation of nano phases? How can biological systems inspire us to formulate nano scale architectures, in the way nature has always done and continues to do? These are two main areas of focus in this book.

The aim of this book is to take you to the root of these issues: the solid–fluid interfacial structures and the basic interactions between nano particles determine the kinetics of nano particles and formation of structures, and consequently the resulting structures and functionalities of the nano particle systems and devices. By taking a fresh look at the novel assembly and surface probing techologies from the global viewpoint of fundamental principles, the two volumes of this book allow us to zoom our focus from the macroscopic phase to the nano structures within a broad spectrum of phenomena. Featuring contributions from a number of international experts in the related fields, this book offers a comprehensive and synergistic look into these challenging issues in tackling topics like theoretical modeling, computer simulations, advanced surface probing and fabrication and interface characterizations. The book also provides a link to the nanostructure engineering of some novel materials playing an important role in advancing technologies in this field.

Volume I focuses on both the theoretical and experimental aspects of crystal surfaces and solid–fluid interfacial structures, the effect of ordering and disordering of the interfacial molecules on the kinetics of crystalline matter, and in particular on the nano crystalline phase and the formation of self-organised nanofiber networks. Expertly written chapters expand the existing knowledge on surface/interfacial structures associated with bulk phases to the micro/nano structural domain, presenting examples of the characterization and manipulation of self-organized nano structures. The subject matter covers the principles and technologies concerning surface/interface structure formation and characterisation, nanophase fabrication and biomineralisation.

Volume II is devoted to the assembly of bio-related nano structures and hybrid nano materials and systems. The part on bio-related nanostructures focuses on the aggregation and pattern formation of protein molecules, or biomaterials in the bulk and on the surface of

designated substrates. The way to control the process of biomineralization, biological matrices, hierachical structures and other bio-related materials by relying on robust methods, such as templating, will also be treated in detail. Finally, innovative techniques to engineer complex nano structures and similar systems such as molecular design and molecular self assembly are highlighted.

The book covers a broad range of subjects relevant to nano/life sciences and technologies. Due to its fundamental nature, this book functions as a valuable resource for scientists and engineers working in the related areas, as well as an important reference manual for both scientists and graduate students in nano/life sciences, majoring in the design of nano systems and related technologies.

X.Y. Liu
on behalf of the Editors
November 2003, Singapore

List of contributors

Julio A. Camarero, Lawrence Livermore National Laboratory, USA

C.L. Cheung, Lawrence Livermore National Laboratory, USA

Kevin J. Davis, Rice University, USA

James De Yoreo, Lawrence Livermore National Laboratory, USA

Patricia M. Dove, Virginia Polytechnic Institute, USA

Oleg Galkin, University of Houston, USA

Jeffry D. Madura, Duquesne University, USA

Alexander J. Malkin, Lawrence Livermore National Laboratory, USA

Alexander McPherson, University of California, Irvine, USA

Kiyotaka Sato, Graduate School of Biosphere Science, Japan

Peter G. Vekilov, University of Houston, USA

B.L. Weeks, Lawrence Livermore National Laboratory, USA

Andrzej Wierzbicki, University of South Alabama, USA

This page intentionally left blank

1

Modeling of molecular adsorption at crystal surfaces and interfaces

Andrzej Wierzbicki*
Department of Chemistry, University of South Alabama, Mobile, AL 36688, USA

Jeffry D. Madura
Department of Chemistry and Biochemistry, Duquesne University, Pittsburgh, PA 15282, USA

1.1. INTRODUCTION

Molecular modeling has played an important role in developing an understanding of fundamental processes of adsorption on crystal surfaces. Essential contributions from molecular modeling came from the elucidation of molecular aspects of adsorption at crystal surfaces. Thanks to numerous modeling efforts, some of which will be discussed in this chapter, we know that the molecular adsorption at crystal surfaces can be categorized into two major classes.

The first class includes adsorption that is essentially dominated by strong electrostatic interaction. This class predominantly includes, although not exclusively, interactions between mineral crystals and charged adsorbates. Electrostatic and van der Waals forces dominate in the adsorption process and the inclusion of explicit liquid interface at the crystal surfaces generally does not change the adsorbate binding scenario. The binding energy is usually scaled due to the presence of dielectric medium, and almost always the application of explicit solvent is not necessary and may be replaced by a continuum dielectric approach. This class of interactions will be in discussed in details in the following sections. From the studies involving various types of charged inhibitors binding to a broad class of mineral crystals the following conclusion can be drawn: well designed inhibitors of mineral crystals tend to complement the coordination of surface ions disrupted at the cleavage plane. For efficient inhibitors it is strongly desirable that they share many characteristics with the ions of the crystalline phase and yet be dissimilar enough so they can disrupt the addition of mineral material in the direction perpendicular to the adsorption plane. This

---

*Correspondence author. E-mail address: awierzbi@jaguar1.usouthal.edu

point is extensively illustrated in the following sections of this chapter dealing with the adsorption of ionic inhibitors to mineral crystals of biological importance.

The second class of molecular adsorption phenomena at crystal interfaces clearly requires the presence of interface between the liquid and crystalline phase. In general the nature of this interface is still poorly understood, but it is very clear that the liquid medium must be treated explicitly since the binding process includes a subtle energetic competition between the solvation effects of the inhibitor in the liquid medium and the binding to crystalline phase in the interfacial region. Broadly one may think of these binding phenomena as having a substantial entropic component of their total free energy. We will discuss the importance of the liquid interface for the adsorption phenomena at the end of this chapter, especially for the description of adsorption of antifreeze proteins at the water/ice interface.

This area of modeling frequently involves expensive long-time molecular dynamics simulations and often requires calculations of the free energy instead of binding energy only. It promises to give an important insight into the nature of adsorption at interfaces, often involving neutral adsorbates binding to molecular crystals in the presence of intervening liquid interface. The last section of this chapter will provide several important examples of molecular adsorption at liquid/crystal interfaces.

1.2. MODELING OF BINDING OF POLYASPARTATE TO CRYSTALS OF CALCITE

1.2.1. Introduction

Modification of crystal growth has been the subject of numerous studies. There were essentially two primary motivations for these investigations. First, the enormous diversity of biomineralization in nature, expressed in countless examples of modification of inorganic crystals to serve specific purposes in living organisms, poses a serious scientific challenge to explain and possibly mimic the outcomes of biomineralization processes perfected by billions years of evolution [1]. Second, there is certainly a strong desire to learn how to stop many types of unwanted mineralization that result in tremendous financial losses to the world's economy.

Calcium containing biominereals are constituting close to 50% of all known biogenic material [1]. Calcium carbonate in the form of calcite and aragonite (a thermodynamically less stable form of calcium carbonate), play an essential role as skeleton reinforcing minerals in many living organisms. Insightful studies of formation of elaborate mineral structures by organisms have attempted to define the stereochemical interactions of biomolecules with specific crystal surfaces [2–6]. The interactions have been deduced from X-ray diffraction patterns and morphology of crystals and the probable conformation of binding groups of adsorbates. The interplay of polyanionic proteins and other biological adsorbates with lattice surfaces often produces materials of remarkable structure [1]. One example is the calcite of the sea urchin skeleton, which does not have well-developed cleavage planes normally characteristic of calcite, and thus it is more resistant to fracture. It has been proposed that this is due to to the presence of acidic glycoproteins occluded along crystal planes that are oblique to the cleavage planes [1]. Calcite crystals grown in the presence of acidic glycoproteins and studied by X-ray diffraction with synchrotron radiation exhibit stabilized (100) faces [7–9], indicating preferential adsorption of the protein on

those faces. The macromolecules are believed to form the boundaries of mosaic blocks and to interfere with the propagation of a smooth fracture by stabilizing discontinuities at the submicron level [1]. The (100) planes have carbonate ions that are perpendicular to those faces. The protruding carbonate oxygens could maximize binding to calcium-preloaded polyanionic molecules [2]. However, calcium preloading may not be necessary [3,10,11]. One hypothesis [6] is that the binding of acidic macromolecules to calcite surfaces could occur by fitting of carboxylate groups into lattice positions normally occupied by carbonate ions of the (100) plane with the adsorbate roughly parallel to the *c*-axis.

In the study published in [12], the binding to calcite of the polyanionic protein from oyster shell and polyaspartate macromolecules consisting of up to 20 aspartate residues was studied by atomic force microscopy and molecular modeling. The oyster shell protein is representative of a class of acidic proteins from biominerals. It is composed of roughly 90 mole % of about equal amounts of aspartate (Asp), glycine, and phosphoserine/serine (PSer/Ser), with up to 80% of serine residues phosphorylated [13–15]. It has domains of Asp_n and $PSer/Ser_n$ and is a powerful regulator of crystallization [11]. Continuous runs of Asp residues occur in numerous other proteins as well [16]. Polyaspartate has been evaluated as an analog of biomineral protein [17,18] has been tested for for use in a variety of technologies related to regulation of mineral formation [19,20]. The size of polyaspartate molecules observed and modeled in the study [12] fall within the range of the most effective molecular weights for regulation of calcite formation [11,21].

1.2.2. Methods

The work [12] was to our knowledge one of the first published attempts to use Atomic Force Microscopy (AFM) combined with molecular modeling to explain in vitro interaction of acidic proteins extracted from the organic phase of biominerals with calcite crystals. In that study the initial conformation of Asp_{15} chosen was β-sheet based on prior studies [22] and was constructed using QUANTA [23] molecular modeling software, yielding a molecule approximately 50 Å long and 7.2 Å wide. The calcite crystal model was prepared using the materials science modeling software CERIUS [24] with unit cell parameters and fractional coordinates from Lippmann [25]. The calcite model surfaces were cleaved from the bulk crystal. QUANTA was used to position the polyaspartate near the cleaved surface within the electrostatic range of interaction, and CHARMm [26] energy optimization was applied. The minimization procedure took into account the contributions of electrostatic forces, van der Waals forces, bonds, angles, and dihedral angles to the total energy of the system. Starting from the initial position of the polyaspartate–calcite surface system, the total energy was minimized yielding the energy and geometry of the most favorable position of polyaspartate on the crystal surface. The coordinates of lattice atoms were kept fixed and the polyaspartate was allowed to translate, rotate, and adopt any conformation on the surface of calcite. The binding energy was determined as the difference between the energy of the polyaspartate–calcite system and the sum of the calcite and polyaspartate energies when separated beyond the interaction distance. Table 1.1 contains the binding energies obtained in the study [12].

TABLE 1.1.
Characterization of calcite surfaces used for analysis of interactions
with Asp$_{15}$. Binding energies in kcal/mol.

Polyamino acid		Calcite surface binding energy	Binding energy per residue
Asp$_{15}$	(100)‖c	−1565	−104
Asp$_{15}$	100)‖c*	−4303	−287
Asp$_{15}$	(100)⊥c	−1749	−117
Asp$_{15}$	(110)	−452	−30
Asp$_{15}$	(104)	−248	−17
Asp$_{15}$	(001)	−4893	−326
Asp$_5$	(100)‖c	−794	−159
Asp$_5$	(100)⊥c	−773	−155

*Incomplete calcite surface (with carbonate ions removed).

1.2.3. Interaction of polyaspartate with (100) faces of calcite

In the study [12] it has been determined that there were two energetically most favorable directions predicted for polyaspartate along the (100) calcite face: parallel and perpendicular to the c-axis. We will discuss these two cases below.

Binding of polyaspartate in the orientation parallel to the c-axis was predicted to occur very strongly with an energy of −1565 kcal/mol, yielding approximately −104 kcal/mol per residue. As seen in Figure 1.1, the strength of this binding is due to coordination of carboxylate groups of polyaspartate with calcium atoms parallel to [001] direction. In this modeling study, the carboxylate groups oriented themselves to complete the coordination polyhedra of surface calcium ions. Some of the carboxylate groups of Asp$_{15}$ were forced away from the calcite surface due to the translational mismatch between the surface and the chain as a result of protruding carbonate ions of the surface.

On the other hand binding of polyaspartate in the orientation perpendicular to the c-axis was stronger, yielding a binding energy of −1749 kcal/mol, or − 117 kcal/mol per residue. The binding mechanism again involved coordination of carboxylate groups with rows of calcium atoms along [001]. The overall fit of the polyaspartate molecule to the surface in the perpendicular direction (Figure 1.2) was better than in the parallel one. There was no significant chain strain in the perpendicular orientation due to translational mismatch between the surface lattice ions and the adsorbate. It may be important to note, however, that the binding of individual carboxylate groups in the parallel rather than the perpendicular position is calculated to be stronger because the separation of adjacent rows of positive ions better matches the separation between carboxyl groups of polyaspartate in β-sheet conformation. But, due to the translational mismatch along the c-axis, approximately every fifth carboxylate was driven away from the surface, with a resulting decrease of the total binding energy. On the other hand, in perpendicular binding, the carboxylate groups along one side of the β-sheet can easily bind to one row of calcium ions along [001]. The carboxylate groups on the other side would have weaker binding due to less favorable spacing to another surface row of calcium, 8.5 Å distant from the first. Overall, the perpendicular binding of Asp$_{15}$ on preexisting, complete (100) surfaces was more advantageous energetically. Binding of a smaller molecule not subject to chain strain could differ from this. Indeed, in the
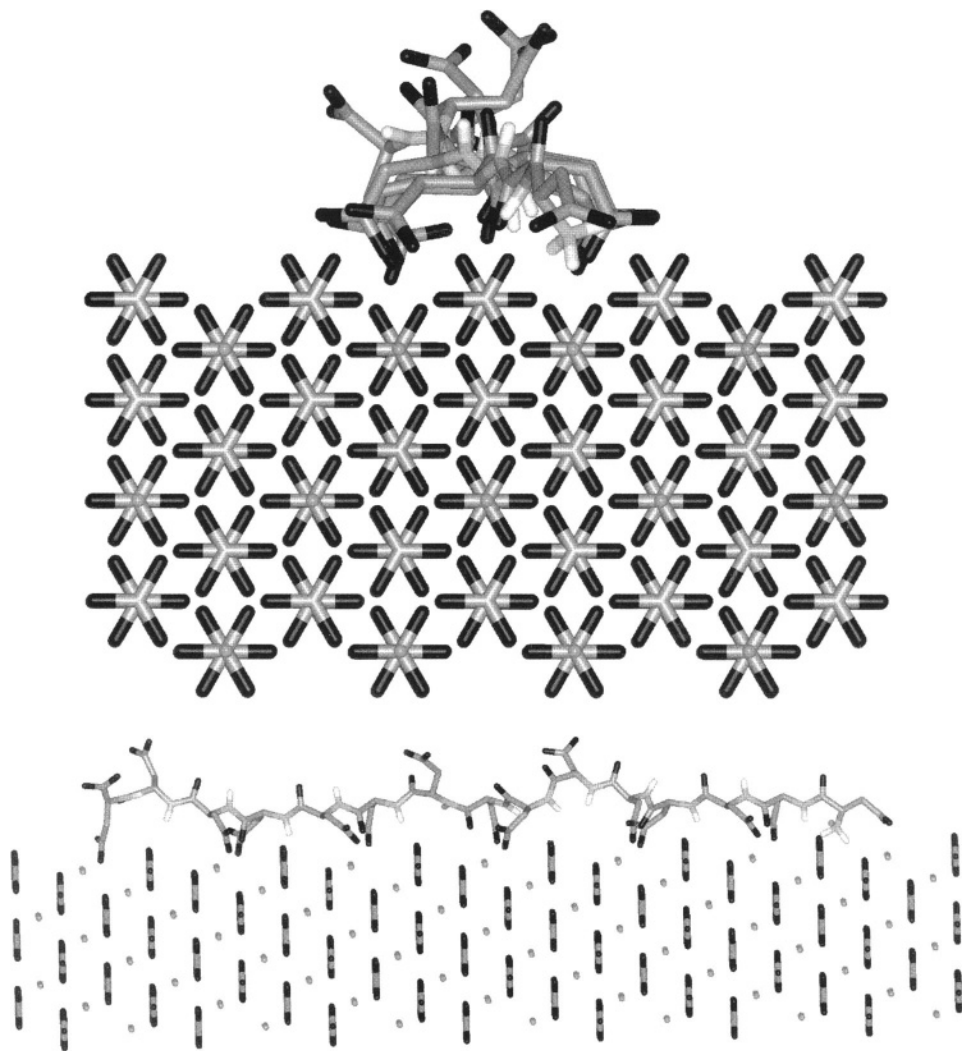
FIGURE 1.1. Asp_{15} adsorbed to the (100) face of calcite in the orientation parallel to the c-axis. Top figure shows the view in the direction perpendicular to the c-axis and bottom figure shows the view rotated 90 degrees with respect to the top view.

case of Asp_5, the parallel binding energy was -794 kcal/mol versus -773 kcal/mol for perpendicular binding.

1.2.4. Substitution of Asp_n carboxylate groups into carbonate lattice positions

When the carbonate ions of the lattice that contribute to chain strain in the parallel position were replaced by carboxylate groups of Asp_{15}, the calculated binding energy in this position was greatly increased to -4303 kcal/mol. Substitution of carboxylate for carbonate groups in the perpendicular orientation did not have such a strong effect on binding. In
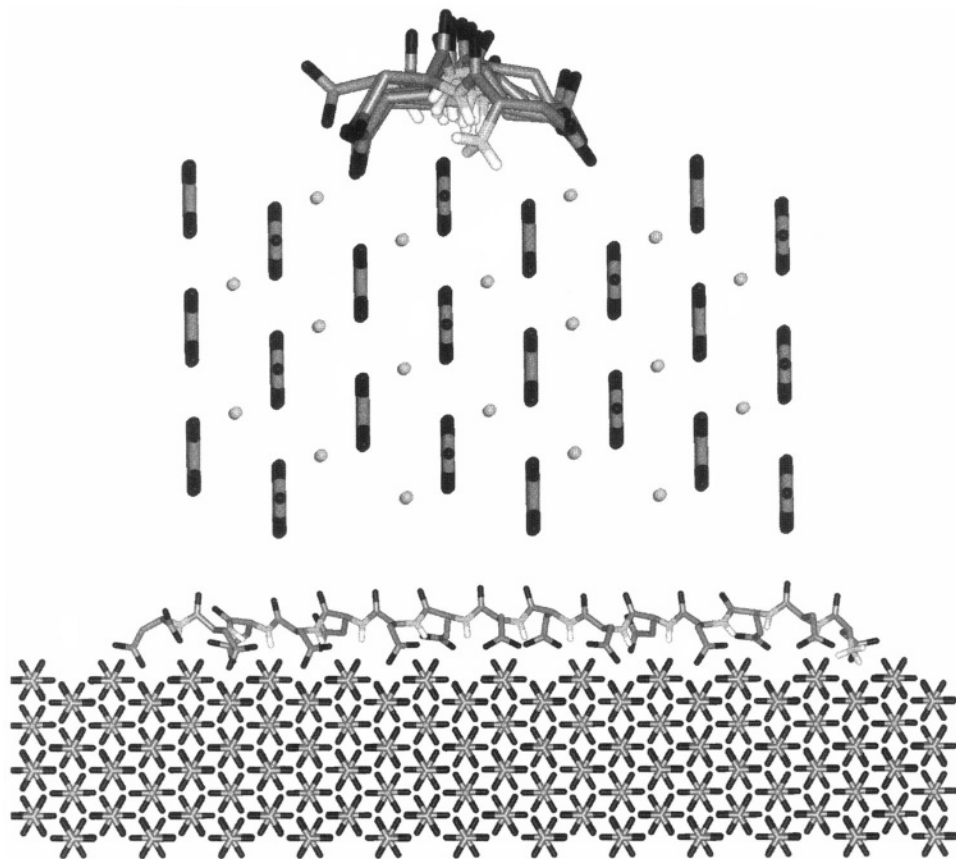
FIGURE 1.2. Asp$_{15}$ adsorbed to the (100) face of calcite in the orientation perpendicular to the *c*-axis. Top figure shows the view in the direction perpendicular to the *c*-axis and bottom figure shows the view rotated 90 degrees with respect to the top view.

the case of a growing crystal rather than a preexisting stable crystal, the surfaces might be expected to be transitional between solid and solution. Therefore, substitution of binding groups of adsorbates for lattice ions is quite plausible and in fact has been postulated for binding of single aspartate and related molecules to (100) surfaces of calcite, including orientations essentially parallel to the *c*-axis [6].

1.2.5. Interaction of polyaspartate with (110), (104) and (001) faces of calcite

The (100) and (110) calcite surfaces have different orientations of carbonate ions, with every other row of carbonate ions of the (110) surface having two rather than one oxygen atom protruding. Also, the distribution of centers of positive and negative charges is more crowded and less favorable on the (110) surface; this distribution would not permit strong, directional binding. Overall, the effect of these differences as revealed by computer simulations was to reduce the fit of Asp$_{15}$ on (110) surfaces such that the calculated binding energy was lowered to −452 kcal/mol. Figure 1.3 shows the binding of Asp$_{15}$ to (110)
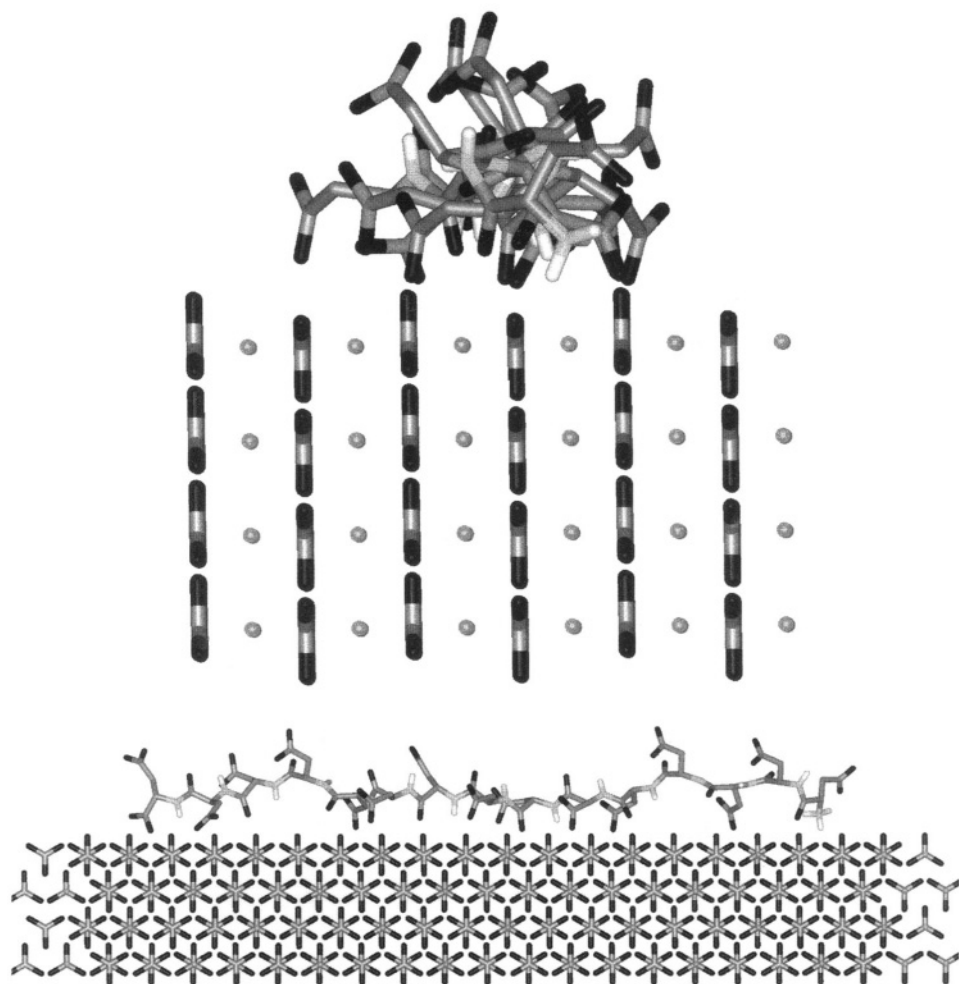
FIGURE 1.3. Asp$_{15}$ adsorbed to the (110) face of calcite in the orientation perpendicular to the c-axis. Top figure shows the view in the direction perpendicular to the c-axis and bottom figure shows the view rotated 90 degrees with respect to the top view.

faces of calcite. The binding direction was nonspecific. This was also true of binding to (104) cleavage faces that commonly are expressed during unmodified growth of calcite. This binding was nonspecific and much weaker at –248 kcal/mol; such binding is likely to be reversible (Figure 1.4). In fact, repeated attempts failed to visualize polyaspartate molecules by AFM on (104) surfaces, even though binding studies with radiolabeled peptides suggest that they were there [18,27]. In these experiments, images were made at doses sufficient to stop crystallization. Adsorbates were added both after and during crystallization. It is probable that such loosely bound adsorbates were not seen because they were dislodged by the force of the AFM tip. Lower binding energies and selectivities would be reflected in lower affinities of adsorbates for crystals and probably greater morphological variability
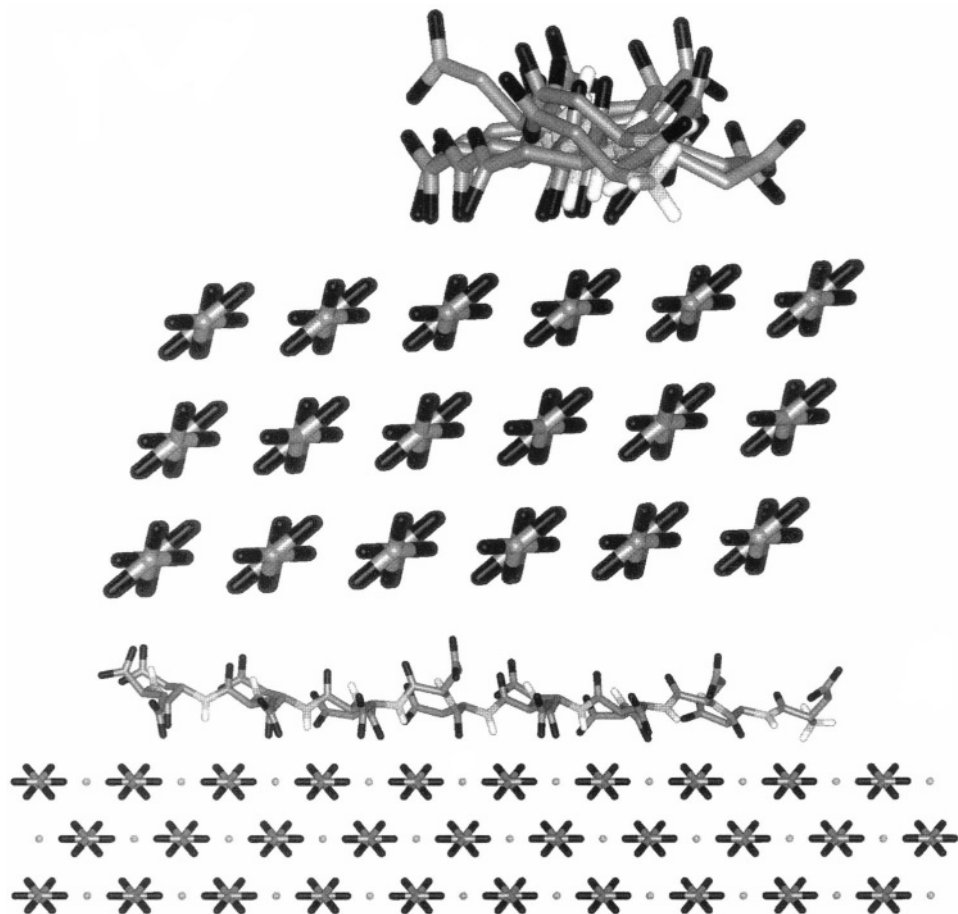
FIGURE 1.4. Asp$_{15}$ adsorbed to the (104) face of calcite. Top figure shows the view along the polypeptide backbone and bottom figure shows the view rotated 90 degrees with respect to the top view.

of crystal habits. Depending on concentrations of adsorbates at the site of crystallization, such interactions also could be quite important in determining, the shape and properties of resultant biominerals.

The binding to (001) basal planes was modeled assuming that the calcium rich plane was exposed to the crystal–liquid interface. The nucleation on a surface of crystals on the basal (001) plane with vertical growth along the *c*-axis has been observed previously for calcite [2,3] and in fact is a common occurrence in biomineralization [1,28]. Exposed basal planes of the biommerals calcite [29] and aragonite [30l as well as other minerals [31] have also been observed by AFM at the atomic level. In general, polyanions such as polyaspartate are potent inhibitors of calcite formation but polycations like polylysine, which might bind to an exposed carbonate plane, are not [11,18]. Therefore, it may be that there were no exposed carbonate planes under the conditions studied.

1.2.6. Binding of proteins to calcite

In [12] we proposed that matrix proteins most likely position themselves along preferred vectors on the calcite surface, presumably with the Asp_n and other anionic domains participating in the binding. As seen in Figure 4 of ref. [12], oyster shell protein lined up consistently in a single orientation on calcite on a set of terraces in troughs along the edges of crystal rhombohedrons. Crystals grown in the presence of polyaspartate also exhibited this morphology. Based on the computer model of calcite morphology the binding sites were tentatively identified as on (100) terraces parallel to the c-axis. Because the crystals were in the process of growing during the binding event, the surfaces were postulated to have been incomplete at that time so that the parallel orientation was favored due to substitution of carboxylate groups of the proteins for carbonate ions of the lattice. As the protein in the medium became depleted during calcite crystallization, some of the crystals would revert to the normal rhombohedral morphology of calcite.

The precise and consistent binding pattern by the oyster shell protein on the hypothesized (100) surfaces of completely separate terraces showed that the orientation was highly selective even for the initial adsorbate molecule because the initial binding event on each terrace must have been the same and without influence by binding events on other terraces.

1.2.7. Summary

In [12] we investigated the binding of polyasparatate to morphologically significant planes of calcite in order to provide a model for binding of oyster shell proteins to calcite that we studied in vitro using AFM and SEM. Computer model of binding of ASP_{15} to prism faces of calcite provided a satisfactory explanation of morphological changes induced by binding of oyster shell protein to growing crystals of calcite. In this work the binding energies and conformations of polyaspartate bound to prismatic (100) and (110) faces, (001) basal planes and (104) cleavage planes were analyzed. Molecular modeling provided a valuable insight into the possible mechanism of morphology control utilized in biomineralization processes.

1.3. MODELING OF BINDING OF CITRATE AND PHOSPHOCITRATE TO CRYSTALS OF CALCIUM OXALATE MONOHYDRATE

1.3.1. Introduction

In the study [32] binding of citrate and phosphocitrate to calcium oxalate monohydrate crystals have been examined using Scanning Electron Microscopy and molecular modeling. In this work for the first time the sodium-phosphocitrate crystal structure has been resolved using low temperature X-ray analysis and *ab initio* computational methods. The identity of crystal surfaces of calcium oxalate monohydrate, (–101), involved in binding of citrate and phosphocitrate were identified by Scanning Electron Microscopy and confirmed by molecular modeling. Citrate and phosphocitrate conformations and binding energies to these faces have been obtained and compared to binding to another set of calcium rich planes (010). Difference in inhibitory properties of these compounds has been attributed to better coordination of functional groups of phosphocitrate with calcium ions distribution in (–101).

Citrate and phosphocitrate (PC) are both recognized to be strong inhibitors of the nucleation, growth and aggregation of calcium oxalate monohydrate (COM) crystals [33,34]. COM is widespread throughout the animal kingdom where it serves a number of functions. For example, in plants it is a useful metabolite and structural component [35,36] whilst in marine organisms, it is found in the main sediment-forming organisms of the oceans, echinoderms and mollusks [37]. In man, unfortunately, the formation of this calcium salt is undesirable as it leads to the development of obstructive calculi in the kidney and urinary tract. Strategies are needed therefore to eliminate such a risk. Information on inhibitor–crystal surface interactions is important toward the development of potent stereospecific compounds to control, and if possible, to eliminate the crystallization and aggregation of this calcium salt. To achieve such a goal we applied computer based molecular modeling techniques, together with electron microscopy of the habits of crystals grown in the presence of these inhibitors, first to elucidate the stereospecificity of action of known inhibitors and second to design even more efficient inhibitors. Scanning electron microscopy (SEM) provided information on crystal morphology changes induced by interactions with atoms and molecules that do not constitute the building elements of a crystal. Expression of designated faces of the crystals indicated possible interactions between the inhibitor and the atomic pattern of a particular crystal surface. Such interactions are very often based upon the stereospecificity of inhibitor–surface recognition. Molecular modeling can provide valuable insight into energetic and spatial feasibility of such recognition. Studies on interactions between acidic matrix macromolecules and calcite [8] and calcium phosphate ester crystals [38], interactions between dicarboxylates and calcite [6], confirm that this mechanism of crystal inhibition based on stereospecificity of interaction is more general and extends to broader classes of crystal forms. Similar conclusions have been reached with respect to barium sulfate inhibition by phosphonates [39].

The same principles were applied to the binding of the citrate and PC molecules to the (–101) planes of COM that contain loci of calcium ions perfectly suited for inhibitor binding which in turn leads to stabilization of these faces and the slowing of the growth in the direction perpendicular to them [40]. Citrate based inhibitors bound to the (–101) planes encounted oxalate groups perpendicular to (–101) that created an excellent binding environment for carboxylate groups of the inhibitor which would complete the coordination polyhedra of calcium cations. This binding scheme is much akin to the calcium carbonate crystal inhibition described above. Of interest, plane (–101) of COM also has been identified as the potential binding plane for nephrocalcin, an acidic macromolecule contained in mammalian urine [41].

In the study presented in [32] the molecular modeling of binding and scanning electron microscopy investigations of crystals grown in the presence of the two compounds were used to explain the inhibitory properties of these molecules and also to account for the observed differences in their inhibitory activity.

1.3.2. Methods

The computational procedure developed earlier for calcium carbonate inhibition by polyaspartate [12] and ice inhibition by antifreeze proteins [42] was used to investigate the stereospecificity of the calcium oxalate inhibitors. Calcium oxalate crystal data were available from the literature [40,43] and for the purpose of modeling, the structure proposed by Deganello [40], and used by him to investigate the interaction between COM and

nephrocalcin [41], was applied. According to this author, COM crystallizes in the monoclinic space group $P2_1/n$ with $a = 9.9763$ Å, $b = 14.5884$ Å, $c = 6.2913$ Å, $\beta = 107.05°$ and $Z = 8$. CERIUS [24], materials science modeling package, enabled the generation of the COM crystal structure from fractional coordinates listed in [40] along with unit cell and symmetry data. Since hydrogen atom positions for the water molecules were not previously resolved [40], CERIUS was used to build hydrogen atoms onto the water oxygen and the hydrogen positions in the lattice were obtained by applying short term dynamics followed by minimization procedures. Consideration of the COM crystal structure showed that COM crystals contain two sets of crystallographically nonequivalent oxalate groups which results in two distinct types of essentially planar packing. One is within (−101) crystal planes and the other interlocks the (−101) along the c axis, being almost perpendicular to it. The structure is additionally stabilized by a network of hydrogen bonding involving water molecules. Plane (−101) is characterized by a high density of calcium ions. Another calcium rich plane is the (010) plane of COM, containing approximately 18.3% less calcium cations per unit area than (−101). Prior to investigation of inhibitor surface interaction, parameters describing the geometry and electrostatic charge distribution, for both citrate, PC and the oxalate anion, was developed as described below.

The geometric structure of citrate was obtained using a series of geometry optimizations for a neutral citrate molecule applying both *ab initio* and semiempirical methods. The citrate structure, but not the PC molecule structure, has been characterized previously by X-ray analysis [44]. Geometry optimization of citrate revealed a structure consistent with the X-ray geometry with a planar backbone and central carboxyl and hydroxyl group lying in the plane perpendicular to the backbone. The hydrogen of the hydroxyl group is within the hydrogen bond distance to oxygen of the central carboxyl. Citrate when present in urine is subject to a pH range between 6–8 which would result in deprotonation of all the carboxyl groups. Therefore, to determine the electrostatic charge distribution for the citrate three valent anion, a single point calculation was run to fit charges from electrostatic potentials [45,46]. This method of charge determination has been proven to determine reliable atomic charges. Both geometry optimization and charge determination were performed using Spartan [47], an electronic structure computational program. Geometric and electrostatic parameters determined in this manner were incorporated into a CHARMm [26] parameters file and used at later stages of modeling for optimizing citrate–COM surface interactions.

Geometry optimizations for PC were derived from semiempirical, MNDO [47], and *ab initio* Hartree–Fock [48], using 6-31G** basis set, and indicated a planar backbone and co-planarity of central carboxyl group with PO_4 group symmetry plane. Since in the pH range 6–8 groups from one of the P–OH, a central $COOH\,(\beta)$, one outer $COOH\,(\alpha)$ and as the more alkaline value is obtained, the second P–OH are deprotonated, single point calculations were run to determine the electrostatic charges from the electrostatic potential for a four valent anion of PC. We call this deprotonation sequence (α, β). Geometrical parameters for the oxalate anion were developed in a similar way using *ab initio* Hartree–Fock calculations with 6-31G** basis set and the charges were determined from electrostatic potentials as above. To confirm the geometry of PC, as obtained by computational methods, we performed low temperature X-ray analysis for the crystals of monosodium phosphocitrate dihydrate.

Using QUANTA [23] molecular modeling software the inhibitor molecule in the initial conformation was positioned near the COM surface within the electrostatic interaction

range and the CHARMm [26] energy optimization procedure was applied. Computation-ally determined geometrical and electrostatic parameters for the COM surface and for the inhibitors were incorporated into CHARMm parameters file. The minimization procedure takes into account the contributions from electrostatic forces, van der Waals forces, hy-drogen bonds, bonds, angles and dihedral angles to the total energy of the system. Start-ing from the initial position of citrate/PC-surface system, the total energy was minimized yielding the energy and geometry of the most favorable position of citrate/PC on the crys-tal surface. During minimization, the coordinates of crystal lattice atoms were kept fixed and the inhibitor molecule was allowed to translate, rotate and adopt any conformation on the COM surface. The binding energy was determined as the difference between the en-ergy of the citrate/PC-COM system and the sum of the citrate/PC and COM energies when separated beyond the interaction distance. Two possible scenarios for interaction between the citrate/PC and the COM surface were considered, namely that the inhibitor molecule interacts with the complete surface of COM or that the inhibitor interacts with the COM surface in which one oxalate group is removed. This approach allows anionic groups of the inhibitor molecule to substitute for oxalate anions lattice position at the surface. The effect of solvent was analyzed by introducing an 8 Å hydration shell around the inhibitor molecule and repeating the minimization procedure. The final configuration of the system was the same since the electrostatic interactions between the COM surface and the inhibitor was the driving force determining the final geometry of the system. The water molecules were accommodated around the inhibitor slightly modifying the attraction of the molecule to the surface but having no effect on mechanism of binding to the surface. For this rea-son further consideration was given to the inhibitor surface system only, using a constant dielectric model with dielectric constant equal to one.

When the crystals were grown subject to interaction with citrate and PC, plane (–101) was clearly stabilized at the expense of the other faces indicating preference for interaction with the atomic motif of this surface for both inhibitors. When citrate was added, in the initial amount of 1.3 mg/ml the faces (–101) of COM were enlarged and the length to width ratio is significantly decreased. There was only slight rounding of the crystal angles suggesting stereospecific interaction with (–101) planes. The effect of PC was even more dramatic. At low concentration 0.05 mg/ml apical planes were not present at all and (–101) faces were well stabilized. Effect of PC at this initial concentration was very similar to the effect observed for nephrocalcin [41]. In some instances, planes (–101) were stabilized but additionally, the curvature of the edges of these faces was enhanced. Slightly curved boat-shape crystals indicated that additional to the specific interactions with (–101) faces, there were other, perhaps nonspecific, interactions between the PC and the crystal. In comparison with citrate this could be attributed, among the other factors discussed below, to higher ionic charge of PC to that of citrate under the conditions studied. This effect was intensified with the increased dosage of 0.25 mg/ml of PC. Resulting in irregularly overgrown COM crystals indicating much less specific inhibition. We have observed that about 20 times smaller dosages of PC than citrate was required to cause similar morphological changes. SEM images also revealed that PC causes significant diminishing of COM crystal size.

1.3.3. Binding of citrate to the complete (–101) surface of COM

Molecular modeling of citrate binding to complete (–101) surface of COM, based on energy minimization, revealed that the citrate molecule orients itself on the surface in the

FIGURE 1.5. Citrate ion interacting with complete (–101) surface of calcium oxalate monohydrate. Citrate ion is coordinated with four calcium ions and is slightly shifted due to citrate hydroxyl group interacting with an oxalate ion.

position that affords all of its carboxylate groups to interact with the calcium ions of the surface. This orientation allowed the carboxylate groups to partially complete calcium co-ordination polyhedra, disrupted due to crystal discontinuity at the surface. Figure 1.5 shows the optimized geometry of interaction between citrate and the surface. The citrate molecule fits well to a trapezoidal arrangement of calcium ions between oxalate groups. Carboxy-late groups of citrate were somewhat rotated when compared to an isolated molecule but overall, no major distortion of the molecule shape was observed. The stereospecificity of the interaction in this case was achieved due to excellent matching of the separation of car-boxylate groups of citrate to the calcium ion distribution at the surface. The molecule was slightly shifted with respect to the calcium ion trapezoid due to the fact that hydrogen from the hydroxyl group interacted with one of oxalate oxygens. Citrate carboxylate groups ap-proached the surface at the angle which would be the closest possible to perpendicular to the surface, just like incoming oxalate ions would if the crystal lattice was to be continued.

1.3.4. Binding of phosphocitrate to the complete (–101) surface of COM

Binding of PC to the complete (–101) surface of COM followed a different pattern as seen in Figure 1.6. Since PC molecule is bigger than citrate it coordinated with six instead of four calcium ions. Binding energy, –717 kcal/mol, was significantly greater than the binding energy of citrate, –546 kcal/mol. In this case the binding-site recognition occurs due to matching of the shape of PC with calcium ions in an hexagonal arrangement at the surface.
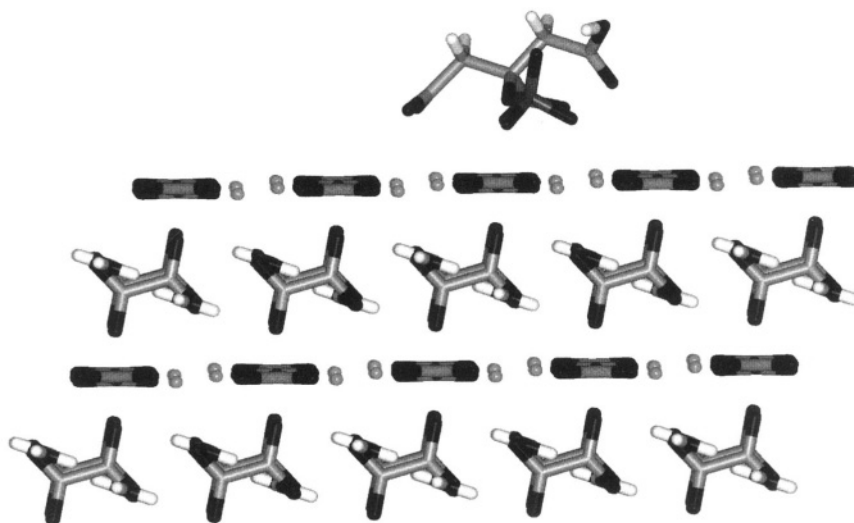
FIGURE 1.6. Phosphocitrate ion interacting with complete (−101) surface of calcium oxalate monohydrate. The phosphocitrate ion is coordinated with six calcium ions. The phosphate group is slightly bent to minimize interaction with the negative charge on an oxalate ion.

1.3.5. Binding of citrate to the incomplete (−101) surface of COM

During COM crystal growth inhibitor molecules may not only interact with complete (−101) surfaces but also they are likely to substitute for oxalate groups into the growing crystal lattice. To investigate the stereospecificity of citrate and PC substitution into the (−101) surface one oxalate group was removed from the surface and the energy minimization procedure was repeated for the inhibitor–surface system. The shape and the charge distribution of the inhibitor is even more important here since the inhibitor must be able to fit into the space created by the oxalate ion removal and to coordinate with neighboring calcium ions. Figure 1.7 shows the optimized geometry of interaction between the citrate and the incomplete (−101) surface. The citrate molecule clearly did fit very well into the oxalate ion position with all three carboxylate groups involved in binding to the surface with binding energy increased significantly to −1071 kcal/mol. All six negatively charged carboxylate groups oxygens were in the distance that is less than 2.6 Å from the neighboring calcium ions.

1.3.6. Binding of phosphocitrate to the incomplete (−101) surface of COM

Figure 1.8 shows the optimal binding geometry of PC to (−101) incomplete planes of COM, where the phosphate group was well coordinated with four calcium ions, with all of its oxygens being less than 2.7 Å away from the closest calcium ions. Moreover the β carboxyl group was coordinated with three calcium ions binding and the binding energy was lowered to −1424 kcal/mol. Analysis of PC binding to (−101) surface indicated high stereospecificity of inhibitor substrate recognition and suggested why PC performs as a better inhibitor than citrate.
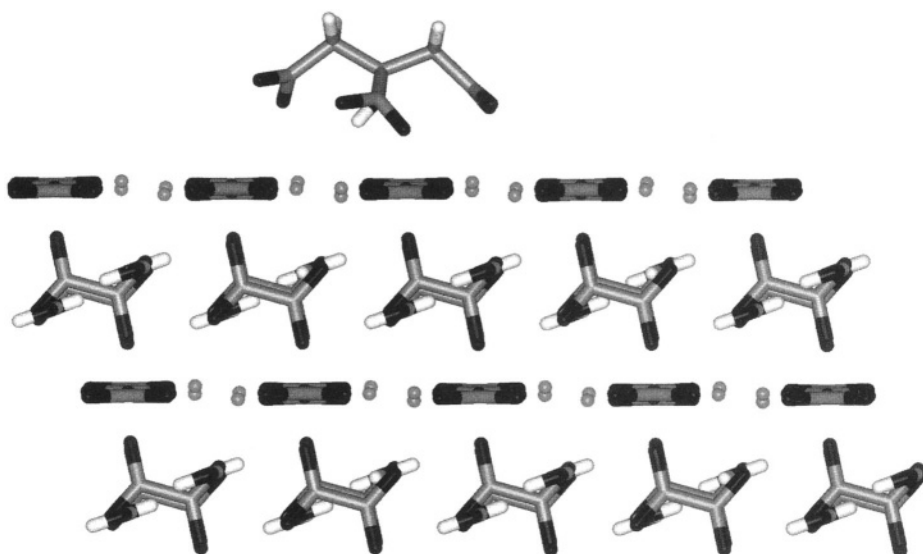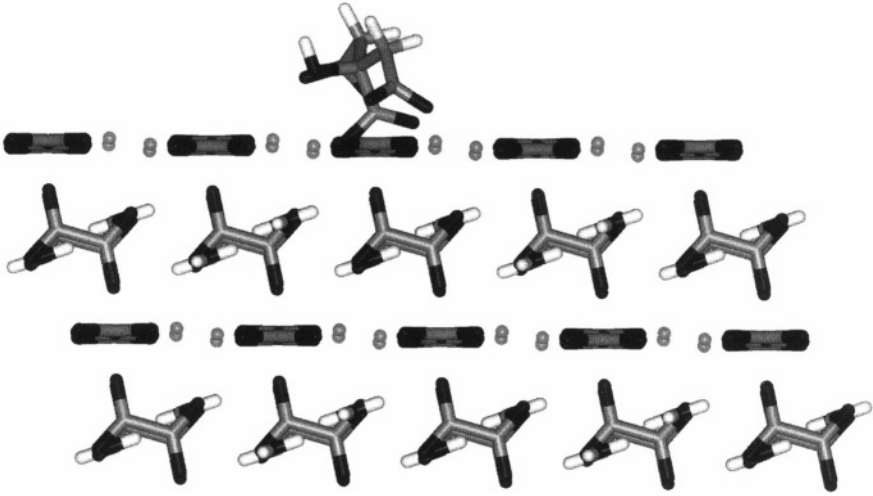
FIGURE 1.7. Citrate ion interacting with incomplete (–101) surface of calcium oxalate monohydrate. The citrate ion is now coordinated with six calcium ions and is somewhat rotated due to slight asymmetry of the crystal electrostatic field, since this structure was obtained using unrestricted energy minimization.
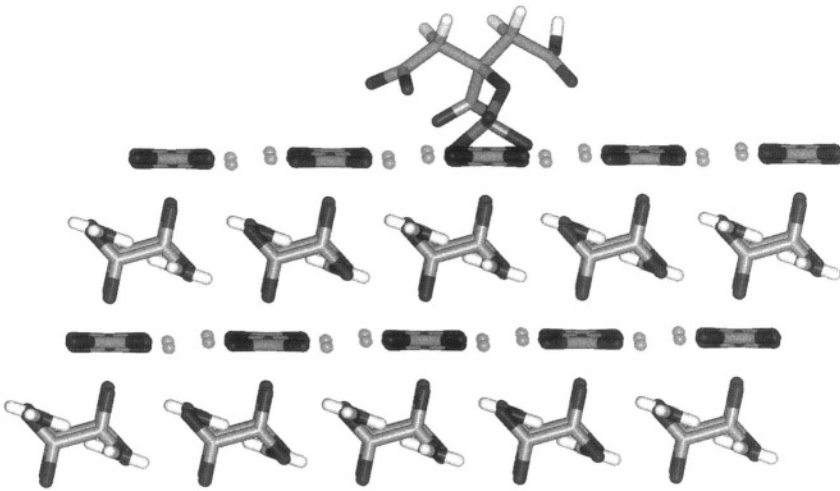
FIGURE 1.8. Phosphocitrate ion interacting with incomplete (–101) surface of calcium oxalate monohydrate. The phosphocitrate ion is more strongly coordinated with six calcium ions than citrate, with three oxygens of the phosphate group driven into the surface.

1.3.7. Binding of citrate and phosphocitrate to the complete and incomplete (010) surfaces of COM

Citrate and PC binding to (010), another calcium rich plane of COM was also compared. Again both complete and incomplete surfaces were considered (Table 1.2). For complete (010) surfaces, interactions of both citrate and PC were not stereospecific and

TABLE 1.2.
Energies of binding of citrate and phosphocitrate to COM. All energies expressed in the units of kcal/mol.

Surface	Complete (−101)	Complete (010)	Incomplete (−101)	Incomplete (010)
Citrate binding energy	−546	−108	−1071	−502
Phosphocitrate binding energy	−717	−142	−1424	−675

the binding energies were much less favorable, −108 and −142 kcal/mol respectively. The geometry of optimal binding revealed no inhibitor–surface recognition which instead was based on the overall attraction between rows of positively charged calcium ions and negatively charged inhibitor molecule that was drawn to the surface. When considering the incomplete (010) surface citrate can almost fit into the space created by oxalate ion removal. However calcium ion distribution did not match the distribution of the functional groups of citrate. Binding of PC to the incomplete (010) surface was also nonspecific and based predominantly on electrostatic interaction between the surface cations and the PO_4 group that was drawn deep into the surface. Binding energies in this case were −675 kcal/mol and −502 kcal/mol for PC and citrate respectively.

1.3.8. Summary

Molecular modeling studies revealed that the negatively charged functional groups of PC better matched of calcium ion distribution of the (−101) surface. SEM images confirmed stereospecificity of this interaction. SEM analysis of morphology changes induced by the inhibitors combined with molecular modeling not only may be used to explain experimentally observed results of inhibition but also to design more potent surface inhibitors based on the stereospecifity of inhibitor surface interaction.

1.4. MODELING OF BINDING OF PHOSPHOCITRATE TO CRYSTALS OF STRUVITE

1.4.1. Introduction

The inhibition by phosphocitrate of struvite crystal formation and growth has been examined in the paper [49]. The effects of inhibition were followed using scanning electron microscopy, optical microscopy, and single crystal X-ray analysis. The presence of phosphocitrate induced very strong, crystal face specific inhibition of struvite, leading to total cessation of crystal growth when sufficient concentration of the inhibitor was made available. Crystal growth studies and results from molecular modeling indicated strong affinity of phosphocitrate to (101) faces of struvite. This in turn led to an alteration in the expression of these faces and the development of a characteristic arrow-head struvite morphology. Similar changes were not observed in the presence of identical concentrations of citrate, acetohydroxamic acid, and N-sulfo-2-amino tricarballylate (an analogue of phosphocitrate), emphasizing the unique interaction of phosphocitrate with the struvite crystal lattice.

Struvite (magnesium ammonium phosphate: $MgNH_4PO_4 \cdot 6H_2O$) is a complex mineral which is known to assume a number of natural morphological forms including coffin, wedge, short prismatic, or short tabular forms [50,51]. The crystallite has been reported to precipitate out in animal urines [52], including human, when a urinary tract infection stimulates the formation of "mixed stones" or infection stones. Increasing urinary alkalization results from ammonia being generated by the infecting microorganism and together with the abundant presence of the magnesium and phosphate ions, rapidly generates the large, relatively soft stone material. These stones have struvite as the predominant crystallite with a minor component of carbonate apatite [53]. Struvite stones in smaller species, particularly rodents and felines, can in addition, be generated from non-infection sources and may occur together with newberyite $(MgHPO_4)$. Blockage of the urinary tract and encrustation of indwelling catheters are two important medical problems that can arise as a consequence of struvite mineralization.

Controlling the formation and growth of struvite requires not only eliminating the primary source driving the reaction (for example, by antibiotic treatment to eliminate infection) but also restricting access of ionic species to the growing face of the crystal. Inhibitors such as pyrophosphate and citrate have been used to slow growth [53] suggesting some form of interaction with the crystallite. Strong inhibition and elimination of the recurrence of crystallites however is not seen with these compounds.

Acetohydroxamic acid (AHA) and other urea analogues have been used to treat infection stone patients as they inhibit urease activity and reduce alkalization [54]. Recent evidence suggests that AHA can induce morphological changes in the struvite crystal [55]. However, the problem remains in that elimination of the formation and growth of stuvite on a pre-existing nidus is not assured with such compounds, indicating that a need exists for having available more powerful chemical inhibitors.

Phosphocitrate (PC) is a natural biological compound [56] which does offer potential to restrict both struvite and newberyite formation *in vivo* [57]. In addition to its ability to control the growth of magnesium crystallites, it has been reported to be a very active inhibitor of the formation of hydroxyapatite [58,59], calcium oxalate [60], calcite and gypsum [61]. Its activity is understood in part to be derived from a stereochemical interaction of its anionic groups, which at pH 7.4 provide a negative charge of -4.0 [32], with the crystal surfaces. Recent molecular modeling studies of binding of PC with calcium oxalate crystal have revealed that PC interacts strongly with the crystal surface and also becomes incorporated into the growing crystal lattice to inhibit crystal growth [32]. In [49] it was shown that a similar mode of action occurred with the magnesium crystallites and that a distorted crystal morphology and alteration of crystal size as a result of inhibition by PC should occur. The study [49] links experimental crystal growth data with computer modeling of the morphology expressed when crystals were formed in the presence of limiting concentrations of PC. The study of interactions of PC with specific faces of the struvite crystal provided insights into why this particular compound is such a powerful inhibitor of this crystal type.

1.4.2. Methods

The model of PC structure was prepared as described above in the study involving PC binding to COM. Models of crystal surfaces of struvite were prepared from the data

provided by the X-ray crystallography and neutron diffraction analysis [62] by use of materials research software Cerius^2 [63]. Several slabs of struvite crystal parallel to (011), (012), and (101) surfaces were prepared. Molecular and atomic charges of the surfaces were determined using the charge equilibration method [64]. The general Universal 1.01 force field parameters of Cerius^2 were used throughout the calculations.

Using Cerius^2 molecular modeling software, the PC inhibitor molecule in the initial conformation was positioned near the struvite surface within the electrostatic interaction range and the conjugate gradient method of Cerius^2 for the energy optimization procedure was applied. The minimization procedure takes into account the contributions from electrostatic forces, van der Waals forces, hydrogen bonds, bond angles and dihedral angles to the total energy of the system. Starting from the initial position of PC–surface system, the total energy was minimized yielding the energy and geometry of the most favorable position of PC on the struvite crystal surface. During the minimization, the coordinates of crystal lattice atoms were kept fixed and the inhibitor molecule was allowed to translate, rotate and adopt any conformation on the struvite surface. The binding energy was determined as the difference between the energy of the PC–struvite system and the sum of the PC and struvite energies when separated beyond the interaction distance.

A constant dielectric model with a dielectric constant equal to unity was used throughout the calculations. To assess the contribution of electrostatic interactions into the binding energy, the procedure of optimization of binding between PC and struvite was repeated for a dielectric constant equal to six, more closely representing the dielectric environment surrounding the growing crystal.

Struvite crystallizes in the orthorhombic space group $Pmn2_1$ with unit cell dimensions $a = 6.955$ Å, $b = 6.142$ Å and $c = 11.218$ Å [62]. In the absence of an inhibitor, struvites form the well described "coffin lid" shape as they grow along the [100] axis of the crystal [50,51]. Crystals grown in the gel medium were relatively large, reaching up to $400\ \mu$m. To identify crystal faces of struvite grown in the gel medium we used morphology modeling software of Cerius^2. Modeling of struvite morphology was complicated by the fact that struvite belongs to a class of hemimorphic crystals [51], for which the crystal habit does not reflect the full symmetry group of the crystal. This effect cannot be accounted for at the level of currently existing software, so modeling predictions need to be closely correlated with the assignment of faces obtained from X-ray crystallography. The occurrence of different sizes of symmetry-related faces of struvite has been explained using the arguments of surface polarization [51]. The hemimorphic character of struvite is clearly seen in its morphology, where smaller (001) faces are accompanied by larger (00–1) faces. Also often seen are (011) faces with a significantly smaller (00–1). This crystal morphology is completed by a set of (101) faces, again accompanied by much smaller symmetry related (10–1) faces.

Struvite crystals grown in the presence of an initial amount of 3 mg/ml of PC show gradual changes in the crystal morphology that reflect the interactions between the inhibitor and the crystal surfaces at a molecular level and can provide an important insight into the nature of the inhibition mechanism. These changes can be clearly identified using the morphology modeling tools since morphological changes at this dosage of the inhibitor are gradual as well. An important issue that had to be solved, however, was whether the faces terminating the top of the coffin-lid and converging at the (001) faces, or entirely displacing them, belonged to the (011) or (012) family of faces. Both faces are reported to

be expressed in natural and synthetic struvites [50,51], with the (011) family of faces being expressed more frequently. This issue was resolved by performing a series of morphology simulations of growth of the (011) and (012) faces and carefully comparing the results with SEM images of struvite grown with the inhibitor at the amount of 3 mg/ml of PC. This morphology analysis clearly indicated that the faces seen in PC inhibited (3 mg/ml) struvite belong to the (011) family of faces. In this case clear reduction to almost total dissapearance of (001) faces occurred. Crystals were still elongated along [100] direction and (101) faces were clearly expressed. Also disparity between (011) and (01–1) was decreased as the (01–1) faces grew in size. Some crystals showed emerging (010) faces. Crystals were still large of the order of $300~\mu m$ as the amount of the inhibitor was not significantly affecting the crystal sizes, only modifying the morphology.

1.4.3. *Modeling of binding PC to the (011) and (012) faces of struvite*

In order to understand the preference of PC binding to (011) over (012) and to elucidate the molecular mechanism of inhibition of struvite crystals by PC, we modeled binding of PC to these faces of struvite. The relative binding energies to specific crystal faces indicate the potential for stereospecific recognition and binding between an inhibitor and crystal surface [32,65]. Inhibitor binding to a specific crystal face in turn leads to an enhanced expression of this face, as it is stabilized and its relative growth rate is decreased, thus modifying crystal morphology. Analysis of PC binding to (011) and (012) faces revealed that PC was not attracted to (012) planes of struvite. Relatively low density of magnesium ions in this plane and the presence of negatively charged phosphate groups in the near vicinity of magnesium ions resulted in the lack of attraction between the PC and (012) faces, thus explaining the absence of (012) faces in struvite morphology as seen in Figure 4 in [49]. In contrast, binding of PC to (011) was relatively strong and utilized both the phosphate group of PC and all negatively charged groups of PC, resulting in a binding energy of –471 kcal/mol (–71 kcal/mol for a dielectric constant equal 6).

Figure 1.9 shows a computer model of binding of PC to (011) face of struvite. The phosphate group of PC positioned itself in perfect register with the underlying (011) surface of struvite, assuming the position of the incoming phosphate ions of struvite, if crystal growth were to continue in the absence of the inhibitor. This affinity of PC to the (011) family of faces was reflected in modification of crystal morphology in the experiment when 3 mg/ml of PC was used.

The sizes of struvite crystals grown in the presence of 3 mg/ml of PC were between $200–300~\mu m$. This was just large enough to afford X-ray assignment of crystal faces. This analysis entirely confirmed the assignment based on morphological and molecular modeling arguments.

1.4.4. *Modeling of binding PC to the (101) faces of struvite*

Increasing the concentration of PC to 6 mg/ml resulted in a dramatic modification of both crystal morphology and size. Characteristic arrow-head morphology now dominated the crystal appearances. The crystals were much smaller in size, reaching dimensions of the order of $100~\mu m$. Modeling revealed that this arrow-head morphology was dictated by dominating (101) faces that frequently converged to form the tip of the arrow-head. Faces
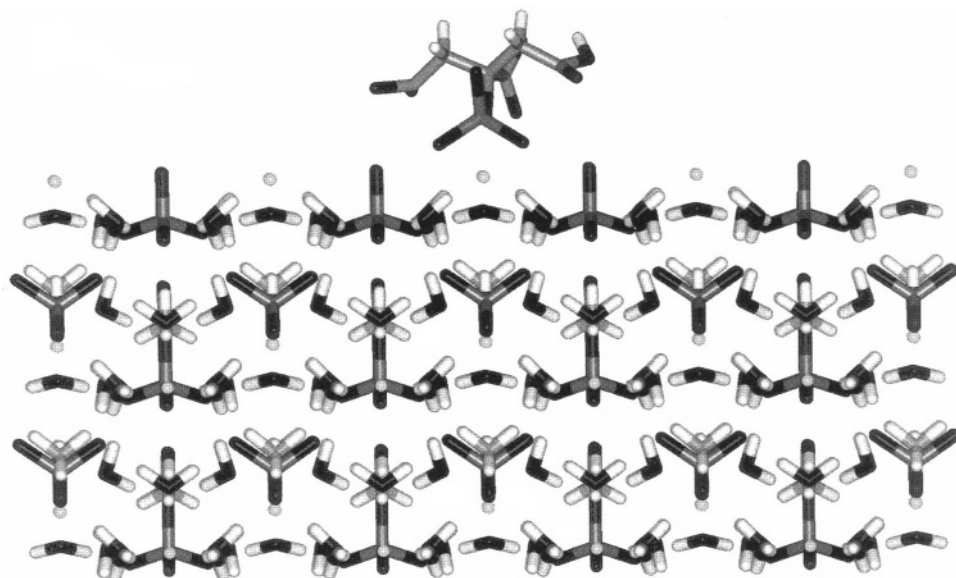
FIGURE 1.9. Computer model of optimized geometry of interactions between phosphocitrate ion and the (011) face of struvite. Phosphate group of phosphocitrate is in excellent register with the phosphate ions of struvite (011) face below. All negatively charged groups of phosphocitrate are participating in binding to the surface.

(001) were virtually nonexistent. Faces (00–1) were also present, often showing twinning parallel to these faces. Faces (011) were well developed with symmetry-related (01–1) faces present as well. The (010) faces were also clearly discernible.

The crystal faces of struvite crystal grown in the presence of 6 mg/ml of PC were indexed using the X-ray Enraf-Nonius CAD4 single crystal automated diffractometer software [66]. To understand the dramatic morphology change of struvite crystals induced by addition of 6 mg/ml of PC, we modeled binding of PC to (101) planes of struvite. A slab of struvite cut parallel to the (101) surface contains planes rich in magnesium ions coordinated with water molecules. These planes provide for a local, positively charged environment perfectly suitable for the binding of the negatively charged PC anions. The PC binding energy to (101) was much stronger than binding to (011), and it was equal to –1403 kcal/mol (–232 kcal/mol for a dielectric constant of 6). From Figure 1.10, one can clearly see that the phosphate group positions itself in place of the phosphate ion of the crystal, participating in the completion of the crystal coordination polyhedra disrupted during cleavage along (101) plane. PC binding to (101) also involved full participation of negatively charged carboxylate groups.

Binding of PC to (101) and (011) planes was an essential factor in the inhibitory activity of PC. Further addition of PC up to 8.3 mg/ml resulted in even greater reduction of crystal size and number. No crystals in fact were formed at the highest dose of 8.3 mg/ml of PC.

In additional studies, we observed that neither citrate nor an analogue of phosphocitrate, N-sulfo-2-amino tricarballylate (SAT), induced comparable change to struvite morphology and size when investigated at levels of 8.3 mg/ml, equivalent to the highest concentration of PC used in this study. This finding is interesting as both compounds are only
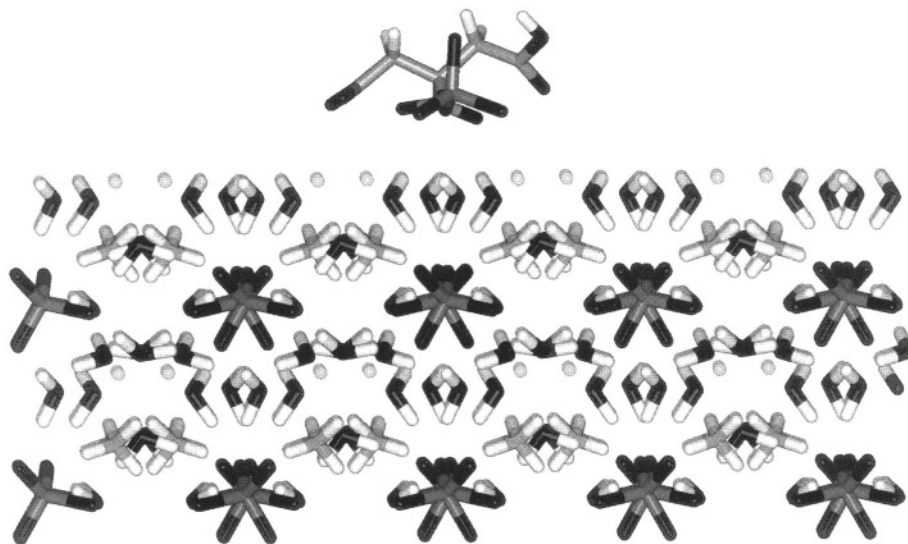
FIGURE 1.10. Computer model of phosphocitrate ion interacting with the (101) faces of struvite. The phosphate group of phosphocitrate is in perfect register with the phosphate groups of the surface. All negatively charged groups of phosphocitrate are participating in binding to the (101) surface of struvite.

slightly less negatively charged than PC. Also, acetohydroxamic acid seemed incapable of significantly affecting struvite growth, although the crystals did appear less bulky and more plate-like, elongating along the [100] direction and sometimes forming characteristic X-shape crystals. This shape seemed to originate from two struvite crystals growing over each other, each of them elongated along its own [100] direction.

1.4.5. Summary

Strong interference by PC to the molecular structure of the growing crystal resulted in significant modification of crystal morphology, crystals were much smaller in size and fewer in number. It seems likely that PC not only had a strong affinity for the selective growing faces but also an ability to get incorporated into the crystal lattice. In studies with calcium oxalate crystals, we had observed a strong crystal–PC interaction based on a similar mechanism [32].

We postulate that the strength of PC as an inhibitor of struvite derives from the fact that PC carries a negatively charged phosphate group, which is also a component of the crystal lattice and therefore is readily incorporated into the growing crystal surface. In addition, the relatively rigid framework of the PC molecule bound to the crystal surface creates a sufficiently large disturbance of the local binding environment for incoming struvite ions to disrupt crystal growth in the direction perpendicular to the binding plane.

We have concluded from both crystal growth experiments and molecular modeling that the adsorption of PC on (101) planes of struvite is of primary importance to its strong inhibitory activity. Incorporation of struvite on these planes leads to the termination of growth along the [100] direction, resulting in the characteristic arrow-head morphology,

significant dwarfing of the crystal size, and total termination of crystal growth at sufficiently high dosages. The importance of the phosphate group of PC is due to its contribution to the overall stereochemistry and total anionic charge of the molecule. This makes PC unique as an inhibitor for controlling the formation and growth of the struvite crystal that significantly exceeds the inhibitory activity of other struvite inhibitors like citrate, SAT, and AHA. *In vivo* and *in vitro* evaluations of the potential of PC, in testing struvite stone formation and encrustation on catheters have been discussed in [57,67].

1.5. MODELING OF BINDING OF PHOSPHOCITRATE TO CRYSTALS OF CALCIUM PYROPHOSPHATE DIHYDRATE

1.5.1. Introduction

Crystalline calcium pyrophosphate dihydrate crystals occur frequently in degenerative joints diseases, causing acute attacks of pseudogout. These crystals appear in cartilage and can engender enzymatic damage to cartilage matrix. Currently no reliable method exists to prevent calcium pyrophosphate dihydrate deposition.

In the study published in [68] we have investigated the role that phosphocitrate, a naturally occurring compound, may play in preventing calcium phosphate precipitation in cells or cellular compartments. Based on the experimental evidence that phosphocitrate blocks ATP-induced CPPD crystals growth in both articular cartilage vesicles and cartilage explants, we used molecular modeling to analyze how the inhibitory activity of phosphocitrate results from the stereospecific interaction between phosphocitrate and the specific faces of calcium pyrophosphate dihydrate crystal.

Our molecular modeling binding studies indicated that phosphocitrate ion is able to bind to (010), (011), (100), (001), (01–1), and (1–10) faces of CPPD crystal with the strongest binding energies obtained for the high calcium density planes (010) and (011). We propose that the binding of phosphocitrate to specific faces of CPPD induces morphological changes that may lead to diminished crystal growth or its total cessation.

Crystalline calcium pyrophosphate dihydrate (CPPD) and basic calcium phosphate (BCP; a term including carbonate-substituted apatite, octacalcium phosphate, and tricalcium phosphate) are the two common forms of pathologic articular mineral [69,70]. Each occurs frequently in degenerative joints, and each may be phlogistic, causing acute attacks of pseudogout, in the case of CPPD crystals, and acute calcific periarthritis, in the case of BCP crystals [69,70]. Both crystal species appear in cartilage [chondrocalcinosis] and can engender enzymatic damage to cartilage matrix. Pathways by which this damage occurs have been studied extensively and have been found to particularly involve the induction of collagenase and stromelysin synthesis and secretion [71]. Formation of these crystals is poorly understood.

Our present understanding of the mechanisms of pathological calcification is limited, therefore no reliable method exists to prevent calcium crystal deposition. Phosphocitrate is a naturally occurring compound which has been identified in mammalian mitochondria [72], and crab hepatopancreas [73]. It has been speculated that PC may have an important role in preventing calcium phosphate precipitation in cells or cellular compartments maintaining high concentration of calcium and phosphate [73]. PC prevents soft tissue cal-

cification *in vivo* and does not produce any significant toxic side effect in rat or mice when administrate through intraperitoneal injection in doses up to 150 mmole/kg/day [74,75].

Although PC is a potent *in vitro* inhibitor of BCP [75,76] and calcium oxalate monohydrate (COM) crystal formation [32,60], it was not known whether PC has any inhibitory effect on CPPD crystallization. Recently, it was reported that PC $(10–1000 \ \mu M)$ blocked ATP-induced CPPD crystal formation in both articular cartilage vesicles (ACV) and cartilage explants [77].

In [68] we postulated that the inhibitory activity of PC resulted from the stereospecific interaction between PC and the specific faces of the CPPD crystal. We employed the molecular modeling technology [12,32,49] to explore whether a binding mechanism similar to that described for inhibition of COM crystals by PC may occur in the interaction of PC and CPPD crystals, resulting in diminished CPPD crystal growth [77].

1.5.2. Methods

Crystal surfaces of triclinic CPPD were generated from data provided by X-ray crystallography [78]. Using $Cerius^2$ [63] software we have prepared several neutral slabs of CPPD crystal, parallel to (100), (010), (001), (01–1), (1–10) and (011) planes. These particular crystal faces were selected due to their importance for the CPPD (triclinic) crystal morphology, and also due to relatively large density of calcium ions in these planes. Molecular and atomic charges of the surfaces were determined using the charge equilibration method [64] and the general Universal 1.01 Force Field parameters of $Cerius^2$ [63].

The morphology of uninhibited CPPD crystal was derived using Bravais–Friedel–Donnay–Harker morphology prediction method of $Cerius^2$ [63] that gives the highest probability to faces (010), (100), (001) and (01–1). These last two faces, i.e. (001) and (01–1) are almost equally probable and they may be preferentially expressed depending on crystal growth circumstances. This can be seen by inspecting the scanning electron microscopy images (SEM) in ref. [79] where CPPD (triclinic) most likely exhibits (100), (010) and (01–1) crystal morphology and in refs [80,81] where (100), (010) and (001) morphology is expressed.

Analysis of the electrostatic charges for the surfaces (010), (001), (100), (01–1), (011) and (1–10) revealed that (010) and (011) surfaces of CPPD had the largest surface density of positive charge. Not surprisingly molecular modeling of PC binding of CPPD, based on the energy minimization, indicated the strongest binding to (010) and (011) surfaces.

1.5.3. Binding of PC to the (010) and (011) surfaces of CPPD

Upon binding the PC molecule orients itself on the surface in the position that allows all of its negatively charged groups to interact with the calcium ions of the surface. This orientation allows the carboxylate groups and negatively charged phosphate group to partially complete calcium coordination polyhedra, disrupted due to crystal discontinuity at the surface. Figure 1.11 shows the optimized geometry of interaction between PC and the (010) surface. The phosphate group of PC positions itself in a site at the surface that would be occupied by pyrophosphate ion if the lattice were continued upward. The PC binding energy to (010) surface is very strong, resulting in binding energy of –2848 kcal/mol. Binding of PC to (011) surfaces was based on a similar scenario, as seen in Figure 1.12, yielding a binding energy of –2961 kcal/mol.
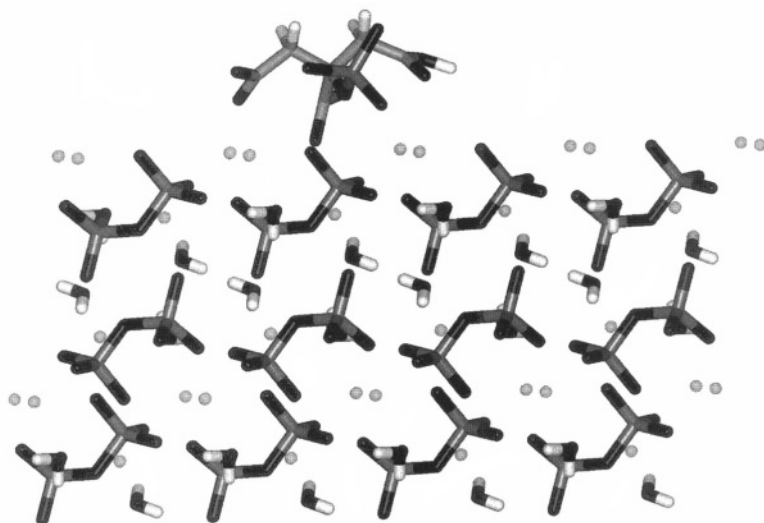
FIGURE 1.11. The optimized geometry of interaction between the PC ion and the (010) surface of CPPD. The PC ion orients itself on the surface in the position that affords all of its negatively charged groups to interact with the calcium ions of the surface. This orientation allows the carboxylate groups and negatively charged phosphate group to partially complete calcium coordination polyhedra, disrupted due to crystal discontinuity at the surface. Note that the phosphate group of PC places itself in the position at the surface that would be occupied by pyrophosphate ion if the lattice were continued upward.

FIGURE 1.12. The optimized geometry of interaction between the PC ion and the (011) surface of CPPD showing strong affinity of the PC molecule to the surface. This affinity results from the presence of double rows of calcium ions sandwiched between rows of pyrophosphate ions. Also relatively low protrusion of negatively charged pyrophosphate groups from these surfaces decreases the repulsion between PC and the surface, leading to further increase in binding energy.

1.5.4. Binding of PC to the (100), (001), (01–1) and (1–10) surfaces of CPPD

In contrast binding to a (100) surface of CPPD, shown in Figure 1.13 reveals only marginal affinity of the PC molecule to the surface. Low calcium density at this surface and the presence of negatively charged pyrophosphate head groups protruding out of the surface does not provide a good binding environment for the phosphocitrate inhibitor. Energy minimization revealed that only the phosphate group of PC is involved in the interaction with the surface, yielding a moderate binding energy of –254 kcal/mol.

Similarly binding to a (001) face, as seen in Figure 1.14, although somewhat stronger, due to a lesser protrusion of pyrophosphate head groups out of the (001) surface, when compared to the (100) surface, allows only the negatively charged phosphate group of PC to participate in binding, resulting in a binding energy of –372 kcal/mol.

Finally binding to (01 –1) and (1 –10) faces of CPPD, Figure 1.15 and Figure 1.16 respectively, is somewhat stronger than binding to the (100) and (001) faces due to more sparse distribution of pyrophosphate ions at the surface resulting in binding energy of –434 kcal/mol and –548 kcal/mol respectively. However it must be emphasized that binding to (01–1) and (1 – 10) faces lacks the strength characterizing binding of PC to (010) and (011) faces.

The above analyses indicate that, although there was some variability in PC binding energy to (100), (001), (01 – 1) and (1–10) faces, resulting from different orientation of pyrophosphate group with respect to these surface planes and different density of calcium ions in these planes, the overall binding scenario is very similar, in all cases showing moderate attraction between PC and these faces. In contrast, binding of PC to (010) and (110) planes was of entirely different nature, resulting from the presence on homoplanes of calcium ions parallel to these planes, leading to a very strong and stereospecific binding of PC to these planes.

Our molecular modeling data strongly indicated the possibility of stereospecific binding of PC to (010) and (011) faces of CPPD. Due to the strength and stereospecific nature of this binding, adsorption of PC on (010) and (011) surfaces of CPPD will result in slowing the growth in the direction perpendicular to this surface resulting in the plate-like crystal morphology and decreasing the size of CPPD crystals for moderate concentration of the PC. In the presence of large doses of PC these crystal plates of CPPD may aggregate leading to spherulitic crystal growth patterns [1] and eventually to cessation of crystal growth altogether. Interestingly (010) face of CPPD (triclinic) has been also recognized as a binding face for alkaline phosphatases [80]. This protein, under experimental conditions [80], is strongly negatively charged, and it is attracted to the CPPD crystal face that has the largest density of positive charge, resulting from coplanar arrangement of calcium ions. It is worth mentioning here that the (010) faces of CPPD crystal are low Miller index crystal faces, predicted using the Bravais–Friedel–Donnay–Harker method of $Cerius^2$ [63] to appear in the morphology of uninhibited CPPD crystal. PC binding will then occur to the existing (010) faces, similarly to phosphocitrate binding to existing (−101) faces of COM [32] or (101) faces of struvite [49]. In contrast binding to (011) faces involves the crystal planes that may not be normally present during uninhibited crystal growth morphology, but nevertheless they can be expressed due to interaction between the inhibitor and the crystal surface, similarly to the expression of (100) faces of calcite grown in the presence of oyster shell proteins [12]. These (100) faces are not normally occurring during uninhibited growth of calcite.
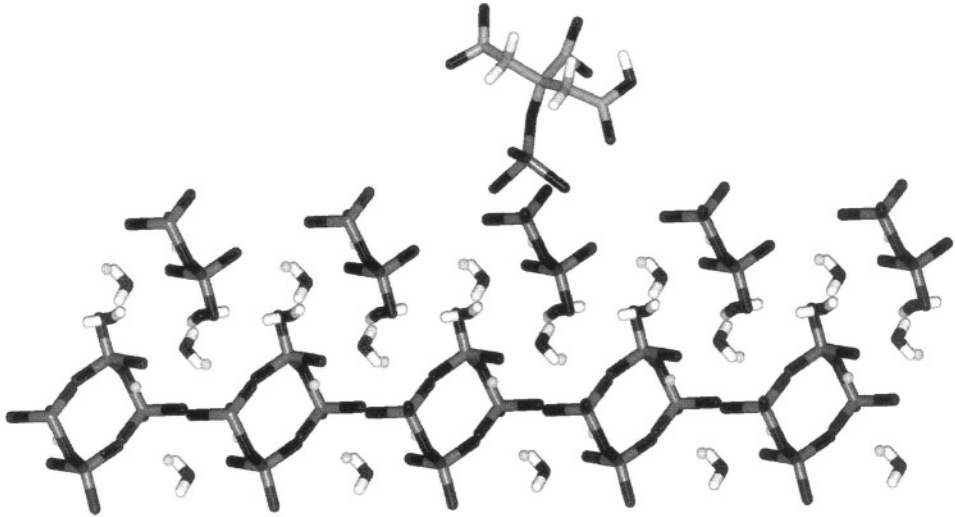
FIGURE 1.13. The optimized geometry of interaction between the PC ion and the (100) surface of CPPD showing only marginal affinity of the PC ion to the surface. Low calcium density at this surface and the presence of negatively charged pyrophosphate head groups protruding out of the surface does not provide for a good binding environment for the phosphocitrate inhibitor.
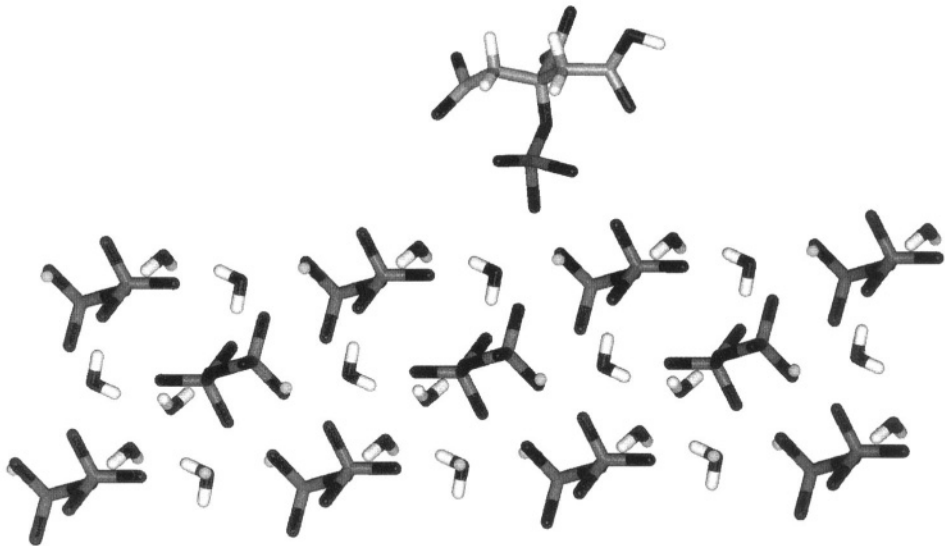
FIGURE 1.14. The binding of PC ion to the (100) face is similar to the binding of PC ion to the (001) face of CPPD, shown in this figure, although it is somewhat stronger due to a lesser protrusion of pyrophosphate head groups out of the (001) surface when compared to the (100) surface. This binding allows only the negatively charged phosphate group of PC ion to participate in binding and results in a relatively low binding energy.
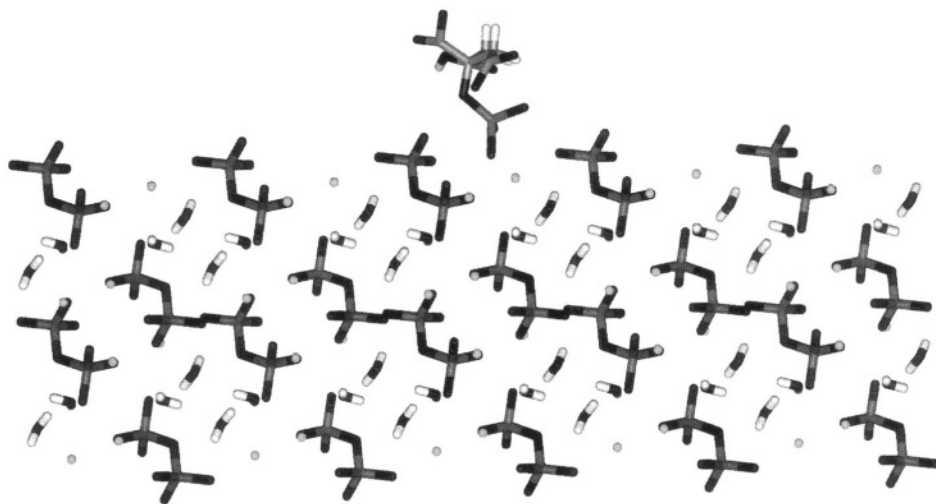
FIGURE 1.15. The optimized geometry of PC ion bound to the (01 –1) face CPPD.
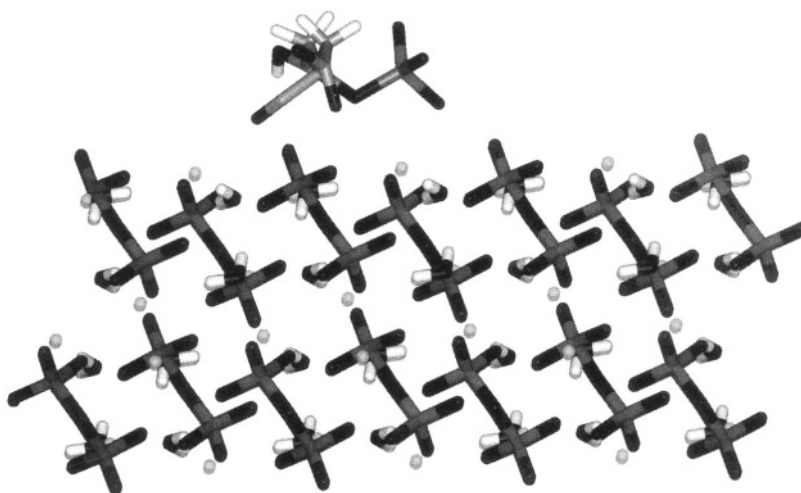
FIGURE 1.16. The optimized geometry of PC ion binding to the (1 –10) face of CPPD.

Also, due to moderate attraction between PC and the remaining crystal faces (100), (001), (01–1) and (1–10) binding to these faces may occur contributing to further diminishing of crystal growth as well.

The best binding energies of phosphocitrate to CPPD (–2848 kcal/mol and –2961 kcal/mol), occurring when inhibition involved (010) and (011) faces respectively, were much stronger than the previously determined binding energy of phosphocitrate to (–101) faces of calcium oxalate monohydrate (–717 kcal/mol) [32] or (101) faces of struvite (–1403 kcal/mol) [49]. The binding to CPPD (010) and (011) is about seven times stronger than binding to other faces of CPPD and is also highly stereospecific.

1.5.5. Summary

All these results strongly suggest that the PC inhibition of ATP-induced CPPD crystal formation in both articular cartilage vesicles and cartilage explants [77] could occur via stereospecific and irreversible binding of phosphocitrate to (010) and (011) faces of CPPD, which in turn leads to the retardation of crystal growth in the direction perpendicular to these faces and eventually cessation of crystal growth. Binding of PC, although of a lesser strength, may also occur on (100), (01−1), (001) and (1−10) faces which also show nonnegligible binding energies, nearly equal to each other.

The affinity of PC to morphologically relevant faces of CPPD, in terms of binding energy, can be summarized as follows:

$$E(010) \approx E(011) \gg E(100) \approx E(01-1) \approx E(001) \approx E(1-10),$$

where $E(h, k, l)$ represents binding energy of PC to a particular crysrallographical face (h, k, l).

The findings reported in [49] helped to explain our earlier findings why PC specifically inhibited the CPPD and BCP crystal-induced mitogen-activated protein kinase cascade signal transduction pathway [82]. In that study, it was speculated that the binding of PC to calcium-containing crystals changes the zeta potential of the crystal surface, thus interfering with the crystal–membrane interactions that lead to cellular responses. This would explain why PC does not inhibit the monosodium urate crystal and peptide growth factor-induction of mitogenesis and metalloproteinase synthesis [83].

Earlier studies had shown that PC specifically inhibits CPPD and BCP crystal-induced metalloproteinase synthesis, and mitogenesis in human fibroblasts *in vitro* while PC has no effect on similar biologic responses induced by EGF, PDGF, monosodium urate crystals, and serum [84]. PC prevents disease progression in murine progressive ankylosis [an animal model of crystal deposition diseases], a condition marked by extensive BCP deposition [85]. Taken together with the present data, PC may be considered as a potential therapeutic agent for both CPPD and BCP crystal deposition diseases. The current hypothesis is that PC will have dual beneficial effects of blocking the degeneration-promoting effects of crystals e.g. metalloproteinase synthesis and mitogenesis [82], and of inhibiting further BCP and CPPD crystal formation in articular tissue [77].

1.6. MODELING OF BINDING OF PHOSPHOCITRATE TO CRYSTALS OF HYDROXYAPATITE

1.6.1. Introduction

Hydroxyapatite is one of the most important minerals in the human body. It constitutes almost the entire mineral phase of bones and tooth enamel. Its ubiquity however, sometimes may lead to cases of unwanted biomineralization that results in many pathological conditions. Recently, it has been shown *in vitro* that the growth of hydroxyapatite crystals can be efficiently controlled using phosphocitrate, a naturally occurring compound. Phosphocitrate has been also shown to prevent sticking of cells to hydroxyapatite crystals. However, the molecular mechanism of phosphocitrate interactions with hydroxyapatite crystals was

almost entirely unknown due to difficulties in analyzing the X-ray geometry of the unit cell of hydroxyapatite, which exhibits disorder in the hydroxyl ion positions.

Presented in [86] was the first, to our knowledge, molecular modeling investigations of inhibition of hydroxyapatite crystals. We used the Generalized Gradient Approximation of Density Functional Theory with the implementation of full periodic boundary conditions to optimize the positions of hydroxyl ions in the unit cell of hydroxyapatite crystal. We applied molecular modeling to show that phosphocitrate binds to (100) crystal faces of hydroxyapatite, and analyzed the nature of stereospecificity of recognition and binding to these planes. In this study we proposed that the binding of phosphocitrate to (100) face of hydroxyapatite induces morphological changes that may lead to diminished crystal growth or to its total cessation, and may also prevent cell sticking to hydroxyapatite.

Hydroxyapatite (HA) is one of the most important biominerals in the human body. Almost the entire mineral phase of human bones and tooth enamel is composed of hydroxyapatite [87]. However, there are also numerous examples in human pathology where formation of this mineral could be associated with unwanted biomineralization such as kidney stone formation, for example. Urolithiasis, a diseased condition resulting from the formation of calculi in the urinary track, develops in 10% of men and in 3% of women during their lifetimes. Although the majority of renal stones contain calcium oxalate, hydroxyapatite is detected in up to 29% of them [88] since HA formation may be a precursory stage in the formation calcium oxalate stones [89]. Recently it has been demonstrated experimentally that PC may also play an important role in the inhibition of HA [90] and that its inhibitory efficiency may be significantly stronger that its parent molecule, citrate [89]. This finding shows that PC not only may inhibit the growth of renal calculi that are already formed (COM crystals), but it may also prevent their nucleation at their early stages of formation (HA).

1.6.2. Methods

In order to use PC as an efficient inhibitor of undesirable HA formation we investigated the mechanism by which PC recognizes and binds to HA. Binding of PC to crystal surfaces of HA may also explain its role in prevention of cell sticking to HA crystals observed experimentally in [90]. Molecular modeling of interactions between hydroxyapatite and its inhibitors was never attempted before our study [86] since the X-ray analysis of the HA crystal structure [91] shows that the hydroxyl ions in the HA lattice is in the four-fold spatial position in two-fold disorder. This results in the number of hydroxyl ions being twice the required stoichiometric amount. Until recently there was no reliable method of optimizing the hydroxyl atom positions when one half of the redundant hydroxyls have been removed from the unit cell. In the study [86] we presented the results of Density Functional Theory optimization of the unit cell of hydroxyapatite and molecular modeling studies of binding of phosphocitrate to the crystal faces of hydroxyapatite. Impact of these studies of molecular recognition and binding of PC to HA on the potential therapeutical properties of PC with respect to prevention of recurring kidney stone formation and other pathological biomineralization in humans was also discussed in [86].

For all our calculations involving the optimization of hydroxyl ion positions in the HA unit cell, the CASTEP (Cambridge Serial Total Energy Package) program was used [92]. The theoretical basis of CASTEP [93] is the Density Functional Theory (DFT) in the local

density approximation (LDA) or gradient-corrected LDA version, as developed by Perdew and Wang (GGA) [94] with the application of a pseudopotential concept [93]. We used a supercell approach by applying the three dimensional periodic boundary condition to the HA unit cell. The geometrical dimensions of the cell were fixed at its crystallographically determined values [91] and all atoms within the unit cell were frozen except the atoms constituting the hydroxyl ions, which were free to move. Optimization calculations were run until convergence criteria, typical for this class of inorganic crystals was met. The original unit cell of HA obtained from its X-ray structure was very difficult to analyze due to the shifted positions of OH^- ions, which are located about 0.35 Å above and below the stable positions of the crystal (mirror planes occurring at $z = 0.25$ and $z = 0.75$) [95].

The crystal surface of HA was generated from the data provided by X-ray crystallography [91]. Using Cerius^2 [92] software we have prepared a neutral slab of HA crystal, parallel to (100) planes. This particular crystal face was selected due to its importance for the HA crystal morphology and the vast experimental evidence implicating this face as the binding site for many anionic species like small molecules [96], polymers [97] and proteins [98]. Molecular and atomic charges of the surfaces were determined using the charge equilibration method [64] and the general Universal 1.02 Force Field parameters of Cerius^2 [92].

Using Cerius^2 [92] molecular modeling software the PC inhibitor molecule in its initial conformation was positioned near the HA surface within the electrostatic interaction range. The conjugate gradient method of Cerius^2 [92] for the energy optimization procedure was applied. The optimization procedure takes into account the contributions from electrostatic forces, van der Waals forces, hydrogen bonds, bond angles, and dihedral angles to the total energy of the system. Starting from the initial position of the PC–surface system, the total energy was minimized, yielding the energy and geometry of the most favorable position of PC on the crystal surface. During the minimization, the coordinates of crystal lattice atoms were kept fixed and the inhibitor molecule was allowed to translate, rotate and adopt any conformation on the HA surface. The binding energy was determined as the difference between the energy of the PC–HA system and the sum of the PC and HA energies when separated beyond the interaction distance, using a constant dielectric model with dielectric constant equal to unity.

The morphology of uninhibited HA crystal was derived using the Bravais–Friedel–Donnay–Harker morphology prediction method of Cerius^2 [92]. This morphology gives the highest probability to faces (100) and (101) respectively. Typical morphology of uninhibited hydroxyapatite often shows in addition to the (100) and (101), the highest probability faces, the (001) faces as well. Although (001) faces are the sixth among the most probable faces of hydroxyapatite, they frequently occur in geologically grown crystals.

1.6.3. Binding of PC to the neutrally charged (100) surfaces of HA

Molecular modeling of PC binding to HA, based on the energy minimization, revealed the energetically most favorable scenario of PC binding to the (100) surface of hydroxyapatite. Figure 1.17 shows the optimized geometry of interaction between PC and the (100) surface of HA with the binding energy equal to −1417 kcal/mol. The PC binding scenario to (100) faces of HA was similar to binding of PC to COM [32], CPPD [68] or struvite [49]. Upon binding, the PC molecule orients itself on the surface in the position that allows all
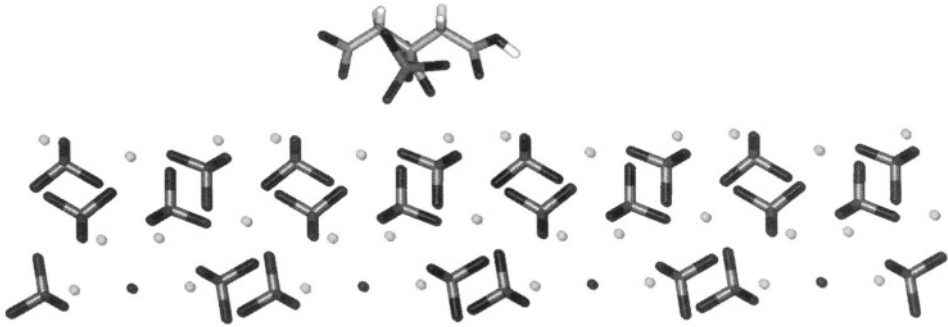
FIGURE 1.17. The optimized geometry of interaction between the PC ion and the neutral slab of the (100) surface of hydroxyapatite. Only a small fragment of the surface used for the modeling is shown. Upon binding the PC ion orients itself on the surface in the position that allows all of its negatively charged groups to interact with the calcium ions of the surface. This orientation allows the carboxylate groups and negatively charged phosphate group to partially complete calcium coordination polyhedra, disrupted due to crystal discontinuity at the surface. The phosphate group of PC positions itself in a site at the surface that would be occupied by phosphate ion if the lattice were continued upward.

of its negatively charged groups to interact with the calcium ions of the surface. This orientation allows the carboxylate groups and negatively charged phosphate group to partially complete calcium coordination polyhedra, which were disrupted due to crystal discontinuity at the surface. The phosphate group of PC positioned itself in a site at the surface that would be occupied by phosphate ion if the lattice were continued upward. In the study [86] we prepared a slab of hydroxyapatite that had a total electric charge equal to zero.

1.6.4. Binding of PC to the negatively charged (100) surfaces of HA

Since it has been reported in the literature that some negatively charged proteins, catalase for example [99], can bind to negatively charged crystals of hydroxyapatite, we also prepared another slab of hydroxyapatite crystal that had a negative –5.4 overall charge. Binding of negatively charged PC to this (100) surface slab (Figure 1.18) although somewhat diminished in its strength, was still substantial, and its binding energy was equal to –667.2 kcal/mol. Closer analysis of the surface electrostatic charges for this (100) slab indicated that it contains loci of positive charges centered on calcium ions. The presence of patches of large positive electrostatic surface charge density in this (100) plane provided for a sufficiently conducive environment for binding of negatively charged functional groups when the distribution of these groups does not overlap with strongly negatively charged phosphate groups protruding from the surface.

1.6.5. Summary

Our present understanding of the mechanisms of pathological calcification is limited, therefore no reliable method exists to prevent calcium crystals deposition. If crystals promote chondrolysis, then removal of crystals from the joint would be therapeutic. This can be accomplished in gout where a systemic accumulation of urate can be targeted and eliminated with hypouricemic therapy. Unfortunately, no systemic defect has been specifically
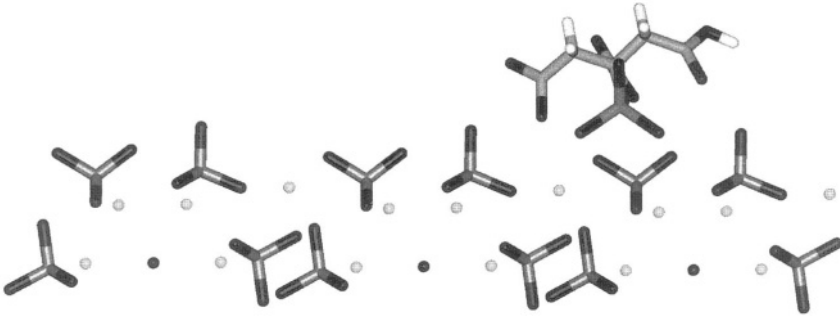
FIGURE 1.18. The optimized geometry of interaction between the PC ion and the negatively charged slab of the (100) surface of hydroxyapatite. The total surface charge is –5.4 and only a small fragment of the surface used for the modeling is shown. Binding of negatively charged PC to this surface although somewhat diminished in its strength, comparing to Figure 1.5, is still substantial Closer analysis of the electrostatic charges for this slab of (100) surface reveals that the patches of large positive electrostatic charge density in this (100) surface provides for sufficiently conducive environment for binding of negatively charged functional groups of phosphocitrate.

recognized underlying most cases of calcium-containing crystal deposits. Directly solubilizing crystals by joint lavage in a patient with CPPD crystal deposition resulted in acute pseudogout attacks.

Phosphocitrate (PC) is a naturally occurring compound, which has been identified in mammalian mitochondria and in human urine [73,100]. PC may protect mitochondria from mineral formation expected due to the high intra-mitochondrial concentrations of phosphate, calcium, and it may prevent mineral interaction with the vulnerable mitochondrial membranes. This blocking effect is likely explained by the influence of PC on the calcium-containing crystals interaction with biomembranes. PC prevents BCP deposition and disease progression in murine progressive ankylosis, an animal model of BCP crystal deposition disease [85]. PC also inhibits CPPD formation in the ATP-induced calcinosis model [77]. We have demonstrated that PC inhibited nitric oxide-induced calcification of articular cartilage and chondrocytes-derived apoptotic bodies. Our working hypothesis is that PC has two beneficial effects. First, PC blocks the deleterious biologic effects of crystals e.g. metalloproteinase synthesis and mitogenesis. Second, PC prevents further crystal formation in the articular tissues, since it has a powerful anti-mineralization effect both *in vivo* and *in vitro* [82].

In the study [86] we have investigated the mechanism by which phosphocitrate binds to hydroxyapatite to prevent its growth in the unwanted events of biomineralization. Since the presence of hydroxyapatite is considered to be a precursory stage in the formation of many calcium-containing crystals in the human body, this work may serve as a starting point in understanding the inhibition of calcium-containing crystals by phosphocitrate. This modeling study together with our earlier findings [32,49,68] helps to explain why PC, as it has been demonstrated in many experimental investigations, outperforms almost all other inhibitors of calcium and/or phosphate containing crystals. The inhibitory strength of PC is derived from its compact and very rigid molecular framework that carries a significant negative charge (up to minus four) in the range of near neutral pH. Ionized carboxylate groups coordinate surface calcium ions whose coordination polyhedra have been disrupted during the crystal cleavage [12]. Moreover, as we have shown in this paper, negatively charged

phosphate groups of PC position themselves in the near perfect registry above the phosphate ions of crystal lattice, as if to continue the ionic arrangement of the lattice, disrupted at the surface. On the other hand, the rigid framework of the molecule creates significant steric hindrance in the vicinity of the adsorbed phosphocitrate. This prevents the incoming lattice ions from being incorporated into the crystal lattice and thus crystal growth is inhibited in the direction perpendicular to the surface. The binding of phosphocitrate to (100) faces of hydroxyapatite will result in significant enlargement of these faces at the expense of the other faces. Flat plate-like crystals, often of elongated hexagonal shape, should be observed. A similar morphological effect was observed in the independent study involving inhibition of hydroxyapatite by the polyacrylic acid, the industrial polymer containing negatively charged carboxylate groups [101].

There is yet another feature of PC that makes it uniquely suited as a versatile inhibitor of calcium-containing crystals. Due to its similarity to citrate, PC most likely utilizes the same routes of transmembrane transport as citrate. Our preliminary studies indicate that PC may bind to Citrate Transport Protein [102] and use it for its passage through the phospholipid bilayer, thus making it readily available at the site of undesirable formation of calcium-containing crystals.

Before the study [86], the way in which PC inhibits one of the most important calcium containing minerals, hydroxyapatite, was unknown due to difficulties resulting from the unresolved structural X-ray data involving inherent disorder in OH^- lattice positions. Applying recently developed methods of Density Functional Theory to periodic systems as implemented in CASTEP, we were able to optimize the positions of hydroxyl ions and perform the molecular binding studies of PC to (100) faces of HA in order to explain how phosphocitrate may work as a therapeutic agent in the treatment of calcium crystal induced diseases.

1.7. MODELING OF MACROMOLECULAR ADSORPTION AT LIQUID/CRYSTAL INTERFACES

1.7.1. Introduction

The adsorption of proteins and peptides to surfaces or within interfacial regions is a topic of considerable interest in the areas of medicine and materials science. Protein and peptide adsorption to crystal surfaces are interesting for several reasons. For example, one may be interested in the actual adsorption mechanism while others are interested in the result of the adsorption. In the first case, a fundamental understanding the adsorption mechanism would yield information on cooperativity between these proteins and peptides, whether the biomolecules bind to the surface, and what intermolecular forces are at play in the process. In the second case, the result of adsorption, seeks to understand from a microscopic perspective, how does the presence of these biomolecules inhibit crystal growth and modify the physical as well as chemical properties. In this chapter we explore, using computation models, the adsorption of biomolecules to ionic and molecular crystals.

As discussed in the preceding sections the exclusion of solvent, or at least treating the solvent as a structureless continuum, from the computations does not effect the interpretation of the data. However in the case of molecular crystals, for example ice, lipids,

etc., neglecting the solvent, in this case liquid water, has a tremendous impact on the computational results. In this section we will discuss the importance of inclusion of solvent molecules at the interface region.

Since their discovery, 28 years ago, there has been a growing interesting in a class of biomolecules commonly referred to as antifreeze proteins/peptides (AFP), antifreeze glycoproteins (AFGP) and thermal hysteresis proteins/peptides (THP) [103–105]. These biomolecules have the unique property of inhibiting ice growth below the normal freezing point; however, they do not change the normal melting point temperature. The difference in temperature between the freezing point of water and the normal melting point of water in the presence of these biomolecules is referred to as thermal hysteresis [103,106]. This unique non-colligative property of these biomolecules is used by Nature to assist fish, insects, plants, and bacteria in their survival in cold environments. During this time, despite the numerous experimental and computational efforts, elucidation of the fundamental behavior of these biomolecules has not been accomplished. In the following paragraphs we will provide a summary of the computational efforts performed in order to provide an insight into this exciting area. The summary will begin with work that was done early on and end with current state of the art simulation efforts.

The computational models and methods that have been used are based on classical molecular mechanics and dynamics methods [107]. In these methods contributions to electrons are neglected. Atoms are treated as spheres while bonds between atoms are modeled as springs. There are three basic relationships used in treating systems in this manner. One begins by representing a molecule using a potential energy function as illustrated in the following equation

$$U(r) = E_{\text{bonds}} + E_{\text{angles}} + E_{\text{torsions}} + E_{\text{vdw}} + E_{\text{Coulombic}}.$$

The potential energy function, which depends on the atomic coordinates (r), is comprised of terms representing the bonds, angles, torsions (improper and proper), van der Waals interactions and Coulombic interactions. The specific form of the potential energy function depends on the implementation one uses. The reader is encouraged to consult any of the many references on a particular potential energy function [107,108]. Once the form of the potential function has been chosen, parameters for the various terms must be determined. The values for these parameters comprise what is known as a force-field. There are several force-fields available today such as CHARMM [109], AMBER [110,111], GROMOS [112], MM3 [113], UFF [114], CVFF [115], Tripos 5.2 [116], MMFF94 [117] and DRIEDING [118] to name a few. In the work described in this chapter we have used CHARMM and UFF potential energy functions and force-fields. Using the potential energy function one can obtain the force between to atoms/molecules using the following relationship

$$F(r) = -\nabla U(r).$$

In this equation one obtains the force by taking the negative gradient ($-\nabla$) of the potential energy. These forces can be used in conjunction with energy minimization techniques

to obtain relaxed, energy-minimized structures. These same forces can also be used with Newton's second law

$$F(r) = ma = m\frac{dr^2}{dt^2}$$

such that when integrated, yields a method in which the atomic positions are obtained as a function of time. This is the basic idea behind molecular dynamic simulations. Using these three basic relationships, one is able to explore, on a fundamental and microscopic level, the interactions between biomolecules and surfaces [119,120].

In the modeling of biomolecule/surface interactions the technique of energy minimization was used. In using this method the interaction between the biomolecule and surface was studied by computing the interaction between them. The interaction energy (ΔE_{inter}) was determined using the following equation

$$\Delta E_{inter} = E_{complex} - (E_{surface} + E_{biomolecule}),$$

where $E_{complex}$ is the molecular mechanical energy of the biomolecule and surface, $E_{surface}$ is the molecular mechanical energy of the surface, and $E_{biomolecule}$ is the molecular mechanical energy of the biomolecule. The "global" minimum was obtained by a survey of the energy landscape through a random search on the surface. Although this does not guarantee that the global minimum is obtained, it is sufficient to provide confidence that a lower minimum is not in the region of interest.

Simulations of a biomolecule at an interface were performed using the method of molecular dynamics. In this case, one is able to compute dynamical as well as static properties. For example, in the ice/water and ice/protein/water simulations we are able to compute various order parameters such as diffusion, orientational, and density. In addition we are able to observe the movement of the protein within the interface as a function of time. Determining static properties such as hydrogen bond analysis along with energetics is possible using the data from the simulations.

The nature of the ice/water interface is slowly being elucidated through experimental and computational efforts. Experimentally the ice/water interface has been examined using X-ray analysis [121], ellipsometry [122], dynamic light scattering [123], and second harmonic generation methods [124]. Based on the results from these experiments the ice/water interface can be summarized in the following manner. There exist an interfacial region in which the dynamics and properties of the water molecules in this region exhibit neither liquid nor solid-like behavior.

Several simulations have been performed on the ice/water interface over the past 10 years [125–135]. The most recent simulations have revealed that the ice/water interface consists of region in which the properties between the two phases smoothly change over a 10–15 Å [127]. This picture is consistent using different water models, for different ice crystal faces, and for different order parameters [127].

In the development of a coherent and fundamental picture of biomolecules at the liquid–solid interface, a basic understanding of all interactions of the biomolecule in the liquid phase as well as the interactions between the biomolecule and the solid. With this in mind our approach has been to perform calculations of the bimolecules in water, on the surface [42,65,136,137], and in the ice/water interfacial region [138]. In the following

paragraphs we will present the current status of our efforts in attempting to elucidate the ability of AFPs to inhibit ice growth [139].

1.7.2. Winter flounder AFP

Most of the computational modeling efforts have focused on the AFP from the *Pleuronectes americanus* winter flounder, specifically the HPLC-6 AFP [140–145]. Figure 1.19 shows that this AFP is α-helical with a regular repeat of threonine residues. These residues are spaced 16.7 Å apart which lead investigators to develop a hypothesis based on hydrogen bonding to describe the interaction between the biomolecule and ice. Using this repeat pattern and the results from ice etching experiments, computer models were developed which explain the "binding" of the AFP to the ice surface [42]. Figure 1.20 summarizes the computer modeling results in which a left-handed and right-handed helix "binds" to the bipyramidal face of ice along their correct vectors. The computer modeling in this case comprised of performing several energy minimizations in order to determine the best "binding" orientation. In these calculations the water molecule oxygen atoms were held fixed in their ice Ih lattice positions while all other atoms were free to move. From these simulations it was determined that the right-handed helix had the lowest energy of interaction lying along the [$\bar{1}12$] direction while the left-handed helix had the lowest energy of

Type I (Winter Flounder)
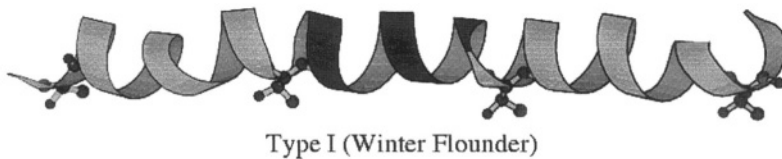
FIGURE 1.19. A ribbon representation of the the HPLC6 fraction of winter flounder antifreeze protein. The red segment of the helix highlights the length of a repeat segment within the protein. The side chaines of the threonine residues are represented in the ball and stick form.
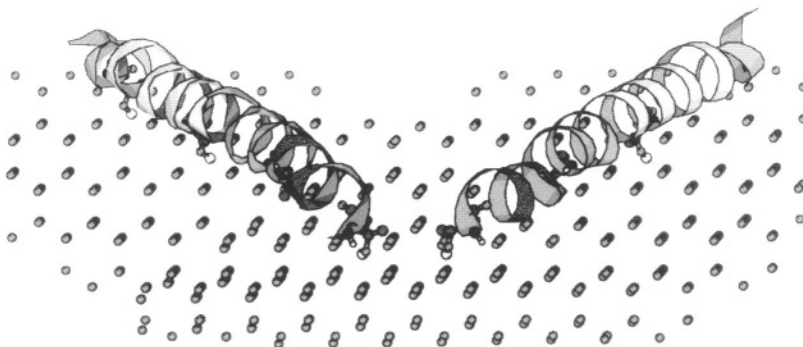
FIGURE 1.20. An illustration of the right and left-handed winter flounder protein on the (201) ice plane. The proteins are represented as ribbon structures while the side chains for the threonine residues are drawn in ball and stick form. The blue end of the helicies is the N-terminus while the orange end is the C-terminus. The ice waters are represented as the red spheres. The orientation is such that the observer is looking down the *c*-axis of the ice crystal.
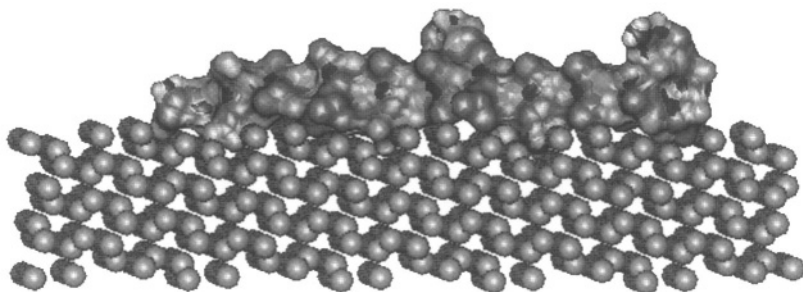
FIGURE 1.21. The protein (represented as a molecular surface) sitting on the (201) ice surface (shown here as red spheres representing the oxygen positions of the ice waters).

interaction lying along the $[1\bar{2}\bar{2}]$ direction with is the mirror image vector of $[\bar{1}12]$. The results from these simulations were summarized as follows. The preferential binding is due to (i) a lattice match between the water oxygens atoms of the ice and the polar groups of the peptide and (ii) the fitting of the peptide shape with that of the ice surface topography (see Figure 1.21). It should be noted here that the water or interface region can adjust better to the outside of the protein than ice (A.D.J. Haymet, personal communication). The concept of topography fitting and lattice match is consistent with two other studies. The first study was performed by Wen and Laursen [146] in which they used a molecular mechanics approach to show the threonine match between AFP and ice. Most recently, Dalal and Sonnichsen [147] have reported using a Monte Carlo rigid body docking of HPLC-6 on various ice planes. They show that although van der Waals interactions are a major source of ice–protein interactions, they cannot be used to completely explain the observed binding specificity. The results from these three studies are relevant as long as one understands that these calculations most closely represent a vacuum/ice interface.

Another approach taken in order to identify unique features of AFPs with respect to other proteins was to study the behavior of these biomolecules in liquid water near freezing. Jorgensen *et al.* [144] reported the first simulations of the winter flounder AFP in a box of water similar to that shown in Figure 1.22. In these simulations the authors looked at possible anomalies in the hydrogen bonding between the AFP and water as well as changes in helicity of the AFP. Simulations by others [140–142,145] obtained similar results to those found by Jorgensen *et al.* A recent simulation of the winter flounder AFP in a box of water in which the simulation temperature is at the phase transition temperature for the water model used and simulation conditions has been performed [140]. These results are consistent with previous simulations.

The next step attempting to analyze the behavior of a protein at the ice water interface was to perform some site-directed mutatgenesis experiments in which the theronine residues were mutated to hydrophobic residues such as valine and alanine [148,149]. The results of these experiments clearly refuted the hydrogen bonding hypothesis and promoted a new hypothesis based on hydrophobic concepts. Figure 1.23 shows a helical wheel representation of the winter flounder antifreeze protein. In Figure 1.23 the two faces in which the protein can interact with the ice are illustrated by a straight line (old hydrogen bonding hypothesis) and a dashed line (new hydrophobic hypothesis).
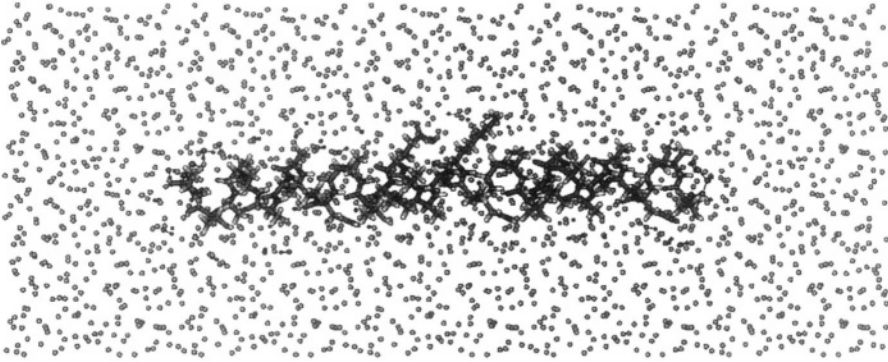
FIGURE 1.22. A snapshot, after 300 ps of molecular dynamics simulation, of the winter flounder antifreeze protein (represented as a coil) in a box of 1000 water molecules. The red and blue spheres represent the water oxygen positions. The blue spheres identify water molecules that are within hydrogen bonding distance of the protein.
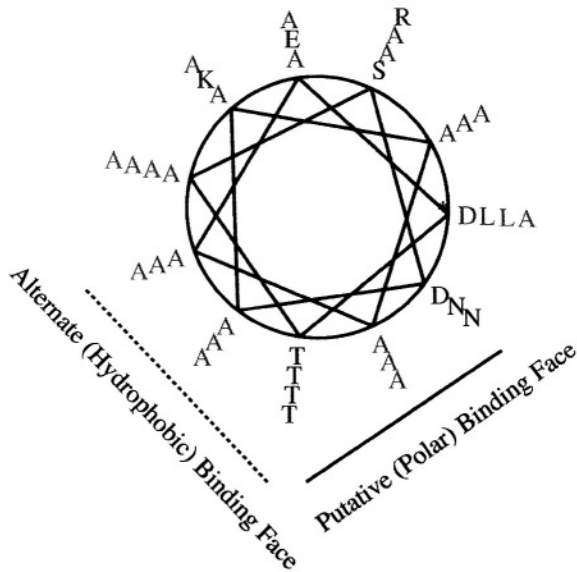
FIGURE 1.23. This figure is shows the positional relationship of winter flounder antifreeze protein residues. An asterisk marks the first residue of the sequence. The next residue in the sequence is the $i + 4$th residue going clockwise around the wheel. This helix wheel is based on a 11-residue repeat instead of the normal 18-residuc repeat [170]. In this representation two binding faces are illustrated. The hydrophilic (TAN) face is indicated by the solid line while the hydrophobic face (AAT) is indicated by the dashed line.

The most recent computational work in this area is the simulation of the antifreeze proteins at the ice/water interface [138]. However, before those simulations could be performed, a series of calculations on the ice/water interface, lead by Haymet and co-workers [127–130], needed to be undertaken. These simulations consist of placing two different phases of water in contact with each other and running long molecular dynamics calcula-
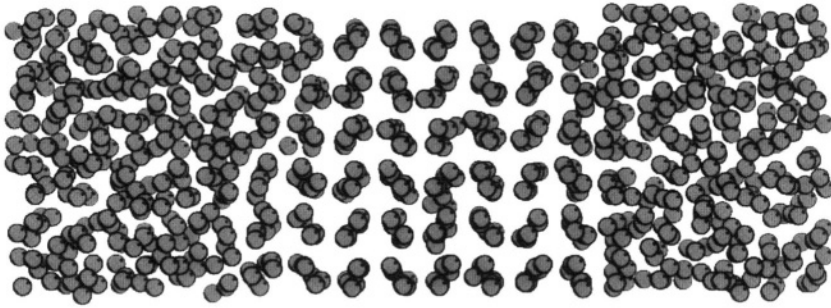
FIGURE 1.24. This figure illustrated a typical (201) ice/water interface used in dynamics simulations. In this case the oxygen atoms of the liquid and solid phase waters are drawn as van der Waal spheres in red. The solid phase water (ice) is sandwiched between two liquid phase water slabs.
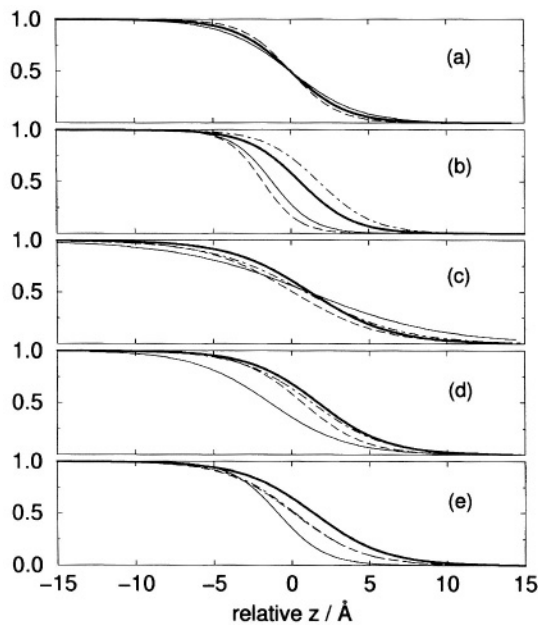
FIGURE 1.25. This figure shows the profiles for various order parameters (a–e) that can be calculated from simulations of ice/water interfaces. The different lines represent different ice/water interfaces [127]. Reprinted with permission from the American Institute of Physics.

tions. Figure 1.24 is a snapshot from a 1 ns molecular dynamics simulation under NVT conditions. From these simulations and from Figure 1.24 it is difficult to observe a well-defined interface. In order to develop an understanding of the properties of the region where the two interfaces meet a clear definition of the interfacial region needs to be identified. Haymet *et al.* [127–130] have accomplished that by investigating various order parameters that can be calculated from the simulation data. The behavior of the various order parameters as a function of ice/water interface are illustrated in Figure 1.25. The result of the
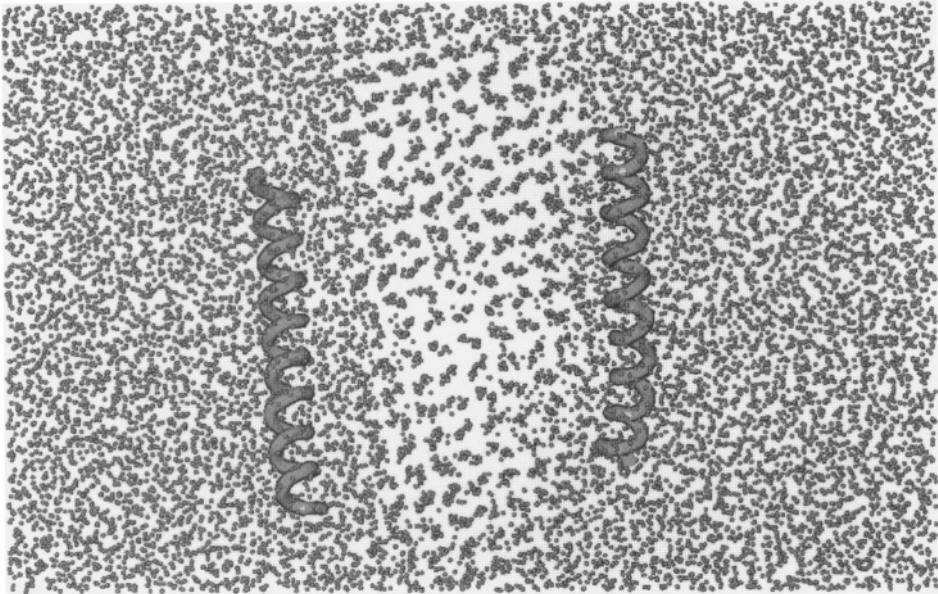
FIGURE 1.26. A figure illustrating two antifreeze proteins in the ice/water interface. This is a snapshot from a water/protein/ice molecular dynamics simulation. The red spheres represent the liquid and solid phase waters while the antifreeze proteins are represented by the yellow coils.

ice/water simulation analysis is that the ice/water interface is a diffuse region approximately 10–15 Å thick and depends on the order parameter used. Using these results a large (201) ice/water interface was constructed and equilibrated. Once this system was equilibrated, the winter antifreeze proteins were introduced to the system in an orientation similar to the (201) ice/vacuum calculations. The water/protein/ice system was further equilibrated. After equilibration, data was collected for over 1 ns. Figure 1.26 shows a snapshot of the water/protein/ice during the 1 ns data collection. Analysis of the simulation results indicates that these proteins are neither at the ice surface nor are they in the water. They are clearly in the interfacial region. During the simulation the proteins move approximately 0.5–0.8 Å to the left and right. Initially they move toward the ice and then move away from the ice.

1.7.3. Shorthorn sculpin

Shortly after obtaining our results from the winter flounder AFP/ice–vacuum calculations we proceeded to study the interactions between the shorthorn sculpin *(Myoxocephalus scorpius)/*ice–vacuum system [65]. This system is interesting for several reasons. Most importantly the shorthorn sculpin AFP is an α-helical protein like the winter flounder, however, it binds to a different ice plane. In this case the short horn sculpin binds to the $(2\bar{1}0)$ ice plane, i.e. secondary prism face. The major difference between the two AFPs is the amino acid sequence. Again we used molecular mechanics minimization methods to locate the best orientation on the $(2\bar{1}0)$ ice plane and determine the binding energy (see Figure 1.27). Analysis of the results from the modeling calculations suggest that this AFP selects this place since the ice channel spacing matches the spacing of the AFP lysine residues [65].
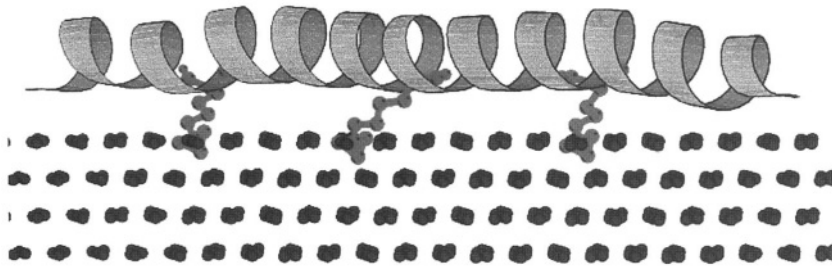
FIGURE 1.27. An illustration of the shorthorn sculpin on the $(2\bar{1}0)$ ice surface. The antifreeze protein is represented as the green ribbon with the lysine side chains highlighted as red ball and sticks. The ice oxygens are represented as blue spheres.
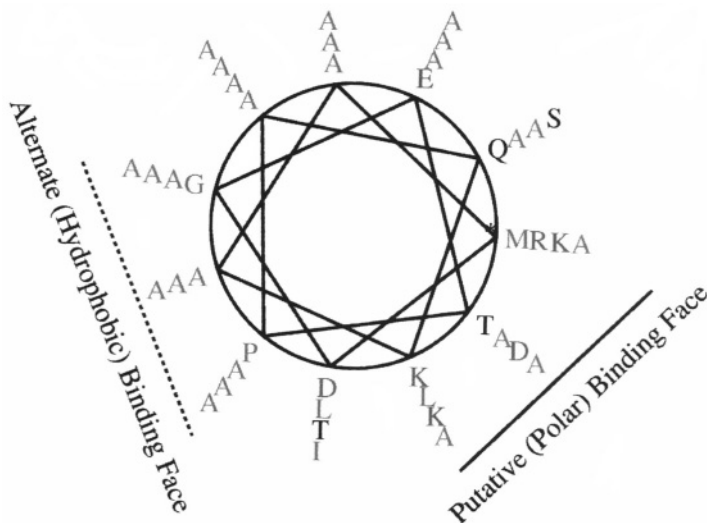
FIGURE 1.28. This figure is shows the positional relationship of shorthorn sculpin antifreeze protein residues. An asterisk marks the first residue of the sequence. The next residue in the sequence is the $i + 4$th residue going clockwise around the wheel. This helix wheel is based on a 11-residue repeat instead of the normal 18-residue repeat [170]. In this representation two binding faces are illustrated. The hydrophilic (KDK) face is indicated by the solid line while the hydrophobic face (AAA) is indicated by the dashed line.

In addition, when a comparison was made between the winter flounder AFP and shorthorn sculpin AFP results, it was observed that the backbone atoms comprising the helix fit into the surface grooves much like the threads of a bolt fitting into the threads of a nut. Unfortunately this does not appear to be the mechanism in which the AFP is interacting within the ice/water interface. Recent experimental results from mutations of the lysine seem to indicate that the lysines are not interacting with the ice in the ice/water interface [150]. In fact Davies *et al.* suggest that it is the alanine residues that are responsible for the "binding" and therefore selectivity of the ice face (see Figure 1.28). Several comments about the use of modeling calculations to substantiate the experimental results and this new hypothesis are needed. Davies *et al.* discuss using a docking simulation to determine the best

"binding" orientation without giving the details of the docking protocol [150]. Our experience with performing such calculations is that one can produce lots of possible solutions. Distinguishing between the correct and unique solution from the incorrect solutions is not possible. The suggestion of a novel N-capped helix based on a molecular mechanical model in which water has not been included is probably incorrect [150]. Based on numerous simulations of Type I AFPs in water, this structure has never been observed. It is also hard to imagine why the alanine face, in which the lysines are in a vacuum, would yield a better energy of interaction than the lysine residues interacting with the ice. It makes more sense for the lysine residues, which are charged, to interact with the ice with stronger electrostatic and hydrogen bonding interactions that the van der Waals interactions found between alanine residues and the ice. Although the lysine residues in reality may be pointing towards the water, the modeling method used by Davies *et al.* to support that hypothesis is invalid. In summary, rationalizations, based on AFP/ice–vacuum models, should not be used to explain the interactions of AFPs at the ice/water interface.

1.7.4. Ocean eel pout

The first globular antifreeze protein structure to be solved was that of the *Macrozoarces americanus* ocean eel pout [151,152]. This structure was solved by analysis of NMR data on this protein. Using this structure and the predicted ice binding plane for the (100) ice plane we performed a systematic scan of the ice surface using molecular mechanics [136]. The results of that scan are shown in Figure 1.29. Analysis of the computational results showed that the best interaction between the protein and ice occurs when the backbone of

FIGURE 1.29. An illustration of the best orientation and position of the ocean eel pout on the (001) plane of ice. The structure of the ocean eel pout antifreeze protein is represented as a ribbon structure. The blue, red, and yellow arrows represent β-strands while the green coil represents an α-helix. The blue spheres represent the oxygen positions of the water positions in ice Ih.

the protein fits into the grooves of the ice plane. These ice/vacuum results are consistent with the findings with the α-helical proteins of winter flounder and shorthorn sculpin.

1.7.5. Sea raven

The comparative modeled structure of the *Hemitripterus americanus* sea raven antifreeze protein [153] was used in our survey of ice/protein binding [137], Again we performed a systematic scan of the antifreeze protein on the ice surface. The computational results again are consistent with our previous efforts in that it is the contour fit of the protein backbone to the corrugation of the (111) ice surface (see Figure 1.30). In addition our analysis revealed strong interactions between the threonine/serine and lysine residues and the ice surface. Although no clear evidence of directionality of bonding was found for this protein, the uniqueness of binding determined by the contoured backbone fit seems to suggest that the preferred angle of binding of the protein may follow the alignment of K91–K122 vector along the bisector of the angle determined by $[10\bar{1}]$ and $[1\bar{1}0]$ surface vectors.

1.7.6. Insect AFPs

Insect AFPs are unlike the AFPs found in fish [154–168]. The beetle AFP *tenebrio molitor* and spruce budworm have thermal hysteresis that are larger than in the fish AFPs

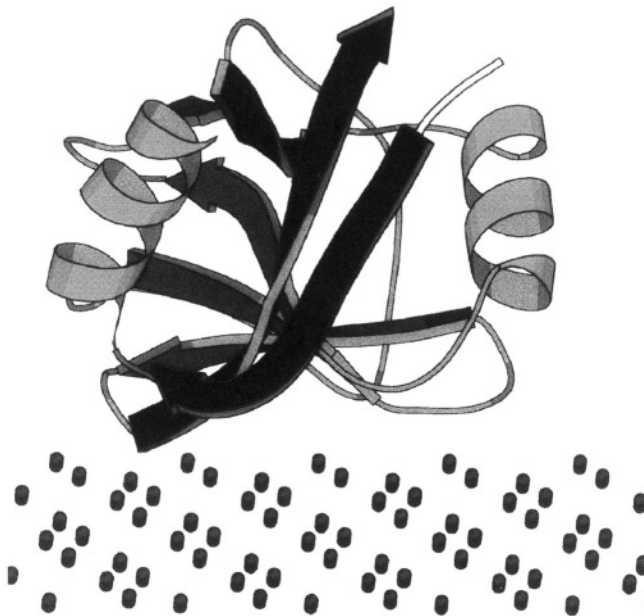FIGURE 1.30. An illustration of the best orientation and position of the sea raven antifreeze protein on the (111) plane of ice. The structure of the sea raven antifreeze protein is represented as a ribbon structure. The blue and red arrows represent β-strands while the green coil represents an α-helix. The blue spheres represent the oxygen positions of the water positions in ice Ih,
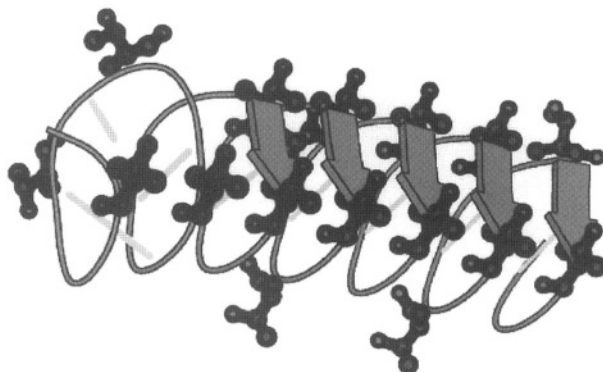
FIGURE 1.31. A ribbon representation of the *Tenebrio molitor* antifreeze protein. The red arrows represent the β-strands, the yellow lines represent the disulfide bridges, and the ball and stick representations highlight the threonine side chain positions.

discussed above. The three-dimensional structures for these AFPs have been determined [160, 164]. The crystal structure for the *tenebio molitor* is illustrated in Figure 1.31. The tertiary structure for this AFP is a right-handed β-helix while that for the spruce budworm is a left-handed β-helix. Both structures have a high percentage of threonine residues which are spaced approximately 4.5 Å apart. Davies *et al.* have used this distance to suggest that these AFPs bind to the prism face of ice or to the basal place of ice in the case of the spruce budworm AFP. The basis of this hypothesis is founded on modeling studies of the AFP at the ice–vacuum interface. What is interesting to note is that Davies *et al.* use a hydrogen-bonding hypothesis to explain the ice-etching patterns they observe and to rationalize the plane in which these proteins "bind" to ice. Yet they disprove the hydrogen bonding theory in the case of the winter flounder AFP "binding" to ice. In the winter flounder AFP situation Haymet *et al.* as well as Davies *et al.,* have demonstrated that hydrophobic interactions are dominant [149,150]. It should be clear from recent experimental work and computational studies that in order to correctly model the interactions between the AFP and ice, liquid water must be included in the calculations before any proper explanation can be made.

1.7.7.   *Modeling of binding of phopsholipid bilaylayers at crystal interfaces*

Recently we have begun molecular simulations in order elucidate the effects that an ionic crystal has on a phospholipid bilayer surface upon binding. Figure 1.32 is a snapshot from a molecular dynamics simulation of the fully solvated POPC phospholipid lipid bilayer in the presence of CPPD crystal.

1.7.8. *Brownian dynamics studies of protein adsorption*

Protein adsorption is an important application in many areas of chemistry, biology and medicine. Unfortunately the process of protein adsorption to surface is poorly understood due to the complex nature of the problem. We have started to address this issue by combining the methods of continuum electrostatic and Brownian dynamics to study the adsorption
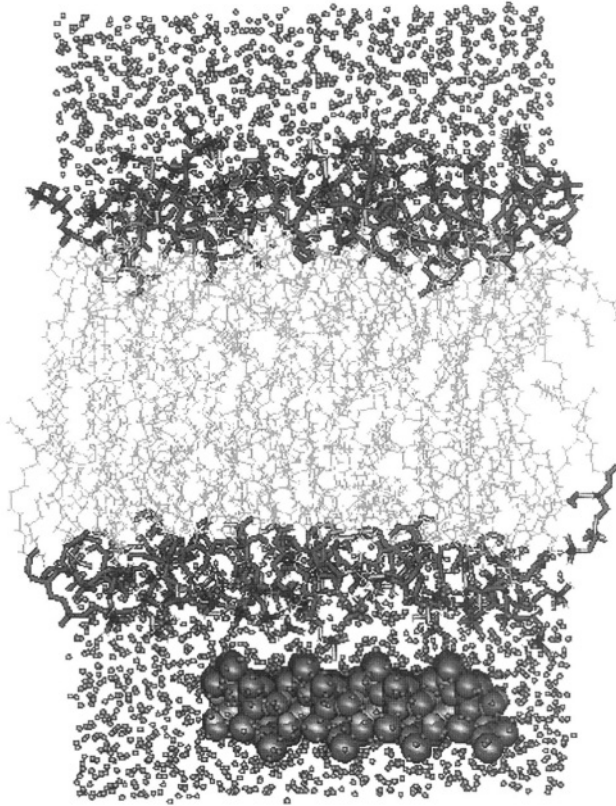
FIGURE 1.32. A snapshot from a 1 ns simulation of a lipid bilayer in contact with an ionic crystal. The ionic crystal is highlighted by van der Waal spheres. The water molecules are illustrated as small red spheres. The lipid head groups are represented as thick sticks and the lipid tails are represented as thin blue sticks.

of a protein to a charged solid surface. Earlier work in this area seemed to indicate that adsorption orientation on charged surfaces would be dictated through charge patches on the protein. However through our simulations we show that it is not the charged patches that dictated the adsorption orientation [169]. In fact one must consider the electric field around the protein. This is the best predictor of the adsorption behavior. Figure 1.33 illustrates the electric field about the protein. The blue region represents positive electrostatic field while the red region represents the negative electrostatic field. Depending on the surface charge, different regions will adsorb to the surface. These calculations were performed using a Brownian dynamics module written to work within MOE. The electrostatic calculations as well as the visualization were also performed using MOE.

ACKNOWLEDGEMENTS
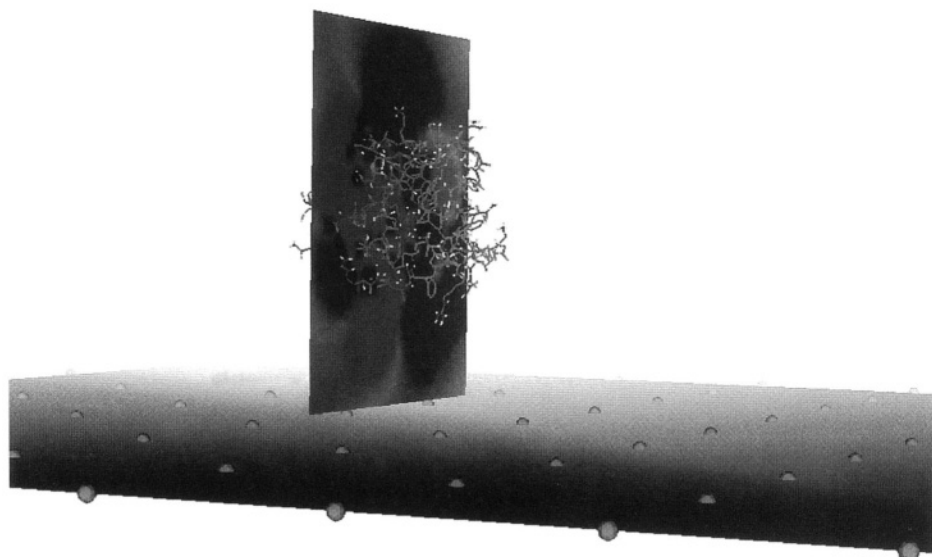
FIGURE 1.33. Lysozyme adsorption to a negatively charges mica surface. The surface is represented by the red sphere sitting within a dark colored slab. The lysozyme is drawn in the stick representation. A slice is draw through the lysozyme and the electrostatic potential (from a Poisson–Boltzmann calculation) is mapped onto the slice. The red regions of the slab represent negative potential and blue region positive potential.

REFERENCES

1. L. Addadi and S. Weiner, Control and design principles in biological mineralization, *Angew. Chem. Int. Ed. Engl.* **31**, 153–169 (1992).
2. L. Addadi and S. Weiner, Interactions between acidic proteins and crystals: stereochemical requirements in biomineralization, *Proc. Natl. Acad. Sci. USA* **82***, 4110–4114 (1985).
3. L. Addadi, J. Moradian, E. Shay, H. Maroudas and S. Weiner, A chemical model for the cooperation of sulfates and carboxylates in calcite crystal nucleation: relevance to biomineralization, *Proc. Natl. Acad. Sci. USA* **84**, 2732–2736 (1987).
4. S. Mann, B.R. Heywood, S. Rajan and J.D. Birchall, Controlled crystallization of $CaCO_3$ under stearic acid monolayers, *Nature* **334**, 692–695 (1988).
5. S. Mann and N.H.C. Sparks, Single crystalline nature of coccolith elements of the marine alga Emiliania huxleyi as determined by electron diffraction and high-resolution transmission electron microscopy, *Proc. R. Soc. Lond. B* **234**, 441–453 (1988).
6. S. Mann, J.M. Didymus, N.P. Sanderson, B.R. Heywoodj and E.J.A. Samper, Morphological influence of functionalized and non-functionalized α, ω-dicarboxylates on calcite crystallization, *J. Chem. Soc. Faraday Trans.* **86**, 1873–1880 (1990).

7. A. Berman, L. Addadi and S. Weiner, Interactions of sea-urchin skeleton macromolecules with growing calcite crystals—a study of intracrystalline proteins, *Nature* **331**, 546–548 (1988).

8. A. Berman, L. Addadi, A. Kvick, L. Leiserowitz, M. Nelson and S. Weiner, Intercalation of sea urchin proteins in calcite: study of a crystalline composite material, *Science* **250**, 664–667 (1990).

9. A. Herman, J. Hanson, L. Leiserowitz, T.F. Koetzle, S. Weiner and L. Addadi, Biological control of crystal texture: a widespread strategy for adapting crystal properties to function, *Science* **259**, 776–779 (1993).

10. A.P. Wheeler, K.W. Rusenko, J.W. George and C.S. Sikes, Evaluation of calcium binding by molluscan shell organic matrix and its relevance to biomineralization, *Comp. Biochem. Physiol.* **87B**, 953–960 (1987).

11. A.P. Wheeler and C.S. Sikes, Matrix–crystal interactions in $CaCO_3$ biomineralization, in: *Biomineralization: Chemical and Biochemical Perspectives,* Ed. R.J.P. Williams (VCH, Weinheim, 1989) p. 95.

12. A. Wierzbicki, C.S. Sikes, J.D. Madura and B. Drake, Atomic force microscopy and molecular modeling of protein and peptide binding to calcite, *Calcified Tissue International* **54**, 133–141 (1994).

13. K.W. Rusenko, J.E. Donachy and A.P. Wheeler, Purification and characterization of a shell matrix phospho-protein from the American Oyster, in: *Surface Reactive Peptides and Polymers: Discovery and Commercialization,* Ed. A.P. Wheeler (ACS Books, Washington, DC, 1991) p. 107.

14. J.E. Borbas, A.P. Wheeler and C.S. Sikes, Molluscan shell matrix phosphoproteins: correlation of degree of phosphorylation to shell mineral microstructure and to in vitro regulation of mineralization, *J. Exp. Zool.* **258**, 1–13(1991).

15. J.E. Donachy, B. Drake and C.S. Sikes, Sequence and atomic force microscopy analysis of matrix protein from the shell of the oyster Crassostrea virginica, *Mar. Biol.* **114**, 423–28 (1992).

16. J.P. Gorski, Acidic phosphoproteins from bone matrix: a structural rationalization of their role in biomineralization, *Calcif. Tissue Int.* **50**, 391–396 (1992).

17. C.S. Sikes and A.P. Wheeler, Regulators of biomineralization, *CHEMTECH* **18**, 620–626 (1988).

18. E.M. Mueller and C.S. Sikes, Adsorption and modification of calcium salt crystal growth by anionic peptides and spermine, *Calcif. Tissue Int.* **52***, 34–41 (1993).

19. J.P. Garris and C.S. Sikes, Use of polyamino acid analogs of biomineral proteins in dispersion of inorganic particulates important to water treatment, *Colloids and Surfaces* **80**, 103–112 (1993).

20. C.S. Sikes, E.M. Mueller, J.D. Madura, B. Drake and B.J. Little, Polyamino acids as antisealants, corrosion inhibitors, and dispersants: atomic force microscopy and mechanisms of action, *Corrosion* **93** (paper 465), 1–21 (1993).

21. C.S. Sikes, M.L. Yeung and A.P. Wheeler, Inhibition of calcium carbonate and phosphate crystallization by peptides enrichedin aspartic acid and phosphoserine, in: *Surface Reactive Peptides and Polymers: Discovery and Commercialization,* Ed. A.P. Wheeler (ACS Books, Washington, 1991) p. 50.

22. L. Addadi and S. Weiner, Interactions between acid macromolecules and structured crystal surfaces. Stereochemistry and biomineralization, *Mol. Cryst. Liq. Cryst.* **134**, 305–322 (1986).

23. QUANTA molecular modeling software (Molecular Simulations Inc., Burlington, MA, 1994).

24. CERIUS molecular modeling software for materials research (Molecular Simulations Inc., Burlington, MA, and Cambridge, UK, 1994).

25. F. Lippmann, *Sedimentary Carbonate Minerals* (Spriger-Verlag, New York, 1973).

26. CHARMm molecular modeling software (Molecular Simulations Inc., Burlington, MA, 1994).

27. A.P. Wheeler, K.C. Low and C.S. Sikes, $CaCO_3$ crystal-binding properties of peptides and their influence on crystal growth, in: *Surface Reactive Peptides and Polymers: Discovery and Commercialization,* Ed. A.P. Wheeler (ACS Books, Washington, 1991) p. 72.

28. H. Lowenstam and S. Weiner, *On Biomineralization* (Oxford Press, New York, 1989).

29. B. Drake, R. Hellman, C.S. Sikes and M.L. Occelli, Atomic scale imaging of albite feldspar, calcium carbonate, rectonte, and bentonite using atomic force microscopy, *SPIE Proc.* **1639**, 151–159 (1992).

30. G. Friedbacher, P.K. Hansma, E. Ramli and G.D. Stocky, Imaging powders with the atomic force microscope: from biominerals to commercial materials, *Science* **253**, 1261–1263 (1991).

31. Y. Kirn and C.M. Lieber, Machining oxide thin films with an atomic force microscopy: pattern and object formation on the nanometer scale, *Science* **257**, 375–377 (1992).

32. A. Wierzbicki, C.S. Sikes, J.D. Sallis, J.D. Madura, E.D. Stevens and K.L. Martin, Scanning electron microscopy and molecular modeling of calcium oxalate monohydrate crystal growth inhibition by citrate and phosphocitrate, *Calcified Tissue International* **56**, 297–304 (1995).

33. H.-G. Tiselius, C. Berg, A.-M. Fornander and M.-A. Nilsson, Effects of citrate on the different phases of calcium oxalate crystallization, *Scanning Microscopy* **7**, 381–390 (1993).

34. J.D. Sallis, M.R. Brown and N.M. Parker, Phosphorylated and nonphosphorylated carboxylic acids, influence of group substitution and comparison of compounds to phosphocitrate with respect to inhibition of calcium salt crystallization, in: *ACS Symposium Series—Surface Reactive Peptides and Polymers,* Ed. A.P. Wheeler (American Chemical Society Pub., Washington, 1990) pp. 149–160.

35. H.J. Arnott, Three systems of biomineralization in plants with comments on the associated organic matrix, in: *Biological Mineralization and Demineralization,* Ed. G.H. Nancollas (Springer-Verlag, New York, 1982) pp. 199–218.

36. K. Simkiss and K.M. Wilbur, *Biomineralization, Cell Biology and Mineral Deposition* (Academic Press Inc., New York, 1989).

37. H.A. Lowenstam, Mineralization processes in monerans and protoctists, *Syst. Assoc. Spec.* **30,** 345–360 (1986).

38. J. Moradian-Oldak, F. Frolow, L. Addadi and S. Weiner, Interactions between acidic matrix macromolecules and calcium phosphate ester crystals: relevance to carbonate apatite formation in biomineralization, *Proc. R. Soc. Lond. B* **247**, 47–55 (1992).

39. S.N. Black, L.A. Bromley, D. Cottier, R.J. Davey, B. Dobbs and J.E. Rout, Interactions at the organic/inorganic interface: binding motifs for phosphonates at the surface of barite crystals, *J. Chem. Faraday Trans.* **87**, 3409–3414(1991).

40. S. Deganello and O.E. Piro, The crystal structure of calcium oxalate monohydrate (Whewellite), *N. Jb. Miner.* **2**, 81–88(1981).

41. S. Deganello, Interaction between nephrocalcin and calcium oxalate monohydrate: a structural study, *Calcified Tissue International* **48**, 421–428 (1991).

42. J.D. Madura, A. Wierzbicki, J.P. Harrington, R.H. Maughon, J.A. Raymond and C.S. Sikes, Interactions of the D- and L-forms of winter flounder antifreeze peptide with the (201) planes of ice, *JACS* **116**, 417–418 (1994).

43. V. Tazzoli and C. Domeneghetti, The crystal structures of whewellite and weddellite: re-examination and comparison, *American Mineralogist* **65,** 3027–3034 (1980).

44. J.P. Glusker, Citrate conformation and chelation: enzymatic implications, *Acc. Chem. Res.* **13**, 345–352 (1980).

45. L.E. Chirlian and M.M. Francl, Atomic charges derived from electrostatic potentials: a detailed study, *J. Computational Chem.* **8**, 894–905 (1987).

46. C.M. Breneman and K.B. Wiberg, Determining atom-centered monopoles from molecular electrostatic potentials: the need for high sampling density in formamide conformational analysis, *J. Computational Chem.* **11**, 361–373 (1990).

47. SPARTAN (Wavefunction Inc., Irvine, CA, 1994).

48. Gaussian92 (Gaussian Inc., Pittsburgh, PA, 1992).

49. A. Wierzbicki, J.D. Sallis, E.D. Stevens, M. Smith and C.S. Sikes, Crystal growth and molecular modeling studies of inhibition of struvite by phosphocitrate, *Calcified Tissue International* **61,** 216–222 (1997).

50. C. Palache, H. Berman and C. Frondel, *The System of Mineralogy of James Dwight Dana and Edward Salisbury Dana,* 7th edn, Vol. II (John Wiley & Sons, New York, 1951).

51. F. Abbona and R. Boistelle, Growth morphology and crystal habit of struvite crystals $(MgNH_4PO_4 \times 6H_2O)$, *Journal of Crystal Growth* **46**, 339–354 (1979).

52. D.P. Griffith, Struvite stones, *Kidney Int.* **13**, 372–382 (1978).

53. Y.M.F. Marickar and P. Koshy, Scanning electron microscopic study of effect of various agents on urine crystal morphology, *Scanning Microscopy* **1**, 571–577 (1987).

54. D.P. Griffith, J.R. Gibson, C.W. Clinton and D.M. Musher, Acetohydroxamic acid: clinical studies of a urease inhibitor in patients with staghorn renal calculi, *J. Urol.* **119**, 9–15 (1978).

55. J.A. Downey, J.C. Nickel, L. Clapham and R.J.C. McLean, In vitro inhibition of struvite crystal growth by acetohydroxamic acid, *British J. Urology* **70**, 355–359 (1992).

56. G. Williams and J.D. Sallis, The sources of phosphocitrate and its influential role in inhibiting calcium phosphate and calcium oxalate crystallization, in: *Urolithiasis, Clinical and Basic Research,* Ed. B. Finlayson (Plenum Press, New York, 1981) pp. 569–577.

57. J.D. Sallis, R. Thomson, B. Rees and R. Shankar, Reduction of infection stones in rats by combined antibiotic and phosphocitrate therapy, *J. Urol.* **140**, 1063–1066(1988).

58. W.P. Tew, C. Mahle, J. Benavides, J.E. Howaro and A.L. Lehninger, Synthesis and characterization of phosphocitrate, a potent inhibitor of hydroxylapatite growth, *Biochemistry* **19**, 1983–1988 (1980).

59. G. Williams and J.D. Sallis, Structural factors influencing the ability of compounds to inhibit hydroxyapatite formation, *Calcified Tissue International* **34**, 169–177 (1982).

60. J.D. Sallis, N.F.G. Parry, J.D. Meehan, H. Kamperman and M.E. Anderson, Controlling influence of phosphocitrate in vitro and in vivo on calcium oxalate crystal formation and growth, *Scanning Microscopy* **9**, 127–136(1995).

61. J.D. Sallis, W. Juckes and M.E. Anderson, PC; potential to influence deposition of scaling salts and corrosion, in: *Mineral Scale Formation and Inhibition,* Ed. Z. Amjad (Plenum Press, New York, 1995) pp. 87–98.

62. G. Ferraris, Neutron diffraction study of $MgNH_4PO_4 \times 6H_2O$ (struvite) and survey of water molecules donating short hydrogen bonds, *Acta Crystallographica* **B42**, 253–258 (1986).

63. *Cerius^2 Molecular Modeling Software for Materials Research* (Molecular Simulations Inc., San Diego, CA, 1997).

64. A.K. Rappe and W.A. Goddard, III, Charge equilibration for molecular mechanics simulations, *J. Phys. Chem.* **95**, 3358–3363(1991).

65. A. Wierzbicki, M.S. Taylor, C.A. Knight, J.D. Madura, J.P. Harrington and C.S. Sikes, Analysis of shorthorn sculpin antifreeze protein stereospecific binding to (2–10) faces of ice, *Biophysical Journal* **71**, 8–18 (1996).

66. B.A. Frenz, *CAD-4 Software* (Enraf-Nonius, Delft, The Netherlands, 1989).

67. L.H. Wills, J.D. Sallis and M.E. Smith, In vitro prevention of struvite encrustation on catheter material with phosphocitrate, in: *Urolithiasis 1996,* Ed. G.M. Preminger (Millet the Printer, Inc., Dallas, 1996) pp. 234–235.

68. A. Wierzbicki and H.S. Cheung, Molecular modeling of inhibition of crystals of calcium pyrophosphate dihydrate by phosphocitrate, *Journal of Molecular Structure THEOCHEM* **454**, 287–297 (1998).

69. L.M. Ryan and D.J. McCarty, Calcium phosphate crystal deposition disease, pseudogout, and articular chondrocalcinosis, in: *Arthritis and Allied Conditions,* Ed. W.J. Koopman (Williams and Wilkins, Baltimore, 1997) pp. 2103–2125.

70. P.B. Halverson and D.J. McCarty, Basic calcium phosphate (apatite, octacalcium phosphate, tricaclium phosphate) crystal deposition diseases; calcinosis, in: *Arthritis and Allied Conditions,* Ed. W.J. Koopman (Williams and Wilkins, Baltimore, 1997) pp. 2127–2146.

71. H.S. Cheung and L.M. Ryan, Role of crystal deposition in matrix degradation, in: *Cartilage Degradation: Basic Research and Clinical Implication,* Ed. D.S. Howell (Marcel Dekker Inc., New York, 1993) pp. 209–223.

72. W.P. Tew, C.D. Mails, J.E. Howard and A.L. Lehninger, Phosphocitrate inhibits mitochondrial and cytosolic accumulation of calcium in kidney cells in vivo, *Proc. Natl. Acad. Sci. USA* **78**, 5528–5532 (1981).

73. J.E. Howard, Studies on urinary stone formation: a saga of clinicalinvestigation, *Johns Hopkins Med. J.* **139**, 239–252(1976).

74. M.R. Brown and J.D. Sallis, N-sulpho-2-amino tricarballylate, a new analogue of phosphocitrate metabolic studies and inhibitory effect on renal calcification, in: *Urolithiasis and Related Clinical Research,* Ed. W. Vahlensieck (Plenum Press, New York, 1985) pp. 891–894.

75. R. Shankar, S. Crowden and J.D. Sallis, Phosphocitrate and its analogue N-sulpho-2-amino tricarballylate inhibit aortic calcification, *Atherosclerosis* **50**, 191–198 (1985).

76. W.P. Tew, C.D. Mahle, J. Benavides, J.E. Howard and A.L. Lehninger, Synthesis and characterization of phosphocitric acid, a potent inhibitor of hydroxylapatite crystal growth, *Biochemistry* **19**, 1983–1988(1980).

77. H.S. Cheung, I.V. Kurup, J.D. Sallis and L.M. Ryan, Inhibition of calcium pyrophosphate dihydrate crystal formation in articular cartilage vesicles and cartilage by phosphocitrate, *J. Biol. Chem.* **271**, 28082–28085 (1996).

78. N.S. Mandel, The crystal structure of calcium pyrophosphate dihydrate, *Acta Cryst.* **B31**, 1730–1734 (1973).

79. G.S. Mandel, K.M. Renne, A.M. Kolbach, A.M. Kaplan, J.D. Millerr and N.S. Mandel, Calcium pyrophosphate crystal deposition disease—preparation and characterization of crystals, *J. Crystal Growth* **87**,453–462 (1988).

80. T. Shinozaki, Y. Xu, T.F. Cruz and K.P.H. Pritzker, Calcium pyrophosphate dihydrate (CPPD) crystal dissolution by alkaline phosphatase: interaction of alkaline phosphatase on CPPD crystals, *J. Rheum.* **22**, 117–123 (1995).

81. T. Shinozaki and K.P.H. Pritzker, Polyamines enhance calcium pyrophosphate dihydrate crystal dissolution, *J. Rheum.* **22**, 1907–1912 (1995).

82. D. Nair, R.P. Misra, J.D. Sallis and H.S. Cheung, Phosphocitrate inhibits a basic calcium phosphate and calcium pyrophosphate dihydrate crystal-induced mitogen-activated protein kinase cascade signal transduction pathway, *J. Biol. Chem.* **272**, 18920–18925 (1997).

83. H.S. Cheung, J.D. Sallis and J.A. Struve, Specific inhibition of basic calcium phosphate and calcium pyrophosphate crystal-induction of metalloproteinase synthesis by phosphocitrate, *Biochim. et Biophys. Acta* **1315**, 105–111 (1996).

84. A.M. Davidson and A.P. Halestrap, Liver mitochondrial pyrophosphate concentration is increased by Ca^{2+} and regulates the intramitochondrial volume and adenine nucleotide content, *Biochem. J.* **246**, 715–723 (1987).

85. H.E. Krug, M.L. Mahowald, P.B. Halverson, J.D. Sallis and H.S. Cheung, Phosphocitrate prevents disease progression in murine progressive ankylosis, *Arthritis Rheum.* **36**, 1603–1611 (1993).

86. A. Wierzbicki and H.S. Cheung, Molecular modeling of inhibition of hydroxyapatite by phosphocitrate, *Journal of Molecular Structure THEOCHEM* **529**, 73–82 (2000).

87. F.C.M. Driessens and R.M.H. Verbeek, *Biominerals* (CRC, Boca Raton, FL, 1990).

88. N.S. Mandel and G.S. Mandel, Urinary tract stone disease in the United States veteran population. II. Geographical analysis of variations in composition, *J. Urol.* **142**, 1516–1521 (1989).

89. I. Hojgaard and H.G. Tiselius, The effects of citrate and urinary macromolecules on the aggregation of hydroxyapatite crystals in solutions with a composition similar to that in the distal tubule, *Urol. Res.* **26**, 89–95(1998).

90. J.C. Lieske, R. Norris and F.G. Toback, Adhesion of hydroxiapatite crystals to anionic sites on the surface of renal epithelial cells, *American Journal of Physiology* **273**, F224-F232 (1997).

91. M.I. Kay, R.A. Young and A.S. Posner, Crystal structure of hydroxyapatite, *Nature* **204**, 1050–1052 (1964).

92. *Cerius*^{2} *Molecular Modeling Software for Materials Research* (Molecular Simulations, Inc., San Diego, CA, 1999).

93. M.C. Payne, M.P. Teter, D.C. Allan, T.A. Arias and J.D. Joannopoulos, Iterative minimization techniques for ab initio total-energy calculations: Molecular dynamics and conjugate gradients, *Rev. Mod. Phys.* **64**, 1045–1097(1992).

94. J.P. Perdew, J.A. Chevary, S.H. Vosko, K.A. Jackson, M.R. Pederson, D.J. Singh and C. Fiolhais, Atoms, molecules, solids, and surfaces: applications of the generalized gradient approximation for exchange and correlation, *Physical Review B* **46**, 6671–6687 (1992).

95. J.M. Hughes, M. Cameron and K.D. Crowley, Structural variations in natural F, OH, and Cl apatites, *American Mineralogist* **74**, 870–876 (1989).

96. J.C. Lieske, R. Leonard, H. Swift and F.G. Toback, Adhesion of calcium oxalate monohydrate crystals to anionic sites on the surface of renal epithelial cells, *American Journal of Physiology* **270**, F192–F199 (1996).

97. E. Bertoni, A. Bigi, G. Falini, S. Panzavolta and N. Roveri, Hydroxyapatite polyacrylic acid nanocrystals, *Journal of Materials Chemistry* **9**, 779–782 (1999).

98. Q. Luo and J.D. Andrade, Cooperative adsorption of proteins onto hydroxyapatite, *Journal of Colloid and Interface Science* **200**, 104–113 (1998).

99. A. Barroug, E. Lerhoux, J. Lemaitre and P.J. Rouxhet, Adsorption of catalase on hydroxyapatite, *Journal of Colloid and Interface Science* **208**, 147–152(1998).

100. D. Zitnan and S. Sitaj, Natural course of articular chondrocalcinosis. *Arthritis Rheum.* **19**, 363–390 (1976).

101. E. Bertoni, A. Biggi, G. Cojazzi, M. Gandolfi, S. Panzavolta and N. Roveri, Nanocrystals of magnesium and fluoride substituted hydroxyapatite, *Journal of Inorganic Biochemistry* **72**, 29–39 (1998).

102. R.S. Kaplan, J.A. Mayor, D.A. Gremse and D.O. Wood, High level expression and characterization of the mitochondrial citrate transport protein from the yeast Saccharomyces cerevisiae, *J. Biol. Chem.* **270**, 4108–4114(1995).

103. P.F. Scholander, L.V. Dam, J. Kanwisher, T. Hammel and M.S. Gordon, Supercooling and osmoregulation in Arctic fish, *J. Cell. Compar. Physiol.* **49**, 5–24 (1957).

104. A.L. DeVries, Glycoproteins as biological antifreeze agents in antarctic fishes, *Science* **172**(3988), 1152–1155(1971).

105. R.E. Feeney, Biological antifreeze, *Am. Set.* **62**(6), 712–719 (1974).

106. A.L. DeVries, Antifreeze peptides and glycopeptides in cold-water fishes, *Annu. Rev. Physiol.* **45**, 245–260 (1983).

107. A.R. Leach, *Molecular Modelling: Principles and Applications* (Prentice-Hall, Harlow, 2001)

108. A.K. Rappe and C.J. Casewit, *Molecular Mechanics Across Chemistry* (University Science Books, Sausalito, 1997).

109. B.R. Brooks, R.E. Bruccoleri, B.D. Olafson, D.J. States, S. Swaminathai and M. Karplus, CHARMM: a program for macromolecular energy, minimization, and dynamics calculations, *J. Comp. Chem.* **4**, 187 (1983).

110. S.J. Weiner, P.A. Kollman, D.A. Case, U.C. Singh, C. Ohio, G. Alagona, S. Profeta and P. Weiner, A new force field for molecular mechanical simulation of nucleic acids and proteins, *J. Am. Chem. Soc.* **106**, 765–784 (1984).

111. W.D. Cornell, P. Cieplak, C.I. Bayly, I.R. Gould, J.K.M. Merz, D.M. Ferguson, D.C. Spellmeyer, T. Fox, J.W. Caldwell and P.A. Kollman, A second generation force field for the simulation of proteins, nucleic acids, and organic molecules, *J. Am. Chem. Soc.* **117**, 5170–5197 (1995).

112. L.D. Schuler, X. Daura and W.F.v. Gunsteren, An improved GROMOS96 force field for aliphatic hydrocarbons in the condensed phase, *J. Comp. Chem.* **22**, 1205–1218 (2001).

113. N.L. Allinger, Y.H. Yuh and J.-H. Lii, Molecular mechanics. The MM3 force field for hydrocarbons. 1, *J. Am. Chem. Soc.* **111**, 8551 (1989).

114. A.K. Rappe, C.J. Casewit, K.S. Colwell, I.W.A. Goddard and W.M. Skiff, UFF, a full periodic table force field for molecular mechanics and molecular dynamics simulations, *J. Am. Chem. Soc.* **114**, 10024–10035 (1992).

115. P. Dauber-Osguthorpe, V.A. Roberts, D.J. Osguthorpe, J. Wolff, M. Genest and A.T. Hagler, Structure and energetics of ligand binding to proteins: E. coli dihydrofolate reductase-trimethoprim, a drug-receptor system, *Proteins: Structure, Function, and Genetics* **4**, 31–47 (1988).

116. M. Clark, I.R.D. Cramer and N.V. Opdenbosch, Validation of the general purpose Tripos 5.2 force field, *J. Comp. Chem.* **10**, 982 (1989).

117. T.A. Halgren, Merck molecular force field I. Basis, form, scope, parameterization, and performance of MMFF94, *J. Comp. Chem.* **17**, 490 (1996).

118. S.L. Mayo, B.D. Olafson and I.W.A. Goddard, DREIDING: a generic force field for molecular simulations, *J. Phys. Chem.* **94**, 8897 (1990).

119. C.L. Brooks, III, M. Karplus and B.M. Pettitt, Proteins: a theoretical perspective of dynamics, structure, and thermodynamics, *Advances in Chemical Physics,* Ed. S. Rice, Vol. LXXI (Wiley, New York, 1988).

120. J.A. McCammon and S.C. Harvey, *Dynamics of Proteins and Nucleic Acids* (Cambridge University Press, Cambridge, 1987).

121. M. Maruyama, T. Satoi, S. Taniguchi, M. Kawamura, S. Kodera, Y. Kishimoto and Y. Furukawa, X-ray analysis of the structure of premelted layers at ice interfaces, *Jpn. J. Appl. Phys., Part 1* **39** (12A), 6696–6699 (2000).

122. Y. Furukawa, T. Ishizaki, I. Ishikawa and M. Maruyama, Experimental study on the melting transition at interface between ice crystal and substrate, *Struct. Surf. IV, Proc. Int. Conf., 4th,* 511–516 (1994).

123. H. Guettinger, J.H. Bilgram and W. Kaenzig, Dynamic light scattering at the ice water interface during freezing, *J. Phys. Chem. Solids* **40**(1), 55–66 (1979).

124. C.M. Bouchez and J.M. Hicks, Second harmonic generation studies of the ice/water interface, *Proc. SPIE— Int. Soc. Opt. Eng.* **2547**(Laser Techniques for Surface Science II), 152–163 (1995).

125. L.A. Baez and P. Clancy, Phase equilibria in extended simple point charge ice-water systems, *J. Chem. Phys.* **103**(22), 9744–9755 (1995).

126. A.D.J. Haymet, Solvation, freezing, and the crystal/liquid interface: modern theories and computer simulation, *Fluid Phase Equilib.* **83**, 415–126 (1993).

127. J.A. Hayward and A.D.J. Haymet, The ice/water interface: molecular dynamics simulations of the basal, prism, {2021}, and {2110} interfaces of ice Ih, *J. Chem. Phys.* **114**(8), 3713–3726 (2001).

128. O.A. Karim and A.D.J. Haymet, The ice/water interface, *Chem. Phys. Lett.* **138**(6), 531–534 (1987).

129. O.A. Karim and A.D.J. Haymet, The ice/water interface: a molecular dynamics simulation study, *J. Chem. Phys.* **89**(11), 6889–6896 (1988).

130. O.A. Karim, P.A. Kay and A.D.J. Haymet, The ice/water interface: a molecular dynamics simulation using the simple point charge model, *J. Chem. Phys.* **92**(7), 4634–4635 (1990).

131. H. Nada and Y. Furukawa, Anisotropic properties of ice/water interface: a molecular dynamics study, *Jpn. J. Appl. Phys., Part 1* **34**(2A), 583–588 (1995).

132. H. Nada, Growth kinetics at ice–water interfaces: a molecular dynamics simulation study, *Int. Conf. Nat. Gas Hydrates, 2nd,* 363–370 (1996).

133. H. Nada and Y. Furukawa, Molecular dynamics study of ice–water interface structures, *Nippon Kessho Sei-cho Gakkaishi* **23**(3), 228 (1996).

134. R.M. Pratt and E.D. Sloan, Jr., A computer simulation and investigation of liquid–solid interfacial phenomena for ice and clathrate hydrates, *Mol. Simul.* **15**(4), 247–264 (1995).

135. T. Yazaki, S. Okawa and A. Saito, Molecular dynamics simulation study of ice crystal growth, *Nippon Reito Kucho Gakkai Ronbunshu* **14**(2), 179–190 (1997).

136. J.D. Madura, M.S. Taylor, A. Wierzbicki, J.P. Harrington, C.S. Sikes and F. Sooennichsen, The dynamics and binding of a type III antifreeze protein in water and on ice, *Theochem.* **388**, 65–77 (1996).

137. A. Wierzbicki, J.D. Madura, C. Salmon and F. Soennichsen, Modeling studies of binding of sea raven type II antifreeze protein to ice, *J. Chem. Inf. Comput. Sci.* **37**(6), 1006–1010 (1997).

138. P. Dalal, J. Knickelbein, A.D.J. Haymet, F.D. Sonnichsen and J.D. Modura, Hydrogen bond analysis of Type 1 antifreeze protein in water and the ice/water interface, *Phys. Chem. Comm.,* Paper No. 7 (2001).

139. J.D. Madura, K. Baran and A. Wierzbicki, Molecular recognition and binding of thermal hysteresis proteins to ice, *J. Mol. Recognit.* **13**(2), 101–113 (2000).

140. J.S. Hong, D.H. Jung and M.S. Jhon, Molecular dynamics study on winter flounder antifreeze protein and its binding mechanism, *Mol. Simul* **20**(5), 303–314 (1998).

141. A. Cheng and K.M. Merz, Jr., Ice-binding mechanism of winter flounder antifreeze proteins, *Biophys. J.* **73**(6), 2851–2873 (1997).

142. C.A. Brooke-Taylor, G.H. Grant, A.H. Elcock and W.G. Richards, Mechanism of action of antifreeze polypeptide HPLC6 in solution: analysis of solvent behavior by molecular dynamics, *Chem. Phys.* **204**(2, 3), 251–261 (1996).

143. S.M. McDonald, A. White, P. Clancy and J.W. Brady, Binding of an antifreeze polypeptide to an ice/water interface via computer simulation, *AIChE J.* **41**(4), 959–973 (1995).

144. H. Jorgensen, M. Mori, H. Matsui, M. Kanaoka, H. Yanagi, Y. Yabusaki and Y. Kikuzono, Molecular dynamics simulation of winter flounder antifreeze protein variants in solution: correlation between side chain spacing and ice lattice, *Protein Eng.* **6**(1), 19–27 (1993).

145. S.M. McDonald, J.W. Brady and P. Clancy, Molecular dynamics simulations of a winter flounder "Antifreeze" polypeptide in aqueous solution, *Biopolymers* **33**(10), 1481–1503 (1993).

146. D. Wen and R.A. Laursen, A model for binding of an antifreeze polypeptide to ice, *Biophys. J.* **63**(6), 1659–1662 (1992).

147. P. Dalai and F.D. Soennichsen, Source of the ice-binding specificity of antifreeze protein type I, *J. Chem. Inf. Comput. Sci.* **40**(5), 1276–1284 (2000).

148. A.D.J. Haymet, L.G. Ward, M.M. Harding and C.A. Knight, Valine substituted winter flounder 'antifreeze': preservation of ice growth hysteresis, *FEBS Lett.* **430**(3), 301–306 (1998).

149. A.D.J. Haymet, L.G. Ward and M.M. Harding, Hydrophobic analogues of the winter flounder 'antifreeze' protein, *FEBS Lett.* **491**(3), 285–288 (2001).

150. J. Baardsnes, M. Jelokhani-Niaraki, L.H. Kondejewski, M.J. Kuiper, C.M. Kay, R.S. Hodges and PL. Davies, Antifreeze protein from shorthorn sculpin: identification of the ice-binding surface, *Protein Science* **10**(12), 2566–2576 (2001).

151. F.D. Soennichsen, B.D. Sykes, H. Chao and P.L. Davies, The nonhelical structure of antifreeze protein type III, *Science (Washington, D.C., I883–)* **259**(5098), 1154–1157 (1993).

152. F.D. Soennichsen, C.I. DeLuca, P.L. Davies and B.D. Sykes, Refined solution structure of type III antifreeze protein: hydrophobic groups may be involved in the energetics of the protein-ice interaction, *Structure (London)* **4**(11), 1325–1337 (1996).

153. F.D. Sonnichsen, B.D. Sykes and P.L. Davies, Comparative modeling of the three-dimensional structure of type II antifreeze protein, *Protein Sci.* **4**(3), 460–471 (1995).

154. J.G. Baust, R.R. Rojas and M.D. Hamilton, Life at low temperatures: representative insect adaptations, *Cryo-Lett.* **6**(3), 199–210(1985).

155. C.-H.C. Cheng, Evolution of the diverse antifreeze proteins, *Curr. Opin. Genet. Dev.* **8**(6), 715–720 (1998).

156. D. Doucet, M.G. Tyshenko, M.J. Kuiper, S.P. Graether, B.D. Sykes, A.J. Daugulis, P.L. Davies and V.K. Walker, Structure–function relationships in spruce budworm antifreeze protein revealed by isoform diversity, *Eur. J. Biochem,* **267**(19), 6082–6088 (2000).

157. D. Doucet, M.G. Tyshenko, P.L. Davies and V.K. Walker, A family of expressed antifreeze protein genes from the moth, Choristoneura fumiferana, *European Journal of Biochemistry* **269**(1), 38–46 (2002).

158. J.G. Duman, Change in overwintering mechanism of the Cucujid beetle, Cucujus clavipes, *J. Insect Physiol.* **30**(3), 235–239 (1984).

159. Y.-b. Fei, Y. Jiang and S.-h. Zhao, Advances in insect antifreeze protein research, *Kunchong Xuebao* **43**(1), 98–102 (2000).

160. S.P. Graether, M.J. Kuiper, S.M. Gagne, V.K. Walker, Z. Jia, B.D. Sykes and P.L. Davies, Beta-helix structure and ice-binding properties of a hyperactive antifreeze protein from an insect, *Nature (London)* **406**(6793), 326–328 (2000).

161. K.L. Horwath and J.G. Duman, Induction of antifreeze protein production by juvenile hormone in larvae of the beetle, Dendroides canadensis, *J. Comp. Physiol.* **151**(2), 233–240 (1983).

162. T. Huang, Expression of insect, Dendroides canadensis, antifreeze proteins in Arabidopsis and cloning of a thermal hysteresis (antifreeze) protein gene in Solanum dulcamara, in: *Univ. Notre Dame, USA* (2000) 129 pp.

163. Y.-C. Liou, Hyperactive insect antifreeze protein from the beetle, tenebrio molitor: from isolation to structure determination, in: *Queen's Univ., Kingston, ON, Can.* (2000) 172 pp.

164. Y.-C. Liou, P.L. Davies and Z. Jia, Crystallization and preliminary X-ray analysis of insect antifreeze protein from the beetle Tenebrio molitor, *Acta Crystallogr., Sect. D: Biol. Crystallogr.* D**56**(3), 354–356 (2000).

165. J.L. Patterson and J.G. Duman, Composition of a protein antifreeze from larvae of the beetle, Tenebrio molitor, *J. Exp. Zool.* **210**(2), 361–367 (1979).

166. M.G. Tyshenko, D. Doucet, P.L. Davies and V.K. Walker, The antifreeze potential of the spruce budworm thermal hysteresis protein, *Nat. Biotechnol.* **15**(9), 887–890 (1997).

167. V.K. Walker, M.J. Kuiper, M.G. Tyshenko, D. Doucet, S.P. Graether, Y.-C. Liou, B.D. Sykes, Z. Jia, P.L. Davies and L.A. Graham, Surviving winter with antifreeze proteins: studies on budworms and beetles, *Insect Timing: Circadian Rhythmicity Seas. [Three Symp.]* (2001) pp. 199–211.

168. D.W. Wu, Structure–function relationships of insect antifreeze proteins, in: *Univ. Notre Dame, Notre Dame, IN, USA* (1991) 187pp.

169. S. Ravichandran, J.D. Madura and J. Talbot, A Brownian dynamics study of the initial stages of hen egg-white lysozyme adsorption at a solid interface, *J. Phys. Chem. B* **105**, 3610–3613 (2001).

170. E.G. Hutchinson and J.M. Thornton, PROMOTIF—a program to identify and analyze structural motifs in proteins, *Protein Sci.* **5**, 212–220 (1996).

This page intentionally left blank

2

Inhibition of $CaCO_3$ crystallization by small molecules: the magnesium example

Patricia M. Dove*
Department of Geosciences, Virginia Polytechnic Institute and State University, Blacksburg, VA 24061, USA

James J. De Yoreo
Chemistry and Materials Science Directorate, Lawrence Livermore National Laboratory, Livermore, CA 94551, USA

Kevin J. Davis
Department of Earth Science, Rice University, Houston, TX 77005, USA

2.1. INTRODUCTION

The ability of organisms to direct the crystallization of inorganic ions into minerals that meet specific needs is highly polyphyletic and has arisen independently many times over earth history. This process, broadly known as biomineralization, yields amorphous and crystalline biogenic materials that often exhibit remarkable morphological and mechanical properties. In the surface waters of the open oceans, biomineralization occurs on such a large scale that it influences many aspects of seawater chemistry. Large amounts of biogenic calcium carbonate are formed primarily as the skeletons of calcitic coccolithophoridae, calcitic foraminifera, and aragonitic pteropoda. Examples of the complex structures formed by coccolithophores are shown in Figure 2.1. In death, the skeletal remains of these organisms sink through the water column to the ocean floor, thereby redistributing the calcium, carbonate, and trace element constituents through dissolution processes. Residual biogenic carbonate skeletons that accumulate on the ocean bottom are eventually incorporated into the sediments and become significant constituents in the sedimentary rock cycle.

*E-mail address: dove@vt.edu
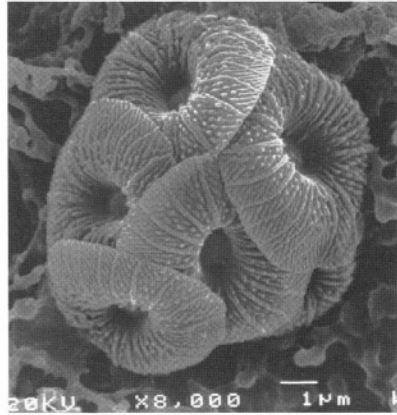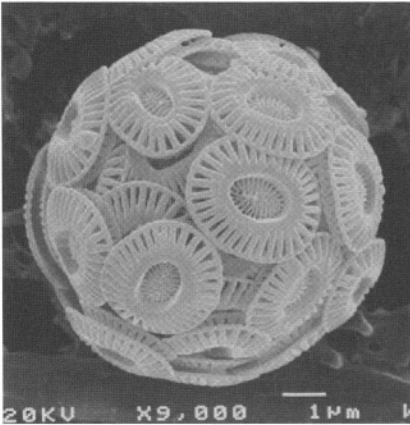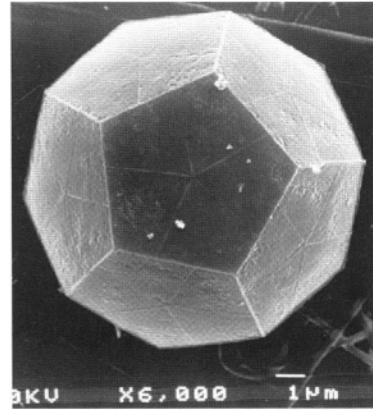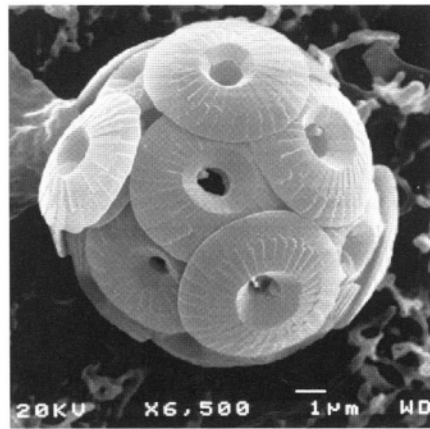
Florisphaera profunda

Umbellosphaera tenuis

Emiliania huxleyi

Braarudosphaera bigelowii

Gephyrocapsa mullerae

Umbilicosphaera sibogue

FIGURE 2.1. Micrographs of calcitic coccoliths (http://www.nhm.ac.uk/hosted_sites/ina/).

TABLE 2.1.
Trace element proxies in foraminiferal calcite [5].

Element	Ion in calcite	Proxy
Magnesium	Mg^{2+}	Temperature
Strontium	Sr^{2+}	Seawater chemistry, pressure?
Boron	$B(OH)_4^-$	pH
Lithium	Li^+	Seawater chemistry
Manganese	Mn^{2+}	Diagenesis
Zinc	Zn^{2+}	Silicic acid
Barium	Ba^{2+}	Alkalinity
Iron	Fe^{2+}?	Diagenesis?
Copper	Cu^{2+}	Nutrient
Neodynium	Nd^{3+}	Seawater chemistry
Cadmium	Cd^{2+}	Phosphate
Vanadium	HVO_4^{2-}	Seawater chemistry
Uranium	UO_2^{2+}	Seawater chemistry

As a result of these processes, many other biogeochemical cycles become dependent on the relative rates of biomineral formation and dissolution in natural waters [1–3]. Of current interest are the possible roles biogenic carbonates play in mediating atmospheric CO_2 concentrations, and the effect that such a process could have on global climate change [4].

The incorporation of foreign elements, such as magnesium, into $CaCO_3$ biominerals has become an important tool for understanding paleoclimates and biogeochemical cycles. Indeed, much of geochemistry is based upon the fundamental concept that the elemental constituents of rocks and minerals indicate the environmental conditions or subsequent history of crystallization. For example, during biomineral formation, trace elements are incorporated directly from seawater during shell precipitation; therefore, biomineral compositions reflect not just seawater composition but also the physical and biological conditions present during precipitation. Accordingly, various trace elements in calcite and aragonite have been shown to vary systematically, with at least one physical or chemical parameter important in the reconstruction of paleoenvironmental conditions. The Mg/Ca ratio in biomineral substrates, for example, has been shown to increase as the temperature rises. Accordingly, due to its reduced susceptibility to changes in salinity and polar ice volume relative to isotopic indicators, the Mg/Ca ratio in biogenic $CaCO_3$ recently has been utilized as an invaluable paleotemperature proxy [6–11]. The virtual "toolbox of elemental proxies available to the paleoceanographer," as summarized by Lea [5], is represented in Table 2.1. As the sheer volume of this "toolbox" indicates, for accurately interpreting biomineral substrates and their reflection of past environments, a fundamental understanding of the thermodynamic and kinetic controls on trace element incorporation in $CaCO_3$ proves crucial.

2.1.1. Nanoscale dimensionality of biominerals

The complexity of processes involved in biomineralization interests a wide array of scientific disciplines [1–3,11]. From the point of view of materials synthesis, in complex molecular systems, biological control over epitaxy represents an elegant example of self-
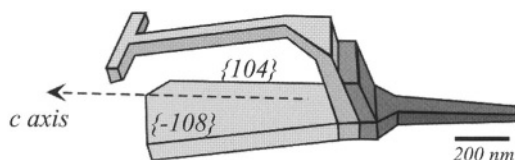
FIGURE 2.2. Individual structural unit from a coccolith plate (redrawn [23]) of *E. huxleyi* showing calcite single crystal.

organization. With such control, organisms can direct surface morphologies [12–15], as well as facet stabilities [13–16] to produce nanophase materials [12,17] topologically-complex single-crystals [18–20], and multi-layer composites [14,21]. The resulting materials possess biological functions as diverse as structural supports, porous filtration media, grinding and cutting tools, lenses, gravity sensors, and magnetic guidance systems.

The aforementioned coccolithophorid organisms provide good examples of biogeochemically-significant organisms that form biomineral structures with nanoscale dimensionalities. The biomineral structures that enclose the mature organism (e.g., Figure 2.1) are believed to play roles in regulating buoyancy, light, and nutrient supply, in addition to offering protective advantages [2]. The most abundant of these structures, *Emiliania huxleyi,* could also be the most abundant calcium carbonate-secreting species on earth [22]. These organisms are particularly interesting to scientists investigating the processes of biomineralization. Initially, coccolith structures of *'Ehux'* form intracellularly as a ring of single rhombohedral calcite crystals, each with a diameter of approximately 40 nm. As the rhombs develop, they differentiate into the delicate structures illustrated in Figure 2.2 [23]. These individual shield elements, which are approximately 1–3 microns long, possess specialized structures with nanoscale dimensionalities. Some of the features, which can be as small as 50–100 nm in diameter, could exhibit the thermodynamically stable {104} surface of calcite. In fact, recent Atomic Force Microscopy studies show that on these nanoscale structures a number of different calcite-mineralizing coccolithophorid species develop {104} [24].

2.1.2. Purpose of this review

This review will provide a framework for understanding how small molecules can selectively inhibit mineral formation at the molecular scale. In particular, this chapter will focus on the chemical and morphological roles of magnesium in affecting the growth of the $CaCO_3$ polymorph, calcite. This system is being extensively studied by the biogeochemistry community owing to the increasing body of evidence that biomineral compositions reflect environments of formation (see Section 2.3.1). By mediating the kinetics and thermodynamics of growth, we focus on the magnesium example to show how minor levels of impurities can affect calcite reactivity at the scale of individual step edges and result ultimately in complex macroscopic morphologies.

The next section of this chapter establishes the various mechanisms by which growth can be inhibited in the context of established crystal growth impurity models. Using this foundation, we present the *magnesium problem.* The final portion of this chapter examines briefly other ions/molecules that could inhibit calcite growth.

2.2. CRYSTAL GROWTH IMPURITY MODELS

The mechanisms by which small molecules inhibit crystal growth can be summarized within the framework of impurity models established by the crystal growth community. These models begin with the assumption that growth occurs by the advancement of step edges as monomolecular units (or small groups of steps). Assuming no changes in supersaturation, ions or molecules can modify step flow by three major processes: incorporation, step blocking, and step-edge adsorption. As this section will show, for each of these major mechanisms inhibiting growth, step migration velocity characteristically depends upon both supersaturation and the impurity-concentration of the growth solution.

2.2.1. Step blocking

Step "pinning" or "blocking" occurs when impurity molecules adsorb to step-edges or accumulate on terraces ahead of migrating steps, thereby decreasing their velocity. Figure 2.3a shows that solutions less supersaturated than σ^d are characterized by no observable crystal growth, a regime termed the "dead zone" of supersaturation [25,26]. At some system-dependent threshold supersaturation, σ^*, the steps break through the chain of adsorbed impurities to result in a sharp rise in v_s. This theory explains the nonlinear dependence of v_s on σ often observed in the presence of impurities at lower supersaturations ($\sigma < \sigma^*$). At still lower supersaturations ($\sigma < \sigma^d$), where no growth is observable, the regime is termed the "dead zone." Above σ^* the linear relationship between v_s and σ, characteristic of the pure system, is reassumed. As illustrated by Figure 2.3b, the width of this "dead zone" of supersaturation increases as the concentration of impurities rises [25,26]. Logically then, the greater the concentration of impurities in solution (C_i), the higher the threshold supersaturation (σ^*) required for steps to break through the impurity fence (where $C_3 > C_2 > C_1$). Accordingly, higher impurity concentrations result in a wider "dead zone" of supersaturation.

While crystal growth literature normally expresses the effect of impurities on kinetic behavior as v_s versus σ, these relations can be revealed further in plots of v_s versus impurity concentration. As a consequence of the relationships illustrated in Figures 2.3a, and 2.3b, theoretical step velocities as a function of impurity concentration at different supersaturations can be represented as shown in Figure 2.3c. In the case of step blocking, solution impurities do not affect step velocity until a threshold impurity concentration is reached; thereafter, a decrease occurs in growth rate. For such retardation in growth, the threshold impurity concentration required is characteristic of the solution's supersaturation, whereas in higher supersaturations (where $\sigma_3 > \sigma_2 > \sigma_1$) cessation of growth requires a greater impurity concentration.

2.2.2. Incorporation

When foreign ions or molecules become captured by advancing steps or otherwise incorporate at kink sites along a step edge to become part of the growing crystal, impurity incorporation occurs. Typically, the impurity molecules distort the crystal structure, thereby through an enthalpic contribution increasing the internal surface free energy of the solid [25,28]. The resulting increase in free energy manifests as an increase in the solubility
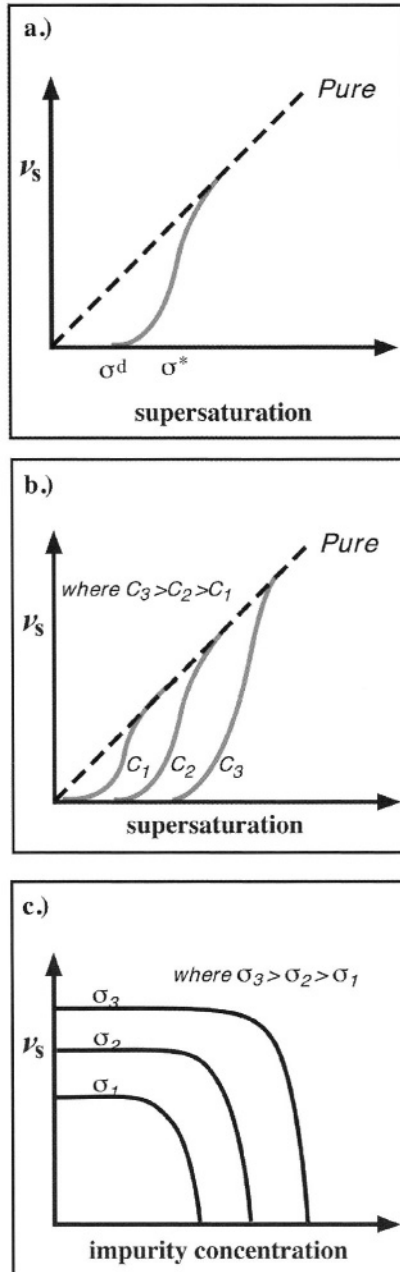
FIGURE 2.3. Theoretical model for growth inhibition by blocking shows. (a) Step velocity is zero at low supersaturation. At higher supersaturations, steps overcome the barrier of the fence of adsorbed impurities and are able to achieve the full velocity associated with the pure system. (b) The dependence of this inhibition upon impurity concentration, c_i, demonstrates that the size of this dead zone is sensitive to impurity concentration [25, 26]. (c) For a constant supersaturation, step velocities are independent of impurity concentration until a critical concentration of impurities creates a dead zone and growth abruptly ceases [27].

(K_{sp}) of the crystal, leading to a lower effective supersaturation. Since σ is defined as the natural logarithm of the ion activity product divided by the solubility constant, an increase in crystal solubility reduces the effective supersaturation (σ_{eff}). As shown in Figure 2.4a, this result shifts step velocity curves to higher equilibrium activities, resulting in an apparent "dead zone" of supersaturation ($\sigma < \sigma^d$). Above σ^*, the linear relationship between step velocity (v_s) and σ characteristic of the pure system is regained. However, at the same supersaturation, the absolute magnitude of the step velocity always remains below that of the pure system.

It is useful to note that upon incorporation of impurities, the kinetic behavior of the system does not significantly deviate from the linear dependence of v_s on σ. Instead, the kinetic curves simply shift over to the higher supersaturations needed to achieve the same growth rate observed in the pure system (Figure 2.4b). The greater the impurity concentration in solution, the wider the dead zone and the farther the curve shifts away from that of the pure system. In this situation, under conditions of impurity incorporation, growth rates at supersaturations above σ^* yield lower growth rates than does the pure system for the same σ [25,28].

This dependence of step velocity on impurity concentration during incorporation is shown in Figure 2.4c. According to the theoretical model, step velocity decreases linearly with increasing impurity concentration. Higher supersaturations (where $\sigma_3 > \sigma_2 > \sigma_1$) result in a faster growth rate at the same impurity concentration.

However, incorporation does not always result in decreasing growth rates. In systems where incorporation results in a large entropic contribution to the free energy of the system, growth rates can exceed that of the pure system [29]. Possible origins of growth enhancement by impurities are discussed by Cabera and Vermilyea [30].

2.2.3. Step edge adsorption

Adsorption of impurity ions or molecules to step edges is implicit to the blocking and incorporation mechanisms discussed in the previous sections. In addition, step edge adsorption of impurities can result in two other growth-modifying phenomena that merit separate consideration.

The first of these phenomena is the weak interaction of the inhibitor ion with individual kink sites, which reduces the number of potential sites to which growth units can attach. In this situation, impurities are not incorporated, nor do they inhibit the flow of step edges by a blocking mechanism to visually roughen or 'scallop' the steps. Rather, decreasing the number of reactive sites physically results in an increase in inter-kink spacing, thereby decreasing the frequency of successful attachments [31,32]. Because step-flow velocity scales with interkink spacing, the slope of the v_s versus supersaturation relation decreases, as illustrated in Figure 2.5a. Since step edge morphology remains unaffected, this type of kinetic inhibition is difficult to discern in experimental studies. Regardless, however, if one suspects the identity of the impurity, one can test for this type of inhibition by measuring the dependence of step velocity on impurity concentration. As shown in Figure 2.5b, step velocity decreases as the impurity content increases, and—with supersaturation of the growth solution—the slope of this relation becomes increasingly negative.

Step edge adsorption can also modify growth by altering step edge energy. Although this process possesses a number of variants, here we consider the end-member situation,
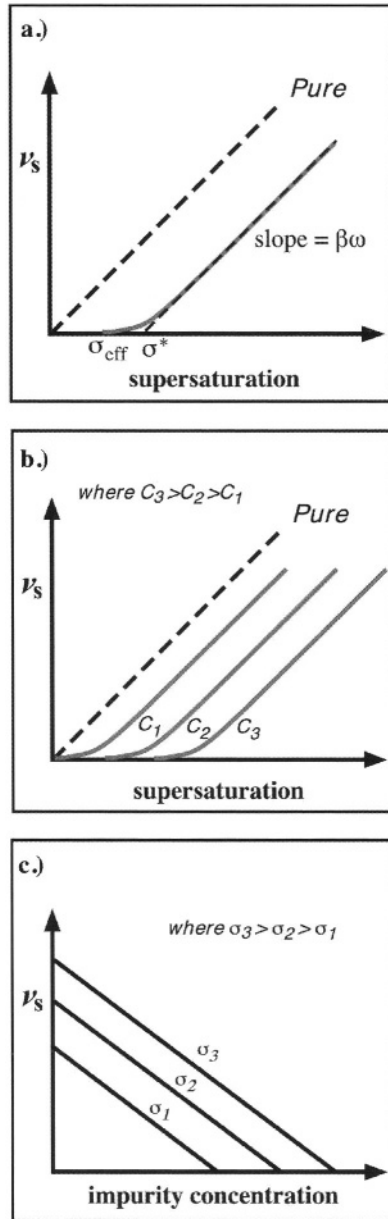
FIGURE 2.4. Theoretical model for growth inhibition by the incorporation mechanism. (a) Impurity incorporation increases the solubility (K_{sp}) of the crystal, leading to a lower effective supersaturation. The reduction in effective supersaturation (σ_{eff}) shifts the kinetic curve to higher equilibrium activities, resulting in a "dead zone" of supersaturation ($\sigma < \sigma^d$). Above σ^*, the linear relationship between step velocity (v_s) and σ characteristic of the pure system is regained. However, the absolute magnitude of the step velocity always remains below that of the pure system at the same σ. (b) The step velocity curves shift to correspond with higher apparent solubilities with increasing impurity incorporation, (c) At constant supersaturation, step velocity decreases linearly with increasing impurity concentration.

FIGURE 2.5. Theoretical model for impurity adsorption at step edges that reduces the number of reactive sites. This mechanism is distinguished by the absence an observable pinning of step edges. (a) By reducing the reactive kink site density, the inhibitor increases the inter-kink spacing. The result is a decrease in the 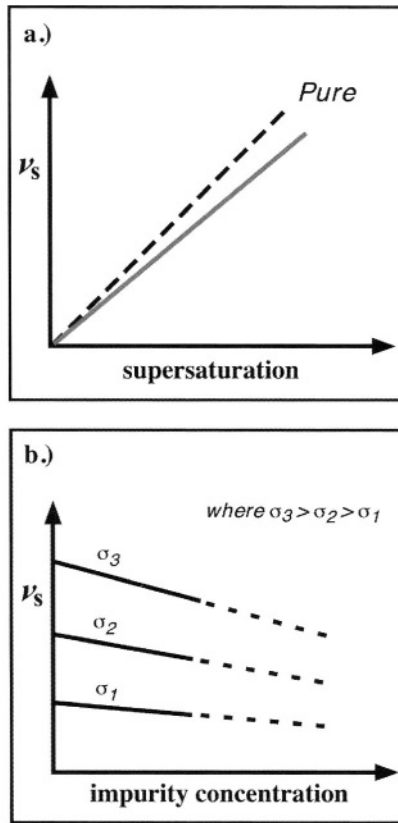frequency of successful attachments of the growth units that becomes more pronounced with increasing saturation or (b) increasing impurity concentration.

whereby modifications in step edge energy, γ, are a purely thermodynamic effect. Under this condition, when the impurity concentration exceeds a threshold value, the minimum energy step shape evolves into a new "lowest energy" form. For the case of a growth hillock that develops in pure and impurity-modified systems, Figure 2.6a uses a Wulff construction of step edge free energy to illustrate such evolution. A complete discussion of this type of interaction is found Kern and coworkers [33,34].

In the absence of a kinetic effect, changes in microscopic (step edge direction) and macroscopic (expression of crystal facets) morphology present evidence for the control of thermodynamics on equilibrium crystal form. Indeed, because step flow rates can exhibit little deviation from the pure system, impurity interactions by step edge adsorption are unique. Figures 2.6b and 2.6c, respectively, illustrate that deviations in growth rates are minimal over a range of supersaturations and impurity concentrations. Small decreases (or increases) in step velocity demand very high concentrations of impurities [35].
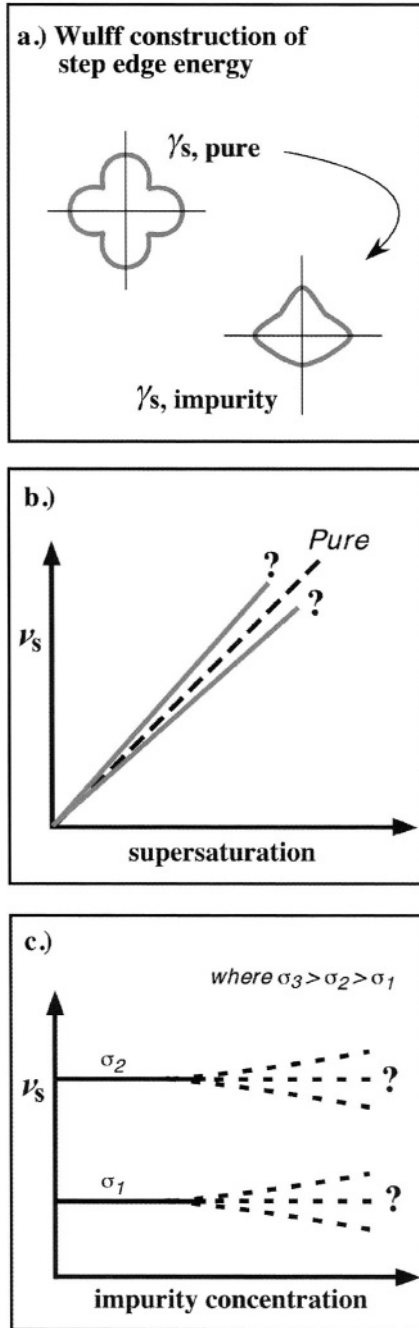
FIGURE 2.6. Theoretical model for impurity adsorption that modifies the step edge energy. (a) This model is distinguished by the development of new energy minima that cause the stabilization of new step directions. Step migration rates may or may not he significantly affected by the introduction of impurities across (b) variable or (c) constant supersaturation.

2.3. THE MAGNESIUM PROBLEM

2.3.1. *Occurrence of Mg^{2+} in calcium carbonate biominerals*

Significant amounts of magnesium occur in calcium carbonate biominerals, a fact first noted in Silliman's 1846 study of biogenic skeletal parts [36]. Since Silliman's research, all comprehensive major-element analyses of calcareous skeletal material not only have recorded at least trace amounts of magnesium but also have demonstrated that, other than calcium, it is the most abundant cation observed to coprecipitate with carbonate biominerals [37]. In the early decades of the twentieth century, Clarke and Wheeler systematically quantified the magnesium composition of marine invertebrates and demonstrated that the carbonate skeletons of calcareous algae could contain as much as 20 mol% $MgCO_3$ [38, 39]. Although Clarke [40] had previously suggested that magnesium carbonate present in skeletal parts was associated primarily with calcitic organisms, determining the exact phase in which magnesium was present in biominerals had to await the development of X-ray diffraction techniques.

After the development of such techniques, the classic work of Chave [41] demonstrated a linear relationship between the position of the {104} diffraction peak of skeletal calcites and their magnesium concentrations over the range of 0–18 mol% $MgCO_3$. As a result of his research, Chave concluded that Mg^{2+} replaced Ca^{2+} in the calcite lattice, thereby shrinking it, and then formed a solid solution between the composition of calcite and dolomite [42]. Subsequent experiments have demonstrated conclusively that, in the cation sites of the calcite-type structure, magnesium is indeed randomly distributed [43]. Utilizing the newly-developed X-ray diffraction technique, Chave systematically studied the distribution of magnesium in the calcareous skeletons of marine organisms as a function of mineralogy, water temperature, and biological complexity [44,45]. (The results of Chave's study [46] are summarized in Table 2.2.) Of the three factors determining the amount of magnesium present in biominerals, Chave concluded that carbonate mineralogy was the most important, with larger amounts of magnesium coprecipitating with calcite than aragonite. He further demonstrated that in the skeletons of all calcitic organisms the magnesium content could be linearly related to the temperature of the water, with greater amounts of magnesium present at higher temperatures. Finally, he observed that the total amount of magnesium in the skeletons decreased as the increasing phylogenetic level (greater complexity) of the organism increased [44].

In an exhaustive study of echinoderm skeletal calcites, Weber [47] reinforced Chave's findings by demonstrating that the distribution of magnesium is a function of both environmental and genetic factors. Observed differences in the magnesium composition within the same echinoderm skeletal material, between different skeletal materials in the same organism, and between skeletons of different genera exposed to the same environmental conditions determined the evidence for genetic factors, which Weber postulated were due to differences in the amino acid composition of protein templates utilized by the organism as a substrate for crystallization. Weber further hypothesized that different biological substrates could vary not merely the rate of crystallization but also the amount of magnesium proximal to the forming mineral, both of which can influence the amount of magnesium incorporated into the biomineral product [47]. Variations in the magnesium content of biominerals—whether a function of biological complexity or genetic factors—indicates an

TABLE 2.2.
Magnesium in various carbonate skeletal biominerals [44–46].

Classification	% Aragonite	Weight % MgCO$_3$
Foraminifera	0	<4–15.9
Sponges	0	5.5–14.1
Madreporian corals	100	0.12–0.76
Alcyonarian corals	0	6.05–13.87
Echinoids	0	4.5–15.9
Echinoid spines	0	<4–10.2
Asteroids	0	8.6–16.17
Ophiuroids	0	9.23–16.5
Crinoids	0	7.28–15.9
Annelid worms	0–99	6.40–16.5
Pelecypods	0–100	0.09–2.80
Gastropods	5–100	0.08–2.40
Cephalopods	0–100	0.05–7.00
Decapod crustaceans	0	5.2–11.70
Ostracode crustaceans	0	<4–10.2
Barnacles	0	1.35–4.60
Calcareous algae	0	7.7–28.75

organism's ability to use biomineralization for influencing the incorporation of magnesium impurities.

2.3.2. Mg as an inhibitor of calcite growth

2.3.2.1. Macroscopic studies   Many investigations have studied the effect of magnesium ions on the nucleation and growth rate of CaCO$_3$ crystallization and have shown that Mg^{2+} can generally inhibit calcite nucleation and growth [48,49,56]. However, the results of these bulk studies vary widely, leading to a considerable amount of confusion in the literature. Much discrepancy can be attributed to the wide range of solution conditions implemented by the various experiments, including differences in supersaturation, ionic strength, and magnesium concentration. Further, important crystallization parameters are often poorly controlled or characterized. For example, the use of seed crystals, surface-controlled versus diffusion-limited growth, and control over the supersaturation state of the solution each can cause critical differences. As a result, such experimental limitations have made more difficult the task of accurately determining the actual crystallization mechanism involved in the presence of each solution composition. An example of this difficulty is shown by Deleuze and Brantley, who determined that Mg^{2+} inhibition depends on the growth regime (supersaturation) and that mechanistic differences can explain much of the discrepancy in the literature [57].

Despite the considerable attention paid by the geochemical community to CaCO$_3$ growth in the presence of magnesium, the actual mechanism of Mg^{2+} inhibition has been a topic of great debate since the 1970's. Two basic mechanisms have received significant experimental support. Berner eloquently articulated the first mechanism: calcite inhibition occurs through an increase in solubility due to lattice strain induced by Mg^{2+} incorporation [58]. Moreover, the works of Folk [59] and Sawada [60] provide additional support

for this mechanism. This theory arises largely from quantitative measurements demonstrating (1) that Mg^{2+} inhibits calcite growth while not influencing aragonite precipitation and (2) that magnesium preferentially incorporates into calcite. Further, it is well known that the greater the amount of Mg^{2+} present in the calcite lattice, the higher the solubility of the mineral [61]. The kinetic data of many other experiments, however, have been proven consistent with a Langmuir adsorption model [50,52,53,56]. Such studies imply that the mechanism of inhibition involves the reversible adsorption of Mg^{2+} ions at kink sites on the calcite crystal surface prior to dehydration and final incorporation. This theory suggests that the higher energy produced by dehydration of Mg^{2+} at the calcite surface acts as the rate-controlling step. Further, in many of these studies, the incorporation of Mg^{2+} into Mg-calcite overgrowths proved unimportant in controlling growth rate [50,53]. A similar adsorption mechanism, coupled with the slow rate of Mg^{2+} dehydration, was first postulated by Lippmann [37] in order to explain why magnesite ($MgCO_3$) fails to precipitate from seawater. Indirect support for the adsorption/dehydration inhibition model arises from the fact that energy of hydration decreases as unhydrated ionic radius increases [62]. From this it can be expected that Ca^{2+} ions are much more strongly hydrated than CO_3^{2-} ions. Therefore, the rate-controlling step in calcite crystallization should be the dehydration of a surface-bound Ca^{2+} cation. When present, the dehydration of the Mg^{2+} cation would be the limiting step and the solution concentration of magnesium would be expected to control growth. The second-order rate law for calcite growth determined by Reddy and Nancollas [63] supports the cation dehydration-limited mechanism, as do the observations of Nancollas and Purdie [64] which suggested that dehydration of growth units often acts as the rate-controlling step in the crystallization of ionically-bonded solids. Finally, the fact that Mg^{2+} does not inhibit aragonite growth can be explained in the context of the adsorption model by observing that Mg^{2+} ions have a much lower affinity for the aragonite surface than for that of calcite [65].

2.3.2.2. Microscopic studies Recent work by Davis *et al.* [66,67] used atomic force microscopy to resolve the mechanism of calcite inhibition by magnesium through molecular-scale determination of the thermodynamic and kinetic controls of Mg^{2+} on calcite growth. This study made in-situ observations of calcite crystallization by observing the growth of single-sourced spiral-growth hillocks generated by screw dislocations on the calcite surface. The typical growth hillock in a control system (absence of Mg^{2+}) exhibits the well-documented surface geometry of calcite (Figure 2.7a). Using carefully characterized solution chemistries that varied Mg^{2+} activities and supersaturation, in-situ measurements were made [66–68] of two fundamental crystal growth parameters, step velocity (v, $nm\,s^{-1}$) and terrace width (λ, nm). Figure 2.7b shows that these kinetic and thermodynamic parameters give the distance traveled by a single monomolecular step as a function of time and the average spacing between individual steps, respectively. Values of v and λ were collected simultaneously with observations of hillock morphology and step-edge roughness.

Observations [66–68] of hillock morphology showed that at step-edges on the calcite surface magnesium caused step direction-specific modifications in the activity of kink-sites (Figure 2.8a–c). In the presence of Mg^{2+}, steps along the negative directions were preferentially roughened, which led to significant rounding of the $-/-$ corner of the hillock. This finding suggests that for Mg^{2+} incorporation, steps along the negative direction provide more energetically favorable. Increasing activities of Mg^{2+} led to the "broadening" of the $+/-$ corner-sites and eventually resulted in the formation of apparently new step directions.
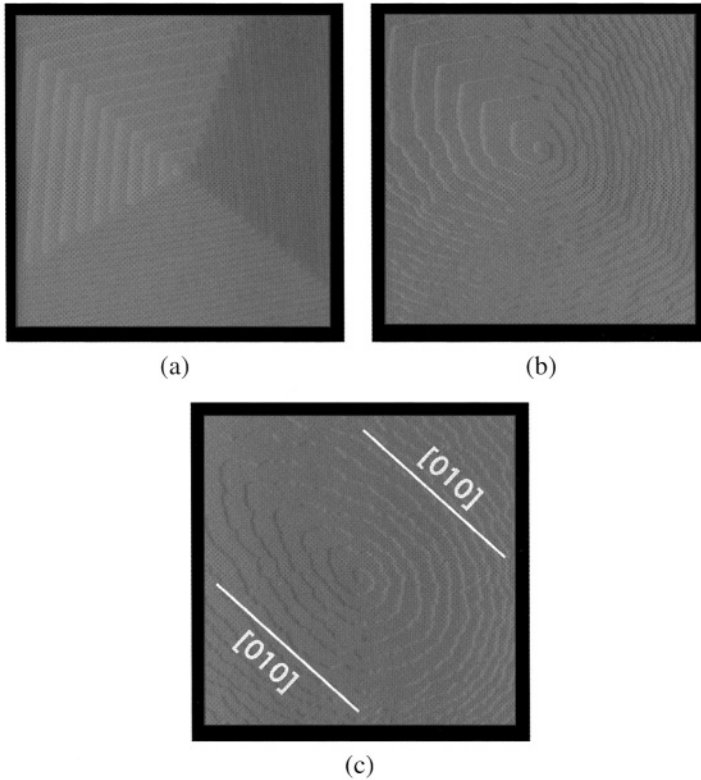
FIGURE 2.7. (a) AFM image of single-sourced growth spiral arising from the (104) cleavage surface of calcite. Image is $3\,\mu\text{m} \times 3\,\mu\text{m}$. (b) Cross-section diagram illustrates, R, the growth rate normal to the calcite surface; step velocity of a given monomolecular step (v_s); terrace width (λ) and the monomolecular step height ($h = 3.1$ Å for calcite). Note the greater terrace width for steps along the positive direction than for steps along the negative direction [67].

Measurements showed that the addition of magnesium to the growth solutions led to a significant decrease in step velocity (v_s) [66–68]. For the positive and negative steps, Figure 2.9 depicts the dependence of step velocities on the activity of magnesium in the growth solution at a constant intermediate supersaturation ($\sigma = 1.20$).

In a suite of solutions containing different activities of Mg (Figure 2.10), measurements of the dependence of v_s upon supersaturation show that for similar magnesium impurity contents step velocities increase with supersaturation. The positive and negative directions exhibit a behavior consistent with the crystal growth impurity models for incorporation (compare Figure 2.4a, 2.4b).

These relations are more clearly illustrated in Figure 2.11, which shows the dependence of step velocity on the activity of the Ca^{2+} cation (proxy for supersaturation) at one magnesium concentration [66–68]. At a unique value of $a_{Ca^{2+}}$ (a_e) on this plot, the experimental solution (containing a certain Mg^{2+} impurity concentration) and the calcite crystal reach thermodynamic equilibrium. Below a_e, steps on the calcite surface retreat, and the crystal begins to dissolve. At Ca^{2+} activities slightly above this value, monomolecular steps begin to advance, and the crystal is observed to grow. However, to achieve the linear relationship
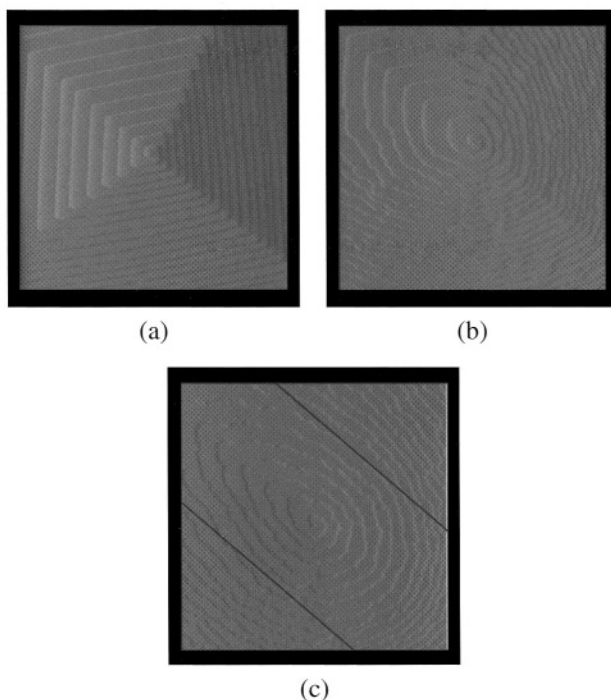
(a)   (b)

(c)

FIGURE 2.8. A series of AFM images show the effect of increasing magnesium activity on calcite hillock morphology at growth conditions of $\sigma = 1.20$, pH = 8.5, and ionic strength = 0.117 [66–68]. (a) Steady-state hillock morphology in Mg-free solutions is characterized by well-formed vicinal faces and straight step-edges. (b) Steady-state hillock morphology in low-Mg solutions shows preferential roughening of steps along the negative directions, indicative of step-specific impurity interactions ($a_{Mg^{2+}} = 6.37 \times 10^{-5}$). (c) As the Mg^{2+} activity in the growth solution further increases to 1.27×10^{-4}, all step-edges roughen, eventually leading to an elongated hillock with apparent step edge directions that correspond to the [0–10]. The crystallographic orientation of these hillocks is the same as Figure 2.6a and all images are 3 × 3 microns.
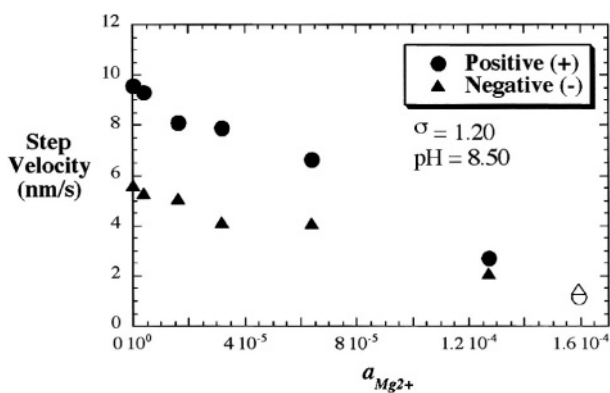

FIGURE 2.9. AFM measurements of positive and negative step edge velocities as a function of magnesium at $\sigma = 1.2$ [66–68]. The measured velocities of steps along both directions were observed to decrease with increasing Mg^{2+} activity in the experimental solutions. (Open symbols denote data for which new step directions may be observed.)
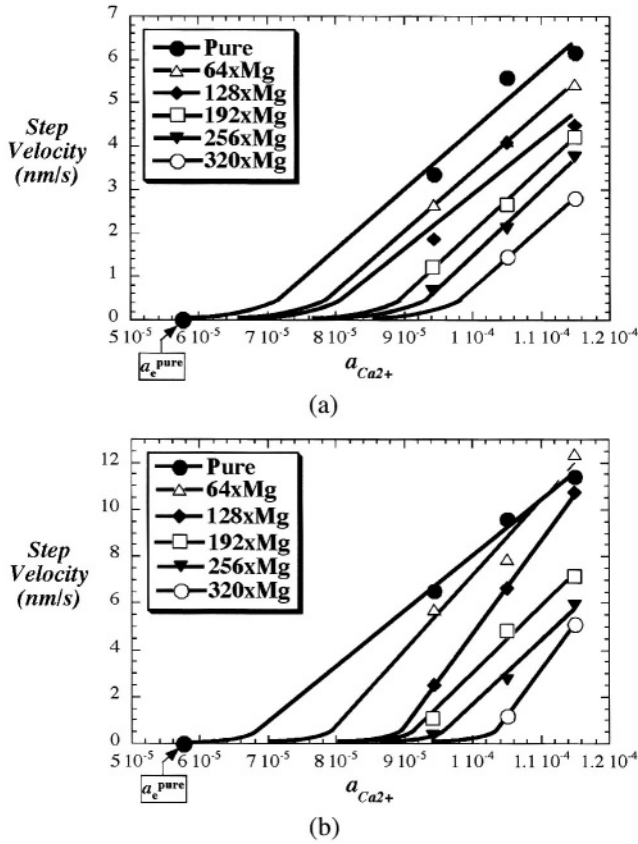
FIGURE 2.10. Step velocity versus calcium activity (proxy for supersaturation) for the: (a) negative and (b) positive directions [66–68]. Contours with magnesium concentration result from the shift in kinetic behavior to increasing equilibrium activities, as expected from the incorporation mechanism.

between step velocity and activity characteristic of the pure system, even greater Ca^{2+} activities are required. Crystal growth theory predicts this linear dependence of a step velocity versus activity plot according to:

$$v_s = \beta\omega(a - a_e), \tag{1}$$

where β is the kinetic coefficient in length/time, ω is the specific molecular volume of calcite (6.13×10^{-23} cm^3/molecule), and $(a - a_e)$ has units of particles/volume [31,69, 70]. Therefore, the kinetic coefficient (β) of growth can be calculated from the slope of the linear portion of the line shown in Figure 2.11. The activity intercept extrapolated from this linear portion of the kinetic curve is termed a^*. For a complete assessment of calcite growth behavior in the presence of magnesium at low supersaturations, the "curvature" that exists between a_e and a^* proves crucial. Further, any experimentally "pure system" also contains a certain amount of background impurities. These were interpreted [71] as the source of deviation from eq. (1) and observed as curvature in the kinetic data at low growth unit activities.
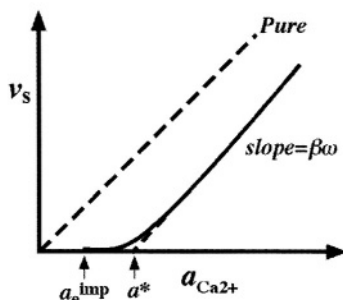
FIGURE 2.11. Illustration of v_s versus $a_{Ca^{2+}}$ relationships shows that the incorporation of magnesium shifts the kinetic curve over to a higher equilibrium activity (a_e^{imp}), where a^* represents the extrapolated activity intercept of the linear portion of the curve [66–68]. "Curvature" in kinetic behavior at low activities occurs between a_e^{imp} and a^*.

Although this study collected measured data only from the linear portions of the kinetic curves, it evaluated the nature of the curvilinear behavior by comparing the extrapolated a^* of this data to the measured equilibrium activities for both the pure system (a_e^{pure}) and for a given magnesium solution ($a_e^{64 \times Mg}$). Linear extrapolations of the step velocity data yield almost identical activity intercepts (a^*) for both the positive and negative steps. If the step velocities of both the positive and negative steps go to zero at the same equilibrium point, such behavior is expected. However, the a^* values determined in this manner were at a substantially higher Ca^{2+} activity than was the measured equilibrium activity for the pure system. Therefore, it becomes evident that significant curvature in step velocity behavior occurs at lower equilibrium activities, even in the pure system. This finding concurs with similar studies of calcite conducted in the pure system [71].

The thermodynamic measurements made in this study also proved consistent with the inhibition of calcite growth through incorporation of Mg^{2+}. According to the Gibbs–Thomson relation [68], the linear increase in terrace width (λ) with increasing magnesium concentration, shown in Figure 2.12, indicates a decrease in the effective supersaturation of the growth solutions due to Mg^{2+} incorporation. As a result, $Ca_{1-x}Mg_xCO_3$ solubilities determined from microscopic observations of step dynamics can be linked to macroscopic measurements. Such findings show the thermodynamic and kinetic measurements independently support the incorporation mechanism of calcite growth inhibition.

Davis *et al.* [66,67] hypothesized that induced lattice strain enhances the solubility of the mineral, resulting in a decrease of the solution's effective supersaturation (σ_{eff}). Accordingly, as was observed, the presence of Mg^{2+} in the growth solutions shifted the kinetic behavior of the system toward higher equilibrium activities. This thermodynamic shift in solution supersaturation accounts for the observed decrease in calcite growth rate as a function of Mg^{2+} activity.

2.3.3. Influence of Mg^{2+} on the polymorphic expression of $CaCO_3$

Possibly no other naturally-occurring compound exhibits polymorphic variation as readily as $CaCO_3$. In addition to calcite, the most stable $CaCO_3$ polymorph, aragonite readily forms in a wide range of natural waters—indeed, in seawater it has been deemed
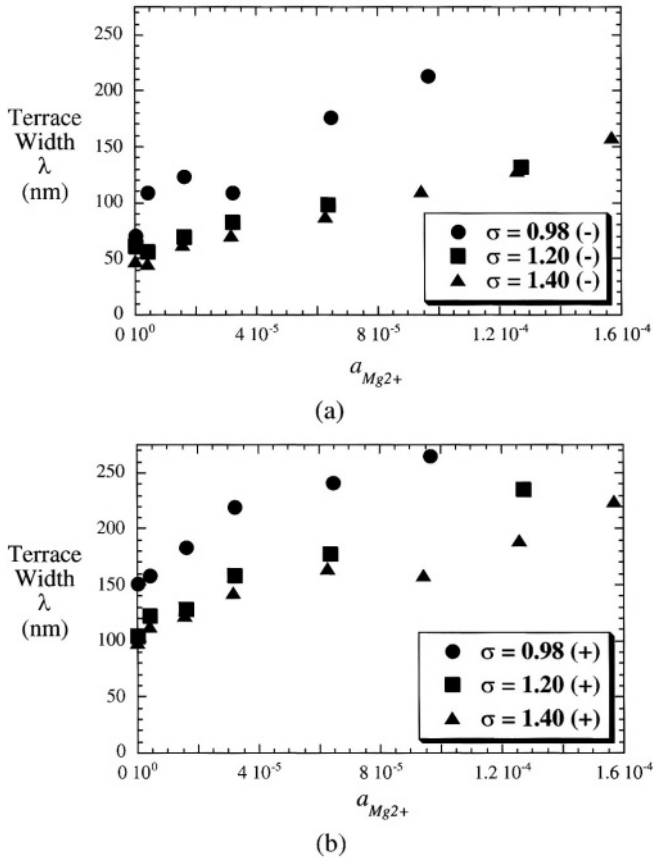
FIGURE 2.12. Dependence of terrace width upon magnesium activity at three saturations for the (a) negative and (b) positive directions. As greater amounts of Mg^{2+} are added to the experimental solutions, the measured terrace widths are observed to increase [68]. This behavior is consistent with a decrease in the apparent supersaturation of the system.

the dominant inorganically precipitated form of $CaCO_3$. With respect to the thermodynamically more stable calcite, the anomalous preferential formation of aragonite in seawater has been attributed [65,37,59] to the ubiquitous presence of Mg^{2+}. Leitmeier was among the first to demonstrate that Mg^{2+} favors the precipitation of aragonite. Through extensive experimentation, he proved that the addition of large amounts of Mg^{2+} to growth solutions caused aragonite to form instead of calcite and that only aragonite would form in Mg^{2+}-rich environments [72,73]. By analyzing natural specimens precipitated from seawater, subsequent investigators have confirmed Leitmeier's observations [44,45,48,74,75].

More recently, Kitamura [76] has shown that Mg suppresses the transformation of vaterite by inhibiting the growth of calcite. Given that in natural waters individual organisms typically exhibit a preference for the formation of a particular polymorph, the apparent control of Mg^{2+} over $CaCO_3$ polymorphism crucially influences the processes of biomineralization. Previous discussions in this chapter suggest a ready explanation for the widespread formation of the metastable aragonite: it has a higher solubility than calcite with values of

TABLE 2.3.

Ionic radius [80] of divalent cations and corresponding isotypes of calcite and aragonite [79].

Cation	Ionic radius (Å)	Mineral
Rhombohedral carbonates		
Ni^{2+}	0.69	Gaspeite ($NiCO_3$)
Mg^{2+}	0.72	Magnesite ($MgCO_3$)
Cu^{2+}	0.73	Un-named ($CuCO_3$)
Zn^{2+}	0.74	Smithsonite ($ZnCO_3$)
Co^{2+}	0.75	Sphaerocobaltite ($CoCO_3$)
Fe^{2+}	0.78	Siderite ($FeCO_3$)
Mn^{2+}	0.83	Rhodochrosite ($MnCO_3$)
Cd^{2+}	0.95	Otavite ($CdCO_3$)
Ca^{2+}	1.00	Calcite ($CaCO_3$)
Orthorhombic carbonates		
Ca^{2+}	1.18	Aragonite ($CaCO_3$)
Sr^{2+}	1.31	Strontianite ($SrCO_3$)
Pb^{2+}	1.35	Cerussite ($PbCO_3$)
Ba^{2+}	1.47	Witherite ($BaCO_3$)

approximately $10^{-8.34}$ and $10^{-8.48}$, respectively [77]. These findings support the idea [59] that in natural waters, magnesium leads to the formation of the more soluble magnesium calcites, moving the solution chemistry into a regime where aragonite becomes the stable $CaCO_3$ polymorph. This process increases the activity of calcium and carbonate into the stability field of aragonite.

The differential interaction of Mg^{2+} with $CaCO_3$ polymorphs can be better understood by contrasting the crystal chemistry and crystallographic structures of calcite and aragonite. Calcite is characterized by a rhombohedral structure in which the Ca^{2+} atom has 6-fold co-ordination, whereas aragonite forms with the orthorhombic structure and the Ca^{2+} is 9-fold coordinated [78]. The ease by which $CaCO_3$ forms both polymorphs on the Earth's surface can be attributed to the size of the Ca^{2+} cation, which nears the limit for 6-fold coordina-tion. Therefore, the divalent cations smaller than Ca^{2+} form single carbonates that have the calcitic structure, while at standard temperature and pressure larger ones tend to crystallize as isotypes of the aragonite structure (Table 2.3) [79,80]. From these structural isotypes of calcite and aragonite, the implication arises that smaller cations, such as Mg^{2+}, will prefer-entially enter the calcite lattice because it is too small to form the 9-coordinated aragonite structure. Coprecipitation studies of the carbonates have validated this assumption with up to 30 mol% $MgCO_3$ occurring in calcites and only negligible amounts of Mg^{2+} found in aragonite.

2.3.4. Effect of Mg^{2+} on the morphology of calcite crystals

In addition to controlling the dominant $CaCO_3$ polymorph observed in natural waters, Mg^{2+} also can influence the morphology of natural calcites. In natural waters, calcite ex-hibits many different crystal morphologies, and natural specimens of it have been collected as micrite, fibers, and as sparry or large equant crystals [81]. Early laboratory experiments
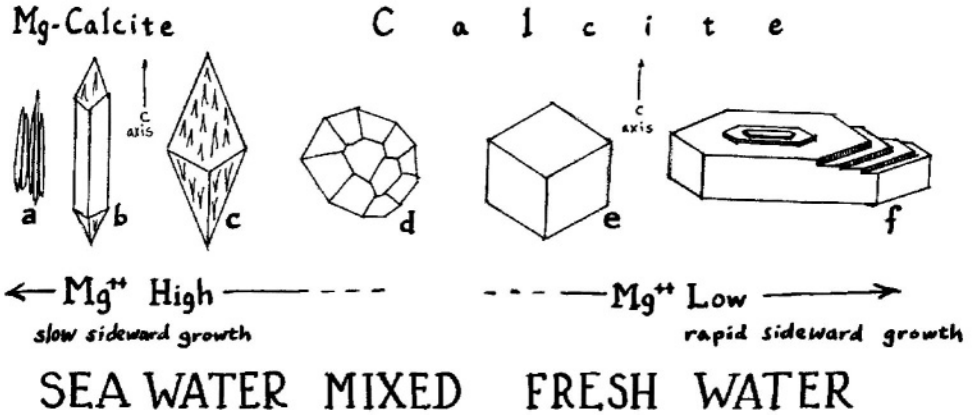
FIGURE 2.13. Proposed influence of Mg^{2+} on calcite morphology [59]. High concentrations of Mg^{2+} selectively poison sideward growth of calcite so that fibrous crystals or elongate rhombs develop. The low Mg^{2+} of fresh waters leads to the formation of complex polyhedra, including the rhomb (e) characteristic of the pure system. It is important to note that a continuum of morphology is observed with change in magnesium concentration. Increasing amounts of magnesium lead to progressive elongation of crystals along the c axis resulting in the growth of prismatic, micritic, and finally fibrous calcites [59].

demonstrated that calcite grown in the presence of very small amounts of Mg^{2+} yielded the unit rhomb characteristic of the pure system [72,73] but that increasing amounts of Mg^{2+} led to the formation of successively steeper rhombs, scalenohedra, and, finally, prism faces. Variations in crystal morphology can result from both the rate of crystallization and the interaction of impurities present in the surrounding solution with certain growth sites on the crystal surface. Probably the most important impurity present in the environments wherein calcite grows is magnesium. Magnesium is in fact present in seawater at a concentration approximately five times higher than that of calcium itself [77]. It is, therefore, not surprising that in natural environments magnesium has been implicated as one of the controlling factors for mediating calcite morphology. However, over the past 25 years of study, the molecular-scale mechanism by which magnesium alters the morphology of natural calcites has been the source of much controversy.

The role Mg^{2+} plays in mediating calcite morphology has been eloquently described by Folk, who pointed out that magnesium selectively so poisons the sideward growth of calcite that fibrous crystals or elongated rhombs tend to develop [59]. This concept derives from observations of calcite morphologies as a function of the Mg^{2+} concentration in fluids adjacent to the developing minerals [59] (Figure 2.13). Folk [59] further postulated that the selective poisoning of calcite growth perpendicular to the c-axis occurred as a result of accumulated lattice strain caused by the incorporation of smaller Mg^{2+} ions (Figure 2.14a). While this mechanism could account for the general inhibition of calcite growth by Mg^{2+}, Lahann [82] disagreed with the idea that it could explain the morphological variation apparent in calcites. Instead, he echoed the earlier proposal of Lippmann [83] that the greater energy required for deydrating the adsorbed Mg^{2+} ions controlled interaction in the morphology of calcites (Figure 2.14b) [82]. Further, modern modeling techniques have indicated that Mg^{2+} might preferentially adsorb to the {100} face of calcite [84]. During
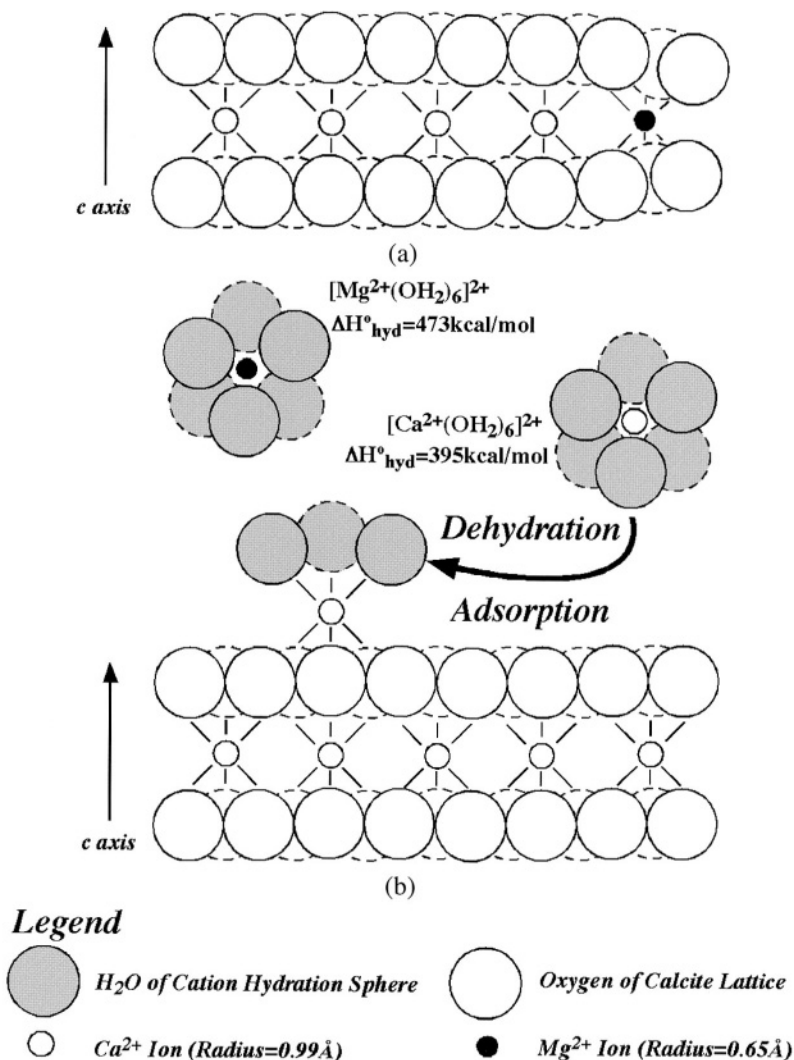
FIGURE 2.14. Proposed mechanisms for Mg^{2+} control on calcite morphology: (a) Folk [59] postulated that the incorporation of the smaller Mg^{2+} ion to the side of the growing crystal causes the neighboring carbonate sheets to shrink. The induced lattice strain retards further sideward growth and the crystal grows much more rapidly in the direction of the c axis, (b) In contrast, Lahann [82] suggested that adsorption of Mg^{2+} to the calcite surface resulted in the poisoning of growth due to the greater enthalphy of hydration [83] for the dehydration of the smaller Mg^{2+} ion than for the Ca^{2+} ion. Adsorption requires the replacement of at least one of the six waters of hydration with an oxygen from the calcite lattice. Shown is the adsorption of Ca^{2+} to a kink site in the calcite lattice where half of the waters of hydration have been replaced by oxygens from carbonates on the calcite surface.

the growth phase, selective inhibition of this face would in fact lead to calcite morphologies similar to those described by Folk (see Figure 2.13) [59].

Recently, a molecular scale explanation for the morphology-governing role of Mg in calcite growth was proposed [85] based upon *in situ* molecular-scale observations of step
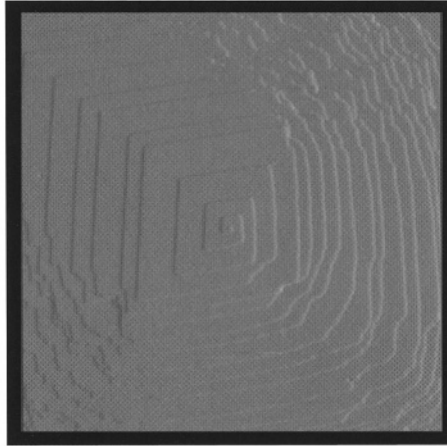
FIGURE 2.15. Recovery of a calcite growth hillock from impurity poisoning [85]. Delayed recovery of step-edges proximal to the intersection of positive and negative steps illustrates a 'memory' of incorporated strain due to differential impurity incorporation into the nonequivalcnt step-types. See text for discussion (4 × 4 μm image).

dynamics and growth hillock morphology. These observations show that Mg^{2+} directly modifies the surface morphology of calcite as a consequence of intrasectoral zoning into vicinal faces on growth hillocks. At low Mg/Ca ratios in solution, the step-specific interactions are especially evident. Those with acute step-edge geometries ($[\bar{4}41]_-$ and $48\bar{1}]_-$) are observed to be rough while obtuse steps ($[\bar{4}41]_+$ and $[48\bar{1}]_+$) remain smooth (Figure 2.8b). Higher Mg/Ca solution ratios cause the edges of both step-types to become rough and the growth spiral to approach a more isotropic form. Coincidentally, decreased growth velocities parallel to the c-glide plane generate new [010] step-directions. Theoretical calculations predict that these new step directions likely result from strain at the intersection of nonequivalent step-types, which result from differential Mg^{2+} incorporation across the boundary of those steps. This hypothesis was validated by observing growth hillock recovery from impurity poisoning, a fact that demonstrated [85] the presence of "remembered" strain at the boundary of the nonequivalent step-types (Figure 2.15). Such findings suggest that habit modification by impurities occur by step-specific impurity interactions rather than by the face-specific interactions postulated by previous theories. This study not only represents a step toward providing a molecular-scale basis by which the anisotropic growth morphologies of many technological and natural crystals can be understood but also offers a plausible molecular-scale explanation for the elongated calcite crystals commonly observed in sedimentary environments.

2.3.5. Inhibition of overall growth rate

The thermodynamic and kinetic measurements made in this study can be used to determine the overall growth rate of calcite normal to the {104} family of surfaces, due to the spiral growth mechanism. According to BCF theory, the overall growth rate (length/time)
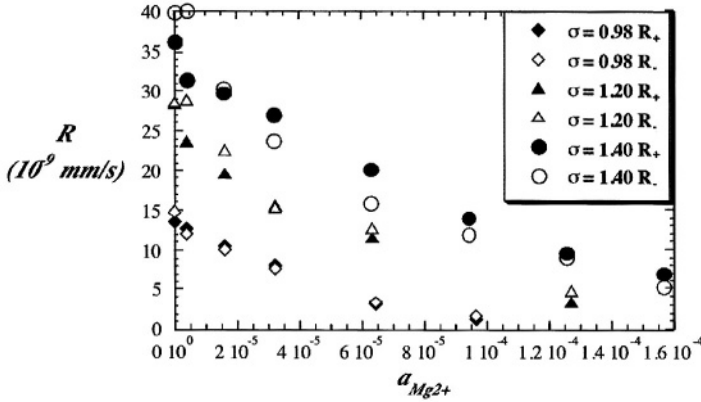
FIGURE 2.16. Surface normal growth rate, *R*, of calcite as a function of Mg^{2+} for the positive and negative step directions at three supersaturations.

of a crystal *(R)* equals the product of the monomolecular step velocity $(v_{s\pm})$ and the slope of the hillock (ρ):

$$R = \rho v_{s\pm}. \tag{2}$$

Since the slope of the hillock (ρ) is equal to the monomolecular step height *(h)*, 3.1 Å for calcite, divided by the terrace width $(\lambda_\pm)$, the overall growth rate *(R)* is a function of the parameters directly measured in this study:

$$R = \frac{h}{\lambda_\pm} v_{s\pm}. \tag{3}$$

The decrease in overall growth rate (*R*) as a function of magnesium is shown in Figure 2.16. This calculated decrease in growth rate represents an integration of the effects of supersaturation state and impurity concentration on both step velocity and terrace width. Higher supersaturation increases monomolecular step velocity and decreases terrace width (increases hillock slope), both of which result in a higher growth rate normal to the calcite surface. Magnesium significantly decreases step velocity and increases terrace width (decreases hillock slope), thereby inhibiting calcite growth. As an independent method for assessing how magnesium inhibits calcite growth, this study proposes calculating the overall growth rate by integrating the key thermodynamic and kinetic measurements identified herein. If this method is used, the resultant growth rate measurement represents a more fundamental and accurate indication than can traditional bulk methods of how Mg^{2+} affects calcite growth kinetics.

2.4. CONCLUSION AND IMPLICATIONS FOR OTHER IONS

This chapter has shown the macroscopic and microscopic roles magnesium plays in significantly inhibiting growth within calcite-mineralizing environments. While many other

divalent and trivalent ions are also known to inhibit calcite growth [86], our microscopic understanding of the mechanisms for inhibition continues to be limited. To date, most knowledge is largely inferred from experiments that employ bulk crystallizers, wherein mechanisms are interpreted from changes that occur in bulk solution chemistry rather than from direct observation of step-edge dynamics. Some ions do, however, appear to fall clearly within the framework of the blocking or incorporation mechanisms presented in Section 2.2. Ions that show good evidence for growth inhibition by blocking [86] are characterized by strong sorption to the calcite surface but do not fit in the lattice during growth, such as ferric iron [87] and phosphate [88–91]. AFM observations of calcite growth in the presence of minute phosphate levels show that in order to directly support blocking mechanisms, step flow ceases and step edges become roughened [92].

Conversely, evidence also suggests that Mn^{2+} inhibits growth through an incorporation mechanism analogous to the model presented here for magnesium [93,29]. If the ability to form solid solutions with calcite can be used as a criterion for inhibition by incorporation, then spectroscopic measurements of impurity concentrations within different crystallographic sectors of a growing hillock suggest a method for predicting probable growth mechanism. This method could be useful for assessing the growth-inhibiting mechanism of numerous ions for which microscopic information does not yet exist. For example, Reeder [94] found preferential incorporation of Ba^{2+} and Zn^{2+} within hillock flanks that correspond to the positive step-edge directions. This finding suggests that, with exposure to these ions, calcite growth could be inhibited by incorporation effects along the positive step directions and inhibited by blocking along the negative directions. Using this analogy, one might expect Sr^{2+} to exhibit a similar effect. However, the opposite microscopic compositional trends reported for Co^{2+} and Zn^{2+} suggest that for these ions an inverse growth inhibiting phenomena might occur. Unfortunately, this type of inference from microscopic compositional data is probably too simplistic because other factors—such as the time scale of ion adsorption/desorption reactions to the step edges relative to step flow rate—likely play an important role in determining the mechanism by which inhibition occurs.

ACKNOWLEDGMENTS

REFERENCES

1. K.E. Chave, Physics and chemistry of biomineralization, *Ann. Rev. Earth Planet. Sci.* **12,** 293–305 (1984).
2. H.A. Lowenstam and S. Weiner, *On Biomineralization* (Oxford University Press, New York, 1989) p. 324.
3. K. Simkiss and K.M. Wilbur, *Biomineralization: Cell Biology and Mineral Deposition* (Academic Press, San Diego, 1989).
4. D. Archer and E. Maier-Reimer, Effect of deep-sea sedimentary calcite preservation on atmospheric CO_2 concentration, *Nature* **367,** 260–263 (1994).
5. D.W. Lea, in: *Modern Foraminifera,* Ed. B.K. Sen Gupta (Chapman & Hall, London, 1999) pp. 253–271.

6. G.S. Dwyer, T.M. Cronin, P.A. Baker, M.E. Raymo, J.S. Buza and T. Cortége, North Atlantic deepwater temperature change during Late Pliocene and Late Quaternary climatic cycles, *Science* **270**, 1347–1351 (1995).

7. T. Mitsuguchi, E. Matsumoto, O. Abe, T. Uchida and P.J. Isdale, Mg/Ca thermometry in coral skeletons, *Science* **274**, 961–963 (1996).

8. D.W. Lea, T.A. Mashiotta and H.J. Spero, Controls on magnesium and strontium uptake in planktonic foraminifera determined by live culturing, *Geochim. et Cosmochim. Acta* **63**, 2369–2379 (1999).

9. L.M.A. Purton, G.A. Shields, M.D. Brasier and G.W. Grime, Metabolism controls Sr/Ca ratios in fossil aragonitic mollusks, *Geology* **27**, 1083–1086 (1999).

10. C.H. Lear, H. Elderfield and P.A. Wilson, Cenozoic deep-sea temperatures and global ice volumes from Mg/Ca in benthic foraminiferal calcite, *Science* **287**, 269–272 (2000).

11. B.R. Heywood, Biomineralization: new directions in crystal science, *Microscopy Research and Technique* **27**, 376–388 (1994).

12. S. Mann, Molecular recognition in biomineralization, *Nature* **332**, 119–124 (1988).

13. A. Berman, L. Addadi and S. Weiner, Interactions of sea-urchin skeleton macromolecules with growing calcite crystals—a study of intracrystalline proteins, *Nature* **331**, 546–547 (1988).

14. S. Mann, J.M. Didymus, N.P. Sanderson, B.R. Heywood and E.J.A. Samper, Morphological influence of functionalized and non-functionalized α,ω-dicarboxylates on calcite crystallization, *J. Chem. Soc. Faraday Trans 86* **10**, 1873–1880 (1990).

15. S. Mann, D.D. Archibald, J.M. Didymus, T. Douglas, B.R. Heywood, F.C. Meldrum and N.J. Reeves, Crystallization at inorganic–organic interfaces: biominerals and biomimetic synthesis, *Science* **261**, 1286–1292 (1993).

16. L. Addadi, J. Moradian, E. Shay, N.G. Maroudas and S. Weiner, A chemical model for the cooperation of sulfates and carboxylates in calcite crystal formation, *Proc. Natl. Acad. Sci.* **84**, 2732–2736 (1987),

17. P. Calvert, Biomimetic ceramics and composites, *Mater. Res. Bull.* **XVII**, 37–40 (1992).

18. J.M. Didymus, S. Mann, N.P. Sanderson, P. Oliver, B.R. Heywood and E.J. Aso-Samper, Modelling biomineralization, in: *Mechanisms and Phytogeny of Calcification in Biological Systems,* Eds S. Suga and H. Nakara (Springer-Verlag, 1991) pp. 267–271.

19. J.R.Young, J.M. Didymus, P.R. Brown, B. Prins and S. Mann, Crystal assembly and phylogenetic evolution in heterococcoliths, *Nature* **356**, 516–518 (1992).

20. A. Berman, J. Hanson, L. Leiserowitz, T.F. Koetzle, S. Weiner and L. Addadi, Biological control of crystal texture: a widespread strategy for adapting crystal properties to function, *Science* **259**, 776–779 (1993).

21. J. Vincent, *Structural Biomaterials* (Princeton University Press, Princeton, 1990).

22. P. Westbroek, P. van der Wal, P.R. van Emburg, E.W. de Vrind-de Jong and W.C. de Bruijn, Calcification in the coccolithophorids E*miliania huxleyi* and *Pleurochrysis carterae.* I. Ultrastructural aspects, in: *Biomineralization in Lower Plants and Animals,* Eds B.S.C. Leadbeater and R. Riding (Clarendon Press, 1986) pp. 189–203.

23. S. Mann, *Biomineralization Principles and Concepts in Bioinorganic Materials Chemistry* (Oxford University Press, 2001).

24. K. Henriksson, S.L.S. Stipp, J.R. Young and P.R. Bown, Calcite biomineralization in coccoliths: Evidence from atomic force microscopy (AFM), *Geochim. Cosmochim. Acta, Special Supplement* **66**, A323 (2002).

25. V.V. Voronkov and L.N. Rashkovich, Influence of a mobile adsorbed impurity on the motion of steps, *Sov. Phys. Crystallogr.* **37**, 289–295 (1992).

26. V.V. Voronkov and L.N. Rashkovich, Step kinetics in the presence of mobile adsorbed impurity, *J. Cryst. Growth* **144**, 107–115 (1994).

27. J.J. De Yoreo, Personal communication (1999).

28. W.J.P. van Enckevort and A.C.J.F. van der Berg, Impurity blocking of crystal growth: a Monte Carlo study, *J. Cryst. Growth* **183**, 441–455 (1998).

29. J.M. Astilleros, C.M. Pina, L. Fernndez-daz and A. Putnis, Molecular-scale surface processes during the growth of calcite in the presence of manganese, *Geochim. Cosmochim. Acta* **66**(18), 3177–3189 (2002).

30. N.Cabera and D.A. Vermilyea, The growth of crystals from solution, in: *Growth and Perfection of Crystals,* eds R.H. Doremus, B.W. Roberts and D. Turnbull (John Wiley & Sons, Inc., New York, 1958) pp. 393–411.

31. A.A. Chernov, The spiral growth of crystals, *Soviet Phys.* **4**, 116–148 (1961).

32. G. Bliznakow, Crystal habit and adsorption of co-solutes, *Fortsch. Min.* **36**, 149–154 (1958).

33. R. Kern, Crystal growth and adsorption, in: *Growth of Crystals,* Ed. N.N. Sheftal' (Consultants Bureau, New York, 1969) pp. 3–23 (and references within).

34. P. Hartman and C.R. Kern, Lechangement de facies par adsorption et la theorie des "PBC", *Acad. Sci. Paris* **258**, 4591–4593 (1964).

35. C.A. Orme, A. Noy, A. Wierzbicki, M.T. McBride, M. Grantham, H.H. Teng, P.M. Dove and J.J. DeYoreo, Formation of chiral morphologies through selective binding of amino acids to calcite surface steps, *Nature* **411**, 775–779 (2001).

36. Silliman, On the chemical composition of the calcareous corals. *Am. J. Science* **1**, 189–199 (1846).

37. F. Lippmann, *Sedimentary Carbonate Minerals* (Springer-Verlag, New York, 1973).

38. F.W. Clarke and W.C. Wheeler, The inorganic constituents of marine invertebrates, *U.S. Geological Survey Professional Paper 102* (1917).

39. F.W. Clarke and W.C. Wheeler, The inorganic constituents of marine invertebrates, *U.S. Geological Survey Professional Paper 124,* 1–62 (1922).

40. F.W. Clarke, Data on geochemistry, *U.S. Geological Survey Bulletin* **770**, 841 (1924).

41. K.E. Chave, A solid solution between calcite and dolomite, *J. Geology* **60**, 190–192 (1952).

42. K.E. Chave, Summary of background information on magnesium calcites, in: *Some Aspects of the Role of the Shallow Ocean in Global Carbon Dioxide Uptake,* Eds R.M. Garrels and F.T. Mackenzie (U.S.D.O.E. Conf. 8003115, National Tech. Inform. Service, Springfield, Virginia, 1981) pp. A4–A9.

43. J.R. Goldsmith, D.L. Graf and O.I. Joensuu, The occurrence of magnesian calcites in nature, *Geochim. Cosmochim. Acta* **7**, 212–230 (1955).

44. K.E. Chave, Aspects of the biogeochemistry of magnesium 1. Calcareous marine organisms, *J. Geology* **62**, 266–283 (1954).

45. K.E. Chave, Aspects of the biogeochemistry of magnesium 2. Calcareous sediments and rock, *J. Geology* **62**, 587–599 (1954).

46. D.L. Graf, Geochemistry of carbonate sediments and sedimentary carbonate rocks, *Illinois State Geol. Survey Circ.,* 297–309 (1960).

47. J.N. Weber, The incorporation of magnesium into the skeletal calcites of echinoderms, *Am. J. Science* **267**, 537–566 (1969).

48. J.L. Bischoff, Kinetics of calcite nucleation: magnesium ion inhibition and ionic strength catalysis, *J. Geophysical Res.* **73**, 3315–3322 (1968).

49. M.M. Reddy and G.H. Nancollas, The crystallization of calcium carbonate: IV. The effect of magnesium, strontium and sulfate ions, *J. Cryst. Growth* **35**, 33–38 (1976).

50. M.M. Reddy and K.K. Wang, Crystallization of calcium carbonate in the presence of metal ions. I. Inhibition by magnesium ion at pH 8.8 and 25°C, *J. Cryst. Growth* **50**, 470–480 (1980).

51. O. Söhnel and J.W. Mullin, Precipitation of calcium carbonate, *J. Cryst. Growth* **60**, 239–250 (1982).

52. A. Mucci and J.W. Morse, The incorporation of Mg^{2+} and Sr^{2+} into calcite overgrowths: influences of growth rate and solution composition, *Geochim. Cosmochim. Acta* **47**, 217–233 (1983).

53. M.M. Reddy, Effect of magnesium ions on calcium carbonate nucleation and crystal growth in dilute aqueous solutions at 25°C, in: *U.S. Geological Survey Bulletin 1578: Studies in Diagenesis,* Ed. F.A. Mumpton (1986) pp. 169–182.

54. R.G. Compton and C.A. Brown, The inhibition of calcite dissolution/precipitation: Mg^{2+} cations, *J. Colloid and Interface Science* **165**, 445–449 (1994).

55. M.M. Reddy, Carbonate precipitation in Pyramid Lake, Nevada: Probable control by magnesium ton, in: *Mineral Scale Formation and Inhibition,* Ed. Z. Amjad (Plenum Press, New York, 1995).

56. A. Gutjahr, H. Dabringhaus and R. Lacmann, Studies of the growth and dissolution kinetics of the $CaCO_3$ polymorphs calcite and aragonite: II. The influence of divalent cation additives on the growth and dissolution rates, *J. Cryst. Growth* **158**, 310–315 (1996).

57. M. Deleuze and S.L. Brantley, Inhibition of calcite crystal growth by Mg^{2+} at 100°C and 100 bars: influence of growth regime, *Geochim. Cosmochim. Acta* **61**, 1475–1485 (1997).

58. R.A. Berner, The role of magnesium in the crystal growth of calcite and aragonite from sea water, *Geochim. Cosmochim. Acta* **39**, 489–504 (1975).

59. R.L. Folk, The natural history of crystalline calcium carbonate: effect of magnesium content and salinity, *J. Sedimentary Petrology* **44**, 40–53 (1974).

60. K. Sawada, Mechanisms of crystal growth of ionic crystals in solution. Formation, transformation, and growth inhibition of calcium carbonates, in: *Crystallization Processes,* Ed. H. Ohtaki (Wiley Series in Solution Chemistry, John Wiley & Sons, New York, 1998).

61. K.E. Chave, K.S. Deffeyes, P.K. Weyl, R.M. Garrels and M.E. Thompson, Observations on the solubility of skeletal carbonates in aqueous solution, *Science* **137**, 33–34 (1962).

62. F.A. Cotton and G. Wilkinson, *Advanced Inorganic Chemistry* (John Wiley and Sons, New York, 1962) p. 959.

63. M.M. Reddy and G.H. Nancollas, The crystallization of calcium carbonate I, *J. Colloid Interface Science* **36**, 166–172 (1971).

64. G.H. Nancollas and N. Purdie, The kinetics of crystal growth, *Quarterly Reviews* **18**, 1–20 (1964).

65. K. De Groot and E.M. Duyvis, Crystal form of precipitated calcium carbonate as influenced by adsorbed magnesium ions, *Nature* **212**, 183–184 (1966).

66. K.J. Davis, P.M. Dove and J.J. De Yoreo, Resolving the control of magnesium on calcite growth: thermodynamic and kinetic consequences of impurity incorporation for biomineral formation, in: *Morphology and Dynamics of Crystal Surfaces in Complex Molecular Systems,* Materials Research Society Symposium Proceedings, Vol. 620, Eds J.J. De Yoreo, W. Casey, A. Malkin, E. Vlieg and M. Ward (2001).

67. K.J. Davis, P.M. Dove and J.J. De Yoreo, The role of Mg^{2+} as an impurity in calcite growth, *Science* **290**, 1134–1137 (2000).

68. K.J. Davis, Magnesium as an impurity in calcite growth: thermodynamic and kinetic controls on biomineral formation (M.S. Thesis, Georgia Institute of Technology, 2000).

69. W.K. Burton, N. Cabrera and F.C. Frank, The growth of crystals and the equilibrium structure of their surfaces, *Phil. Trans. R. Soc.* **243**, 299 (1951).

70. A.A.A. Chernov, *Modern Crystallography, Vol. III: Crystal Growth* (Springer-Verlag, Berlin 1984).

71. H.H. Teng, P.M. Dove and J.J. DeYoreo, Reversed calcium carbonate morphologies induced by microscopic growth kinetics: insight into biomineralization, *Geochim. Cosmochim. Acta.* **63**, 2507–2512 (1999).

72. H. Leitmeier, Zur Kenntnis der Carbonate, Die Dimorphie des Kohlensauren Kalkes. I. Teil. *Neues Jahrb. Mineral.,* Heft **1**, 49–74 (1910).

73. H. Leitmeier, Zur Kenntnis der Carbonate. II. Teil. *Neues Jahrb. Mineral.,* Beilageband **40**, 655–700 (1915).

74. R.A. Berner, Chemical diagenesis of some modern carbonate sediments, *Am. J. Science* **264**, 1–36 (1966).

75. J.L. Bischoff and W.S. Fyfe, Catalysis, inhibition, and the calcite-aragonite problem. I. The aragonite-calcite transformation. *Am. J. Science* **266**, 65–79 (1968).

76. M. Kitamura, Crystallization and transformation mechanism of calcium carbonate polymorphs and the effect of magnesium ion, *J. Colloid and Interface Science* **236**, 318–327 (2001).

77. E.K. Berner and R.A. Berner, *Global Water Cycle Geochemistry and Environment* (Prentice-Hall, Englewood Cliffs, NJ, 1987).

78. W.A. Deer, R.A. Howie and J. Zussman, *An Introduction to the Rock-Forming Minerals* (Halsted Press, 1966).

79. J.A. Speer, Crystal chemistry and phase relations of orthorhombic carbonates, in: *Carbonates: Mineralogy and Chemistry,* MSA Vol. 11, Ed. R.J. Reeder (1983).

80. R.D. Shannon, Revised effective ionic radii and systematic studies of interatomic distances in halides and chalcogenides, *Acta Cryst.* **A32,** 751–767 (1976).

81. T.P. Scoffin, *An Introduction to Carbonate Sediments and Rocks* (Chapman and Hall, New York, 1987).

82. R.W. Lahann, A chemical model for calcite growth and morphology control, *J. Sedimentary Petrology* **48**, 337–344 (1978).

83. F. Lippmann, Versuch zur Aufklarung der Bildungsbedeingungen von Kalzit under Aragonit, *Fortschr. Miner.* **38**, 156–161 (1960).

84. J.O. Titiloye, S.C. Parker, D.J. Osguthorpe and S. Mann, Predicting the influence of growth additives on the morphology of ionic crystals, *J. Chem. Soc. Commun.* (1991).

85. K.J. Davis, P.M. Dove, L.E. Wasylenki and J.J. De Yoreo, Morphological consequences of intrasectoral zoning of Mg^{2+} in calcite: a plausible mechanism for crystal elongation, *American Mineralogist* (2004) in press.

86. H.J. Meyer, The influence of impurities on the growth rate of calcite, *J. Cryst. Growth* **66**, 639–646 (1984).

87. A. Katz, The interaction of magnesium with calcite during crystal growth at 25–90°C and one atmosphere, *Geochim. Cosmochim. Acta* **37**, 1563–1586 (1973).

88. J.W. Morse, Dissolution kinetics of calcium carbonate in sea water. V. Effects of natural inhibitors and the position of the chemical lysocline, *Am. J. Science* **274**, 638–647 (1974).
89. M.M. Reddy, Crystallization of calcium carbonate in the presence of trace concentrations of phosphorus-containing anions, *J. Cryst. Growth* **41**, 287–295 (1977).
90. W.A. House, Inhibition of calcite crystal growth by inorganic phosphate, *J. Colloid and Interface Science* **119**, 505–511 (1987)
91. E.A. Burton and L.M. Walter, Relative precipitation rates of aragonite and Mg calcite from seawater: temperature or carbonate ion control?, *Geology* **15,** 111–114 (1987).
92. P.M. Dove and M.F. Hochella, Jr., Calcite precipitation mechanisms and inhibition by orthophosphate: in situ observations by scanning force microscopy, *Geochim. Cosmochim. Acta* **57**, 705–714 (1993).
93. E.L. Dromgoole and L.M. Walter, Inhibition of calcite growth rates by Mn^{2+} in $CaCl_2$ solutions at 10, 25 and 50°C, *Geochim. Cosmochim. Acta* **54**, 2991–3000 (1990)
94. R.J. Reeder, Interactions of divalent cobalt, zinc, cadmium, and barium with the calcite surface during layer growth, *Geochim. Cosmochim. Acta* **60,** 1543–1552 (1994).

3

Kinetics of liquid–solid transformation in emulsion droplets

Kiyotaka Sato*
Graduate School of Biosphere Science, Higashi-Hiroshima, 739-8528, Japan

Attempts have been made recently to develop novel methods of crystallization for producing functional materials, resulting in increased exploration of crystallization phenomena in encapsulated systems like emulsions, vesicles, and foams [1,2]. Emulsion particles are confined systems of an aqueous or non-aqueous phase, dispersed in a continuous phase in which the confined dispersed-phase materials are insoluble in the continuous phase (Figure 3.1). In most cases, the non-aqueous phase is made of oil and the aqueous phase of water, and the two phases are dispersed using techniques suitable for the specific properties needed for forming the emulsion. Two types of emulsions, oil-in-water (O/W) and water-in-oil (W/O), can be made based on the ratio of the oil and water phases, the methods of dispersion techniques, and the nature of the amphiphilic molecules (emulsifiers).

Turnbull *et al.* were the first to explore the nucleation processes of organic substances dispersed in an aqueous phase [3]. Skoda and Tempel extended the emulsion crystallization experiments towards natural fats [4]. Both groups clearly showed that supercooling of the
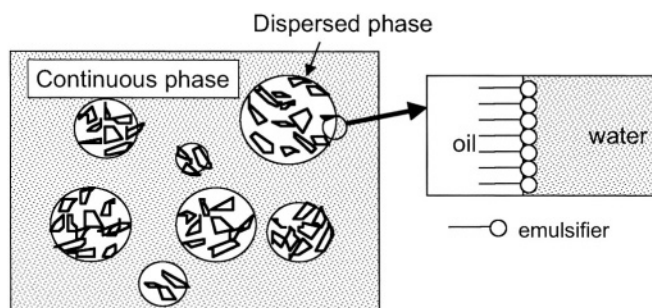

FIGURE 3.1. Emulsion droplets (oil-in-water type).

*E-mail address: kyosato@hiroshima-u.ac.jp

nucleation in the O/W emulsion droplets increased compared to the bulk phase. After their pioneering work, the research on crystallization in emulsion droplets has been conducted on widely diversified systems of crystallizing materials and emulsion droplets, as recently reviewed [5,6].

Despite its complexity, liquid–solid transformation in emulsion droplets has recently attracted attention as a novel area of crystal growth for both hard and soft materials. This complexity is revealed in the rate and extent of crystallization of the materials in the droplets. Numerous factors are involved in the complicated crystallization phenomena: the effects of droplet size and distribution [7]; droplet–droplet interactions [8,9]; and additives in the dispersed phase [10]. To explore the complexity of these origins, many researchers have focused on observing nucleation processes of crystals in emulsion droplets, bearing in mind that post-nucleation crystal-growth processes in the droplets may not differ from those in the bulk state.

In this chapter, we summarize our recent experimental results to better understand the interfacial nucleation of crystals in emulsion droplets [10,12–15]. We employed non-destructive techniques to monitor the events of crystal nucleation in the emulsion droplets, e.g., synchrotron radiation, X-ray diffraction, DSC, and ultrasound velocity.

3.1. CHARACTERISTICS OF CRYSTAL NUCLETION IN EMULSION DROPLETS

In this section, we will briefly discuss the characteristic properties of crystallization processes of crystals in an emulsion.

3.1.1. Nucleation: homogeneous vs. heterogeneous

Crystallization in emulsion occurs by nucleation and growth of crystals consisting of the materials contained in the droplets, after dissolving materials in the droplets. We can reasonably assume that post-nucleation growth processes in the emulsion are basically the same as those observed in the bulk state. It is worth noting that the dispersed phase, in which the crystallization occurs, contains minor components of amphiphilic substances that are employed for emulsification (Figure 3.1). If these substances interfere with solute molecules at the growth interface, the post-nucleation growth of crystals differs from the same growth in pure liquid.

Nucleation in the pure liquid in the emulsion droplets becomes homogeneous under two conditions [16]: (a) when the crystalline embryos are entirely immersed in the droplets, and (b) when the small size of the droplets induces changes in the thermodynamic properties of the embryos. If these conditions are not met, nucleation becomes heterogeneous.

In addition to emulsifiers, catalytic foreign materials present in liquid when the droplets contain foreign molecules behaving as nucleation-catalytic centers, lead to heterogeneous nucleation [5] (Figure 3.2). In the emulsion system, the dispersed phase is divided into a number of droplets. When the size distribution of the droplets is wide (poly-dispersed droplets), nucleation-catalytic materials (hereafter referred to as impurities) are distributed unequally throughout some of the droplets. Most probably, larger droplets will have higher impurity concentrations. In such a case, we can reasonably assume that nucleation assisted by the impurities is more pronounced in larger droplets than in smaller ones, through volume heterogeneous nucleation (Figure 3.3A).
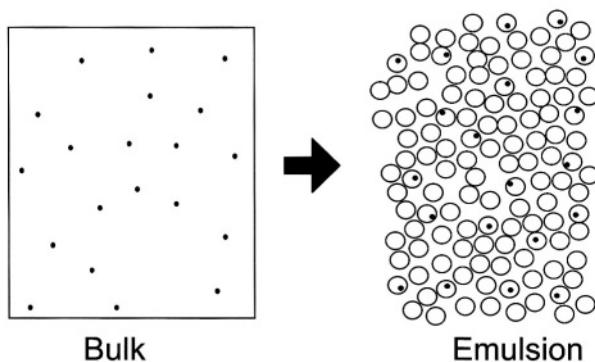
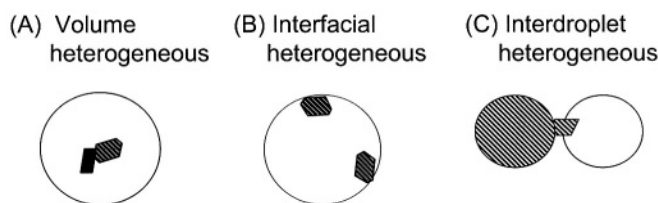FIGURE 3.2. Nucleation-catalytic impurities in bulk and emulsion droplets.

FIGURE 3.3. Heterogeneous nucleation processes in emulsion droplets.

The membrane itself, encapsulating the liquid from the continuous phase, can also be catalytic for nucleation when molecular interactions between constructing moieties of the membrane and the solute molecules or ions are operative. Examples of this are van der Waal's interactions between the hydrophobic moieties of the membrane and the organic molecules, and electrostatic interactions and hydrogen bonding between polar molecules and polar moieties of the membrane. Such nucleation may be called interfacial heterogeneous nucleation (Figure 3.3B). The present chapter focuses on this nucleation process.

3.1.2. Droplet–droplet interactions

In the emulsion state, droplets are rapidly moving and frequently collide with one another because of their Brownian motion and gravity. Thermal movement and droplet–droplet interactions cause various destabilization mechanisms, in which the crystallization due to droplet–droplet interactions plays an important role (Figure 3.3C). The already crystallized dispersed-phase droplets colliding with the other droplets emulsifying the supercooled liquid cause interdroplet nucleation, provided that the crystal phase comes in contact with the supercooled liquid. Dickinson's group [17] first demonstrated this nucleation using time-dependent measurement of ultrasound velocity when they observed the kinetics of the crystallization of supercooled oil droplets in emulsions containing a mixture of solid and liquid n-hexadecane droplets at constant temperature.

The ultrasound velocity (USV) through oil-in-water emulsions is proportional to the extent of the crystallization of oil droplets [18]. For example, when an emulsion is kept at a constant temperature far below the melting point of the droplet material, the progressive
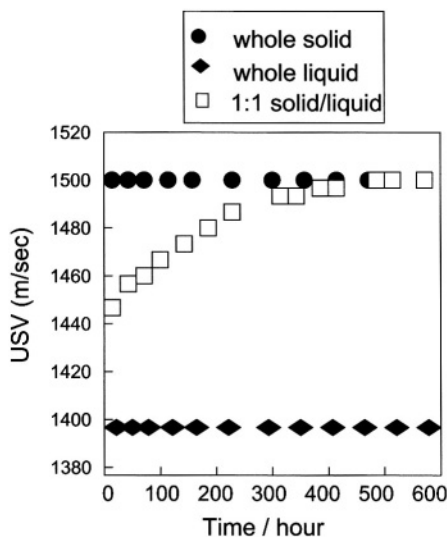
FIGURE 3.4. Ultrasound velocity (USV) of oil-in-water emulsion of n-hexadecane measured at 6°C.

crystallization of the droplets in the emulsion brings about a gradual change of USV in accordance with the nucleation and crystal growth of the materials in the droplets. Based on the USV values for solid and liquid of the dispersed phase, and for continuous water phase at different temperatures, we may relate the USV to the percent of crystallized droplets.

Figure 3.4 shows time variation in USV (m/s) of n-hexadecane-in-water emulsion (volume ratio, 20:80) prepared with the emulsifier (non-ionic surfactant, Tween 20) measured at 6°C, which is far below the melting temperature (18°C) [17]. No crystallization occurred when the droplets containing supercooled liquid were kept over 600 hours. However, crystallization was induced in the liquid droplets when solid droplets were present and reached the USV values of the whole solid, as shown by the increase in the USV values of the droplets containing 50% solid and 50% liquid during the isothermal crystallization. It was assumed that the mechanism of the inter-droplet crystallization involves crystals on the solid droplets penetrating supercooled liquid droplets during collision, thereby acting as nucleation cites for crystal growth as depicted in Figure 3.3C.

3.1.3. Effects of droplet size distribution

In addition to the factors mentioned above, crystallization in emulsion droplets is also influenced by the size distribution of the droplets. The emulsion is referred to as *monodispersed* if all the droplets in the emulsion are of the same size. If this not the case, the emulsion is referred to as *polydispersed*. Actually, most emulsions are polydispersed, mainly because widely employed emulsification techniques form polydispersed emulsion droplets, and it is difficult to obtain monodispersed emulsion droplets. It is interesting to compare the crystallization rate of the polydispersed emulsion to that of the monodispersed emulsion.

We analyzed the kinetics of isothermal crystallization of the droplets in polydispersed emulsions under conditions where each emulsion droplet gives birth to one nucleus only (mono-nucleus model) [19]. We derived expressions for the time dependences of the num-
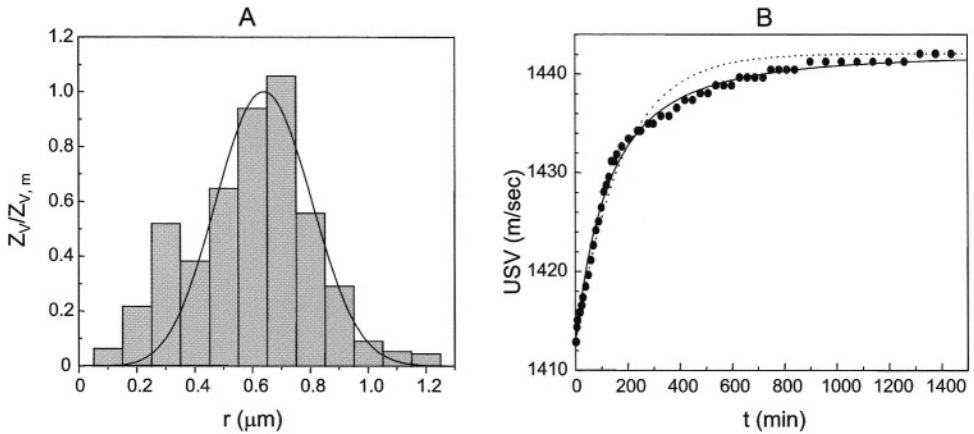
FIGURE 3.5. (A) Size distributiom of oil (palm oil)-in-water emulsion droplets and (B) ultrasound velocity (USV). For (A), bars are actual size distribution. For (B), closed circles are experimental data, solid and dotted curves are calculations based on polydisperse and monodisperse emulsion, respectively.

ber of crystallized droplets and the fraction of crystallized droplet volume, and compared them to the experiments obtained by the ultrasound velocity technique. Figure 3.5A shows the size distribution of polydispersed emulsion droplets of palm oil in the water phase and measurement of USV values at constant temperature (10°C). Since the melting temperature of palm oil (a multiple-component vegetable fat) is around 30°C, the USV value of the emulsion measured at 10°C increased with time due to the nucleation and crystal growth of the palm oil (Figure 3.5B). The evolution of the USV value with time best fit the calculation of the polydispersed emulsions (solid curve) rather than the monodispersed emulsions (dotted curve). Polydispersed, n-hexadecane-in-water emulsions were similarly analyzed. It would be quite interesting to compare the results of the polydispersed and monodispersed emulsions, since it is easier to numerically evaluate monodispersed volume nucleation and surface nucleation than polydispersed emulsion droplets. This has not been done because it is difficult to obtain finely monodispersed emulsions.

3.2. INTERFACIAL NUCLEATION IN EMULSION ACCELERATED BY ADDITIVES

In the case of emulsion systems where an oil phase is emulsified in a water phase (O/W emulsion), the transformation from liquid oil to fat crystals remarkably influences the physical properties of the emulsions, such as stability, rheology, and appearance [20]. Therefore, it is important to clarify the mechanisms of nucleation and crystal growth of the oil phase in the O/W emulsions. We have recently studied the effects on crystallization behavior of n-alkanes in the O/W emulsions by adding various hydrophobic emulsifiers [10–15] (Figure 3.6 and Table 3.1). Below, we summarize the results of the experiment regarding how additives accelerate nucleation of crystals and modify the polymorphic occurrence, both of which are observed in emulsion systems and not in the bulk state.

Sucrose fatty acid oligo-ester(SOE)
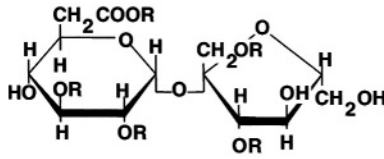
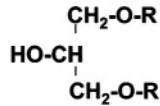Polyglycerine fatty acid ester (PGE)
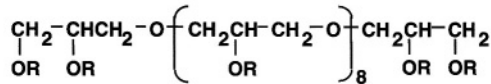
Diacyl-glycerol(DAG)

FIGURE 3.6. Additives of high-melting emulsifiers put in O/W emulsion (R; fatty acid).

TABLE 3.1.
Temperatures of crystallization (T_c) and melting (T_m) of
additives employed for modifying crystallization properties of
oil phase in O/W emulsion droplets; SOE: sucrose fatty acid
oligo-ester, PGE: polyglycerine fatty acid ester, DAG:
diacyl-glycerol.

Additive	T_c (°C)	T_m (°C)
SOE (R)		
stearic (S-170)	58.2	68.0
palmitic (P-170)	52.6	61.5
PGE (R)		
stearic (10G10S)	46.9	53.2
DAG (R)		
behenic (DB)	72.7	77.7
stearic (DS)	66.6	74.7
palmitic (DP)	58.7	69.0
lauric (DL)	48.1	56.6
oleic (DO)	6.4	20.5

3.2.1. Effects on nucleation rates

We studied crystallization rates of n-hexadecane dispersed in the O/W emulsion (oil 20 wt%, water 80 wt%) using a USV measurement technique. We employed Tween 20 for emulsification to form the O/W emulsion, which we measured with a laser diffraction particle analyzer (Shimadzu, SALD-2000A and 2000J) soon after homogenization. The
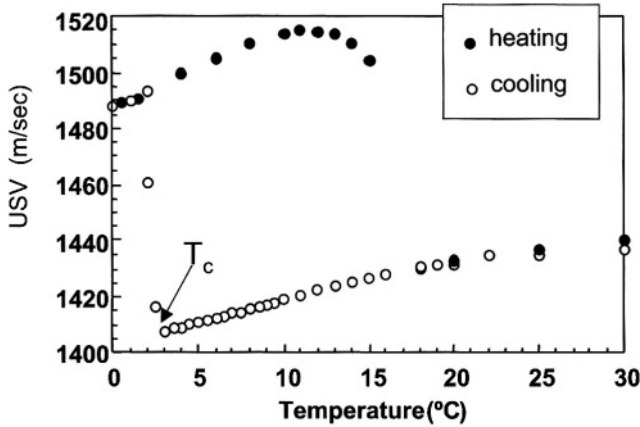
FIGURE 3.7. Temperature dependence of ultrasound velocity (USV) of n-hexadecane-in-water emulsion without additives.

average droplet diameter was calculated as $0.8 \ \mu m$, and the size distribution of emulsion droplets was similar to that in Figure 3.5A. We added the highly hydrophobic emulsifiers shown in Figure 3.6 to n-hexadecane in an attempt to modify the rate of crystallization of n-hexadecane. We paid particular attention to the opposing effects of additives on the rates of nucleation and crystal growth in the emulsion droplets.

Figure 3.7 shows the USV values of n-hexadecane-in-water emulsion without additives (pure emulsion) measured during the cooling and heating processes. The USV suddenly jumps around 3°C, corresponding to the crystallization of n-hexadecane, and then remains at 1480 m/s on further cooling. Crystallization temperature (T_c) was thus defined as shown by the arrow in Figure 3.7. In contrast, USV gradually increased on heating from 0°C to 14°C, started to decrease around 15°C, and returned to the initial values around 18°C. This indicates that melting occurred at almost the same temperature as bulk n-hexadecane. When the melting temperatures of the additives were high, we found that the addition of the emulsifiers listed in Figure 3.6 increased the T_c as the amount of the additives increased.

Figure 3.8A shows the results of the DAG additives [14]. Adding DL (dilauroyl-glycerol) and DO (dioleoyl-glycerol) did not increase T_c at an additive concentration of 1 wt% with respect to n-hexadecane. However, T_c increased with the increased concentration of DP (dipalmitoyl-glycerol), DS (distearoyl-glycerol), and DB (dibehenoyl-glycerol), and the extent of this increase in T_c was enhanced by increasing the melting and crystallization temperatures of the DAGs (see Table 3.1). Figure 3.8B shows the variation in T_c with increasing amounts of the three additives.

We measured the growth rate of n-hexadecane crystals in bulk liquid with additives of P-170, using an optical microscope to separately examine the effects of additives on nucleation and crystal growth [10]. The rate of displacement of the growing surface of crystals was monitored *in-situ* at 17.1°C and 16.7°C, showing clearly that adding P-170 remarkably retarded the rate of crystal growth of n-hexadecane, as shown in Figure 3.9. The same results were obtained for the additives listed in Figure 3.6. Interestingly, we found that both the additives that increased T_c and the low-melting-point additives that did
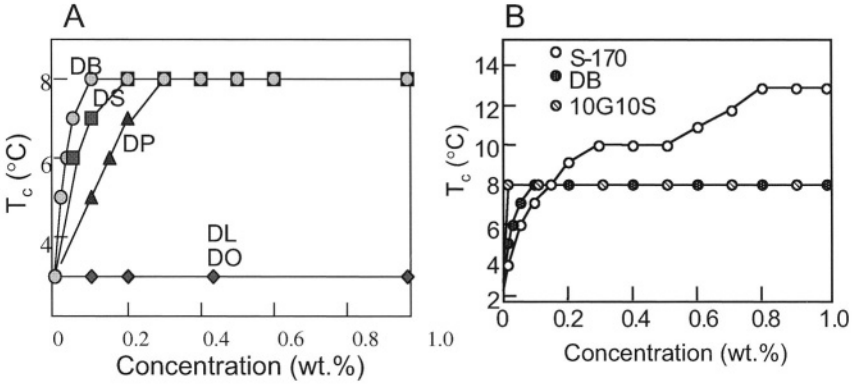
FIGURE 3.8. Variation in crystallization temperature (T_c) of n-hexadecane-in-water emulsion measured by ultrasound velocity measurements. (A) Comparison with different diacylglycerols additives, and (B) comparison with three different additives.
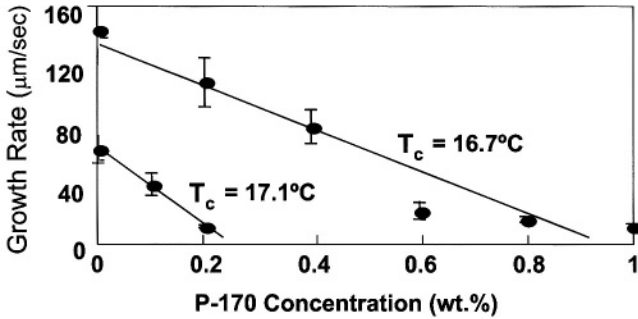

FIGURE 3.9. Linear crystal growth rate of n-hexadecane in bulk with P-170 measured at two crystallization temperature (T_c).

not change T_c retarded crystal growth. This leads us to conclude that the increase in T_c in the emulsion system is due to the acceleration of nucleation.

3.2.2. Optical observation of crystallization in emulsion droplets

To observe the crystallization in the droplet *in-situ*, we prepared a mixture of n-octadecane ($T_m = 27.9°C$) and n-dodecane (C_{12}, $T_m = -9.6°C$) as the dispersed phase (hereafter $C_{18} + C_{12}$ emulsion) [15]. It was shown that the mixture of n-octadecane and n-dodecane in a 50/50 wt% ratio exhibited a high degree of supersaturation in the crystallization of n-octadecane due to the solubilization effect of n-dodecane. Therefore, the acceleration of crystallization caused by the additive (10G10S) was easily observed in the $C_{18} + C_{12}$ emulsion using an optical microscope equipped with a high-speed video system. We prepared mono-dispersed droplets with a 34 μm diameter using a micro-channel technique. We formed all the emulsion droplets at 60°C to avoid fat crystallization, and cooled them to various crystallization temperatures.
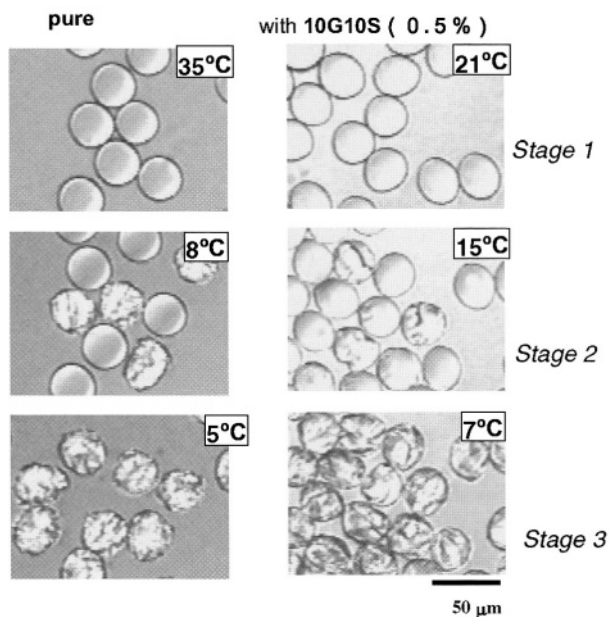
FIGURE 3.10. Optical micrographs of *in-situ* observation of crystallization of n-octadecane in C_{18+12} emulsion droplets.

Successive video images in Figure 3.10 show morphological changes of the $C_{18} + C_{12}$ emulsion droplets: without and with 10G10S additive (0.5 wt%). In the pure $C_{18} + C_{12}$ emulsion, there were no detectable morphological changes in the spherical droplet shape during the cooling process until n-octadecane crystallized at 8°C. When we added 10G10S, we observed complicated morphological changes at temperatures far above the T_c of n-octadecane. First, the spherical droplet shape we observed at high temperature deformed into an ellipsoid around 25°C. To quantify the degree of deformation, we calculated the average S/L values over 40 droplets at each temperature below 30°C, as shown in Figure 3.11. The S/L value was 1.0 at 30°C, representing a spherical droplet, but gradually decreased around 25°C and reached 0.8 around 22°C. We defined this deformation of the droplet shape of the $C_{18} + C_{12}$ emulsion as stage 1.

On further cooling, we detected the next stage of morphological change as the formation of an aggregate in the droplet around 22°C. We defined this process as stage 2. When temperature was reduced from 22°C, the size of the aggregate in the droplet became larger, and the number of droplets forming such an aggregate increased. Finally, the droplets deformed drastically around 8°C, with every droplet becoming polygonal. We defined this process as stage 3, thought to represent the crystallization of n-octadecane in the mixed phase of n-octadecane and n-dodecane. Figure 3.11 shows the variation in the number of droplets exhibiting stage 3 characteristics with and without 10G10S of the $C_{18} + C_{12}$ emulsion. In the only pure emulsion that exhibited stage 3, the number of crystallized droplets increased drastically between 8°C and 5°C. The 10G10S containing $C_{18} + C_{12}$ emulsions, entered stage 3 at 10°C and was fully in stage 3 at 6°C.
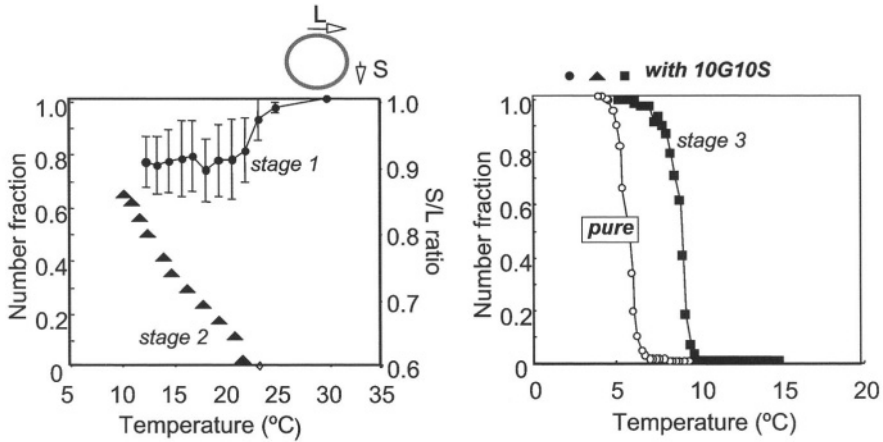
FIGURE 3.11. Fractions of droplet numbers that exhibited stage 1 (droplet deformation), stage 2 (aggregate formation) and stage 3 (crystallization) with and without additive of 10G10S.
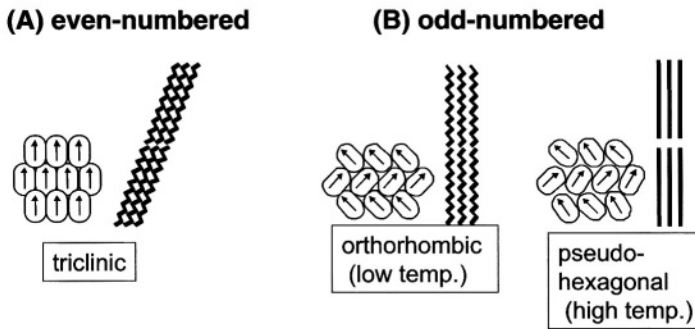

FIGURE 3.12. Polymorphism in n-alkane crystals.

3.2.3. Effects on crystal structure modification

We report here the *in-situ* measurements of the crystallization of the emulsion droplets, showing that additives introduced into the droplets cause the formation of crystal structures that are different from those formed in the bulk [21]. To determine the crystal structure, we employed synchrotron radiation (SR) X-ray diffraction of small-angle and wide-angle areas combined with differential scanning calorimetry (hereafter SAXS/WAXS-DSC analyses). Although even-numbered n-alkanes always crystallize in a triclinic structure from the bulk phase [22] (Figure 3.12A), our measurements revealed that these oils nucleated into pseudo-hexagonal and orthorhombic crystal structures when certain additives were mixed with the droplets, similar to the crystals of odd-numbered n-alkanes (Figure 3.12B).

Simultaneous SR-XRD/DSC measurements were performed on the 15A-beam line at the Photon Factory in Tsukuba, Japan. Using a modified DSC (Mettler model FP 84), we obtained time-resolved XRD and thermal data simultaneously from the same sample. The wavelength of the SR X-ray beam was 0.1506 nm. The samples (10 mg) were sealed in a
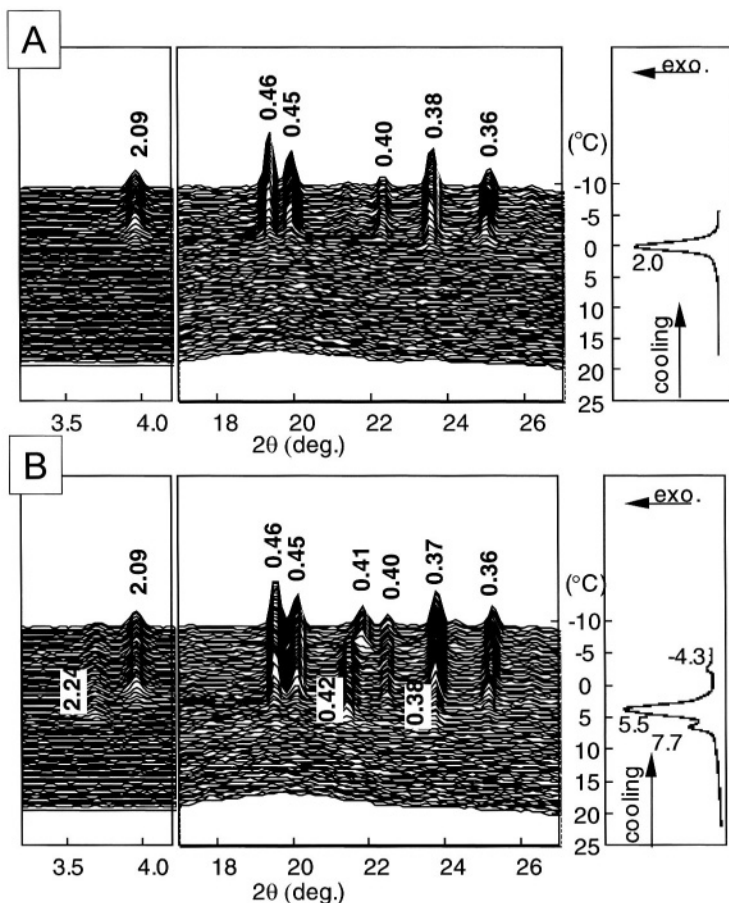
FIGURE 3.13. SAXS/WAXS-DSC data of n-hexadecane ($n_c = 16$)-water emulsion without additive (A), and with additive (B) during cooling processes.

1.5 mm-thick aluminum cell. We performed all experiments in both heating and cooling modes with a scan rate of 2.0°C/min, and we recorded the X-ray diffraction spectra at 10-s intervals.

Figure 3.13 shows the SAXS/WAXS-DSC data obtained during cooling of an n-hexadecane ($C_n = 16$)-in-water emulsion with and without the additive 10G10S. In the pure emulsion (Figure 3.13A), an exothermic peak appeared at 2.0°C, corresponding to the crystallization of triclinic n-hexadecane crystal as revealed in the SAXS (2.09 nm) and WAXS (0.46 nm, 0.45 nm, 0.40 nm, 0.38 nm and 0.36 nm) patterns that appear at the DSC crystallization temperature. On heating, the triclinic crystal of n-hexadecane melted at 19.0°C (not shown). The SR-XRD patterns clearly indicated that the triclinic structure crystallized at 2.0°C and then melted at 19.0°C. The same structure was crystallized at 18.5°C from the bulk liquid. Hence, the supercooling of these n-hexadecane droplets (15°C) was much greater than the supercooling (0.5°C) for the bulk liquid, as observed by the ultrasound velocity measurements (Figure 3.7).
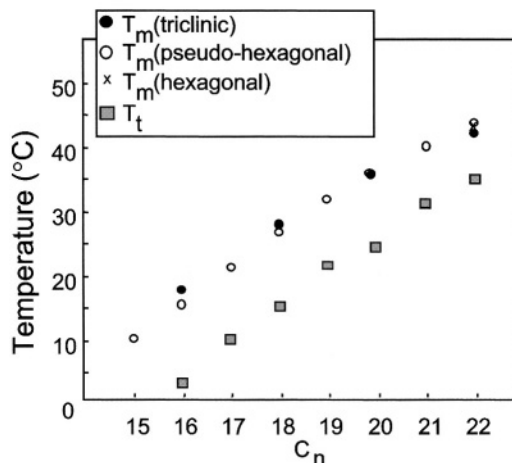
FIGURE 3.14. Temperatures of transformation (T_t) and melting (T_m) of n-alkane crystals formed in O/W emulsion droplets with the additive of 10G10S. C_n; number of carbon atoms in n-alkanes.

Figure 3.13B shows the SAXS/WAXS-DSC data obtained during cooling of the C_{16} emulsion with the 10G10S additive. Three exothermic DSC peaks appeared: a big peak (5.5°C) and two small peaks (7.7 and –4.3°C). Each DSC peak appeared at the same time that new peaks appeared in the SR-XRD SAXS/WAXS patterns. The crystallization of a non-triclinic structure is indicated by an exothermic DSC peak and by SAXS/WAXS patterns at 7.7°C, before the crystallization of the triclinic structure at 5.5 °C. The non-triclinic structure had a solid-state transformation to a low-temperature structure at –4.3°C. The reverse transformations occurred during heating (not shown here). The low-temperature structure was transformed to a high-temperature structure at 4.3°C. The high-temperature structure melted at 16.6°C, and the triclinic structure melted at 19.4°C. The WAXS patterns of the high-temperature (low-temperature) forms corresponded to the pseudo-hexagonal (orthorhombic) structures in odd-numbered n-alkanes that crystallized from the bulk liquid, and in the emulsion droplets. The SAXS peak at $2\theta = 3.7$°C for the pseudo-hexagonal structure corresponds to a 2.24 nm-thick layer. The same features of C_{16} with 10G10S were observed in the SAXS/WAXS-DSC data for C_{16}, C_{18}, C_{20}, and C_{22} emulsions containing the additives of DAS-750, P-170, and DB.

Figure 3.14 shows the melting (T_m) and transformation (T_t) temperatures for the crystal forms observed in the emulsion droplets of the even-numbered n-alkanes with and without the additives, and of the odd-numbered n-alkanes without the additives. T_t corresponds to the transformation from orthorhombic to pseudo-hexagonal polymorphs in the crystals of the odd-numbered alkanes, and in the additive-induced crystals of the even-numbered alkanes. We observed the triclinic structures, both in pure and additive-containing emulsion droplets for the even-numbered n-alkanes.

To summarize, we note the following results in Figures 3.13 and 3.14.

(a) T_m and T_t of all crystalline forms increased when C_n of the n-alkanes increased, because the latent heats of melting and transformation of the n-alkanes increased with the increasing chain length.

(b) The T_m values of the pseudo-hexagonal forms were less than (for $C_n = 16$, 18) or the same as (for $C_n = 20$, 22) those of the triclinic forms, even though crystallization of the pseudo-hexagonal forms always occurred at higher temperatures than the triclinic forms.

It is obvious that the additive-induced pseudo-hexagonal forms of the even-numbered alkanes were thermodynamically less stable than the triclinic forms, whereas the nucleation rate of the pseudo-hexagonal forms was higher than that of the triclinic forms. We observed this result only in the emulsion droplets, not in the bulk state. As for the structural properties of the additive-induced new polymorphs in the even-numbered alkanes, it was also evident that the aliphatic chain axis of the pseudo-hexagonal and orthorhombic forms was perpendicular to the lamellar plane, in the same manner as those of the odd-numbered n-alkanes. Therefore, we reached the important conclusion that the high-melting emulsifier additives put in the O/W emulsion droplets of the even-numbered alkanes induced the crystallization of new polymorphic forms at a greater rate of nucleation than the basic triclinic polymorph, as metastable forms.

3.2.4. Interfacial heterogeneous nucleation assisted by the additives

To interpret the results of acceleration of nucleation (Section 3.2.1) and formation of new n-alkane crystals (Section 3.2.3) in emulsion droplets with the additives, we compared the nucleation rates of the two crystal forms by considering the Gibbs free-energy difference between the liquid and crystal phases (ΔG) and activation free energy of nucleation ($\Delta G^{\#}$) (Figure 3.15). In this figure, dark (open) ovals at the oil–water boundary mean polar
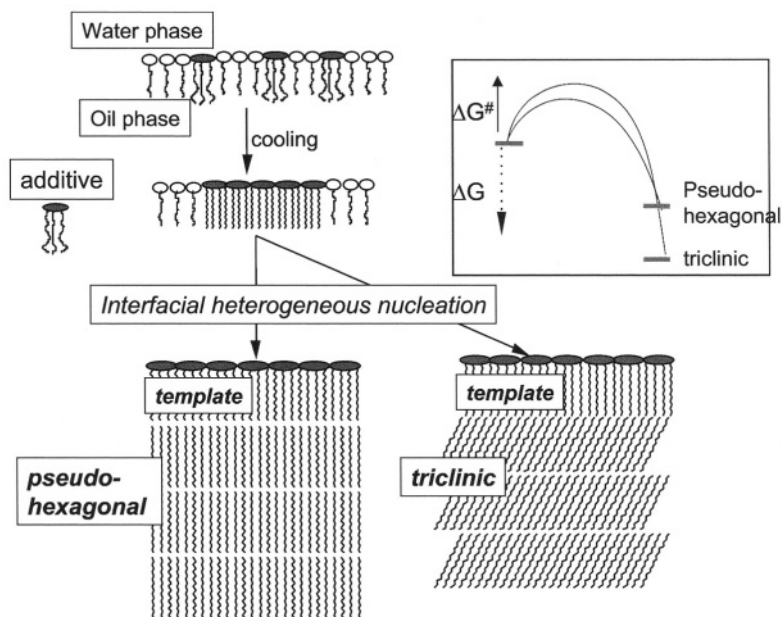

FIGURE 3.15. A model of interfacial heterogeneous nucleation in O/W emulsion with additives.

head groups of additive molecules (Tween 20 molecules). Zigzag lines are aliphatic chains of the additive and n-alkane. The template films are likely aliphatic chains that crystallized at the oil-in-water interface. We propose that the additive film promotes the nucleation of the pseudohexagonal form over that of the triclinic form, even though the latter crystalline structure is more stable. Here, $\Delta G^{\#}$ is the barrier for nucleation and ΔG is the free-energy change for crystallization (see box at upper right).

For n-hexadecane, the fact that T_m of the pseudo-hexagonal form is less than that of the triclinic form means that ΔG of the triclinic form exceeds that of the pseudo-hexagonal form. However, the higher nucleation rate of the pseudo-hexagonal form means that $\Delta G^{\#}$ is smaller for the pseudo-hexagonal form than for the triclinic form. The nucleation rate, J, depends on $\Delta G^{\#}$ and absolute temperature as,

$$J = A \exp\left(-\Delta G^{\#}/k_B T\right), \tag{1}$$

where A is a pre-exponential factor and k_B is Boltzmann's constant. $\Delta G^{\#}$ is

$$\Delta G^{\#} = f\left(V^2 \gamma^3\right)(\Delta\mu)^{-2}, \tag{2}$$

where f is a geometrical factor for the nucleus, V is the molecular volume, γ is the interfacial energy of the nucleus, and $\Delta\mu$ is the difference in chemical potential between liquid and crystal. The fact that the nucleation rate of the pseudo-hexagonal form is greater than that of the triclinic form leads us to assume that $\Delta G^{\#}$ of the pseudo-hexagonal form is less than that of the triclinic form. Although numerical values of the factors appearing in eqs (1) and (2) are lacking for the pseudo-hexagonal form, an argument can be made that $\Delta\mu$ is greater for the triclinic form than for the pseudo-hexagonal form.

This indicates that the interfacial energy γ of the pseudo-hexagonal form decreased below that of the triclinic form through an interaction between the crystalline n-alkane molecules and an additive film or additive crystals at the interface. Such an interaction can arise by freezing the aliphatic chains of the high-melting-point additive molecules that are adsorbed on the oil–water interface due to their amphiphilic property. Because of limited solubility in oil and water, and because the temperatures in the experiments are below the melting temperatures of the additives, the additives should crystallize at the oil–water interfaces with their aliphatic chains aligned normally to their lamellar plane. These crystals could decrease the γ-values in contact with pseudo-hexagonal forms more than those for the triclinic forms, which contain tightly and obliquely arranged aliphatic chains, as shown in the crystal structure model in Figure 3.12. An *in-situ* optical observation of large monodispersed droplets of C_{18}-emulsion (Figure 3.10) and interfacial tension measurement [15] supports the model depicted in Figure 3.15.

The present results indicate that specific crystal structures can be nucleated under a critical influence of the interfacial heterogeneous nucleation occurring at the membrane around the droplets, by determining how various additives modify the interface structure. This phenomenon may be related to the significance of the ordering process of surface molecules during nucleation, as shown for surface freezing of the n-alkane monolayer [23], and formation of the metastable rotator phase as transient phases of short n-alkanes involving n-hexadecane [24], both of which occur in the bulk phase.

3.3. NUCLEATION AND TRANSFORMATION IN NANOMETER-SIZE EMULSION DROPLETS

3.3.1. *Significance and characteristics of crystallization in nanometer-size emulsion*

We recently investigated formation of O/W emulsion particles with diameters far less than 200 nm (hereafter referred to as nanometer-size emulsion) with a particular emphasis on application to Pharmaceuticals [25]. Nanometer-size emulsion generally exhibits many advantages such as lowered melting point, increased solubility of foreign materials in the droplets, transparency, permeability, and easy handling during and after the droplet production processes [26–28]. The O/W nanometer-size emulsion involving fat crystals within the particles also exhibits preferable properties such as controlled release of functional lipophilic materials that are incorporated in the dispersed phase [29]. Multiple techniques have been used to study physical properties of melting, crystallization, and polymorphic transformation in the nanometer-size emulsion droplets.

Westesen and co-workers have performed X-ray diffraction studies using synchrotron radiation (SR-XRD) to observe structural and thermal properties of crystalline nanoparticles [30–35]. Precise correlation of line width of small-angle SR-XRD spectra with the DSC thermopeaks has particularly shown that reduction in melting temperature of fat crystals was ascribed to reduction in their particle size. The number of long-chain lamella in a crystal was also reduced to two to three when the particle diameter was reduced to tens of nanometers.

Figure 3.16 shows DSC heating thermopeaks of bulk and O/W emulsion droplets of trimyristoylglycerol (MMM) with different mean particle sizes. The raw material is dis-
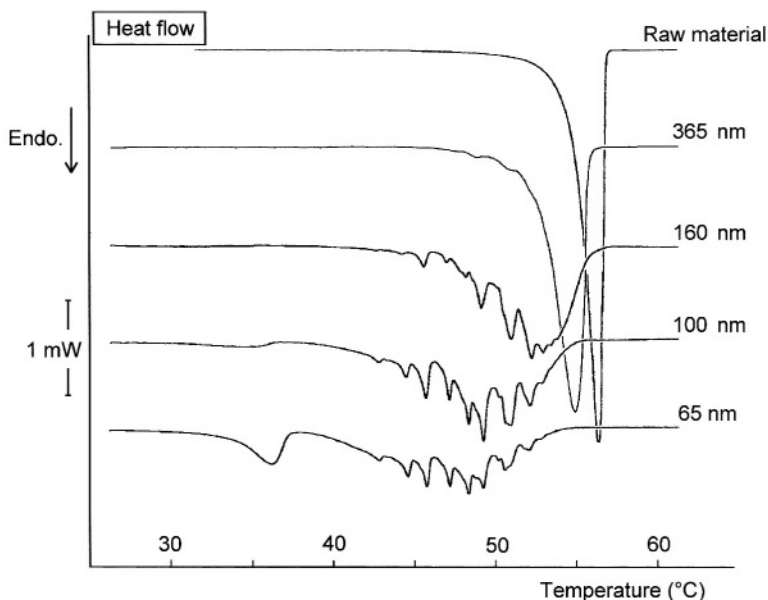

FIGURE 3.16. Heating DSC thermopeaks of nano-size emulsion droplets of tripalmitoyl glycerol with different diameters.

persed in a bile salt solution. It is evident that the DSC melting behavior of the nanosized particles strongly depends on their size. The DSC peaks broaden and shift to lower temperatures with decreasing particle size. Several discrete melting peaks appear when the particle size is less than 163 nm, and the lowest T_m is 36°C for droplets with an average diameter of 65 nm. The split in the melting peaks is not due to polymorphic transformation [36], since the SR-XRD study shows that the polymorphic forms of the particles showing the DSC peaks in Figure 3.16 are all of the most stable β form. It was assumed that the solid nano-particles of MMM with comparatively small thickness may only take on discrete values corresponding to multiples of the thickness of a single molecular MMM layer (3.6 nm). Discrete melting peaks mean a stepped increase in T_m with the increasing numbers of the MMM (001) lamella-type layer of the β crystal. This assumption was confirmed by precise analysis of the SR-XRD pattern.

The next section shows our recent results of the nanometer-size emulsion particles of trilauroylglycerol (LLL) whose crystallization, polymorphic transformation, and melting behavior was observed *in-situ* using a simultaneous SAXS/WAXS-DSC study [37].

3.3.2. Crystallization and transformation of fats in nano-size emulsion

We prepared the O/W nanometer-size emulsions with average diameters of 42 to 120 nm by applying mechanical shear using a high-pressure homogenizer. Figure 3.17A shows the simultaneous SR-SAXS/WAXS/DSC measurements of the bulk LLL samples. LLL has three polymorphs with T_m values of α (14°C), β' (34°C) and β (45°C). In Figure 3.17A, crystallization of β' of LLL at 19.2°C is shown as exhibited in a SAXS peak at 3.5 nm, two WAXS peaks at 0.42 and 0.37 nm, and a DSC exothermic peak. Figure 3.17B, taken during reheating of the sample after cooling, shows that β' transformed to β at 22.8°C and β crystals melted at 46.5°C on further heating.

Figures 3.18A and 3.18B show the SR-SAXS/WAXS/DSC data during cooling and heating of nanosize emulsion samples with an average diameter of 100 nm. Figure 3.18A shows a DSC exothermic peak and a corresponding single SAXS peak (3.6 nm) and WAXS peak (0.42 nm) at – 7.6°C, both indicating the crystallization of the α form of LLL. During further cooling to –20°C, the SAXS and WAXS peaks converted from 3.6 nm to 3.5 nm, and from the single pattern of 0.42 nm to split patterns of 0.42 nm and 0.37 nm around – 10°C. This change corresponds to the transformation from α to β', although it is not detectable by DSC. Figure 3.18B shows that the SAXS and WAXS peaks of β' gradually convert to those of β around 0°C during heating. On further heating, the SR-SAXS/WAXS spectra of β remain stable to about 40°C, where the all-SR-XRD spectra disappear due to melting.

Figure 3.19 shows the temperature dependence of the intensity of the SAXS peaks of β of LLL in both the bulk and the nanosize emulsion droplets shown in Figure 3.18. The spectral intensity for the bulk samples starts to decrease around 41°C, rapidly decreases around 45°C, and disappears at 49°C. As for the nanosize emulsion sample, reduction in diffraction intensity begins around 31 °C, a gradual decrease is exhibited at 38 to 41 °C, and then the spectra disappear at 42°C.

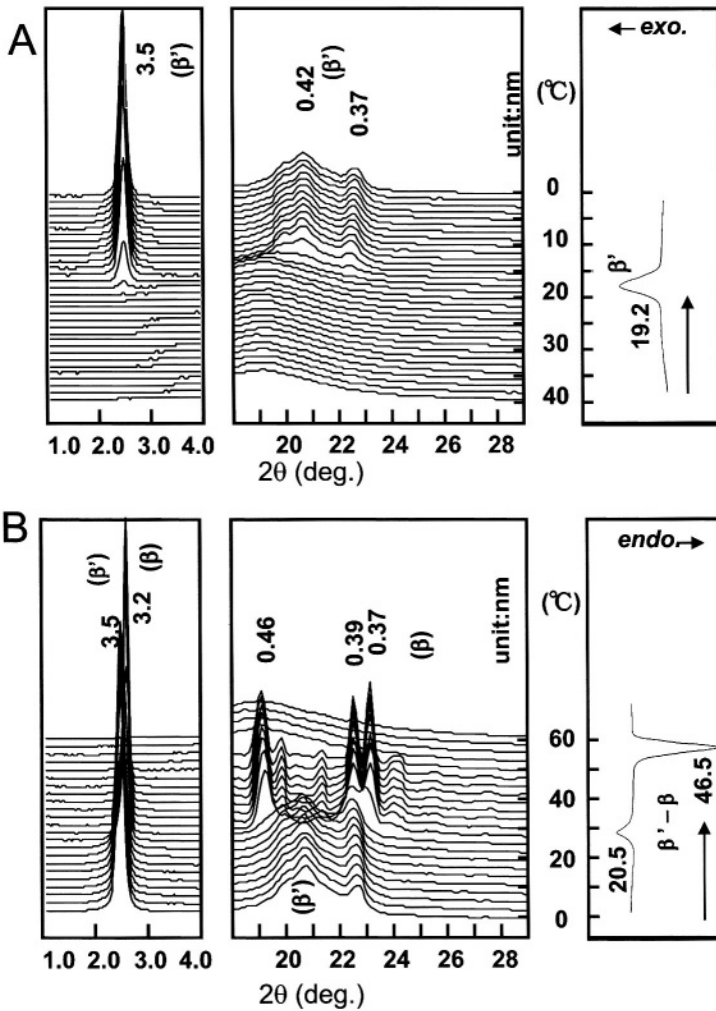The results for the nanosize emulsion of LLL are summarized below.

FIGURE 3.17. SR-XRD-SAXS/WAXS/DSC simultaneous patterns of (A) cooling and (B) heating (2°C/min) processes of trilauroyl-glycerol (LLL) in bulk state.

(a) The melting temperature of the stable β form of LLL was reduced from 46°C (bulk) to 26.5 to 44.0°C (nanosize emulsion). Crystallization temperature was also reduced from 18.9°C (bulk) to -9.5 ± 0.5°C (nanosize emulsion).

(b) The first occurring polymorph of LLL in the bulk liquid was β', whereas α was first nucleated and transformed to β' around -10°C during cooling in the nanosize emulsion.

(c) During the heating process from -20°C after crystallization, β' transformed to β around 0°C, β started to melt at 30°C, and melting ended at 44°C. The two transformations occurred far below the same transformation temperatures in the bulk state.
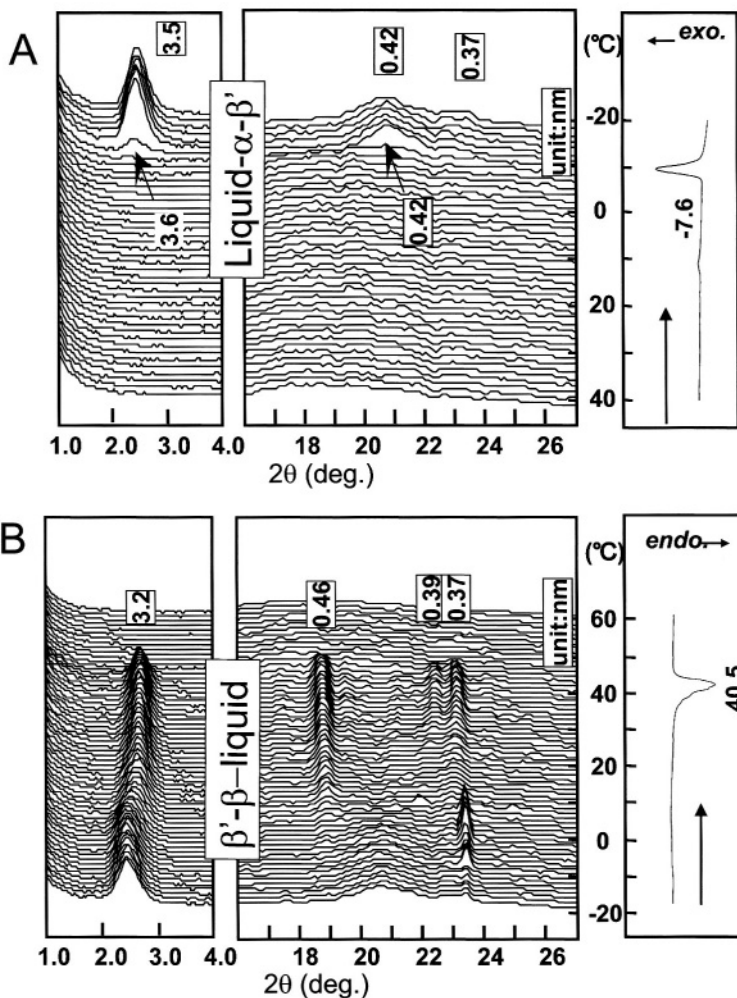
FIGURE 3.18. SR-XRD-SAXS/WAXS/DSC simultaneous patterns of (A) cooling (2°C/min) and (B) heating (2°C/min) processes of trilauroyl-glycerol (LLL) in nano-size (diameter around 100 nm) emulsion droplets.

We can interpret the reduction in T_m in the nanosize emulsion based on the size effects discussed in Section 3.3.1. The features of reduced polymorphic crystallization and promoted polymorphic transformation may be considered in the following.

The reduced rate of nucleation of crystals, which is represented in the increase of supercooling for crystallization, was also observed in the micrometer-size particles, and the argument discussed for the micrometer-size particles (see Section 3.2.3) can be applied to the nanometer-size emulsions.

We will consider two main causes for the promoted rates of polymorphic transformation in crystals formed in the nanosize emulsion droplets. The first cause is due to surface effects, in which excess surface free energy raised the total Gibbs free energy that causes a decrease in melting point and an increase in solubility (Gibbs–Thomson effect). The
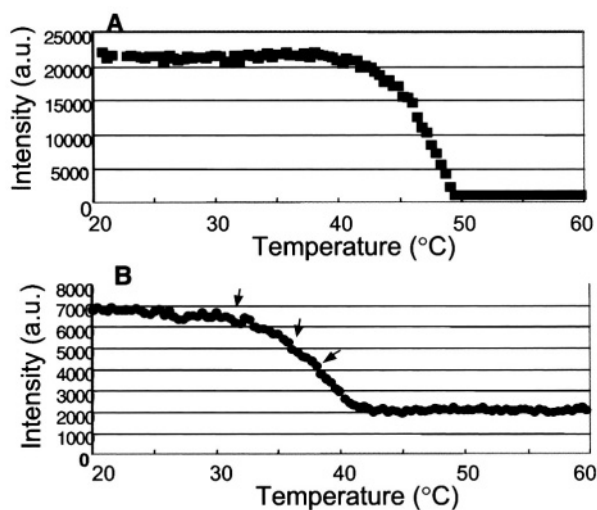
FIGURE 3.19. Variation in intensity of SAXS patterns (β form) during heating.

polymorphic transformation associated with conversion in the sub-cell structure and inter-lamellar distance reveals this surface effect, since this polymorphic transformation may be initiated from a crystal surface that is a kind of planar defect. In the second cause, lattice defects may initiate the polymorphic transformations. These lattice defects include dislocation or stacking faults, and may be introduced more easily when the nanometer-sized particles are compared with the bulk crystals.

3.4. CONCLUSION

We have discussed the transformations from liquid to solid, and from one solid structure to another in the emulsion droplets with average diameters of micrometer-dimensions and nanometer-dimensions, mainly by arguing recent experimental results with *in-situ* monitoring techniques. The heterogeneous nucleation behavior in terms of nucleation kinetics and structural modification, both in the emulsion droplets with μm-dimension and nm-dimension, has revealed the particular uniqueness of crystallization in the emulsion droplets. We also observed this uniqueness for the nanometer-dimension droplets in the thermodynamic effects that appeared in their melting behavior. We have extensively presented these experimental findings, yet there are many questions open to microscopic and mechanistic interpretations. Recent theoretical work of heterogeneous nucleation mechanisms [38–40] may shed new light on the experimental findings of the crystal nucleation in the emulsion droplets.

REFERENCES

1. K. Sato, in: *Advances in Crystal Growth Research,* Eds K. Sato, Y. Furukawa and K. Nakajima (Elsevier Science, Amsterdam, 2001) pp. 401–419.

2.   B.-D. Chen, J.J. Cilliers, R.J. Davey, J. Garside and E.T. Woodburn, Templated nucleation in a dynamic environment: crystallization in foam lamellae, *J. Am. Chem. Soc.* **120**, 1625–1626 (1998).

3.   R.L. Cormia, F.P. Price and D. Turnbull, Kinetics of crystal nucleation in polyethylene, *J. Chem. Phys.* **37**, 1333–1340 (1962).

4.   W. Skoda and M. van den Tempel, Crystallization of emulsified triglycerides, *J. Coll. Sci.* **18**, 568–574 (1963).

5.   M.J.W. Povey, in: *Crystallization and Process in Fats and Lipid Systems,* Eds N. Garti and K. Sato (Marcel Dekker, New York, 2001) pp. 251–288.

6.   J.N. Coupland, Crystallization in emulsions, *Curr. Opin. Coll. Interface Sci.* **7**, 445–450 (2002).

7.   E. Dickinson, D.J. McClements and M.J.W. Povey, Ultrasonic investigation of the particle size dependence of crystallization in n-hexadecane-water emulsions, *J. Colloid Interface Sci.* **142**, 103–110 (1991).

8.   D.J. McClements, E. Dickinson, S.R. Dungan, J.E. Kinsella, J.G. Ma and M.J.W. Povey, Effect of emulsion type on the crystallization kinetics of oil-in-water emulsions containing a mixture of solid and liquid droplets, *J. Colloid Interface Sci.* **160**, 293–297 (1993).

9.   S. Hindle, M.J.W. Povey and K. Smith, Kinetics of crystallization in n-hexadecane and cocoa butter oil-in-water emulsions accounting for droplet collision-mediated nucleation, *J. Colloid Interface Sci.* **232**, 370–380 (2000).

10.   N. Kaneko, T. Horie, S. Ueno, J. Yano, T. Katsuragi and K. Sato, Impurity effects on crystallization rates of n-hexadecane in oil-in-water emulsions, *J. Crystal Growth* **197**, 263–270 (1999).

11.   T. Katsuragi, N. Kaneko and K. Sato, Effects of addition of hydrophobic sucrose fatty acid oligoesters on crystallization rates of n-hexadecane in oil-in-water emulsions, *Colloids Surf. B* **20**, 229–237 (2001).

12.   T. Awad and K. Sato, Effects of hydrophobic emulsifier additives on crystallization behavior of palm mid fraction in oil-in-water emulsion, *J. Am. Oil Chem. Soc.* **78**, 837–842 (2001).

13.   T. Awad and K. Sato, Acceleration of crystallization of palm kernel ooil in oil-in-water eemulsion by hydrophobic emulsifier additives, *Coll. Surf. B* **25***, 45–53 (2002).

14.   T. Awad, Y. Hamada and K. Sato, Effects of addition of diacylglycerols on fat crystallization in oil-in-water emulsion, *Eur. J. Lipid Sci. Technol.* **103**, 735–741 (2001).

15.   Y. Hamada, I. Kobayashi, M. Nakajima and K. Sato, Optical and interfacial tension study of crystallization of n-alkane in oil-in-water emulsion using monodisopersed droplets, *Cryst. Growth Des.* **2***, 579–584 (2002).

16.   B. Mutaftschiev, *The Atomistic Nature of Crystal Growth* (Springer, Berlin, 2001).

17.   E. Dickinson, F.-J. Kruizenga, M.J.W. Povey and M. van der Molen, *Coll. Surf. A* **81**, 273–279 (1993).

18.   J. Coupland, E. Dickinson, D.J. McClements, M.J.W. Povey and C.R. Mimmerand, in: *Food Colloids and Polymers: Stability and Mechanical Properties,* Eds E. Dickinson and P. Walstra (Royal Society of Chemistry, Cambridge, 1993) pp. 243–249.

19.   D. Kashchiev, N. Kaneko and K. Sato, Kinetics of crystallization in polydisperse emulsions, *J. Colloid Interface Sci.* **208**, 167–177 (1998).

20.   P. Walstra, W. Kloek and T. van Vliet, in: *Crystallization and Process in Fats and Lipid Systems,* Eds N. Garti and K. Sato (Marcel Dekker, New York, 2001) pp. 289–328.

21.   S. Ueno, Y. Hamada and K. Sato, Controlling polymorphic crystallization of n-alkane crystal in emulsion droplets through interfacial nucleation, *Cryst. Growth & Design* **3**, 935–939 (2003).

22.   D.M. Small, *The Physical Chemistry of Lipids* (Plenum Press, New York, 1986) pp. 183–232.

23.   X.Z. Wu, B.M. Ocko, E.B. Sirota, S.K. Sinha, M. Deutch, B.H. Cao and M.W. Kim, Surface tension measurements of surface freezing in liquid normal alkanes, *Science* **261**, 1018–1021 (1993).

24.   E.B. Sirota and A.B. Herhold, Transient phase-induced nucleation, *Science* **283**, 529–531 (1999).

25.   W. Mehnert and K. Mader, Solid lipid nanoparticles production: characterization and applications, *Adv. Drug Del. Rev.* **47**, 165–196 (2001).

26.   C. Washington and K. Evans, Release rate measurement of model hydrophobic solutes from submicron triglyceride emulsions, *J. Control. Release* **33**, 383–390 (1995).

27.   B. Siekmann and K. Westesen, Investigations on solid lipid nanoparticles prepared by precipitation in O/W emulsions, *Eur. J. Pharm. Biopharm.* **43**, 104–109 (1996).

28.   T.P. Norden, B. Siekmann, S. Lundquist and M. Malmsten, Physicochemical vharacterisation of a drug-containing phospholipid-stabilised O/W emulsion for intravenous administration, *Eur. J. Pharm. Sci.* **13**, 393–01 (2001).

29.   V. Jenning, M. Schafer-Korting and S. Gohla, Vitamin A-loaded solid lipid nanoparticles for topical use: drug release properties, *J. Controlled Release* **66**, 115–126 (2000).

30. K. Westesen, B. Siekmann and M.H.J. Koch, Investigations on the physical state of lipid nanoparticles by synchrotron radiation X-ray diffraction, *Int. J. Pharm.* **93**, 189–199 (1993).
31. H. Bunjes, K. Westesen and M.H.J. Koch, Crystallization tendency and polymorphic transitions in triglyceride nanoparticles, *Int. J. Pharm.* **129**, 159–173 (1996).
32. T. Unruh, H. Bunjes, K. Westesen and M.H.J. Koch, Observation of size-dependent melting in lipid nanoparticles, *J. Phys. Chem. B* **103**, 10373–10377 (1999).
33. H. Bunjes, M.H.J. Koch and K. Westesen, Effect of particle size on colloidal solid triglycerides, *Langmuir* **16**, 5234–5241 (2000).
34. T. Unruh, H. Bunjes, K. Westesen and M.H.J. Koch, Investigations on the melting behavior of triacylglyceride nanoparticles, *Colloid Polym. Sci.* **279**, 398–403 (2001).
35. T. Unruh, K. Westesen, P. Boecke, P. Lindner and M.H.J. Koch, Self-assembly of triglyceride nanoparticles in suspension, *Langmuir* **18**, 1796–1800 (2002).
36. K. Sato, S. Ueno and J. Yano, Molecular interactions and kinetic properties of fats, *Prog. Lipid Res.* **38**, 91–116 (1999).
37. M. Higami, S. Ueno, T. Segawa, K. Iwanami and K. Sato, Simultaneous synchrotron radiation X-ray diffraction-DSC analysis of melting and crystallization behavior of trilauroylglycerol in nanoparticles of oil-in-water emulsion, *J. Am. Oil Chem. Soc.* **80**, 731–739 (2003).
38. D. Kashchiev, *Nucleation: Basic Theory with Applications* (Butterworth Heinemann, Oxford, 2000).
39. X.Y. Liu, A new kinetic model for three-dimensional heterogeneous nucleation, *J. Chem. Phys.* **111**, 1628–1635 (1999).
40. X.Y. Liu, Interfacial effect of molecules on nucleation kinetics, *J. Phys. Chem. B* **105**, 11550–11558 (2001).

This page intentionally left blank

4

Fundamental aspects of nucleation theory revealed in experiments with protein solid phases

Peter G. Vekilov*, Oleg Galkin**
Department of Chemical Engineering, University of Houston, Houston, TX 77204, USA

Only Jesus and Gibbs never erred and this has been strictly shown for Gibbs only.

E.D. Shchukin

4.1. INTRODUCTION

Nucleation is one of the two major mechanisms of first order phase transitions, the process of generation of a new phase from an old phase whose free energy has become higher than that of the emerging new phase [1,2]. Nucleation occurs via the formation of small embryos of the new phase inside a large volume of old phase. Another prominent feature of nucleation is the metastability of the old phase—the transition requires the passage over a free energy barrier [3]. At sufficiently high supersaturations, the barrier vanishes and the old phase becomes unstable, so that an infinitesimal fluctuation of an order parameter, such as density, can lead to the appearance of the new phase. The rate of generation and growth of the new phase is then only limited by the rate of transport of mass or energy. This second process is referred to as spinodal decomposition, and the boundary between the regions of metastability and instability of the old phase is called spinodal line [4,5].

The main concepts in the area of equilibrium between large and small phases and the generation of the first "globulae" of a new phase from an old were introduced by J.W. Gibbs in two monumental papers published in 1876 and 1878 [6,7]. In the first application of the method of the thermodynamic potential functions, he considered the stability and instability of a phase with respect to another phase. Among many other issues, Gibbs considered nuclei of a fluid embedded in another fluid. He viewed the nuclei, or "globulae", of the new phase arising from "variations of the old phase". We now use "fluctuations" instead of

---

*E-mail address: vekilov@uh.edu
**E-mail address: ogalkin@uh.edu

FIGURE 4.1. J.W. Gibbs (1839–1903) at about forty, at the time that the two papers on equilibria in heterogeneous systems were published.

"variations of phase", somewhat confining the content of the term to fluctuations along an order parameter, such as density in Figure 4.2—"variations of phase" encompasses fluctuations along all possible order parameters. Evaluating of the free energy barrier for nucleation, Gibbs concluded that the likely shape of the "globulae" of the new fluid was spherical, because it minimizes the total surface free energy. Gibbs was careful to point out that the composition of the "globulae" would likely differ from the composition of a large sample of the new phase. Since the surface tension of the "globulae", the main factor that determines the height of the barrier for nucleation, is not necessarily related to the surface tension of the interface between bulk samples of the two phases, and cannot be measured independently, it should be viewed as an adjustable parameter.

In further developments, some of the Gibbs's assumptions regarding the thermodynamics of nucleation of a fluid phase were transferred to the nucleation of ordered solids, such as crystals, from dilute or condensed fluids, or from other solid states, Figure 4.3 [8–11]. The classical nucleation theory emerged, in which so called "capillary approximation" was widely used. In application to crystals, the approximation means that the molecular arrangement in a crystal's embryo is identical to that in a large crystal, and hence, the surface free energy of the nuclei will equal the one of the crystal interface. It was also assumed that the size of the nuclei, either the radius, for spherical nuclei, or the side length, for "cubic" clusters, decreases smoothly as supersaturation increases.

An initial basic assumption in the considerations of the kinetics of nucleation was that the rates of growth and decay of the fluctuations are so high that the fluctuations which overcome the barrier, the nuclei, always have equilibrium structure and shape, and their
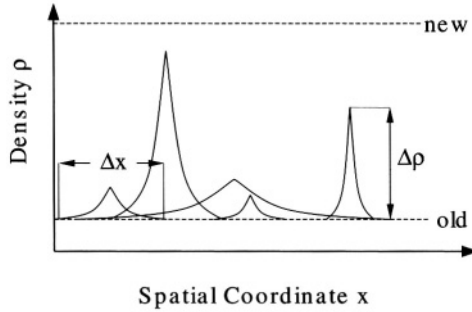
FIGURE 4.2. A schematic representation of the density fluctuations in a fluid. The free energy of a fluctuation ΔG depends on its characteristic length Δx, and amplitude $\Delta\rho$. Even fluctuations with a density lower than that of the new phase may have $\Delta G \geqslant \Delta G^*$, the free energy barrier for nucleation, and become nuclei of the new phase. Classical nucleation theory assumes that only fluctuations with $\Delta\rho$ such that $\rho_{old} + \Delta\rho \geqslant \rho_{new}$ can become nuclei, and defines a critical lengthscale, the radius of the critical nucleus, from the condition $\Delta G \geqslant \Delta G^*$.
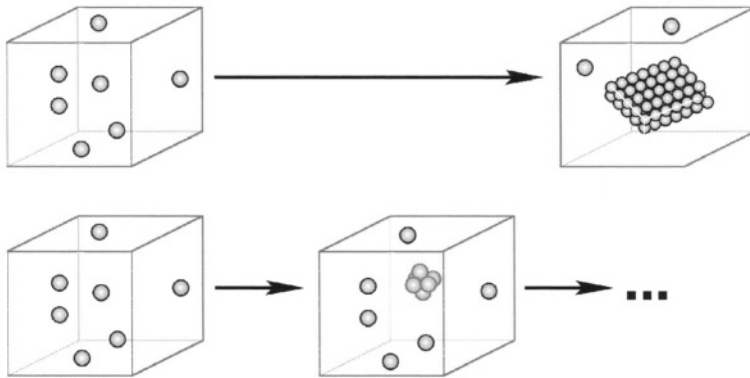

FIGURE 4.3. The formation of crystals, whereby a highly ordered phase emerges from a disordered medium, is often viewed as one of the miracles of nature, i.e., one of the most difficult problems to tackle, top. Even the simple picture given by the classical nucleation theory that the crystal starts with a tiny ordered nucleus, bottom, is extremely informative.

number is determined by equilibrium considerations. These two approximations afforded the convenience of easy separation of the thermodynamic and kinetic factors for nucleation [12]. Zeldovich found that the assumption of equilibrium number of nuclei can be relaxed and proposed an elegant way to calculate the steady-state number of nuclei [13]. Kashchiev evaluated the time-dependent concentration of nuclei in non-steady state nucleation processes [14,15]. However, the assumption of equilibrium shape of the nucleus has been preserved, and the separation of the thermodynamic and kinetic factors is not questioned even in recent papers [16–18].

The kinetic theory of generation of new phase at high supersaturations was developed in the 1950's [19]. It considered processes on both sides of the spinodal line, i.e., nucleation at high supersaturations, and spinodal decomposition. One of the main conclusions was that at the spinodal, the characteristic lengthscales of the of phase transition, nucleus size on the side of nucleation, and correlation length on the side of spinodal decomposition,

diverge towards infinity. This means that for some phase transitions, one can never quench into the region of spinodal decomposition and all phase separations are initiated by nucleation, while for other systems, one always gets spinodal decomposition. More elaborate theoretical discussions showed that no point of divergence exists, and a smooth transition from nucleation to spinodal decomposition should be observed [4,20–22]. Note that no experiments showing smooth transition between the two regimes have carried out for any system [4].

In this chapter, we use recent results on the structure of nuclei and the nucleation kinetics of protein crystals during crystallization of two proteins from their solutions to examine some of the assumptions of the classical nucleation theory. First, we show that nuclei of the protein apoferritin have a quasi-planar structure, in obvious deviation from the typical assumption of compact shape. We argue that this shape is selected because it provides faster kinetics of formation of sub-critical clusters, i.e., it is not an equilibrium shape. Despite that, we show that the arrangement of the molecules is the same as in the crystal, i.e., the capillary approximation holds. Note that since the nucleus shape determines the height of the nucleation barrier, it follows that thermodynamic factors in the nucleation rate cannot be considered independently of the selected kinetic pathway.

We then discuss results on the kinetics of nucleation of the protein lysozyme. We show that the nuclei consist of fewer than ten molecules, and the changes of nucleus size are step-wise. At high supersaturations, the nucleus consists of a single molecule, i.e., the rate of phase transformation is only limited by the rate of transport of molecules. We use this as a kinetic definition of a spinodal line for the solution–solid phase transitions. We also show that the nucleation of crystals is severely affected by another phase transition in the solution, the formation of a second, dense liquid phase. The nucleation rate reaches a maximum outside of the phase diagram region of liquid–liquid coexistence. We use these and other pieces of evidence to argue that the nucleation of ordered solids occurs via a superposition of fluctuations along two order parameters: a density fluctuation, and a "structure" fluctuation. Depending on where in the phase diagram the system is, density fluctuations may never or may selectively lead to the formation of dense liquid droplets. A crystalline nucleus appears when a fluctuation over a second order parameter, "structure", occurs within the quasi-droplet resulting from the density fluctuation, i.e., the structure fluctuation is superimposed on the density fluctuation. This "superposition of fluctuations" outlook of the nucleation of ordered solids from dilute phases suggests that the rate of nucleation can be controlled either by shifting the phase region of the dense liquid phase, or by facilitating the structure fluctuations in the dense liquid droplet. We close by discussing tests of these nucleation control mechanisms.

4.2. THE NUCLEUS STRUCTURE

4.2.1. *Imaging of sub-critical and near critical clusters*

Although the compact three-dimensional arrangement of the molecules in the nucleus is one of the main assumptions of mainstream nucleation theories [23,24], there was no direct experimental evidence of the nucleus shape and structure for any system. The problem is very intriguing: molecular dynamics simulations predict a compact nucleus structure for

atoms or molecules with a spherical interaction field [25,26], while strongly anisotropic, dipolar molecules may have a nucleus consisting of a single chain of molecules [27]. Furthermore, a recent theory, which accounts for the relaxation of the surface layer atoms or molecules in a cluster and its dependence on the thickness of the underlying crystalline matter, predicts, for some cases, planar critical clusters [28]. As these theories only consider equilibrium shapes of the critical clusters, accounting for the possibility of non-equilibrium shapes increases significantly the importance of imaging of near-critical clusters.

The experimental difficulties in visualization of the structure of the critical clusters can be grouped into four categories: (a) the constituent atoms or molecules are so small that even if the clusters are detected, their structures cannot be discerned by most microscopic techniques. (b) The critical clusters exist for extremely short times after which they either grow to macroscopic crystals or decay. (c) The critical clusters are relatively small and due to Brownian diffusion, they freely move throughout the available volume of the mother phase. (d) The detected clusters need to be identified as belonging to the nucleation pathway and representing the near-critical steps.

The former two of these difficulties can be overcome by using a protein crystallization model system. The sizes of the protein molecules are a few nanometers [29] and the typical times between sequential discrete growth events are a few seconds [30]. These sizes and time scales are within the reach of the modern atomic force microscopy (AFM) techniques [31]. A further advantage of AFM is that this method allows *in situ,* real-time, molecular-resolution monitoring of the processes of interest at room temperatures and atmospheric pressures, i.e., at conditions under which protein crystallization typically occurs [32–35].

Atomic force microscopy can be applied to visualize clusters that appear in the solution bulk only if they reach a surface of AFM cell and adsorb on it without changing their structure. We can evaluate the time τ required for a cluster formed within a distance $x = 100$ μm from the cell bottom to reach it through Brownian motion from Einstein's relation $x^2 = 2D\tau$ [36]. A lower estimate for cluster diffusivity D can be obtained from the diffusivity of single apoferritin molecules, 3.2×10^{-7} cm^2 s^{-1} [37,38] using Stokes law and assuming that the clusters behave like particles with several molecules at an edge: $D \approx 5 \times 10^{-8}$ cm^2 s^{-1}. Substituting, we get $\tau \approx 1000$ s ≈ 15 min. (The times for sedimentation of particles whose density is only slightly higher then the solution density [39] in the Earth's gravity field are longer by more than an order of magnitude [40].) Thus, in its random walk throughout the solution, a near-critical cluster may land on the cell bottom.

4.2.2. Non-compact nucleus shape and the nucleation pathway

We monitored the glass bottom of the AFM cell prior to the formation of any crystals at supersaturations σ between 0.5 and ~2.5. ($\sigma \equiv \Delta\mu/k_B T = \ln(a/a_e) \cong \ln(C/C_e)$; $\Delta\mu$ is the difference between the apoferritin chemical potential in solution and in the crystal, a and C are, respectively activity and concentration, subscript e denotes equilibrium, $a \cong C$—as shown in [32], at the conditions employed, the activity coefficient of apoferritin $\gamma \cong 1$.) A disordered apoferritin layer of molecules with roughly hexagonal co-ordination covers the glass [41]. With a glass substrate, this layer was always of single molecule thickness, while more hydrophobic substrates, such as Teflon or silane-coated glass, were covered with many layers thick accumulations of apoferritin molecules. We saw numerous clusters ranging from 2–3 to 50–70 molecules (we never saw single molecules) land

on the apoferritin-covered glass, stay adsorbed for 1 to 30 min and then dissolve or des-orb. Typically, smaller clusters, such as those in Figures 4.4a and 4.4b had significantly shorter residence times on the surface. Hence, although the occurrence of smaller clusters appeared higher, comparisons of the populations of large and small clusters with theoretical predictions would be unjustified [41].

It was noted that: (a) in the smallest clusters the molecules occupy the corners of a flat polygon, e.g., four-member clusters are shaped as quadrangles. (b) Clusters of ~ 10–20 molecules consist of two parallel molecular rows. (c) Two structures were possible for clus-ters of 20 or more molecules: a few molecular rows in a plane, or disordered aggregates. (d) Apoferritin molecules attached to and detached from the ordered clusters, while (e) the disordered ones were "dead". (f) The larger ordered clusters were not seen at the high su-persaturations. The images of the molecules constituting the clusters were somewhat fuzzy in comparison with the molecules from the layer coating the glass bottom. We attributed this to the relatively weak attachment of the landing clusters to the structureless apoferritin layer [41].

For better images of the clusters, the top [111] surfaces of large apoferritin crystals were used as substrates—these surfaces have characteristic lengthscales, which exactly fit the size of the molecules in the clusters. The top faces of large apoferritin crystals were monitored for periods of several hours in the σ range from 0.5 to 1.6 [41,42] and clusters landing on the top $\langle 111 \rangle$ crystal surfaces were detected. Figure 4.4c, taken a few minutes after cluster landing, shows an example representative of more than 15 such events. In all cases, the molecules in a cluster are arranged in rows of 4–8 molecules, while 3–7 rows assemble in planar domains with additional 2–3 rows forming a second layer. The cluster in Figure 4.4c contains two domains linked by a longer row of ~ 10 molecules. The center-to-center distance between adjacent molecules in a row is 13 nm, equal to that along the close-packed $\langle 110 \rangle$ direction in the crystal. Hence, these are clusters of apoferritin molecules, which, unlike occurrences in other systems [43,44], have the same arrangement as in the crystal [42].

The quasi-planar cluster shape precludes the clusters being pieces chopped off a large crystal. It was concluded that the clusters form in the solution bulk and then land on the monitored surface since: (i) the clusters consist of {110} planes, Figure 4.5, rather than {111} planes, typical of "2 dimensional" nuclei of a new layers replicating the {111} molecular arrangement of the crystal surface [30]. (ii) The molecular rows in the clus-ters in Figure 4.4c are at an angle with the crystal's [110] direction. (iii) The clusters are often are out of registry with the crystal's own layer causing a boundary free of molecules or consisting of strained molecules. (iv) Often, the clusters are pushed back into the solu-tion by the advancing crystal layers. (v) If trapped by the crystal layers a misfit boundary between the two structures appears.

Did the cluster structure change after landing under the influence of the translationally-symmetric force field exerted by the underlying crystal? Apparently, no: one would expect that in such a case there would be an exact match and continuity between the structures of the cluster and the underlying crystal, as observed before [43,45].

Numerous observations revealed that molecules attach to and detach from clusters. The attachment and detachment frequencies are comparable, which is unusual for the su-persaturated conditions of the observation. Comparable rates of molecular attachment and detachment, and bifurcation of their subsequent evolution into either growth or dissolution
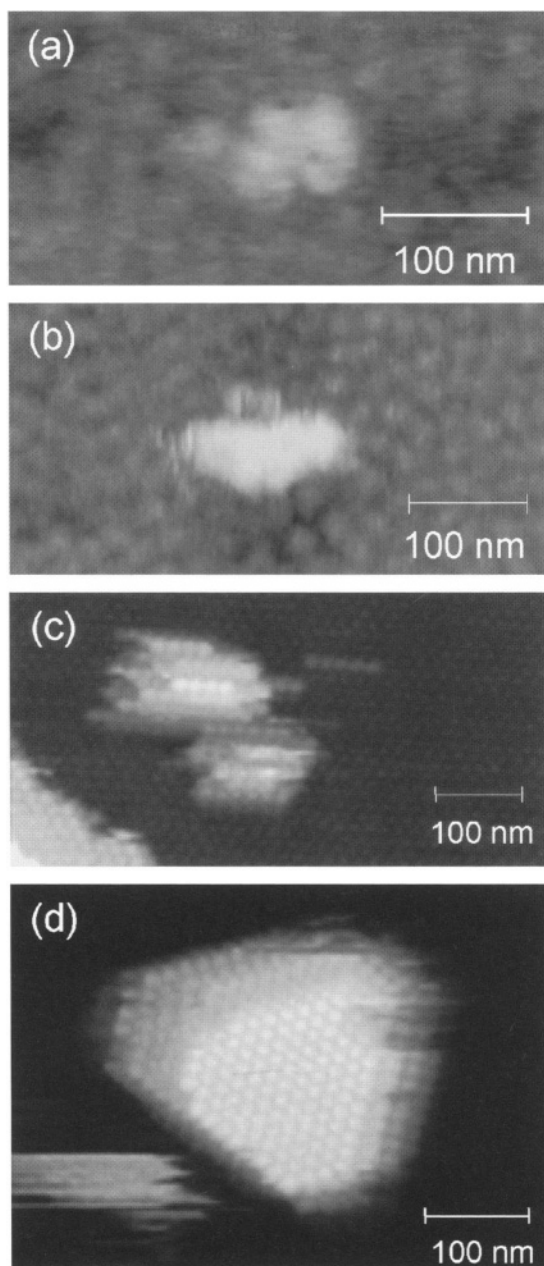
FIGURE 4.4. Sub-critical, near-critical clusters, and super-critical crystallites in the nucleation pathway of the apoferritin crystals. Brighter coloring codes for higher altitude. (a, b) Clusters that have landed on the bottom of the AFM cell covered with a single layer of apoferritin molecules [41]; (a) apoferritin concentration $C = 0.23$ mg ml^{-1}, supersaturation $\sigma = 2.3$, a cluster consisting of two molecules. (b) $C = 0.04$ mg ml^{-1}, $\sigma = 0.5$, a cluster consisting of six molecules in two rods with four and two molecules in each of the rods. (c) A near critical cluster that has landed on the (111) face of a apoferritin crystal at $\sigma = 1.1$. (d) A crystallite of ~ 150–180 molecules on a large crystal at $\sigma = 1.1$.
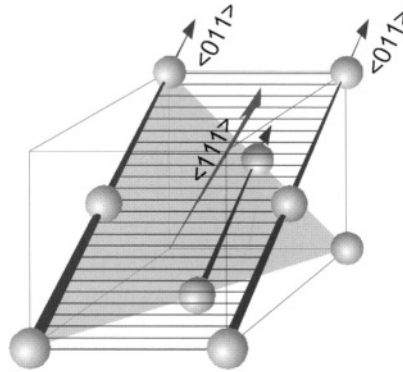
FIGURE 4.5. Schematic of [111] and [110] planes and $\langle 110 \rangle$ molecular rows in a face-centred cubic (f.c.c.) crystal lattice.

were observed for all clusters of such sizes seen experimentally. Estimating the average net frequency of molecular attachment, we found ~4 molecules/43 s $\cong 0.1$ s^{-1} for the ~20 possible attachment sites at the ends of the molecular rows, or 0.005 s^{-1} per attachment site. This frequency is more than one order of magnitude lower than the net frequency of attachment to a growth site on the surface of a large crystal—0.065 s^{-1} [30,32]. The ratio of the two rates indicates that the size of the observed clusters is just above the critical. In other series of observations we monitored clusters that were just below the critical for that supersaturation [42].

In numerous instances, the clusters that form in the solution were seen to develop into {111} facetted f.c.c. crystals, Figure 4.4d. We concluded that the clusters, illustrated in Figure 4.4a–c are sub-critical and near-critical clusters for the phase transformation occurring in the system, crystallization of apoferritin. Their structure is representative of the structure of the nucleus [42].

The nucleation pathway emerging from the above observations is schematically summarized in Figure 4.6 [42]. The planar structure of the sub-critical clusters and the nuclei, consisting of {110} layers, illustrated by the sequence in Figure 4.6a, rather than an evolution of a compact shape as shown in Figure 4.6b [23,24], is surprising. In a subsection below, we show that the lower-dimensional shapes of the sub-critical and near critical clusters are selected because the kinetics of their formation is faster.

This nucleus structure may have drastic consequences for the nucleation process. A planar cluster has larger surface area than a compact cluster with the same number of molecules n. As a result, a larger contribution to the crystallization energy gain is needed to compensate for the greater surface energy loss, and hence the number of molecules in the critical cluster n^* is greater. Since the nucleation barrier [23,46–48]

$$\Delta G^*(n^*) \approx n^* \Delta \mu / 2, \tag{1}$$

the higher nucleation barriers lead to slower nucleation kinetics than predicted by the classical theories based compact spherical nuclei. Furthermore, the rough surface of the nuclei in Figure 4.4c may result in a surface energy that is not a smooth and monotonic function of n. This may result in unusual dependencies of the nucleation rate on $\Delta \mu$.
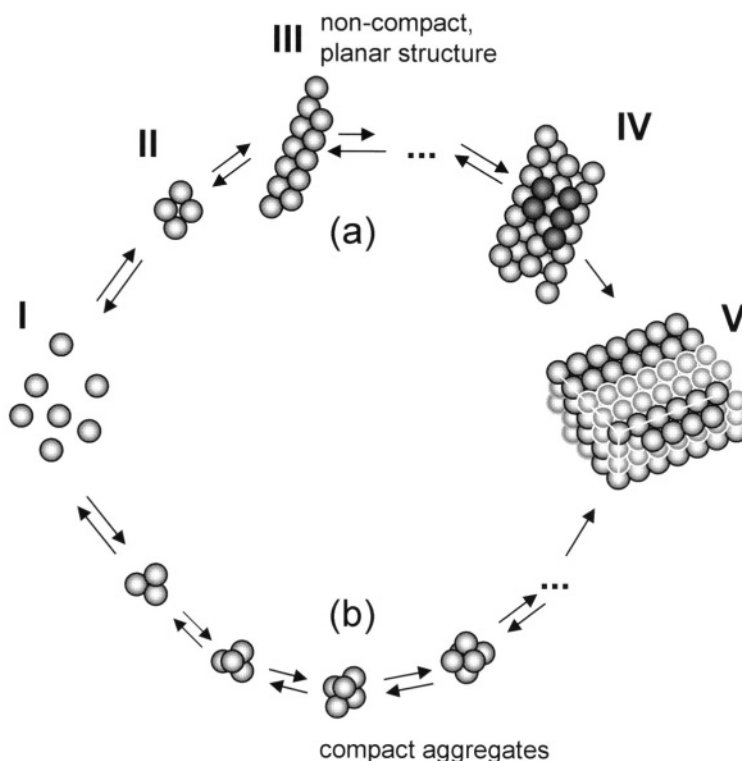
FIGURE 4.6. Schematic illustration of nucleation pathways. (a) Via planar critical cluster: Stage I—single mole-cules in the solution; the lack of any significant concentration of dimers, trimers, etc. has been evidenced by static and dynamic light scattering [37,38]. II—a few molecules at the corners of a polygon as seen in Figure 4.4a. III—linear array as seen in Figure 4.4b. IV—a quasi-planar critical cluster with (110) orientation, similar to struc-tures seen in Figure 4.4c; molecules belonging to the second layer are shown in lighter shade. V—microcrystal facetted by (111) planes, the (110) layers that stack up to form this crystal are delineated by lighter and darker contours, as in Figure 4.4c. (b) Via compact critical cluster [23,24]. From refs [41,42].

4.2.3. The capillary approximation holds

As noted above the arrangement of the molecules in the nucleus is the same as inside large crystals. This is the prerequisite for the capillary approximation. In this subsection, we test if the energetics of nucleus formation also conforms with this approximation. Typically, the size of the near-critical clusters seen at $\sigma = 1.6$ was ~ 16–20 molecules, i.e., four or five molecular rows with four molecules per row, Figure 4.7b. At $\sigma = 1.1$, the observed clusters contain ~45–50 molecules, i.e., seven or eight rows of ~six molecules Figure 4.7a. On the average, smaller near-critical clusters were observed at higher supersaturations. These observations agree with the predictions of the classical and advanced treatments of nucleation [46,49,50].

For a quantitative comparison of the sizes of the critical clusters, observed as discussed above, to predictions using the capillary approximation, we used the fact that the nucleus evolves into a crystal by accumulating new layers. For a rough quantification of the nucle-ation process, we approximate the critical cluster with a square of one or two crystalline
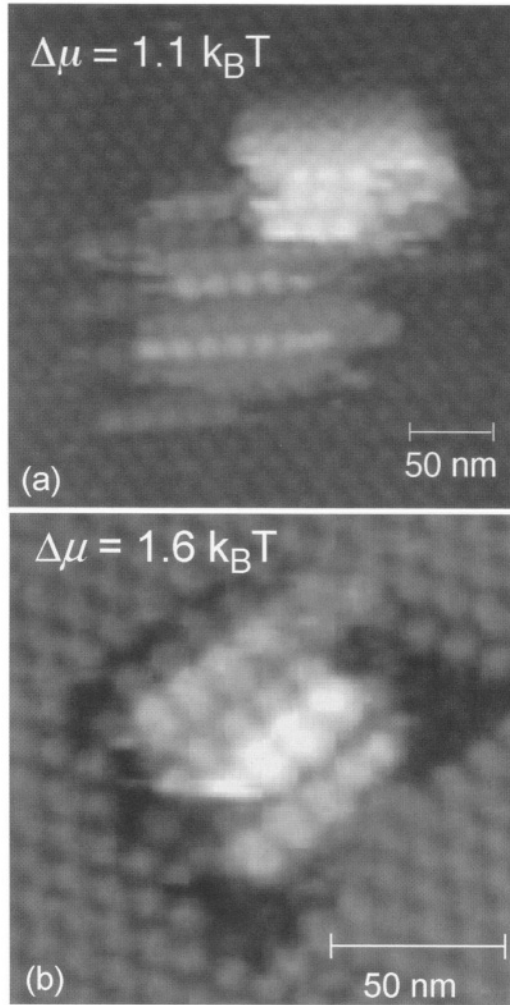
FIGURE 4.7. Two clusters that have landed on the top [111] surface of a apoferritin crystal at the supersaturation indicated in the frames. Brighter coloring codes for higher altitude. (a) $C = 0.07$ mg ml^{-1}, $\sigma = 1.1$, dark beehive pattern in background is the [111] face of the apoferritin crystal used as a substrate. A cluster consisting of two domains, the upper domain consist of six or seven rods of four to seven molecules in each. The rods are parallel and positioned alternatively higher and lower in a harmonica pattern, in an arrangement corresponding to a [110] crystal layer, see Figure 4.5. (b) $C = 0.115$ mg ml^{-1}, $\sigma = 1.6$ s. A cluster, consisting of four or five rods in a harmonica arrangement typical for the (110) layer of the apoferritin crystals, is surrounded on three sides by a layer of the underlying crystal formed after landing. Each rod has four to six molecules. The lower left rod of the cluster has initiated an island parallel to the crystal [111] planes. The molecules in this cluster are horizontally shifted from the crystallographic positions of the underlying crystal, resulting in a misfit boundary around the cluster and the crystal layer. From refs [41,42].

layers, with n_e molecules on its edge. The labile equilibrium of the critical cluster with the medium represented as IV in Figure 4.6, is around states in which the second layer is being built. To calculate the average reversible work per molecule $\Delta G/\Delta n$, $\Delta n = n_e \times n_e$,

needed to build the second layer, we follow derivations in refs [51–53]. At constant temperature and pressure, $\Delta G/\Delta n$ for the addition of a [110] layer consisting of $n_e \times n_e$ molecules to a (110) surface is [41]

$$\frac{1}{n_e^2}\left(6n_e^2\phi - 2n_e\phi\right) = 6\phi - \frac{2\phi}{n_e}. \tag{2}$$

Here ϕ is the free energy of formation of one intermolecular bond [32]. The sum in eq. (2) contains the work to add $(n_e - 1)^2$ molecules to kinks on (110) surfaces by forming alternatively 8 or 4 bonds with neighbors from the new and the lower layers, $2(n_e - 1)$ molecules along the edges of the layer than are bound to 5 or 3 molecules, and one molecule bound to three or one molecules from the lower (110) layer. Ignoring the crystallization entropy change due to the protein molecules (significantly smaller than the contribution of the water molecules [32,54]) the first term in eq. (2) is the average change of free energy upon crystallization per molecule, i.e., $\Delta\mu$. The second term is the excess free energy of the cluster surface. For a critical cluster in labile equilibrium with the solution, the difference in eq. (2) equals zero, and the discrete Gibbs–Thomson equation obtains [51–53]

$$\Delta\mu = 2\phi/n_e. \tag{3}$$

Monitoring the dynamics of molecular incorporation on the (111) apoferritin surface the value obtained for ϕ was $\phi = 3.2k_BT$ [30], in agreement with the corresponding free energy for crystallization, determined from solubility data [32,54,55]. Substituting in eq. (3), with $\Delta\mu/k_BT = 1.1$ and 1.6 the values of n_e are 6 and 4, respectively, i.e., in near-perfect agreement with the numbers of molecules on the edges of the respective clusters in Figure 4.7.

The first conclusion from this correspondence is that eq. (3) applies, and ϕ is the molecular-level equivalent to surface tension that governs nucleation [51–53]. To compare the estimated ϕ to previous results, a corresponding effective macroscopic surface energy γ was defined as [42]

$$\gamma_{\text{eff}} = n_{\text{free}}\phi/S. \tag{4}$$

Here n_{free} is the number of unsaturated bonds of a molecule on the surface of a nucleus, S is the surface area of a molecule. With n_{free} on the average 7–8 for the clusters that expose two sides of many molecules, one gets $\gamma_{\text{eff}} \approx 0.2$ mJ m^{-2}. Light scattering determinations of apoferritin nuclei sizes averaged over all body angles [56] at $\sigma = 0.92$ yielded values of ~40 nm (or ~3.5 molecular dimensions, compatible with the cluster in Figure 4.7b). Assuming spherical nucleus shape, the authors obtained $\gamma = 0.027$ mJ m^{-2} [56]. As discussed above, the surface energy should be lower for a spherical than for a flat cluster. Likely, this underlies the lower estimate of γ. Similarly, AFM studies of virus crystallization kinetics [57] produced γ-values higher by about the same factor than the evaluation based on light scattering [56].

Since the value of ϕ was taken from thermodynamic determinations with large crystals [32,54,55], we reach the far more potent conclusion that the capillary approximation is strictly obeyed by the apoferritin nuclei.

4.2.4. Non-compact shape of the nucleus is selected by kinetics

As noted above, the standing paradigm is that polar molecules self-assemble into chains [27], while isotropic molecules form compact three-dimensional clusters [58]. Linear and planar arrays of isotropic molecules can be assembled only on suitable substrates [59], or by introducing bonds of deliberately chosen lower symmetry [60–63]. The justifications for this model assume intermolecular interaction potentials with a single minimum and monotonically decaying attraction at longer distances. Yet recent data show that for many proteins, long-range repulsion exists and introduces a maximum in the potential at a distance form the minimum [37,38,64]. Below, we show that non-monotonic potentials are may be correlated with lower cluster dimensionality, and that this correlation may explain the quasi-planar nuclei for crystallization of apoferritin.

Apoferritin crystallizes from solutions containing Na^+ at 0.2 M and Cd^{2+} at 2.5% [65–67]. With only Na^+ present, it was found that at $[Na^+] > 0.15$ M, a non-DLVO repulsion arises, Figure 4.8 [37]. This was attributed to the build-up of hydrated Na^+ counterions at the apoferritin surface, schematically depicted in Figure 4.9b [37,68,69]. These interactions have been called hydration forces [70–73]. The relation linking the hydration potential U_{hyd} and the intermolecular separation $(r - a)$, $a = 13$ nm is the apoferritin molecular diameter,

$$U_{hyd}(r) = \pi(a/2)Lf_0 \exp\left[-(r - a)/L\right], \tag{5}$$

where $L = 1.44$ nm, the double diameter of the hydrated Na^+ [74], and $f_0 = 12.5$ mJ m^{-2}, surface energy density [71] represented by the dashed curve in Figure 4.9a, quantitatively describes the apoferritin data at $[Na^+] = 0.20$ M [37].

The addition of Cd^{2+} induces crystallization [38]—the Cd^{2+} ions embed between adjacent apoferritin molecules in the crystal and form strong coordination-type bonds with the carboxylic groups of the aspartic and glutamic acid residues [66,75]. Two such bonds form in each intermolecular contact. The strong bond induced by Cd^{2+} in the crystal is represented in Figure 4.9a as a deep short-range minimum. Since Cd^{2+} might affect the hydration shell around the apoferritin molecules, we carried out determinations of the second virial coefficient B_2 (for experimental details on the determination, see [38,55]). Figure 4.10
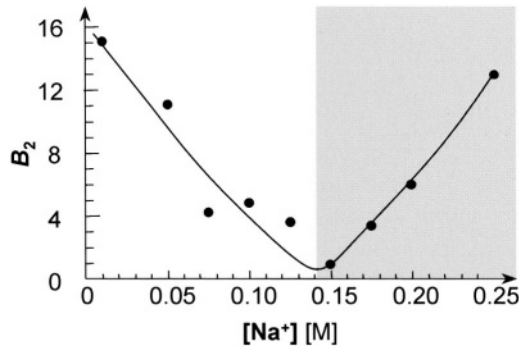

FIGURE 4.8. Dimensionless second osmotic virial coefficient B_2 for the apoferritin monomer as a function of the sodium cation concentration $[Na^+]$. Solid line is just a guide for the eye. Gray highlights area of non-DLVO increase of B_2 at $[Na^+] \geqslant 0.15$ M attributed to the hydration interactions. From refs [37,38].
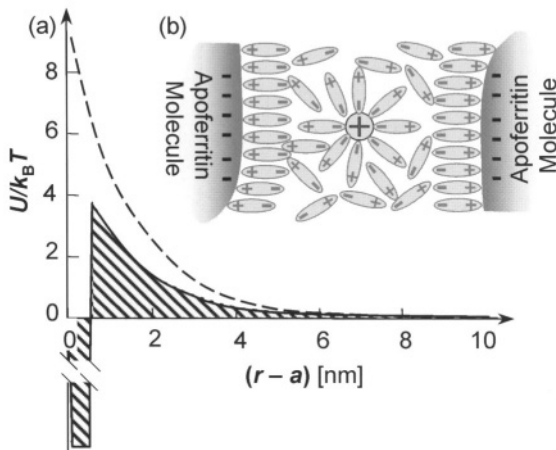
FIGURE 4.9. (a) The potential of pair interactions between apoferritin molecules. Dashed line—in the presence of $[Na^+] = 0.20$ M according to eq. (5). Solid line—schematic representation of the interaction potential after the addition of Cd^{2+}. (b) Schematic representation of the build-up of counterions at the surface of the protein molecules that leads to the hydration repulsion reflected in (a).
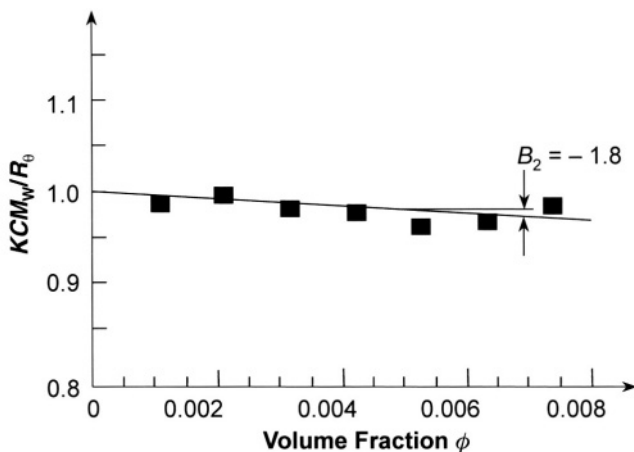

FIGURE 4.10. Static light scattering results with apoferritin in the presence of $[Na^+] = 0.20$ M and $[Cd^{2+}] = 0.22$, M = 2.5%. K—instrumental constant; $M_w = 450$ kDa—apoferritin molecular mass; R_θ—Rayleigh ratio; C—apoferritin concentration. The slope of this line yields the shown second virial coefficient B_2.

shows that in a crystallizing solution containing Na^+ and Cd^{2+} B_2 is only slightly negative. B_2 corresponds to the hatched area in Figure 4.9a, thus $|B_2| \sim 0$ indicates a positive section at longer ranges that compensates the negative contribution from the Cd^{2+} bond. Hence, Cd^{2+} ions do not destroy the hydration shell, and the intermolecular interaction potential can be qualitatively described with the solid non-monotonic curve in Figure 4.9a—a deep narrow minimum followed by a maximum.
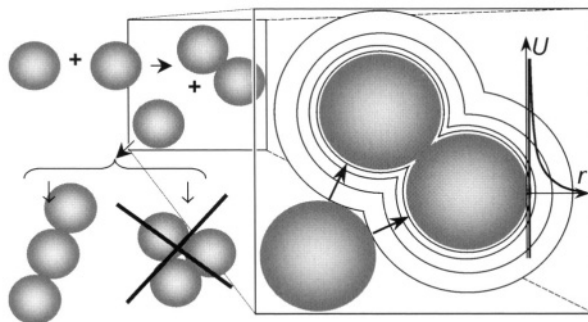
FIGURE 4.11. Schematic of formation of a trimer of molecules with an interaction potential consisting of long range repulsion and short range attraction, highlighted on $U(r)$ plot far right. Contours around zoomed-in dimer represent repulsive potential lines in the plane of the image.

The non-monotonic potential of the apoferritin molecules may explain the linear and planar sub- and near-critical clusters along the nucleation pathway of this protein. Figure 4.11 schematically shows that in the case of the non-monotonic potential in Figure 4.9a, a molecule attempting to join an existing cluster from the side encounters stronger repulsion than if it tries to join along the dimer axis. This makes attachment along the dimer axis and a linear arrangement faster. A self-consistent solution for diffusion-limited aggregation in two dimensions has shown that this scenario indeed results in aggregates of lower dimension [76]. The attachment symmetry of the clusters and the deviations from the simplified model are likely determined by the fine details of the molecular shape, as well as by random factors.

As the clusters grow into crystallites, the thermodynamic gain from molecules in the potential minimum at short separations in Figure 4.9a becomes the main structure-determining factor and compact structures evolve. This growth scenario is similar to the collapse of longer chains of polar molecules into compact shapes [27].

These considerations suggest that the shape and the arrangement of the molecules in the sub- and near-critical clusters for apoferritin nucleation are determined by the kinetics of passing over the potential maximum, which is faster for the linear arrays. This is not the equilibrium cluster structure—Monte-Carlo simulations with spherical molecules interacting with non-monotonic potentials similar to the one shown in Figure 4.9a, show that after a sufficient number of steps, even the small pieces of solid phase are three-dimensional and with f.c.c. structure (S. Brandon *et al.*, in preparation). Thus, we conclude that the non-monotonic potential leads to a nucleation pathway, for which the nucleus shape and structure are selected because they provide for faster nucleation and *not because* they have the lowest free energy.

Another example of nuclei of non-equilibrium shape and structure comes from experiments with mono-disperse colloid particles [58]. Even though the nuclei were monitored at relatively low supersaturations, they were found to have an ellipsoidal shape and rough surface, which obviously does not ensure a minimal surface free energy. Furthermore, the colloid particles were arranged in randomly stacked hexagonal and f.c.c. layers [58], although a consistent f.c.c. arrangement would offer a slight free energy advantage [77,78].

4.3. NUCLEATION KINETICS AND MECHANISMS

To address the issues related to nucleation at high supersaturations and possible transition to spinodal decomposition, interaction between the phases, etc., we relied on data on the kinetics of homogeneous nucleation of crystals of the protein lysozyme.

4.3.1. Techniques for nucleation rates determinations

Some of the methods for determinations of homogeneous nucleation rates applied to inorganic crystals would be inapplicable or produce ambiguous results if applied to protein systems. For instance, different variants of cloud chamber [79] and supersonic nozzle expansion techniques [80] are specific for vapor–liquid nucleation. Techniques that use levitating droplets [81,82] are prone to evaporation of solution from the liquid–air interface and may lead to biases due to effects of the nucleation field on the nucleation process [83].

Direct counting of protein crystals grown to optically detectable size in supersaturated solutions [84–88] allows rough evaluations of the nucleation rate, J (in units $cm^{-3} s^{-1}$), i.e., the number of stable nuclei appearing in a unit volume per unit time. These studies, unfortunately, are limited to the overall number of crystals, thus giving only an integral of J over time and supersaturations and do not account for the inevitable heterogeneous nucleation events [89].

Another method applied to identify nucleation events has been dynamic light scattering [56,90]. The method was used with several proteins and protein complexes: ferritin, pumpkin seed globulin, and the satellite tobacco mosaic virus, whose size is sufficiently large to be detected by dynamic light scattering. In a supersaturated solution, with time a signal indicating the appearance of aggregates larger than the size of one molecule appears. The average size of the aggregate was found to slowly increase. These aggregates have been assumed to correspond to pre-critical clusters, and in this way the time evolution of the pre-critical sizes has been monitored for several proteins [56,90].

In pursuit of data allowing definitive conclusions about the nucleation mechanism, a novel technique that allows direct determinations of the steady-state rate of homogeneous nucleation was recently developed. In the beginning of an experiment run, the temperature is lowered to a selected T_1 at which nucleation occurs, Figure 4.12. After a time period of Δt_1 temperature is raised from the nucleation temperature T_1 to the growth temperature T_2. The temperature T_2 is chosen so that the supersaturation is at a level where nucleation rate is practically zero, but the crystals already formed can grow to detectable dimensions [91]. This regime allows nucleation to occur at constant supersaturation during Δt_1 at T_1 without solution depletion due the growth of the nucleated crystals at T_2. After the growth stage, the crystals nucleated at T_1 during Δt_1 are counted.

To obtain reproducible statistical characteristics of the random nucleation process, 400 simultaneous trials take place under identical conditions, in solution droplets of volume $0.7\ \mu$l. To suppress the undesired nucleation at the solution/air interface, the droplets were suspended in inert silicone oil, used in optimizations of the crystallization conditions of a variety of proteins [92]. To extract the nucleation rate from the time dependence of the number of nucleated crystals, five arrays of 400 droplets are subjected to the nucleation supersaturation at increasing time intervals Δt_1. These Δt_1's ranged from 12 minutes to 8 hours. Thus, the determination of one nucleation rate data point is based upon statistics
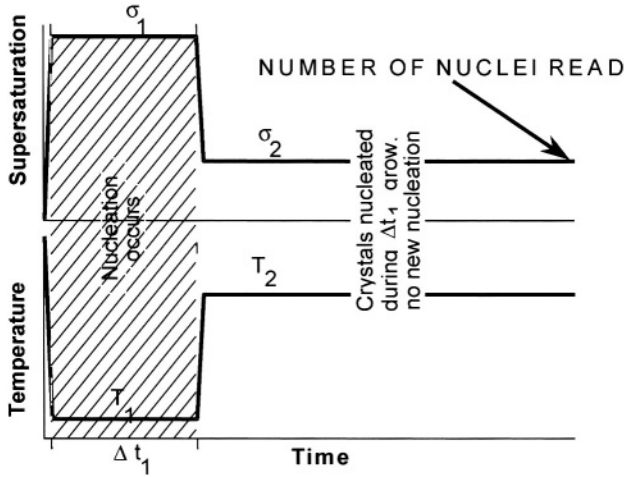
FIGURE 4.12. Temperature regimes and corresponding supersaturation levels used to induce nucleation during the time Δt_1 and to develop the crystals to detectable dimensions for a system with normal temperature dependence of the solubility, such as lysozyme used here. From ref. [93].

over 2000 protein solution droplets. The experiment setup, experimental and data collection procedures, and the extensive tests to validate this technique are described in detail in ref. [93].

Although the number of crystals in a droplet is a random variable, Figures 4.13 and 4.14, the mean number of nucleated crystals is reproducible and increases linearly with time, see Figure 4.15 and ref. [94], indicating steady-state nucleation at the chosen experimental conditions. Although heterogeneous nucleation was significantly reduced through various precautions [89,93,94], apparently it still occurs—note the non-zero intercept of the data in Figure 4.15 at $t = 0$. Likely centers for this process may be the small ($<0.22 \ \mu$m) particles remaining in the solution after filtration. The good linearity of the $N(t)$ at $t > 0$ indicates that the heterogeneous nucleation is limited to times shorter than those accessible to our technique. This mode of fast crystal nucleation leads to a constant additive to the number of nucleated crystals at all times. Thus, the intercept of the dependence with Y-axis in Figure 4.15 can be used to characterize the rate of *heterogeneous* nucleation and the slope of this dependence yields the *homogeneous* nucleation rate.

4.3.2. Kinetics of the nucleation processes

The variations of the homogeneous nucleation rate of lysozyme crystals with protein concentration at three different concentrations of the precipitant, NaCl, determined with the direct method discussed above, are presented in Figure 4.16. In agreement with general expectations, the nucleation rate increases exponentially with protein concentration at each precipitant concentration, and, overall, is higher at higher precipitant concentrations. However, at the highest precipitant concentration, $C_{\text{NaCl}} = 4\%$, the $J(C)$ dependence contains three peculiarities.

(i) The dependence breaks at $C^* = 33.5$ mg/ml, with the sections at $C < C^*$ and $C > C^*$ following different exponents.
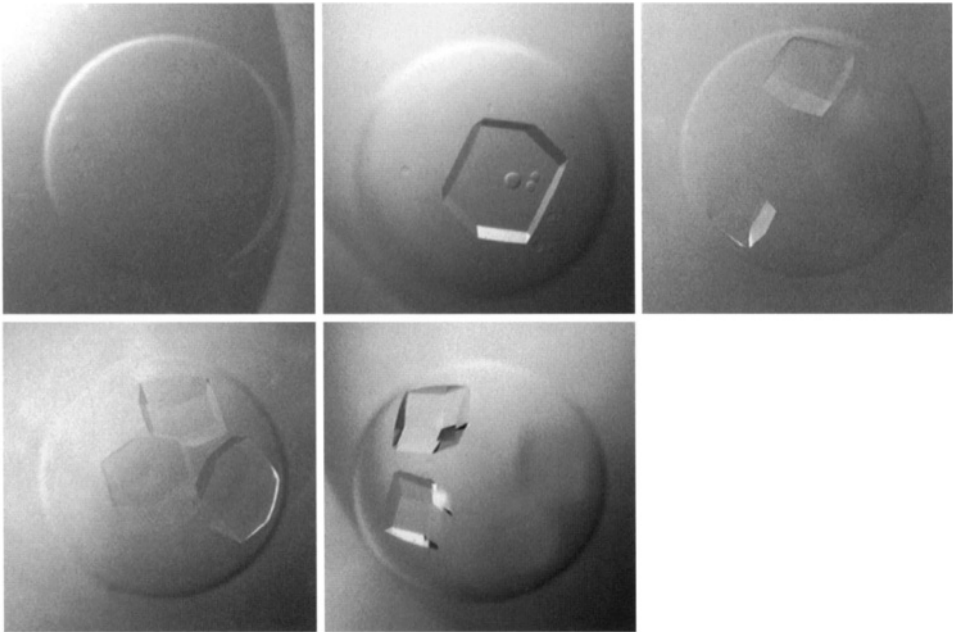
FIGURE 4.13, Variations in the number of crystals nucleated in a droplet between none and four under identical conditions. From ref. [93].

(ii) The data point at the highest lysozyme concentration, $C = 68$ mg/ml and $C_{NaCl} = 4\%$ is lower than the data point determined at lower C and C_{NaCl}, 64 mg/ml and 3%, respectively. During the determination of the data point at $C_{NaCl} = 4\%$, the crystallization solutions in all 2000 droplets became cloudy immediately after temperature was lowered to the nucleation temperature and became clear again when T was raised to T_2. This indicates that this set of conditions (C, C_{NaCl}, T) is below the liquid–liquid coexistence boundary for the lysozyme–water–NaCl system. After the growth stage, most of the crystals found in the droplets appeared like regular tetragonal lysozyme crystals. However, in a few (~20 out of 2000) droplets spherulitic crystals with thin needles growing radially outward from a center ("sea urchin" morphology) were detected, see Figure 4.17. No correlation between the nucleation times and the number of droplets with "sea urchin" morphology crystals was found. The presence of crystals with such unusual shape has been related to crystallization starting below the liquid–liquid co-existence curve [95].

(iii) At $C > 48$ mg/ml the dependence bifurcates with the data points belonging to either of two branches. In the runs leading to J's from the upper branch, in a few droplets (~2–3 out of ~2000) spherulitic crystals, similar to those in Figure 4.17, were noticed. This suggests that the closeness of the liquid–liquid coexistence boundary may be affecting crystallization in those runs [96].
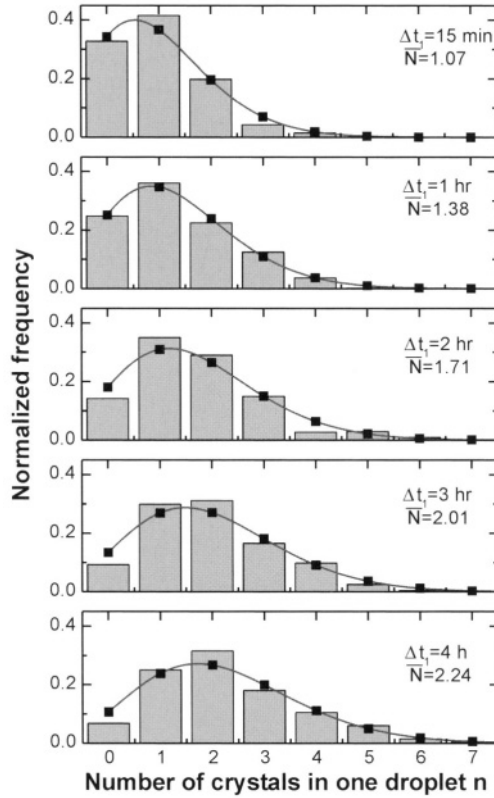
FIGURE 4.14. Distributions of the number of lysozyme crystals n appearing in one droplet as a result of increasing nucleation times Δt_1 indicated in the plots. Each distribution presents the result of simultaneous experiments in 400 droplets with volume $V = 0.7\ \mu l$ each, lysozyme concentration $C = 55.5$ mg/ml, precipitant NaCl concentration $C_{NaCl} = 3\%$. Bars: experiment results; lines and symbols: fits with Poisson distribution. From ref. [94].
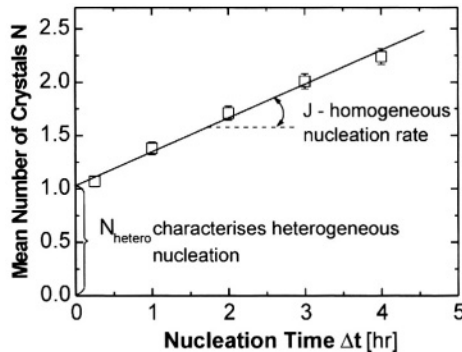

FIGURE 4.15. Time Δt_1 dependence of the mean number of crystals in one droplet N. Each N value is determined from the Poisson distributions for simultaneous experiments in 400 droplets with volume $V = 0.7\ \mu l$, lysozyme concentration $C = 55.5$ mg/ml, precipitant NaCl concentration $C_{NaCl} = 2.5\%$. Error bars correspond to $\sqrt{N/N_{trial}}$. The slope of the straight line is used to calculate the nucleation rate J in cm^{-3} s^{-1}, the intercept N_{hetero} characterizes heterogeneous nucleation. From ref. [93].
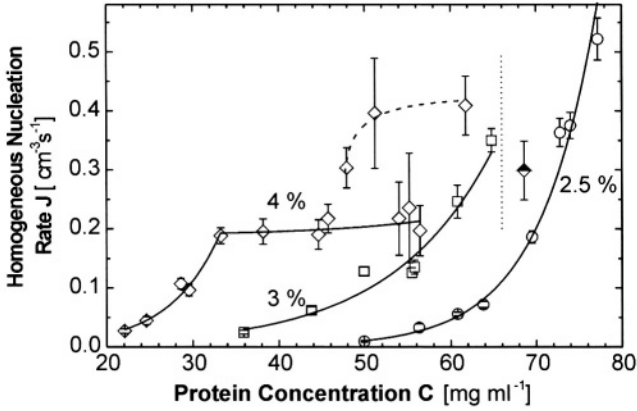
FIGURE 4.16. Dependencies homogeneous nucleation rates J of lysozyme crystals on protein concentration C at $T = 12.6°C$ and the three precipitant concentrations C_{NaCl} indicated in the plots. Solid lines—fits with exponential functions; dashed line for data points at $C_{NaCl} = 4\%$ is just a guide for the eye. Datum point at $C_{NaCl} = 4\%$ and lysozyme $C = 68$ mg/ml was obtained in a cloudy solution and was not used in fitting procedures. Vertical dotted line at $C = 66$ mg/ml indicates the liquid–liquid demixing boundary at this T and $C_{NaCl} = 4\%$. From ref. [94].
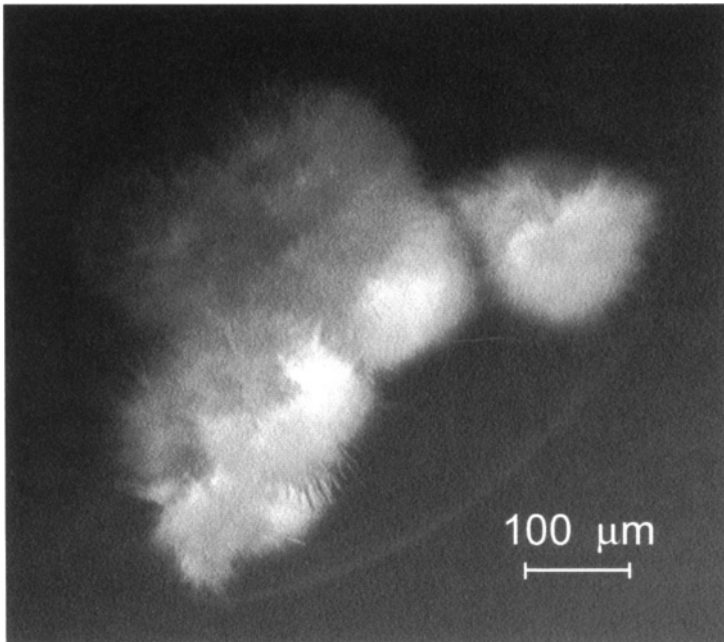

FIGURE 4.17. "Sea urchin" morphology of crystals observed in a few of the droplets during runs at $C_{NaCl} = 4\%$ and $T = 12.6°C$ yielding higher J's, as well as the run at $C_{NaCl} = 4\%$ and lysozyme $C = 68$ mg/ml in which the crystals nucleated in a cloudy solution. From ref. [94].
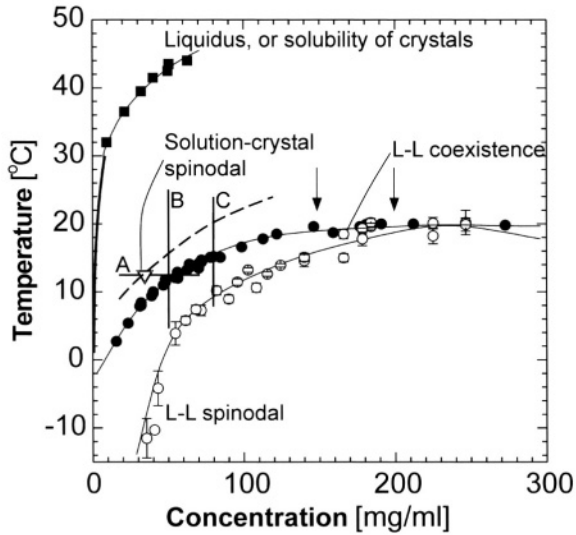
FIGURE 4.18. A section of the phase diagram of lysozyme solutions in the presence of 4% NaCl. As shown in [112,113,140], for many proteins the L-L coexistence line is below the liquidus line because of the very short range of attractive interactions. The liquid–liquid co-existence line and the corresponding spinodal are from [I53|. Error bars for L-L binodal are within the size of the symbols. Solubility of tetragonal crystals at low lysozyme concentrations calculated using empirical formula from [97]. Solubility at higher lyso/yme concentrations—independently measured using methods discussed in [154]. Error bars are smaller than symbol size. Lines A, B and C mark conditions used in the studies reviewed here.

4.3.3. Effects of liquid–liquid separation on the crystal nucleation rate

The liquid–liquid (L-L) phase lines, the coexistence curve and the spinodal, in the system lysozyme– 4% NaCl–water at pH = 4.5 maintained by acetate buffer, are plotted in Figure 4.18 together with the solubility [97] curve at these conditions. For 3% NaCl, all three phase lines are shifted to lower temperature by ~8°C [96].

The line A in Figure 4.18 shows the locations in the (T, C) plane of all nucleation experiments discussed above. The experimental conditions are far from the L-L separation curve for $C_{NaCl} = 3\%$ and should be even further away for $C_{NaCl} = 2.5\%$. Thus, one should not expect any effects of the L-L demixing on the nucleation of crystals at these two precipitant concentrations. Correspondingly, no solution clouding or spherulitic crystals were found in these series of experiments. However, the line A crosses the L-L separation curve for $C_{NaCl} = 4\%$. The data point at this precipitant concentration and $C = 68$ mg/ml in Figure 4.16 was recorded below this curve in the region of liquid–liquid co-existence, and, during nucleation, the solution was cloudy. Crystal nucleation occurring below the L-L phase separation boundary is predicted to have higher energy barriers than at the boundary, or slightly above it [26]. We attribute the slow nucleation at these experimental condition (slower that the nucleation at a lower protein and precipitant concentration) to this effect.

As shown below, the vicinity of the L-L separation boundary is a location of enhanced nucleation of crystals. Minor variations of the solution composition that cause small changes in the locations of the L-L curve may have a strong effect on the nucleation rate. We attribute the kinetic instability in $J(C)$ for $C > 48$ mg/ml to such variations [94].

4.3.4. Number of molecules in the nucleus is small

The nucleus or critical cluster of the new phase is a cluster that has equal probability to grow or to dissolve and is in a labile equilibrium with the supersaturated solution [49,50,98,99]. The number of molecules in the nucleus is an important characteristic of the nucleation process. The nucleus size and shape largely determine the height of the free energy barrier for nucleation (i.e., the reversible work for nucleation), ΔG, and hence the nucleation rate J. The relation between ΔG and the excess number of molecules in a solution volume holding the nucleus n^* over those in an equal solution volume without the nucleus n_0, is treated by the nucleation theorem of Kashchiev and Oxtoby [47,48], a universal, model-independent nucleation law. Since the nucleation work ΔG can be estimated from the logarithm of the nucleation rate J, in terms of J and n^* the nucleation theorem becomes

$$n^* - n_0 = k_\mathrm{B} T \frac{\partial \ln J}{\partial \Delta \mu} + \alpha, \tag{6}$$

where α is a correction that takes values between 0 and 1 [48].

To present the dependencies of the nucleation rates on the concentrations of the protein and precipitant in Figure 4.16 in the variables of the nucleation theorem, the data were re-plotted in Figure 4.19 in terms of functions of thermodynamic supersaturation σ.

Figure 4.19b indicates that at $C_\mathrm{NaCl} = 2.5$ and 3% n^* does not change throughout the respective supersaturation ranges, while at $C_\mathrm{NaCl} = 4\%$ the nucleus size changes abruptly at $\sigma = 3.1$, corresponding to $C = 33.5$ mg/ml. The values of $n^* - n_0$ extracted from the four linear segments in Figure 4.19b are shown in Table 4.1. Since supersaturation is denned as the logarithm of the ratio of C to C_eq, the exact value of C_eq does not affect the slope of the straight lines in Figure 4.19b. Hence, the values of $n^* - n_0$ are independent of possible experimental errors of the solubility measurements.

To roughly evaluate n_0, the molecular diameter, ~30 Å, was compared to the distance between the molecular centers $n_1^{-1/3}$, where n_1 is the protein *molecular* concentration. At $C \approx 70$ mg/ml, $n_1 = 2.9 \times 10^{18}$ cm^{-3} and the distance is ≈ 70 Å. At 2.5% NaCl and a protein concentrations close to 70 mg/ml, in the volume occupied by a crystal consisting of ~10 molecules, there may be $n_0 \approx 1$ solute molecule. At the other precipitant concentrations, the $n^* - n_0$ values in Table 4.1 and the volume occupied by the nuclei are smaller, hence, n_0 is smaller and the correction it introduces in the nucleus size is comparable or smaller than α. With this in mind, the n*'s corresponding to the $n^* - n_0$ values in Table 4.1 were extracted: for $C_\mathrm{NaCl} = 2.5\%$ n^* is 10 or 11, at $C_\mathrm{NaCl} = 3\%$, $n^* = 4$ or 5, at $C_\mathrm{NaCl} = 4\%$, $n^* = 4$ or 5 and then 1 or 2 molecules.

4.3.5. Comparison with predictions of classical nucleation theory

One of the basic assumptions of classical nucleation theory (CNT) is the assumption of continuous cluster size changes. This is a good approximation to reality only for large nuclei. Thus, the size of the nuclei determined above precludes application of CNT to our data. We compared our experimental results to the predictions of this theory only for the
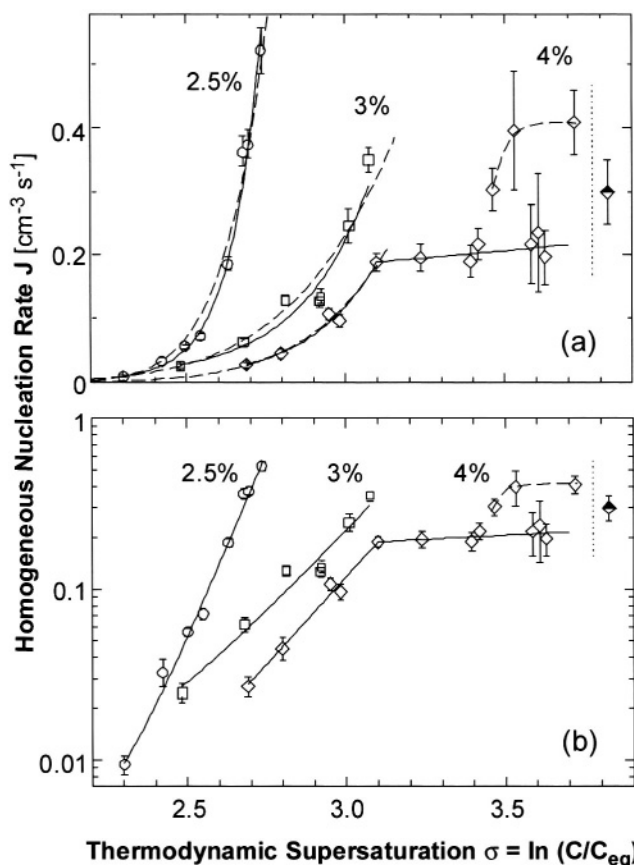
FIGURE 4.19. Dependencies of homogeneous nucleation rate J on supersaturation $\sigma \equiv \Delta\mu / k_B T$ at $T = 12.6°C$ and at the three precipitant concentrations indicated on the plots. Solid lines—fits with exponential functions; dashed lines fits with the classical nucleation theory expression, eq. (6). Data points with higher J's at $C_{NaCl} = 4\%$, and datum point obtained in a cloudy solution at $C_{NaCl} = 4\%$ and lysozyme $C = 68$ mg/ml were not used in fitting procedures, see text for details. Vertical dotted lines at $\sigma = 3.9$ indicate the liquid–liquid demixing boundary at this T and $C_{NaCl} = 4\%$. (a) Linear coordinates; (b) semi-logarithmic coordinates. From ref. [94].

TABLE 4.1.

Characteristics of nucleation process determined from fits of eqs (2)--(5) to data. For definitions and details, see text.

C_{NaCl}	$n^* - n_0$	A (s^{-1})	B	γ (mJ/m^2)	n^*_{CNT}
2.5%	9.6 ± 0.2	$(9 \pm 5) \times 10^{-16}$	65 ± 4	0.64	11–7
3%	4.2 ± 0.2	$(4 \pm 2) \times 10^{-18}$	33 ± 4	0.51	4–2
4%	4.7 ± 0.3	$(1.4 \pm 0.7) \times 10^{-17}$	44 ± 4	0.56	5–3
4%	0.2 ± 0.3	–	–	–	–

sake of completeness. Within the framework of this theory, the dependence of the nucleation rate on supersaturation σ and protein molecular concentration n_1 is [46,85]

$$J = An_1 \exp\left(-B/\sigma^2\right). \tag{7}$$

The coefficient A is a complicated function of the molecular-level attachment-kinetics parameters. There have been attempts to analytically derive an expression for this coefficient for nucleation from solution [9–11,100]. In all cases, the final formulae for A contain variables that are often impossible to determine independently.

The parameter B is related to the thermodynamic barrier for the creation of the critical cluster ΔG^* and for a spherical cluster can be written as

$$B = \frac{16\pi}{3} \frac{\Omega^2 \gamma^3}{(k_{\mathrm{B}}T)^3}, \tag{8}$$

where Ω is the protein molecular volume in the crystal and γ is the surface free energy of the critical cluster. Two-parameter fits of our data with eq. (7) show reasonably good correspondence Figure 4.19a. The best-fit values of A and B are shown in Table 4.1. From the values of B we estimate the surface free energy γ.

Classical nucleation theory also allows determinations of the nucleus size as

$$n_{\mathrm{CNT}}^* = \frac{2B}{\sigma^3}. \tag{9}$$

This size continuously changes in the supersaturation ranges of the experiments. The nucleus sizes determined using eq. (9) straddle the more accurate determinations based on the nucleation theorem, eq. (6). This correspondence seems to support the general belief that CNT provides a fair approximation for the nucleation barrier [101–103], while failing to predict the pre-exponential factors.

4.3.6. Spinodal for the solution–solid phase transition

Critical clusters consisting of one molecule have been encountered before in investigations of electrochemically-driven nucleation of new phases under high overvoltages/supersaturations [23]. Similar to the case of nucleation of lysozyme crystals, discussed above, it was concluded that the nucleation rate is determined only by the kinetics of attachment of molecules to this critical cluster. The lack of a thermodynamic barrier for the formation of nuclei of the new phase in this regime allows us to view it as spinodal decomposition. The location in the phase diagram, where the transition to $n^* = 1$ occurs can be viewed as the spinodal line for the solution-solid phase transformation.

This would constitute a kinetic definition of the spinodal line, and differs form the thermodynamic definitions employed for fluid–fluid, or solid–solid systems. For fluid–fluid or solid–solid phase transitions unified expressions for the free energy exist which encompass both the old and new phase. The spinodal line has been sought as the location where the second derivative of the free energy with respect to the order parameter defining the phase transition vanishes. Since a unified expression for the free energy of an ordered and a disordered phase in equilibrium cannot be written, it is sometimes claimed that the spinodal for

the phase transition between fluid and solid phase does not exist. We see that this spinodal line can be defined from kinetic considerations and in the phase diagram in Figure 4.18, we have marked its location for the temperature probed in Figure 4.16, and likely location for similar temperatures.

In Figure 4.16 the transition form nucleation to spinodal decomposition regimes occurs at $C = 33.5$ mg ml^{-1}. The break in the nucleation rate at this concentration is what is expected at any step-wise change of nucleus size [23,104]. Thus, we conclude that the transition from nucleation to spinodal decomposition is not a point of singularity and divergence of lengthscales.

4.3.7. Nucleation of ordered solids as superposition of fluctuations along two order parameters

The phase diagram in Figure 4.18 contains there phases: the "normal" dilute solution, the dense liquid phase, and crystals. The transitions between the three phases require at least two order parameters for a complete description. The phase diagram also contains two spinodal lines—for the solution–solid, and for the liquid–liquid transitions. Since the spinodal is the location where the "old" phase looses stability, we conclude that dilute solution may loose stability with respect to fluctuations along both order parameters.

It has been suggested the formation of crystals should be viewed as a transition along two order parameters: density and "structure" [26]. Below, we provide some considerations that may help to distinguish between density and structure fluctuations.

A "pure" density fluctuation may lead to the formation of a stable droplet of dense liquid depending on the region of the phase diagram in which it occurs. Above the L-L coexistence line, all density fluctuations decay. In the region between the L-L binodal and L-L spinodal, only density fluctuations exceeding the critical size and amplitude, see Figure 4.2, lead to nuclei of dense liquid droplets. Below the L-L spinodal, all density fluctuations, even those of infinitesimal amplitude result in formation of a new liquid phase.

"Pure" structure fluctuations are only possible in melts, whose density is similar to that of the emerging crystalline phase. Depending on the location in the phase diagram, a structure fluctuation may lead to the formation of an ordered crystalline nucleus. The smallest fluctuation can be viewed as a pair of atoms or molecules from the melt that has an orientation similar to the orientation of a pair of atoms or molecules in the crystal, for informative examples, see Refs [58,105]. This crystals-like orientation in the pair is preserved over times significantly longer than the lifetime of a "bond" in the melt. A nucleus arises as a result of accumulation of such ordered pairs into an ordered piece of new phase. In a sense, structure fluctuations can be viewed as fluctuations of the density of ordered pairs.

If a crystal nucleates not from its melt, but from a dilute solution or gas, a density and a structure fluctuation are needed so that a crystalline nucleus may form.

The phase diagram in Figure 4.18 helps us to add important features to the idea of two order parameters, illustrated in Figure 4.20. Since the spinodal for solution–crystal transition is above the L-L coexistence line, the solution may be unstable with respect to structure fluctuations even in phase diagram regions where none of the density fluctuations grows into a new phase droplet. Thus, in contrast to earlier suggestions [25,26,106,107], in order to overcome their barrier and become crystalline nuclei, structure fluctuations do not require (i) stable droplets, or (ii) density fluctuations of large amplitude, such as those
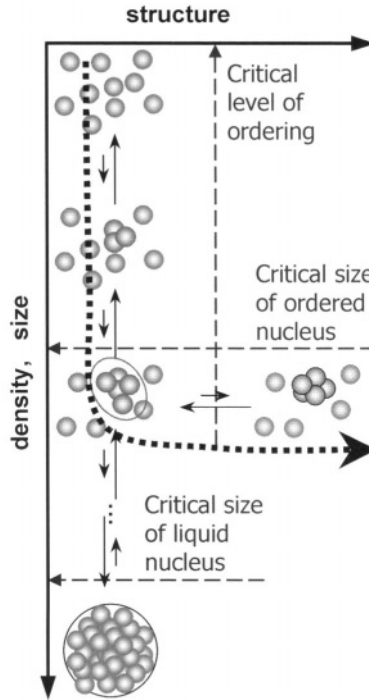
FIGURE 4.20. A schematic illustrating the formation of ordered crystalline nuclei as a result of the superposition of a density and a structure fluctuations. This schematic corresponds to a location in the phase diagram just below the L-L coexistence lines. At locations between the liquidus and the L-L coexistence lines, the critical liquid nucleus size is infinite, i.e., no density fluctuation can lead to a stable droplet. At locations between below the L-L spinodal line, any density fluctuation leads to a stable droplet.

in the critical region. On the other hand, (iii) density fluctuations occurring below the L-L coexistence line lead to droplets that may never become crystals. Two conclusions can be drawn from observations (i)–(iii): (a) a density and a structure fluctuation that result in a crystalline nucleus occur not simultaneously, but in sequence. The structure fluctuation is superimposed on the density fluctuation in such a way that for the lifetime of a density fluctuation, as it grown and decays, the material in the quasi-droplet may attain structure. (b) There exist density fluctuations with optimal size and density, which provide the highest probability that a structure fluctuation may occur in the quasi-droplet. Density fluctuations of larger sizes and amplitudes may spend less time in the optimal parameter region and decrease the probability of superposition of a structure fluctuation.

4.4. NUCLEATION OF CRYSTALS AND DENSE LIQUID DROPLETS

The viewpoint that nucleation of ordered solid phases occurs via the superposition of fluctuations along two ordered parameters, density and structure, was formulated above on the basis of data on the nucleation rate in the vicinity of the liquid–liquid co-existence line. In the experiments discussed above, the L-L coexistence boundary was crossed along a

constant temperature line. For further tests of this mechanism, we carried out a series of experiments, in which we kept the concentration of the protein constant and crossed into the L-L coexistence region by varying the temperature. In both series of experiments, we use L-L separation as a probe for the mechanisms of crystal nucleation that operate not only in the vicinity of the L-L separation phase region, but also away from it.

4.4.1. Enhanced nucleation around T_{L-L}

Figure 4.21 presents the dependencies of the homogeneous nucleation rate J on the temperature T recorded at two solution compositions. The conditions of these experiments are represented with lines B and C in the phase diagram in Figure 4.18. In all cases, we see that as T is lowered, J increases, reaches a maximum near the respective T_{L-L} and then decreases as the system enters the L-L separation region. Thus, the maxima in $J(T)$ curves are related to the L-L separation, although in both case it occurs at temperatures higher by 1–1.5°C from the respective T_{L-L}'s.

Experiments at protein concentrations of 150 and 200 mg/ml revealed the expected [25, 26] extremely high crystal nucleation rates close to (C^{crit}, T^{crit}). However, a few minutes after T was lowered to the chosen value, solution gelation [95,108] occurred and, accordingly [106], nucleation was arrested.

Factors that may underlie the increase of J before its maximum as T is lowered in Figure 4.18 are: (i) increase of supersaturation for crystallization as the system moves away from the solubility line. (ii) The approach to the spinodal lying below the L-L coexistence line $T_{L-L}(C)$ similar to the theoretical predictions for approaches to (C^{crit}, T^{crit}) [25,26,109]. At the spinodal, $(\partial^2 \Delta G / \partial C^2)_T = 0$ (ΔG being the free energy of the so-
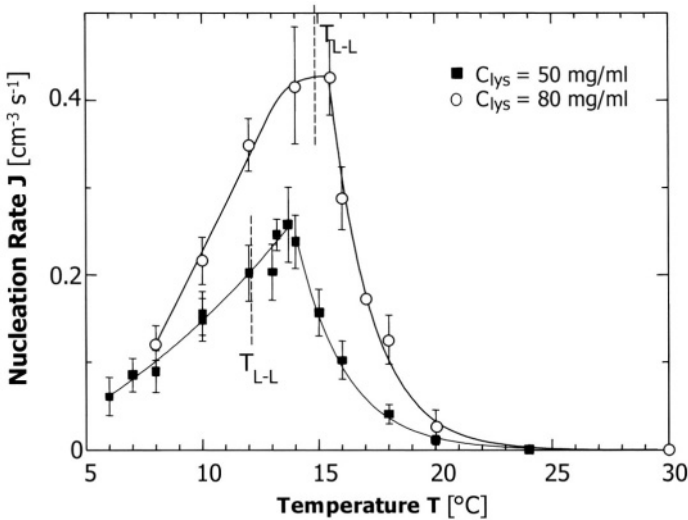

FIGURE 4.21. Dependencies of the rate of homogeneous nucleation of lysozyme crystals J on temperature T at pH = 4.5 by 50 mM sodium acetate buffer and 4% (w/v) NaCl. (■) Lysozyme concentration $C_{lys} = 50$ mg/ml, (○) $C_{lys} = 80$ mg/ml. Vertical dotted lines indicate respective temperatures of liquid-liquid separation T_{L-L}. Curves are just guides for the eyes. From ref. [148].

lution) ([110], p. 202). (iii) Lower free energy barrier for nucleation of crystals from the dense liquid phase [25]. Note that factors (ii) and (iii) have not been separately considered by theory. The theoretical treatments of nucleation enhancement due to L-L separation [25, 26,109] concentrate on the region around the critical point, where the binodal and spinodal coincide.

To evaluate the effect of supersaturation increase, (i) above, we note that at 20°C the concentration of a solution without additives and in equilibrium with crystals is $C_{eq} = 3.4$ mg/ml, while for $T = 14$°C, $C_{eq} = 2.3$ mg/ml [97]. For a solution containing 50 mg/ml lysozyme, these correspond to $\sigma = 2.7$ and 3.1, respectively. Figure 4.19 indicates that in this supersaturation range, the σ increase should lead to at most a fourfold increase of the nucleation rate. The actual increase between these two temperatures is ~25-fold. Furthermore, it is unlikely that this conclusion could be affected by possible changes in the surface free energy of the nuclei with temperature. Surface free energy affects the nucleation kinetics through the nucleus size, while we found above that in this supersaturation range, this size is fixed at four or five molecules. We attribute the residual ~six-fold increase to the L-L separation related factors (ii) or (iii) above.

The same conclusion stems from the $J(T)$ dependencies at protein concentration $C = 80$ mg ml^{-1} in Figure 4.21—J increases by a factor of ~17× as T decreases from 20 to 15°C. The corresponding supersaturations are 3.15–3.5. As shown above, in this σ range, the critical cluster contains one or two molecules, J is a very weak function of σ [94] and increase in J under these conditions is almost entirely attributable to the liquid-liquid phase separation.

4.4.2. Alternative mechanisms of nucleation enhancement around $T_{L\text{-}L}(C)$

To distinguish between lower nucleation barriers at the L-L coexistence line, and density fluctuations enhancement around the spinodal, we correlate the $J(T)$ dependencies in Figure 4.21 to the phase diagram in Figure 4.18. The data in Figure 4.18 show that the spinodal is below the L-L coexistence line by 2 to 8°C, depending on the protein concentration. At the concentration of 50 mg/ml of the experiments in Figure 4.21, the maximum occurs at temperature higher by ~6°C from the temperature of the spinodal. At $C = 80$ mg ml^{-1}, the descending branch of $J(T)$ below the L-L coexistence line crosses the spinodal at $T = 9.5$°C. There is no enhancement of nucleation at that temperature. Thus, we conclude that density fluctuations alone do not contribute to higher nucleation rates. This conclusions is contrary to the predictions of the simulations in ref. [25], but agrees with expectations stemming from the model of superposition of density and structure fluctuations, and in particular with the concept of optimal density fluctuation, discussed above.

It is tempting to use the illustrative concept of wetting to describe the enhancement of the nucleation of crystals in the area around the L-L separation boundary [111]. It seems to us that this may be misleading: if the liquid wets the crystal nucleus, lowers its surface energy, and thus decreases the nucleation barrier, it is hard to understand why this does not occur at temperatures below $T_{L\text{-}L}$. Furthermore, as pointed out above, the critical cluster consists of as few as 10, or 4 or 1–2 molecules—with so few molecules, it would be difficult to assign some of them to the crystal, and others to the liquid that wets it. Note that the calculation of the nucleation rates in ref. [25] was based on a model phase diagram that has been shown to underestimate the separations between the liquidus and the L-L coexistence

lines [112–114]. As a result, the size of the crystal nucleus near the L-L coexistence line, emerging from the simulations, was unrealistically large, and one could speculate that it could accommodate a liquid layer wetting a crystalline nucleus. The overall conclusion from these considerations is that the macroscopic concepts of wetting or surface tension are not readily applicable to the nucleation of protein solid phases.

Another mechanism that has been invoked to explain the enhancement of nucleation by the dense liquid phase is the higher protein concentration in it. Although appealing in its obviousness, this mechanism fails to explain the decrease in nucleation rate seen in Figure 4.21 at temperatures deeper into the L-L co-existence region. Further evidence that the presence of stable droplets of dense liquid is not a prerequisite for enhanced nucleation comes from Figure 4.22. It shows that the numerous dense liquid droplets do not cause the nucleation of new crystals. A single crystal, present from the beginning of the monitoring period grows and the recruitment of material into it leads to gradual disappearance of the dense liquid droplets. The coupled growth and dissolution are possible because the solubility of the crystals in Figure 4.18 is significantly lower than the concentration of the solution in equilibrium with the dense phase; this observation is an illustration of the metastability of the dense liquid phase with respect to the crystals. The transfer of protein molecules from the dense liquid phase to the crystals shows that the protein in the droplets is not denatured, and the reason for suppression of nucleation should be sought elsewhere.

Note that in some cases, the presence of dense liquid does facilitate the nucleation of ordered solid phases. Figure 4.23 shows an example of nucleation of bundles of linear arrays, often called polymers, of deoxy-hemoglobin S; the formation these polymers is the primary pathogenic event in the deadly sickle cell anemia [115–119]. The temperature is changed from a value in which the droplets are the main phase co-existing with the normal solution, to a value where the droplets are unstable and the polymers are in equilibrium with the solution, for further details, see [120]. Smaller droplets disappear within several seconds, while the larger droplets, that have not disappeared, serve as centers for nucleation of deoxy-HbS polymers. Additional spherulites emerge at the locations where the smaller droplets have been, most likely due to high deoxy-HbS concentrations undissipated within the short times for the onset of polymerization. This last observation allows us to attribute the enhanced nucleation of polymers in the dense liquid droplets to the higher hemoglobin concentration in them.

We would like to attribute the difference in nucleation behavior within the dense liquid droplets to the viscosity of the dense liquid phase [106]. Hemoglobin molecules were designed by evolution to operate in environments where their concentration is very high, 35% (w/v) in the red cell cytosol, yet remain non-aggregated and preserve the flexibility of the red cell as it squeezes and slithers along the narrow capillaries. Hence, the hemoglobin molecules exhibit week repulsion [121,122], and the mutation in sickle cell hemoglobin that enables the formation of the polymers only induces a very short-range attraction [122]. The long-range repulsion underlies the unusually low viscosity of native and mutant hemoglobins even at the high concentration in the red cell cytosol [123,124], or in the dense liquid phase. On the other hand, attraction is the dominant force acting between pairs of molecules in crystallizing protein solutions, and correspondingly, we expect high viscosity in the respective dense phases. Such high viscosity would arrest nucleation.
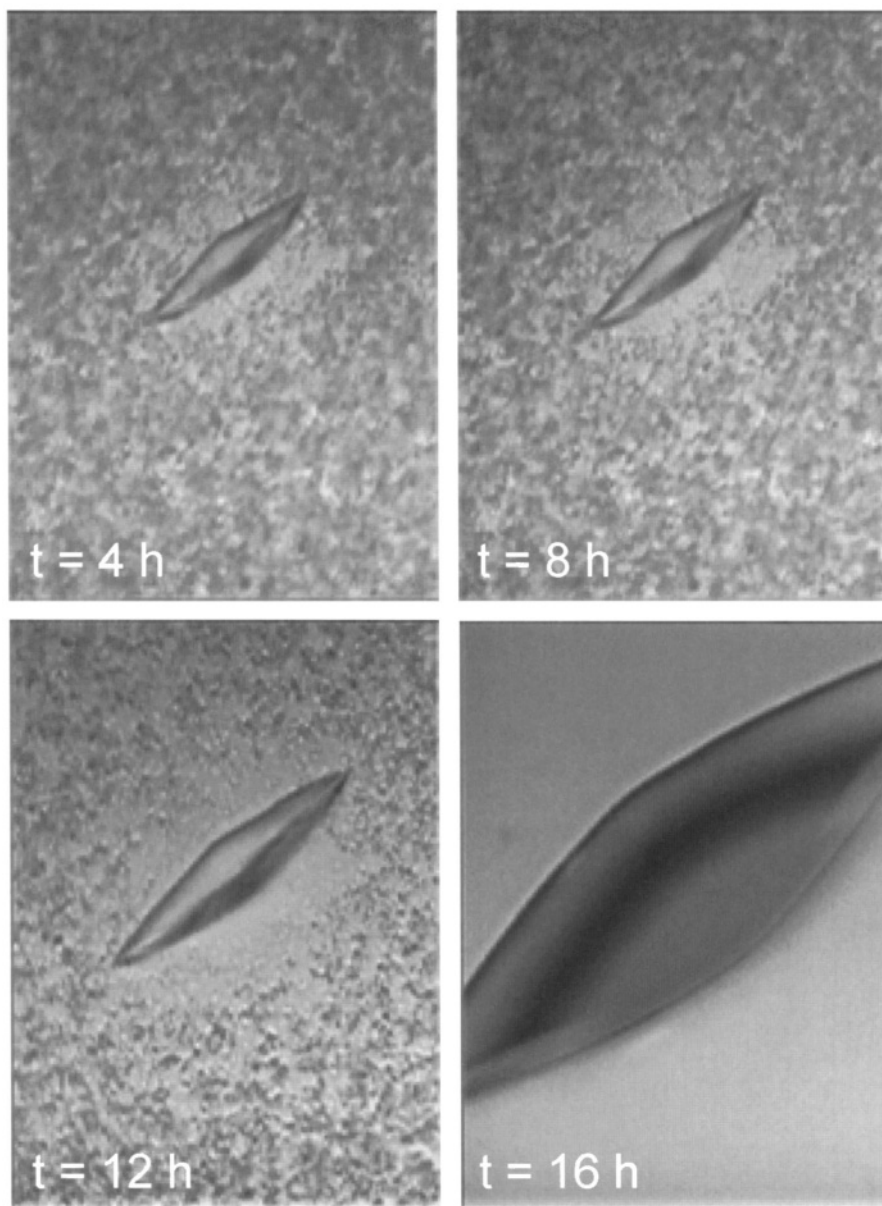
FIGURE 4.22. A single tetragonal crystal of lysozyme grows while surrounded by numerous droplets of the dense liquid phase at $C_{lys} = 80 \, \text{mg ml}^{-1}$ and $T = 12°C$. Time on frames is measured from the moment in which T was set at its value. Crystal fills $\sim 20 \, \mu\text{m}$ space between two coverslips and its shape is accordingly distorted.

There is abundant evidence in literature that shows that the stable macroscopic dense liquid phase *does not* promote the nucleation of crystals [125]. In many cases, similar to the example discussed above, crystals and dense liquid droplets were found to coexist for
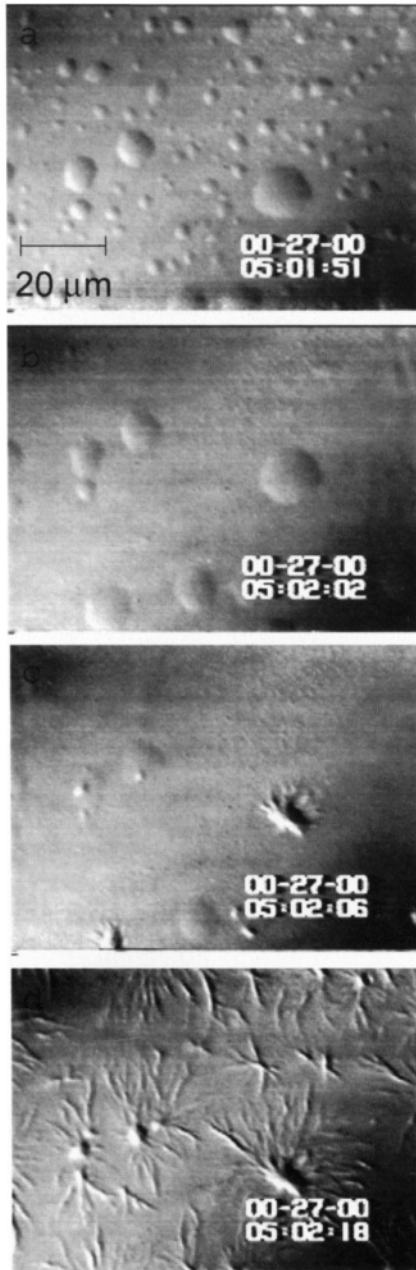
FIGURE 4.23. Link between liquid–liquid separation and formation of ordered linear arrays in deoxy-HbS solutions. Concentration of HbS is 22 g/dl. (a–d) when temperature is lowered from 42 to 35°C, the smaller of the dense liquid droplets disappear, while the larger ones serve as nucleation centers for HbS spherulites. Spherulites also appear at the locations where smaller droplets have been, apparently because of the undissipated locally higher concentration. From ref. [120].

extended lengths of time without the droplets generating additional crystal nuclei. In some cases, crystals that were nucleated on the droplet boundaries grew into the dilute solution, rather than into the dense liquid [125].

4.4.3. Correlation between dense-phase formation and crystal nucleation

The above considerations suggest that although the experiential evidence indicates strong effect of the dense liquid phase on the nucleation of the ordered phases, neither enhanced density fluctuations, nor the presence of stable dense liquid phase are factors that by themselves could explain the correlation. On the other hand, the mechanism of crystal nucleation as a superposition of density and structure fluctuations schematically depicted in Figure 4.20, well fits the experimental data. Indeed, the relative distance of the operating point of the system from the L-L coexistence line in the plane of the phase diagram in Figure 4.18 determines the prevailing sizes and the amplitudes of the density fluctuations. This is why the behavior of the $J(T)$ curves is correlated with the $T_{L-L}(C)$. Furthermore, the existence of optimal size and amplitude of the density fluctuation explains why the strongest enhancement of the nucleation of crystals does not occur at the spinodal for L-L separation, where the density fluctuations are strongest. Since the optimal density fluctuation may occur above the L-L coexistence line, we understand why the strongest enhancement and the $J(T)$ maximum are located above this line.

4.4.4. Control of nucleation

The capability to enhance or suppress the rate of nucleation of protein crystals opens broad avenues in the area of protein crystallization for X-ray structure studies [126]. For instance, in some cases, the highsupersaturations needed to achieve crystal nucleation lead to fast growth of poor-quality crystals [127]. Seeding can in some cases help to circumvent the problem [128–130], however, often the surface of the seeds is contaminated or otherwise pacified and the technique is inapplicable. If protein crystal nucleation could be enhanced, this would allow crystal nucleation to occur at lower supersaturations, at which growth of higher-quality crystals may be expected. In other cases, new crystals are continuously nucleated throughout a crystallization run and may be incorporated into previously nucleated, larger crystals. Such incorporation may remain undetected and lead to mosaicity and lattice strain. Hence, for systems of this latter type, suppression of the secondary nucleation events should contribute to higher perfection. Control of protein crystal nucleation is needed in other health-related areas: production of protein crystalline Pharmaceuticals [131], protein separation [132], and treatment of protein condensation diseases [119,133–136].

Control of the spatial distribution, of the orientation and polymorphism is sought if crystals of microcrystalline particles are to be used in devices [16,137,138].

The realization that the nucleation of ordered solid phases occurs as a superposition of fluctuations along two order parameters offers two handles for control of the spatiotemporal characteristics of nucleation—its rate and the distribution and orientation of the nuclei. The first one involves enhancing the desired structure fluctuation in the quasi-droplet comprising the density fluctuation. This has been done by applying electric field to a supersaturated solution. In one instance, a flat microscope slide with supersaturated solution of the protein lysozyme was placed between two electrodes and a field of

~ 1500 V cm^{-1} was imposed [83]. It was found that the nucleation rate increased significantly, and that the crystals were preferentially oriented with their c-axis along the field lines. While the crystal orientation could be due to rotation of the crystallites after nucleation, the increased rate of nucleation suggests that the electric field stabilizes some of the structures that form and decay within a density fluctuation quasi droplet, and the stabilized structures are compatible with those leading to a crystalline nucleus. Note that orienting the protein molecules in the direction of the field should lead to suppression of nucleation— in tetragonal crystals, the molecules are oriented along evenly distributed angles along all three axes.

In another series of experiments, high power laser pulses were shone on supersaturated solutions of glycine [16]. It was fond that the nucleation rate increases as a result of the illumination by eight-nine orders of magnitude and that by using elliptically or linearly polarized light, α- or γ-glycine crystals could be preferentially nucleated. Since glycine does not absorb the illumination wavelength, and the electric filed intensity was insufficient to orient single glycine molecules, it was concluded that the elliptically or linearly polarized pulses stabilize the structure fluctuations leading to the respective solid phases, and in this way help the selection of the polymorph and speed up the rate of nucleation [16,17].

Another way to control nucleation, suggested by the superposition mechanism, is by shifting the L-L coexistence line and in this way controlling the density fluctuations.

4.4.5. Nucleation control by shifting T_{L-L}

The finding of a maximum in crystal nucleation rate near the L-L separation boundary suggests that shifting this boundary to lower temperatures can reduce J. One may attempt this by increasing the repulsion between the protein molecules [106,139,140]. Recent work with a trypsin inhibitor suggests that glycerol increases such repulsion [141]. Glycerol is preferentially rejected from the surroundings of the protein molecules [142], stabilizes their native structures [143], enhances their folding in aqueous media [144]. The $J(T)$ curve in the presence of glycerol in Figure 4.24 shows that, indeed, T_{L-L} is lowered by 5°C, see also Figure 4.25, and, at temperatures above the T_{L-L} for solutions sans glycerol, the nucleation rate is lowered by a factor of about three. Note that this suppression cannot be attributed to viscosity increase due to the glycerol: 5% glycerol causes a viscosity higher by only $\sim 13\%$ [145], which should affect the nucleation rate by the same factor [11].

In other applications, enhancement of crystal nucleation is sought. Polyethylene glycol (PEG) has been expected to increase the attraction between colloid particles solely due to the system's drive to minimize the excluded volume inaccessible to the polymer between two particles, often called depletion attraction [139,140,146,147]. It has been suggested that such non-adsorbing, non-bridging polymers should enhance nucleation [25]. The data on $J(T)$ in the presence of 0.2% (w/v) PEG with molecular mass 5000 Da (PEG 5000) are shown in Figure 4.24. This low concentration of PEG does not measurably affect the solubility or the L-L separation points, Figure 4.26 [148]. Despite that, the rate of nucleation is increased three fold at T_{L-L} and less than that at higher or lower T's. Using PEG of various molecular masses in concentrations higher than 0.5% resulted in very fast nucleation often accompanied by solution gelation or amorphous precipitation of the protein, indicating strong isotropic intermolecular attraction [149].

The effect of PEG on J is considerably stronger than that of glycerol. The phase diagram of the protein solution in the presence of PEG in Figure 4.26 shows that PEG effects
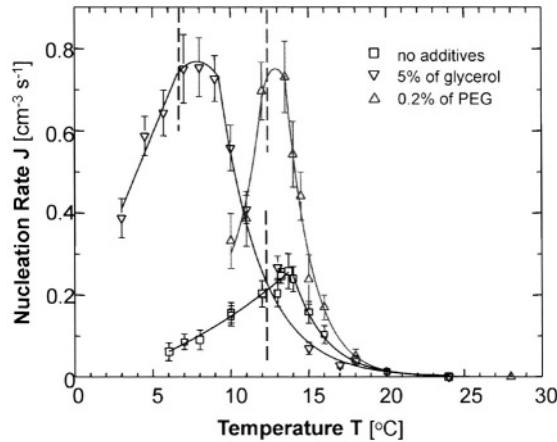
FIGURE 4.24. Dependencies of the rate of homogeneous nucleation of lysozyme crystals J on temperature T at pH = 4.5 by 50 mM sodium acetate buffer and 4% (w/v) NaCl. (□) Lysozyme concentration $C_{lys} = 50$ mg/ml, no additives; (∇) lysozyme concentration $C_{lys} = 50$ mg/ml; 5% (vol.) glycerol; (△) $C_{lys} = 50$ mg/ml, 0.2% (w/v) polyethylene glycol 5000. Vertical dotted lines indicate respective temperatures of liquid–liquid separation T_{L-L}. Curves are just guides for the eyes. From ref. [148].
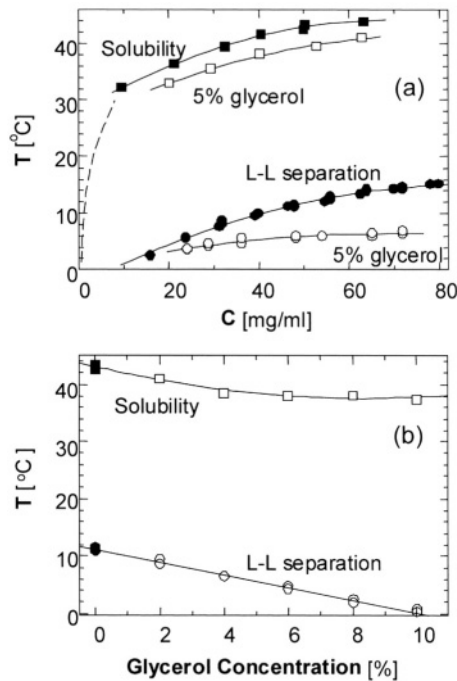

FIGURE 4.25. Effects of glycerol on the phase diagram of a lysozyme solution containing 4% (w/v) NaCl with a pH = 4.5 by 50 mM sodium acetate buffer. (a) Changes in the solubility and liquid–liquid (L-L) separation boundaries introduced by the addition of 5% (vol.) glycerol. Dashed line—solubility from ref. [97]. (b) Dependence of the solubility and L-L separation temperatures on the concentration of glycerol in a 50 mg/ml lysozyme solution. From ref. [148].
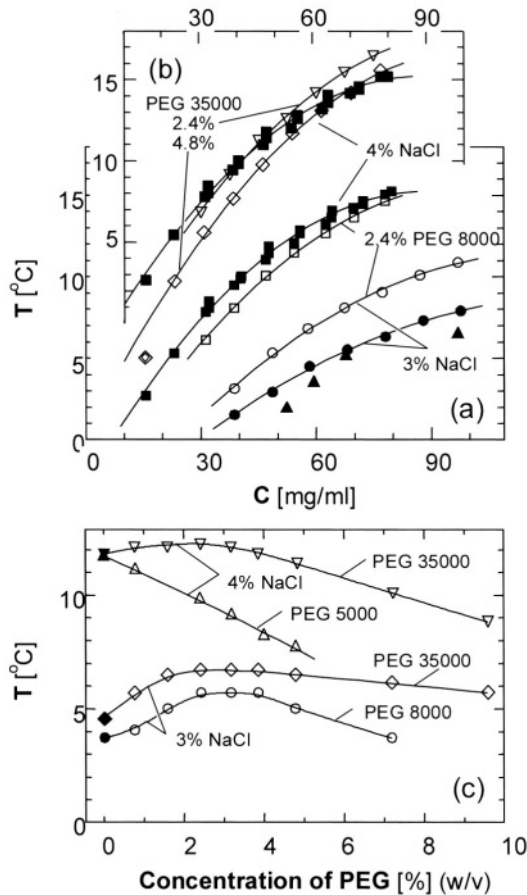
FIGURE 4.26. Effects of polyethylene glycol (PEG) with molecular mass and concentration indicated in the plots on the liquid–liquid separation in a lysozyme solution containing 3 or 4% NaCl with a pH = 4.5 by 50 mM sodium acetate buffer. Full symbols—no additive; open symbols—PEG added as indicated in the plots. Curves are just guides for the eye. (a and b) Changes in the liquid–liquid (L-L) separation boundary introduced by the addition of PEG. (▲) Data of ref. [95] for 3% NaCl. (c) Dependence of the L-L separation temperature on the concentration of PEG in a 50 mg/ml lysozyme solution. From ref. [148].

cannot be understood simply in terms of enhanced attraction due to restricted volume accessible to non-adsorbing non-interacting polymers. Recent models and experiments [139, 150,151], allowing for interactions between the polymer molecules, predict that, as the PEG concentration increases into the semidilute regime (where the polymer coils overlap), the attraction between the protein molecules should gradually taper off. The emerging complex picture of the interactions in a PEG–protein system agrees with recent direct force measurements [152]. They show strong, non-entropic attraction at high polymer–protein separations, corresponding to low PEG concentrations, and strong repulsion at short separations. The conclusions of these studies may at least partially explain the strong action of PEG on the nucleation kinetics.

ACKNOWLEDGMENT

REFERENCES

1. P.C. Hohenberg and B.I. Halperin, Theory of dynamic critical phenomena, *Rev. Mod. Phys.* **49**, 435–479 (1977).

2. P.M. Chaikin and T.C. Lubensky, *Principles of Condensed Matter Physics* (Cambridge Unversity Press, Cambridge, 1995).

3. D. Kashchiev, *Nucleation. Basic Theory with Applications* (Butterworth, Heinemann, Oxford, 1999).

4. K. Binder and P. Fratzl, Spinodal decomposition, in: Ed. G. Kostorz, *Phase Transformation in Materials* (Wiley, New York, 2001).

5. D. Kashchiev, Thermodynamically consistent description of the work to form a nucleus of any size, *J. Chem. Phys.* **118**, 1837–1851 (2003).

6. J.W. Gibbs, On the equilibrium of heterogeneous substances, *Trans. Connect. Acad. Sci.* **3**, 108–248 (1876).

7. J.W. Gibbs, On the equilibrium of heterogeneous substances, *Trans. Connect. Acad. Sci.* **16**, 343–524 (1878).

8. J.L. Katz and B.J. Ostermier, Diffusion cloud chanber investigation of homogeneous nucleation, *J. Chem. Phys.* **47**, 478–487 (1967).

9. A.E. Neilsen, Nucleation in aqueous solutions, in: Ed. S. Peiser, *Crystal Growth* (Pergamon, Oxford, 1967) pp. 419–426.

10. M. Kahlweit, Nucleation in liquid solutions, in: Ed. H. Eyring, *Physical Chemistry,* Vol. VII (Academic Press, New York, 1969) pp. 675–698.

11. A.G. Walton, Nucleation in liquids and solutions, in: Ed. A.C. Zettlemoyer, *Nucleation* (Marcel Dekker, New York, 1969) pp. 225–307.

12. J.L. Katz, Three dimensional nucleation, in: Ed. B. Mutaftschiev, *Interfacial Aspects of Phase Transformations* (Kluwer, Boston, 1982).

13. J.B. Zeldovich, On the theory of formation of new phases. Cavitation, *J. Theor. Experimen. Phys. (USSR)* **12**, 525–538 (1942).

14. D. Kashchiev, Solution of the non-steady state problem in nucleation kinetics, *Surf. Sci.* **14**, 209–220 (1969).

15. D. Kashchiev, Nucleation, in: Eds J.P.v.d. Eerden and O.S.L. Bruinsma, *Science and Technology of Crystal Growth* (Kluwer Academic Publishers, 1995) pp. 53–56.

16. B. Garetz, J. Matic and A. Myerson, Polarization switching of crystal structure in the nonphotochemical light-induced nucleation of supersaturated aqueous glycine solutions, *Phys. Rev. Lett.* **89**, 175501 (2002).

17. D.W. Oxtoby, Crystals in a flash, *Nature* **420**, 277–278 (2002).

18. N.M. Dixit and C.F. Zukoski, Crystal nucleation rates for particles experiencing short-range attractions: applications to proteins, *J. Colloid Interface Sci.* **228**, 359–371 (2000).

19. J.W. Cahn and J.E. Hilliard, Free energy of a nonuniform system. I. Interfacial free energy, *The Journal of Chemical Physics* **28**, 258–267 (1958).

20. K. Binder, Dynamics of first order phase transitions, in: Ed. T. Riske, *Fluctuations and Instabilities in Phase Transitions* (Plenum, New York, 1975) pp. 19–42.

21. J.S. Langer, Spinodal decomposition, in: Ed. T. Riske, *Fluctuations and Instabilities in Phase Transitions* (Plenum, New York, 1975) pp. 19–42.

22. K. Binder, Spinodal decomposition, in: Ed. P. Haasen, *Phase Transformations of Materials,* Vol. 5 (VCH Verlag, Weinheim, 1990).

23. A. Milchev, Electrochemical phase formation on a foreign substrate—basic theoretical concepts and some experimental results, *Contemp. Phys.* **32**, 321–332 (1991).

24. A.A. Chernov, *Modern Crystallography III, Crystal Growth* (Springer, Berlin, 1984).

25. PR. ten Wolde and D. Frenkel, Enhancement of protein crystal nucleation by critical density fluctuations, *Science* **277**, 1975–1978 (1997).

26. V. Talanquer and D.W. Oxtoby, Crystal nucleation in the presence of a metastable critical point, *J. Chem. Phys.* **109**, 223–227 (1998).

27. P.R. ten Wolde, D.W. Oxtoby and D. Frenkel, Coil–globule transition in gas–liquid nucleation of polar fluids, *Physical Review Letters* **81**, 3695–3698 (1998).

28. W.T. Lee, E.K.H. Salje and M.T. Dove, Effect of surface relaxations on the equilibrium growth morphologies of crystals: platelet formation, *J. Phys. Condensed Matter* **11**, 7385–7410 (1999).

29. T.E. Creighton, *Proteins: Structure and Molecular Properties* (W.H. Freeman, New York, 1993).

30. S.-T. Yau, B.R. Thomas and P.G. Vekilov, Molecular mechanisms of crystallization and defect formation, *Phys. Rev. Lett.* **85**, 353–356 (2000).

31. G. Binnig, C. Gerber, E. Stoll, R.T. Albrecht and C.F. Quate, Atomic resolution with atomic force microscope, *Europhys. Lett.* **3**, 1281–1286 (1987).

32. S.-T. Yau, D.N. Petsev, B.R. Thomas and P.G. Vekilov, Molecular-level thermodynamic and kinetic parameters for the self-assembly of apoferritin molecules into crystals, *J. Mol. Biol.* **303**, 667–678 (2000).

33. T.A. Land, J.J. DeYoreo and J.D. Lee, An in-situ AFM investigation of canavalin crystallization kinetics, *Surf. Sci.* **384**, 136–155 (1997).

34. A.J. Malkin, Y.G. Kuznetsov and A. McPherson, In situ atomic force microscopy studies of surface morphology, growth kinetics, defect structure and dissolution in macromolecular crystallization, *J. Crystal Growth* **196**, 471–488 (1999).

35. Y.G. Kuznetsov, A.J. Malkin, T.A. Land, J.J. DeYoreo, A.P. Barba, J. Konnert and A. McPherson, Molecular resolution imaging of macromolecular crystals by atomic force microscopy, *Biophys. J.* **72**, 2357–2364 (1997).

36. T.L. Hill, *Thermodynamics of Small Systems* (Benjamin, New York, 1963).

37. D.N. Petsev and P.G. Vekilov, Evidence for non-DLVO hydration interactions in solutions of the protein apoferritin, *Phys. Rev. Lett.* **84**, 1339–1342 (2000).

38. D.N. Petsev, B.R. Thomas, S.-T. Yau and P.G. Vekilov, Interactions and aggregation of apoferritin molecules in solution: effects of added electrolytes, *Biophysical J.* **78**, 2060–2069 (2000).

39. L.K. Steinrauf, Preliminary X-ray data for some crystaline forms of β-lactoglobulin and hen egg-white lysozyme, *Acta Crystallogr.* **12**, 77–78 (1959).

40. P.G. Vekilov and A.A. Chernov, The physics of protein crystallization, in: Eds H. Ehrenreich and F. Spaepen, *Solid State Physics,* Vol. 57 (Academic Press, New York, 2002) pp. 1–147.

41. S.-T. Yau and P.G. Vekilov, Direct observation of nucleus structure and nucleation pathways, *J. Am. Chem. Soc.* **123**, 1080–1089(2001).

42. S.-T. Yau and P.G. Vekilov, Quasi-planar nucleus structure in apoferritin crystallisation, *Nature* **406**, 494—497 (2000).

43. Y.G. Kuznetsov, A.J. Malkin and A. McPherson, Atomic force microscpopy studies of phase separations in macromolecular systems, *Phys. Rev. B* **58**, 6097–6103 (1998).

44. Y. Georgalis, P. Umbach, J. Raptis and W. Saenger, Lysozyme aggregation studied by light scattreing. I. Influence of concentration and nature of electrolyte, *Acta Crystallogr. Section D* **53**, 691–702 (1997).

45. Y.G. Kuznetsov, A.J. Malkin and A. McPherson, AFM stuides of the nucleation and growth mechanisms of macromolecular crystals, *J. Crystal Growth* **196**, 489–502 (1999).

46. B. Mutaftschiev, Nucleation theory, in: *Handbook of Crystal Growth,* Vol. I, Ed. D.T.J. Hurle (Elsevier, Amsterdam, 1993) pp. 189–247.

47. D. Kashchiev, On the relation between nucleation work, nucleus size, and nucleation rate, *The Journal of Chemical Physics* **76**, 5098–5102 (1982).

48. D.W. Oxtoby and D. Kashchiev, A general relation between the nucleation work and the size of the nucleus in multicomponent nucleation, *The Journal of Chemical Physics* **100**, 7665–7671 (1994).

49. J.W. Gibbs, *The Collected Works of J.W. Gibbs,* Vol. 1 (Yale University Press, New Haven, 1961).

50. D.W. Oxtoby, Nucleation of first order phase transitions. *Accounts of Chemical Research* **31**, 91–97 (1998).

51. I.N. Stranski and R. Kaischew, Über den Mechanismus des Gleichgewichtes kleiner Kriställchen. I, *Z. Phys. Chem.* **B26**, 100–113 (1934).

52. I.N. Stranski and R. Kaischew, Über den Mechanismus des Gleichgewichtes kleiner Kriställchen. II, *Z. Phys. Chem.* **B26**, 114–116 (1934).

53. R. Kaischew and I.N. Stranski, Über die Thomson–Gibbs'sche Gleichung bei Kristallen, *Z. Phys. Chem.* **B35**, 427–432 (1937).

54. P.G. Vekilov, A.R. Feeling-Taylor, S.-T. Yau and D.N. Petsev, Solvent entropy contribution to the free energy of protein crystallization, *Acta Crystallogr. Section D* **58**, 1611–1616 (2002).

55. D.N. Petsev, B.R. Thomas, S.-T. Yau, D. Tsekova, C. Nanev, W.W. Wilson and P.G. Vekilov, Temperature-independent solubility and interactions between apoferritin monomers and dimers in solution, *J. Crystal Growth* **232**, 21–29 (2001).

56. A.J. Malkin and A. McPherson, Light scattering investiagtion of the nucletion processes and kinetics of crystallization in macromolecular systems, *Acta Crystallogr. Section D* **50**, 385–395 (1994).

57. A.J. Malkin, T.A. Land, Yu.G. Kuznetsov, A. McPherson and J.J. DeYoreo, Investigation of virus crystal growth mechanism by in situ atomic force microscopy, *Phys. Rev. Lett.* **75**, 2778–2781 (1995).

58. U. Gasser, E. Weeks, A. Schofield, P. Pusey and D. Weitz, Real-space imaging of nucleation and growth in colloidal crystallization, *Science* **292**, 258–262 (2001).

59. H. Shi, W.-B. Tsai, M.D. Garrison, S. Ferrari and B.D. Ratner, Template-imprinted nanostructured surfaces for protein recognition, *Nature* **398**, 593–597 (1999).

60. M. Böhringer, K. Morgenstern and W.-D. Schneider, Two-dimensional self assembly of supramolecular clusters and chains, *Phys. Rev. Lett.* **83**, 324–327 (1999).

61. R. Elghanian, J.J. Storhoff, R.C. Mucic, R.L. Letsinger and C.A. Mirkin, Selective colorimetric detection of polynucleotides based on the distance-dependent optical properties of gold nanoparticles, *Science* **277**, 1078–1081 (1997).

62. E. Braun, Y. Eichen, U. Sivan and G. Ben-Yoseph, DNA-templated assembly and electrode attachment of a conducting silver wire, *Nature* **391**, 775–778 (1998).

63. E. Winfree, F. Liu, L.A. Wenzler and N.C. Seeman, Design and self-assembly of two-dimensional DNA crystals, *Nature* **394**, 539–544 (1998).

64. A. Tardieu, S. Finet and F. Bonnete, Structure of macromolecular solutions that generate crystals, *J. Cryst. Growth* **232**, 1–9 (2001).

65. P.D. Hempstead, S.J. Yewdall, A.R. Fernie, D.M. Lawson, P.J. Artymiuk, D.W. Rice, G.C. Ford and P.M. Harrison, Comparison of the three dimentional structures of recombinant human H and horse L ferritins at high resolution, *J. Mol. Biol.* **268**, 424–448 (1997).

66. D.M. Lawson, P.J. Artymiuk, S.J. Yewdall, J.M.A. Smith, J.C. Livingstone, A. Trefry, A. Luzzago, S. Levi, P. Arosio, G. Cesareni, C.D. Thomas, W.V. Shaw and P.M. Harrison, Solving the structure of human H ferritin by genetically engineering intermolecular crystal contacts, *Nature* **349**, 541–544 (1991).

67. W.H. Massover, Ultrastructure of ferritin and apoferritin: a review, *Micron* **24**, 389–437 (1993).

68. V. Paunov, E. Kaler, S. Sandler and D. Petsev, A model for hydration interactions between apoferritin molecules in solution, *J. Colloid Interaface Sci.* **240**, 640–643 (2001).

69. M. Manciu and E. Ruckenstein, Long range interations betwen apoferritin molecules, *Langmuir* **18**, 8910–8918(2002).

70. J. Israelachvili and H. Wennerstrom, Role of hydration and water structure in biological and colloidal interactions, *Nature* **379**, 219–225 (1996).

71. J.N. Israelachvili, *Intermolecular and Surface Forces* (Academic Press, New York, 1995).

72. R.M. Pashley and J.N. Israelachvili, DLVO and hydration forces between mica surfaces in Mg^{2+}, Ca^{2+}, Sr^{2+} and Ba^{2+} chloride solutions, *J. Colloid Interface Sci.* **97**, 446–452 (1984).

73. D. Leckband and J. Israelachvili, Intermolecular forces in biology, *Quart. Rev. Biophys.* **34**, 105–267 (2001).

74. Y. Marcus, Ionic radii in aqueous solutions, *Chem. Rev.* **88**, 1475–1498 (1988).

75. P.M. Harrison and P. Arosio, The ferritins: molecular properties, iron storage function and cellular regulation, *Biochim. Biophys. Acta* **1275**, 161–203 (1996).

76. A.J. Hurd and D.W. Shaefer, Diffusion-limited aggregation in two dimensions, *Phys. Rev. Lett.* **54**, 1043–1046 (1985).

77. P.G. Bolhuis, D. Frenkel, S.-C. Mau and D.A. Huse, Entropy difference between crystal phases, *Nature* **388**, 235–236 (1997).

78. L.V. Woodcock, Reply: entropy difference between crystal phases, *Nature* **388**, 237–238 (1997).

79. C.-H. Hung, M.J. Krasnopoler and J.L. Katz, Condensation of a supersaturated vapor. VIII. The homogeneous nucleation of n-nonane, *Journal of Chemical Physics* **90**, 1856–1865 (1989).

80. L.S. Bartell and T.S. Dibble, Electron diffraction studies of the kinetics of phase changes in molecular clusters. Freezing of CCl_4 in supersonic flow, *The Journal of Physical Chemistry* **95**, 1159–1167 (1991).

81. S. Arnold, N.L. Goddard and N. Wotherspoon, Convertible electrodynamic levitator trap to quasielectrostatic levitator for microparticle nucleation studies, *Review of Scientific Instruments* **70**, 1473–1477 (1999).

82. A.F. Izmailov, A.S. Myerson and S. Arnold, A statistical understanding of nucleation, *Journal of Crystal Growth* **196**, 234–242 (1999).

83. C.N. Nanev and A. Penkova, Nucleation of lysozyme crystals under external electric field, *J. Cryst. Growth* **232**, 285–293 (2001).

84. Z. Kam, H.B. Shore and G. Feher, On the crystallization of proteins, *J. Mol. Biol.* **123**, 539–555 (1978).

85. P.G. Vekilov, L.A. Monaco, B.R. Thomas, V. Stojanoff and F. Rosenberger, Repartitioning of NaCl and protein impurities in lysozyme crystallization, *Acta Crystallogr. Section D* **52***, 785–798 (1996).

86. R.A. Judge, R.S. Jacobs, T. Frazer, E.H. Snell and M.L. Pusey, The effect of temperature and solution pH on the nucleationof tetragonal lysozyme crystals, *Biophysical J.* **77**, 1585–1593 (1999).

87. M.W. Burke, R.A. Judge and M.L. Pusey, The effect of solution thermal history on chicken egg white lysozyme nucleation, *J. Crystal Growth* **232**, 301–307 (2001).

88. G. Sazaki, E. Yoshida, H. Komatsu, T. Nakada, S. Miyashita and K. Watanabe, Effect of a magnetic field on the nucleation and growth of protein crystals, *J. Cryst. Growth* **173**, 231–234 (1997).

89. P.G. Vekilov and O. Galkin, On the methods of determination of homogeneous nucleation rates of protein crystals, *Colloids and Surfaces A* **215**, 125–130 (2003).

90. A.J. Malkin and A. McPherson, Light scattering investigations of protein and virus crystal growth: ferritin, apoferritin and satellite tobacco mosaic virus, *J. Crystal Growth* **128**, 1232–1235 (1993).

91. G. Tammann, *Die Aggregatzustaende* (Voss, Leipsig, 1922).

92. N.E. Chayen, Crystallization with oils: a new dimension in macromolecular crystal growth, *J. Crystal Growth* **196**, 434–441 (1999).

93. O. Galkin and P.G. Vekilov, Direct determination of the nucleation rate of protein crystals, *J. Phys. Chem.* **103**, 10965–10971 (1999).

94. O. Galkin and P.G. Vekilov, Are nucleation kinetics of protein crystals similar to those of liquid droplets?, *J. Amer. Chem. Soc.* **122**, 156–163 (2000).

95. M. Muschol and F. Rosenberger, Liquid–liquid phase separation in supersaturated lysozyme solutions and associated precipitate formation/crystallization, *J. Chem. Phys.* **107**, 1953–1962 (1997).

96. M. Muschol and F. Rosenberger, Interaction in undersaturated and supersaturated lysozyme solutions: static and dynamic light scattering results, *J. Chem. Phys.* **103**, 10424–10432 (1995).

97. E. Cacioppo and M.L. Pusey, The solubility of the tetragonal form of hen egg white lysozyme from pH 4.0 to 5.4, *Journal of Crystal Growth* **114**, 286–292 (1991).

98. M. Volmer, *Kinetik der Phasenbildung* (Steinkopff, Dresden, 1939).

99. D.W. Oxtoby, Homogeneous nucleation: theory and experiment, *Journal of Physics: Condensed Matter* **4**, 7627–7650 (1992).

100. D. Turnbull and J.C. Fisher, Rate of nucleation in condensed systems, *J. Chem. Phys.* **17**, 71–73 (1949).

101. A. Laaksonen, V. Telaquer and D.W. Oxtoby, Nucleation: measurements, theory and atmospheric applications, *Annu. Rev. Phys. Chem.* **46**, 489–524 (1995).

102. G.K. Schenter, S.M. Kathmann and B.C. Garrett, Dynamical nucleation theory: a new molecular approach to vapor liquid nucleation, *Phys. Rev. Lett.* **82**, 3483–3487 (1999).

103. R. McGraw and A. Laaksonen, Scaling properties of the critical nucleus in classical and molecular-based theories of vapor–liquid nucleation, *Phys. Rev. Lett.* **76**, 2754–2757 (1996).

104. A. Milchev, *Elecrocrystallization: Fundamentals of Nucleation and Growth* (Kluwer, Dordrecht, The Netherlands, 2002).

105. M. Matsumoto, S. Saito and I. Ohmine, Molecular dynamics simulation of the ice nucleation and growth process leading to water freezing, *Nature* **416**, 409–413 (2002).

106. R.M.L. Evans, W.C.K. Poon and M.E. Gates, Role of metastable states in phase ordering transitions, *Europhys. Lett.* **38**, 595–600 (1997).

107. V.J. Anderson and H.N.W. Lekkerkerker, Insights into phase transition kinetics from colloid science, *Nature* **416**, 811–815 (2002).

108. W.C.K. Poon, A.D. Pirie and P.N. Pusey, Gelation in colloid–polymer mixtures, *Faraday Discuss.* **101**, 65–76 (1995).

109. K.G. Soga, J.M. Melrose and R.C. Ball, Metastable states and the kinetics of colloid phase separation, *J. Chem. Phys.* **110**, 2280–2288 (1999).

110. P. Atkins, *Physical Chemistry* (Freeman, New York, 1998).

111. C. Haas and J. Drenth, The interface between a protein crystal and an aqueous solution and its effects on nucleation and crystal growth, *J. Phys. Chem.* **104**, 358–377 (2000).

112. N. Asherie, A. Lomakin and G.B. Benedek, Phase diagram of colloidal solutions, *Phys. Rev. Lett.* **77**, 4832–4835 (1996).

113. A. Lomakin, N. Asherie and G.B. Benedek, Monte Carlo study of phase separation in aqueous protein solutions, *J. Chem. Phys.* **104**, 1646–1656 (1996).

114. A. Lomakin, N. Asherie and G. Benedek, Aelotopic interactions of globular proteins, *Proc. Natl. Acad. Sci. USA* **96**, 9465–9468 (1999).

115. M.H. Steinberg, B.G. Forget, D.R. Higgs and R.L. Nagel (Eds), *Disorders of Hemoglobin: Genetics, Pathology, Clinical Management* (Cambridge University Press, Cambridge, 2000).

116. A. Cole-Strauss, K. Yoon, Y. Xiang, B.C. Byrne, M.C. Rice, J. Crynn, W.K. Holloman and E.B. Kmiec, Correction of the mutation responsible for sickle cell anemia by an RNA-DNA nucleotide, *Science* **273**, 1386–1389 (1996).

117. E.V. Hahn and E.B. Gillespie, Sickle cell anemia: report of a case greatly improved by splenectomy. Experimental study of sickle cell formation, *Arch. Int. Med.* **39**, 233–254 (1927).

118. H.R. Sunshine, J. Hofrichter, F.A. Ferrone and W.A. Eaton, Oxygen binding by sickle cell hemoglobin polymers, *J. Mol. Biol.* **158** (1982).

119. W.A. Eaton and J. Hofrichter, Sickle cell hemoglobin polimerization, in: Eds C.B. Anfinsen, J.T. Edsal, F.M. Richards and D.S. Eisenberg, *Advances in Protein Chemistry,* Vol. 40 (Academic Press, San Diego, 1990) pp. 63–279.

120. O. Galkin, K. Chen, R.L. Nagel, R.E. Hirsch and P.G. Vekilov, Liquid–liquid separation in solutions of normal and sickle cell hemoglobin, *Proc. Natl. Acad. Sci. USA* **99**, 8479–8483 (2002).

121. A.P. Minton, Non-ideality and the thermodynamics of sickle cell hemoglobin gelation, *J. Mol. Biol.* **110**, 89–103 (1977).

122. P.G. Vekilov, A.R. Feeling-Taylor, D.N. Petsev, O. Galkin, R.L. Nagel and R.E. Hirsch, Intermolecular interactions, nucleation and thermodynamics of crystallization of hemoglobin C, *Biophys. J.* **83**, 1147–1156 (2002).

123. R.W. Briehl, Rheology of hemoglobin S gels: possible correlation with impaired microvascular circulation, *Am. J. Ped. Hem. Onc.* **5***, 390–398 (1983).

124. R.W. Briehl and P. Nikopoulou, Kinetics of hemoglobin polymerization and gelation under shear: shape of the viscosity progress curve and dependence of the delay time and reaction rate on shear rate and tempature, *Blood* **81**, 2420–2428 (1993).

125. Y.G. Kuznetsov, A.J. Malkin and A. McPherson, The liquid protein phase in crystallization: a case study intact immunoglobins, *J. Crystal Growth* **232**, 30–39 (2001).

126. P.C. Weber, Overview of protein crystallization methods, in: Eds C.W. Carter, Jr. and R.M. Sweet, *Methods in Enzymology,* Vol. 276 (Academic Press, New York, 1997) pp. 13–22.

127. A. McPherson, *Crystallization of Biological Macromolecules* (Cold Spring Harbor Laboratory Press, Cold Spring Harbor, New York, 1999).

128. E.A. Stura and I.A. Wilson, Seeding techniques, in: Eds A. Ducruix and R. Giege, *Crystallization of Nucleic Acids and Proteins: A Practical Approach* (Oxford University Press, Oxford, 1992) pp. 99–126.

129. E.A. Stura, A.C. Satterwait, J.C. Calvo, D.C. Carslow and I.A. Wilson, Reverse screening, *Acta Crystallogr. Section D* **50**, 448–455 (1994).

130. E.A. Stura, J.-B. Charbonnier and M.J. Taussig, Epitaxial jumps, *J. Crystal Growth* **196**, 250–260 (1999).

131. J. Brange, *Galenics of Insulin* (Springer, Berlin, 1987).

132. H. Mahadevan and C.K. Hall, Theory of precipitation of protein mixtures by non-ionic polymer, *AIChE J.* **38**, 573–591 (1992).

133. M.L. Broide, C.R. Berland, J. Pande, O.O. Ogun and G.B. Benedek, Binary liquid phase separation of lens proteins solutions, *Proc. Natl. Acad. Sci. USA* **88**, 5660–5664 (1991).

134. A. Lomakin, D.S. Chung, G.B. Benedek, D.A. Kirschner and D.B. Teplow, On the nucleation and growth of amyloid b-protein fibrils: detection of nuclei and qualification of rate constants, *Proc. Natl. Acad. Sci. USA* **93**, 1125–1129 (1996).

135. Y. Kusimoto, A. Lomakin, D.P. Teplow and G.B. Benedek, Temperature dependence of amyloid β-protein fibrilation, *Proc. Natl. Acad. Sci. USA* **95**, 12277–12282 (1998).

136. Y.V. Zastavker, N. Asherie, A. Lomakin, J. Pande, J.M. Donovan, J.M. Schnur and G.B. Benedek, Self-assembly of helical ribbons, *Proc. Natl. Acad. Sci. USA* **96**, 7883–7887 (1999).

137. J. Aizenberg, A.J. Black and G.M. Whitesides, Control of crystal nucleation by patterned self-assembled monolayers, *Nature* 495–498 (1999).

138. I. Weissbuch, M. Lahav and L. Leiserowitz, Toward stereochemical control, monitoring and understanding of crystal nucleation, *Crystal Growth and Design* **3**, 125–150 (2003).

139. A.P. Gast, C.K. Hall and W.R. Russel, Phase separations induced in aqueous colloidal suspensions by dissolved polymer, *Faraday Discuss. Chem. Soc.* **76**, 189–201 (1983).

140. S.M. Illett, A. Orrock, W.C.K. Poon and P.N. Pusey, Phase behavior of a model colloid–polymer mixture, *Phys. Rev. E* **51**, 1344–1352 (1995).

141. M. Farnum and C. Zukoski, Effect of glycerol on the interactions and solubility of bovine pancreatic trypsin inhibitor, *Biophys. J.* **76**, 2716–2726 (1999).

142. K. Gekko and S.N. Timasheff, Mechanism of protein stabilization by glycerol: proferential hydration in glycerol–water mixtures, *Biochemistry* **20**, 4667–4676 (1981).

143. R. Sousa, Use of glycerol, polyols and other protein structure stabilizing agents in protein crystallization, *Acta Crystallogr. Section D* **51**, 271–277 (1995).

144. R.V. Rariy and A.M. Klibanov, Correct protein folding in glycerol, *Proc. Natl. Acad. Sci. USA* **94**, 13520–13523 (1997).

145. H. Borchers (Ed.), *Landoldt–Bornstein Numerical Data and Functional Relationships.* Vol. IV, part II, *Materials Values and Mechanical Behaviour of Nonmetals* (Springer, Berlin, 1955).

146. S. Asakura and F. Oosawa, Interaction between particles suspended in solutions of macromolecules, *J. Polymer Sci.* **33**, 183–192 (1958).

147. R. Verma, J.C. Crocker, T.C. Lubensky and A.G. Yodh, Entropic colloidal interactions in concentrated DNA solutions, *Phys. Rev. Lett.* **81**, 4004–4007 (1998).

148. O. Galkin and P.G. Vekilov, Control of protein crystal nucleation around the metastable liquid–liquid phase boundary, *Proc. Natl. Acad. Sci. USA* **97**, 6277–6281 (2000).

149. R.P. Sear, Phase behaviour of a simple model of globular proteins, *J. Chem. Phys.* **111**, 4800–4806 (1999).

150. A.P. Chatterjee and K.S. Schweizer, Microscopic theory of polymer-mediated intercations between spherical particles, *J. Chem. Phys.* **109**, 10464–10476 (1998).

151. A.M. Kulkarni, A.P. Chatterjee, K.S. Schweitzer and C.F. Zukoski, Depletion interactions in the protein limit: effects of polymer density fluctuations, *Phys. Rev. Lett.* **83**, 4554–4557 (1999).

152. S.R. Sheth and D. Leckband, Measurements of attractive forces between proteins and end-grafted poly(ethylene glycol) chains, *Proc. Natl. Acad. Sci. USA* **94**, 8399–8404 (1997).

153. D.N. Petsev, X. Wu, O. Galkin and P.G. Vekilov, Thermodynamic functions of concentrated protein solutions from phase equilibria, *J. Phys. Chem. B* **107**, 3921–3926 (2003).

154. A.R. Feeling-Taylor, R.M. Banish, R.E. Hirsch and P.G. Vekilov, Miniaturized scinitillation technique for protein solubility determinations, *Rev. Sci. Instr.* **70**, 2845–2849 (1999).

5

Microscopic, mesoscopic, and macroscopic lengthscales in the kinetics of phase transformations with proteins

Peter G. Vekilov*

Department of Chemical Engineering, University of Houston, Houston, TX 77204-4004, USA

The structure of landscape is infinitesimal,
Like the structure of music, seamless, invisible,
Even the rain has larger sutures.

Charles Wright, 2002

5.1. INTRODUCTION

   Phase transformations occur through a combination of processes at molecular, meso-scopic, and macroscopic length scales. Molecular-level phenomena include the interactions between the molecules that alter the free energy landscape to cause the formation of the new phase and determine the driving force for the phase transformation; attachment of molecules to the new phase during growth; formation of sites suitable for molecular attachment; generation of defects; etc. On the mesoscopic lengthscale, one could consider the nucleation of droplets, clusters or crystallites of the new phase; generation of new layers of a crystal controlled by capillarity; interactions between growth steps as they propagate along crystals' surfaces; etc. Macroscopic lengthscales govern the fluxes of energy and mass through the interface, i.e., the transport of building blocks to the growing phase and the dissipation of heat from it, as well as the balance and distribution of stress and strain in a solid and the transition form elastic to plastic deformations.

   A common point of view is that the causality flow is from the bottom up, from finer to coarser lengthscales, whereby molecular-level processes determine those on the meso-scopic lengthscales; the combination of microscopic and mesoscopic processes determine

---

*E-mail address: vekilov @ uh.edu

the macroscopic pathways of the phase transformation. Some of the examples discussed in this chapter illustrate this viewpoint, however other sets of data show a more complex picture in which mesoscopic and macroscopic-level phenomena and processes directly affect the behavior of individual molecules.

It is important to emphasize that there are two microscopic lengthscales in a protein solution—the one determined by the size of the water and other small molecules and ions, and the one determine by the significantly larger protein molecules [1]. These size differences are particularly important if the interactions between protein molecules in solution and the resulting effects of the phase diagrams are discussed [2–4]. In this chapter, I focus on the processes of growth of an exiting phase, and I limit myself to the microcosmic lengthscale of the protein molecules. The significantly smaller size of the water molecules will only come up in Section 5.7, where I address the role of water structuring on the repulsive potential between the protein molecules.

Below, I discuss the coupling and the interplay between microscopic, mesoscopic, and macroscopic processes during the growth of crystals, such as the one shown in Figure 5.1, of the pair of proteins ferritin and apoferritin. I start by defining the methods used to characterize the growth kinetics on the three lengthscales. Then, I discuss the tests of the correspondence between discrete approaches to the kinetics of attachment, in which the growth rate and other spatial and temporal characteristics of the growth process are represented as statistical averages of events involving individual atoms or molecules, to the continuous approaches, in which fluxes of matter towards the growth interface are evaluated. Next, I show that the kinetics of incorporation of the molecules into growth sites on the surface of a crystal are not determined by a decay of a high-energy transition state, but are only limited by the diffusion of the incoming molecule over a barrier due to the hydration shells around incoming molecules. This is an example in which a molecular process is determined by a typical macroscopic phenomenon—diffusion. Next, I discuss the interactions between the moving steps, a mesoscopic lengthscale phenomenon, and its correlation with the microscopic structure of the step edge, and the formation of step patterns, occurring on the
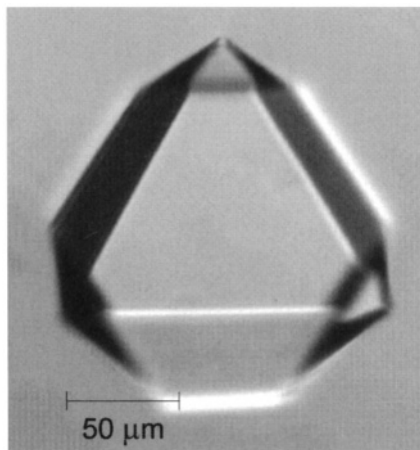

FIGURE 5.1. A typical octahedral crystal of apoferritin, resting on the cell bottom with a (111) face facing upward. Ferritin crystals appear identical except for the ruby red color.

macroscopic lengthscales. Last, I illustrate how the accumulation of molecular-level defects causes lattice strain, resolved in mosaicity, i.e., the formation of macroscopic blocks in the crystal.

5.2. METHODS

To capture the dynamics of processes occurring on microscopic, mesoscopic and macroscopic lengthscales and for crosschecks of the veracity of the kinetics data, we employed a combination of scanning probe and interferometry techniques, illustrated in Figure 5.2. Modifications of the scanning probe techniques, discussed below, allow monitoring of processes occurring at 1/3–1/2 seconds with resolution ~1 nm. The phase-shifting interferometry that we used probes processes with characteristic times of 0.1 second, occurring over lengthscales from 0.5 mm to several millimeters.

5.2.1. Atomic force microscopy

We used Nanoscope IIIa or Nanoscope IV Multimode atomic force microscopes (AFM) from Digital Instruments, equipped with a 120 μm ("J") scanner and a Tapping Mode fluid cell. The preparation of crystals and solutions, the cell loading, are discussed in detail in ref. [5].

Temperature in the laboratory was stabilized to ~22 ± 0.5°C. To control the temperature in the crystallization solution, we mounted the sample on to a Peltier-cooled disk firmly attached to the scanner. This allowed imaging in the range 28 to 45°C; to access 25 and 20°C, the room temperature was set to 18–20°C. Temperature in the fluid cell was monitored with a thermocouple imbedded into the metal disk under the solution droplet and was found to be steady within 0.1 °C.

All images were collected *in-situ* during the growth of the crystals using the less intrusive tapping-imaging mode [6,7]. This allows visualization of adsorbed protein and impurity species (tip impact in contact imaging mode often prevents such imaging).

We used the standard SiN tips and tapping drive frequency was adjusted in the range 25–31 kHz to the resonance value for specific tip used. Other scanning parameters were
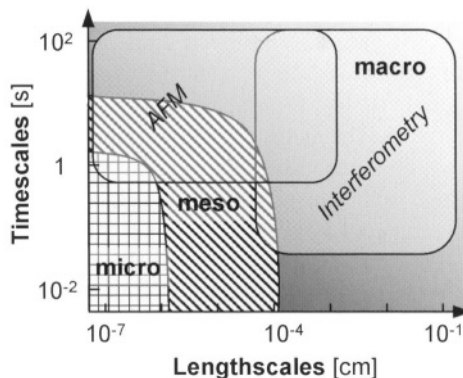

FIGURE 5.2. Schematic illustration of the lengthscales over which the processes discussed here occur and the techniques employed to probe these processes.

adjusted such that continuous imaging affected neither the surface structure, nor the process dynamics. For verification, we varied the scan sizes and the time elapsed between image collections, and saw that neither the spatial nor the temporal characteristics of the processes changed.

5.2.2. AFM data collection

We employed four types of AFM data collection. The first type consists of images of sizes 200 nm to 1 μm, such as the one in Figure 5.3, on which the protein molecules, 13 nm in size were clearly detectable. Calibration of the microscope was verified by determining the spacing of molecules along a dense packed direction in the lattice and the thickness of the top crystalline layer. As Figure 5.3 reveals, the respective numbers for one of the systems, used for the studies summarized here, the protein apoferritin, are 13.1 and 10.5 Å These are in good agreement with the evaluations from the X-ray structure of the crystal. Using the crystal lattice parameter of $a = 18.4$ nm for the crystallographic group $F432$ [8,9], the intermolecular spacing is $(1/2) \cdot (2a^2)^{1/2} = 13.0$ nm, and the layer thickness is $(1/3) \cdot (3a^2)^{1/2} = 10.6$ nm.

To evaluate the maximum resolution of molecular-scale imaging attainable *in-situ,* during crystallization with the proteins ferritin and apoferritin, we scanned a 200×200 nm square on the surface of a ferritin crystal, Figure 5.4a. The two-dimensional Fourier transform of the image in Figure 5.4b has the expected hexagonal symmetry, with the distance between the peaks in the first hexagon and the center of the plot corresponding to resolution equal to the molecular size of 13 nm. The maximum resolution, determined from the location of the most distant peak is 1.6 nm. This resolution allows us to distinguish some of the sub-molecular level details of the molecules on the crystal surface in Figure 5.4c. Comparison with the structure of the molecules coming from an X-ray determination in Figure 5.4d [9] shows that the triangular formation on Figure 5.4c likely corresponds to bundles of α-helices.

The second type of AFM data consisted of images on the mesoscopic lengthscales— from several tens of nanometers to a several micrometers—as in many previous AFM studies of crystallization from solution [10–21]. These images, similar to the one in Figure 5.5, with viewfield width between 2 and 40 μm, allow characterization of growth steps and step patterns.

For the third type of AFM data we employed scans with disabled y-axis [22,23], as in previous STM work on metals and semiconductors in ultra-high vacuum [24–27]. The AFM tip is drawn over a single line on the crystal surface. In the collected pseudo-images, the vertical axis represents time. The technique allows monitoring of processes with characteristic times of fractions of a second. If the scan widths were 600 nm and less, the displacement of a single site on the step could be monitored with molecular resolution, i.e., we could trace the attachment and detachment of single molecules to and from steps [5,22,28]. Data collection lasted typically for 2–3 min. Immediately after such scans, area scans that include the line along which the tip was drawn. In about 80% of the cases, these tests reveled that the tip impacted over the same location has delayed the growth. These data were discarded, and only data sets that did not show tip impact are discussed below.

The fourth type of AFM data was also based on disabled y-axis scans, albeit with scan widths of 10–20 μm. This allowed monitoring the location along the line of scanning of
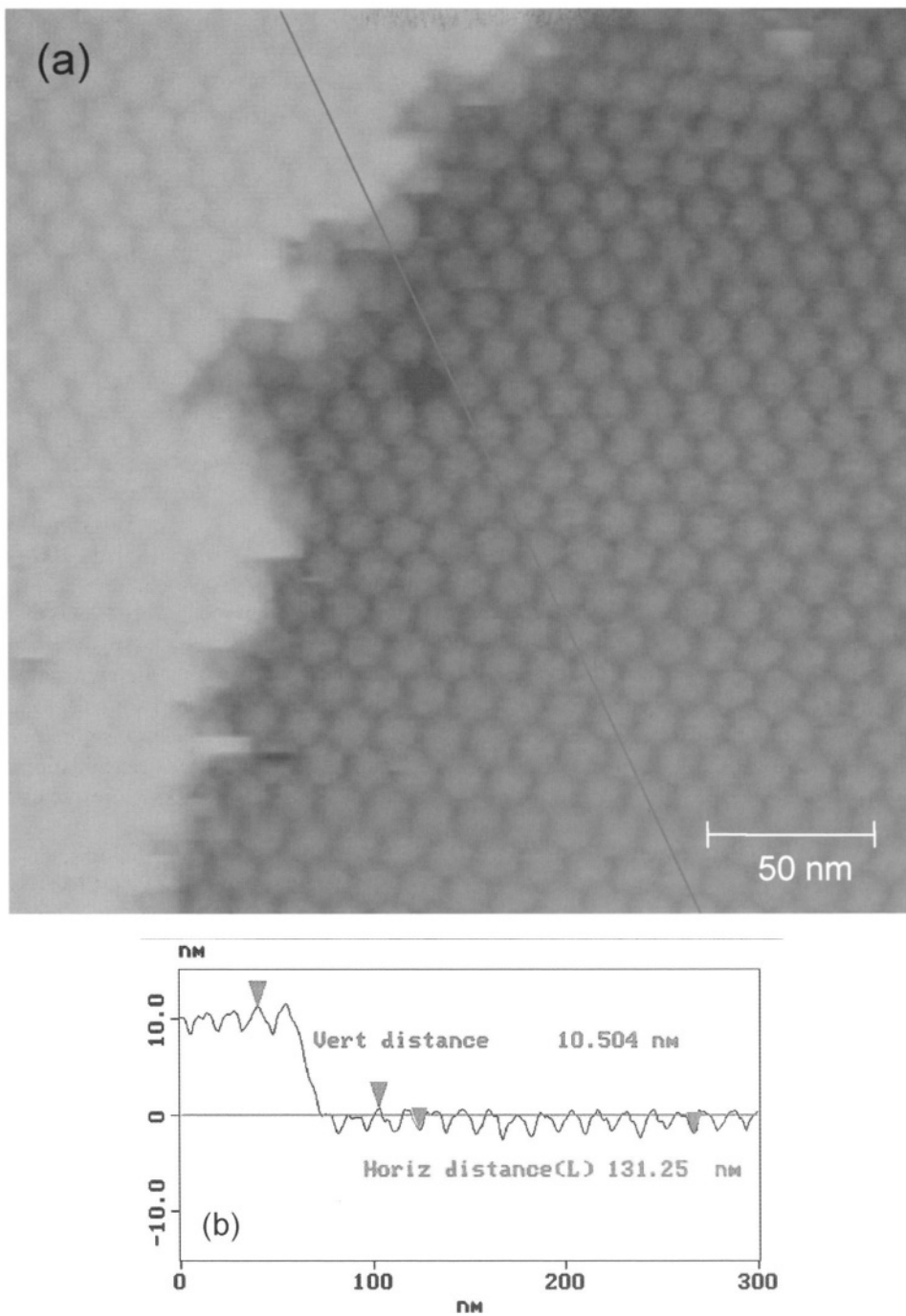
FIGURE 5.3. Accuracy of atomic force microscopy imaging. (a) View of a (111) apoferritin crystal face. (b) Height profile along line in (a) allowing determination of layer thickness and molecular spacing. From ref. [5].
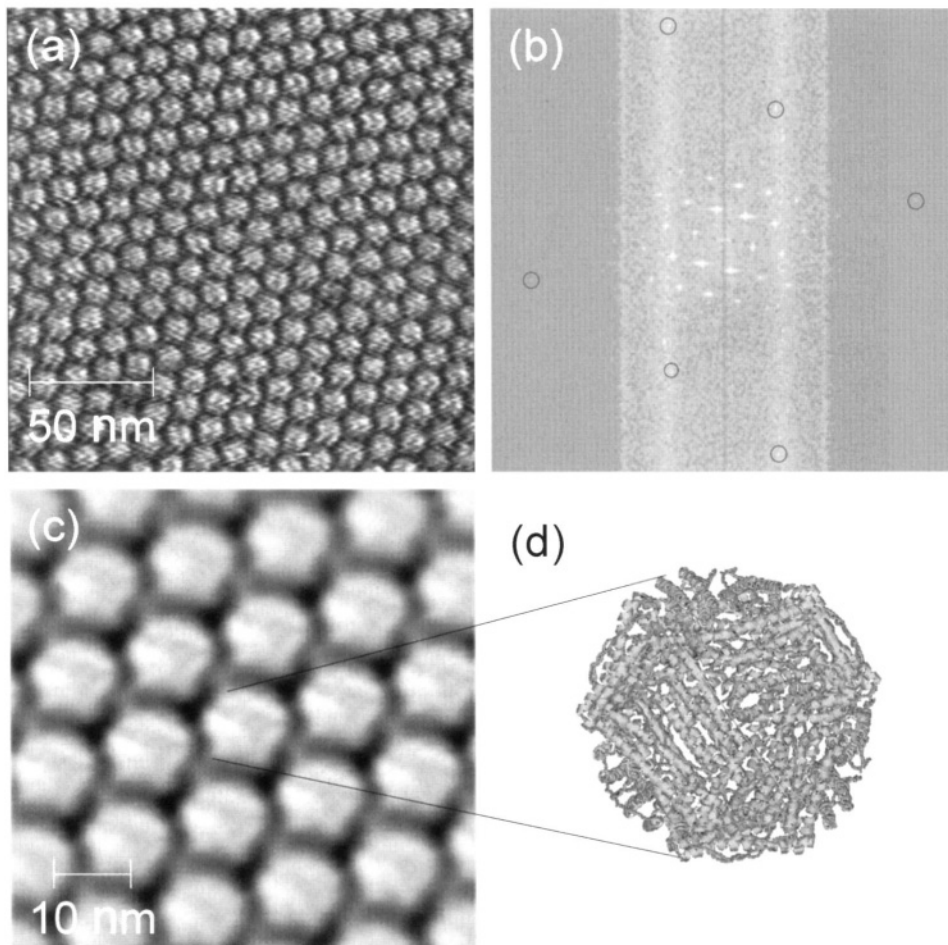
FIGURE 5.4. Resolution of atomic force microscopy imaging. (a) Real space high-resolution image of a (1 1 1) apoferritin crystal face [5]. (b) (d) Fourier transform of (a), circles highlight high-resolution peaks; 8-th order peaks at top and bottom of image correspond to resolution of ~1.6 nm [5]. (c) Real-space image in which each molecule is replaced by the average of all molecules in frame; processed with the SEMPER Software package (N. Braun, S. Weinkauf). (d) Ribbon presentation of the X-ray structure of an apoferritin molecule viewed along the (1 1 1) direction. Images of molecules in (c) appear to have similar triangular features.

~10–20 steps for about 1–1.5 hours [23]. Area scans that include the line along which the tip was drawn, performed immediately after such data collection, revealed tip impact in about 20% of the data sets, which were duly discarded.

5.2.3. Differential phase-shifting interferometry

To access faster processes, as well as those occurring over lengthscales of up to several millimeters, we applied differential phase shifting interferometry [29]. While inferior in spatial resolution to atomic force microscopy, this technique is non-intrusive and allows
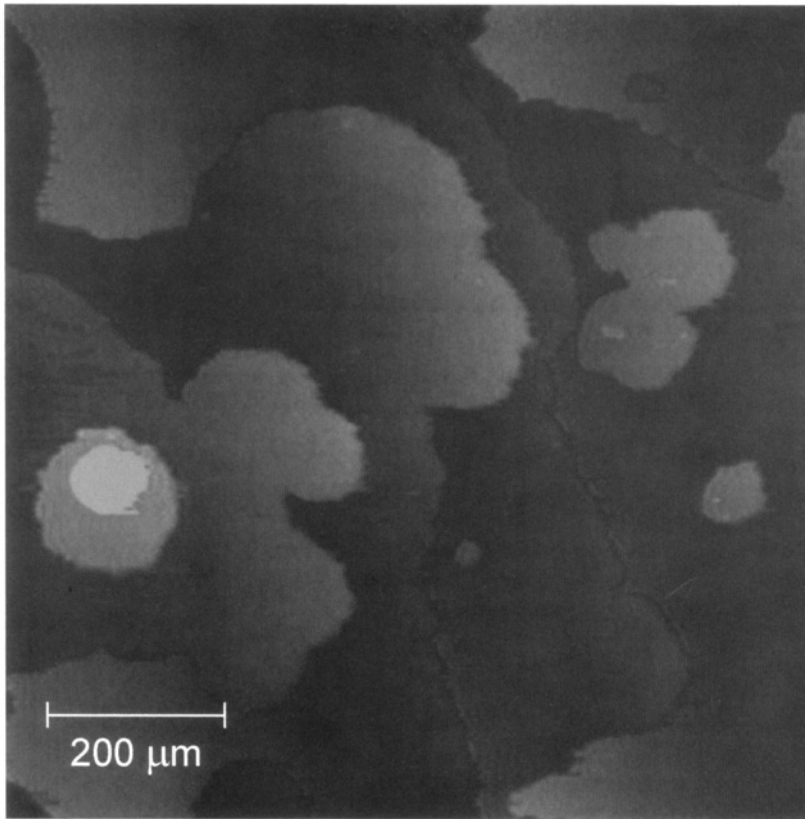
FIGURE 5.5. Atomic force microscopy images of the surface of growing apoferritin crystals taken near the center of the respective facet. Facet size is ~90 μm, ensuring near uniform supersaturation over the facet. New crystal layers are generated at random locations by surface nucleation and spread to merge with other islands and cover whole facet.

imaging and monitoring of entire crystal faces as large as 1 mm. The development of a fast phase-shifting procedure significantly increased the depth resolution and shortened the accessible time scales [30]. A schematic diagram of the phase-shifting interferometer is presented in Figure 5.6, for details see [29]. The linearly polarized light from a He–Ne laser is filtered, broadened, and an area of practically uniform intensity in the center of the broadened beam is obtained. This beam is divided into two arms by a beam splitter. As in the first interferometry applications to crystal growth, the surface of growing crystal reflects one of the arms, while a high flatness mirror is used in the reference arm [31]. To introduce phase shift, we placed a liquid crystal variable retarder in the reference arm. This "phase-shifter" operates by discretely changing the applied voltage to an element containing nematic liquid crystals to vary their refractive index [32]. As a result, the optical pathway of the reference beam is varied, and this shifts the phase of the interferograms. The interference pattern is magnified by an optical microscope and acquired to a high resolution, high capture frequency CCD video camera [29,33].
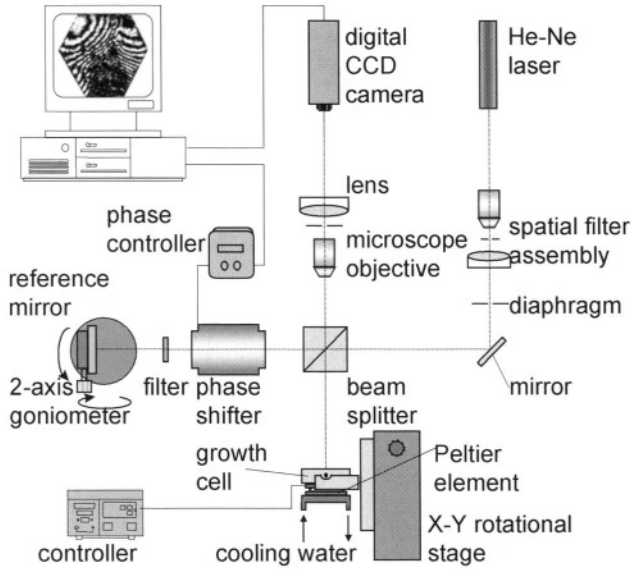
FIGURE 5.6. Schematic of the experimental setup for phase-shifting interferometry. From ref. [29].

We employ a five-step phase-shifting algorithm. As shown in [32], this number is a compromise between the length of the data collection times, determined by the number of images, and noise reduction, better with higher number of images. A sequence of five interferograms is recorded and digitized, Figure 5.7a–e. In the sequence, the interferograms differ by a $\pi/2$ optical phase shift, introduced into the reference beam between each of sequentially recorded interferograms. In each of the five interferograms, the interference intensity at a point (x, y) is described by

$$I_i(x, y) = I_r + I_c + 2\sqrt{I_r I_c} \cos\left[\phi(x, y) + \delta_i\right], \tag{1}$$

where I_r and I_c are the intensities of the reference and crystal beams, respectively. We split the phase difference into two components: $\phi(x, y)$ is the phase difference attributed to the deviations of the crystal surface from ideally flat and parallel to reference mirror, while δ_i is the phase difference introduced by the phase-shifter. The phase shift δ_i takes on five discrete values:

$$\delta_i = 0,\ \pi/2,\ \pi,\ 3\pi/2,\ 2\pi; \quad i = 1, 2, 3, 4, 5. \tag{2}$$

The set of eq. (1) with varying δ_i's can be solved for the phase difference $\phi(x, y)$:

$$\phi(x, y) = \tan^{-1}\left[\frac{2(I_2 - I_4)}{2I_3 - I_5 - I_1}\right], \tag{3}$$
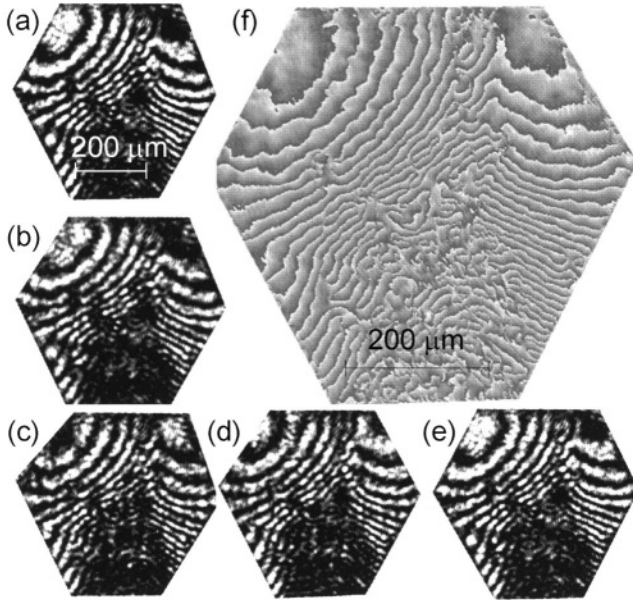
with each $I_i = I_i(x, y)$.

FIGURE 5.7. (a–e) A sequence of five interferometric images from the surface of ferritin crystal recorded with a phase shift of $\pi/2$. (f) The phase-wrapped image. The gray scale values discontinuities correspond to phase difference of π. Supersaturation $\Delta\mu/k_BT = 3.0$. Because of the higher local supersaturation at the facet corners [130], the growth layers are generated by 2D nucleation near the facet corners. From ref. [36].

The calculated phase is related to the crystal surface height $h(x, y)$:

$$\phi(x, y) = \frac{4\pi n h(x, y)}{\lambda}, \tag{4}$$

where n is the refractive index of protein solution and λ is the laser wavelength. Using this expression we reconstruct the microscopic morphology relief of the growing crystal surface.

With the chosen magnification of the optical system, each pixel in an image corresponds to 1×1 μm^2 area of the crystal surface. The time taken to capture five-image sequence is about 1 s. Because the tangential growth rates of ferritin do not exceed the value of 40 nm/s in our experiments, fringes do not move from one pixel to another during this time.

The "phase-wrapped" image calculated using eq. (3) is shown in Figure 5.7f. The gray scale is proportional to the surface height. The discontinuities in gray scale and surface height result from the calculation algorithm based on the $\tan^{-1}$ function and correspond to a height difference of $\lambda_{laser}/4n$, where $\lambda_{laser} = 0.6328$ μm is the wavelength of the He–Ne laser and $n = 1.3320$ is the refractive index of the solution, largely determined by its acetate and $CdSO_4$ components [34] and measured as in ref. [35].

For further processing we chose a rectangular region of the crystal surface, Figure 5.8. The reconstruction of the surface relief is illustrated in Figure 5.8b. The height profile along the line depicted in Figure 5.8a is shown in Figure 5.8e, with the profile of the wrapped
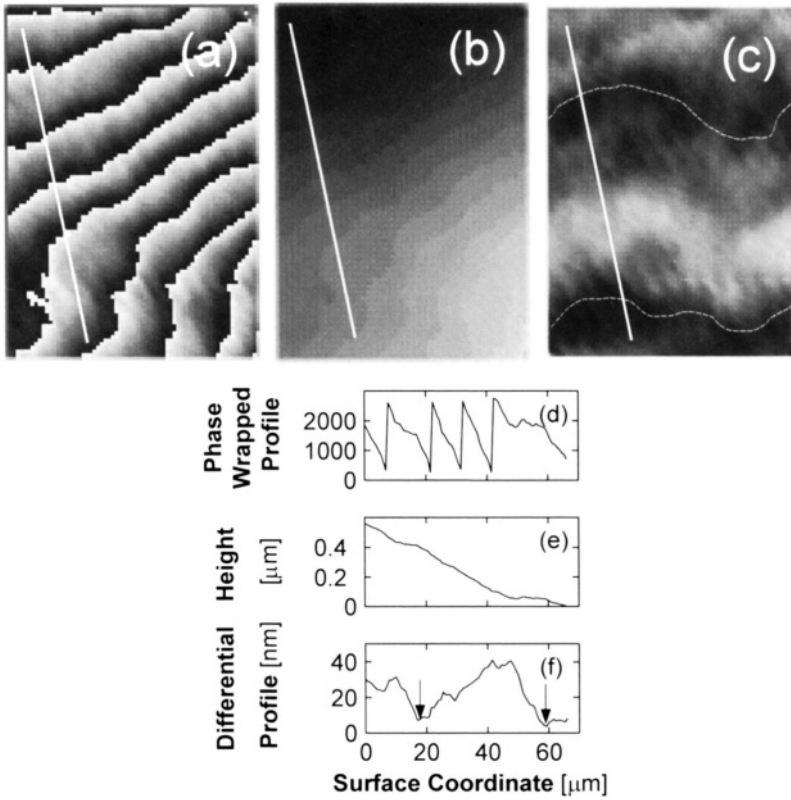
FIGURE 5.8. Illustration of surface relief reconstruction. (a) The phase-wrapped image; (b) reconstructed surface relief image; (c) image produced from (b) by subtracting the average slope; (d–f) the phase-wrapped, height and differential profiles along the line depicted in (a–c), respectively. From ref. [29].

phases in Figure 5.8d. Subtracting the average surface slope, calculated by linking the first and the final point of the profiles similar to the one in Figure 5.8e with a straight line, reveals the local variations of the surface height in Figure 5.8c and f. The latter figure illustrates the depth resolution of the surface image of 5 nm, which is determined by the roughness of the reference mirror. The step bunches, seen in Figure 5.8f at 30 and at $50\ \mu$m are highlighted in Figure 5.8c by dashed lines [36].

A second interferometry data collection routine is based on the intensity of the interference image at up to 10 locations recorded over periods of several hours with time resolution of 1 s. The traces are processed to obtain the values of normal growth rate, local slope and step velocity, as described earlier and illustrated in Figure 5.9 [37].

5.2.4. Methods to determine step velocities

During growth of crystals by the generation and spreading of layers, the rate of growth of the newly-formed layers, often called step velocity, is the main kinetic variable, and its link to the driving force determines the step kinetic coefficient. In the studies discussed here, we employed three methods of step velocity determination.
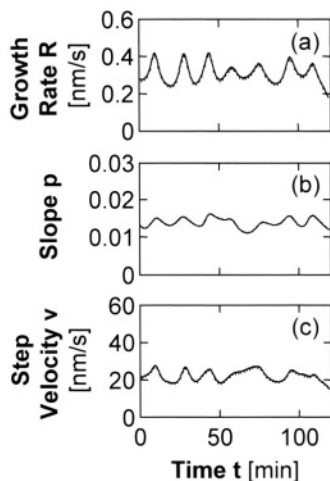
FIGURE 5.9. Time traces of (a) growth rate R, (b) local slope p and (c) step velocity v recorded on a ferritin crystal surface at $\Delta\mu/k_\mathrm{B}T = 3.0$. From ref. [36].

As a first method, we used sequences of molecular resolution *in-situ* AFM images of the advancing steps as in Figure 5.3. The step velocities were determined as the ratio $Na/\Delta t$, where N is the number of molecular sizes a that the step advances for the time between two sequential images Δt. For each concentration of ferritin or apoferritin, ~20 determinations of v were done and averaged [38]. This method is applicable to step velocities $<5\ \mathrm{nm\,s^{-1}}$, at which a step would advance by several molecular sizes for the time required for image collection, ~1 min [5,22].

For step velocity data at higher driving forces, we disabled the slow scanning axis of the AFM [22]. This allowed us to monitor for times of 60 to 90 min with a frequency $2–4\ \mathrm{s^{-1}}$ the propagation of 15–30 steps within $10\ \mu\mathrm{m}$ segments of a growing crystal surface [23].

As a third method, applicable to step velocities as fast as $100\ \mathrm{nm\,s^{-1}}$, we extracted averaged values of the step velocities from time traces of this variable recorded using diferentrial phase-shifting interferometry, such as those in Figure 5.9. We averaged ~1000 measurements [29,39], the data scatter intervals were evaluated as 90% confidence interval for this average [38].

5.3. THE FERRITIN/APOFERRITIN SYSTEM

5.3.1. The proteins

Ferritin is the main non-heme iron storage protein in the cytosol [40–42]. The protein shell consists of 24 subunits, arranged in pairs along the 12 facets of a rhombododecahedron [8,9]. Ferritins have been extensively studied as an example of biological mineralization occurring *in-vivo* [43,44]. The iron-containing core of ferritin can be replaced with other organic, inorganic and bioorganic compounds for various applications in the areas of nanoassembly, drug delivery, biomineralization, etc. [45,46]. Apoferritin is the protein shell from which the ferrite core has been removed by dissolution into an acidic solution. The

structures of the proteins from various species are known down to 1.90 Å resolution [9]. An ongoing effort is aimed at better and larger ferritin and apoferritin crystals that would allow higher resolution X-ray or neutron structure determinations to better understand the hydrophobic and hydrophilic channels through the shell, the possible binding or catalytic sites on the inside and on the outside of the shell [144,47–50].

In the presence of Cd^{2+}, ferritin and apoferritin crystallize in the cubic $F432$ group [9, 42]. Contrary to typical protein crystallization cases, where the electrolyte serves to screen the repulsion between the similarly charged protein molecules, in the apoferritin case Cd^{2+} is involved in specific bonds between the molecules [9]. This specificity makes the case of apoferritin crystallization a relevant first-approximation model of other self-assembling systems: viri, protein complexes, etc.

The crystals, such as the one in Figure 5.1, are typically facetted by octahedral $\{111\}$ faces pierced by the three-fold axis belonging to the $F432$ symmetry group. The highly symmetric shape of the ferritin and apoferritin molecules makes the approximation of isotropic molecular shape realistic. In addition, the symmetry of the environment of a molecule in a crystal makes quantitative insight easier to obtain and comprehend. Because of these two factors, ferritin and apoferritin crystallization is a particularly appealing system for in-depth investigations of the thermodynamics and kinetics of phase transitions.

5.3.2. Molecular mass and intermolecular interactions

The molecular mass of apoferritin has been determined by many techniques to be $M_w = 450,000 \text{ g mol}^{-1}$ [41,42], with the mass of a molecule $m = 7.47 \times 10^{-19}$ g. However, the average M_w of ferritin varies between 550,000 and 950,000 g mol^{-1}, depending on the size of the ferrite core [41,42]. To determine the M_w of ferritin in the samples used here, we performed static light scattering [35] in 0.05 M $NaOOCCH_3$ solutions. The molecular masses M_w and the second osmotic virial coefficients A_2 in dimensional form were determined from the Debye plots, $KC/R_\theta = 1/M_w + 2A_2C$ in Figure 5.10, where R_θ is the Raleigh ratio of the scattered to the incident light intensity, K is a system constant, $K = \frac{1}{N_A}(\frac{2\pi n_0}{\lambda^2})^2(\frac{dn}{dC})^2$, $n_0 = 1.3320$ is the refractive index of the solvent at the wavelength of the laser beam $\lambda = 0.6328\ \mu$m [34,51], dn/dC is the n-increment with the protein concentration C, determined for each protein at $\lambda = 0.628\ \mu$m by a differential refractometer; for ferritin $dn/dC = 0.290\ \text{cm}^3\ \text{g}^{-1}$, for apoferritin, $dn/dC = 0.159\ \text{cm}^3\ \text{g}^{-1}$.

The Debye plots in Figure 5.10 show that for ferritin, $M_w = 780,000\ \text{g mol}^{-1}$, $m = 1.30 \times 10^{-18}$ g, while, as expected, for apoferritin, $M_w = 450,000\ \text{g mol}^{-1}$.

Figure 5.10 also shows that values of the second osmotic virial coefficients A_2 for the two proteins are similar. This is not surprising—the A_2's characterize the pair interactions between the solute molecules, determined by the identical surfaces of the molecules.

Figure 5.11 displays the size distributions of the scatterers in solutions of the two proteins resulting from a dynamic light scattering determination as discussed in detail in ref. [35]. We see that the size distributions are narrow, and the two proteins have identical diameters of 13 nm. This is equal to their identical crystallographic diameters [8,41,42]. Since these sizes are calculated from the set of experimentally-determined diffusivities using the Einstein–Stokes law of diffusion, the equality to the crystallographic data indicates that the diffusion of both molecules obeys this law [52].
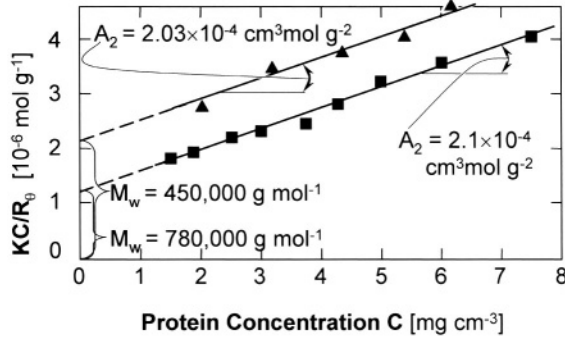
FIGURE 5.10. Static light scattering characterization of ferritin and apoferritin molecules in 0.05 M $NaOOCCH_3$ solutions. Debye plots, $KC/R_\theta = 1/M_w + 2A_2C$, ($R_\theta$ is the Raleigh ratio of the scattered to the incident light intensity, K is a system constant, C is protein concentration in $mg\,ml^{-1}$). The molecular masses M_w and the second osmotic virial coefficients in the dimensional form A_2 of the two proteins are shown in the plot. The repulsion between the protein molecules [35,106] ensures non-aggregating sample of well-separated monomers. From ref. [105].
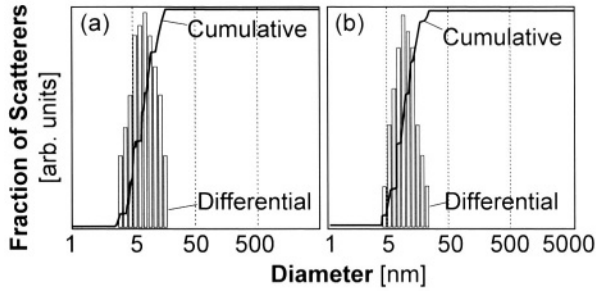
FIGURE 5.11. Dynamic light scattering results. Size distributions of scatterers in (a) ferritin, and (b) apoferritin solutions.

5.3.3. Solubility and driving force for crystallization

The crystallization driving force is written as

$$\{\exp[-(\mu_c - \mu_s)/k_B T] - 1\} \cong (C/C_e - 1) = (n/n_e - 1), \tag{5}$$

where

$$\mu_s = \mu_0 + k_B T \ln(\gamma C), \quad \text{and} \quad \mu_c = \mu_0 + k_B T \ln(\gamma_e C_e). \tag{6}$$

In these expressions, subscripts c and s denote crystal and solute, respectively, C is mass concentration and n is molecular number concentration, $n = C/m$, for determinations of the molecular masses m of ferritin and apoferritin, see preceding subsection; the subscript e indicates their values at equilibrium with the crystal; γ and γ_e are the respective activity coefficients.

To determine the solubility of ferritin and apoferritin at 27°C, we monitored trains of growth steps and gradually decreased the apoferritin concentration in the solution. We
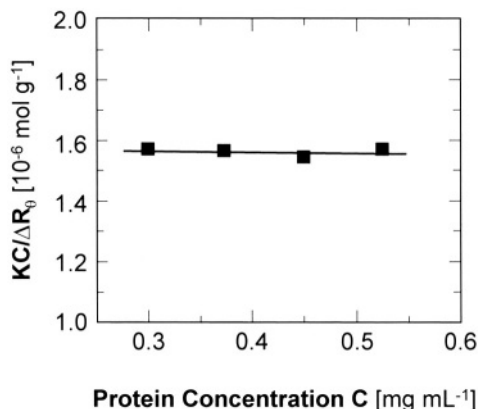
FIGURE 5.12. Static light scattering characterization of apoferritin molecules in crystallizing solutions containing 0.05 M $NaOOCCH_3$ and 2.5% $CdSO_4$.

found that at a certain C, the propagation of the steps stops, and when the concentration is lowered below this value, the step movement is backwards and the crystal is dissolving. The concentration of equilibrium between crystal and solution C_e is for ferritin 35 ± 5 $\mu g\,ml^{-1}$, and for apoferritin it is 23 ± 4 $\mu g\,ml^{-1}$.

To evaluate the activity coefficients of the proteins in crystallizing solutions, i.e., in the presence of both Na^+ and Cd^{2+} ions, we used again static light scattering [35]. The Debye plot is shown in Figure 5.12. The straight line through the experimental points allows determinations of the second virial coefficient $A_2 = -2.35 \times 10^{-5}$ $cm^3\,mol/g^2$. The good fit of the Debye plot in Figure 5.12 to a straight line indicates that effects accounted for by higher order virial coefficients are insignificant at the apoferritin concentrations employed. The activity coefficients γ and γ_e were evaluated according to the relationship $\ln \gamma = 2A_2 M_w C$ [5,53]. We get $\gamma = 0.996$ in 100 $\mu g\,ml^{-1}$ solution of ferritin, and $\gamma = 0.998$ in an apoferritin solution of the same concentration.

Note that for other proteins under crystallizing conditions, the values of A_2 are limited from below to $\sim -8 \times 10^{-4}$ $cm^3\,mol/g^2$ [54–56]. The higher magnitudes of A_2, in particular in combination with higher concentrations of proteins of higher molecular masses, may lead to significant deviations from ideality, with the non-ideality correction lowering the supersaturation significantly below estimates assuming ideal behavior.

5.3.4. Independence of solubility on molecular mass—statistical thermodynamics arguments

The values for n_e, determined as discussed in the preceding subsection and in [5,22] $n_e = (2.7 \pm 0.5) \times 10^{13}$ cm^{-3} for ferritin and $n_e = (3.0 \pm 0.5) \times 10^{13}$ cm^{-3} for apoferritin. The two n_e's are equal within their error limits, suggesting that the solubilities of these proteins do not depend on their molecular mass. Below, we provide statistical-mechanical arguments that indicate that this may be the case for protein molecules with near-spherical symmetry.

To rationalize the apparently equal solubility of ferritin and apoferritin, we consider the equilibrium between the solution and a crystal. This is equivalent to equilibrium between

the states of a molecule in a kink on the crystal surface and in the solution [57–59]. At constant temperature and pressure, the activity of a molecule in the crystal does not depend on the concentration of the solute and is equal to the activity of the standard crystal state [60,61]. Then, the equilibrium constant K_{cryst} can be written as

$$K_{cryst} = (\gamma_e C_e)^{-1} \cong C_e^{-1}, \tag{7}$$

where γ_e is the protein activity coefficient at a protein concentration equal to the solubility, and C_e is the solubility. The activity coefficient depends on the protein concentration and on the intermolecular interactions. Hence, we expect equal γ's in solutions of ferritin and apoferritin of equal concentration. As shown in the preceding subsection, determinations of γ for apoferritin solutions of concentrations up-to 20-fold higher than the solubility have yielded $\gamma \cong 1$ [5]. We expect the same to be true for ferritin, and this is the basis of the second equality above for these two proteins.

From the point of view of statistical thermodynamics, the equilibrium constant for crystallization K_{cryst} can be written as [53]

$$K_{cryst} = q_0 \exp(\mu_0/k_B T), \tag{8}$$

where q_0 is the partition function of a molecule in a kink (which is only a function of temperature and pressure), and μ_0 is the standard chemical potential of a molecule in the solution

To evaluate q_0 and μ_0, we assume that the internal molecular vibrations in the solution are the same as in the crystal and are decoupled from the other degrees of freedom. This allows us to neglect the internal vibrational partition function for both states. Furthermore, we limit ourselves to only translational contributions to the solute partition function, neglecting the rotational contributions, and those stemming from the intermolecular interactions. This limits the validity of the considerations below to molecules similar to the ferritin–apoferritin pair: with symmetry close to spherical, and that only exhibit very week intermolecular interactions and activity coefficients close to 1.

We do not take into account the contribution of the release or binding of the solvent molecules to the free energy changes of the phase transition. Although arguments presented in Section 5.5.2 below indicate that these contributions may be significant [5], we expect the contributions of the solvent effects to be identical for ferritin and apoferritin. This justifies neglecting them while aiming at comparisons between the two proteins. We also neglect the rotational vibrations in the crystal.

With these assumptions, we can use the expressions for the partition functions from ref. [53], and write

$$q_0 = q_x q_y q_z \cong (q_{vib})^3, \tag{9}$$

where q_i $(i = x, y, z)$ is the partition functions for translational vibrations along the respective coordinate. In turn, with h—the Planck constant, ν—the vibration frequency, and U—the mean-force potential of a molecule in a kink,

$$q_{vib} = \frac{\exp\left(-\frac{h\nu}{k_B T}\right)}{1 - \exp\left(-\frac{h\nu}{k_B T}\right)} \approx \frac{k_B T}{h\nu}, \quad \nu = \frac{1}{2\pi}\sqrt{\frac{f}{m}}, \quad \text{where } f = \left(\frac{\partial^2 U}{\partial i^2}\right)_{min}. \tag{10}$$

Combining, we get for q_{vib} and q_0

$$q_{vib} = \frac{2\pi k_B T}{h}\sqrt{\frac{m}{f}}, \qquad q_0 = \left(\frac{2\pi k_B T}{h}\right)^3\left(\frac{m}{f}\right)^{\frac{3}{2}}. \tag{11}$$

For μ_0, we have [53]

$$\frac{\mu_0}{k_B T} = -\ln\left[\left(\frac{2\pi m k_B T}{h^2}\right)^{\frac{3}{2}} k_B T\right] \quad\text{and}\quad \exp\left(\frac{\mu_0}{k_B T}\right) = \frac{1}{k_B T}\left(\frac{h^2}{2\pi m k_B T}\right)^{\frac{3}{2}}. \tag{12}$$

We see that q_0 contains $m^{3/2}$, while $\exp(\mu_0/k_B T)$ is proportional to $m^{-3/2}$, i.e., their product K_{cryst}, and C_e do not depend on the mass of the molecule.

It is important reemphasize two issues. (i) The thermodynamic considerations above are simplified and they only aim to address the issue of the equal solubility of two species that are identical in every respect but their mass. The equations above cannot be used to calculate values of thermodynamic functions. (ii) We did not account for the rotational degrees of freedom of the solute. This limits even this simplified model to molecules with close to spherical symmetry.

5.4. STATISTICS OF GROWTH SITES

5.4.1. Kinks and kink density

Under all conditions used in the experiments reported here, the crystals of ferritin and apoferritin as seen in the optical microscope attached to the AFM had the typical octahedral shapes with sharp edges. Accordingly, the AFM images in Figure 5.5 and all figures below indicate growth by layer generation and spreading to cover the whole facet.

The molecular structures of a {111} apoferritin face and of a growth step are shown in Figure 5.13. A molecule attached at a kink has half of the neighbors that a molecule in the crystal bulk has; in the f.c.c. lattice of ferritin and apoferritin, the half-number equals six, with three molecules belonging to the underlying layer, and three molecules from the step [57,58,62]. Since kinks at a step are the sites where incoming molecules attach, kink density is a fundamental variable that determines the ability of the crystal to incorporate solute molecules and grow [63,64].

From Figure 5.13 and ~15 other similar images, we determine the kink density along a step by counting the molecules between two kinks, n_k, also called kink length [65] and plot the distribution of the counts in Figure 5.13b–d for apoferritin, and in Figure 5.14b for ferritin. Note that kink density is affected by the presence of surface point defects, such as vacancies or vacancy clusters, seen in Figure 5.13a, as well as impurity cluster adsorbed on the surface [35]. These features act as stoppers: straight step segments as long as eight molecules form and the step propagation is locally delayed [22]. Hence, for the statistics in Figures 5.13 and 5.14 we did not consider step segments around such stoppers. We get $\bar{n}_k = 3.5$ for both proteins.
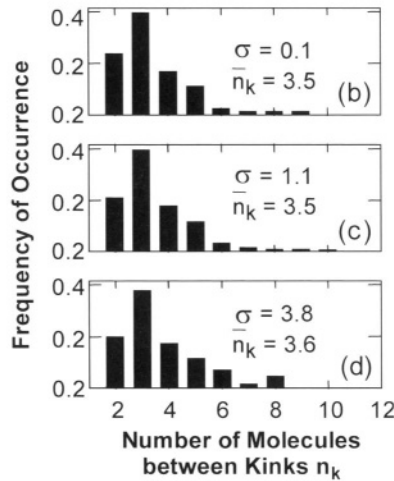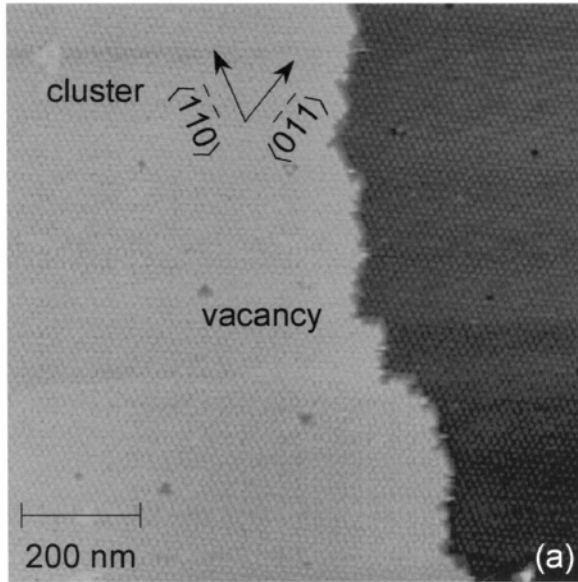
FIGURE 5.13. (a) Molecular structure of a growth step on an apoferritin crystal at protein concentration of 70 μg/ml, corresponding to supersaturation $\sigma = \Delta\mu/k_B T = 1.1$, $(C/C_e - 1) \approx 2.04$. Dark color: lower layer; light color: advancing upper layer. Adsorbed impurity clusters and surface vacancies are indicated. (b–d) Distribution of number of molecules between kinks on steps located >0.5 μm apart, obtained from images similar to Figure 5.1 at the three supersaturations σ indicated in the plots, the mean values of the distributions for each case are also shown. The protein concentrations corresponding to these σ's are (a) 25 μg/ml, (b) 70 μg/ml and (c) 1 mg/ml. From ref. [5].

Comparing Figure 5.13b, c and d, we see that the n_k distributions are nearly the same near equilibrium, as well as at very high supersaturations (provided that the distance between the steps is higher than ~200 nm, cases with closely located steps, where step–step interactions affect kink density are discussed in Section 5.8.1 below).

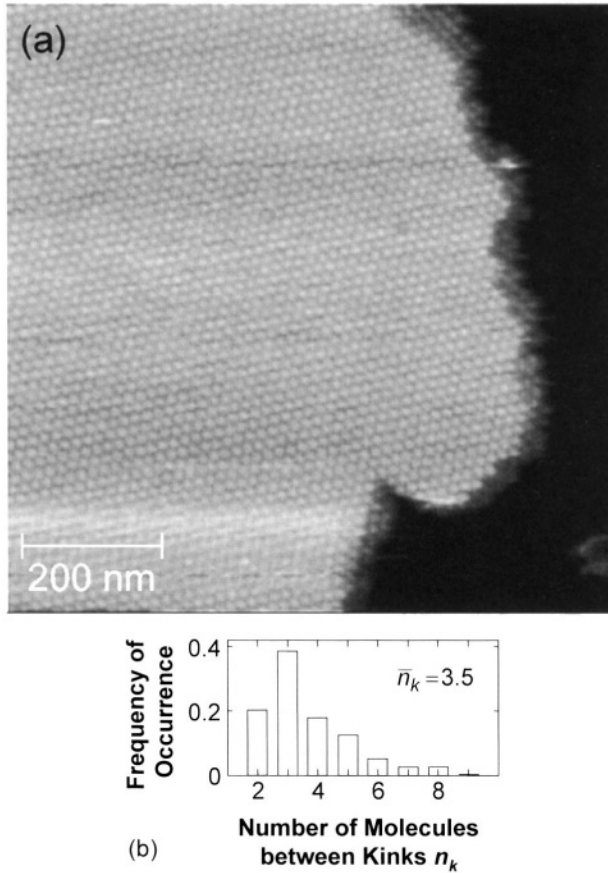FIGURE 5.14. (a) Molecular structure of a growth step on a ferritin crystal at protein concentration of $70 \ \mu$g/ml, corresponding to supersaturation $\sigma = \Delta\mu/k_B T = 0.7$, $(C/C_e - 1) = 1$. Dark color: lower layer; light gray: advancing upper layer. (b) Distribution of molecules between kinks on steps located $\sim 0.5 \ \mu$m apart, obtained from images similar to (a) at the same $(C/C_e \sim 1) = 1$. From ref. [28].

5.4.2. Energy of kinks and molecular interaction energy

The lack of dependence of the kink density on the thermodynamic supersaturation suggests that the kinks are not created by nucleation of molecular rows along a step: such nucleation would result in a steep dependence of kink density on supersaturation [66,67]. Hence, the kink density $1/n_k$ is an equilibrium property of this surface. In this case, the number of molecules between the kinks n_k is solely determined by the balance of molecular interactions and thermal fluctuations in the top crystal layer [25,26,68,69], and should be a function of the energy w needed to create a kink. Derivations have shown [63] that the average $\bar{n}_k$

$$\bar{n}_k = \frac{1}{2}\exp(w/k_B T) + 1. \tag{13}$$

From the value of $\bar{n}_k$ in Figures 5.13 and 5.14, $w = 1.6\,k_B T$. Quite surprisingly, the value of w for ferritin and apoferritin is only slightly lower than the energy of kinks on Si crystals [27]: one would expect the strong covalent bonds in the Si crystal lattice to lead to significantly higher kink energies. For the orthorhombic form of lysozyme it was found $w = 7.4\,k_B T$ [66]. This significantly higher value leads to an extremely low kink density with n_k as high as 400–800, and step propagation limited by the rate of kink generation [66].

If we assume first-neighbor interactions only, we can evaluate the intermolecular bond energy, ϕ. When a molecule is moved from within the step on a (111) face of a f.c.c. crystal to a location at the step, four kinks are created. For this, seven bonds (four in the top layer and three with molecules from the underlying layer) are broken, and five are formed. Then, $w = \phi/2$ and $\phi = 3.2\,k_B T \cong 7.8\,\text{kJ/mol} = 0.09\,\text{eV}$.

The intermolecular bonds in ferritin and apoferritin crystals involve two chains of bonds $\text{Asp–Cd}^{2+}\text{–Glu}$ between each pair of adjacent molecules [8,9]. The above value of ϕ seems significantly lower than the typical coordination bond energies. This low value may stem from the need to balance Cd^{2+} coordination with the aminoacid residues and with the water species (H_2O and OH^-), or from free energy loss due to spatially and energetically unfavorable contacts by the other aminoacid residues involved in the intermolecular contacts.

5.5. THERMODYNAMICS OF CRYSTALLIZATION AND CRYSTAL MORPHOLOGY

5.5.1. Macroscopic thermodynamics aspects

To test of the solubility of ferritin depends on temperature, ferritin crystals were grown under optical microscopic observation. At various stages in the crystal development of the individual crystals, corresponding to crystal sizes between 20 and $400\,\mu\text{m}$, the temperature was varied in the range between 0°C and 40°C. We did not notice significantly faster growth rate, that would correspond to a higher supersaturation at a lower solubility neither at the low, nor at the high limits of this temperature range. Furthermore, no rounding of the crystal edges was detected that would indicate crystal dissolution due to higher solubility. We interpret these observations as an indication of none or very weak temperature dependence of the solubility [70].

Temperature independent solubility means that the equilibrium constant of crystallization is also independent of temperature. Hence [71]

$$\left(\frac{\partial \ln K}{\partial T} \right)_p = -\left(\frac{\partial \Delta G^0/RT}{\partial T} \right) = \frac{\Delta H^0}{RT^2} = 0, \tag{14}$$

where R is the gas constant, or

$$\left(\frac{\partial \Delta G^0}{\partial T} \right) = \frac{\Delta G^0}{T}. \tag{15}$$

The latter equation has a simple solution

$$\Delta G^0 = \text{const} \times T. \tag{16}$$

Using $\Delta G^0 = \Delta H^0 - T\Delta S^0$, we obtain that $\Delta H^0 = 0$ and $\Delta S^0 = \text{const}$.

Since solubility has been found to correlate to the second virial coefficient for many proteins [56,72] we performed measurements of the second virial coefficients of apoferritin at the same conditions using static light scattering. Varying the temperature between 15°C and 35°C indicated no dependence of the virial coefficient and it remained constant, $A_2 = -7.5 \times 10^{-5}$ ml mol/g^2 [70]. This independence of temperature leads to the same results for the enthalpy and entropy of crystallization as those suggested by eq. (16): (i) the enthalpy of crystallization is zero (or extremely small) and (ii) the entropy of crystallization is temperature independent (or a weak function of temperature).

5.5.2. Molecular processes underlying the enthalpy, entropy and free energy for crystallization

The intermolecular bond energy ϕ contains both enthalpy and entropy components [73, 74]. The enthalpy contributions are due to the ion-mediated, hydrogen, and other bonds between the molecules, while the entropy components stem from the net release or binding of water and other small molecules upon crystallization [60], p. 164. With this in mind, we can write an expression for the free energy for crystallization as

$$\Delta G^0 = \Delta H^0 - T\Delta S^0_{\text{solvent}} - T\Delta S^0_{\text{protein}}. \tag{17}$$

Here $\Delta H^0 - T\Delta S^0_{\text{solvent}}$ are contributions associated with ϕ, and $\Delta S^0_{\text{protein}}$ is the loss of entropy of the protein molecules. A crude estimate of $\Delta S^0_{\text{protein}}$ and of the relative weights of the two entropy contributions can be obtained by comparing the standard free energy change for apoferritin crystallization ΔG^0 determined from the solubility, to the value corresponding to the intermolecular bond *free* energy ϕ.

Converting the solubility of the apoferritin 23 μg/ml, to molality, $C_e = 5.2 \times 10^{-8}$ mol kg^{-1}. At equilibrium between crystal and solution, for apoferritin

$$\Delta G = G^0(\text{crystal}) - \left[G^0(\text{solution}) + N_A k_B T \ln(C_e) \right] = 0, \tag{18}$$

where N_A is the Avogadro number, and the product $N_A k_B = R$ is the universal gas constant. Hence,

$$\Delta G^0 = G^0(\text{crystal}) - G^0(\text{solution}) = N_A k_B T \ln C_e, \tag{19}$$

$\Delta G^0 = -42$ kJ/mol.

To get $\Delta H^0 - T\Delta S^0_{\text{solvent}}$ from $\phi = 3\,k_B T \cong 7.3$ kJ/mol, we have to multiply ϕ by $Z_1/2 = 6$, the half number of neighbors in the crystal lattice (two molecules partake in a bond, in a f.c.c. lattice $Z_1 = 12$) and, accounting for the sign, we get −44 kJ/mol. The closeness of $\Delta H^0 - T\Delta S^0_{\text{solvent}}$ to ΔG^0 indicates the insignificance of $\Delta S^0_{\text{protein}}$ for the free energy of crystallization.

As shown above, the enthalpy of crystallization and the related energy of pair interactions in the solution are close to zero. In combination with the insignificance of $\Delta S^0_{\text{protein}}$, this allows us to conclude that crystallization is mostly driven by the maximization of the entropy of the solvent. Such disordering may stem from the release upon crystallization of the water and other solvent components bound to the protein molecules in the solution. A similarity can be traced to the processes that underlie hydrophobic attraction that governs many processes in nature [75], including some stages of protein folding [76].

The standard free energy of formation of a single intermolecular bond in apoferritin crystals ϕ is -7.8 kJ mol^{-1}, see above, and is fully attributable to the entropy gain due to the release of water, $\Delta S^0_{\text{solvent}} = 26.6 \text{ J mol}^{-1} \text{ K}^{-1}$ per intermolecular bond [5].

This conclusion allows us to crudely estimate the number of water molecules n_{w} released at the contact between two hemoglobin molecules. Following an analogy first put forth by Tanford [77], we compare the entropy effect of Hb crystallization to the entropy change for melting of ice, at 273 K, $\Delta S^0_{\text{ice}} = 22 \text{ J mol}^{-1} \text{ K}^{-1}$ [60,78,79]. Similarly, estimates of the entropy loss due to the tying up of hydration water in crystals have yielded 25–$29 \text{ J mol}^{-1} \text{ K}^{-1}$ [79]. Using these numbers, the above values of $\Delta S^0_{\text{solvent}}$ reflect the release of one or two water molecules per intermolecular bond.

This low number of water molecules can be linked to the structure of the intermolecular bonds in apoferritin crystals. The X-ray structure reveals that each of the twelve such bonds consists of a pair of Cd^{2+} ions [8]. Around each Cd^{2+} ion of the pair, two of the six coordination spots are occupied by an aspartic acid residue from the one apoferritin molecule partaking in the bond and a glutamic acid residue from the other [9]. A Cd^{2+} ion in water has all six coordination sites taken by water molecules. The fact that the entropy change corresponds to the release of one or two, rather than four water molecules (two from each Cd^{2+} ions in the bond) suggests that the Cd^{2+} ions may be pre-bound to either the incoming apoferritin molecule, or to the apoferritin molecules already in the crystal.

Thus, as suggested by the crystal structures of ferritin and apoferritin [8,9,42], the main component of the crystallization driving force stems from the strong Cd^{2+}-mediated bond between each pair of molecules. The unexpected part of our conclusion is that this driving force is not of enthalpy origin (the likely large negative enthalpy of such a bond must have been compensated for by unfavorable enthalpy effects of other patches of the molecules), but by the entropy of the water released during the formation of this bond.

5.5.3. Faceted or rough crystals

The selection between faceted and rough interfaces determines the density of growth sites on the crystal surface, the rate of growth, the crystal shape, and ultimately, the crystal quality and utility. The above determination of the intermolecular bond energy allows a better understanding of the transitions between rough and faceted crystal morphology. There may be thermodynamic and kinetic factors for crystal roughening. The thermodynamic criteria for roughening [80] are based on the ratio between the bond energy between two molecules in the crystal and the thermal energy of a molecule. If this ratio

$$\phi/k_{\text{B}}T > 2/Z_1, \tag{20}$$

where Z_1 is the number of neighbors in the crystal lattice, the crystal is faceted. For crystal surfaces below the roughening transition temperature, the kinks can only be located at

the edges of unfinished crystal planes on the surface, as in Figures 5.4 and 5.5. The emergence of such growth steps is associated with 2D or surface nucleation of new layers as in Figure 5.5 [59,62,81,82], or dislocations cropping out on the face [63].

For growth above the roughening transition temperature, kinks are abundant even at equilibrium [80]. The frequency with which molecules are incorporated into the crystal structure depends only on the impingement frequency and the attachment activation energy. For rough surfaces, transport processes responsible for delivering growth material to the interface, or heat away from the interface, control the growth rate and the crystal shape [83,84].

To check if normal growth mode in the apoferritin system can be thermodynamically induced, we substitute $\phi = 3.2\ k_B T$ and $Z_1 = 12$ in eq. (20). The inequality is fulfilled and we conclude that no thermodynamic roughening transitions are likely for the studied system at the typical experimental temperature around 300 K.

Even crystals that grow below the roughening transition temperature may exhibit rough surfaces due to kinetics factors. First, at very high supersaturations, layer generations becomes so intense that the step density becomes comparable to the density of kinks along the step. Individual steps are then indistinguishable and the crystal grows by the normal mode [85]. Second, adsorption of foreign molecules, "impurities" on the flat terraces between the steps may facilitate the nucleation of new layers and bring about roughening even at moderate supersaturations and at temperatures far below the roughening temperature. Since commercial ferritin and apoferritin preparations contain up to 50% of other protein species [86], the normal growth mode for ferritin crystals observed in experiments in which ferritin was used without additional purification, is, most likely, impurity induced [16].

5.6. MOLECULAR-LEVEL KINETICS OF GROWTH

While the kink density is a thermodynamic growth variable that characterizes the affinity of the crystal to the solute molecules, the kinetics of incorporation are reflected by the flux of molecules into a growth site. To monitor these fast incorporation events, we disabled the slow scanning axis of the AFM. The advance of a step site is shown in Figures 5.15 and 5.16. Area scans immediately following the trace in Figures 5.15 and 5.16 and revealed that step motion is not inhibited or accelerated at the location of scanning, i.e., the chosen scanning parameters ensured that step propagation was not affected by scanning over the same line for ~3 min.

Despite the relatively high solution supersaturation $\sigma = 1.1$, the time trace in Figure 5.15 reveals not only 25 arrivals to but also 22 departures of molecules from the monitored site. All arrivals and departures of molecules to and from the monitored site involve single molecules. Thus, in contrast to claims of preformed multiple-molecule growth units for the protein lysozyme [87–89], apoferritin and ferritin crystal growth by the attachment of single molecules.

This type of data collection does not allow observations of the neighboring sites at the step. Hence, we cannot distinguish between attachment/detachment from molecules in the kinks or at the steps. Still, we notice that the residence times τ between these events fall into either $\tau \leqslant 1$ s or $\tau > 5$ s. In Figure 5.15 we have six events of the second type and 19 events of the first. Their ratio is roughly equal to the kink density along the step, suggesting
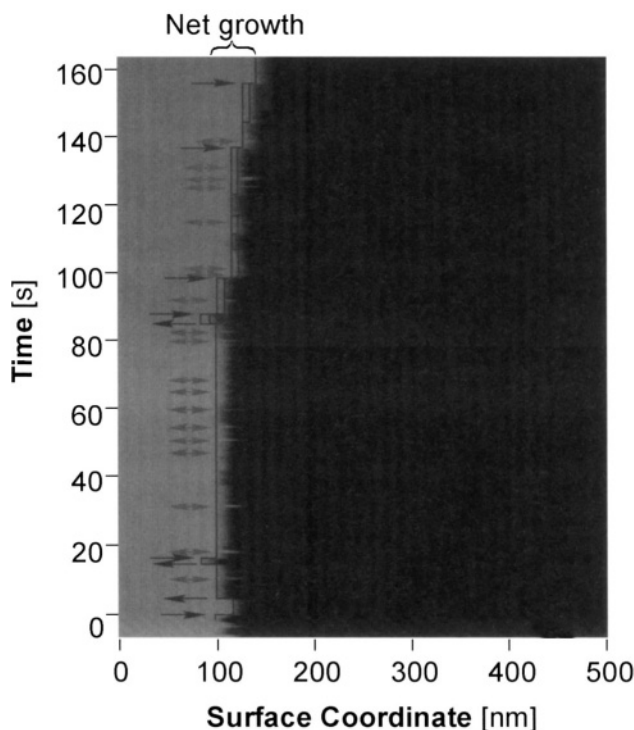
FIGURE 5.15. Incorporation of molecules into steps at apoferritin concentration of 70 μg/ml, $\sigma = 1.1$, $(C/C_e - 1) = 2.04$. Pseudo-image recorded using scanning frequency of 3 Hz with the Y scan axis disabled at time = 0 shows displacement of one step site. Contour traces step position. Red arrows indicate attachment and detachment events with residence time > 1 s, blue double-sided arrows—with residence time < 1 s, for details, see text. Appearance of ½ molecule attachments at times > 80 s, highlighted in green, is due to events at a neighboring site that enters image due to scanner drift.

that the long-time events may be attachments/detachments to/from a kink, while the short ones may be sightings of molecules at the step edge.

Furthermore, molecules may enter the line of observation due either to molecular diffusion along the step or to exchange with either the terrace between the steps or the adjacent solution. While the latter results in step propagation and growth, the former is a process that only involves rearrangement of molecules already belonging to the crystals and may not be associated with growth. To distinguish between the two, as done before for steps on metal and semiconductor surfaces [25,68,90–92], we calculated the time correlation function of the step position x (in molecular size units) as $\langle [x(t + \Delta t) - x(t)]^2 \rangle_{\Delta t}$, with averaging over the respective Δt. In Figure 5.17 it is plotted as a function of Δt. Theoretical analyses of the exchange of the steps with the medium at equilibrium [25,68,92–94] predict that if diffusion along the step edge dominates the advance of the step site, the cross-correlation should follow $\Delta t^{1/4}$ dependence [25,68,92–94]. We found no theory dealing with supersaturated conditions. However, motion of a site on the step edge is similar to Brownian motion [92,93]. For Brownian diffusion, the coefficient relating $\langle [x(t + \Delta t) - x(t)]^2 \rangle_{\Delta t}$ and $\Delta t^{1/2}$ may vary, but the exponent 1/2 of Δt does not depend on the presence or ab-
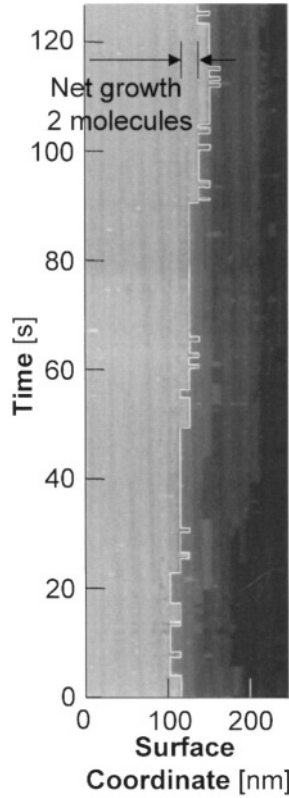
FIGURE 5.16. Incorporation of molecules into steps on a ferritin crystal at protein concentration of $70 \, \mu g/ml$, corresponding to supersaturation $\sigma = \Delta\mu/k_B T = 0.7$, $(C/C_e - 1) = 1$. A pseudoimage recorded with the scan axis parallel to the step disabled at time = 0 shows the displacement of one molecular site at the step. In this imaging mode, the molecules in the upper and lower layers appear as vertical columns. Red contour traces step position. Left shifts of this contour indicate detachment of a molecule from the monitored site, right shifts—molecular attachment into the monitored site. From ref. [28].

sence of concentration/chemical potential gradients [71]. Hence, we use only the exponents of Δt stemming from the data in Figure 5.17 for further discussion.

The data in Figure 5.17 do not fit a single exponential. The deviation from ¼ at times longer than 20 s allows us to conclude that the trace in Figure 5.15 likely reflects exchange of molecules between the step and interstep terraces or the adjacent solution. This conclusion allows us to extract from Figures 5.15 and 5.16 net frequencies of attachment of molecules to kinks. For apoferritin at $(C/C_e - 1) = 2$, from the net attachment of 3 molecules for 162 s and the probability of viewing a kink of $1/n_k = 1/3.5$, we get for the difference between the incorporation and detachment fluxes, or the "net flux" $(j_+ - j_-) = 0.065 \, s^{-1}$, or one molecule for ~15 s. For ferritin at $(C/C_e - 1) = 1$, Figure 5.16 shows net growth of two molecules for 128 s, leading to an average net flux $(j_+ - j_-) = 0.054 \, s^{-1}$ into the growth sites distributed with mean density $\bar{n}_k^{-1} = 0.28$. Thus, even at the relatively high supersaturation in Figures 5.15 and 5.16, incorporation of molecules into the crystal is extremely slow and occurs over macroscopic time scales.
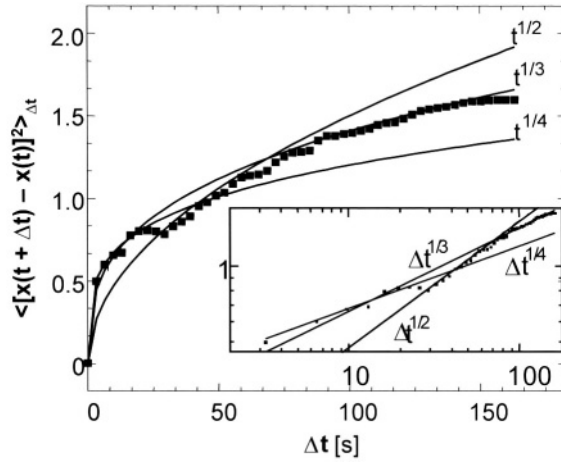
FIGURE 5.17. Time correlation curve, characterizing mean square displacement of a location at a step for a time interval Δt as a function of this Δt, corresponding to the trace of step location in Figure 5.15; inset: logarithmic plot. Solid squares—data; lines fits with exponential dependencies on time as indicated in plots. From ref. [22].
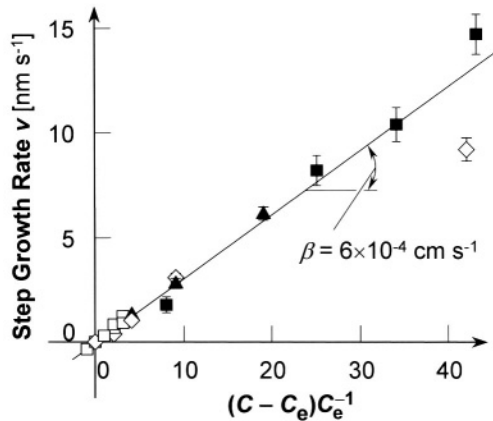

FIGURE 5.18. Determination of the kinetic coefficients for step growth for ferritin and apoferritin. Dependencies of the step growth rates v on the crystallization driving force $(C/C_e - 1)$. Open squares and diamonds denote v-values for, respectively, ferritin and apoferritin, from sequences of molecular resolution *in-situ* AFM images of the advancing steps. The reason for the lower value of the point for apoferritin at $(C/C_e - 1) = 42$ is not well understood. This point was not use in the determination of the kinetic coefficient β. Solid triangles—data for apoferritin extracted from disabled-*y*-axis scans. Solid squares—data for ferritin from time traces of the step growth rate using laser interferometry. Straight line corresponds to the step kinetic coefficient $\beta = 6 \times 10^{-4}$ cm s^{-1}. From ref. [105].

The step velocities v for the two proteins, determined using the three methods discussed in Section 5.2.4 above are shown in Figure 5.18. The data fit well the proportionalities between v and $(C/C_e - 1)$ and $(n/n_e - 1)$

$$v = \beta \Omega C_e (C/C_e - 1) = \beta \Omega n_e (n/n_e - 1) \tag{21}$$

with $\Omega = 1/4a^3 = 1.56 \times 10^{-18}$ cm^3—the crystal volume per ferritin or apoferritin molecule, and step kinetic coefficient β [64,95] is $(6.0 \pm 0.4) \times 10^{-4}$ cm s^{-1} for ferritin and $(6.0 \pm 0.3) \times 10^{-4}$ cm s^{-1} for apoferritin.

Since there are no sources or sinks of molecules at the step other than the attachment sites, the step growth rate v should equal $a\bar{n}_k^{-1}(j_+ - j_-)$ [64,96]. At $(C/C_e - 1) = 1$, at which all data in ferritin in Figure 5.16 were collected, the value of the step growth rate for ferritin from Figure 5.18 is $v = 0.20$ nm s^{-1}, equal to the product $a\bar{n}_k^{-1}(j_+ - j_-)$. For apoferritin, the average step velocity at $(C/C_e - 1) = 2$, $\sigma = 1.1$, is $v = 0.26$ nm/s. The product $a\bar{n}_k^{-1}(j_+ - j_-)$ determined at the same conditions is 0.24 nm/s.

The closeness of the values of the product $a\bar{n}_k^{-1}(j_+ - j_-)$ and measured v's indicates that the step propagation in ferritin crystallization occurs only due to incorporation of molecules into the kinks along the steps [5,22].

5.7. WHAT LIMITS THE RATE OF INCORPORATION OF A MOLECULE IN A KINK?

5.7.1. Diffusion-limited versus transition-state kinetics

I discuss below the factors that determine the rate of the last, the chemical, stage in the growth mechanism—the incorporation into a kink of a molecule standing in front of this kink. In this way, I eliminate from consideration the rate of supply of the molecules from the solution bulk to the kink, constituting the transport stage of the growth mechanism. The kinetics of chemical reactions in solutions are either limited only by the rate of diffusion of the species [97], or additionally slowed down by a high-energy transition state [98]. The former kinetics pathway does not exclude the presence of potential or free energy barriers. It has been shown that if molecules have to overcome a repulsive maximum to reach the bonding minimum, the rate of binding can be evaluated as diffusion over the barrier. The resulting kinetic law contains an exponential dependence on the barrier height [98].

For the kinetics of the phase transitions in solutions, it is generally accepted that colloid particles follow the diffusion-limited model, while the growth rates of new phases of small molecules are thought to be governed by a transition state [95,96,99–101]. For the intermediate case of protein solid phases, the growth kinetics largely resemble those of small-molecules, and it was assumed that transition-state laws apply [102]. While rate laws reminiscent of diffusion-limited mechanisms have been postulated for small-molecule phase transitions [63,84,103], they were viewed as equivalent to respective transition-state expressions [84,103] and no critical tests to discriminate between the two mechanisms were suggested or performed.

In the transition-state kinetics, the rate coefficients are: (i) mass-dependent [64,104], (ii) independent on the diffusivity [98], and (iii) faster for high-symmetry molecules, because of the transition-state entropy [96]. Below, we discuss evidence indicating that (i) is violated for the ferritin/apoferritin pair of proteins, and violations of (ii) and (iii) for many other systems suggesting that the rate of many phase transitions is in fact diffusion limited.

The data in Figure 5.18 show that at equal driving forces, the step growth rates are equal for the two proteins. Since in the preceding subsections we have shown that the mechanism of attachments of molecules to kinks are identical for the two proteins, we conclude that this observation is in apparent contradiction with transition-state type kinetic laws, in which

the vibrational components of the transition-state partition function lead to proportionality of β to $m^{-1/2}$, characteristics (i) of transition-state kinetics discussed above. We conclude that the kinetics of incorporation into the kinks are only limited by diffusion [105].

As an aside, Figure 5.18 shows that the proportionality between the step growth rate v and the crystallization driving force $(C/C_e - 1) = (n/n_e - 1)$ is valid in a broad range of concentrations of both proteins. When the protein concentration is lower than the solubility, the steps retreat with a velocity symmetric to that in growth, as expected from the microscopic reversibility of the growth-dissolution processes [5,22].

5.7.2. Evaluation of the kinetic coefficient for step motion in the case of diffusion-limited kinetics

We derive an expression for the flux of molecules into a kink for diffusion over an energy barrier U, followed by unimpeded incorporation [97,98]. The barrier U may be of electrostatic origin [98]; however, for the ferritin/apoferritin pair, it probably accounts for the need to expel the water molecules attached to the incoming molecules and to the growth site [106]. Repulsive potentials due to water structuring at hydrophobic and hydrophilic surface patches can have significant strength and range [107,108].

In Figure 5.19 the resulting potential relief is schematically depicted. The potential maximum U_{max} is due to the crossing of the increasing branch, due to the repulsion between the incoming solute molecules and the crystal surface at medium separations, and the receding branch, which corresponds to the short-range attraction required if the molecules should enter the growth site. We position the beginning of the coordinate axis $x = 0$ at the location of this maximum. We assign a finite curvature of $U(x)$ about this maximum and link it with the expulsion of the last few solvent molecules as an incoming solute molecules joins the crystal. The finite curvature assumption follows previous solutions to similar problems [109,110]. The distance δ, used below as an upper integration limit, is bound from below by the range of interaction of the solute molecules with the surface, which can be a few solute molecular sizes, and from above by the distances between the solute molecules in the solution bulk, $n^{-1/3} \approx 0.2 \ \mu m$. Thus, δ can be chosen significantly longer than the molecular sizes and kink lengths, and using a one-dimensional model is justified. Since the rate of diffusion over a sharp barrier only depends on the curvature around the maximum [109,110], the choice of δ does not affect the result.

To calculate the flux J of molecules with concentration n that, driven by a concentration gradient, overcome a barrier $U(x)$, we use the generalized Fick's law, $J =$
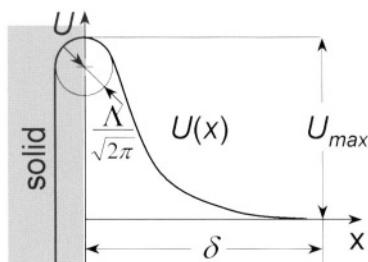

FIGURE 5.19. A schematic illustrating the potential energy relief in front of the growth interface. For details, see text.

$(nD/k_BT)\mathrm{d}\mu/\mathrm{d}x$, with $\mu(T,x) = \mu_0(T) + k_BT\ln[\gamma n(x)] + U(x)$ and $\gamma \approx 1$ [5], J is linked to $U(x)$, $n(x)$ and the gradient of n as [97,110]

$$J = D\left[\frac{\mathrm{d}n(x)}{\mathrm{d}x} + n(x)\frac{\mathrm{d}(U(x)/k_BT)}{\mathrm{d}x}\right], \quad x > 0 \tag{22}$$

with D being the Stokes diffusion coefficient of the molecules. Solving for a steady $J = $ const, we integrate the above equation with two sets of boundary conditions: (i) that at $x \geqslant \delta$, $U = 0$, and $n = n_\delta$; and, (ii) that in the crystal, i.e., at $x \leqslant 0$, $n = 0$.

Dividing by D and multiplying both sides by $\exp(U(x)/k_BT)$, we get

$$\frac{J}{D}\exp\left[U(x)/k_BT\right] = \frac{\mathrm{d}}{\mathrm{d}x}\left\{n(x)\exp\left[U(x)/k_BT\right]\right\}. \tag{23}$$

Integrating from $x = 0$ to $x = \delta$, using the boundary conditions at $x = 0$ and $x \geqslant \delta$, we get

$$J = \frac{n_\delta D}{\int_0^\delta \exp[U(x)/k_BT]\mathrm{d}x}, \tag{24}$$

an analogue to eq. (9.51) in ref. [98] and the Fuchs expression for coagulation of particles interacting through $U(x)$.

If $U(x)$ has a sharp maximum at $x = 0$, we can represent it with a symmetric function around the point of the maximum. As shown below, in many cases $|\mathrm{d}^2U/\mathrm{d}x^2| < a$ and this justifies the assumption of a sharp maximum. We use only the first two members of its Taylor series: $U(x) = U_{max} - \frac{1}{2}|\mathrm{d}^2U/\mathrm{d}x^2|x^2$. The minus sign stems from $\mathrm{d}^2U/\mathrm{d}x^2 < 0$ at the maximum. Then, the integral

$$\int_0^\delta \exp\left[U(x)/k_BT\right]\mathrm{d}x = \exp\left(\frac{U_{max}}{k_BT}\right)\int_0^\delta \exp\left[-\frac{1}{2}\left|\frac{\partial^2(U/k_BT)}{\partial x^2}\right|_{x=0}x^2\right]\mathrm{d}x$$

$$\approx \exp\left(\frac{U_{max}}{k_BT}\right)\int_0^\infty \exp\left[-\frac{1}{2}\left|\frac{\partial^2(U/k_BT)}{\partial x^2}\right|_{x=0}x^2\right]\mathrm{d}x$$

$$= \exp\left(\frac{U_{max}}{k_BT}\right)\left[\frac{2}{\pi}\left|\frac{\partial^2(U/k_BT)}{\partial x^2}\right|_{x=0}\right]^{-1/2}. \tag{25}$$

The approximate equality above is based on $\delta \gg [1/2\,|\,\mathrm{d}^2U/\mathrm{d}x^2|]^{-1/2}$, the half-width of the Gaussian function in eq. (25). Finally,

$$J = D\sqrt{\frac{2}{\pi k_BT}}\left\{\left|\frac{\partial^2U}{\partial x^2}\right|_{max}\right\}^{1/2}\exp\left(-\frac{U_{max}}{k_BT}\right)n_\delta. \tag{26}$$

Note that only half of the flux J from this equation contributes to growth: on top of the barrier, the force driving the molecules into the crystal is zero, and a molecule has equal chances of getting incorporated, or going back to the solution [111]. With this, and introducing the parameter Λ as the radius of curvature of $U(x)/k_B T$ at its maximum:

$$\Lambda = \left(\frac{1}{2\pi} \left| \frac{\partial^2 (U/k_B T)}{\partial x^2} \right|_{\text{max}} \right)^{-1/2}, \tag{27}$$

the expression for J becomes

$$J = \frac{D}{\Lambda} \exp\left(-\frac{U_{\text{max}}}{k_B T} \right) n_\delta. \tag{28}$$

This last equation is essentially identical to the nucleation rate expression derived by Zeldovich [110] as a diffusion flux over a potential barrier in the space of cluster sizes.

If U_{max} is due to the hydration of the incoming molecule and the site where it attaches, the radius of curvature of $U(x)$ around U_{max} should be the size of a few water molecules, 2–4 Å, and the length Λ should be ~5–10 Å. Note that in this evaluation, we apply discreet considerations to a continuous model. Still, we expect the estimate of Λ to be roughly correct.

To evaluate the step velocity, we note that if all molecules that overcome the barrier are incorporated into a kink, the incoming flux into a kink is $j_+ = J \Delta S_{\text{kink}} \approx J a^2$, where a^2 is an effective surface area of a kink. If there are no solute transport constraints (kinetic growth regime), n_δ is equal to that in the solution bulk n. Furthermore, in equilibrium, when n equals the solubility, n_e, $j_+ = j_-$. Since $j-$ does not depend on n in the solution, the step velocity v is

$$v = \frac{a}{\bar{n}_k}(j_+ - j_-) = \frac{a^3}{\bar{n}_k} \frac{D}{\Lambda} \exp\left(-\frac{U_{\text{max}}}{k_B T} \right)(n - n_e). \tag{29}$$

Since Brownian diffusion does not depend on the molecular mass, the above model yields a mass-independent kinetic coefficient, for details, see the Supplementary information.

With $a^3 = \Omega$, we can re-write eq. (29) in the typical form of eq. (21) that is readily comparable to experimental data [105]. This defines β as

$$\beta = \frac{1}{\bar{n}_k} \frac{D}{\Lambda} \exp\left(-\frac{U_{\text{max}}}{k_B T} \right). \tag{30}$$

The parameters in this expression, $\bar{n}_k^{-1}$, D, Λ, and U_{max} have a clear physical meaning, and can be independently measured [105].

5.7.3. How broad is the class of molecules that follow diffusion-limited kinetics law?

The ratio $D/\Lambda \bar{n}_k$ has been used [112] as a kinetic coefficient for crystallization from the melt, with Λ defined as the "free pathlength" of the building blocks, atoms or molecules, in the melt. In further work, this law was shown to poorly predict the behavior of metals during solidification [113]. Note that in contrast to the above expression for melt growth, eq. (30) treats growth from solutions with Einstein–Stokes diffusion of the solute molecules.

In a classical paper [63], the ratio of the diffusivity to the mean distance between kinks, $D/a\bar{n}_k$ was used as a kinetic coefficient. This definition misses the energy barrier for growth, demonstrated by numerous later experiments [104]. In a further development [103], the kinetic coefficients for motion of steps were postulated as $\beta = (D/\Lambda)\exp(-U/k_B T)$, with Λ introduced as a "jump length in the solution". Comparing this formula with our eq. (30), we see that eq. (30) explicitly accounts for the mean kink density $\bar{n}_k^{-1}$ and provides a clear definition of Λ.

Evidence for diffusion-limited kinetics in other solution crystallization systems can be found in experiments on growth of protein crystals in gels, where the protein diffusivity is significantly lower than in a "free" solution. It was found with two proteins that the maximum value of the growth rate, recorded at the early stages of growth before solution depletion and transport control set in, is 1.5–3× lower than the equivalent value in free solutions [114]. This suggests that the kinetic coefficient of growth is correlated to the diffusivity, which lower in gells. In another work with the protein lysozyme, it was found that in gelled media, the protein concentration at the growth interface is essentially equal to the one in free solutions, while the concentration gradient at the interface, proportional to the growth rate, is lower by ~1.5× [115]. This is only possible if the kinetic coefficient in gels is lower, supporting the correlation between β and D and contradicting characteristics (ii) of the transition state kinetic laws, discussed above.

Table 5.1 shows that the known kinetic coefficients for crystallization of about a dozen proteins, protein complexes and viri are in the range 0.8–400×10^{-4} cm s^{-1} [14,19,22, 116,117]. The molecular symmetry groups have orders ranging from 1, through 3, to 24 for the ferritins, and 60 for the satellite tobacco mosaic virus. No correlation exists between higher molecular symmetry and higher kinetic coefficients. This suggests that the rate-limiting step is not the decay of a transition state that should be facilitated for high symmetry molecules with higher transition-state entropies, characteristics (iii) discussed above.

Evidence in favor of the applicability of the diffusion-limited kinetics to phase transitions involving small-molecule substances, comes from detailed data on the adsorption kinetics on the surface of a growing ammonium-dihydrogen phosphate (ADP) crystal [118, 119]. The data for the temperature range 29–67°C were fitted to an equivalent of eq. (30) with $\bar{n}_k^{-1} = 1$ to account for the suspected density of the adsorption sites [118,119]; for the surface diffusion mechanism selected by this system, adsorption is the process to be limited by either diffusion, or by a transition-state decay rate. The fit yielded $\Lambda = 13$ Å and $U = 27$ kJ/mol. The closeness of Λ to the range suggested above for the diffusion-limited case suggests that this mechanism is the rate-determining one for the investigated phase transition.

TABLE 5.1.
Kinetic coefficient, β, diffusivities, D, effective molecular diameter a, point symmetry group of molecule G, order of symmetry group Z, for various systems.

System	β, 10^{-4} (cm s^{-1})	D, 10^{-6} (cm^2 s^{-1})	a (nm)	G	Z	Source
Insulin			6.5	$\bar{3}m$	6	[168]
No acetone	90	0.79				
~5% acetone	420					
Apoferritin	6	0.32	13	432	24	[22]
Ferritin	6	0.32	13	432	24	[105]
Canavalin, R3 form	5.8–26	0.4	3.5–8	3	3	[19]
Catalase	0.32	n.a.	11.5	222	4	[169]
Lysozyme {101}		0.73	3	1	1	
Typical	2–3					[170]
No step bunching	22–45					[117]
Lysozyme {110}	2–3					[171]
STMV	4–8	0.2	16	$m5$	60	[14]
Thaumatin	2	0.6	4.0	1	1	[172]
Various inorganic systems (ADP, KDP, alums, etc.)	~100–1000	~1–5	0.5	1, 2, $\bar{2}$, m etc.	1, 2	[1]

Further evidence in favor of the applicability of this mechanism to small molecules comes from the unusually narrow grouping of the kinetic barriers for growth of ~10 diverse substances at $28 \pm 7 \text{ kJ mol}^{-1}$ [104]. The chemical nature of these substances ranges from inorganic salts, through organic molecular compounds, to proteins and viri. Hence, the narrow range of the activation barriers is unexpected for transition-state kinetics, where the activated complexes should reflect the chemical variety of the crystallizing compounds. On the other hand, assuming diffusion-limited kinetics, we note that the diffusivities in aqueous solutions have effective activation energies of $\sim 8-17 \text{ kJ mol}^{-1}$ [34,120]. If, as suggested by eq. (30), we subtract these values from the barriers of $28 \pm 7 \text{ kJ mol}^{-1}$ [104] characterizing the overall kinetics, only $\sim 10-20 \text{ kJ mol}^{-1}$ remain for the barriers due to the interactions between the solute and the crystal surface. The above range of $\pm 7 \text{ kJ mol}^{-1}$ is sufficiently broad to accommodate the chemical specificity of the solutes.

Thus, our experimental data in the context of other recent findings show that the kinetics of attachment of molecules to a growing phase during crystallization or other phase transitions in solution are, in many cases, diffusion limited. This applies to proteins, as well as to small-molecule systems. It is important to once again state that this result concerns the kinetics of incorporation of the solute molecules into existing attachments sites. In the cases where such sites are few, or transport from the solution bulk is slow, the kinetics of creation of attachment sites, or of transport may control the overall kinetics. What we argue is that after an attachment site exists, and the solute molecules are standing in front of it, the rate of incorporation is solely limited by diffusion, and not restricted by the decay of an intermediate state [105].

5.8. INTERACTIONS BETWEEN STEPS AND THE MOLECULAR PATHWAY FROM SOLUTION TO CRYSTAL

5.8.1. Step–step interactions

To test if step–step interactions, typical mesoscale phenomena, affect the kink density, a microscopic characteristics of growth, I show in Figure 5.20 the distribution of n_k along steps spaced about 10 molecules $(0.13 \, \mu\text{m})$ apart, as opposed to 0.5 to 1 μm in Figures 5.13 and 5.14. The kink density and step meandering are lower, indicating interactions between neighboring steps. Such interactions may occur through the solution or the adsorption layer and consist of competition between the steps for nutrient supply. Competition for supply effectively reduces the supersaturation to which a step is exposed. However, the results in Figure 5.13 indicate that the kink density is independent of the supersaturation within very broad limits. Hence, step–step interactions are not mediated by the supply fields. Other interaction types include step–step repulsion [90,91] associated with the entropy loss of closely spaced steps [65,121], or overlapping of the relaxation elastic fields of neighboring step edges [122,123]. Our observations are evidence that such interactions may be present even during solution growth of protein crystals [5,28].

For insight into step interactions and step pattern dynamics, we consider the spatio-temporal evolution of the step train. For this, we chose a fast scanning direction perpendicular to the steps and disabled the slow scanning axis of the AFM. In the collected pseudo-images, the vertical axis represents time. An example of such data is shown in Figure 5.21a. The diagram in Figure 5.21b traces the locations x of each step in Figure 5.21a at time t. These lines fully characterize the dynamics of the monitored step train segment. Thus, the slope of a line tracing a step is reciprocal to the step velocity v, the local step density l^{-1} and vicinal slope $p = h_0 l^{-1}$ ($h_0 = 10.5 \, \text{nm}$ is the thickness of a (111) layer in ferritin/apoferritin) can be determined from the distances between the lines l at a chosen time t. The time intervals between subsequent steps Δt at a chosen location x determine the normal growth rate $R = h_0 / \Delta t$ at this location [23,28].

Observation of the step traces in Figure 5.21b reveals numerous twinning (two step joining into a single one) and de-twining events. Only steps separated prior to twinning by distances of $<100 \, \text{nm} \approx 7$ lattice parameters twin, indicating the presence of a short-range step–step attraction. In the subsequent subsection, see also ref. [28], we show that this attraction is likely due to the overlapping of the fields of surface diffusion of adjacent steps; the characteristic surface diffusion length, determined from these results, is a few lattice parameters. This short length determines the range of the attraction. The numerous twinning events suggest that the repulsion between steps that may be associated with entropic or elastic interactions, often present in semiconductor systems [65,124], is weaker that the attraction [23].

5.8.2. The molecular pathway from the solution into a growth site

During crystal growth from solution, the solute molecules have two possible pathways between the solution and the kinks: they can be directly incorporated [63,95], or they can first adsorb on the terraces between the steps, diffuse along them, and then reach the steps [62,63].
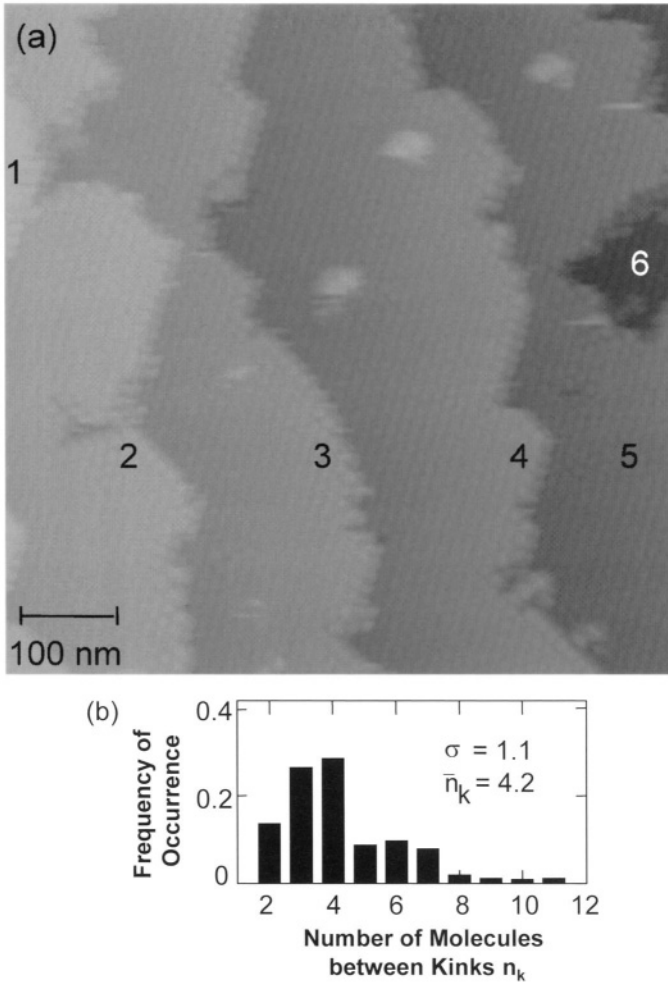
FIGURE 5.20. (a) Structure of steps and (b) kink distribution for closely spaced steps at apoferritin concentration of 70 μg/ml, $\sigma = 1.1$, $(C/C_e - 1) = 2.04$. Clusters similar to the one in Figure 5.15 are seen on the terraces behind steps 3, 4, and 5 in (a). From ref. [5].

If a crystal grows by the direct incorporation mechanism, the competition for supply between adjacent steps is mild [95]. On the contrary, competition for supply confined to the adsorption phase is acute [103]; it retards step propagation and acts as a strong effective attraction between the steps. This dramatically affects the stability of the step train, the appearance and evolution of step bunches [65], and ultimately the crystal quality and utility [125].

The two mechanisms can be directly discerned by monitoring the adsorbed solute molecules on the crystal surface, similar to experiments with metal atoms at lowered temperatures [126]. However, during solution growth at room temperature, the diffusivity of the adsorbed species is $\sim 10^{-8}$ cm^2 s^{-1} [19,118], i.e., a molecule passes 100 nm in ~ 0.01 s. With *in-situ* atomic force microcopy, this distance is covered by the scanning tip typically
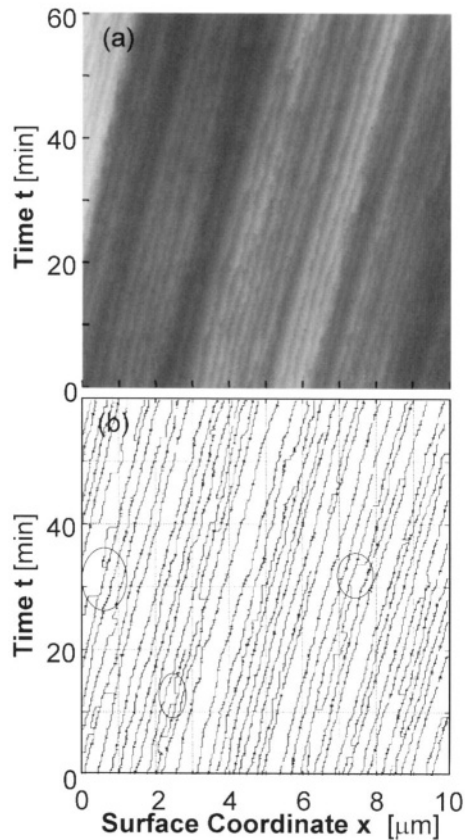
FIGURE 5.21. Quantification of the step train dynamics. (a) A pseudo-image of a 10 μm section of a step train recorded by orienting the fast scanning axis perpendicular to the dominant step direction and disabling the slow scanning axis of the atomic force microscope. In this imaging mode, the vertical axis represents the elapsed time. (b) Digital version of the image in (a) in which each point represent the position of a step along the surface coordinate x at time t. Ellipses mark pairs of twinning-de-twinning events. From ref. [23].

~0.1 s, i.e., imaging is too slow to detect and monitor the adsorbed molecules. Electron microscopy of flash-frozen samples has in several cases revealed the presence of adsorbed solute molecules on the crystal surface [127]; however, their participation in growth cannot be confidently judged by this technique. As direct tests appear impossible, indirect evidence for the growth mechanism of several systems has been sought.

For several solution-grown crystals the growth mechanism has been deduced by comparing the velocities of isolated steps to those of closely spaced steps. Similar values of the two velocities for silver [128] and calcite [12,13] were taken as evidence for the direct incorporation mechanism. Conversely, slower growth of dense step segments was interpreted in favor of the surface diffusion mechanism for KDP/ADP [18,118], lysozyme [129] and canavalin [19]. A known problem for such mesoscale data is that the data sets interpreted in favor of direct incorporation could also reflect a surface diffusion range shorter than the shortest step separation probed [12,13]. Thus, critical evidence about the growth mode should be sought by studying the growth processes at the molecular level [5,22].

In the case of direct incorporation from the solution, as shown in the preceding section and in [96,102],

$$j_+ - j_- = \nu_+ C_e \Omega \exp\left(-\frac{U_{\max}}{k_B T}\right)\left[\frac{C}{C_e} - 1\right], \quad \nu_+ = \frac{D}{\Lambda a}, \quad \text{and} \quad \frac{j_+}{j_-} = \frac{C}{C_e}. \quad (31)$$

Here $U_{\max}$, is the energy barrier for incorporation into the kinks [64,95]; in the case of ferritin, it likely accounts for the need to expel the water molecules structured around hydrophilic patches on the surfaces of the incoming molecules and the molecules forming the kink [106]. $\Omega = 1.56 \times 10^{-18}$ cm^3 is the crystal volume per ferritin molecule, $D = 3.2 \times 10^{-7}$ cm^2 s^{-1} is the ferritin diffusivity [35], and Λ is the radius of curvature of the surface-molecule interaction potential around its maximum at $U_{\max}$ [97,98], and hence, should be of the order of a few water molecule sizes, ~5–10 Å [119]. The step velocity v for this growth mode is

$$v = \frac{a}{\bar{n}_k}(j_+ - j_-) = \frac{\Omega C_e}{\bar{n}_k} \frac{D}{\Lambda} \exp\left(-\frac{U_{\max}}{k_B T}\right)\left[\frac{C}{C_e} - 1\right]. \quad (32)$$

For the case of growth via surface diffusion, analogous considerations yield for the net flux into the step from the surface

$$j_{s+} - j_{s-} = \nu_{s+} n_e a^2 \exp\left(-\frac{U_{s0}}{k_B T}\right)\left[\frac{n_s}{n_e} - 1\right], \quad \nu_{s+} = \frac{D_s}{\Lambda_s a} \quad \text{and} \quad \frac{j_+}{j_-} = \frac{n_s}{n_e}, \quad (33)$$

where n_s and n_e are the surface concentration of adsorbed ferritin, and its equilibrium value, respectively; U_{s0} is the energy barrier for incorporation into the kink from the surface, D_s and Λ_s are, respectively, the surface diffusivity and curvature of the surface U_s. For the step velocity, one gets through $v = a/\bar{n}_k(j_{s+} - j_{s-})$ an expression analogous to eq. (32).

To evaluate the ratios of the in- to out-fluxes, we use that Figure 5.16 reveals that for ferritin at $C/C_e = 2$, $j_+/j_- \leqslant 1.105$. For apoferritin, similar experiments in Figure 5.15 show that at $C/C_e = 3$, $j_+/j_- \leqslant 25/22 = 1.14$. For both proteins, these ratios represent gross violations of the last equality of eq. (31). These violations cannot be attributed to depletion of the solution layer adjacent to the crystal—this factor becomes significant at ~100× higher growth rates [130], and suggest that the direct incorporation mechanism may not apply. In the case of Langmuir adsorption, $n_s = n_{s\infty}C(B + C)^{-1}$ (B—Langmuir constant) and $n_s/n_e < C/C_e$. Hence, the lower ratios of the in- to out-flux are compatible with a mechanism of incorporation from the state of adsorption on the surface.

Estimates of the ratio $n_s/n_{s\infty}$ using the $j+/j-$ ratios above yield 0.82 at $C = C_e$, 0.9 at $C = 2C_e$, and 0.93 at $C = 3C_e$. Typically, in considerations of the surface diffusion mechanism, it is assumed that one adsorption site is equivalent to one lattice site so that $n_s/n_{s\infty} = 1$ corresponds to a full crystal layer. If this were the case here it is unlikely that the closely packed adsorbed molecules would have the surface mobility required for growth. This contradiction suggests that the molecular adsorption sites are not the crystal lattice sites in the layer under construction. The most likely candidates for adsorption sites are the three types of surface vacancies, discussed in ref. [22]. As shown below, see also [131], the surface density of these defects is up to 10%, with distances between them 2–5 molecular sizes. Note that assuming adsorption on such sites would require significant
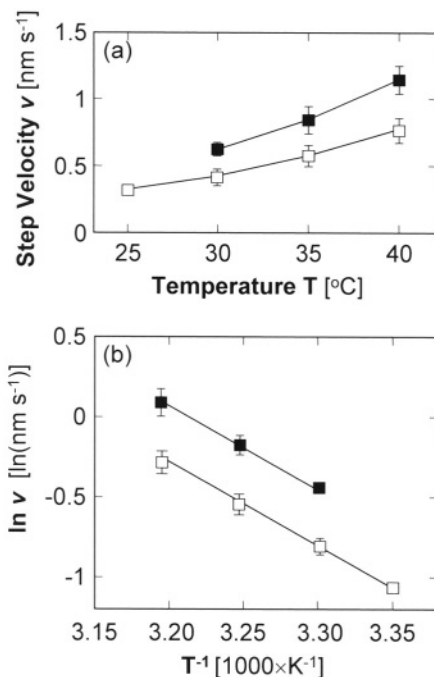
FIGURE 5.22. Dependencies of the step velocity v for growth of ferritin on the temperature (a), and in Arhenius coordinates (b). Solid squares at $C/C_e = 4$, open squares at $C/C_e = 3$. For each point, positions of advancing steps were compared in sequences of molecular resolution *in-situ* AFM images; ~20 such determinations of v were averaged. The error bars represent the 90% confidence interval of the average. From ref. [28].

modifications in the surface diffusion model: (i) since their elastic energy varies [131], this would mean variable adsorption energy, contrary to a basic assumption of Langmuir adsorption; (ii) the exchange of molecules between the randomly distributed non-identical sites may follow unusual statistics and dynamics. It is conceivable that the suspected unconventional adsorption state may be the main factor underlying the short characteristics surface diffusion length, discussed above.

For further tests of the applicability of growth mechanism to ferritin and apoferritin crystallization, we examine the step velocity law in eq. (29). The only unknown parameter here is the energy barrier U_{max}. Determinations of v at four temperatures and two ferritin concentrations in Figure 5.22 yield $E_{total} = 41 \pm 3$ kJ/mol. In eq. (29), C_e [70] and Ω do not depend on temperature, Λ is about the size of a few water molecules and in a first approximation does not depend on T [119]. For a molecule following the Stokes law, $D = D_0 \exp(-E_{visc}/k_B T)$, where E_{visc} is the temperature factor in an Arhenius-type expression for the dependence of the solvent viscosity on temperature. For NaCl solutions in Na acetate buffer it is $E_{visc} = 7.4$ kJ mol^{-1} [34]. As shown in [22], $\bar{n}_k$ has a weak near-exponential dependence on T through the kink energy $w = 3.8$ kJ mol^{-1}. This leaves for $U_{max} \approx 30$ kJ mol^{-1}. This value is close to the 28 kJ mol^{-1} found as the average over systems ranging from inorganic salts, through organics, to proteins and viri [104].

Substituting these value of U_{max} into eq. (29), we get at $C/C_e = 2$, $v = 0.0014$ nm s^{-1}, and at $C/C_e = 3$, $v = 0.0028$ nm s^{-1}. These values are more than two orders of magnitude
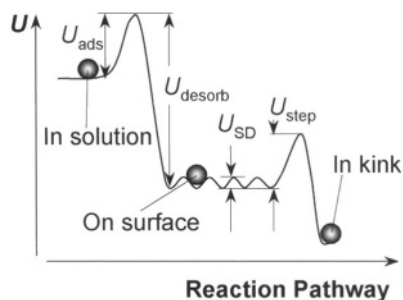
FIGURE 5.23. The energy landscape of the surface diffusion mechanism. For notations, see text. After ref. [173].

lower than actually observed. The measured values of 0.20 and 0.31 nm/s would require $U_{max} \approx 18 \text{ kJ mol}^{-1}$, beyond the range of the determination in Figure 5.22. This discrepancy supports the assertion that the direct incorporation mechanism is inapplicable to the growth of ferritin. We conclude that a mechanism involving adsorption on the terraces better corresponds to the available data for ferritin. As noted above, in the ferritin/apoferritin system the steps only exhibit attraction at very short separations. We conclude that the characteristic surface diffusion length [63] must be shorter than a few lattice parameters to account for this. Note that an investigation limited to data on the mesoscale step kinetics would have concluded that the growth mechanism is direct incorporation.

A relevant question is why the energetics of the system select the surface diffusion mechanism over the direct incorporation. This question can only be addressed with the molecular-level data available for the system. We note that when the surface diffusion mechanism operates, the energy barrier determined from the data in Figure 5.22 is a function of the barriers of the elementary steps of this mechanism and should be denoted as U_{sum}. As shown in [103,119] $U_{sum} = U_{ads} - U_{desorb} + U_{SD} + U_{step}$, which are the barriers, respectively, for adsorption, desorption, surface diffusion, and incorporation into the step, Figure 5.23. Since the energy effect of one intermolecular bond of ferritin should be equal to that of apoferritin, $\phi \approx 3k_B T = 7.4 \text{ kJ mol}^{-1}$ [22], we can safely assume that for adsorption–desorption on a (111) f.c.c. surface, $U_{ads} - U_{desorb} = \Delta H_{ads} = -3\phi = -22 \text{ kJ mol}^{-1}$. Ignoring interactions between the adsorbed molecules, the lowest possible value of U_{SD} occurs when only one bond is broken upon passage between two adsorption sites, hence $U_{SD} \geqslant \phi$. This yields $U_{step} \leqslant 44 \text{ kJ mol}^{-1}$, similar to the ADP value [119]. Since an equal number of bonds, three, are created during adsorption and incorporation into the step, we can roughly assume $U_{ads} \approx U_{step}$. Thus, the highest barrier encountered by a molecule en route to the kink is $\leqslant 44 \text{ kJ mol}^{-1}$. For direct incorporation into kinks, for which all of the six bonds are created simultaneously, $U_{kink} \sim U_{ads} + U_{step} \approx 88 \text{ kJ mol}^{-1}$. A crude estimate yields that this would make growth via this pathway slower by a factor of $\sim \exp[(88000 - 44000)/RT] \sim 10^8$.

5.9. IMPURITY-INDUCED LATTICE DEFECTS

Incorporation of impurities (other proteins or macromolecules or modifications of the native protein) having sizes similar to those of the crystallizing proteins has been identified

as a major factor of protein crystal imperfection [132–135]. Recent evidence suggests that other proteins are more readily removable upon purification [86,136] and even at high levels in the solution their incorporation into the crystals may be low [137]. Thus, in many cases, the impurity species responsible for the deterioration of the crystal quality are non-dissociable aggregates (oligomers, clusters) of native protein molecules [138,139].

While the mechanisms leading to relatively perfect protein crystals have been studied in great detail at both the mesoscopic [16,19,140] and the molecular level [5,20–22,141], only a few of the processes leading to defects have been monitored [142–144]. Below I summarize data that characterize at the molecular level the processes with the participation of impurity species that accompany crystallization: adsorption at the growth interface, incorporation be the growing step, resulting defects, and associated lattice strain and potential plastic deformations such as mosaicity.

It has been shown that the major contaminants are ferritin and apoferritin species with molecular masses double that of the native proteins [86]. The levels of these impurities can be brought down to at most ~5%; over 30 days or more, the dimers are regenerated. Thus, it was found that after storage for a year at 5°C the dimer concentration reached as high as 40% (w/w) [86]. A static and dynamic light scattering investigation revealed that the likely shape of the dimer is of two bound monomer spheres [35]. The same study found that dimer molecules attract in a solution in which the monomers strongly repel, suggesting a partial unfolding of the monomers upon dimerization that exposes the attractive hydrophobic residues [35].

5.9.1. Characterization of the crystal surface during growth

Figure 5.24 figure illustrates the three common types of defects observed on the surfaces of ferritin and apoferritin crystals: single-molecular-site vacancies, triple vacancies (trivacancies) and trivacancies containing a species to be identified below. These defects exist for unlimited time in the top surface layer of both ferritin and apoferritin crystals under all studied growth conditions, at supersaturations as high as 3.8 and at conditions close to equilibrium. Sometimes, clusters of four or five vacancies exist for a few minutes after a growing layer surrounds an underlying defect. They turn into trivacancies by incorporating one or two molecules. Figure 5.24 also shows about 20 unknown heterogeneities adsorbed on the surface. The acts of adsorption are random events, independent of the terrace age. Adsorption on a fresh surface may occur after < 1 s: for instance, a heterogeneity molecule is present close to the edge of step 2 in Figure 5.24 where the surface age is ~ 1 s.

The identification of the heterogeneities, the correlation between these formations and the defects, and the consequences for the crystal perfection are the subject of the discussion below.

5.9.2. Identification of the adsorbed heterogeneity molecules

Since the molecular dimer is the predominant impurity present in solutions of both ferritin and apoferritin [86], and it is the impurity preferentially incorporated into the respective crystals [137], we suspect that the adsorbed heterogeneities are these dimers. However, the image of an adsorbed cluster is a convolution of the cluster shape and its molecular vibrations, with effects due to multiple AFM tips, and this precludes unambiguous AFM
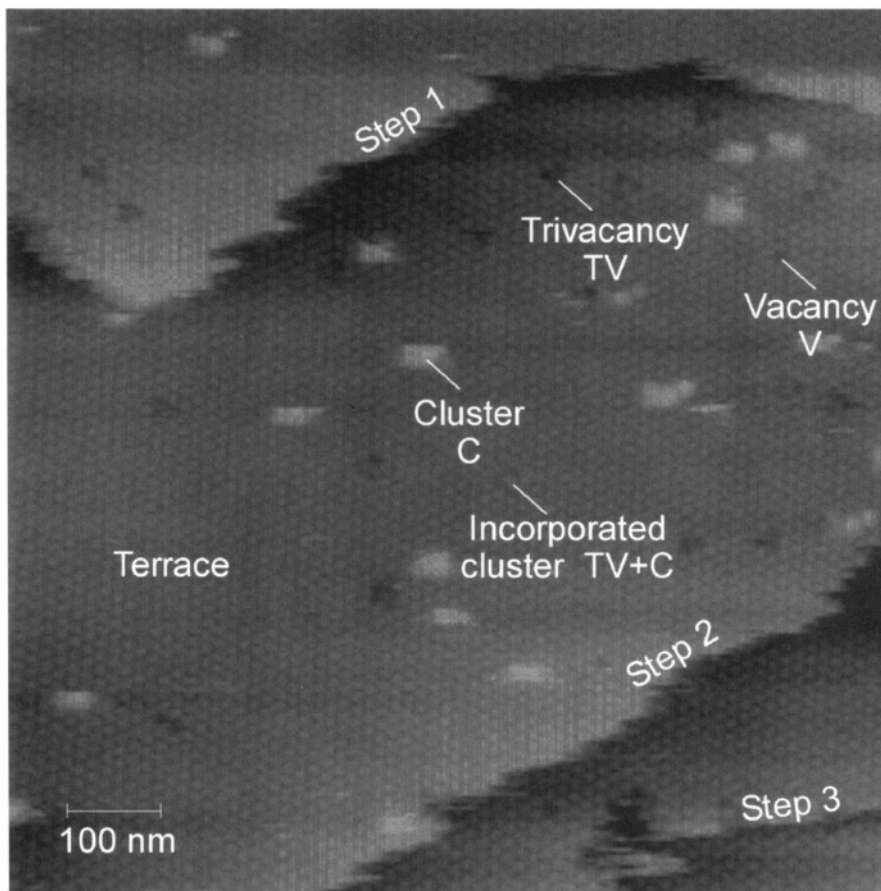
FIGURE 5.24. *In-situ* atomic force microscopy images of a ferritin surface crystal growing from a solution containing $1 \, \text{mg ml}^{-1}$ ferritin in 2.5% $CdSO_4$ and 0.05 M acetate buffer with pH 4.5. Note the growth steps with adsorbed impurity clusters and related point defects on the terraces between the steps. From ref. [131].

identification. Monitoring a step approach and incorporate the cluster in Figure 5.25 removes these obscuring effects—Figure 5.25b and c show that the heterogeneities are molecular dimers, in this case of apoferritin, shaped as two bound monomer spheres, and seen by electron microscopy [145]. This shape agrees with the result of a combined light scattering and chromatography characterization of the crystallizing solution in our laboratory [35]. The dimers in Figure 5.25 occupy three, rather than two monomer lattice sites, for a discussion of this phenomenon, see below. Numerous other image sequences with the two proteins showed that: (i) detachments of the heterogeneities are extremely rare and that most adsorbed dimers get incorporated into the crystal, and (ii) although the two-sphere shape was not always apparent, the incorporated heterogeneity molecules always displace three monomer molecules form the lattice. Based on these considerations, we conclude that all heterogeneities that adsorb on the surface and are seen in Figure 5.24 are the molecular dimers of, respectively, ferritin or apoferritin.
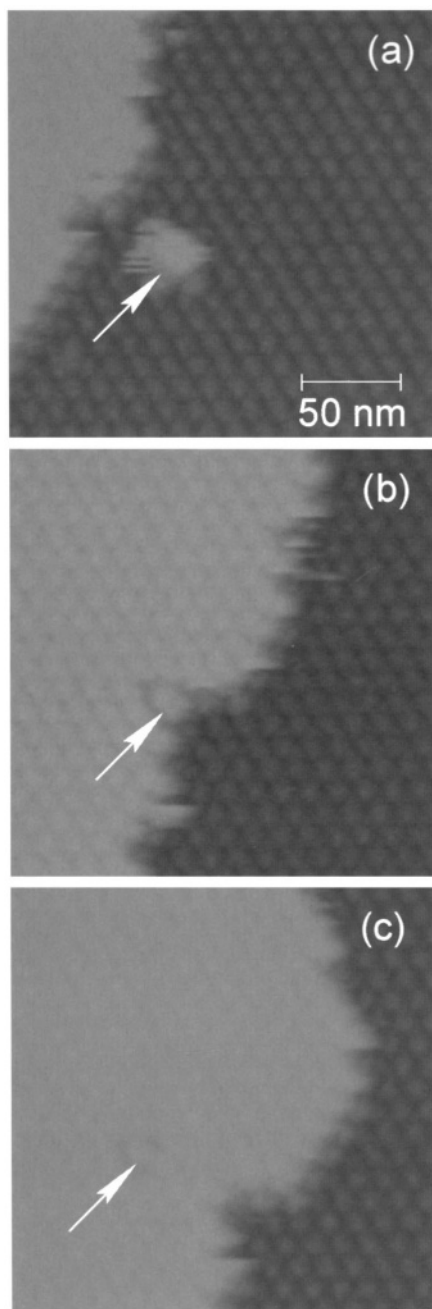
FIGURE 5.25. Incorporation of a cluster, indicated by arrows, by a step on the surface of an apoferritin crystal growing from a 0.12 mg ml^{-1} solution: (a) the cluster adsorbed on the crystal surface in front of the step. (b, c) The step incorporates the cluster and its shape is deconvoluted from vibration and multiple-tips effects to allow identification as a ferritin dimer. From ref. [131].

5.9.3. *The surface concentration of the dimer*

From Figure 5.24, the dimer surface concentration is $22\ \mathrm{dimers}\,\mu\mathrm{m}^{-2} = 2.2 \times 10^9\ \mathrm{dimers}\,\mathrm{cm}^{-2}$. A 10 nm thick layer above the crystal would have dimer concentration $2.2 \times 10^{15}\ \mathrm{dimer\,molecules\,cm}^{-3}$. This is 100–1000-fold higher than typical dimer concentrations in the bulk solution: 5% w/w of the dimer corresponds to 2.5 dimer molecule/100 monomer molecules or $3 \times 10^{12}\ \mathrm{dimer\,molecules\,cm}^{-3}$ in a $0.1\ \mathrm{mg\,ml}^{-1}$ solution. Note, however, that the surface concentration of the dimmers is likely reduced by the interactions with the AFM tip during imaging—we notice that after imaging for times of the order of 1/2 hour this concentration is reduced about twofold. The following considerations suggest that even stronger reduction of the surface concentration due to tip impact may occur immediately upon the commencement of imaging and, hence, remain undetected.

We use the fact discussed above that most adsorbed dimers are incorporated into the crystals. We determined the relative amount of dimers incorporated into the crystals by dissolving the crystals and quantifying the monomer and dimer concentrations in the resulting solution. The found dimer segregation coefficient was between 2.5 and 4 [137], i.e., there is that-fold more dimers per monomer molecule in the crystals than in the solution. One square micrometer of the top crystal layer contains about 12000 monomers that occupy triangles of 13 nm on a side. Hence, since all adsorbed dimers are incorporated, the expected surface dimer concentration would be $>750\ \mu\mathrm{m}^{-2}$. Thus, even in the gentler tapping mode, atomic force imaging cannot be used to determine the surface concentration of the adsorbed dimers.

There are two possible selection criteria that determine if an adsorbed heterogeneity molecule will be removed by the AFM tip, or will stay and be incorporated as we watch it. (i) There are two dimer populations, and only one of them, namely the two-sphere-shaped dimer, is sufficiently strongly adsorbed. (ii) All dimers are identical, but we only see those adsorbed at special surface sites; the reasons for the strong adsorption at these sites cannot be identified by the techniques used in this study. In view of the light scattering and gel electrophoresis results in refs [35,86] that show that in ferritin and apoferritin solutions there is a single dimer population with the same shape as the one revealed by AFM, we conclude that possibility (i) is unlikely. Then, (ii) acts and the AFM observations of the dimer incorporation and its consequences for the crystal quality are relevant to the understanding of the crystallization and crystal perfection of these proteins.

5.9.4. *Surface properties and formation mechanisms of the dimer*

Figure 5.25c shows that (i) upon incorporation the dimers occupy three, rather than two, monomer lattice sites. Furthermore, as shown in refs [35,106] (ii) in the absence Cd^{2+} the overall interactions between native monomers are repulsive and should preclude dimer formation; (iii) dimers are present in the initial solution prior to the addition of the $\mathrm{CdSO_4}$ precipitant.

These observations suggest that the arrangement of the two monomers in the dimer is different from that between two neighboring monomers in the lattice. Thus, only monomers that have undergone a partial unfolding, e.g., a rearrangement of the 24 subunits, or opening of the loop regions in the peptide chain to reveal the hydrophobic regions of the helices, can partake into the formation of dimers. This unfolding only slightly changes the shape and size of the constituent monomers (strong changes would be detectable by the light

scattering technique), and exposes groups that locally increase the attraction between the monomers. Still, the changes are sufficient to preclude incorporation of the dimers in the ferritin and apoferritin crystal lattices as integral components, and to result in the displacement of three monomers seen in Figures 5.24 and 5.25. The increased hydrophobicity of the dimer surface underlies the attraction between the dimers under conditions where the monomers strongly repel [35]. The exposed attractive contact sites are the likely cause for the increased attraction of the dimers to a monomer crystal surface and for the preferential adsorption of the dimers on the crystal surface. Furthermore, note that since the dimers are not generated by addition of Cd^{2+} ions to the solution, they are not a preliminary step in the ferritin and apoferritin crystal nucleation or growth [35,131].

5.9.5. Dimer incorporation by the growing steps

A possible mode of the effects of impurity molecules on the spreading of layers during growth of various materials has been postulated by Cabrera and Vermileya [146]. According to this mechanism, impurities that are strongly adsorbed on the terraces between steps should impede their advancement. The characteristic capillary length—the radius of the two-dimensional critical nucleus—is the parameter that determines the velocity of the steps squeezing between the impurity stoppers [147,148]. This mechanism has been supported by indirect evidence form crystallization experiments with various materials [64,149], including proteins [150,151] however, since imaging of individual adsorbed molecules on the surface of a growing crystal was not possible, direct visualization of the action of this mechanism and possible deviations from the original postulate was lacking.

In Figure 5.26, we monitor the interactions between two advancing steps and the surface defects and adsorbed dimers. Figure 5.26a shows two clusters adsorbed on the lower terrace. This lower terrace also contains a trivacancy with an incorporated dimer, and a vacancy. Figure 5.26b and c shows that the growth steps are retarded not only by adsorbed dimers as in Figure 5.26d, but by the trivacancy as well. Other similar sequences demonstrate retardation by single vacancies and trivacancies.

With all types of stoppers, a channel with the stopper at the far end forms as shown in Figure 5.26b for the dimer-containing trivacancy. This channel does not close until a certain critical number n^* of molecules in the steps forming the channel is reached. For this and other series of images at $\sigma = 1.6$, the value of n^* that occurred most frequently was 4. At $\sigma = 1.1$ the most frequently occurring n^* increased to 6, i.e., n^* roughly scales with $1/\sigma$. This appears to suggest that the short steps are retained because of capillarity factors, as suggested by theory. To test this hypothesis, we recall that at the scales of a few molecules as here, the excess capillary energy corresponds to energy of the unsaturated bonds of the molecules at the end of the channel. Detailed analyses lead to the discrete form of the Gibbs–Thomson relation [58,59,81]

$$\Delta\mu = \phi/n^*, \tag{34}$$

where $\phi = 3.2k_BT$ is the free energy of the bond between two molecules in the crystal [22]. Substituting the values of n^* in the eq. (34) and using the above ϕ, we get $\Delta\mu$ values about half of the values at which the respective n^* were found. This suggests a deviation from the classical Cabrera–Vermileya theory: that the elastic strain field around defect, discussed below, may also affect the behavior of the steps around the cluster [131].
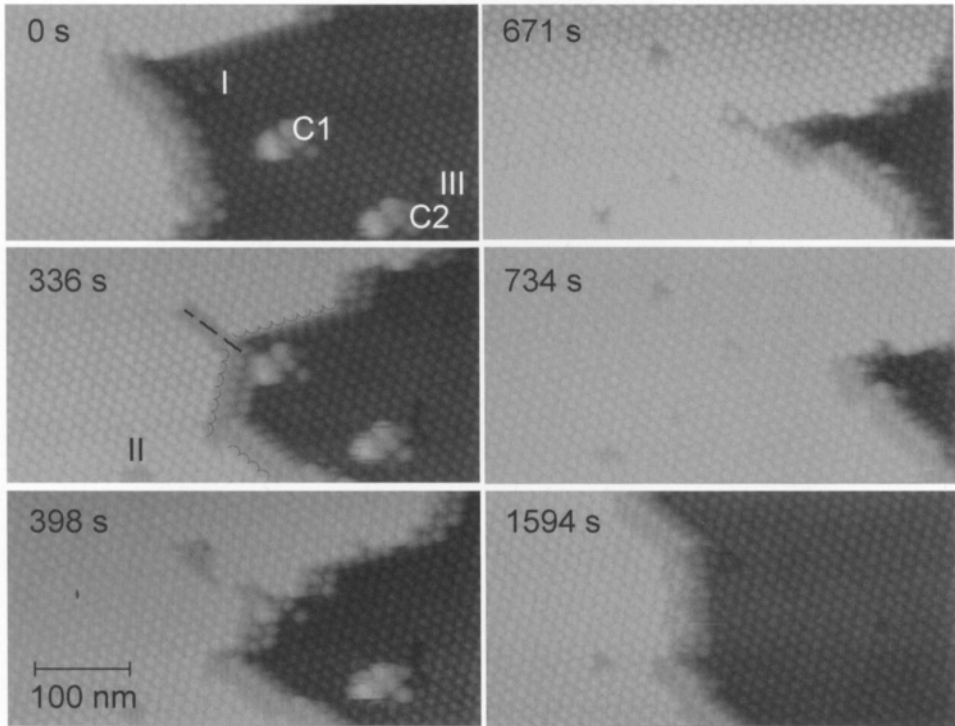
FIGURE 5.26. Creation and evolution of defects on an apoferritin crystal at supersaturation $\sigma = 1.6$. (a–e) Interactions between advancing step and trivacancies with a cluster, vacancy, and two clusters, C1 and C2. Dashed line indicates channel formed at detect I. (f) A new step is stopped by trivacancies with clusters, empty trivacancies, and single vacancies; a trivacancy is created in the new layer on top of the one first seen in (b) after a shift of the view field. From ref. [22].

5.9.6. Formation and replication of defects

Steps longer than n^* are not hindered by the line tension factors and the elastic barriers and move to close the channel in Figure 5.26c. However, the elastic field does not allow molecules to attach on top of the trivacancy with the cluster, and an empty trivacancy is created in the next layer, Figure 5.26c–e. Cluster C2 is pushed away by the step. The vacancy next to it in Figure 5.26a, after some configurational variations in Figure 5.26b–d, is replicated in the advancing layer, Figure 5.26f. Figure 5.26f also shows that the third layer is retarded by all the defects in the second layer and the trivacancy in the second layer in Figure 5.26b is also replicated in the third layer.

Thus, Figure 5.26 illustrates the series of transformations: adsorbed cluster $\rightarrow$ trivacancy with a cluster $\rightarrow$ trivacancy in subsequent crystal layers. In numerous similar image sequences, we found that both empty and cluster-containing trivacancies may produce a single vacancies and trivacancies and single vacancies often replicate in the next layer. A column of vacancies may be terminated by the incorporation of a molecule. The resulting average length of these cigar-shaped cavities is about 5 crystal layers. Note that we never saw point defects that were not initiated by a cluster adsorbed on the crystal surface. Unlike Schottky and Frenkel defects [152,153], none of the defects observed here
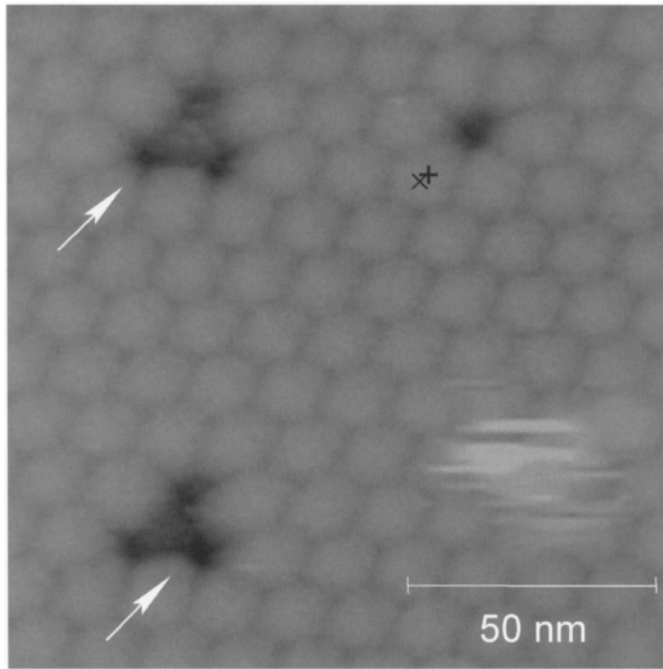
FIGURE 5.27. Lattice strain in a apoferritin crystal introduced by dimer molecules. X indicates anticipated location of molecule center based on the three molecular rows that it belongs to. (+) mark actual location of molecule center, shifted by ~1.5 nm because of the vacancy next to it. Arrows indicate other monomers around the three types of point defects that are shifted from their crystallographic positions. From ref. [131].

are equilibrium defects induced by the thermal vibrations of the lattice molecules and their lattice sites have never been occupied by apoferritin monomer molecules. Since they are bound to the incorporated cluster, these defects have zero translational mobility [131].

5.9.7. Consequences for crystal quality: lattice strain and mosaicity

The strain caused by the various defects in a stack is evidenced in Figure 5.27 by the ~1–2 nm displacements of the molecules around the defects from their crystallographic positions (intermolecular distance is ~13 nm). With nine lattice monomers around a trivacancy, average height of defect stack of five layers, and one dimer molecule per of ten or twenty monomers, the strain should affect all lattice sites and have noticeable contribution to the background X-ray scattering [131].

Even stronger effects on the crystal quality and utility for diffraction studies arise due to the impurity-induced strain. Mosaicity is one of them, and a mechanism leading to it and based on impurity-induced strain is summarized below. The elastic energy of a strained crystal increases as the crystal grows proportionally to L^3, L being the crystal size. On the other hand, the emergence of unstrained blocks separated by a dislocation network would minimize the crystal's energy with the grain boundary energy $\sim L^2$. The balance between the elastic strain and the interblock surface energy determines the critical size for the onset of mosaicity [135,154].

Indeed, mosaic blocks ∼20–50 μm wide were observed for ferritin and apoferritin crystals larger than ∼200 μm growing from solutions 2–3 months old in which the concentration of the dimers is higher [86]. Growth steps were confined within the individual blocks and the growth of each block was independent from the others. Similarly, independent growth of blocks of a satellite tobacco mosaic crystal were reported in ref. [142].

5.9.8. *Other sources of mosaicity*

Arguments have been put forth that crystals' quality and utility for diffraction studies is only affected by short-scale molecular disorder and not by mosaicity and block structures [155]. There are examples in which heavily mosaic crystals diffract to high resolution [156]. On the other hand, the diffraction resolution is determined by the signal-to-noise ratio of high-index reflections. Since high-index crystal planes have low molecular density, larger areas of rotationally and translationally aligned molecules are needed to enhance the intensity of the reflections from these planes. Hence, crystal imperfections on the scale of microns could affect the diffraction resolution obtainable from a crystal [157]. Mosaicity, striae and block structures often lead to broader or split diffraction spots, and, hence, lower accuracy of the structure determination [158–160]. However, if the crystal consists of a few large blocks, the beam in a X-ray diffraction experiments can be focused on only one of these blocks, and high resolution structure determinations can still be achieved [156,161]. Hence, studies of mosaicity and the molecular mechanisms leading to it are relevant to the understanding of the factors underlying crystal perfection.

Figure 5.28 illustrates the incorporation of a formation that has landed on the growing crystal surface of an apoferritin crystal in Figure 5.28a. Besides this formation, heterogeneities, likely the apoferritin molecular dimer discussed above, are also adsorbed on the surface. Their surface concentration is roughly equal to the one in Figure 5.24. Zooming in, we find in Figure 5.28b that the formation is an apparently perfect microcrystal consisting of three layers—the section in Figure 5.28c was taken after the incoming layer visible in Figure 5.28a surrounded the microcrystal—with about 60 molecules in each layer. Upon landing, the microcrystal may have covered an adsorbed heterogeneity cluster and this could explain its inclination with respect to the surface in Figure 5.28c.

After about 15 min new crystal layers reach the microcrystal and surround it, Figure 5.28d and e. Judging from the orientation of the {110} molecular rows in the microcrystal and the large crystals in Figure 5.28b, d and e, the two crystals are in registry. Still, the tilt seen in Figure 5.28c leads to a far from perfect fit between the microcrystal and the surrounding material—a boundary with a thickness comparable to the molecular size obtains in Figure 5.28d and e. In analogy to the strain caused by a single vacancy in Figure 5.27, we can expect this boundary to induce significant strain in the lattice of the large crystal. Unfortunately, the detrimental effects for the crystal quality from the incorporation of the microcrystal are not limited to this boundary and the strain associated with it. Figure 5.28e–i show that even after the microcrystal is covered with new layers, a cluster of vacancies forms all the way up to the 5-th layer above it. This vacancy cluster is due to the strain caused by the trapped microcrystal in the layers above it. It is quite surprising that the strain field around a microcrystal has the same characteristic lengthscale as the strain field around a single heterogeneity molecule or a vacancy in the lattice. As a result, the perturbation in the lattice due to the trapping of larger objects is localized around these objects.
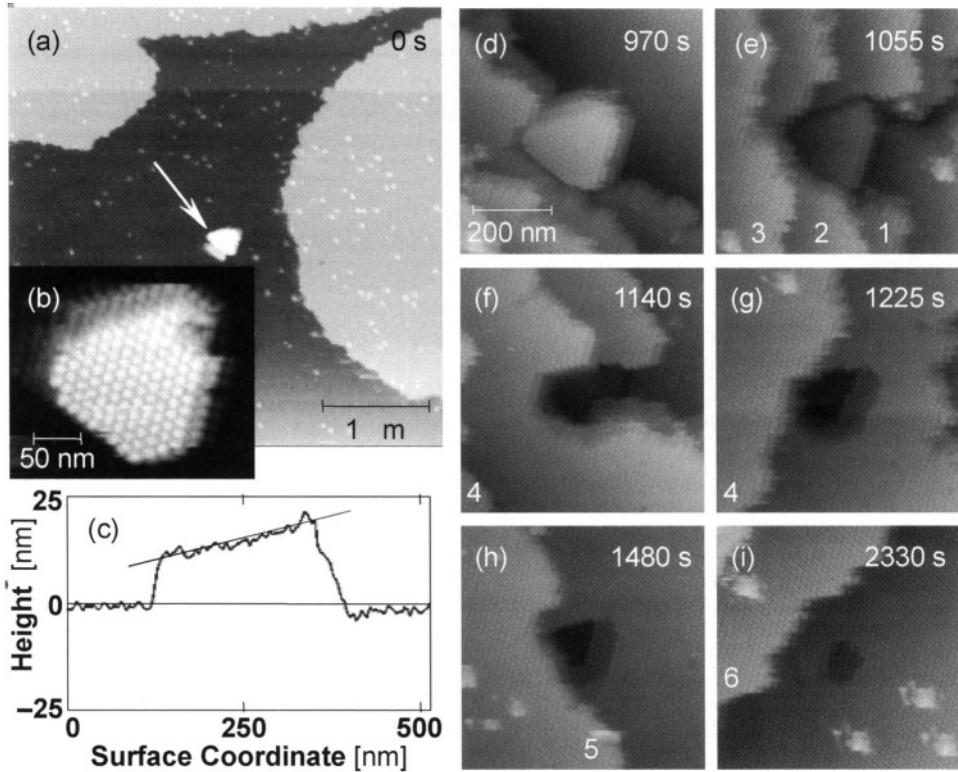
FIGURE 5.28. Incorporation of a microcrystal by a growing apoferritin crystal. (a) A microcrystal, identified by zoom in (b) and indicated by an arrow lands on the surface. (c) Height profile along diagonal in (b) showing the inclination of the microcrystal with respect to the underlying plane of the large crystal. (d–i) Stages of the incorporation of the microcrystal, times shown are after the image in (a) was recorded; the Arabic numerals at the bottom of (e–i) count the layers on top of the incorporated microcrystal. From ref. [131].

There are numerous observations of the incorporation of microcrystals in protein crystals in literature [15,116,141–143,162,163]. The novel insight contributed by the molecular resolution images in Figure 5.28 consists in the finding that even microcrystals that appear well aligned with the underlying lattice cause significant lattice strain, and that the strain field stretches to about five molecular dimensions around the trapped microcrystal [131].

5.9.9. Can trapping of microcrystal be avoided?

Obviously, if the growth conditions are chosen such that no nucleation of microcrystals occurs, there will be no trapping. However, often, as in the cases of ferritin and apoferritin, the growth conditions change during growth due to, e.g., solution depletion, and may pass through a set inductive of nucleation. As a second line of defense, it has been argued that in a microgravity environment, for instance aboard a spacecraft, the microcrystals will not of sediment on the growing crystal [164].

Other than sedimentation driven by Earth's gravity, a microcrystal may reach the surface of a growing larger crystal by Brownian diffusion. Let us consider these two transport

pathways. The velocity of sedimentation v of a particle of radius r with density ρ_1 falling in a liquid with viscosity η and density ρ_2 is $v = 2r^2(\rho_1 - \rho_2)g/9\eta$, where g is the free fall acceleration. This velocity is determined by the balance of the buoyancy, $(4/3)\pi r^3(\rho_1 - \rho_2)g$, and the viscous, $6\pi\eta r v$, forces [71,165]. For the microcrystal in Figure 5.28, $r \approx 130$ nm, and assuming density difference between crystal and solution similar to that of lysozyme $\rho_1 - \rho_2 \approx 0.3 \, \mathrm{g\,cm}^{-3}$ [166], we get $v = 1.2 \times 10^{-6} \, \mathrm{cm\,s}^{-1}$. If the microcrystals form at a height of about $100 \, \mu$m, they would take more than 2 hours to reach the surface. The corresponding characteristic Brownian diffusion time τ to reach the substrate for a cluster formed at a distance $x = 100 \, \mu$m from the surface can be evaluated from Einstein's relation $x^2 = 2D\tau$. A lower estimate for cluster diffusivity D can be obtained form the diffusivity of single apoferritin molecules, $3.2 \times 10^{-7} \, \mathrm{cm}^2/\mathrm{s}$ [35,106] using Stokes low and assuming that the microcrystal behaves like a particle with 10 molecules at an edge: $D \approx 3.2 \times 10^{-8} \, \mathrm{cm}^2/\mathrm{s}$. Substituting, $\tau \approx 1500 \, \mathrm{s} \approx 25$ min. Hence, Brownian diffusion is a more efficient method of transfer of microcrystals to the surface of a large crystal than sedimentation, and even in the absence of gravity, microcrystals can still reach the surface and get trapped [131].

5.9.10. Is there a critical size for the onset of mosaicity?

To further explore the onset of a mosaic block structures in ferritin and apoferritin crystals larger than $200 \, \mu$m, we grew numerous crystals of the two proteins under careful microscopic observation. Typically, crystals smaller than 200–$300 \, \mu$m appeared perfect without any visible boundaries or any other defects, an example is shown in Figure 5.29a. As they grew larger, one and then more boundaries appeared, separating the crystal into two, three, etc., blocs as in Figure 5.29b. The sizes of these blocs varied between 20 and about $100 \, \mu$m. If older solutions that contain higher levels of the dimer are used, the size at which the crystal breaks into individual domains shifts downward.

Figure 5.29b also shows the trapping of a few 10–$15 \, \mu$m crystals and smaller objects. Since the strain filed around the trapped crystals and objects is short ranged, and there is relatively few of them, we conclude that their contribution to the overall strain in the crystal is insignificant. Furthermore, although we did not carry out X-ray characterization of the grown crystals, we offer that since the trapped crystal and objects occupy a small fraction of the total volume of the large crystal, diffraction from them is a minor contribution to the mosaicity of the diffraction pattern.

These observations of the onset of mosaicity show that (i) there is critical size, below which even defect-rich crystal will not be mosaic; (ii) trapping of smaller crystals does not significantly contribute to the mosaicity; and (iii) mosaicity is primarily due to the accumulation of strain associated with the incorporation of the ferritin and apoferritin molecular dimers into the lattice.

Theoretical predictions of the critical size for the onset of mosaicity due to the elastic strain associated with the incorporated impurity molecules have only been performed for the protein lysozyme. Using a recently determined Young modulus for lysozyme crystals, the critical size was evaluated to be in the range 100–$500 \, \mu$m [135]. As with ferritin and apoferritin, the typical impurities for this protein are covalently bound dimers at ~ 1–2% of the dry protein mass [136,167]. They cannot be fully removed, recur after purification, and readily incorporate into crystals. Observations with lysozyme crystals, discussed in [131],
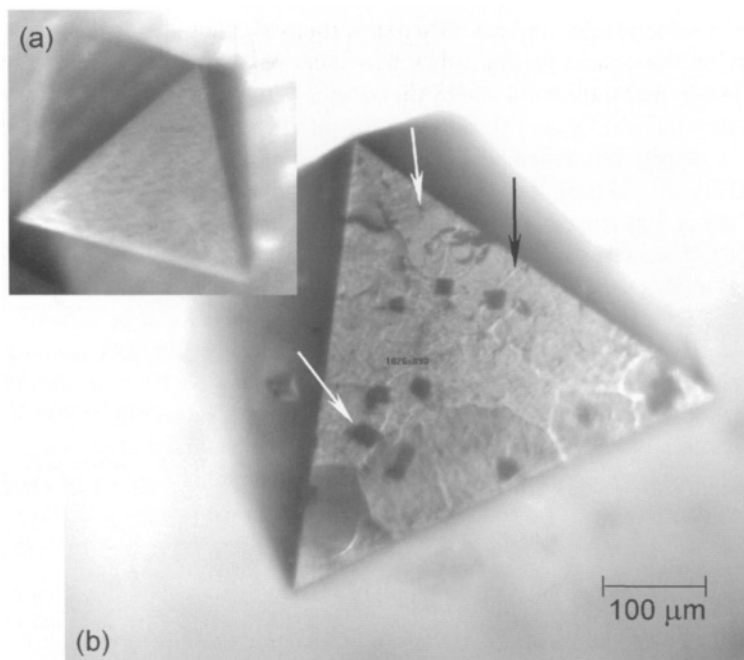
FIGURE 5.29. Optical micrograph of ferritin crystals. (a) Typical crystal smaller than ~ 300 μm—no detects or block boundaries are discernible. (b) Typical crystal larger than ~ 300 μm—black arrow indicates a block boundary, white arrows indicate incorporated crystals and microscopic objects. From ref. [131].

reveal that below ~ 170 μm, the crystal consists of a single block. This is the critical size for the onset of mosaicity, within the range of the theoretical estimates in ref. [135]. Crystals grown from solutions containing lower impurity amounts did not reveal such mosaic structure. This allows us to correlate the mosaicity to the lattice strain introduced by the impurity incorporation.

Since this critical size for the onset of this type of mosaicity for ferritin and apoferritin is of ~ 200 μm is in the range expected and demonstrated for lysozyme, we may conclude that the Young modulus of these two crystals is close and does not differ much from the one for lysozyme.

The existence of a critical size for the onset of mosaicity suggests that in some cases smaller crystal may be more suitable for diffraction studies than larger crystals. On the other hand, for other proteins, the critical size may be too small for practical use of sub-critical crystals. Note that the perfect faceting of a crystal, such as the one in Figure 5.29, does not indicate the lack of mosaicity. High magnification optical observations with specialized techniques are required to see the block structure.

ACKNOWLEDGEMENTS

REFERENCES

1. P.G. Vekilov and A.A. Chernov, The physics of protein crystallization, in: Eds H. Ehrenreich and F. Spaepen, *Solid State Physics,* Vol. 57 (Academic Press, New York, 2002) pp. 1–147.

2. N. Asherie, A. Lomakin and G.B. Benedek, Phase diagram of colloidal solutions, *Phys. Rev. Lett.* **77**, 4832–4835 (1996).

3. P.R. ten Wolde and D. Frenkel, Enhancement of protein crystal nucleation by critical density fluctuations, *Science* **277**, 1975–1978 (1997).

4. M.G. Noro, N. Kern and D. Frenkel, The role of long range forces in the phase behavior of colloids and proteins, *Eurpophys. Lett.* **48**, 332–338 (1999).

5. S.-T. Yau, D.N. Petsev, B.R. Thomas and P.G. Vekilov, Molecular-level thermodynamic and kinetic parameters for the self-assembly of apoferritin molecules into crystals, *J. Mol. Biol.* **303**, 667–678 (2000).

6. P.K. Hansma, J.P. Cleveland, M. Radmacher, D.A. Walters, P. Hillner, M. Bezanilla, M. Fritz, D. Vie, H.G. Hansma, C.B. Prater, J. Massie, L. Fukunaga, J. Gurley and V. Elings, Tapping mode atomic force microscopy in liquids, *Appl. Phys. Lett.* **64**, 1738–1740 (1994).

7. A. Noy, C.H. Sanders, D.V. Vezenov, S.S. Wong and C.M. Lieber, Chemically sensitive imaging in tapping mode by chemical force microscopy: relationship between phase lag and adhesion, *Langmuir* **14**, 1508–1511 (1998).

8. D.M. Lawson, P.J. Artymiuk, S.J. Yewdall, J.M.A. Smith, J.C. Livingstone, A. Trefry, A. Luzzago, S. Levi, P. Arosio, G. Cesareni, C.D. Thomas, W.V. Shaw and P.M. Harrison, Solving the structure of human H ferritin by genetically engineering intermolecular crystal contacts, *Nature* **349**, 541–544 (1991).

9. P.D. Hempstead, S.J. Yewdall, A.R. Fernie, D.M. Lawson, P.J. Artymiuk, D.W. Rice, G.C. Ford and P.M. Harrison, Comparison of the three dimentional structures of recombinant human H and horse L ferritins at high resolution, *J. Mol. Biol.* **268**, 424–448 (1997).

10. S.D. Durbin and W.E. Carlson, Lysozyme crystal growth studied by atomic force microscopy, *J. Crystal Growth* **122**, 71–79(1992).

11. S.D. Durbin, W.E. Carson and M.T. Saros, In situ studies of protein crystal growth by atomic force microscopy, *J. Phys. D: Appl. Phys.* **26**, B128–B132 (1993).

12. P.E. Hillier, S. Manne, P.K. Hansma and A.J. Gratz, Atomic force microscope: a new tool for imaging crystal growth processes, *Faraday Discuss.* **95**, 191–197 (1993).

13. A.J. Gratz, P.E. Hillner and P.K. Hansma, Step dynamics and spiral growth on calcite, *Geochimica and Cosmochimica Acta* **57**, 491–495 (1993).

14. A.J. Malkin, T.A. Land, Yu.G. Kuznetsov, A. McPherson and J.J. DeYoreo, Investigation of virus crystal growth mechanism by in situ atomic force microscopy, *Phys. Rev. Lett.* **75**, 2778–2781 (1995).

15. A. McPherson, A.J. Malkin and Y.G. Kuznetsov, The science of macromolecular crystallization, *Structure* **3**, 759–768 (1995).

16. A.J. Malkin, Y.G. Kuznetsov, T.A. Land, J.J. DeYoreo and A. McPherson, Mechanisms of growth of protein and virus crystals, *Nature Struct. Biol.* **2**, 956–959 (1996).

17. J.D. Ng, Y.G. Kuznetsov, A.J. Malkin, G. Keith, R. Giege and A. McPherson, Visualization of RNA crystal growth by atomic force microscopy, *Nucleic Acids Res.* **25,** 2582–2588 (1997).

18. J.J. DeYoreo, T.A. Land and B. Dair, Growth morphology of vicinal hillocks on the {101} face of KH_2PO_4: from step flow to layer-by-layer growth, *Phys. Rev. Lett.* **73**, 838–841 (1994).

19. T.A. Land, J.J. DeYoreo and J.D. Lee, An in-situ AFM investigation of canavalin crystallization kinetics, *Surf. Sci.* **384**, 136–155 (1997).

20. C.M. Yip and M.D. Ward, Atomic force microscopy of insulin single crystals: direct visulization of molecules and crystal growth, *Biophysical J.* **71**, 1071–1078 (1996).

21. C.M. Yip, M.R. DePhelippis, B.H. Frank, M.L. Brader and M.D. Ward, Structural and morphological characterization of ultralente insulin crystals by atomic force microscopy: evidence of hydrophobically driven assembly, *Biophysical J.* **75**, 1172–1179 (1998).

22. S.-T. Yau, B.R. Thomas and P.G. Vekilov, Molecular mechanisms of crystallization and defect formation, *Phys. Rev. Lett.* **85**, 353–356 (2000).

23. H. Lin, S.-T. Yau and P.G. Vekilov, Dissipating step bunches during crystallization under transport control, *Phys. Rev. E* **67**, 0031606 (2003).

24. M. Giesen-Seibert, R. Jentjens, M. Poensgen and H. Ibach, Time dependence of step fluctuations on vicinal copper (1119) surfaces investigated by tunneling microscopy, *Phys. Rev. Letters* **71**, 3521–3524 (1993).

25. M. Poensgen, J. Wolf, J. Frohn, M. Giesen and H. Ibach, Step dynamics on Ag(111) and Cu(100) surfaces, *Surface Science* **274**, 430–140 (1992).

26. N. Kitamura, M.G. Lagally and M.B. Webb, Real-time observations of vacancy diffsusion on Si(001)-(2x2) by scanning tuneling microscopy, *Phys. Rev. Lett.* **71**, 2081–2085 (1993).

27. B.S. Swartzentruber, Y.-W. Mo, R. Kariotis, M.G. Lagally and M.B. Webb, Direct determination of site and kink energeis of vicinal Si(001), *Phys. Rev. Lett.* **65**, 1913–1916 (1990).

28. K. Chen and P.G. Vekilov, Evidence for the surface diffusion mechanism of solution crystallization from molecular-level observations with ferritin, *Phys. Rev. E* **66**, 021606 (2002).

29. O. Gliko, N.A. Booth, E. Rosenbach and P.G. Vekilov, Phase-shifting interferometry for the study of the step dynamics during crystallization of proteins, *Crystal Growth and Design* **2**, 381–385 (2002).

30. K. Onuma, T. Kameyama and K. Tsukamoto, In-situ study of surface phenomena by real time phase shift interferometry, *Journal of Crystal Growth* **137**, 610–622 (1994).

31. A.A. Chernov, N.L. Rashkovich and A.A. Mkrtchan, Solution growth kinetics and mechanism: primatic face of KDP, *J. Crystal Growth* **74**, 101–112 (1986).

32. N.A. Booth, B. Stanojev, A.A. Chernov and P.G. Vekilov, Differential phase-shifting interferometry for *in-situ* surface characterization during solution growth of crystals, *Rev. Sci. Instr.* **73**, 3540–3545 (2002).

33. O. Gliko, N.A. Booth and P.G. Vekilov, Step bunching in a diffusion-controlled system: phase-shifting interferometry investigation of ferritin, *Acta Crystallogr. Section D* **58**, 1622–1627 (2002).

34. W.J. Fredericks, M.C. Hammonds, S.B. Howard and F. Rosenberger, Density, thermal expansivity, viscosity and refractive index of lysozyme solutions at crystal growth concentrations, *J. Crystal Growth* **141**, 183–192 (1994).

35. D.N. Petsev, B.R. Thomas, S.-T. Yau and P.G. Vekilov, Interactions and aggregation of apoferritin molecules in solution: effects of added electrolytes, *Biophysical J.* **78**, 2060–2069 (2000).

36. O. Gliko and P.G. Vekilov, Spatio-temporal step patterns during crystal growth in a transport controlled system, *J. Phys. Chem.* **106**, 11800–11804 (2002).

37. P.G. Vekilov, L.A. Monaco and F. Rosenberger, High resolution interferometric technique for in-situ studies of crystal growth morphologies and kinetics, *J. Crystal Growth* **146**, 289–296 (1995).

38. S.C. Choi, *Introductory Applied Statistics in Science* (Prentice Hall, Englewood Cliffs, NJ, 1978).

39. P.G. Vekilov, J.I.D. Alexander and F. Rosenberger, Nonlinear response of layer growth dynamics in the mixed kinetics–bulk transport regime, *Phys. Rev. E* **54**, 6650–6660 (1996).

40. E.C. Theil, Ferritin: structure, gene regulation, and cellular function in animals, plants and microorganisms, *Annual Reviews of Biochemistry* **56**, 289–315 (1987).

41. W.H. Massover, Ultrastructure of ferritin and apoferritin: a review, *Micron* **24**, 389–437 (1993).

42. P.M. Harrison and P. Arosio, The ferritins: molecular properties, iron storage function and cellular regulation, *Biochim. Biophys. Acta* **1275**, 161–203 (1996).

43. K.L. Taft, G.C. Papaefthymiou and S.J. Lippard, A mixed-valent polyiron oxo complex that models the biomineralization of the ferritin core, *Science* **259**, 1302–1305 (1993).

44. A.S. Pereira, P. Tavares, S.G. Lloyd, D. Danger, D.E. Edmondson, E.C. Theil and B.H. Huynh, Rapid and parallel formation of Fe^{3+} multimers, including a trimer, during H-type subunit ferritin mineralization. *Biochemistry* **36**, 7917–7927 (1997).

45. S. Gider, D.D. Awschalom, T. Douglas, S. Mann and M. Chaparala, Classical and quantum magnetic phenomena in natural and artificial ferritin proteins, *Science* **268**, 77–80 (1995).

46. D. Yang and K. Nagayama, Permeation of small molecules into the cavity of ferritin as revealed by proton nuclear magnetic resonance relaxation, *Biochem. J.* **307**, 253–256 (1995).

47. R.R. Crichton, J.A. Soruco, F. Roland, M.A. Michaux, B. Gallois, G. Precigoux, J.P. Mahy and D. Mansuy, Remarkable ability of horse spleen apoferritin to demetallate hemin and to metallate protoporphyrin IX as a function of pH, *Biochemistry* **36**, 15049–15054 (1997).

48. S. Levi, P. Santambrogio, A. Cozzi, E. Rovida, B. Corsi, E. Tamborini, S. Spada, A. Albertini and P. Arosio, The role of the L-chain in ferritin iron incorporation. Studies of homo and heteropolymers, *J. Mol. Biol.* **238**, 649–654(1994).

49. A. Treffry, Z. Zhao, M.A. Quail, J.R. Guest and P.M. Harrison, Iron(II) oxidation by H chain ferritin: evidence from site-directed mutagenesis that a transient blue species is formed at the dinuclear iron center, *Biochemistry* **34**, 15204–15213 (1995).

50. S. Allen, X. Chen, J. Davies, M.C. Davies, A.C. Dawkes, J.C. Edwards, C.J. Roberts, J. Sefton, S.J. Tendler and P.M. Williams, Detection of antigen-antibody binding events with the atomic force microscope, *Biochemistry* **36**, 7457–7463 (1997).

51. M. Muschol and F. Rosenberger, Interaction in undersaturated and supersaturated lysozyme solutions: static and dynamic light scattering results, *J. Chem. Phys.* **103**, 10424–10432 (1995).

52. S.F. Sun, *Physical Chemistry of Macromolecules* (John Wiley & Sons, New York, 1994).

53. T.L. Hill, *Introduction to Statistical Thermodynamics* (Dover, New York, 1986).

54. A. George and W.W. Wilson, Predicting protein crystallization form a dilute solution property, *Acta Crystallogr. Section D* **50**, 361–365 (1994).

55. D.F. Rosenbaum, P.C. Zamora and C.F. Zukoski, Phase behavior of small attractive colloid particles, *Phys. Rev. Lett.* **76**, 150–153 (1996).

56. B. Guo, S. Kao, H. McDonald, W.W. Wilson, A. Asanov and L.L. Combs, Correlation of second virial coefficients and solubilities useful in protein crystal growth, *J. Crystal Growth* **196**, 424–33 (1999).

57. I.N. Stranski, Zur Theorie des Kristallwachstums, *Z. Phys. Chem.* **136**, 259–278 (1928).

58. I.N. Stranski and R. Kaischew, Über den Mechanismus des Gleichgewichtes kleiner Kriställchen. I, *Z. Phys. Chem.* **B26**, 100–113(1934).

59. R. Kaischew and I.N. Stranski, Über die Thomson-Gibbs'sche Gleichung bei Kristallen, *Z. Phys. Chem.* **B35**, 427–132(1937).

60. D. Eisenberg and D. Crothers, *Physical Chemistry with Applications to Life Sciences* (The Benjamin/Cummins, Menlo Park, 1979).

61. P.S. Berry, S.A. Rice and J. Ross, *Physical Chemistry* (Oxford University Press, New York, 2000).

62. M. Volmer, *Kinetik der Phasenbildung* (Steinkopff, Dresden, 1939).

63. W.K. Burton, N. Cabrera and F.C. Frank, The growth of crystals and equilibrium structure of their surfaces, *Phil. Trans. Roy. Soc. London Ser. A* **243**, 299–360 (1951).

64. A.A. Chernov, *Modern Crystallography III, Crystal Growth* (Springer, Berlin, 1984).

65. E.D. Williams and N.C. Bartelt, Thermodynamics of surface morphology, *Science* **251**, 393–400 (1991).

66. A.A. Chernov, L.N. Rashkovich, I.V. Yamlinski and N.V. Gvozdev, Kink kinetics, exchange fluxes, 1D "nucleation" and adsorption on the (010) face of orthorhombic lysozyme crystals, *J. Phys.: Condens. Matter* **11**, 9969–9984(1999).

67. H.H. Teng, P.M. Dove, C.A. Orme and J.J. De Yoreo, Thermodynamics of calcite growth: baseline for understanding biomineral formation, *Science* **282**, 724–727 (1998).

68. L. Kuipers, M. Hoogeman and J. Frenken, Step dynamics on Au(110) studied with a high-temperature, high-speed scanning tunneling microscope, *Phys. Rev. Letters* **71**, 3517–3520 (1993).

69. B.S. Swartzentruber, Fundamentals of surface step and island formation mechanisms, *J. Crystal Growth* **188**, 1–10 (1998).

70. D.N. Petsev, B.R. Thomas, S.-T. Yau, D. Tsekova, C. Nanev, W.W. Wilson and P.G. Vekilov, Temperature-independent solubility and interactions between apoferritin monomers and dimers in solution, *J. Crystal Growth* **232**, 21–29(2001).

71. P. Atkins, *Physical Chemistry* (Freeman, New York, 1998).

72. C. Haas, J. Drenth and W.W. Wilson, Relation between the solubility of proteins in aqueous solutions and the second virial coefficient of the solution, *J. Phys. Chem. B* **103**, 2808–2811 (1999).

73. P.G. Vekilov, A.R. Feeling-Taylor, D.N. Petsev, O. Galkin, R.L. Nagel and R.E. Hirsch, Intermolecular interactions, nucleation and thermodynamics of crystallization of hemoglobin C, *Biophys. J.* **83**, 1147–1156 (2002).

74. P.G. Vekilov, A.R. Feeling-Taylor, S.-T. Yau and D.N. Petsev, Solvent entropy contribution to the free energy of protein crystallization, *Acta Crystallogr. Section D* **58**, 1611–1616 (2002).

75. J.N. Israelachvili, *Intermolecular and Surface Forces* (Academic Press, New York, 1995).

76. W.A. Eaton, V. Munoz, P.A. Thompson, C.K. Chan and J. Hofrichter, Submillisecond kinetics of protein folding, *Curr. Opin. Struct. Biol.* **7,** 10–14 (1997).

77. C. Tanford, *The Hydrophobic Effect: Formation of Micelles and Biological Membranes* (John Wiley & Sons, New York, 1980).

78. D. Eisenberg and W. Kauzmann, *The Structure and Properties of Water* (University Press, Oxford, 1969).

79. J.D. Dunitz, The entropic cost of bound water in crystals and biomolecules, *Nature* **264**, 670–670 (1994).

80. K.A. Jackson, Interface structure, in: Eds R.H. Doremus, B.W. Roberts and D. Turnbull, *Growth and Perfection of Crystals* (Chapman and Hill, London, 1958) pp. 319–323.

81. I.N. Stranski and R. Kaischew, Über den Mechanismus des Gleichgewichtes kleiner Kriställchen. II, *Z. Phys. Chem.* **B26,** 114–116 (1934).

82. A. Milchev, Electrochemical phase formation on a foreign substrate—basic theoretical concepts and some experimental results, *Contemp. Phys.* **32**, 321–332 (1991).

83. G.H. Gilmer, Atomic scale models of crystal growth, in: Ed. D. Hurle, *Handbook of Crystal Growth,* Vol. 1a (North Holland, Amsterdam, 1994) pp. 583–638.

84. J.P. Van der Eerden, Crystal growth mechanisms, in: Ed. D. Hurle, *Handbook of Crystal Growth,* Vol. 1a (North Holland, Amsterdam, 1994) pp. 307–76.

85. A.A. Chernov, Growth of crystals from solutions, *Contemp. Phys.* **30**, 251–276 (1989).

86. B.R. Thomas, D. Carter and F. Rosenberger, Effects of microheterogeneity on horse spleen apoferritin crystallization, *J. Crystal Growth* **187**, 499–510 (1997).

87. M. Li, A. Nadarajah and M.L. Pusey, Growth of (101) faces of tetragonal lysozyme crystals: determination of the growth mechanism, *Acta Cryst. Section D* **55**, 1012 (1999).

88. M. Li, A. Nadarajah and M.L. Pusey, Determining the molecular-growth mechanisms of protein crystal faces by atomic force microscopy, *Acta Cryst. Section D* **55**, 1036 (1999).

89. A. Nadarajah and M.L. Pusey, Growth mechanism of the (110) face of tetragonal lysozyme crystals, *Acta Cryst. Section D* **53**, 524 (1997).

90. C. Alfonso, J.M. Bermond, J.C. Heyraud and J.J. Metois, The meandering of steps and the terrace width distribution on clean Si(111), *Surf. Sci.* **262**, 371–381 (1992).

91. N.C. Bartelt, T.L. Einstein and E.D. Williams, The influence of step–step interactions on step wandering, *Surf. Sci. Lett.* **240**, L591–L598 (1990).

92. T. Ihle, C. Misbah and O. Pierre-Louis, Equilibrium step dynamics of vicinal surfaces revisited, *Phys. Rev. B* **58**, 2289–2309 (1998).

93. A. Pimpinelli, J. Villain, D.E. Wolf, J.J. Metois, J.C. Heyraud, I. Elkinari and G. Uimin, Equilibrium step dynamics on vicinal surfaces, *Surf. Sci.* **295**, 143–153 (1993).

94. L. Kuipers, M.S. Hoogeman and J.W.M. Frenken, Step and kink dynamics on Au(110) and Pb(111) strudied with a high-speed STM, *Phys. Rev. B* **52**, 11387–11397 (1995).

95. A.A. Chernov, The spiral growth of crystals, *Sov. Phys. Uspekhi* **4**, 116–148 (1961).

96. A.A. Chernov and H. Komatsu, Topics in crystal growth kinetics, in: Eds J.P. van der Eerden and O.S.L. Bruinsma, *Science and Technology of Crystal Growth* (Kluwer Academic, Dordrecht, 1995) pp. 67–80.

97. M. Smoluchowski, Drei Vorträge über Diffusion, Brownsche Bewegung und Koagulation von Kolloidteilchen, *Physik Z.* **17**, 557–585 (1916).

98. H. Eyring, S.H. Lin and S.M. Lin, *Basic Chemical Kinetics* (John Wiley and Sons, New York, 1980).

99. A.E. Neilsen, Nucleation in aqueous solutions, in: Ed. S. Peiser, *Crystal Growth* (Pergamon, Oxford, 1967) pp. 419–426.

100. M. Kahlweit, Nucleation in liquid solutions, in: Ed. H. Eyring, *Physical Chemistry,* Vol. VII (Academic Press, New York, 1969) pp. 675–698.

101. A.G. Walton, Nucleation in liquids and solutions, in: Ed. A.C. Zettlemoyer, *Nucleation* (Marcel Dekker, New York, 1969) pp. 225–307.

102. A.A. Chernov and H. Komatsu, Principles of crystal growth in protein crystallization, in: Eds J.P. van der Eerden and O.S.L. Bruinsma, *Science and Technology of Crystal Growth* (Kluwer Academic, Dordrecht, 1995) pp. 329–353.

103. G.H. Gilmer, R. Ghez and N. Cabrera, An analysis of combined volume and surface diffusion processes in crystal growth, *J. Crystal Growth* **8**, 79–93 (1971).

104. J.J. DeYoreo, Eight years of AFM: what has it taught us about solution crystal growth, in: Eds T. Hibiya, J.B. Mullin and M. Uwaha, *13 International Conference on Crystal Growth* (Elsevier, Kyoto, Japan, 2001).

105. D.N. Petsev, K. Chen, O. Gliko and P.G. Vekilov, Diffusion-limited kinetics of the solution–solid phase transition of molecular substances, *Proc. Natl. Acad. Sci. USA* **100,** 792–796 (2003).

106. D.N. Petsev and P.G. Vekilov, Evidence for non-DLVO hydration interactions in solutions of the protein apoferritin, *Phys. Rev. Lett.* **84**, 1339–1342 (2000).

107. J. Israelachvili and R. Pashley, The hydrophobic interaction is long range decaying exponentially with distance, *Nature* **300**, 341–342 (1982).

108. J. Israelachvili and H. Wennerstrom, Role of hydration and water structure in biological and colloidal interactions, *Nature* **379**, 219–225 (1996).

109. M. von Smoluchowski, *Z. Phys. Chem.* **92**, 129–135 (1918).

110. J.B. Zeldovich, On the theory of formation of new phases. Cavitation, *J. Theor. Experimen. Phys. (USSR)* **12**, 525–538 (1942).

111. R. Zwanzig, *Nonequilibrium Statistical Mechanics* (Oxford University Press, Oxford, 2001).

112. J. Frenkel, *Phys. J. USSR* **1**, 498–510 (1932).

113. J.Q. Broughton, G.H. Gilmer and K.A. Jackson, Crystallization rates of a Lennard–Jones liquid, *Phys. Rev. Lett.* **49**, 1496–1500(1982).

114. J.M. Garcia-Ruiz and A. Moreno, Growth kinetics of protein single crystals in the gel acupuncture technique, *J. Crystal Growth* **178**, 393–401 (1997).

115. W.B. Hou, A.B. Kudryavtsev, T.L. Bray, L.J. DeLucas and W.W. Wilson, Real time evolution of concentration distribution aroud teragonal lysozyme crystal: case study in gel and free solution, *J. Crystal Growth* **232**, 265–272 (2001).

116. A.J. Malkin, Y.G. Kuznetsov, W. Glanz and A. McPherson, Atomic force microscopy studies of surface morphology and growth kinetics of thaumatin crystallization, *J. Phys. Chem.* **100**, 11736–11743 (1996).

117. P.G. Vekilov, B.R. Thomas and F. Rosenberger, Effects of convective solute and impurity transport on protein crystal growth, *J. Phys. Chem.* **102**, 5208–5216 (1998).

118. P.G. Vekilov, Y.G. Kuznetsov and A.A. Chernov, Interstep interaction in solution growth; (101) ADP face, *J. Crystal Growth* **121**, 643–655 (1992).

119. P.G. Vekilov, Y.G. Kuznetsov and A.A. Chernov, The effect of temperature on step motion; (101) ADP face, *J. Crystal Growth* **121**, 44–52 (1992).

120. H. Borchers (Ed.), *Landoldt–Bornstein Numerical Data and Functional Relationships,* Vol. IV, Part II. *Materials Values and Mechanical Behaviour of Nonmetals,* Vol. IV, Part II (Springer, Berlin, 1955).

121. D. Wolf and J.A. Jaszczak, On the interaction between steps on vicinal fcc surfaces, *Surf. Sci* **277**, 301–322 (1992).

122. V.I. Marchenko and A.Y. Parshin, Elastic properties of crystal surfaces. *Sov. Phys. JETP* **52**, 129–131 (1980).

123. B. Houssmandzadeh and C. Misbah, Elastic interaction between modulated steps on a vicinal surface, *J. Phys. I France* **5**, 685–698 (1995).

124. G.S. Bales and A. Zangwill, Morphological instability of a terrace edge during step flow growth, *Physical Review B* **41**, 5500–5508 (1990).

125. E. Bauser, Atomic mechanisms in semiconductor liquid phase epitaxy, in: Ed. D.T.J. Hurle, *Handbook of Crystal Growth,* Vol. 3b (North Holland, Amsterdam, 1994) pp. 879–911.

126. G. Ehrlich and F.G. Hudda, Asymmetric capture at steps, *J. Chem. Phys.* 44, 1039–1052 (1966).

127. N. Braun, J. Tack, M. Fischer, A. Bacher, L. Bachmann and S. Weinkauf, Electron microscopic observations on protein crystallization: adsorption layers, aggregates and crystal defects, *J. Crystal Growth* **212**, 270–282 (2000).

128. V. Bostanov, G. Staikov and D.K. Roe, Rate of propagation of growth layers on cubic crystal faces in electrocrystallization of silver, *J. Electrochem. Soc.* **122**, 1301–1305 (1975).

129. P.G. Vekilov, L.A. Monaco and F. Rosenberger, Facet morphology response to non-uniformities in nutrient and impurity supply. I. Experiments and interpretation, *J. Crystal Growth* **156**, 267–278 (1995).

130. H. Lin, D.N. Petsev, S.-T. Yau, B.R. Thomas and P.G. Vekilov, Lower incorporation of impurities in ferritin crystals by suppression of convection: modeling results, *Crystal Growth and Design* **1**, 73–79 (2001).

131. S.-T. Yau, B.R. Thomas, O. Galkin, O. Gliko and P.G. Vekilov, Molecular mechanisms of microheterogeneity-induced defect formation in ferritin crystallization, *Proteins: Structure, Function, Genetics* **43**, 343–352 (2001).

132. R. Giege, B. Lorber and A. Theobald-Dietrich, Crystallogenesis of biological macromolecule—facts and perspectives, *Acta Crystallogr. Section D* **50**, 339–350 (1994).

133. F. Rosenberger, P.G. Vekilov, M. Muschol and B.R. Thomas, Nucleation and crystallization of globular proteins—what do we know and what is missing?, *J. Crystal Growth* **167**, 1–27 (1996).

134. A. McPherson, A.J. Malkin, Y.G. Kuznetsov and S. Koszelak, Incorporation of impurities in macromolecular crystals, *J. Crystal Growth* **168**, 74–92 (1996).

135. A.A. Chernov, Estimates of internal stress and related mosaicity in solution grown crystals: proteins, *J. Crystal Growth* **196**, 524–534 (1999).

136. B.R. Thomas, P.G. Vekilov and F. Rosenberger, Heterogeneity determination and purification of commercial hen egg white lysozyme, *Acta Crystallogr. Section D* **52**, 776–784 (1996).

137. B.R. Thomas, A.A. Chernov, P.G. Vekilov and D.C. Carter, Distribution coefficients of protein impurities in ferritin and lysozyme crystals. Self-purification in microgravity, *J. Crystal Growth* **211**, 149–156 (2000).

138. A.R. Ferre-D-Amare and S.K. Burley, Use of dynamic light scattering to assess crystallizability of macromolecules and molecular assemblies, *Structure* **15**, 357–359 (1994).

139. T.-S. Yoon, S. Tetreault, H.E. Bosshard, R.M. Sweeet and J. Sygush, Mosaic spread analysis of Canadian advanced protein crystallization experiments on the Russian space station Mir, *J. Crystal Growth,* accepted (2000).

140. S.D. Durbin and G. Feher, Protein crystallization, *Annu. Rev. Phys. Chem.* **47**, 171–204 (1996).

141. A.J. Malkin, Y.G. Kuznetsov, R.W. Lucas and A. McPherson, Surface processes in the crystallization of turnip yellow mosaic virus visalized by atomic force microcsopy, *J. Struct. Biol.* **127**, 35–43 (1999).

142. A.J. Malkin, Y.G. Kuznetsov and A. McPherson, Defect structure of macromolecular crystals, *J. Struct. Biol.* **117**, 124–137 (1996).

143. A.J. Malkin, Y.G. Kuznetsov and A. McPherson, Incorporation of microcrystals by growing protein and virus crystals, *Proteins: Structure, Function and Genetics* **24**, 247–252 (1996).

144. P.G. Vekilov and J.I.D. Alexander, Dynamics of layer growth in protein crystallization, *Chem. Rev.* **100**, 2061–2089 (2000).

145. D. Yang, K. Matsubara, M. Yamaki, S. Ebina and K. Nagayama, Heterogeneities in ferritin dimers as characterized by gel filtration, nuclear magnetic resonance, electrophoresis, transmission electron microscopy, and gene engineering techniques, *Biochim. Biophys. Acta* **1206,** 173–179 (1994).

146. N. Cabrera and D.A. Vermileya, The growth of crystals form solution, in: Eds R.H. Doremus, B.W. Roberts and D. Turnbul, *Growth and Perfection of Crystals* (Wiley, New York, 1958).

147. S.Y. Potapenko, Threshold for step percolation through impurity fence, *J. Crystal Growth* **133**, 141–146 (1993).

148. V.V. Voronkov and L.N. Rashkovich, Step kinetics in the presence of mobile adsorbed impurity, *J. Crystal Growth* **144**, 107–115 (1994).

149. K. Onuma, K. Tsukamoto and I. Sunagawa, Step motion of CdI_2 crystals growing from aqueous solution, *Microgravity Sci. Technol.* **2,** 62–66 (1992).

150. P.G. Vekilov, Elementary processes of protein crystal growth, in: Ed. H. Komatsu, *Studies and Concepts in Crystal Growth* (Pergamon, Oxford, 1993) pp. 25–49.

151. T. Nakada, G. Sazaki, S. Miyashita, S.D. Durbin and H. Komatsu, Direct AFM observations of impurity effects on a lysozyme crystal, *J. Crystal Growth* **196**, 503–510 (1999).

152. C. Kittel, *Introduction to Solid State Physics* (John Wiley and Sons, New York, 1986).

153. H.J. Queisser and E.E. Haller, Defects in semiconductors, some vital, some fatal, *Science* **281**, 945–950 (1998).

154. A.A. Chernov, Crystal growth and crystallography, *Acta Crystallographica Section A* **54**, 859–872 (1998).

155. A. Shaikevich and Z. Kam, Investigation of long range order in protein crystals by X-ray diffraction, *Acta Crystallographica Section A* **37**, 871–875 (1981).

156. R. Fourme, A. Ducruix, M. Ries-Kaut and B. Capelle, The perfection of protein crystals probed by direct recording of Bragg reflection profiles with a quasi-planar X-ray wave, *J. Synchtron Rad.* **2,** 136–142 (1995).

157. P.G. Vekilov and F. Rosenberger, Intrinsic kinetics fluctuations as cause of growth inhomogeneity in protein crystals, *Phys. Rev. E* **57,** 6979–6981 (1998).

158. S. Weisgerber and J.R. Helliwell, Improvements in lysozyme crystal perfection through microgravity growth, *Acta Cryst. Section D* **51**, 1099–1102 (1995).

159. N.E. Chayen, T.J. Boggon, A. Casseta, A. Deacon, T. Gleichmann, J. Habash, S.J. Harrop, J.R. Helliwell, Y.P. Neih, M.R. Peterson, J. Raftery, E.H. Snell, A. Hädener, A.C. Niemann, D.P. Siddons, V. Stojanoff, A.W. Thompson, T. Ursby and M. Wulff, Trends and challenges in experimental macromolecular crystallography, *Quarterly Reviews of Biophysics* **29**, 227–278 (1996).

160. E.H. Snell, A. Cassetta, J.R. Helliwell, T.J. Boggon, N.E. Chayen, E. Weckert, K. Hoelzer, K. Schroer, E.J. Gordon and P.F. Zagalski, Partial improvement of crystal quality for microgravity grown apocrystacyanin-C1, *Acta Crystallogr. Section D* **53**, 231–239 (1997).

161. A. Guinier, Is the imperfect crystal in fact the best?, *Cryst. Res. Technol.* **33**, 543–545 (1998).

162. A.J. Malkin, Y.G. Kuznetsov and A. McPherson, In situ atomic force microscopy studies of surface morphology, growth kinetics, defect structure and dissolution in macromolecular crystallization, *J. Crystal Growth* **196**, 471–488 (1999).

163. A. McPherson, A.J. Malkin and Y.G. Kuznetsov, Atomic force microscopy in the study of macroimoleular crystal growth, *Ann. Rev. Biomol. Struct.* **20**, 361–410 (2000).

164. A. McPherson, A.J. Malkin, Y.G. Kuznetsov, S. Kozselak, M. Wells, G. Jenkins, J. Howard and G. Lawson, The effects of microgravity on protein crystallization: evidence for concentration gardients around growing crystals, *J. Crystal Growth* **196**, 572–586 (1999).

165. E.A. Moelwyn-Hughes, *Physical Chemistry* (Pergamon, London, 1961).

166. L.K. Steinrauf, Preliminary X-ray data for some crystaline forms of β-lactoglobulin and hen egg-white lysozyme, *Acta Crystallogr.* **12**, 77–78 (1959).

167. B.R. Thomas, P.G. Vekilov and F. Rosenberger, Effects of microheterogeneity on hen egg white lysozyme crystallization, *Acta Crystallogr. Section D* **54**, 226–236 (1998).

168. I. Reviakine, D.K. Georgiou and P.G. Vekilov, Capillarity effects on the crystallization kinetics: insulin, *J. Am. Chem. Soc.* **125**, 11684–11693 (2003).

169. A. Malkin, Y. Kuznetsov and A. McPherson, An in situ AFM investigation of catalase crystallization, *Surf. Sci.* **393**, 95–107 (1997).

170. P.G. Vekilov, M. Ataka and T. Katsura, Laser Michelson interferometry investigation of protein crystal growth, *J. Crystal Growth* **130**, 317–320 (1993).

171. P.G. Vekilov and F. Rosenberger, Dependence of lysozyme growth kinetics on step sources and impurities, *J. Crystal Growth* **158**, 540–551 (1996).

172. Y.G. Kuznetsov, J. Konnert, A.J. Malkin and A. McPherson, The advancement and structure of growth steps on thaumatin crystals visualized by atomic force microscopy at molecular resolution, *Surf. Sci.* **440**, 69–80 (1999).

173. P. Bennema, Analysis of crystal growth models for slightly supersaturated solutions, *J. Crystal Growth* **1**, 278–286 (1967).

This page intentionally left blank

6

Probing of crystal interfaces and the structures and dynamic properties of large macromolecular ensembles with *in situ* atomic force microscopy

Alexander J. Malkin[*]
BioSecurity and NanoSciences Laboratory, Department of Chemistry and Materials Science, Lawrence Livermore National Laboratory, Livermore, CA 94551, USA

Alexander McPherson
Department of Molecular Biology and Biochemistry, University of California, Irvine, CA 92697-3900, USA

Abstract: The crystallization of more than a dozen biological macromolecules, including proteins, nucleic acids, viruses, membrane proteins and the 50S ribosomal subunit has been studied *in situ* by atomic force microscopy (AFM), and evidence was found that macromolecules utilize all of the growth mechanisms found in the crystallization of conventional molecules. Estimates of fundamental kinetic and thermodynamic parameters for the crystallization of a number of macromolecules have been obtained. The influence of impurities on the growth of macromolecular crystals, as well as defect structure, and mechanisms of defect formation were also studied. For virus crystals the sources of mosaicity and local disorder that, to a great extent, determine the resolution limit and the ultimate quality of X-ray structure determinations were identified. Molecular dynamics on crystalline surfaces were investigated, and the structures of growth step edges were visualized. From these, attachment frequencies and probabilities for incorporation of macromolecules into crystals were estimated. High-resolution imaging can also yield unit cell dimensions, the number of molecules per asymmetric unit, and in favorable cases, gross structural features of the molecules themselves. The capsomere structures of several $T = 3$ virions have been visualized. Application of high-resolution AFM has further been extended to the probing of structures of several microbial pathogens, while the dissection of viral particles with detergents and enzymes has revealed the internal structures of some large viruses.

[*]Corresponding author. Mailing address: Department of Chemistry and Materials Science, Lawrence Livermore National Laboratory, L-234, P.O. Box 808, Livermore, CA 94551, USA. E-mail address: malkin1@llnl.gov

6.1. INTRODUCTION

Protein molecules play critical roles in living systems such as signal transducers, protective agents, transport molecules, or as structural materials. Many important functions of proteins could well be transposed from cells to in vitro processes or products if the molecules were modified to maintain their structure and function necessary to accomplish an intended chemical or physical task.

Monoclonal antibodies could be designed and conjugated with reporter groups to act as molecular sensors for detecting and signaling the presence of specific compounds at otherwise immeasurably low concentrations. These would have uses ranging from medical diagnosis to pollutant monitoring and the detection of carcinogens in the environment. Transport proteins could be designed to carry specified drugs in the blood and constructed to deliver them only to designated target tissues. Proteins with unique physical properties such as collagen and elastin that make up the connective tissues of the body might be modified in useful ways to create new materials for a broad spectrum of products ranging from prostheses to electronics.

Another example of this "new polymer chemistry" is that of protein engineering in agriculture and nutrition. The storage proteins found in cereal grains, beans and other plant seeds comprise major protein food sources worldwide. Unfortunately, many of these proteins are lacking in certain essential amino acids. By redesigning these storage proteins to contain a better balance of nutritionally important components, without otherwise impairing their physiological roles, enhanced crops could be created. By similar means, the abilities of plants to resist disease and withstand environmental extremes might be fortified and the palatability and taste of plant proteins altered, thereby generating new classes of food materials.

It requires little imagination to see that detailed knowledge of the target macromolecule could be of great service in directing a chemist more rapidly toward synthesis of the most effective compound. Presently, and in the foreseeable future, the only technique that can yield atomic level structural images of biological macromolecules is X-ray diffraction analyses as applied to single macromolecular crystals.

The objectives of the new polymer chemistry are attainable only for those cases where the gene for the target macromolecule can be isolated for subsequent manipulation, and the target protein can be crystallized and subjected to X-ray diffraction analysis to reveal its structure at atomic resolution. For example, to design pharmacologically important ligands, that is drugs, the target protein or enzyme must be crystallized and the structure of its active form determined.

Application of X-ray crystallography is absolutely dependent on crystals of the macromolecule, and not simply crystals, but crystals of sufficient size and quality to permit accurate data collection. The quality of the final structural image is directly correlated with the perfection, size, and physical properties of the crystalline specimen; hence the crystal becomes the keystone element of the entire process, and the ultimate determinant of its success.

Macromolecular crystallization is now widely regarded as the rate-limiting step in X-ray structure analyses. This is in part because macromolecules are extremely complex physical-chemical systems whose properties vary as a function of many environmental influences such as temperature, pH, ionic strength, contaminants, and solvent composition,

to name only a few [1,2]. They are structurally dynamic, microheterogeneous, aggregating systems, and they change conformation in the presence of ligands. There are extensive empirical studies and a vast collection of observations relating to macromolecular crystallization. Numerous physical and chemical factors have been observed to influence the success and reproducibility of crystallization, and a variety of reagents, precipitating agents, and other chemical compounds have proven useful in promoting and supporting the process [1,2].

However, quantitatively, the physics of macromolecular crystallization is rather poorly understood. In particular, quantitative predictions of growth and perfection for a given crystal are impossible, as is our ability to predict optimum growth conditions. This is true because of limited understanding of the mechanisms operative in crystallization, and their impact on the solid-state properties of macromolecular crystals. In spite of much recent progress in the physical analyses of macromolecular crystallization, important questions still remain largely unanswered, particularly, which kinds of disorder limit the diffraction resolution, and what are the sources of the disorder that arise during growth? Furthermore, studies on molecular dynamics on surfaces of macromolecular crystals, which are vital for the further development of a quantitative understanding of the crystal growth process, and the processes involved in defect formation have been conducted for only a few macromolecules.

On the other side of the ledger, however, macromolecular crystals are almost ideal systems for studying crystal growth as a general phenomenon using *in situ* atomic force microscopy (AFM). Particle sizes are relatively large, 3 to 10 nm diameters for most proteins, several times that for viruses, which is an order of magnitude or more larger than conventional molecules that crystallize. Thus their aggregates can be seen on the surfaces of crystals, even the incorporation of single molecules can be observed. The kinetics of the growth processes of macromolecular crystals are several orders of magnitude slower than for conventional crystals, thus the course of events during growth are fully compatible with the temporal resolution of the AFM technique.

AFM was first applied to study macromolecular crystallization by S. Durbin in 1992 using crystals of lyzozyme [3,4]. In our laboratory in a last 9 years we applied AFM to studies of more than a dozen macromolecular systems. These included protein, nucleic acid, antibody, membrane protein and virus crystals [5–22]. In a past several years a number of studies from several other laboratories on AFM studies of protein crystal growth have also been reported [23–36].

AFM can also provide important structural information on large macromolecular ensembles, such as human and animal viruses. Complex viruses can, otherwise, be difficult to characterize at the topographical level. Fragility and structural heterogeneity can render them troublesome targets for X-ray crystallography. The only alternative approach to date, electron microscopy (EM), yields resolutions ranging from 8 nm upwards. In our laboratory we demonstrated recently [37,38] that for large human viruses, AFM yields resolutions similar to EM and allows, in addition, the study of the dynamic properties of these viruses *in situ.*

6.2. ATOMIC FORCE MICROSCOPY STUDIES OF MACROMOLECULAR CRYSTALLIZATION

6.2.1. Probing crystal surfaces with AFM

The technique of atomic force microscopy (AFM) was introduced in 1986 [39] and it has already had a major impact in the characterization of surface structures in both material science [40,41] and biology [42–45]. In all AFM instruments, one of which is shown schematically in Figure 6.1 the sample surface is scanned with a probe, which consists of a miniature cantilever and a sharp tip. AFM probes made from silicon and silicon nitride are typically utilized for imaging in air and in the liquid respectively. When imaging is performed in contact mode the AFM tip is in continuous contact with the surface of the sample. Scanning is accomplished by tracing the probe, which is under piezoelectric control, along a series of raster lines. As the probe tip moves over the surface, it interacts through aggregate atomic forces with topological features on the surface. As a consequence of the interactions, the probe is deflected. The force between the sample and the tip is deduced from the position of a laser beam reflected from the upper surface of the cantilever onto a four-quadrant photo detector, which detects bending deflections.

In contact mode the AFM can be operated in both constant height and deflection modes. With the former, a feedback mechanism raises and lowers the sample to maintain the can-
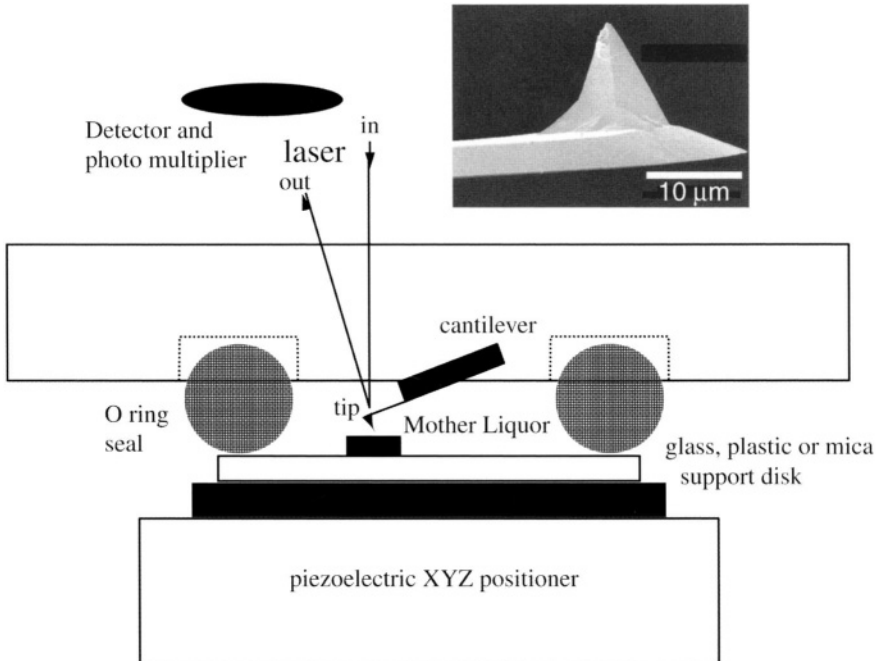
FIGURE 6.1. Schematic diagram of an atomic force microscope. A laser beam is reflected from the upper surface of the cantilever and detected with a four-quadrant photo detector. Scanning takes place in a fluid filled cell of about 50–75 μl volume. The sample is translated in a raster manner by a piezoelectric positioner upon which the fluid cell is mounted. Shown in the insert is an TEM image of a cantilever tip.

tilever deflection nearly constant. The system monitors the piezo "height", and produces the corresponding image information, a topographic profile of the surface. In "deflection" mode, the piezo remains stationary and actual cantilever deflection data are recorded. This mode of operation is particularly useful for imaging surfaces features with significant differences in height.

It was found in AFM applications to soft materials, such as biological samples and polymers, that lateral forces and relatively high tip-to-sample interactions utilized in the contact mode of operation often resulted in mechanical damage to the surface. These problems have been overcome by the development of tapping mode [46]. In tapping mode the vertical position of the sample is continually adjusted by a feedback mechanism to maintain the amplitude of the freely oscillating probe constant. Tapping mode minimizes contact between the probe tip and the sample surface and greatly reduces lateral forces. The tapping mode technique has proven a significant advance as it has permitted the visualization of materials that would otherwise be too soft or too fragile to withstand contact mode examination.

AFM can be applied to scan fields ranging in size from less than 20 nm up to about 150 μm, and with a spatial resolution on biological, soft materials of about 1 nm, with a height resolution as great as 0.1 nm. Thus it provides precise visual detail over a size range that is impossible for most other techniques. Its application extends over the range lying between individual macromolecules, which are accessible by X-ray crystallography, macromolecular assemblies amenable to electron microscopy, to living cells which can just be seen using light microscopy. Because visualization is carried out in a fluid environment, the specimens suffer no dehydration as is generally necessary with electron microscopy, they require no fixing or staining.

AFM allows the investigator to record not simply a single image, but a series of images that may extend over hours or even days. This is ideal of course for the study of the growth of macromolecular crystals, which develop over such periods of time. A further property of AFM carried out in fluid cells, is that the fluid can be changed during the course of experiments. This is of great value in the study of macromolecular crystal growth because it allows the study of growth process under different conditions of supersaturation using a single growing crystal.

6.2.2. *Mechanisms of growth*

AFM studies of macromolecular crystallization demonstrated that surfaces of virtually all macromolecular crystals are smooth and that growth proceeds layer-by-layer. Sources of the growth layers are either two-dimensional (2D) nuclei or screw dislocations. For most proteins (i.e. catalase, Ben-Jones protein) [7,11,18,20] and all virus crystals [5,14,20,22] investigated, the dominant source of the growth layers over a broad supersaturation range was exclusively two-dimensional (2D) nuclei (Figure 6.2a–c). For other protein crystals (i.e. lysozyme, t-RNA, xylanase, and canavalin), at low supersaturations growth proceeded from dislocations (Figure 6.2d–f), with 2D nucleation taking over at relatively high supersaturations [7,12,15,18,24]. For several macromolecules it was found that while crystals of one form are dislocation-free, crystals of other forms have high dislocation densities, the most notable case being hexagonal and rhombohedral canavalin. (111) faces and (001) of apoferritin [7] and hexagonal canavalin crystals were found to be rough and grew by a
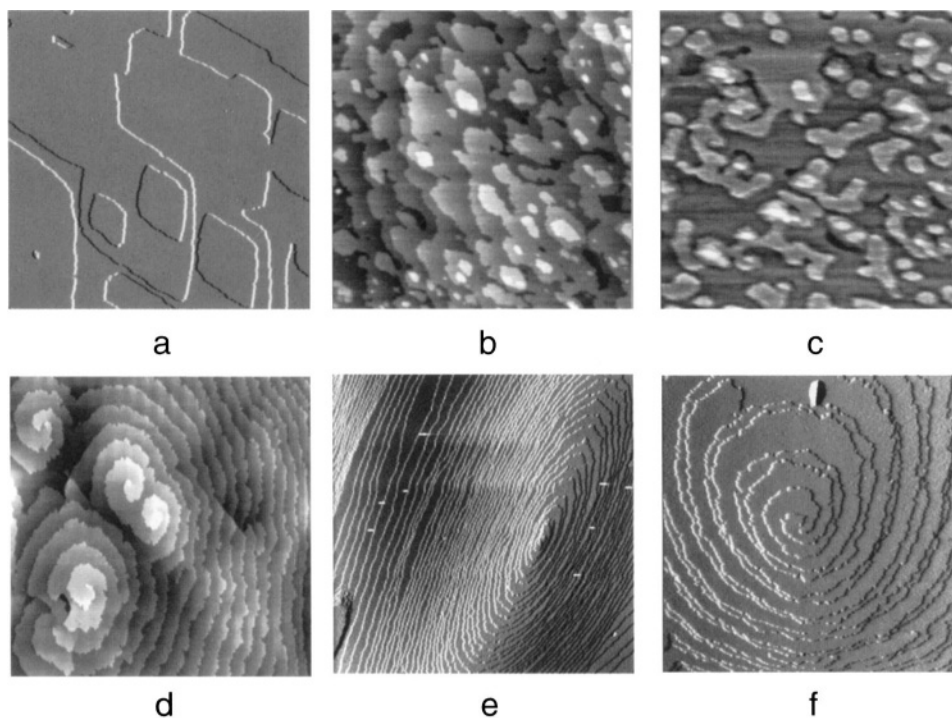
FIGURE 6.2. *In situ* AFM images showing 2D nucleation (a–c) and dislocation growth (d–f) on the surfaces of various macromolecular crystals. In (a) glucose isomerase, 11×11 μm; (b) hexagonal canavalin, 19×19 μm; (c) membrane protein bacteriorhodopsin, 500×500 nm; (d) rhombohedral canavalin, 10×10 μm; (e) lysozyme, 12×12 μm, and (f) trypsin, 30×30 μm.

normal mechanism which has also been described for a number of systems growing from a melt or from the vapor phase. Comprehensive studies of apoferritin crystallization [33, 34] revealed growth by strictly 2D nucleation, presumably due to a lower impurity content compared with commercial protein utilized in earlier studies [7].

AFM studies have demonstrated that macromolecules utilize all of the growth mechanisms found in the crystallization of conventional molecules from solution, including normal growth, which is practically unheard of for growth of inorganic and organic crystals from solution. At high solution supersaturation a novel mechanism of growth by adsorption of 3D clusters (Figure 6.3) was also observed on the surfaces of macromolecular crystals investigated in our laboratory [7,15,16,18]. Upon interaction with the underlying lattice the 3D clusters restructured themselves into multilayer stacks, which then advanced tangentially and in the normal direction due to 2D nucleation. In all of those cases, multilayer stacks (typical height 2–15 layers) assumed characteristic morphologies and orientations consistent with the lattice of the underlying crystal.

Based on a number of experimental observations [16] it was proposed that multilayer stacks were formed upon adsorption on the crystalline surface of protein-rich droplets possessing short-range order. These clusters are known to appear in bulk, concentrated macromolecular solutions due to fluctuations in density [48,49]. Upon adsorption, 3D clusters
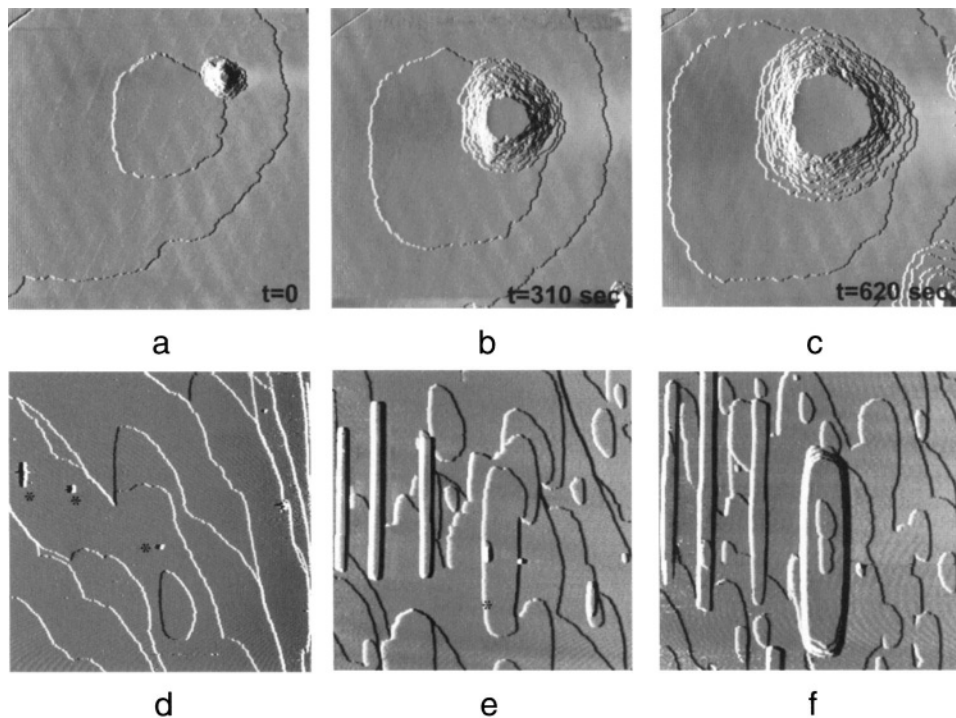
FIGURE 6.3. (a–c) 15×15 μm images showing appearance and development of 3D multiplayer stack on the surface of STMV crystal. In (d–f) is a sequence of images taken at (d) 0, (e) 20, and (f) 81 minutes showing the growth of 3D nuclei on the surface of a catalase crystal. In (b) three-dimensional clusters (in the upper left portion of the image indicated with *) sediment and adsorb on the surface of a catalase crystal. In (e–f) they produce misaligned microcrystals. In (d) a three-dimensional cluster (in the middle of the image indicated with *) adsorbs on the surface and develops, in (e–f), into a multilayer stack. The scan sizes for the images are (d–f) 35×35 μm^2.

transform into crystallites, the process being guided by the underlying lattice. As a result, the lattices of 3D crystalline nuclei are consistently aligned with the lattices of the underlying crystals, and layers from stacks merge flawlessly both with other steps on the crystal surface and with each other. When a 3D cluster becomes crystalline, its lattice occasionally misaligns with respect to the lattice of the underlying crystal. In those cases misaligned 3D nuclei develop into discreet microcrystals. Both possible pathways for the development of protein-rich clusters on the surfaces of catalase crystals are illustrated in Figure 6.3.

Generally, crystal faces in a particular direction *(hkl)* are expected to grow with layers of thickness d_{hkl}. Indeed layer-by-layer growth of the vast majority of macromolecular crystals proceeds by the advancement of growth steps with a height equal to the unit cell along the direction perpendicular to the crystal face. However, the Bravais Friedel Donnay Harker (BFDH) criterion [50] contains exemptions for structures with centered cells, glide planes and screw axes, which all lead to reduced growth layer thickness. Indeed AFM studies conducted in our laboratory demonstrated the validity of the BFDH criterion. Thus orthorhombic catalase, trigonal trypsin and tetragonal BJP crystals all follow the exemption
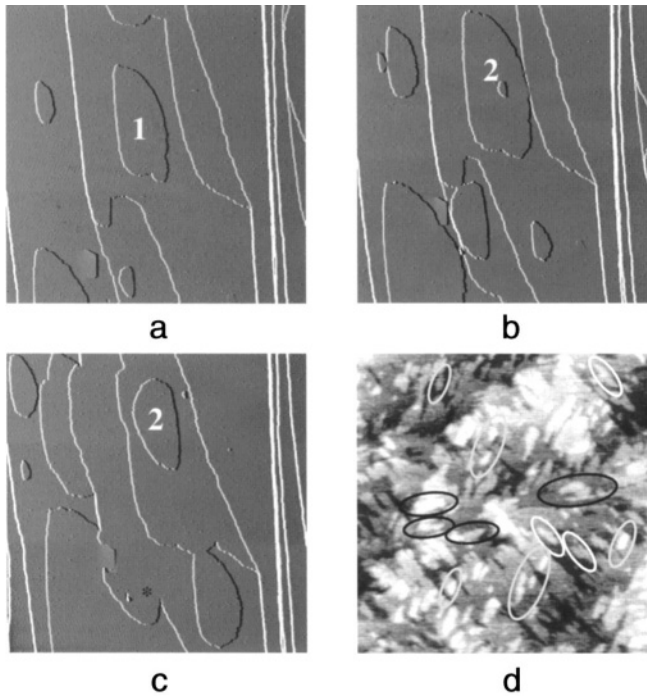
FIGURE 6.4. A sequence of $25 \times 25\ \mu\mathrm{m}$ *in situ* AFM images taken at: (a) 0; (b) 11; and (c) 30 min showing nucleation of symmetry-related 2D nuclei on the (001) face of orthorhombic catalase crystal. (d) $5 \times 5\ \mu\mathrm{m}$ image showing symmetry-related 2D nuclei (indicated by differently colored ellipses) on the (001) faces of trigonal trypsin crystal.

rule which implies that the existence of a screw axis in a crystal structure leads to the formation of reduced growth layers d_{nhnknl} on the face *(hkl)* perpendicular to that axis. In the case of screw axes perpendicular to (001), growth layers have a thickness of d_{00n}. From symmetry considerations, the unit cell should be divided into two equivalent layers for 2_1, 4_2, and 6_3 screw axes ($n = 2$), three equivalent layers for 3_1, 3_2, 6_2, and 6_4 ($n = 3$), four layers for 4_1 and 4_3 ($n = 4$), and six layers for 6_1 and 6_5 screw axes ($n = 6$).

In the case of catalase crystals [11] the step heights of the nuclei are equal to 11.5 ± 0.2 nm, which corresponds to half of the unit cell dimension along *c*. Each successive layer derived from a 2D island is related by a 180°, 2-fold rotation to the preceding layer (Figure 6.4a–c). The formation of two alternating growth layers on the (001) face of catalase crystals is caused by the presence of a 2_1 screw axis in the structure perpendicular to this face. This screw axis divides the unit cell into two symmetrically equivalent layers rotated by 180°, which indeed should lead to the observed equivalent, but rotated half-layers. As seen in Figure 6.4d 2D nuclei on the (001) face of trigonal trypsin forming each successive growth layer of thickness 3.2 ± 0.5 nm are related by a counterclockwise rotation of 120° with respect to the shape of the initiating nuclei of the preceding layer [47]. This observed 3-fold symmetric growth behavior of the trigonal (001) face can be explained by the presence of the 3_1 screw axis parallel to *c* in the $P3_121$ crystal structure. The six molecules in the unit cell with a height of $c = 10.9$ nm can, in accordance with
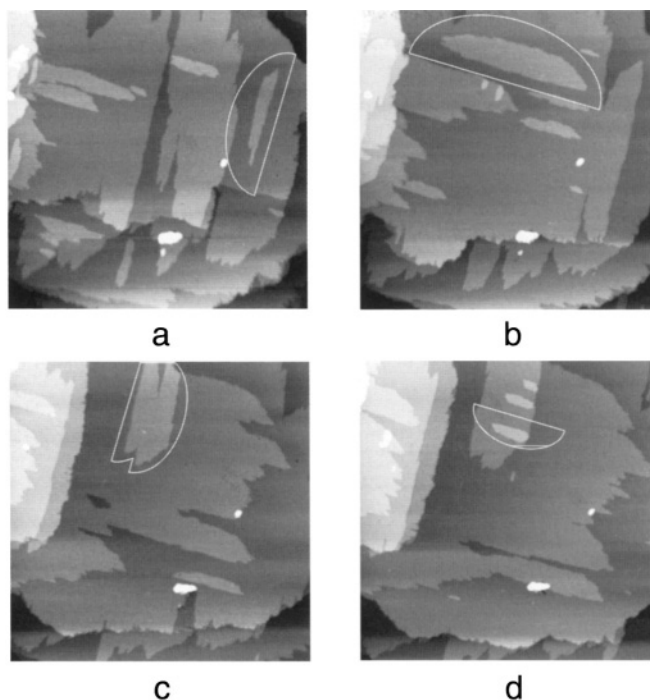
FIGURE 6.5. A sequence of 2×2 μm *in situ* AFM images taken at: (a) 0; (b) 11 ; and (c) 25 and (d) 32 min showing nucleation of symmetry-related 2D nuclei (indicated by half-ellipses on the (001) face of tetragonal Bence-Jones protein.

the space group symmetry, be sorted into three groups consisting of two molecules each, that are mutually related by a 3-fold screw axis. This results in three triad-related growth layers within a unit cell, each with height of $d_{003} = 1/3|c| = 3.6$ nm, which corresponds well to the experimentally observed growth steps of height 3.2 ± 0.5 nm. In the case of growth of the (001) face of tetragonal BJP crystals [47], symmetry-related layers produced exclusively by 2D nucleation were again encountered. These were related by a rotation of 90° clockwise for each subsequent layer (Figure 6.5). The step height of the nuclei was 4.6 ± 0.2 nm. This corresponds well to $d_{004} = 4.49$ nm. These observations indicate that the observed symmetry-related layers are caused by the presence of the 4_3 screw axis.

In case of catalase, trypsin and BJP because of multiple asymmetric units in the unit cell there are potentially several ways to distribute them into two equivalent sub-layers. To delineate the division of molecules into the three layers that occur in the course of crystallization, a basic periodic bond chain (PBC) [50] analysis can be performed using atomic coordinate data from the Protein Database [51] This analysis was performed for trypsin crystals [21].

Thus according to the X-ray diffraction data as illustrated in Figure 6.6, trypsin molecules, numbered here as 1 through 6 are stacked in the c-direction in the order ..3..5..1..4..2..6..3..5... Molecules in positions 1, 2 and 3 are directly symmetry-related by the three-fold-axis as are those in positions 4, 5 and 6. Every molecule has crystal con-
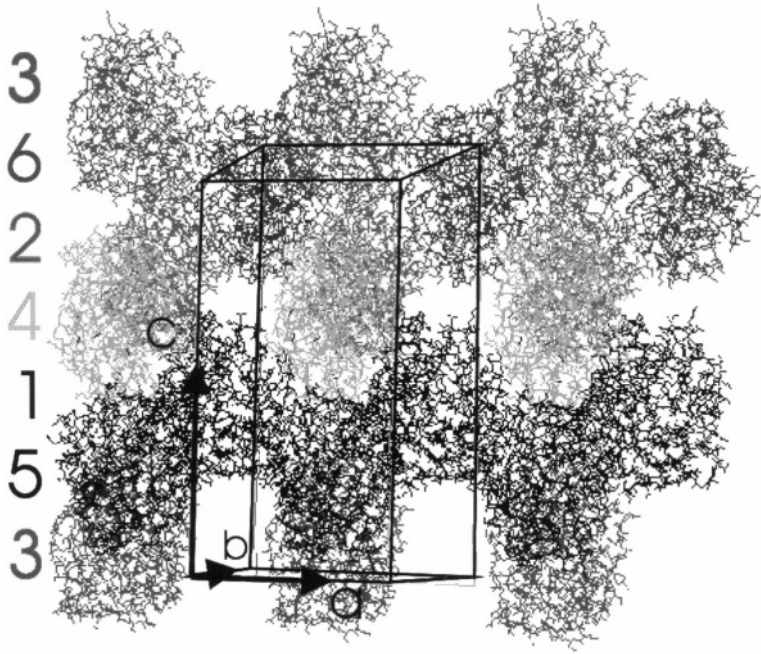
FIGURE 6.6. $P3_121$ trigonal trypsin crystal structure. The molecules are numbered according to their general Wyckoff positions, the unit cell is indicated in white. Molecules in positions 1, 2 and 3 are symmetry-related by the three-fold screw-axis, as those in positions 4, 5 and 6. There are two ways to distribute the molecules in three layers of d_{003}, which are layers formed by molecules in positions ..3–5..1..4..2–6..3–5.. or 6–3..5–1..4–2..6–3...

tacts with seven other molecules, which can be either molecules within the same unit cell or molecules within neighboring cells. From the molecular stacking ..3..5..1..4..2..6..3..5.., two different divisions into d_{003} growth layers are possible. These are layers formed by molecules in positions ...3–5...1–4...2–6...3–5... or ...6–3...5–1...4–2...6–3... respectively. From X-ray diffraction data, all crystal contacts between neighboring molecules in the unit cell within a range less than 4 Å were tabulated [21]. According to PBC theory, for a given slice d_{hkl}, all crystal interactions add up to the slice energy E_{slice}. Based on the basic connected net criterion [50], the net with the highest E_{slice}, i.e. with the strongest bonds inside the layer, will be the one forming growth layers during the crystallization process. It was demonstrated [21] that the 1–5 type growth layers have a much higher E_{slice}, which makes them, and not the 1–4 type layers, the obvious choice for the actual growth steps.

In the case of a growth spiral originating from a screw dislocation, the origin of each new growth layer is pinned to exactly the same point (i.e. the dislocation outcrop), and therefore successive symmetry-related layers demonstrating rotated step velocity anisotropy can be significantly restrained. For crystal faces with relatively low anisotropy it is still possible for dislocation spirals to grow, and they will develop growth patterns with multiple (e.g. double for 2_1 or triple for 3_1) growth steps. In growth directions where small and large step velocities of subsequent layers change, the pairing of steps will alternate. This leads to the formation of "zig-zag" patterns known as 'step interlacing'. In the case of macromolecular crystals, interlacing at a spiral was observed for the (001) face of a ri-
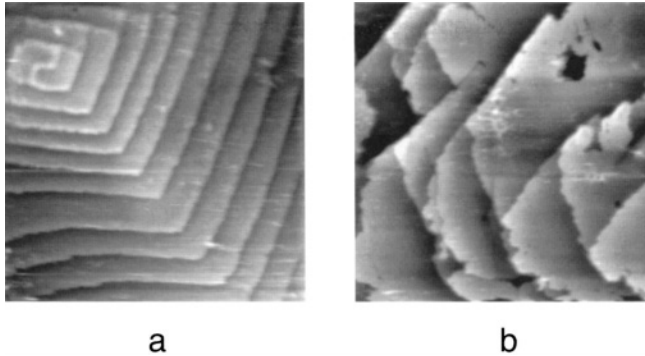
FIGURE 6.7. (a) *In situ* AFM 60×60 μm image showing a dislocation spiral on the (001) face of ribosomal 50s subunit crystal. (b) *In situ* AFM 25×25 μm image showing step interlacing on the (001) face of a ribosomal 50s subunit crystal growth steps.

bosomal 50s subunit crystal (Figure 6.7) with space group $C222_1$ (which has a 2_1 screw axis perpendicular to the (001) face). The greater anisotropy of the growth layers, the more severe the steps restrain one another. Eventually, this can lead to 'self-inhibition' of growth spirals, as was shown for the case of *Pnma* barite (001), having screw axes parallel to c [52]. In this case, the growth rate of the spirals was so reduced (because of step hindrance) that 2D nucleation alone determined the growth rate of the face. Growth by symmetry related layers has so far been reported only for catalase, trypsin, Ben-Jones proteins, ribosomal 50s subunit crystals and barite crystals in the crystallization of inorganic, organic and biological macromolecules.

6.2.3. Growth step kinetics. Fundamental growth parameters

For macromolecular crystal interfaces, AFM allows direct measurement of supersaturation dependencies of tangential step rates, slopes of dislocation hillocks, step critical lengths, as well as rates of two-dimensional nucleation over a broad range of supersaturations. From these data important parameters which govern crystallization process, such as kinetic coefficient of steps β and surface energy of the step edge α can be deduced.

Thus for example, the combination of a stacking fault with a dislocation source on the (001) face of orthorhombic glucose isomerase crystals resulted in rotation of two growth steps around the stacking fault (insert in Figure 6.8a). This allowed simultaneous measurement of the supersaturation dependencies of tangential step rates for four orthogonal crystallographic directions (Figure 6.8a) using the stacking fault as a reference point.

The tangential step rate, v is given by [53]

$$v = \Omega\beta(c - c_e), \tag{1}$$

where $\Omega = 4.8 \times 10^{-19}$ cm^3 is the specific volumes of glucose isomerase tetramers in the crystal, c and $c_e = 2.1 \times 10^{15}$ cm^{-3} are initial and equilibrium concentrations of protein respectively, and β is the step kinetic coefficient [53]. The kinetic coefficient is the aggregate measure of the kinetics of diffusion, adsorption, and incorporation of macromolecules
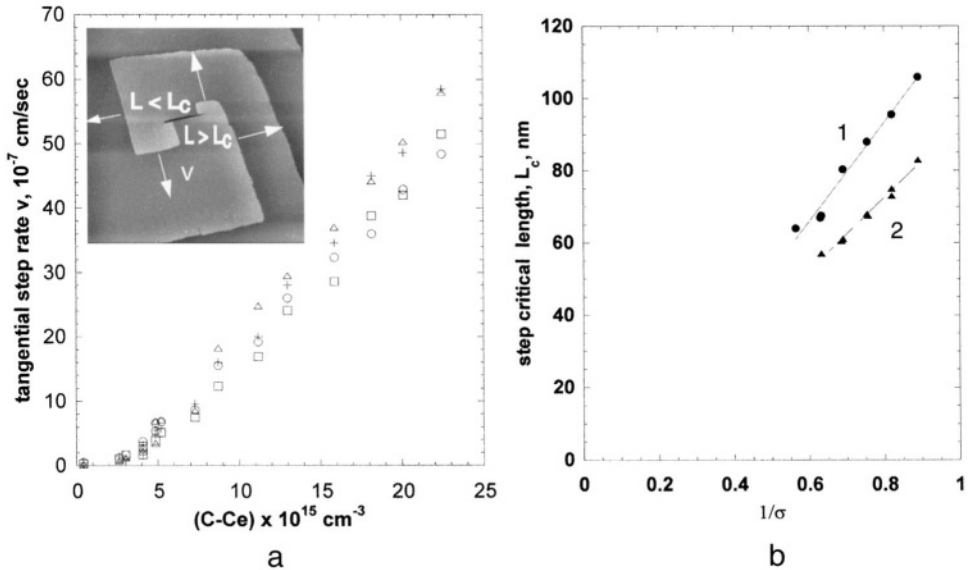
FIGURE 6.8. (a) Supersaturation dependencies of tangential step growth rates in different crystallographic directions. ($\square$) $\langle 010 \rangle$; (∇) $\langle 100 \rangle$; (+) $\langle 100 \rangle$ and ($\circ$) $\langle 010 \rangle$. Insert: 11×11 μm image showing growth steps advancing around the stacking fault. Arrows indicate advancing steps segments. (b) Dependence of step critical length on supersaturation for 1, $\langle 010 \rangle$; 2, $\langle 100 \rangle$.

with the rate-limiting step dominant. For several macromolecular systems it was demonstrated [9,11] that velocities of single steps do not differ significantly from ones for steep macrosteps. This suggests, that like the crystallization of most inorganic crystals from solution [53], growth is limited by the kinetics of incorporation rather than by surface or volume diffusion. For canavalin crystallization, however, based on experimental data, it was suggested [24,25] that surface diffusion rather than bulk diffusion is the controlling mechanism of solute transport to the steps with the length scale for diffusion being on the order of 1 μm.

From the linear portion of v $(c - c_e)$ dependencies for $(c - c_e) > 10^{14}$ cm^{-3} (Figure 6.8a), the kinetic coefficient β for glucose isomerase crystallization was estimated to be 4.7×10^{-4} cm/s, 5.2×10^{-4} cm/s, 4.4×10^{-4} cm/s and 5.4×10^{-4} cm/s for crystallographic directions $\langle 010 \rangle$, $\langle 100 \rangle$, $\langle 010 \rangle$ and $\langle 100 \rangle$ respectively.

Values for the kinetic coefficient measured for the crystallization of several other macromolecules using both AFM and Michelson interferometry techniques were found to be in the same range and varied from 3.2×10^{-5} cm/s for catalase [15] to 1.6×10^{-3} cm/s for canavalin [24]. For inorganic crystals grown from solution a typical value of β is on the order of 10^{-2} to 10^{-1} cm/s, i.e., 2–4 order orders of magnitude higher [54]. The lower values of β for macromolecular crystallization compared with inorganic crystallization are most likely due to several factors such as lower diffusivity, larger barriers for adsorption, and most important the necessity of the pre-kink selection of the proper orientation of an incoming macromolecule for incorporation into the growth step. It was estimated [54] that the steric probability factor (probability of the correct spatial orientation of the incoming molecule for incorporation in the lattice, relative to all other orientations) for macromole-

cules is on the order of 10^{-2}–10^{-3} compared with values close to unity for small inorganic molecules. Indeed, from direct AFM observations, as demonstrated in Section 6.2.4, the attachment probabilities of macromolecules varied from 10^{-2} to 5×10^{-4} for highly symmetrical virions on the one hand to thaumatin molecules on the other (which can have only one correct molecular orientation for incorporation into the crystal). Note that values of β scale with the size of the macromolecule [25], with larger molecules having slower kinetics. This is consistent with the facts that diffusion of the larger macromolecule, as well as rotation into a proper orientation, is likely to take longer compared with smaller macromolecules.

Values for interfacial free energies can also be deduced from AFM measurements. Thus, growth steps advance (Figure 6.8a, insert) only when their length L exceeds a critical value, L_c, [53]. Critical length L_c is related to the free energy of the step edge α by [53]:

$$L_c = 2\Omega\alpha/kT\sigma, \tag{2}$$

where k is Boltzmann's constant and T is temperature. Supersaturation dependence of step critical length, L_c, was measured as the average of growth step length immediately before and after the growth step started to advance (Figure 6.8b). From the slope of L_c ($1/\sigma$) dependencies, according to eq. (2), surface free energies of the step edge α were estimated to be 0.5 erg/cm^2 and 0.37 erg/cm^2 for $\langle 010 \rangle$ and $\langle 100 \rangle$ crystallographic directions respectively.

From successive AFM images rates of 2D nucleation J (cm^{-2} s^{-1}) were calculated for the crystallization of thaumatin and catalase over a broad supersaturation range [15]. These rates varied from only 25 cm^{-2} s^{-1} (for catalase at supersaturation $\sigma = 0.9$) to 2.2×10^6 cm^{-2} s^{-1} (for thaumatin at supersaturation $\sigma = 2.3$). The supersaturation dependencies of the normal growth rates were based on experimentally measured values of J. This dependency can be presented in coordinates $[\ln(R/\sigma^{5/6})] - 1/\sigma$ as [53,55]

$$\ln\left[R/\sigma^{5/6}\right] = \ln\left\{hc_e\beta\left[\Omega^2 han_s\right]^{1/3}\right\} - \pi\Omega\alpha^2 h/3(kT)^2\sigma, \tag{3}$$

where a is the distance between adjacent molecules, n_s is the number of nucleation centers, k is Boltzmann's constant, and T is temperature. With known values of Ω, c_e, β, T and h, values of α and n_s can be measured directly from experimentally determined data of the normal growth rates versus supersaturation in the coordinates $\ln[R/\sigma^{5/6}]$–$1/\sigma$ (Figure 6.8b). As illustrated in Figure 6.8b, instead of a straight line, different slopes at low ($1/\sigma > 1.2$, $\alpha \sim 0.2$ erg/cm^2) and higher supersaturations ($1/\sigma < 1.2$, $\alpha \sim 0.4$ erg/cm^2) were observed. Similar supersaturation dependencies of the normal growth rate were obtained for the two dimensional growth of catalase crystals and of inorganic crystals of ADP [55]. It is likely that at low supersaturation, 2D nucleation does not occur homogeneously but at hyperactive sites (defects and impurity particles), which would require significantly less surface free energy. The number of nucleation sites was estimated [9] to be $n_s \sim 1.6 \times 10^8$ cm^{-2} and 5×10^4 cm^{-2} at higher and lower supersaturations respectively.

Surface free energies of the step edge measured for several macromolecular crystals varied in the range of 0.3–5 erg/cm^2 for catalase [15], thaumatin [9] and glucose isomerase [20], to 2 erg/cm^2 for canavalin [25], and 5 erg/cm^2 for orthorhombic trypsin crystals [21]. For canavalin and trypsin crystals, which have relatively high crystal-solution interfacial energies, 2D nucleation was not observed at the highest supersaturation values

utilized, while in the case of catalase, thaumatin, and glucose isomerase, crystallization by 2D nucleation took place at relatively low supersaturations. Values for macromolecular crystals appear to be considerably lower than those estimated for inorganic crystals grown from solution [54]. However, upon scaling by the molecular sizes both values of α for macromolecular and inorganic crystals become comparable [54].

6.2.4. Growth step structures. Incorporation of macromolecules into growth steps: attachment frequencies and probabilities

Knowledge of the morphology and structure of crystal surfaces on a scale of nanometers is a governing factor in the development of a quantitative understanding of crystal growth processes. In contrast with crystallization in high vacuum, experimental data on molecular dynamics on surfaces of macromolecular crystals are virtually absent. Because of the large sizes of macromolecules, AFM allowed us, for the first time in solution crystallization, to monitor structures of growth steps and incorporation of individual macromolecules into step edges. As illustrated in Figure 6.10 these observation were performed recently for the proteins lipase [13], thaumatin [13] and for turnip yellow mosaic (TYMV) [14] and cucumber mosaic (CMV) [22] viruses. In all cases, except apoferritin, step propagation was controlled by 1D nucleation. Advancement of growth steps proceeded by one-dimensional nucleation of kinks formed by single or multiple macromolecules, with subsequent lateral extension of molecular rows by addition of macromolecules into kinks. An in-depth description of mechanisms of 1D nucleation, first introduced by V. Voronkov in late 1960's, is presented in [32,56].
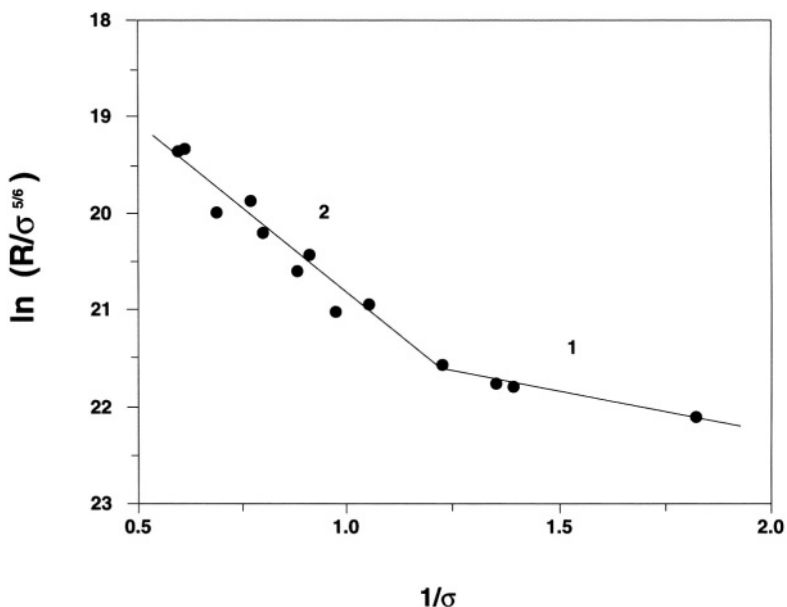
FIGURE 6.9. Supersaturation dependence of the normal growth rate for the (101) face of thaumatin crystals produced by 2D nucleation. The slope of curve 1 yields the value for the surface free energy of the step edge $\alpha \sim 0.2$ erg/cm^2; the slope of curve 2 yields $\alpha \sim 0.4$ erg/cm^2.
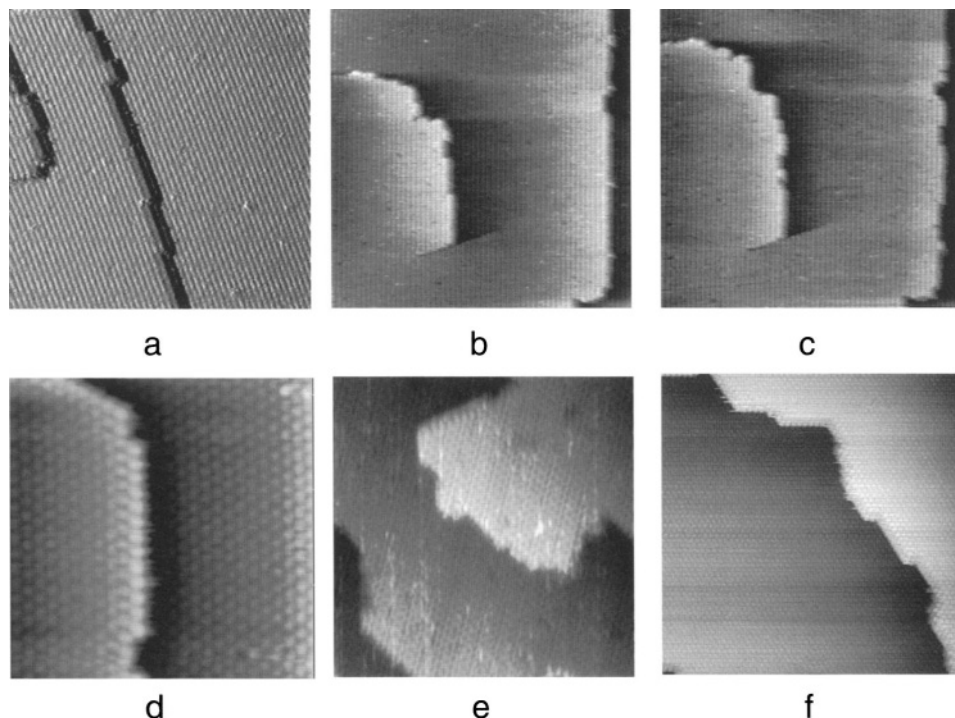
FIGURE 6.10. Structure of the growth step and one-dimensional nucleation on the step edges on surfaces of several macromolecular crystals. (a) Lipase, 880×880 nm; (b–c) thaumatin, 1×1 μm; (d) CMV, 800×800 nm; (e)TYMV, 2.25×2.25 μm and (d) STMV, 1×1 μm.

In the case of thaumatin crystallization it was demonstrated directly (Figure 6. 10b, c) that although the height of growth steps corresponds to the unit cell containing eight molecules, step advancement occurs by ordered addition of individual protein molecules [13], and the formation of 1D nuclei of varying sizes, rather than preformed multiple-molecule growth units as were suggested for tetragonal lysozyme [30]. AFM studies of step advancement on surfaces of apoferritin (Figure 6.11a [33]) and viruses [14,22] also demonstrated growth by attachment of single macromolecules.

In the case of orthorhombic lysozyme [32] only kinks of one unit cell thickness were observed (Figure 6.11b), which was due either to insufficient time resolution, or stronger binding of lysozyme molecules (compared with thaumatin) within the unit cell compared with binding along single rows parallel to the step. At relative supersaturation near unity, steps were observed to be molecularly straight (Figure 6.11b) with a very low kink density of approximately 1.7×10^{-3} kinks nm^{-1}. From experimental data for solution supersaturation of $\sigma = 1$, the rate of 1D nucleation was found to be $J = 2.7 \times 10^{-5}$ nm^{-1} s^{-1} and attachment and detachment frequencies from a kink were estimated to be approximately 50 and 25 molecules s^{-1} respectively.

Another interesting experimental observation, which could have important fundamental implications in the understanding of molecular processes in crystallization, emerged recently from AFM studies of orthorhombic lysozyme. It was reported that for the step
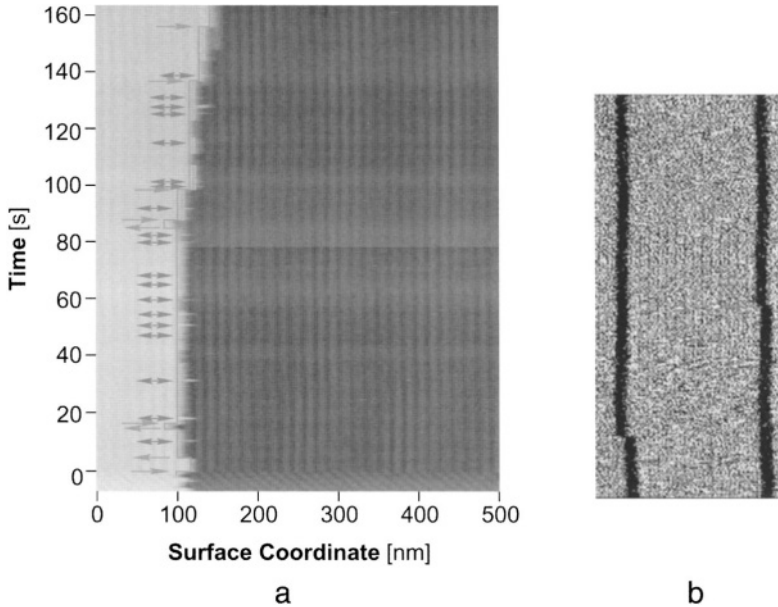
FIGURE 6.11. (a) Displacement of one step site (recorded with the Y scan axis disabled) and incorporation of apoferririn molecules into the step. Arrows indicate attachment and detachment events (courtesy of P.G. Vekilov). (b) Orthorombic lysozyme. Low kink density on the steps, 110 × 240 nm (courtesy of L.N. Rashkovich and A.A. Chernov).

segment, the large value of the critical step length, as well independence of step velocity on the segment length, are determined by low kink densities [56]. This implies that the thermodynamic Gibbs–Thomson law may applicable for short step segments only at very low supersaturations where kinetic effects become unimportant [56].

Formation of kinks at the step edges of apoferritin crystals (Figure 6.11 a) was found to be strictly due to thermal fluctuations of the molecules at the crystal–solution interface [33], opposed to a nucleation of molecular rows along a step as described above. Kink densities were found to be virtually independent of the solution supersaturation, with approximately 3 molecules between kinks in the supersaturation range of $\sigma = 1.1$–3.8. At $\sigma = 1.1$ it was estimated that one apoferritin molecule was attached in roughly 15 seconds. Free energy of intermolecular bond was estimated to be 7.3 KJ/mol.

The structures of growth steps on surfaces of CMV crystals at conditions close to equi-librium are shown in Figure 6.12. In these experiments (Figure 6.12) the concentration of CMV was only 0.04–0.06 mg/ml. At these virus concentrations no attachment of virus particles was observed during approximately one hour of imaging. Furthermore, no detach-ment of single virus particles was observed during more than 30 minutes of imaging, with the structure of the step edge remaining unchanged (Figure 6.12a, b). At increased super-saturation conditions, again no detachment of virions from the step edge was observed. Absence of detachment of macromolecules from the step edge was also observed in the crystallization of thaumatin, lipase and orthorhombic STMV crystals [13,18]. Apparently in all of these cases, macromolecules, once incorporated into the step edge, remain because thermal energy is insufficient to promote detachment of molecules from the crystal. It is
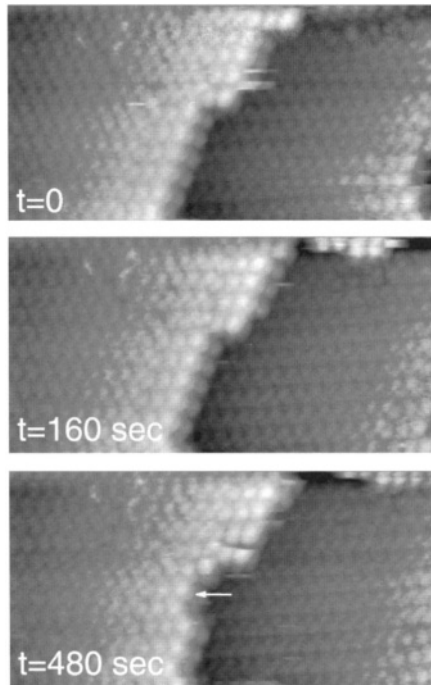
FIGURE 6.12. $1.25 \times 1.25 \ \mu m$ AFM images of the step edge on the surface of CMV crystal at conditions close to the equilibrium. No attachment or detachment of CMV virions were recorded at these conditions (a and b). In (c) the force applied to the surface was increased during the scanning (indicated with an arrow c). This resulted in the detachment of two CMV virions.

important to emphasize that for all of these macromolecular systems, no reverse movement of growth steps was observed even at zero virus concentration in precipitant. What's more, STMV crystals remain completely insoluble, once grown, and even when placed in distilled water, indicating that the energy barrier for removal of macromolecules from the crystalline lattice is substantial. This is different compared with lysozyme and apoferritin crystallization where reverse movement of growth steps and detachment of the macromolecules from the step edge were reported [32,33].

In the case of inorganic crystals grown from solution, solvatation and desolvatation processes typically exhibit relatively high activation energies [53] while the entropic activation barrier can be relatively low. The corresponding steric factor, which is the probability of a particle having the proper spatial orientation, is close to unity. In the crystallization of complex macromolecules, the necessity of desolvatation is likely less important than in the crystallization of inorganic molecules. However, macromolecules in an arbitrary orientation cannot join a growth site. Thus the entropic activation barrier must play an important role. Pre-kink selection would be expected for the approaching macromolecule to assume an acceptable orientation for incorporation into the growth step.

Because of their relatively large size of 28 nm, CMV virions can be seen by AFM as they incorporate into growth steps as individuals, thus allowing measurement of attachment frequencies under controlled supersaturation conditions. From attachment frequen-
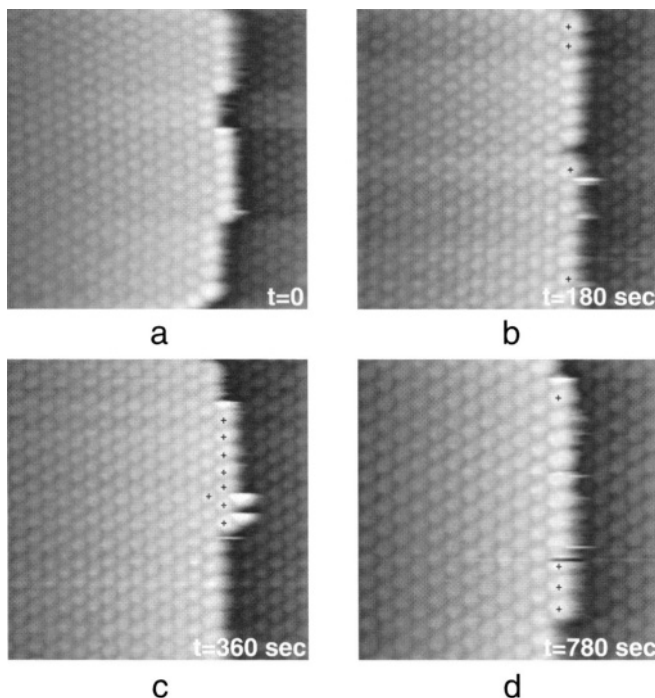
FIGURE 6.13. AFM images or an advancing growth step on the (001) face of a CMV crystal. Newly incorporated virions are indicated with (+). AFM images are 670 × 670 nm in (a–c), and 560 × 560 nm in (d).

cies, attachment probabilities can be estimated. In CMV crystals, icosahedral virions are connected in the surface layer through hexameric capsomers [57], hence there are 60 identical orientations for correct incorporation, far more than for most proteins. This should result in relatively high attachment probabilities.

As seen in Figure 6.13, advancement of growth steps proceeds by 1D nucleation of kinks, formed by single or multiple virions, with subsequent lateral extension of molecular rows by addition of virions into kinks. Under the supersaturation conditions here (~0.1 mg/ml CMV), the attachment frequency of virus particles was found to be ~2.3×10^{-2} virions/s. Again, as indicated above, there was no detachment of virus particles, either at supersaturated or equilibrium conditions, hence, thermal energy is insufficient to displace a particle from the step edge.

In these experiments the concentration of virions in solution was $c = 7 \times 10^{12}$ cm^{-3}, corresponding to an average distance between virions of $L = 5 \times 10^{-5}$ cm. Assuming that growth proceeds by direct incorporation of virions from the bulk solution into the step edge [53], and that the concentration of virions at the crystalline interface is zero, then the diffusive flux can be estimated as $J = D(C - C_0)/L = 2.2 \times 10^{10}$ s^{-1} cm^{-2}. $D = 1.6 \times 10^{-7}$ cm^2/s is the diffusivity of CMV determined from light scattering experiments. From this, virus particles encounter a kink having a size of approximately 30 × 30 nm with a frequency of approximately ~0.2 s^{-1}. Using the attachment frequencies of 2.3×10^{-2} s^{-1} measured from AFM (Figure 6.13), the attachment probability is ~10^{-2}. Thus,

approximately one out of every 100 CMV virions that approach the step edge incorporates into the step.

This probability of attachment can be related in large part to pre-kink selection of proper molecular orientation for incorporation into the growth step. For high symmetry particles, as might be expected, pre-kink selection of the proper molecular orientation is considerably less than for most macromolecules. Indeed, from the same calculation using AFM data for step advancement in thaumatin crystallization [13], the attachment probability of those protein molecules, which can have only one correct molecular orientation for incorporation into the crystal, was estimated to be $\sim 5 \times 10^{-4}$.

We would like to end our description of AFM studies of step edge structures on a cautious note. In the extensive high-resolution studies of CMV crystallization, in all cases where detachment of virions from step edges was observed, it was strictly due to the influence of the AFM tip. This is illustrated in Figure 6.12. While scanning, the force was increased by decreasing a setpoint (defines the amplitude of the cantilever oscillation signal to be maintained by the feedback loop) by the smallest value allowed by the software of only 10^{-3} V. This immediately resulted in the detachment of two virus particles (indicated with an arrow in Figure 6.12c) from the step edge. We then immediately decreased the force to the initial value and continued to image the step edge. With these conditions neither attachment nor detachment of virions was observed for the next 20 minutes of imaging. Typically, due to density fluctuations in supersaturated solution, a force should be constantly adjusted in order to prevent perturbation of the step edges. These adjustments are typically considerably larger than that described above (Figure 6.12), where even a relatively small change in the force applied to the crystalline surface results in the detachment of virions from the step edge.

Recently a first attempt was made to directly map local energy dissipation while scanning polypropylene particles embedded in a polyurethane matrix, in tapping mode [58]. According to [58] the power dissipation is $P \propto kw$, where w is the oscillation frequency and k is spring constant of cantilever. It was found that the softer polyurethane exhibits a maximum energy dissipation of about 200 eV per tap, while the same value for harder polypropylene was three times lower. These are the amounts of energy dissipated across the complete contact area, which is typically several nanometers across. Measurements were made in air using silicon cantilevers, which are about 50 times stiffer than silicon nitride cantilevers utilized in *in situ* imaging of macromolecular crystal growth. Taking into account that the oscillation frequency while imaging in the air is also higher, extrapolation of data give a rough estimate of the order of magnitude of energy dissipation of 10^{-1} eV. This value is comparable with intermolecular bond energy for most macromolecular crystals [33]. Thus, forces involved in tip–sample interactions can cause detachment of macromolecules from step edges even when imaging in tapping mode.

6.2.5. Molecular mobilities on crystalline surfaces

Because of the large sizes of virions, not only were structures of step edges and the attachment of individual virus particles to step edges visualized, but adsorption of virions and their aggregates to crystalline surfaces could also be observed. Two types of virus particles and their aggregates were observed on crystalline surfaces. In the first case, upon
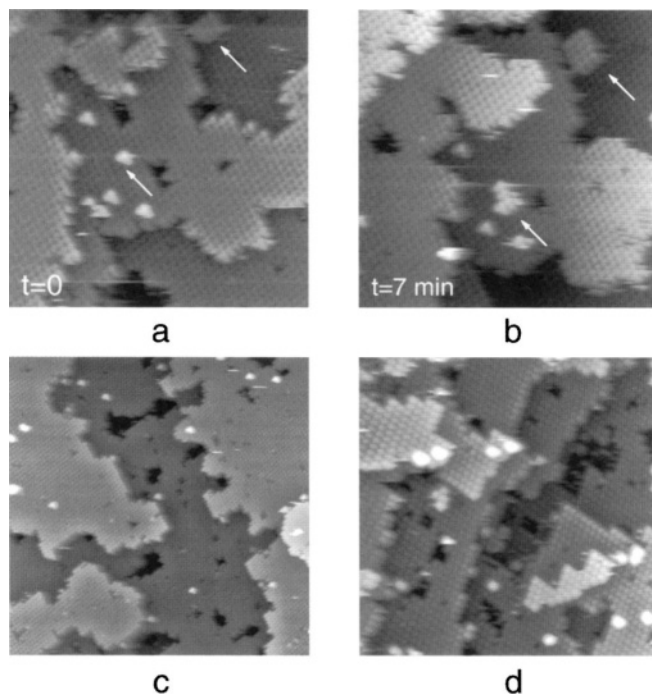
FIGURE 6.14. In (a–b) growth of two-dimensional islands (indicated with arrows) on a CMV crystal surface. A number of adsorbed virions on the crystalline surface are seen in (c) and (d). The scan sizes are (a); (b) 860×860 nm and (c) $1.6 \times 1.6 \ \mu$m and (d) $1.35 \times 1.35 \ \mu$m.

adsorption, virus particles formed small clusters, which developed into two-dimensional nuclei and provided sources of growth steps. Thus, in Figure 6.14a, a 2D island consisting of approximately 9 virus particles expanded over a time period of seven minutes by the addition of 3–4 virions. In these experiments the concentration of CMV was approximately 0.1 mg/ml. This supersaturation is relatively low for 2D nucleation compared with the crystallization of other macromolecules [18]. Furthermore, at such low solution supersaturation, the formation of a cluster containing only two virions (Figure 6.14a) results, in Figure 6.14b, in the development of a supercritical 2D nucleus containing approximately 8 virions. Here the critical 2D nucleus consists of only two virions.

Virus particles and their clusters, which adsorb to the crystalline surface but never develop into two-dimensional nuclei (Figure 6.14c, d), were consistently observed in experiments. These virus particles appear to be firmly attached to the surface and can be seen in subsequent images over long periods of time. This suggests that their interactions with the underlying surface are probably non-crystallographic. Ultimately these virions and their clusters become incorporated into growth steps, often causing defect formation. Capsids of these virions may have been modified during purification procedures. Alternatively, microhetergenity of virions could arise from differing amounts of divalent cations bound to virions.

Larger scan areas of the surface layers of the (101) planes of TYMV crystals revealed three distinctive arrangements of viral particles on surfaces and these are presented in Fig-
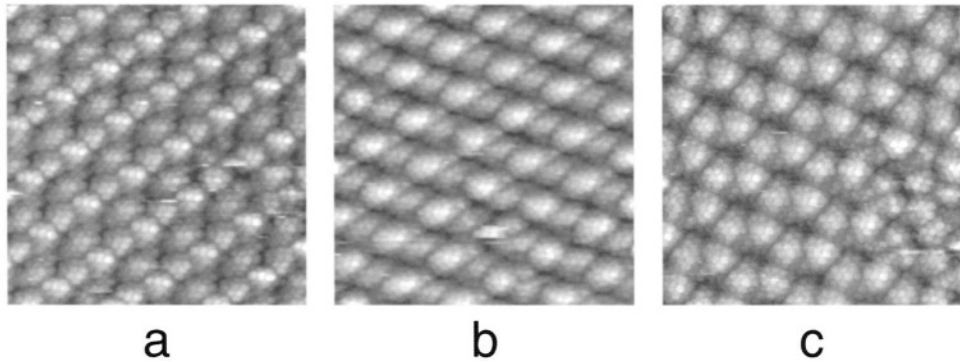
FIGURE 6.15. (a–c) 300 × 300 nm AFM images recording sequential transformations of the surface layer of the (101) face of the TYMV crystals, when exposed to equilibrium conditions. Vacancies in the surface layer, where one or more individual particles are absent, were occasionally observed.

ure 6.15. When the supersaturation was reduced to equilibrium, it was observed on a number of TYMV crystals that the patterns transformed in time from one to another. Transitions occurred rapidly, as one motif was seen at the end of a scan and another motif at the beginning of the next, where a scan period was about 4–6 minutes. The pattern seen in Figure 6.15a was initially observed on the (101) surface layer. Transformation then occurred to yield that seen in Figure 6.15b, which subsequently restructured to yield the pattern seen in Figure 6.15c. The relationship between the three motifs, and the mechanism of transformation from one to another, is shown in Figure 6.16. Starting with the motif in Figure 6.15a, and corresponding Figure 6.16a, removal of all particles of class A, which occupy specific locations in the crystallographic unit cells, yields the motif of Figure 6.15b, and corresponding Figure 6.16b. Further removal of all particles of class B, as seen in Figure 6.16b, produces the motif appearing in Figure 6.15c, and in corresponding Figure 6.16c. The process of surface restructuring was not reversible and the structure presented in Figure 6.15c was stable for prolonged periods over the course of experiments, which typically lasted for 6–8 hours. Thus the transformations can be described as an organized emission from the lattice of distinct classes of virus particles occupying specific crystallographic lattice positions. In each transition, the class of particles lost is that which protrudes highest above the surface, and which maintains least contact with the viruses forming the remainder of the crystal lattice. That is, the class which is least firmly bound and has the highest chemical potential.

6.2.6. Impurities and defect formation

A number of important properties of macromolecular crystals can be affected by the incorporation of impurities into their crystalline lattices. These include, among others, the kinetics of growth, anisotropy of the step velocities for different crystallographic directions, defect formation and defect densities, crystal habit, morphology, ultimate size, and most important, diffraction resolution and mosaicity. It is very difficult to purify macromolecular solutions to complete homogeneity and solution impurity concentrations are typically at least several molecular percent. Macromolecular solutions utilized for crystallization can
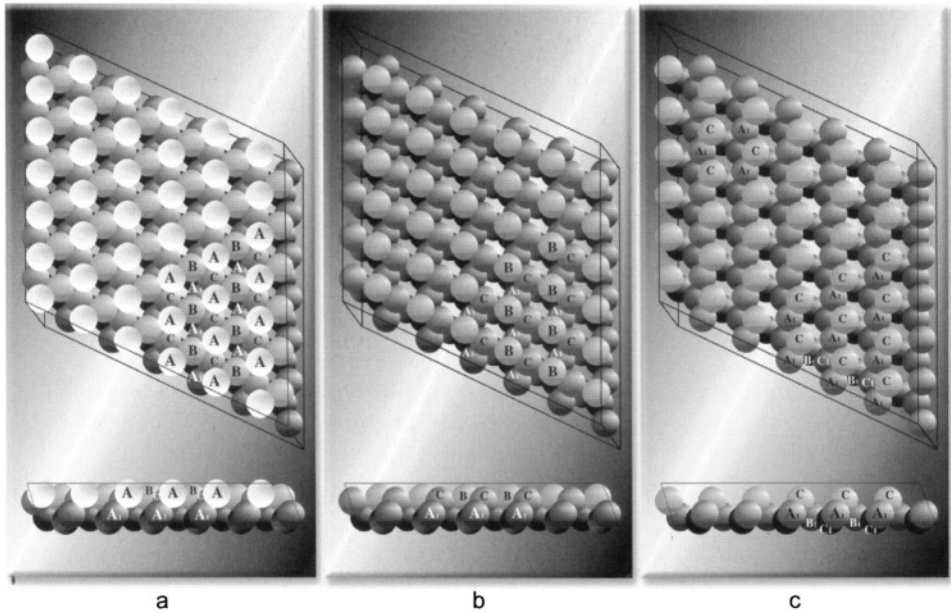
FIGURE 6.16. Computer simulated orthogonal images of the different surface structures of the (101) faces of the TYMV crystals based on the packing of the particle known from X-ray diffraction. Each class of particles A, B and C correspond to viruses occupying symmetry related positions in the unit cell. Although these units are identical in the interior of the crystal, they are unique when in a surface layer. Sequential loss of particle class A from the motif in (a), corresponding to Figure 6.15a, yields the motif in (b), corresponding to Figure 6.15b. Subsequent loss of particle class B in (b) yields the motif in (c), which corresponds to that observed in Figure 6.15c.

contain a wide variety of macromolecular impurities including modified, proteolytically altered, and partially denatured macromolecules, molecules with alternate conformations or chemically damaged residues, as well as a host of structurally unrelated molecules [1,2]. In addition, even highly purified macromolecules, may be chronically heterogeneous due to modifications, ligand binding, and denaturation [1,2].

AFM studies of macromolecular crystals [18,19] revealed a wide variety of defects parallel to those found in inorganic crystals. As illustrated in Figure 6.17 these include point defects, dislocations, and stacking faults. Total defect densities for different macromolecular crystals were found to be in the range of 10^4–10^6 cm^{-2}. At high supersaturations, typically utilized in macromolecular crystallization, microcrystals form in the bulk solutions and sediment (Figure 6.18) on the surfaces of growing crystals [18,19].

As illustrated in Figure 6.19a, b, AFM reveals impurity molecules adsorbed on the surfaces of growing macromolecular crystals, here glucose isomerase and canavalin. High densities of dimers were also found on the surfaces of growing apoferritin crystals and high-resolution images of their incorporation into the growing crystals revealed the formation of vacancies, which cause lattice stress [36]. Adsorption of covalently bound lysozyme dimers was revealed on the (101) faces of lysozyme crystals as well [31]. Trapping of impurities was found to be correlated with the diffraction properties of lysozyme crystals. Thus the distribution coefficient for this impurity was found to be 9 and 2 for lyzozyme crystals grown in ground-based laboratory and microgravity condi-
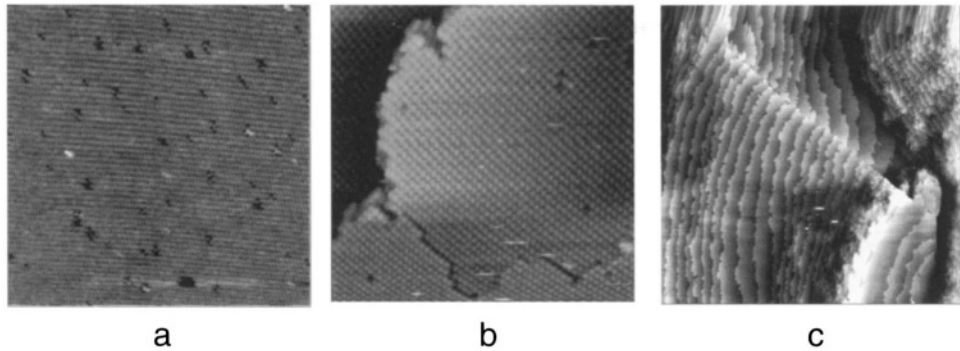
FIGURE 6.17. (a) Point defects in the crystalline lattice of CMV crystals, $3.4 \times 3.4 \ \mu$m; In (b) domain bouadary on the surface of CMV crystal, $2.25 \times 2.25 \ \mu$m and in (c) stacking fault on the surface of trypsin crystal, $40 \times 40 \ \mu$m.
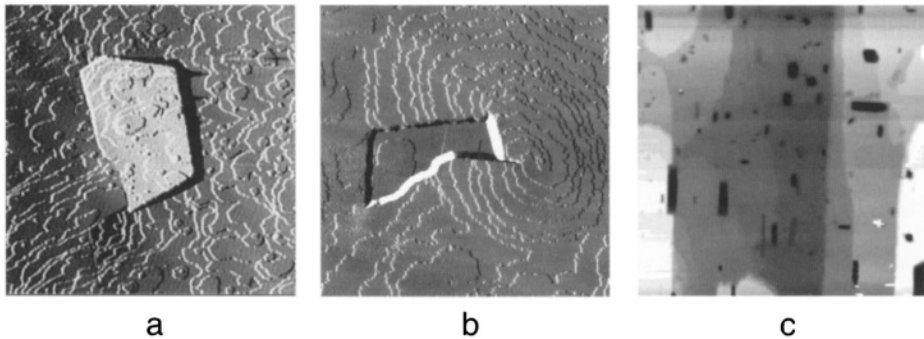
FIGURE 6.18. Incorporation of microcrystals from solution into growing crystals. In (a) thaumatin, $3 \times 3 \ \mu$m; (b) canavalin, $20 \times 20 \ \mu$m. In (c) the catalase crystal has been etched to reveal the embedded microcrystals, $42 \times 42 \ \mu$m.

tions respectively, with corresponding diffraction resolutions of 1.6 Å and 1.35 Å [59]. Based on these observations it was suggested [56] that, in the absence of solutal convection, the concentration of impurities in the solution surrounding growing crystals decreases. Thus formation of an impurity depletion zone could be responsible for improvement of diffraction properties of macromolecular crystals grown under microgravity conditions.

Incorporation of microcrystals, impurities, foreign particles, and fibers of microbial origin often results in formation of multiple defects and introduces both local and long range disorder in crystals. A striking example of how impurities can affect the diffraction properties of macromolecular crystals was demonstrated in a study, currently in progress, of impurity effects on canavalin crystallization [60]. High densities of impurities were found on the surfaces of canavalin crystals [60] with growth steps exhibiting extreme roughness (Figure 6.19c). Upon purification, a considerably lower density of impurities was observed on the crystalline surfaces, along with significant changes in surface morphology. This resulted in polygonalized dislocation spirals and straight growth steps (Fig-
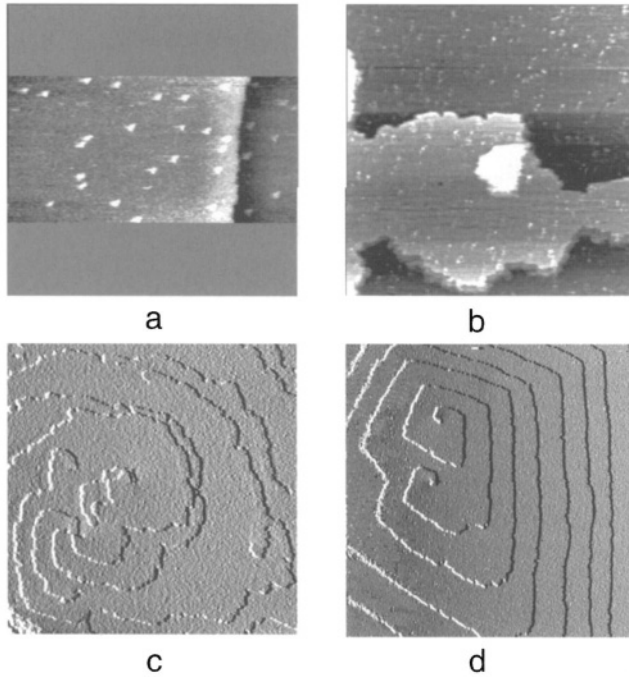
FIGURE 6.19. Visualization of adsorbed impurities on the surface of macromolecular crystals (a) glucose iso-merase, 5.5×11 μm; (b) hexagonal canavalin, 1.8×1.8 μm. In (c) and (d) change in the surface morphology and step roughness for rhombohedral canavalin crystals grown from (c) unpurified and (d) purified solutions. Scan areas are (c) 20×20 and (d) 18×18 μm.

ure 6.19d). Canavalin crystals grown from unpurified solutions diffracted to no better than 2.8 Å, while the diffraction resolution of crystals grown from purified solution improved to 2.0 Å. Here it was demonstrated directly for canavalin crystals that incorporation of impurities resulting in macroscopic stress in the crystalline lattice affect diffraction prop-erties.

Growth of macromolecular crystals typically proceeds by depletion of protein concen-tration with a consequent decrease in solution supersaturation. At low supersaturations, adsorption of impurities may result in sufficient surface stopper concentrations that steps cannot progress, and this results in cessation of growth, a phenomenon commonly observed in macromolecular crystallization. As seen in Figure 6.20a, the surface of a CMV crystal which ceased to grow is covered by a mass of virions. As illustrated in Figure 6.20b the surface of a xylanase crystal is also completely covered by a layer of adsorbed impuri-ties. When the impurity shield was partially removed, by scratching the surface with the AFM tip, growth steps appeared and growth resumed (Figure 6.20c, d). These results sug-gest that cessation of growth of macromolecular crystals is likely due to the formation of dense impurity adsorption layers. Thus it appears that the growth of macromolecular crys-tals might be sustained at appropriate, controlled supersaturations, when the exposure time of a surface between deposition of successive growth layers is less than that necessary for the adsorption of impurities. Cessation of growth of dislocation-free crystals could also be
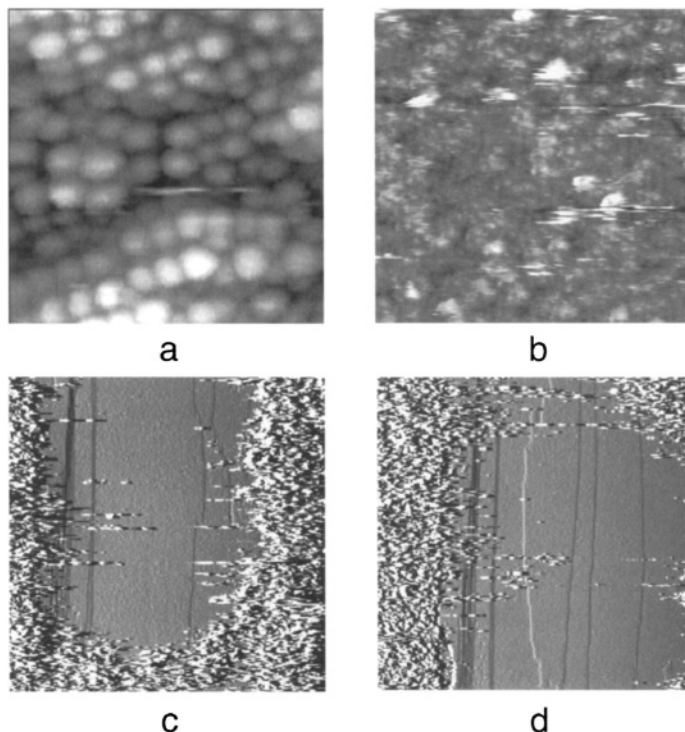
FIGURE 6.20. Surface of a CMV (a) xylanase (b) crystals is completely covered by the impurity adsorption layer resulting in a cessation in growth. On the surface of xylanase crystal this layer was partially scratched and distracted by the AFM tip, which revealed in (c) growth steps, which were buried under the impurity adsorption layer. In (d) a newly formed two-dimensional nucleus and resumption of growth. The scan areas for the AFM images are (a) 450×450 nm; (b) $8 \times 8 \ \mu$m ; (c) $15 \times 15 \ \mu$m and (d) $15 \times 15 \ \mu$m.

caused by depletion of protein concentration, since growth by two-dimensional nucleation typically requires a certain critical supersaturation.

Macrosteps and step bunching are often observed on the surfaces of macromolecular crystals. Morphological instabilities of crystalline surfaces resulting in step bunching can be responsible for defect formation in macromolecular crystals as well. Thus growth bands with different defect densities and liquid inclusions in growing crystals can be formed [53, 61]. Numerous attempts have been made in studies of inorganic crystals from solution to understand the mechanisms of macrostep formation and their decay, and to find growth conditions at which these instabilities are less likely. Interferometric studies of lysozyme crystallization revealed significant fluctuations in growth rates, and in local vicinal slopes. It was suggested that fluctuations occur through the formation and decay of step bunches that originate from the coupling of bulk transport with nonlinear interface kinetics [62]. Our AFM studies of several macromolecular crystals revealed [15] that step bunching on crystalline surfaces occurred either due to two- or three-dimensional nucleation on the terraces of vicinal slopes or as a result of uneven step generation by complex dislocation sources. No step bunching arising from the interaction of individual steps in the course of an experiment was observed.

6.2.7. Defect structure of virus crystals

In our laboratory we are carrying out both AFM and X-ray diffraction investigations of crystals of several icosahedral plant viruses. Virus crystals generally diffract to lower resolutions than do protein crystals, typically to no better than 3 Å resolution [63–66]. Crystals of CMV crystals diffracted to only 8–10 Å resolution. As illustrated in Figure 6.21, AFM images of the (001) face of CMV crystals revealed numerous domains with sizes in the range of 0.2 μm^2 to 50 μm^2. In some cases the virion surface lattice within an individual domain was misoriented with respect to the virion lattice outside the domain, as shown in Figure 6.21. The height differences between domains within the same surface growth layer varies from 0.6 nm to almost 5 nm, that is, by 2% to 18% of the diameter of the virus particles making up the lattice.

Layer growth on the (001) face of hexagonal crystals of CMV occurs by the progression of steps generated exclusively by two-dimensional nucleation (Figure 6.22). It was found that heights of growth steps produced exclusively by 2D nucleation are not equal for different steps, but vary in the range of 25–30 nm. Such differences in step heights of this magnitude on the faces of macromolecular crystals, or indeed any crystals, have not previously been observed. The smallest measured step heights of 25 nm correspond to precise alignment of growth steps upon the previous layer. Virions forming a new growth layer position themselves in triangular depressions formed by virions in the layer below, as shown in Figure 6.22c (position A). Steps having heights of 30 nm, on the other hand, have their constituent virions positioned atop particles in the preceding layer (position B in Figure 6.22c). CMV virions, it appears, form weak and geometrically imprecise bonds upon incorporation into crystals. The broad and continuous range of height differences among growth steps (0.5–5 nm) suggests that virions creating a new two dimensional nucleus may attach arbitrarily at intermediate sites between positions A and B (Figure 6.22c) on the proceeding layer. Remarkably, even within a single domain a height difference between virions of up to 1.5 nm is observed. A two-dimensional nucleus, therefore, can grow by addition of virions, which come to occupy significantly different crystallographic positions within the same growth layer.

Due to height variations, a significant number of individual two-dimensional nuclei are formed on the (001) face, which are crystallographically misoriented with respect to one another. It was demonstrated [22] that, apparently because of the non-rigorous nature of the molecular contacts in the lattice coupled with an unusually high elasticity, growth
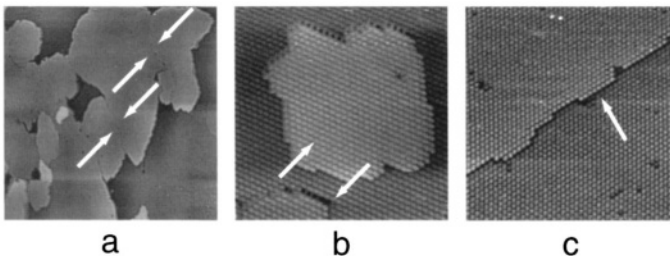
FIGURE 6.21. AFM images of the (001) face of CMV crystals showing in (a) large area revealing multiple domains (indicated with arrows). In (b–c) higher magnification AFM images of domains (indicated with arrows). The scan areas are 18×18 μm in (a), 1.3×1.3 μm in (b), and 1.5×1.5 μm in (c).
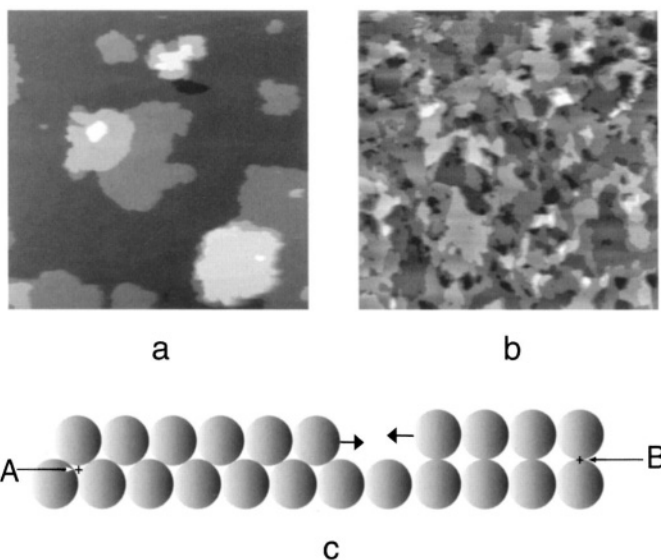
FIGURE 6.22. AFM images of the (001) face of CMV crystals showing 2D nucleation at relatively low (a) and high supersaturations (b). A cross section of the (001) face showing arbitrary attachment of virions on the underlying growth layer is in (c). AFM images are $16 \times 16\ \mu m$ in (a), and $18 \times 18\ \mu m$ in (b).

layers with height differences of up to 2 nm may, nonetheless, merge without formation of defects. At the same time coalescence of growth steps with larger height differences, in the neighborhood of 3 nm and larger, results in the formation of domain boundaries. Since growth steps cannot pass through domain boundaries, these defects propagate throughout the volume of the crystal. Growth by formation of misoriented 2D nuclei resulting in this kind of domain structure has not been previously reported, to our knowledge, either in the crystallization of conventional or macromolecular crystals.

As illustrated in Figure 6.23, surface layers of CMV crystals reveal the unexpected presence of abnormal virions with diameters in the range of 22–36 nm. As seen in Figure 6.23a incorporation of abnormal virions causes local distortion that propagates through several adjacent rows of virions and results in defect formation and accumulation of lattice strain. Density of these defects can be very high, up to $10^9\ cm^2$, which are several orders of magnitude greater than point defect densities visualized for other macromolecular crystals. As described in Section 6.3.5, a considerable number of modified virions incorporate into growing crystals. In either case, in spite of their differences, both aberrant and modified virions apparently form sufficient crystallographic interactions to be incorporated into the crystalline lattice.

AFM also proved effective in the molecular scale manipulation of defects in CMV crystals. For example, in the time between the AFM scans shown in Figure 6.23b and Figure 6.23c, an anomalously large virion (indicated by the number 3 in Figure 6.23b) was displaced from the surface layer by applying an increased force with the AFM tip. This resulted in an immediate local rearrangement of virions in the crystalline lattice and disappearance of the point defect. This, in turn, was accompanied by a further repositioning of two other virions (indicated with arrows).
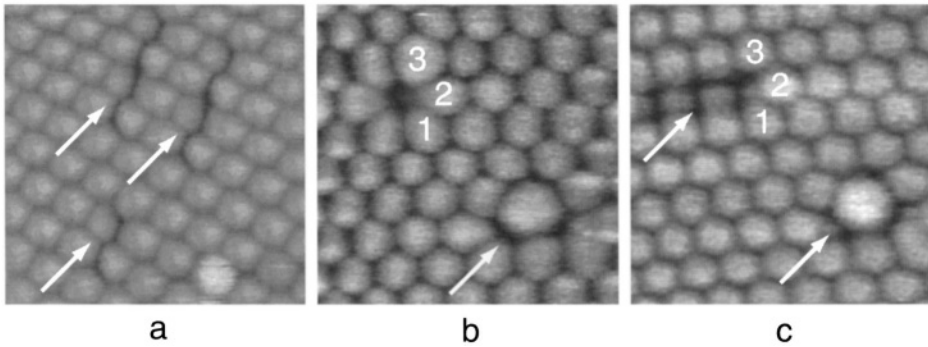
FIGURE 6.23. In (a) the incorporation of abnormal CMV virions with diameters in the range of 22–26 nm (indicated with arrows) results in defect formation. In (b) the incorporation of two abnormally large virions into the crystalline lattice is seen. Anomalous particle incorporation can proceed either without delect formation, as in the example indicated by an arrow, or result in the formation of a point defect (where the aberrant particle is indicated by the number 3). In (c), the abnormally large virion indicated by the number 3 in (c), was displaced from the surface layer by the AFM tip. This was followed by a rearrangement of the surrounding virions in the crystalline lattice. AFM images are 230 × 230 nm in (a), 190 × 190 nm in (b), and 210 × 210 nm in (c).

Particle variability within the CMV lattice due to virion microheterogeneity results in poorer long-range order compared with other macromolecular crystals. In addition, weak intermolecular bonding produces CMV crystals having extremely high mosaicity. Both of these sources of disorder are consistent with the poor diffraction properties of the crystals.

Macromolecular crystals, in general, exhibit greater mosaic spread compared with conventional small-molecule crystals [67,68]. Crystals, including those of macromolecules and viruses, are traditionally described as consisting of misoriented, mosaic blocks. Each mosaic block is, in turn, treated as a perfect crystal composed of molecules exhibiting varying degrees of local disorder [68]. In CMV crystals, blocks disrupted both long- and short-range lattice order, and the mechanisms by which they formed were evident. Mosaic block structure generally assumes that variation in domain orientation occurs on a length scale comparable to the crystal size. It arises from the domain structure of the crystalline faces, and those domains are, in turn, due to the coalescence of misoriented two-dimensional islands. Thus the observations presented here are important in identifying the sources of mosaicity, which, to a great extent, determines the resolution limit and the ultimate quality of X-ray structure determinations. Here, the classical theory of mosaic blocks achieves physical reality.

Because of the arbitrary disposition of virions within individual domains and growth layers, their deviations from average lattice orientations and positions are considerable. This produces local disorder within the CMV crystals. Mosaicity and local disorder both affect diffraction properties. The local disorder we observe for CMV crystals is likely common to crystals of most viruses, and probably crystals of most macromolecules, and this could help explain their generally poor diffraction properties [63–66] compared with conventional crystals. Effects are simply accentuated in virus crystals because of the large particle size and unit cell dimensions.

CMV crystals diffract to little more than 10 Å resolution. It is quite likely that the disorder of most icosahedral virus crystals reflects the fundamental sources identified in this investigation, but generally to lesser degrees. It is noteworthy that chemical treatments
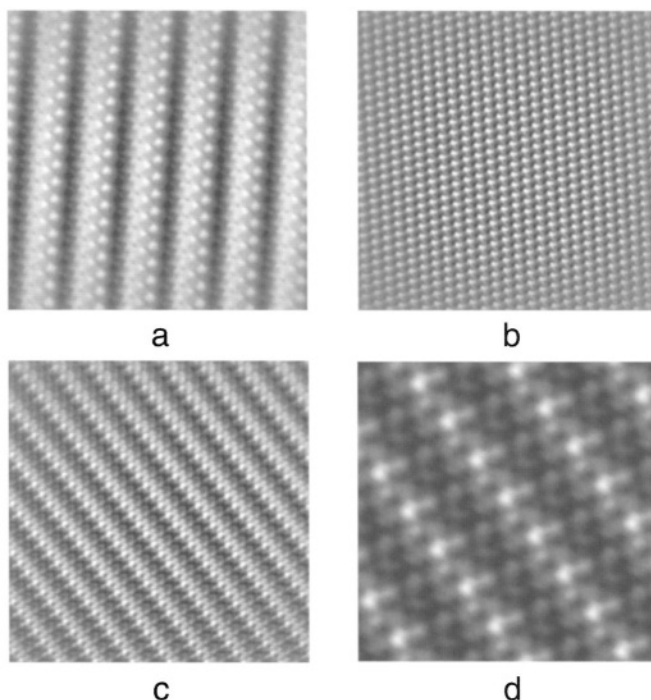
FIGURE 6.24. Lattice-resolution AFM images of macromolecular crystals. In (a), (b) and (c) are crystals of thaumatin, canavalin and lipase respectively. In (d) Fourier-filtered image (5 × 5 unit cells) of the lipase crystal. Scan sizes are (a) 100 × 100 nm; (b) 300 × 300 nm and (c) 200 × 200 nm.

during purification procedures as well as modifications of virions during storage can affect diffraction properties of virus crystals as well. This was demonstrated, for example, in the crystallization of satellite tobacco mosaic virus (STMV), where changes that occurred to individual virus particles during storage or upon exposure to different pHs resulted in structural changes to virions and these alterations were subsequently responsible for a decrease in the diffraction properties of STMV crystals [69].

6.2.8. High resolution imaging

AFM can provide molecular resolution images of the surface layers of macromolecular crystals [10,18], as exemplified by Figure 6.24. Information obtained from these images can facilitate structural studies of macromolecular crystals by providing data which accelerate and enhance X-ray diffraction analyses. Such images may yield cell dimensions, the number of molecules per asymmetric unit; provide information on the packing of molecules within the unit cell, and on the relative dispositions of molecules within the unit cells. In addition, because height information is preserved, the handedness of molecular arrangements arising from screw axes can be deduced. Thus AFM may provide a means of discriminating a screw axis from its enantiomorph [10] as was done for crystals of fungal lipase (Figure 6.23c, d), something often difficult early in an X-ray structure analysis.

AFM also allows one to obtain molecular resolution images from crystals with surfaces as small as $10\,\mu$m, which can be too small for X-ray diffraction studies. For example, AFM allowed molecular resolution studies of therapeutically important ultralente insulin crystals [28], which typically have very small sizes and diffract only to low resolution. AFM images revealed that crystal faces of these crystals exhibited cylindrical features formed by close packed insulin hexamers. It was suggested that the observed structures of these crystals prohibit solvent access to the center of the insulin hexamers and to the interiors of crystals, which could explain the slow dissolution rates of ultralente insulin formulations.

In the case of large viruses, AFM allows resolution of the gross structural features of the virions themselves. Indeed, this was demonstrated in the first direct visualization of the capsomere structure of a small virus by AFM [14]. Here Figure 6.25a, b presents AFM images of individual virus particles making up the (101) plane of hexagonal crystals of turnip yellow mosaic virus (TYMV). TYMV is a $T = 3$ icosahedral plant virus of 28 nm diameter. The structure of the virus, shown in Figure 6.25c, was determined by X-ray diffraction analysis [63]. The surfaces of individual virions within crystals as seen is Figure 6.25 were visualized and seen to be quite distinctive, with hexameric and pentameric capsomers of the $T = 3$ capsids being clearly resolved. The noteworthy features of the particles, which in this view are in the canonical orientation of the virion seen in Figure 6.25c, are the capsomers. Twelve of these are composed of five, and twenty of six protein subunits. In these images, the pentameric and hexameric clusters can be discriminated from one another and the difference between the highest and lowest points on the capsid surface, about 40 A [63] is accurately reflected by AFM. Also apparent in the images are broad, solvent filled channels that permeate the crystals and which have diameters roughly equivalent to that of a virion. Recently the orientations of individual brome grass mosaic virions (BMV), and the capsomere structure of their surfaces was also visualized by AFM [18].

The images of single virus particles provided by AFM, the accurate depiction of their structural characteristics, as well as their exact positions and orientations in the crystal lattice, may prove useful for deducing initial phase information for X-ray diffraction. Initial phase information in virus crystallography is of particular value because structure determination relies on extension of initial phases to high resolution using the icosahedral symmetry of the particles. The success of that process is directly dependent on the quality of the starting model used to formulate the initial phase set.

6.3. PROBING STRUCTURES OF HUMAN PATHOGENS WITH AFM

The clarity with which structural detail can be recorded on the surfaces of small plant viruses, like TYMV described above and which has a diameter of only 28 nm, suggests that AFM may be even more broadly useful as an analytical tool for structural investigations of large animal and human viruses. These viruses typically cannot be crystallized either because of their structural heterogeneity, or because of difficulties in producing sufficient quantities for crystallization. Moreover, large sizes of human and animal viruses often places them outside the range of X-ray crystallography. An alternative that has proven effective, though at significantly lower resolution compared with the X-ray diffraction technique, is cryo-electron microscopy (cryo-EM), often coupled with image reconstruction
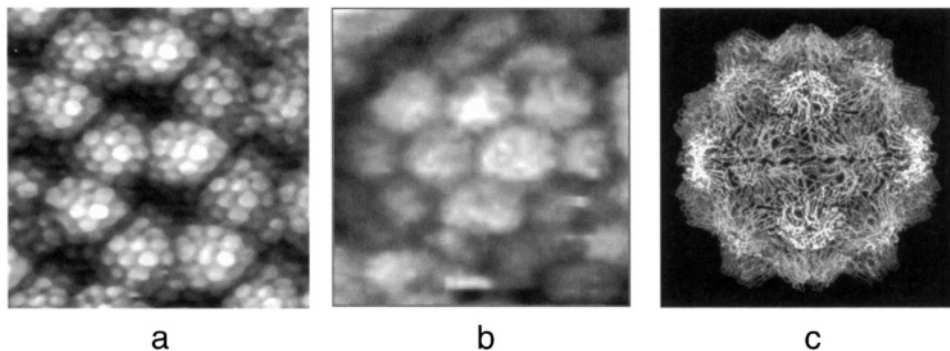
FIGURE 6.25. In (a–b) *in situ* AFM images of TYMV particles immobilized in the crystalline lattice clearly display capsomers on the surface of the $T = 3$ icosahedral virions. The capsomers, from both X-ray diffraction and AFM, are roughly 60 Å across and protrude above the viral surface by about 45 Å. (c) The structure of the capsid of TYMV based on X-ray diffraction analysis. The scan areas are (a) 140 × 140 nm and (b) 38 × 38 nm.

techniques. This approach has yielded excellent images of animal viruses at resolutions ranging from 8 Å upwards [70].

AFM can also provide a means for obtaining structural information directly from individual virus particles immobilized on a substrate. In our laboratory we tested the potential of AFM for molecular pathology with one of the most widespread human viruses, Herpes Simplex Virus 1 (HSV-1) [37]. The 8.5 Å cryo-EM model of the HSV-1 capsid structure [71] provides a standard against which AFM studies could be compared. HSV-1 consists of an icosahedral capsid of protein containing a double stranded DNA genome, and which is itself surrounded by a lipid envelope with embedded proteins. Between the membrane and the capsid are tegument proteins of various sizes. The intact virion is about 200 nm in diameter with the capsid shell of 125 nm in diameter and approximately 15 nm thick.

In Figure 6.26a an AFM image of the enveloped HSV-1 virions is presented with a number of features having dimensions in the range of 10–25 nm clearly visible on the surface of the lipid envelope. These features correlate well with the dimensions of virus-encoded glycoproteins, which are essential for virion infectivity and penetration into the host cell, and which are incorporated into the virion envelope. As illustrated in Figure 6.26b removal of the lipid envelope upon treatment with detergent allows visualization of both the tegument and capsomere structure (seen on the upper part of virus capsid). Here a capsid is seen to be covered with an irregular coating of particles of various sizes up to 10 nm. These are more likely tegument proteins, which are known to have a complex non-icosahedrally ordered arrangement and contains at least 18 different viral proteins, the largest of which, VP 1-3, has a predicted size of 336 kD [72]. This corresponds well with the observed particles of ~10 nm and smaller.

Structures of HSV-1 icosahedral capsids revealed by vigorous treatment of virions with detergent, are is presented in Figure 6.26c, d at different magnifications. The main components of the icosahedral capsid of triangulation number $T = 16$, as determined by cryo-EM, are 12 pentameric capsomeres and 150 hexameric capsomeres. These capsomeres are interconnected by 320 smaller protein complexes known as triplexes [71]. As illustrated in Figure 6.27a, b the pentameric and hexameric capsomeres can be discriminated from one
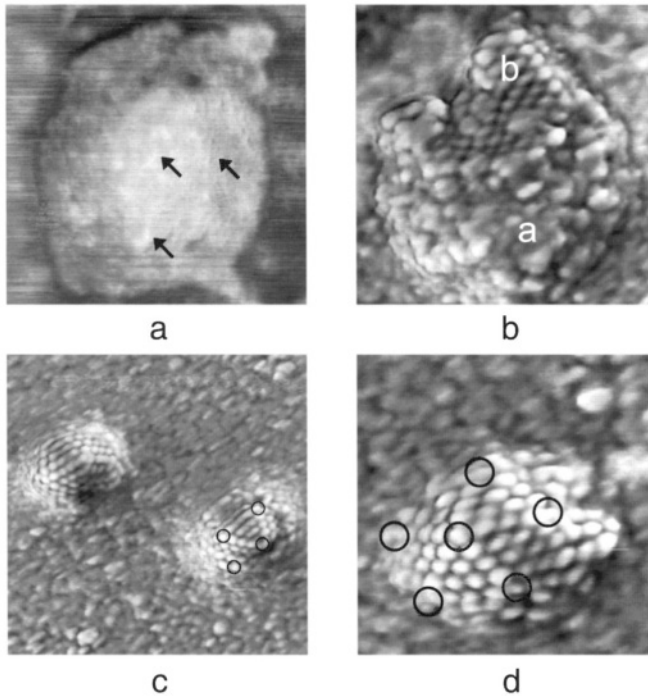
FIGURE 6.26. In (a) The HSV-1 capsid is still covered by the lipid envelope. Some elongated features of sizes 10–25 nm elongated features which may correspond to glyco-proteins are denoted by arrows. These may correspond to glyco-proteins. In (b–d) addition of 0.2% Triton X-100 removes the lipid envelope. (b) Most of this capsid is covered by a irregular collection of particles of approximately 10 nm in size (area a), which correspond to tegument proteins. In a smaller region the underlying, highly regular capsid is exposed (area b). (c) Two particles with lipid bilayer and tegument completely removed. Black circles denote pentons in one of the capsids. In (d) a completely stripped capsid at higher magnification. Again, black circles denote the pentons. The scan areas are: (a) 360 × 360 nm; (b) 650 × 650 nm; (c) 800 × 800 nm and (d) 300 × 300 nm.

another in AFM images. Diameters of capsomers of approximately 15 nm are accurately reflected by AFM. In Figure 6.27a, b not only the substructures of individual capsomeres (such as holes in the centers consistent with the structure of the capsid determined from EM), but also small protein clusters, corresponding to triplexes linking adjacent capsomeres are seen.

The capsids seen in the AFM images don't exhibit perfection implied by the cryo-EM structure (Figure 6.27c, d), though all are consistent, in a general sense, with that model. The adsorbed virions reveal the range of eccentricities that characterize the individual members of the purified population. Not only does AFM permit visualization of a-periodic features of the virions, it shows us the natural variation about the mean structure. When compared to EM single images [72], the resolution is similar.

A limitation of the EM technique is that it benefits greatly from high particle symmetry, such as icosahedral symmetry, but it is far less powerful for non-symmetrical macromolecular ensembles. Thus, for example, a number of features of vaccinia virus assembly and maturation have been revealed by thin-section EM and cryo-EM. However, because of the
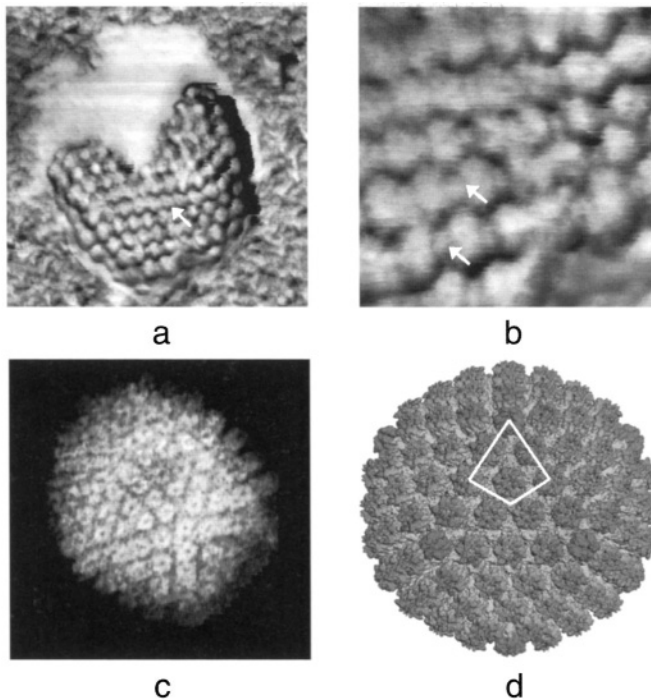
FIGURE 6.27. In (a) a HSV-1 capsid is partly covered with (white) lipid envelope with arrow pointing at capsomere with visible hollow channels in their center. In (b) triplexes, indicated with arrows are consistent with image reconstruction EM models of HSV-1 (Zhou et al., 2000). Scan areas are (a) 200 × 200 nm and (b) 100 × 100 nm. In (c) HSV-1 capsid structure visualized by electron microscopy (courtesy of Z.H. Zhou). In (d) HSV-1 capsid at 8.5 Å resolution, reconstructed by from of cryo electron microscopy images (courtesy of Z.H. Zhou). The asymmetric unit is indicated by the white line.

non-symmetrical structure of vaccinia virus, structural information derived from EM is rather limited and is not amenable to EM-image reconstruction procedures. Vaccinia virus is historically significant as a smallpox vaccine [73]. The similar structure and architecture of vaccinia virus makes it the best model system for studies of smallpox. Vaccinia is one of the more voluminous and largest human viruses with a size of approximately 450 × 350 nm. Its structure is one of the most complex known among the human viruses and rivals that of some bacteria [73].

As illustrated in Figure 6.28 AFM images of surfaces of hydrated vaccinia virions, imaged in physiological buffer, show a striking morphological feature that has not heretofore been observed for the poxviruses, namely, a highly-density array of punctuate protrusions with diameters in the range of 25–30 nm [38].

AFM can probe not only the structures of large macromolecular complexes, as illustrated in Figures 6.29, but also dynamic processes associated with the assembly or with other processes that take place under physiological conditions. Thus, as illustrated in Figure 6.29a, under reducing conditions vaccinia virus undergoes a drastic morphological change and disassembly. This is of considerable interest because reducing conditions are similar to those in the cytoplasm upon infection. The protein packing within vaccinia viral
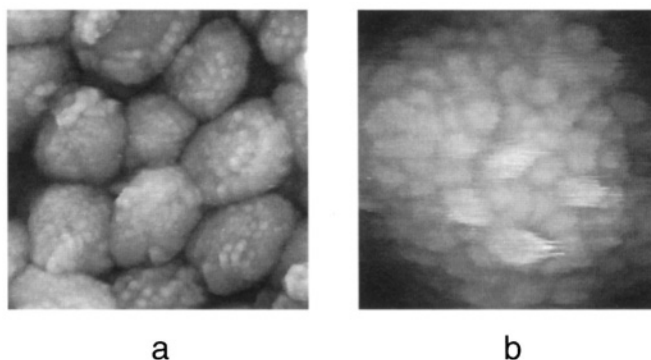
FIGURE 6.28. Fully hydrated vaccinia virions imaged *in situ* under physiological suspensions. Scan areas are (a)1.2 × 1.2 μm and (b) 365 × 365 nm.
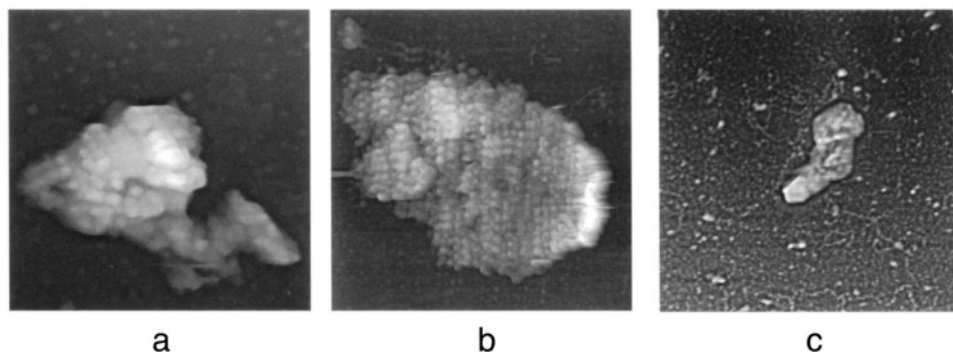
FIGURE 6.29. In (a) disassembly of vaccinia virions upon exposure to reducing conditions. In (b) protein packing in the viral membrane. In (c) DNA extrusion upon treatment with proteinase K. Scan areas are: (a) 1.25 × 1.25 μm; (b) 1.2 × 1.2 μm and (c) 2.0 × 2.0 μm.

membranes is seen in Figure 6.29b. Investigations of the extrusion of vaccinia DNA, seen in Figure 6.29c, can be important for understanding DNA packing in the virion, and for simulating DNA exit from the virion *in vivo*. AFM studies of vaccinia virus may provide important information on its structure, architecture, and dynamic properties [38].

In our laboratory we have also applied AFM to the investigation of the bacterium *Chlamedya trachomatis.* Both uninfectious elementary (EB) and infectious reticulate bodies (RB) of *Chlamedya trachomatis* were imaged *in situ* by AFM under physiological conditions (Figure 6.30). The structural basis of the outer membrane for the bacterium *Chlamedya trachomatis* (COMC) was visualized *in situ* by AFM in unanticipated detail. As illustrated in Figure 6.30b, the AFM images revealed that the COMC exhibits a supromolecular structure containing proteins with a size of approximately 50 Å. This corresponds to that of the major outer membrane protein (MOMP) trimers. The individual molecules in Figure 6.30b are readily distinguished and even some sub-molecular details are detectable. Attachment of monoclonal antibody Mab40 to COMC was also visualized *in situ* by AFM. Again, AFM was demonstrated to be a powerful and complementary experimental tool for
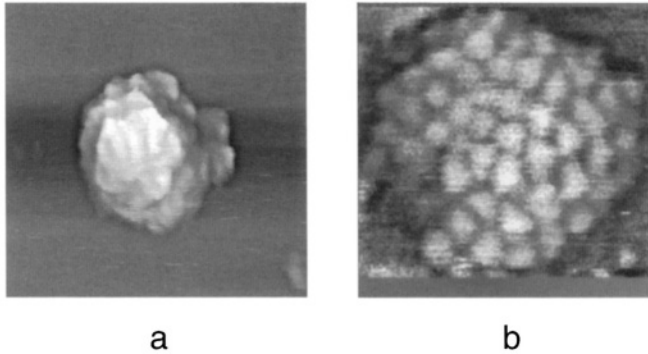
FIGURE 6.30. *In situ* AFM image of (a) *Chlamedia trachomatis* elementary body and (b) supramolecular structure of COMC. The image areas are 450 × 450 nm (a) and 80 × 80 nm (b).

a structural and functional analysis of the OM of the *C. trachomatis* MoPn serovar. Such data can be essential to the understanding of the mechanisms of transformation from EB to RB as well as for a fundamental understanding of the pathogenesis of the organism.

Currently, the principal limitation to the application of the powerful technique of atomic force microscopy in structural biology and molecular pathology is the resolution limit imposed by the finite tip radius which is typically larger than 10 nm. Overall tip sharpness becomes, furthermore, particularly important in imaging the relatively rough structures of pathogens having deep crevasses, and delineating details of protein complexes. Recently carbon nanotubes (NT) have emerged as the next generation of force microscopy probes [74,75]. These probes typically have an aspect ratio of more than 100 and end radii of curvature of only several nanometers. This presents an obvious advantage over conventional AFM probes and may provide the essential enhancement in imaging capability that is required for visualization of the molecular scale details of surfaces of pathogens. Based on recent improvements in the fabrication of ultrasharp tips, it is reasonable to expect that AFM resolution will considerably improve in the near future, making AFM resolution comparable to that of conventional EM. In addition to high-resolution imaging of pathogens itself, AFM potentially may be used to image immuno-reactions and cell infection by viruses. Its high-resolution capacity combined with its capability of imaging in aqueous environments make AFM well suited for this, and will further increase its use in the field of molecular pathogenesis.

ACKNOWLEDGMENTS

REFERENCES

1. A. McPherson, *Crystallization of Biological Macromolecules* (Cold Spring Harbor Laboratory Press, Cold Spring Harbor, New York, 1998).
2. A. Ducriux and R. Giege, *Crystallization of Nucleic Acids and Proteins* (Oxford University Press, New York, 1992).
3. S.D. Durbin and W.E. Carlson, Lysozyme crystal growth studied by atomic force microscopy, *J. Cryst. Growth* **122,** 71–79(1992).
4. S.D. Durbin, W.E. Carlson and M.T. Saros, *In situ* studies of protein crystallization by atomic force microscopy, *J. Phys. D Appl. Phys.* **26,** 128–135 (1993).
5. A.J. Malkin, T.A. Land, Yu.G. Kuznetsov, A. McPherson and J.J. DeYoreo, Investigation of virus crystal growth by *in situ* atomic force microscopy, *Phys. Rev. Letters* **75,** 2778–2781 (1995).
6. T.A. Land, A.J. Malkin, Yu.G. Kuznetsov, A. McPherson and J.J. DeYoreo, Mechanisms of protein crystal growth: an atomic force microscopy study of Canavalin crystallization, *Phys. Rev. Letters* **75,** 2774–2777 (1995).
7. A.J. Malkin, Yu.G. Kuznetsov, T.A. Land, J.J. DeYoreo and A. McPherson, Mechanisms of growth for protein and virus crystals, *Nature Structural Biology* **2**(11)**,** 956–959 (1995).
8. A.J. Malkin, Yu.G. Kuznetsov and A. McPherson, Defect structure of macromolecular crystals, *J. Struc. Biol.* **117,** 124–137 (1996).
9. A.J. Malkin, Yu.G. Kuznetsov, W. Glantz and A. McPherson, Atomic force microscopy studies of surface morphology and growth kinetics in thaumatin crystallization, *J. Phys. Chem.* **100,** 11736–11743 (1996).
10. Yu.G. Kuznetsov, A.J. Malkin, T.A. Land, J.J. DeYoreo, A.P. Barba de la Rosa, J. Konnert and A. McPherson, Molecular resolution imaging of macromolecular crystals by atomic force microscopy, *Biophys. J.* **72,** 2357–2364 (1997).
11. A.J. Malkin, Yu.G. Kuznetsov and A. McPherson, An *in situ* AFM investigation of catalase crystallization, *Surface Sci.* **393,** 95–107 (1997).
12. J.D. Ng, Yu.G. Kuznetsov, A.J. Malkin, G. Keith, R. Giege and A. McPherson, Visualizaton of nucleic acid cyrstal growth by atomic microscopy, *Nucleic Acids Research* **25**, 2582–2588 (1997).
13. Yu.G. Kuznetsov, J. Konnert, A.J. Malkin and A. McPherson, The advancement and structure of growth steps on thaumatin crystals visualized by atomic force microscopy at molecular resolution, *Surface Science* **440,** 69–80 (1999).
14. A.J. Malkin, Yu.G. Kuznetsov, R.W. Lucas and A. McPherson, Surface processes in the crystallization of turnip yellow mosaic virus visualized by Atomic Force Microscopy, *Journal of Structural Biology* **127,** 35–43 (1999).
15. A.J. Malkin, Yu.G. Kuznetsov and A. McPherson, *In situ* atomic force microscopy studies of surface morphology, growth kinetics, defect structure and dissolution in macromolecular crystallization, *J. Cryst. Growth* **196**, 471–488 (1999).
16. Yu.G. Kuznetsov, A.J. Malkin and A. McPherson, Atomic force microscopy studies of phase separation in macromolecular systems, *Phys. Rev.* **B58**(10), 6097–6103 (2000).
17. Yu.G. Kuznetsov, J. Day, R. Newman and A. McPherson, Chimeric human-simian anti-CD4 antibodies form crystalline high symmetry particles, *J. Struct. Biol.* **131**, 108–115 (2000).
18. A. McPherson, A.J. Malkin and Yu.G. Kuznetsov, Atomic force microscopy in the study of macromolecular crystal growth, *Annual Review of Biophysics and Biomolecular Structure* **29**, 361–410 (2000).
19. A. McPherson, A.J. Malkin, Yu.G. Kuznetsov and M. Plomp, Atomic force microscopy applications in macromolecular crystallography, *Acta Cryst.* **D57**, 1053–1060 (2000).
20. A.J. Malkin, Yu.G. Kuznetsov and A. McPherson, Viral capsomere structure, surfaces processes and growth kinetics in the crystallization of macromolecular crystals visualized by in situ atomic force microscopy, *J. Cryst. Growth* **232,** 471–488 (2001).
21. M. Plomp, A. McPherson, S.B. Larson and A.J. Malkin, Growth mechanisms and kinetics of trypsin crystallization, *J. Phys. Chem.* **105**(2), 542–551 (2001).
22. A.J. Malkin and A. McPherson, Novel mechanisms for defect formation and surface molecular processes in virus crystallization, *J. Phys. Chem. B* **106,** 6718–6722 (2002).
23. J.H. Konnert, P. D'Antonio and K.B. Ward, Observation of growth steps, spiral dislocations and molecular packing on the surface of lysozyme crystals with the atomic force microscope, *Acta Cryst.* **D50,** 603–613 (1994).

24. T.A. Land, J.J. DeYoreo and J.D. Lee, An *in situ* AFM investigation of canavalin crystallization kinetics, *Surface Science* **384,** 136–155 (1997).

25. T.A. Land and J.J. DeYoreo, The evolution of growth modes and activity of growth sources on canavalin investigated by in situ atomic force microscopy, *J. Cryst. Growth* **208,** 623–637 (2000).

26. M. Yip and M.D. Ward, Atomic force microscopy of insulin single crystals—direct visualization of molecules and crystal growth, *Biophys. J.* **71,** 1071–1078 (1998).

27. C.M. Yip, M.L. Brader, M.R. DeFelippis and M.D. Ward, Atomic force microscopy of crystalline insulins: the influence of sequence variation on crystallization and interfacial structure, *Biophys. J.* **74,** 2199–2209 (1998).

28. C.M. Yip, M.R. DeFelippis, B.H. Frank, M.L. Brader and M.D. Ward, Structural and morphological characterization of ultralente insulin crystals by atomic force microscopy: evidence of hydrophobically driven assembly, *Biophys. J.* **75,** 1172–1179 (1998).

29. H.Y. Li, M.A. Perozzo, J.H. Konnert, A. Nadarajah and M.L. Pusey, Determining the molecular-packing arrangements on protein crystal faces by atomic force microscopy, *Acta Cryst.* **D55,** 1023–1035 (1999).

30. M.R. Li, A. Nadarajah and M.L. Pusey, Determining the molecular growth mechanisms of protein crystal faces by atomic force microscopy, *Acta Cryst.* **D55,** 1036–1045 (1999).

31. T. Nakada, G. Sazaki, S. Miyashita, S.D. Durbin and H. Komatsu, Direct AFM observations of impurity effects on a lysozyme crystal, *J. Cryst. Growth* **196,** 503–510 (1999).

32. A.A. Chernov, L.N. Rashkovich, I.V. Yaminski and N.V. Gvozdev, Kink kinetics, exchange fluxes, 1D "nucleation" and adsorption on the (010) face of orthorhombic lysozyme crystals, *J. Physics—Condensed Matter* **11,** 9969–9984 (1999).

33. S.T. Yau, B.R. Thomas and P.G. Vekilov, Molecular mechanisms of crystallization and defect formation, *Phys. Rev. Lett.* **85,** 353–356 (2000).

34. S.T. Yau, D.N. Petsev, B.R. Thomas and P.G. Vekilov, Molecular level thermodynamic and kinetic parameters for the self-assembly of apoferritin molecules into crystals, *J. Mol. Biol.* **303,** 667–678 (2000).

35. S.T. Yau and P.G. Vekilov, Quasi-planar nucleus structure in apoferritin crystallization, *Nature* **406,** 494–497 (2000).

36. S.T. Yau, B.R. Thomas, O. Galkin, O. Gliko and P.G. Vekilov, Molecular mechanisms of microheterogenity-induced defect formation in ferritin crystallization, *Proteins: Structure, Function, and Genetics* **43,** 343–352 (2001).

37. M. Plomp, M.K. Rice, E.K. Wagner, A. McPherson and A.J. Malkin, Rapid visualization at high resolution of pathogens by atomic force microscopy: structural studies of Herpes Simplex Virus-1, *American J. Pathology* **160,** 1959–1966 (2002).

38. A.J. Malkin, A. McPherson and P.D. Gershon, Structure of intracellular mature vaccinia virus visualized by *in situ* atomic force microscopy, *J. Virology* **77,** 6332–6340 (2003).

39. G. Binning, C.F. Quate and C. Gerber, Atomic force microscope, *Phys. Rev. Lett.* **56,** 930–933 (1986).

40. C.J. Chen, *Introduction to Scanning Tunneling Microscopy* (Princeton University Press, Princeton, 1993).

41. S.N. Magonov and D.H. Reneker, Characterization of polymer surfaces with atomic force microscopy, *Ann. Rev. Mater. Sci.* **27,** 175–222 (1997).

42. C. Bustamante and D. Keller, Scanning force microscopy in biology, *Phys. Today* **48**(12), 32–38 (1995).

43. C. Bustamente, C. Rivetti and D. Keller, Scanning force microscopy under aqueous solutions, *Curr. Opin. Str. Biol.* **7,** 709–716 (1997).

44. I. Revenko, Probing the life sciences with atomic force microscopy, in: *Micro- and Nanostructures in Biological Systems,* Eds G. Bischoff and H.J. Hein (Martin Luther University, Halle-Wittenberg, 2000) pp. 1–51.

45. C. Bustamante and D. Keller, Scanning force microscopy in biology, *Phys. Today* **48**(12), 32–38 (1995).

46. P.K. Hansma, J.P. Cleveland, M. Radmacher, D.A. Walters, P.E. Hillner, M. Bezanilla, M. Fritz, D. Vie, H.G. Hansma, C.B. Prater, J. Massie, L. Fukunage, J.V. Gurley and V. Elings, Tapping mode atomic force microscopy in liquids, *Applied Physics Letters* **64,** 738–1740 (1994).

47. M. Plomp, A. McPherson and A.J. Malkin, Crystal growth of macromolecular crystals: correlation between crystal symmetry and growth mechanisms, *J. Cryst. Growth* **237,** 306–311 (2002).

48. C. Lui, A. Lomakin, G.M. Thurston, D. Hayden, A. Pande, J. Pande, O. Ogun, N. Asherie and G.B. Benedek, Phase separation in multicomponent aqueous-protein solutions, *J. Phys. Chem.* **99,** 454–461 (1995).

49. P.R. Ten Wolde and D. Frenkel, Enhancement of protein crystal nucleation by critical density fluctuations, *Science* **277,** 1975–1978 (1997).

50. P. Hartman, in: *Crystal Growth, an Introduction* (North-Holland, Amsterdam, 1973) pp. 319–367.

51. Protein Data base: http://www.rcsb.org/pdb/

52. C.M. Pina, U. Becker, P. Risthaus, D. Bosbach and A. Putnis, *Nature* **395,** 483–486 (1998).

53. A. Chernov, *Modern Crystallography,* vol. III: *Crystal Growth* (Springer-Verlag, Berlin, 1984).

54. A.A. Chernov and H. Komatsu, in: *Science and Technology of Crystal Growth,* Eds J.P. van der Eerden and O.S.L. Bruinsma (Kluwer Academic Publishers, 1995) pp. 327–353.

55. A.J. Malkin, A.A. Chernov and I.V. Alekseev, Growth of dipiramidal face of dislocation-free ADP crystals. Free energy of steps, *Journal of Crystal Growth* **97,** 765–770 (1989).

56. A.A. Chernov, Crystal growth science between the centuries, *J. Mat. Science: Materials in Electronics* **12**, 437–449 (2001).

57. T.J. Smith, E. Chase, T. Schmidt and K.L. Perry, The structure of cucumber mosaic virus and comparison to cowpea chlorotic mottle virus, *J. Virology* **74,** 7578–7586 (2000).

58. B. Anczykowski, B. Gotsmann, H. Fuchs, J.P. Cleveland and V.B. Elings, How to measure energy dissipation in dynamic mode atomic force microscopy, *Appl. Surf. Sci.* **140,** 376–382 (1999).

59. R. Thomas and A.A. Chernov, Acetylated lysozyme as impurity in lysozyme crystals: constant distribution coefficient, *J. Cryst. Growth* **232,** 237–243 (2001).

60. M. Plomp, A.J. Malkin, B.R.Thomas, A. McPherson and A.A. Chernov, unpublished.

61. S.R. Coriell, B.T. Murray, A.A. Chernov and G.B. McFadden, Step bunching on a vicinal face of a crystal growing in a flowing solution, *J. Cryst. Growth* **169,** 773–785 (1996).

62. P.G. Vekilov, J.I.D. Alexander and F. Rosenberger, Nonlinear response of layer growth dynamics in the mixed kinetics-bulk-transport regime, *Phys. Rev.* **E54,** 6650–6660 (1996).

63. M.A. Canady, S.B. Larson, J. Day and A. McPherson, Crystal structure of turnip yellow mosaic virus, *Nat. Struct. Biol.* **3,** 771–781 (1996).

64. R.W. Lucas, Yu.G. Kuznetsov, S.B. Larson and A. McPherson, The crystallization structure of Brome Mosaic Virus, *Virology* (2002) in press.

65. S.B. Larson, J. Day, A. Greenwood and A. McPherson, Refined structure of satellite tobacco mosaic virus at 1.8 Å resolution, *J. Mol. Biol.* **277,** 37–59 (1998).

66. S.B. Larson, J. Day, M.A. Canady, A. Greenwood and A. McPherson, Refined structure of desmodium yellow mottle tymovirus at 2.7 Å resolution, *J. Mol. Biol.* **301,** 625–642 (2000).

67. T.L. Blundell and L.N. Johnson, *Protein Crystallography* (Academic Press, New York, 1992).

68. R. Helliwell, *Macromolecular Crystallography with Synchrotron Radiation* (Cambridge University Press, New York, 1992).

69. Yu.G. Kuznetsov, A.J. Malkin and A. McPherson, Growth kinetics and diffraction properties of STMV crystals, *Mat. Res. Soc. Symp.* **620,** M8.4.1-M8.4.11 (2000).

70. T.S. Baker, N.H. Olson and S.D. Fuller, Adding the third dimension to virus life cycles: three-dimensional reconstruction of icosahedral viruses from cryo-electron micrographs, *Microbol. Mol. Biol. Reviews* **63,** 862–922 (1999).

71. Z.H. Zhou, M. Dougherty, H.J. Jakana, F.J. Rixon and W. Chiu, Seeing the herpesvirus capsid at 8.5 Å, *Science* **288,** 877–880 (2000).

72. M. Stannard, A.O. Fuller and P.G. Spear, Herpes simplex virus glycoproteins associated with different morphological entities projecting from the virion envelope, *J. Gen. Virol.* **68,** 715–725 (1986).

73. S. Dales and B.G.T. Pogo, *Biology of Poxviruses* (Virol. Monogr., 1981) pp. 1–156.

74. H. Hafner, C.L. Cheung and C.M. Lieber, Growth of nanotube for probe microscopy tips, *Nature* **398,** 761–762 (1999).

75. J.H. Hafner, C.L. Cheung and C.M. Lieber, Direct growth of single-walled carbon nanotube scanning probe microscopy tips, *J. Am. Chem. Soc.* **121,** 9750–9751 (1999).

7

Chemoselective ligation methods for the ordered attachment of proteins to surfaces

Julio A. Camarero*

Laboratory of Protein Engineering, Chemical Biology and Nuclear Sciences Division, Lawrence Livermore National Laboratory, University of California, 7000 East Avenue, L-232, Livermore, CA 94550, USA

7.1. INTRODUCTION

Many experimental techniques in biology and biophysics, and applications in diagnosis and drug discovery, require proteins immobilized on solid substrates [1–3]. In fact, the concept of arrays of proteins attached to a solid support has attracted increasing attention over the last three years due to the sequencing of several genomes, including the human genome. When a genome has been deciphered, the daunting task of determining the function of each protein encoded in the genome still remains. Protein arrays can be used easily for such analysis in a parallel fashion [4,5]. Another powerful application employs ordered nanometric arrays of proteins as nucleation templates for protein crystallization. Recent advances in nanoprinting techniques have allowed the creation of sub-micrometer arrays of proteins [6,7]. All these applications demonstrate the use of protein arrays and also highlight the need for methods able to attach proteins in a well defined and ordered way onto a solid supports.

Various methods are available for attaching proteins to solid surfaces. Most rely on non-specific adsorption [7,8], or on the reaction of chemical groups within proteins (mainly, amino and carboxylic acid groups) with surfaces containing complementary reactive groups [9,10]. In both cases the protein is attached to the surface in random orientations. The use of recombinant affinity tags addresses the orientation issue. However, in most cases the interactions of the tags are reversible (e.g., glutathione S-transferase, maltose binding protein and poly-His [11,12]) and therefore not stable over the course of subsequent assays or require large mediator proteins (e.g., biotin-avidin and antigen antibody [13,14]).

---

*E-mail address: camarerol@llnl.gov

Covalent attachment and orientation of a protein to a solid support requires two unique and mutually reactive groups on the protein and the support surface. The reaction between these two groups should be highly chemoselective, thus behaving like a molecular *'velcro'*. Also, the reaction should work under physiological conditions (i.e. in aqueous buffers around pH 7) in order to avoid the denaturation of the protein during the coupling step. Finally, it is desirable that the reactive group on the protein could be obtained using recombinant protein expression techniques.

The scope of this chapter is to review in detail all the chemoselective methods reported in the literature for immobilizing proteins on surfaces through covalent bonds and in well defined orientations.

7.2. SHORT SURVEY IN PROTEIN CHEMISTRY

Naturally occurring proteins contain combinations of many or all the 20 genetically coded L-α-amino acids (Table 7.1). Every different amino acid has slightly different physicochemical and structural properties. These properties play a key role in protein structure [15]. The individual amino acids in a protein or peptide are linked together via amide (peptide) bonds forming a linear sequence of amino acids (see Figure 7.1). This sequence is called the primary structure of a protein or peptide. According to the Nobel winning work of Anfinsen [16], all the information required for protein folding is somehow encoded within that sequence. As shown in Figure 7.1 the peptide bond is rigid and planar and for thermodynamic reasons always adopts a nearly *trans* conformation (note that Pro may also adopt sometimes the *cis* conformation due to a lower barrier for the *cis–trans* isomerism). The adoption of planar structure allows the partial delocalization of the carbonyl π-system on the C–N bond, which gives it some double bond character and explains its higher stability versus other chemical functionalities like the ester or thioester functions.

The secondary structure of a protein is defined as the localized three-dimensional (3D) structure of the amino acid sequence. The most common types of secondary structure are helixes (α and 3_{10}), β-sheets and turns (Figure 7.2). These secondary structural elements are mainly stabilized by backbone hydrogen bonding interactions and in most proteins are able to orient themselves with respect to one another in a relatively well defined three-dimensional structure. This three-dimensional structure is referred as the folded state of the protein or tertiary structure (see Figure 7.2). The folded state of a protein is stabilized by three classes of interactions, which are hydrogen bonding (e.g., involving side-chains containing the –OH groups such as in Tyr, Thr and Ser), electrostatic bonding (involving coulombic bonding interactions between the negatively charged carboxylate side chains of Asp and Glu and the positively charged side-chains of Arg, His and Lys) and van der Waals bonding (namely, dipole/dipole, dipole/induced-dipole and induced-dipole/induced-dipole). In addition, covalent crosslinking (disulfide formation between the side-chain of Cys residues) sometimes may help to stabilize the folded state of some proteins.

Some larger proteins contain more than one polypeptide chain. These multisubunit proteins have a more complex shape, although they are still governed by the same forces that twist and fold a single polypeptide chain. The unique three-dimensional interactions between different polypeptide chains defines the quaternary structure. It is important to remark that all the chemical, physical and biological properties of a given protein will be defined by its three-dimensional structure.

TABLE 7.1.

Structure and chemical properties of the 20 proteinogenic amino acids. Note that except for glycine, all of the remaining amino acids are chiral with L configuration (S configuration except for cysteine that is R in the Cahn–Ingold–Prelog system).

Symbol	Name	Structure	Properties	Occurrence (%)	Side-chain pKa
A, Ala	Alanine		non-charged non-polar	7.49	-
C, Cys	Cysteine		non-polar unless ionized	1.82	≈8.5
D, Asp	Aspartic acid		negatively-charged polar	5.22	4.5
E, Glu	Glutamic acid		negatively-charged polar	6.26	4.6
F, Phe	Phenylalanine		non-charged non-polar	3.91	-
G, Gly	Glycine		non-charged non-polar	7.10	-
H, His	Histidine		positively-charged polar	2.23	6.2
I, Ile	Isoleucine		non-charged non-polar	5.45	-
K, Lys	Lysine		positively-charged polar	5.82	10.4
L, Leu	Leucine		non-charged non-polar	9.06	-
M, Met	Methionine		non-charged non-polar	2.27	-
N, Asn	Asparagine		non-charged polar	4.53	-
P, Pro	Proline		non-charged non-polar	5.12	-
Q, Gln	Glutamine		non-charged polar	4.11	-
R, Arg	Arginine		positively-charged polar	5.22	≈ 12.0
S, Ser	Serine		non-charged polar	7.34	-
T, Thr	Threonine		non-charged polar	5.96	-
V, Val	Valine		non-charged non-polar	6.48	-
W, Trp	Tryptophan		aromatic non-polar	1.32	-
Y, Tyr	Tyrosine		aromatic polar	3.25	9.7
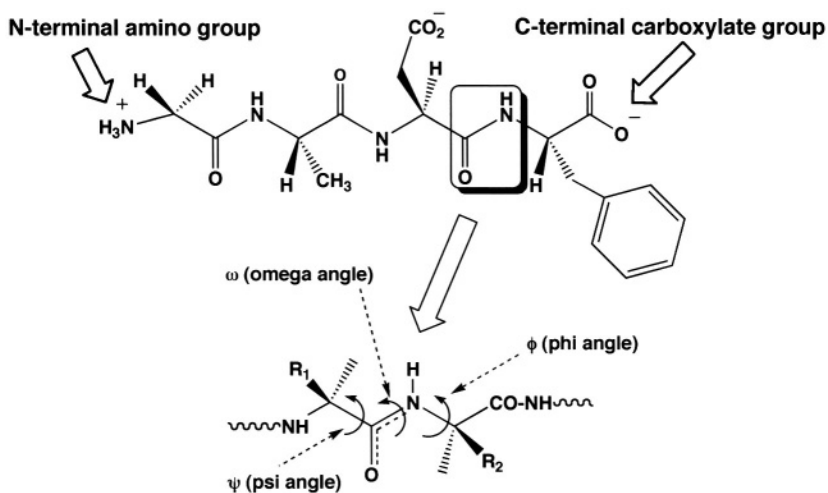
FIGURE 7.1. Nomenclature of proteins and peptides. Graphical representation of the extended conformation of tetrapeptide H–Gly–Ala–Asp–Phe–OH. Note that the sequence is always described from the N-terminal amino group to the C-terminal carboxylate group. The shadowed box shows in larger detail the planarity of the peptide bond as well as the angles that define the peptide backbone three-dimensional structure. The dihedral angle ω contains the peptide bond and it is either equal or close to 0 or 180° (i.e. *cis* or *trans* configuation).

The opposite of a well defined folded state is the so-called random coil state, which has no well defined or long lived architecture. All proteins can be induced into a random coil state (a process known as unfolding) by thermal or chemical denaturation (using chaotropic agents, extreme pH and organic solvents) as well as chemical modification. In most cases the unfolding of a protein will result in the loss of its biological activity.

This brief introduction should allow the reader to visualize proteins as very large and complex organic molecules rather than featureless solid objects as represented in some biology text-books.

7.3. CONCEPT OF CHEMOSELECTIVE ATTACHMENT AND ITS REQUIREMENTS

The principle of chemoselectivity is fundamental to modern protein chemistry, and it describes the ability to selectively modify one functional group in the presence of other chemical groups. Sometimes chemoselectivity is also referred as orthogonality.

We are interested in the reaction between a unique chemical group present in the protein with a complementary one contained on a surface where the protein is to be attached (Figure 7.3). This reaction must not be affected by the presence of the other reactive groups in the protein (i.e. amino, carboxylic acid, thiol and hydroxyl). In this way the protein is specifically attached to the surface through a unique reacting moiety which provides control of the orientation of the protein on the surface. A successful outcome requires the introduction of complementary reactive groups into the protein and surface respectively. In organic chemistry these complementary groups are often referred to as electrophiles and nucleophiles and correspond to Lewis acids and Lewis bases respectively. The reaction be-

Primary Structure of Egg-Lysozyme

KVFGRCELAAAMKRHGLDNYRGYSLGNWVCAAKFESNFNTQATNRNT
DGSTDYGILQINSRWWCNDGRTPGSRNLCNIPCSALLSSDITASVNCAK
KIVSDGNGMNAWVAWRNRCKGTDVQAWIRGCRL

Secondary structure
elements

Protein Folding

Tertiary structure

N

C
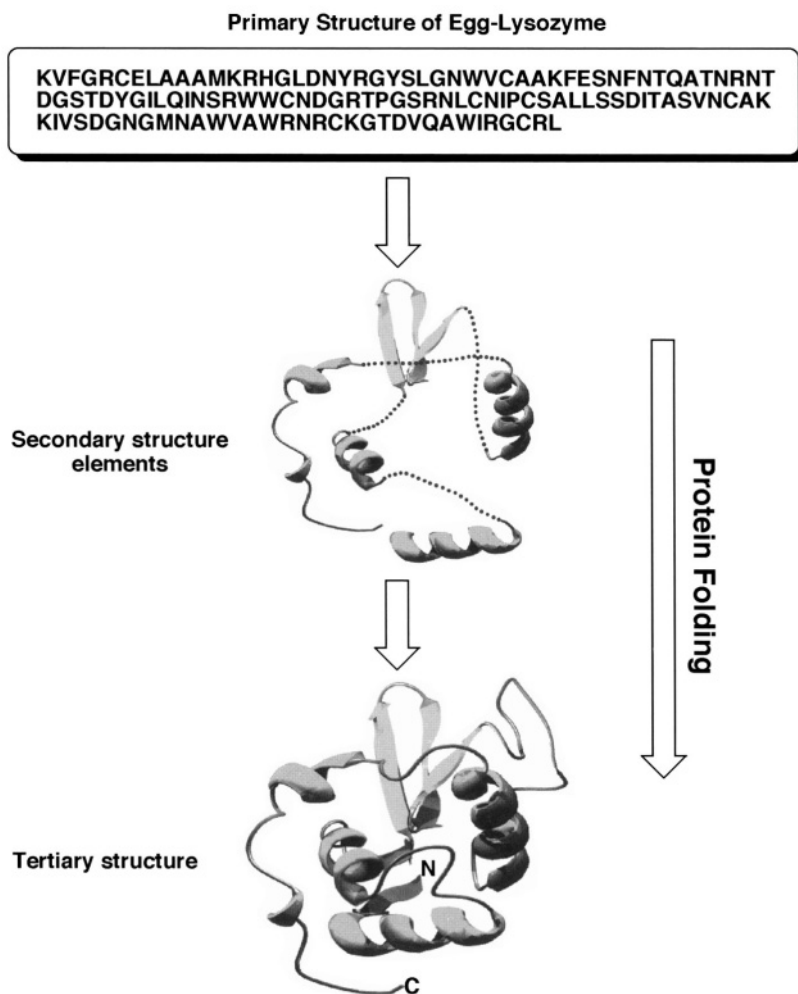
FIGURE 7.2. Example of how the amino acid sequence of a protein (i.e. primary structure) defines the three-dimensional structure of a protein (lysozyme).

tween the two complementary groups has to be compatible with physiological conditions (i.e. aqueous buffers at neutral pH) in order to avoid the denaturation of the protein during the coupling step. Furthermore, since most of the proteins can only be obtained through recombinant methods, it also desireble to have an easy and general way to introduce these reactive groups into the protein using protein expression techniques.

Although proteins contain a great variety of functional groups (see Table 7.1), it is important to note that these chemical functionalities are basically nucleophiles (i.e. amino, guanidino, hydroxyl, thiol and imidazole), and with three notable exceptions, all are protonated and hence unreactive at or around neutral pH. The exceptions are the imidazole ring (His side-chain, see Table 7.1), the thiol (Cys side-chain) and the α-amino groups (see
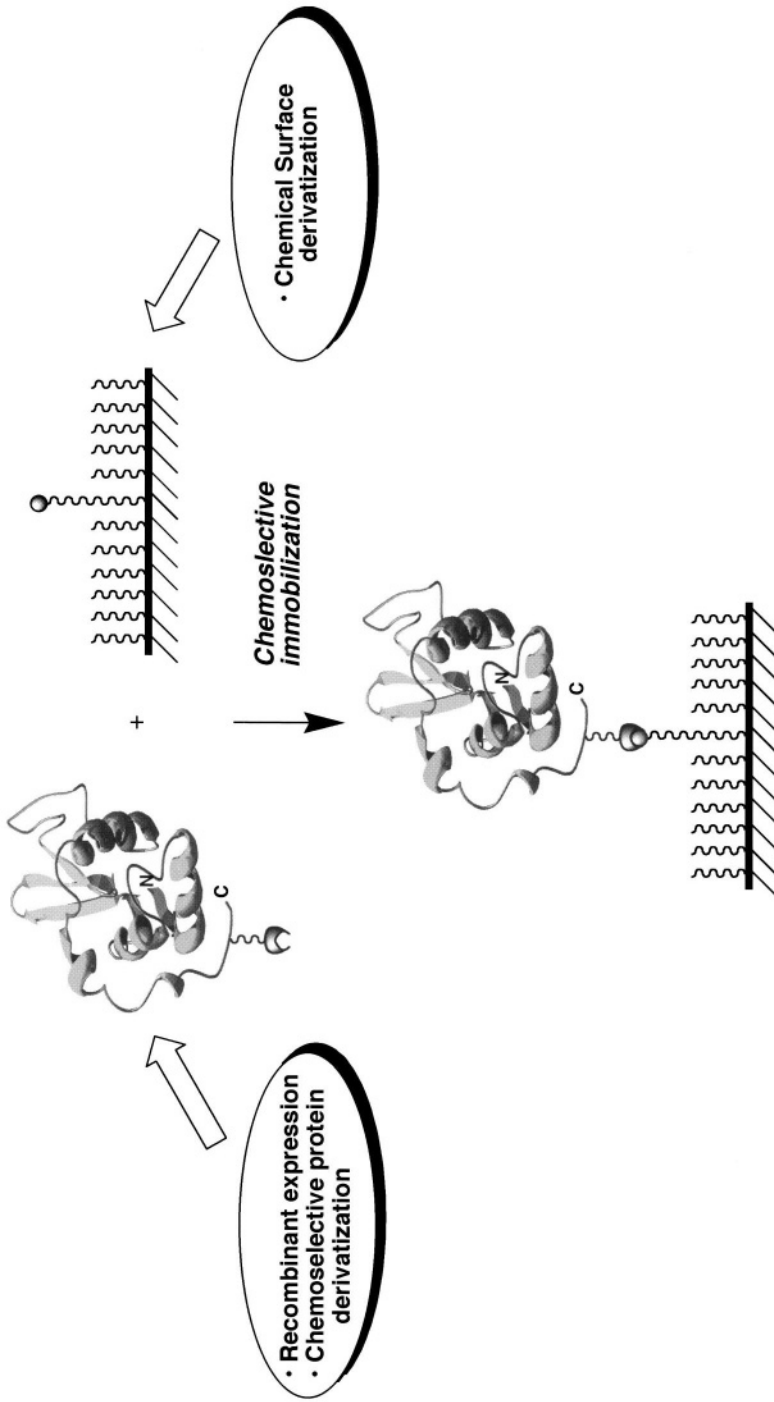
FIGURE 7.3. General concept of chemoselective reaction between a protein and a appropriately chemically modified surface. Key to this concept is the introduction of two reactive groups that will react chemoselctively in the presence of other chemical moieties (i.e. they work like a 'molecular velcro').

Figure 7.1). Note also the lack of electrophiles in the 20 genetically coded amino acids. This is important as we will see later in some chemoselective attachment strategies.

7.4. METHODS FOR THE CHEMOSELECTIVE ATTACHMENT OF PROTEINS TO SURFACES

Most of the methods suitable for the chemoselective attachment of proteins to surfaces are based on ligation methods originally developed for the synthesis, semisynthesis and selective derivatization of proteins by chemical means [17–24]. As shown in Figure 7.4, all these methods involve the derivatization of a protein with a unique chemical group at a defined position, which will be later reacted chemoselectively with a complementary group previously introduced into the surface.

7.4.1. *Chemical modification of surfaces*

When trying to attach proteins to surfaces the most common employed surfaces are silicon based (e.g. glass slides or Si/SiO_2 wafers) or metals (mainly Au and Ag).

The most used agent for chemically derivatizing silicon based surfaces is γ-aminopropyl)trialkosysilane [25–28] (APS, see Figure 7.5A) which is relatively cheap and easy to handle. Moreover, the presence of the amine group allows to carry out a variety of subsequent chemical transformations to produce the desired complementary chemical moieties that will react with the appropriately modified protein. The reaction between the silane and the surface hydroxyl groups seems rather simple but is nevertheless rather complex. In aqueous solvents the amino group rapidly catalyzes the hydrolysis of the alkoxy groups. These hydrolyzed silane molecules do not only react easily with the surface silanol groups but also condense with each other to form siloxane oligomers. Remaining alkoxy groups and hydroxyl groups can form then hydrogen bonds with surface silanols and amine groups or form cross-links within the coupling layer (Figure 7.5B). Baking the silanized surface for a short period of time after the silanization process has been shown to help in increasing the degree of crosslinking and hence the hydrolytic stability of the corresponding surface [29].

Structural investigations have shown, that in fact the APS molecules in these three-dimensional polysiloxane networks can be in many conformations and orientations with respect to the surface and form definitely no monolayers [30]. Ideal APS monolayers, as shown in Figure 7.5C, are only formed by vapor phase silanization techniques [25,26]. Although in some applications the smoothness of the surface is not normally an issue, in some other applications (e.g. creation of molecular templates as crystallization seeds) it is critical. One way to avoid structural randomness is to use long-chain trichlorosilanes. These molecules react faster with the silanol groups of the surface and also due to self-assembling character of the long alkyl chains, as result of the lateral van der Waal forces between the alky chains, are able to form densely packed highly ordered monomolecular assemblies with solid-state-like properties [31]. Unfortunately, the use of APS analogues with long alkyl chains such as (17-aminoheptadecil)trimethoxysilane, does not give rise to well ordered monolayers [32]. This is very likely due to the hydrogen bond formation between the amine group and silanol surface. Proper chemical derivatization of the resulting monolayer can be achieved by using 1-bromo-16-(trichlorosilyl)hexadecane, which forms close

	Protein			Surface		Type of
Reactive group	Introduction	Location	Reactivity	Reactive group	Reactivity	covalent bond
R—SH	Natural Cys residue or introduced by mutation	C-terminal N-terminal Accessible loops	Nucleophile	I—CH₂—C(O)—NH~ / maleimide	Electrophile	Thioether
R—CHO	Oxidation of glycoproteins and N-terminal Ser, Cys or Thr residues	N-terminal and glycosylation site	Electrophile	H₂N-HN~ / H₂N-O~	Nucleophile	Hydrazone or oxime
R—C(O)—SR″	Express protein as C-fusion with intein then treatment with soluble R″-SH	C-terminal	Electrophile	HS~ / H₂N~ / H₂N-HN~ / H₂N-O~	Nucleophile	Amide, hydrazide or oxamate
R—C(O)—NHNH₂	Express protein as C-fusion with intein then treatment with hydrazine	C-terminal	Nucleophile	OHC~	Electrophile	Hyfrazone
R—C(O)—SH	Express protein as C-fusion with intein then treatment with bisulfide	C-terminal	Nucleophile	X-CH₂-C(O)-NH~ X: I, Br / maleimide	Electrophile	Thioester
H₂N-CH(R)-XH Z X: O,S Z: -H,-CH₃	Natural N-terminal Ser, Thr or Cys residues, otherwise introduced by mutation	N-terminal	Nucleophile	OHC~	Electrophile	thiazolidine or oxazolidine
R—N₃	Replacement of Met residues with azidohomoalanine	Anywhere, preferentially accessible loops	Electrophile	Ph₂P-C₆H₄-C(O)-S~	Nucleophile	Amide

FIGURE 7.4. Summary of different chemoselective approaches that can be used for the attachment of proteins to surfaces with total control over the orientation.
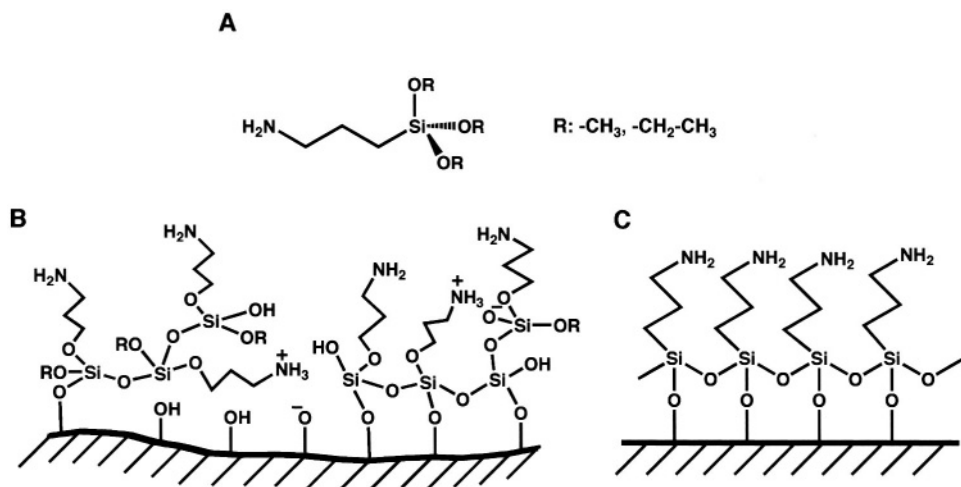
FIGURE 7.5. Derivatization of silicon-based surfaces using (γ-aminopropyl)trialkoxysilane (APS, note the the methoxy derivative is more reactive than the ethoxy one). (A) Structure of the APS molecule. (B) Schematic representation of a real APS multilayer obtained by liquid-phase deposition. (C) Schematic representation of an ideal APS monolayer.
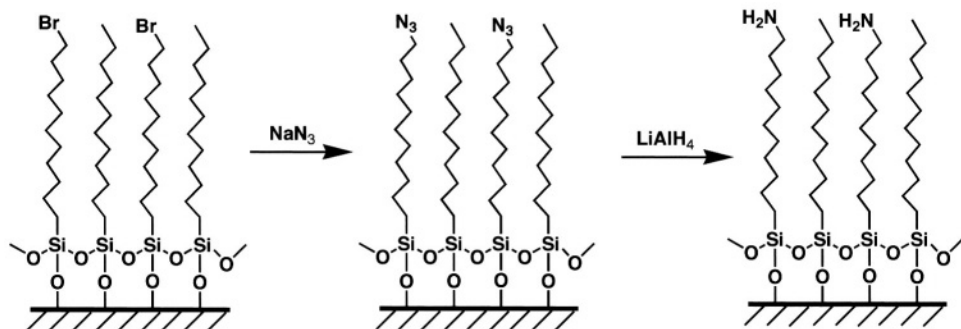
FIGURE 7.6. Schematic representation of a mixed silane self-assembled monolayer (SAM) and subsequent *in situ* modification for the introduction of a primary amino group.

packed ordered monolayers [33]. The bromo groups can be later substituted by azide anions which can be subsequently reduced to amine groups. Heise and co-workers [34] have also shown that mixed self-assembled monolayers (also known as SAMs) can be used for tuning the concentration of amine groups on the surface (Figure 7.6). As described before, these amino groups can be easily derivatized with the desired complementary chemical group for the reaction with the adequate protein derivative (Figure 7.4).

Another approach for derivatizing a surface suitable for the attachment of proteins is the use of a metal substrate like gold. Sulfur and selenium compounds have a strong affinity for this transition metal and they are also able to coordinate very strongly to other transition metals such as silver, copper and platinum [35].

The most studied system, however, is the use of alkanethiols on Au(111) surfaces. Chemisorption of alkanethiols as well as alkyl disulfides on clean gold gives rise to similar levels of surface coverage, although thiols react faster than disulfides [36]. The reaction between the gold surface and the disulfide happens through a simple oxidative addition of the S–S bond to the gold surface:

$$RS-SR + Au_n^0 \rightarrow RS^- Au^+ \cdot Au_n^0$$
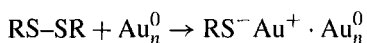
In the alkanelthiol case, the reaction may be considered formally as an oxidative addition of the S-H bond to the gold surface, followed by a reductive elimination of the hydrogen. When a clean surface is used this hydrogen probably ends as a H_2 molecule:

$$R-S-H + Au_n^0 \rightarrow R-S^- Au^+ \cdot Au_n^0 + 1/2H_2$$
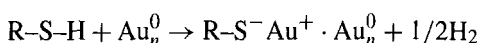
The combination of hydrogen atoms at the metal surface to yield molecular hydrogen is thought to be an important exothermic step in the overall chemisorption energetics. The bonding of the thiolate to the gold surface is very strong (homolytic bond strength is approximately $40 \, kcal \, mol^{-1}$) [37].

Alkylaminothiols are the most common species used for the preparation of functionalized gold surfaces. Among them, cysteamine ($HS-CH_2-CH_2-NH_2$) is probably the most used [38–41], in part due to its availability. Mercaptoalkyl carboxylic acids [$HS-(CH_2)_x-CO_2H$)] can also be used to introduce a reactive group on the gold surface [41], however the amine group has slightly more potential than the carboxylic group for introducing chemical diversity on the surface, as we will see later.

As stated earlier for the silanes, the thiol molecule should contain long alkyl chains when ordered and packed surfaces are a requirement. Whitesides and coworkers have developed several chemical approaches for the synthesis of functionalized long chain alkane thiols [11,42,43]. Key to all these approaches is the incorporation of a tri(ethylene glycol) moiety to the alkanethiol, which has been shown to decrease the non-specific adsorption of proteins to surfaces [43,44]. However, all of these synthetic approaches involve the use of liquid-phase methodologies, which are very time consuming. In our group we have developed a new solid-phase scheme for the rapid generation of modified long alkanethiols [45] (see Figure 7.7). The first step involves the immobilization of the corresponding ω-mercaptoalkanoic acid on a trityl chloride resin. The thiol moiety of the carboxylic acid reacts selectively with the trityl chloride resin forming a thioether which results in the immobilization of the ω-mercaptoalkanoic acid on the solid-support. The free carboxylic function is then activated with HBTU (2-(1H-benzotriazole-1-y1)-1,1,3,3-tetramethyuronium hexafluorophosphate) (HBTU) in DMF (dimethylformamide) after which is reacted with a mono-protected diamine. This step transforms the previous carboxylic function in a more versatile amino group. After the deprotection step, the amino group is then acylated with a tri(ethylene glycol) molecule incorporating both a protected amino and carboxylic groups. This step incorporates a tri(ethylene glycol) moiety to the thiolalkane at the same that keeps the amino group that can be then derivatized with the appropriate complementary reactive moiety (see Figure 7.4). The final step involves the cleavage and deprotection of the product from the resin, which is accomplished by treatment with trifluoroacetic acid.
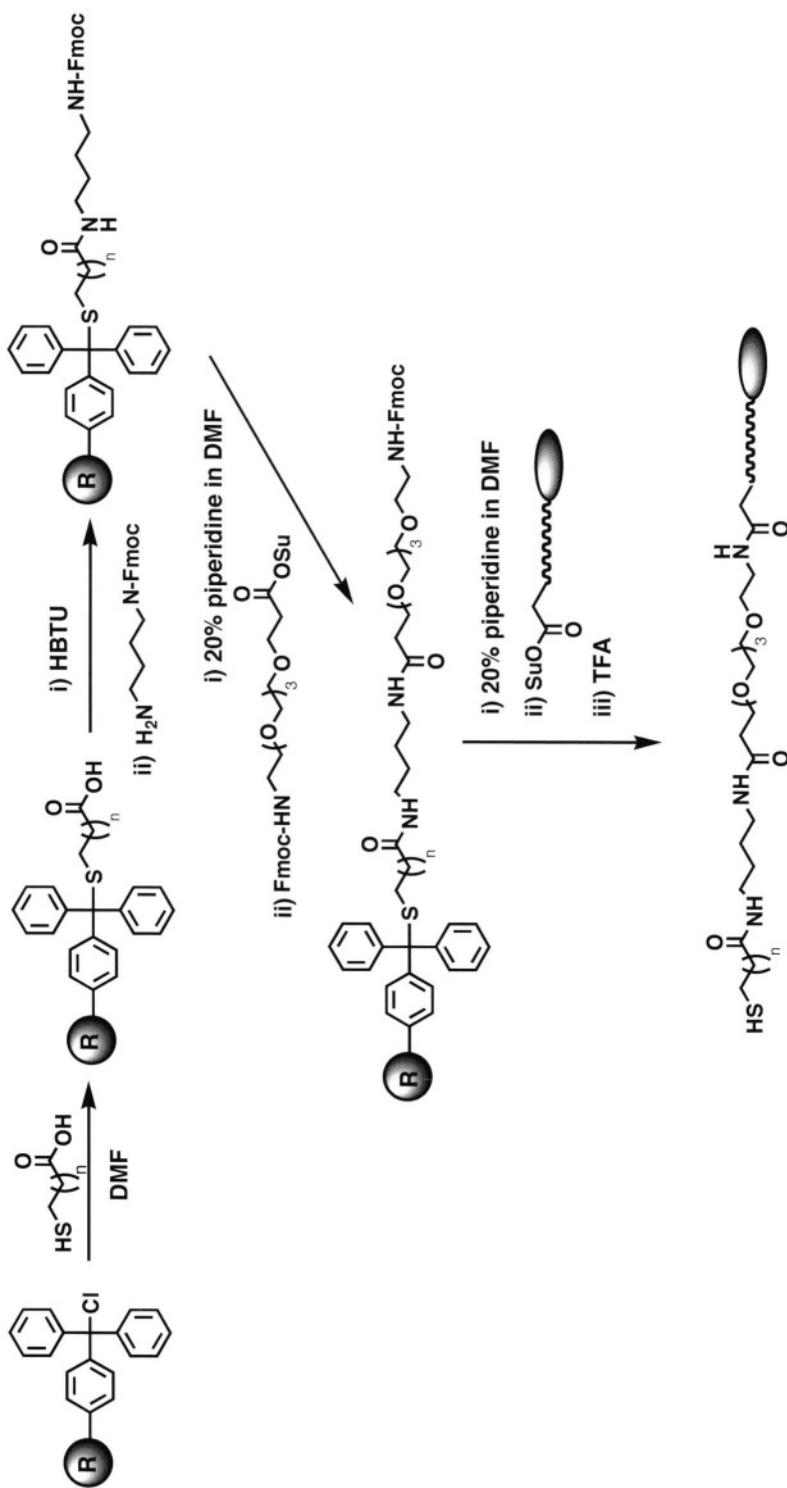
FIGURE 7.7. Synthetic scheme developed in our group for the rapid and efficient preparation of chemically modified thioalkanes. In this case the solid elipsoid represents the reactive group to be introduced in the surface.

7.4.2. Chemoselective attachment of proteins

In this section we will study in more detail all the methods available for the chemose-lective derivatization of proteins summarized on Figure 7.4 and their corresponding reac-tivities.

7.4.2.1. Attachment through the thiol group

The only amino acid containing a thiol group in its side-chain is the Cys residue (see Table 7.1) and its relative abundance in the average protein is rather small. Thiols have a pK_a of around 8.5 and they are nucleophilic at pH 7. Under these conditions they can be reacted with high selectivity with some chemical groups like alkyl halides and maleimides compounds to form a stable thioether covalent bond (see Figure 7.8).

One of the most commonly used alkyl halide derivatives is the iodoacetyl group, which can be easily introduced on amine-modified surfaces through its symmetrical anhydride (see the following references [21,46] for the *in situ* preparation of this derivative). It is important to remark that the iodoacetyl group can potentially react at neutral pH with other nucleophiles present in the protein (e.g., the imidazole ring of His and the α-amino group). However, when the iodoacetyl derivative is present in limiting quantities and the ligation is carried out at slightly alkaline pH, the alkylation of the Cys thiol group will be the exclusive reaction.

Another thiol-reactive group is the maleimide function. As shown in Figure 7.8, the double bond of the maleimide function undergoes a selective addition reaction by the thiol group. This reaction is extremely selective in the pH range 6.5–7.5 [47] and only at higher pH values some cross-reactivity with amino groups may be observed. There are a great variety of commercial available reagents that can be used for introducing maleimide groups on an amine-derivatized surface [27]. All of them contain both the maleimido and N-hydroxysuccinimide groups.

All of this provides a unique window of reactivity for the chemoselective attachment of proteins to surfaces through the thiol group of the amino acid Cys. Hence, the only requirements are: (1) complementary reactive groups (i.e., maleimide or iodoacetyl groups) onto the appropriate surface and (2) a unique and reactive Cys residue (i.e. amino acid on the primary sequence of the protein) on the protein. Reactive Cys residues should not be involved in any structural element (i.e. disulfide bonds, Zn fingers, etc.) and should be exposed in solvent accessible region of the protein. In the absence of an endogenous Cys residue, it will be necessary to introduce a Cys residue through mutation of a native residue. The effect of this Cys mutation on the structure and function of the protein can be easily minimized by following a few simple rules: (1) if the tertiary structure of the protein is known, choose a region remote from the active site of the protein, preferably in a flexible surface loop; (2) choose the mutation to be as conservative as possible, e.g., Ser → Cys or Ala → Cys; (3) avoid mutation of residues that are conserved across a gene family and (4) take advantage of any known mutational data on the system since the effect on structure/function of a specific residue mutations may already be known.

Bonn and co-workers [29] have used this approach for the preparation of ori-ented citochrome b_5 nanostructures on a Ti:Zn glass substrate. In this case the surface was silanized with APS and then the resulting amino group was acylated with EMCS (N-hydroxysuccidinimyl 6-maleimidocaproate). The maleimido group was then reacted chemoselectively with a mutant of cytochrome b_5 where the residue of Thr [8] was mu-tated to Cys which produced an ordered protein film. The same authors also investigated
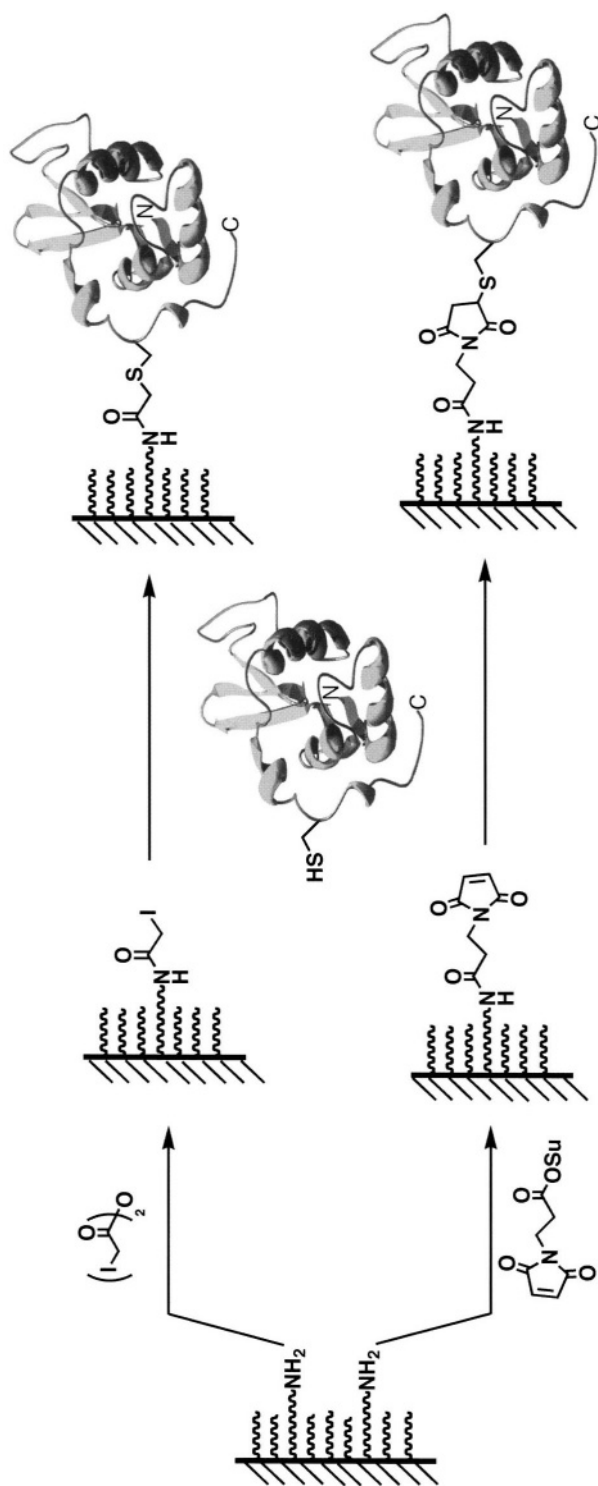
FIGURE 7.8. Chemoselective reactions of the thiol group and its applications for attaching proteins to chemically modified surfaces containing an iodoaceteamido or maleimido functions. In both cases the reacting groups are introduced into an amine-coated surface by the symmetrical anhydride of the corresponding acids.

the effect of the linker length on the orientation of proteins specifically attached through a unique Cys residue [48]. For that purpose they used a genetically engineered myoglobin where the original residue Ala^{126} was mutated to Cys to introduce a unique thiol group in the protein. The mutated myoglobin was then reacted with self-assembled bromoalkylsilylated silica surfaces employing different linear alkyl chains varying in length. The results showed that the best ordering was accomplished with short ($n = 2–3$) and long ($n > 11$) alkyl chains. However, the stability of the protein was marginal when attached to long alkyl chains. This apparent instability was very likely due to the increased hydrophobic character of the surface. Edwards *et al.* [49] used in this case the naturally occurring thiol group of the Cys^{102} of yeast cytochrome c for the creation of a vectorially oriented monolayer of the bimolecular complex between yeast cytochrome c and bovine heart cytochrome c oxidase on both quartz and Ge/Si multilayer substrates. In both cases the surfaces were silanized with APS (Figure 7.5A) and then treated with EMCS. Xiao *et al.* [50] has also reported another example of selective attachment of a polypeptide through the thiol group of a Cys residue. In this case, two short cell-adhesive peptides containing single Cys residues were selectively immobilized onto a Ti surface previously treated first with APS and then with different maleimido amine-reactive compounds.

The thiol group can also react in an oxidative way with other thiols to form disulfides linkages. This approach has been used by several authors for attaching heme proteins containing single Cys residues to thiol-containing surfaces [29,51]. The thiol group can be easily introduced on silicon-based surfaces using thiol thioalkylsilanes. However the disulfide linkage is less stable than the thioether bond described previously and can be easily reduced under slightly reductive conditions.

Other authors have used the thiol or the disulfide group as a way to attach proteins to an underivatized gold surface. As stated before, the thiol and disulfide groups can react with gold surfaces to form a relatively stable covalent bond. Aizawa and co-workers [52] used this approach for attaching protein A fragments to a gold surface through a unique Cys residue introduced at the C-terminus of the protein fragment by genetic engineering. The resulting attached protein A fragment retained the same IgG binding activitiy as the intact protein A and it was used for the highly oriented immobilization of antibodies. Mirkin and co-workers [6] have also used this kind of covalent immobilization for the creation of nano-metric patterns using collagen-peptide fragments containing a unique Cys residue in combination with the atomic force microscopy technique of dip-pen nanolithography.

More recently Wang *et al.* [53] introduced a single Cys residue by genetic engineering into one of the solvent accessible loops of the capsomer protein of the cowpea mosaic virus. They showed that this genetically engineered virus was able to chemoselectively bind maleimido-containing gold nanoparticles and consequently it could be used for the creation of highly ordered films of virus on appropriately modified surfaces [45]. Cavarelly *et al.* [54] also used the naturally occurring and unique disulfide bond present in the protein azurin. This protein was able to form highly ordered films when reacted with gold. In contrast, the same protein gave random orientations when adsorbed on a self-assembled monolayer of 11 -mercaptoundecanoic acid on gold.

This is a powerful technique for achieving ordered immobilization of proteins and virus onto solid surfaces. It should be noted, however, that is not general method and can be only applied when there is only one reactive Cys residue, either artificially introduced or naturally occurring, on the protein to be attached. When the protein contains multiple Cys residues it is better to use alternative chemoselective methods.

7.4.2.2. Attachment through the carbonyl group As can be seen in Table 7.1, none of the genetically coded amino acids contain carbonyl groups (i.e., aldehyde and ketone groups) in the side-chain, only some glycoproteins which have been post-translationally modified by glycosylation with reductive sugars.

The carbonyl function reacts at pH 5–6 very efficiently and selectively with hydrazine- and hydroxylamine-containing substances to yield the relatively stable hydrazones and oximes, respectively (Figure 7.9, note that aldehydes react faster than ketones due to sterical reasons). The hydrazone function can be further stabilized by mild reduction with $NaBH_4$ (sodium borohydride) or $NaBH_3CN$ (sodium cyanoborohydride).

These two facts open the possibility of using these well known chemical reactions for the selective attachment of proteins to solid supports with total control over the orientation. The only requirements are the introduction of a unique carbonyl group in a well defined and solvent accessible position on the protein surface and the preparation of a hydrazine- or hydroxylamine-containing chemical surface. The hydrazine and hydroxylamine function can be easily introduced onto an amine-containing surface (see Section 7.4.1) using the corresponding symmetrical anhydrides of the N-protected hydrazinoacetic acid (Boc–NH–NH–CH_2–CO_2H) or N-protected aminoxyacetic acid (Boc–NH–O–CH_2–CO_2H) as depicted in Figure 7.9A. The Boc (*t*-butoxycarbonyl) protecting group prevents self-condensation of the $-NH_2$ group with the activated carboxylic groups. The hydrazino group can be also easily introduced onto an aminated surface by using 2-bromoacetic acid and *t*-butyl carbazate as it is shown in Figure 7.9B.

The hydrazide function also readily reacts with carbonyl groups (see Figure 7.10) and can be easily introduced onto a silicon-based surface by using first thiolalkylsilanes and then a heterobifunctional crosslinker such as MBPH [55] (4-(4-N-maleimidophenyl)-butyric acid hydrazide, Figure 7.10). In this case the maleimido group reacts selectively with the thiol-covered surface to introduce the hydrazide function onto the surface, which can react with any carbonyl-containing protein to give a highly ordered protein film (Figure 7.10).

Carbonyl groups can also reversibly react with amino groups to give the corresponding imines, which can be reduced with $NaBH_3CN$ to provide more stable amine derivatives.

The most common method of introducing a carbonyl function into a protein is by mild sodium periodate oxidation. Oxidation of 1,2-diols (present in the polysaccharide chain of glycoproteins) and β-**aminoethanol** derivatives (N-terminal Ser and Thr residues contain a β-**aminoethanol** function) to the corresponding aldehydes derivatives (Figures 7.11A and 7.11C). The periodate anion also oxidizes Met (to its sulfoxide) and some thiol groups (usually to disulfides). These reactions, however, occur at slower rates than the oxidation of 1,2-diols and β-**aminoethanol** derivatives. Another milder procedure for introducing carbonyl groups into glycoproteins is the use of specific sugar oxidases. However, these enzymes only catalyze the oxidation of a specific monosaccharide and not with other sugars present in the polysaccharide chain. The most often used oxidase for this purpose is galactose oxidase, which forms C-6 aldehydes on terminal D-galactose or N-acetyl-D-galactose residues (Figure 7.11B). When galactose residues are penultimate to sialic acid, another enzyme, the enzyme neuramidase is used first to remove the sialic residue thus exposing the galactose residue for the enzymatic oxidation. Using these two independent methods, the sugar moiety of glycoproteins (including antibodies) can be oxidized to introduce selectively aldehyde groups in the glycosylation site of the protein. Note that the use of oxidized proteins, requires unique glycosylation sites if total control of the orientation of the
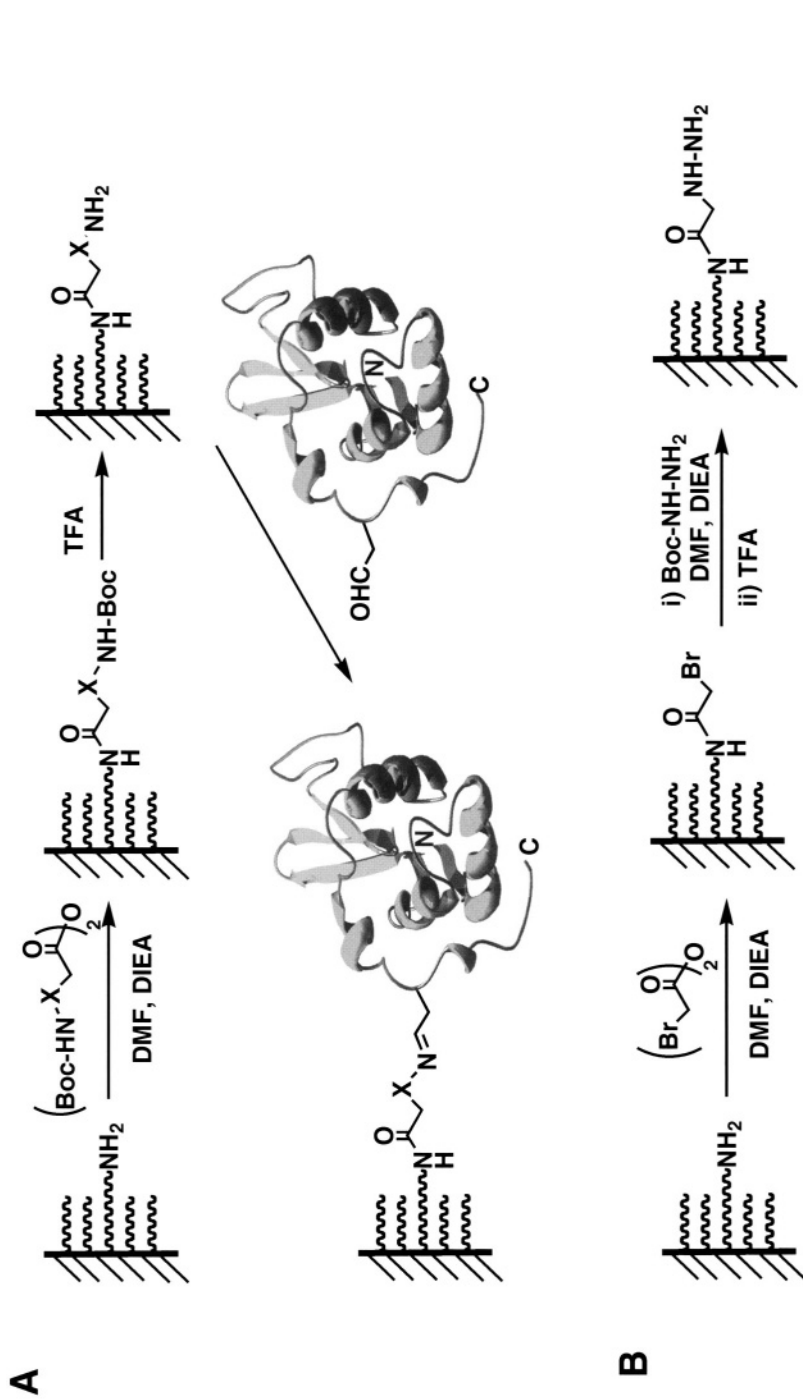
FIGURE 7.9. Chemoselective reactions of the carbonyl group. (A) Attachment of a protein through its carbonyl group to a surface containing the hydrazino (X = −NH−) or the aminooxy (X = −O−) group. (B) Alternative introduction of the hydrazino group into an amine-coated surface by using 2-bromoacetic acid and *t*-butyl carbazate.
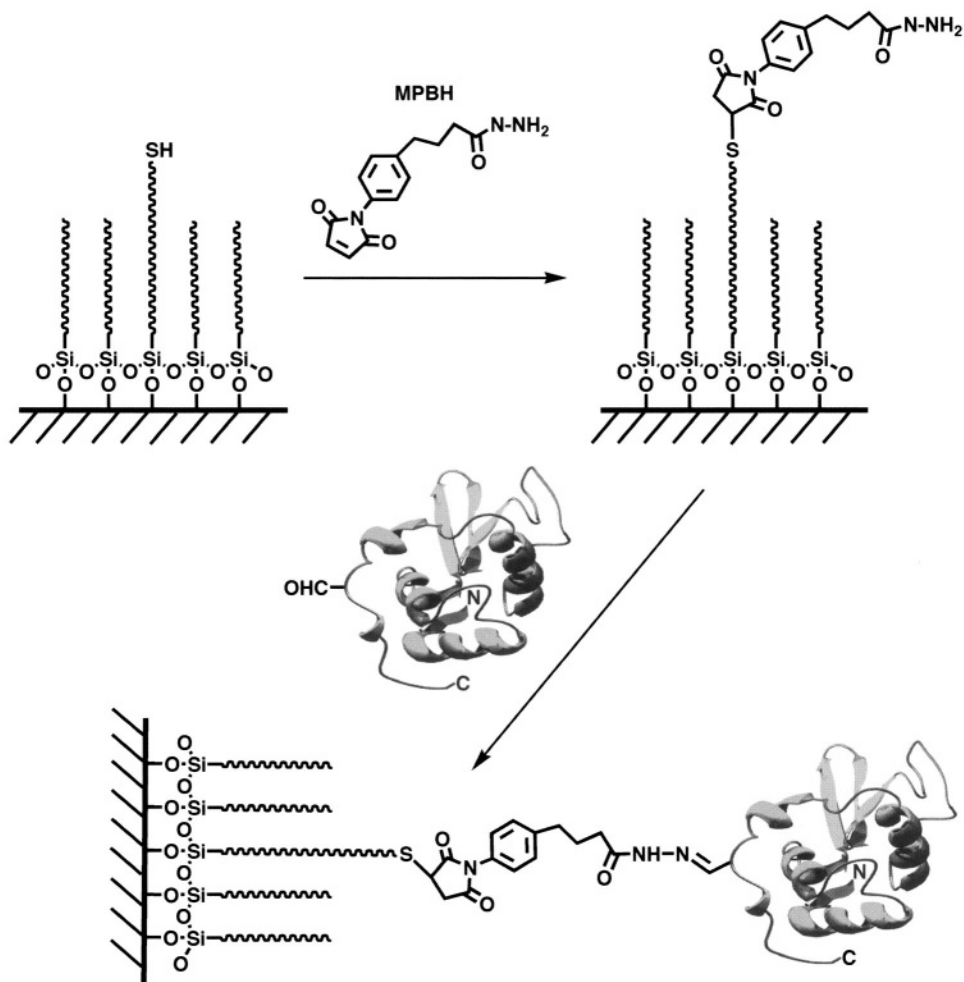
FIGURE 7.10. Site-directed immobilization of carbonyl-containing proteins on glass by using the 4-(4-N-maleimidophenyl)butyric acid hydrazide (MPBH) heterofunctional crosslinker.

attached protein is desired. It should be noted, however, that glycosylation patterns are usually heterogeneous and therefore some heterogeneity should be expected in the location of the carbonyl groups within the polysaccharide chain.

As stated before, N-terminal Ser and Thr residues can also be selectively oxidized to yield aldehyde groups [56–58] (Figure 7.11C). PCR-driven mutagenesis can be used for the introduction of the dipeptide Met–Ser/Thr– at the N-terminus of recombinant protein (note that the Met residue is always the first amino acid to be translated by the ribosome). Once the protein has been fully translated, the Met residue is then removed *in vivo* by the methionine aminopeptidase enzyme yielding the corresponding N-terminal Ser or Thr residue [59]. Verdine and co-workers [60] have also used an enzymatic approach for introducing a N-terminal Ser residue into a protein. In this case, the leader peptide sequence
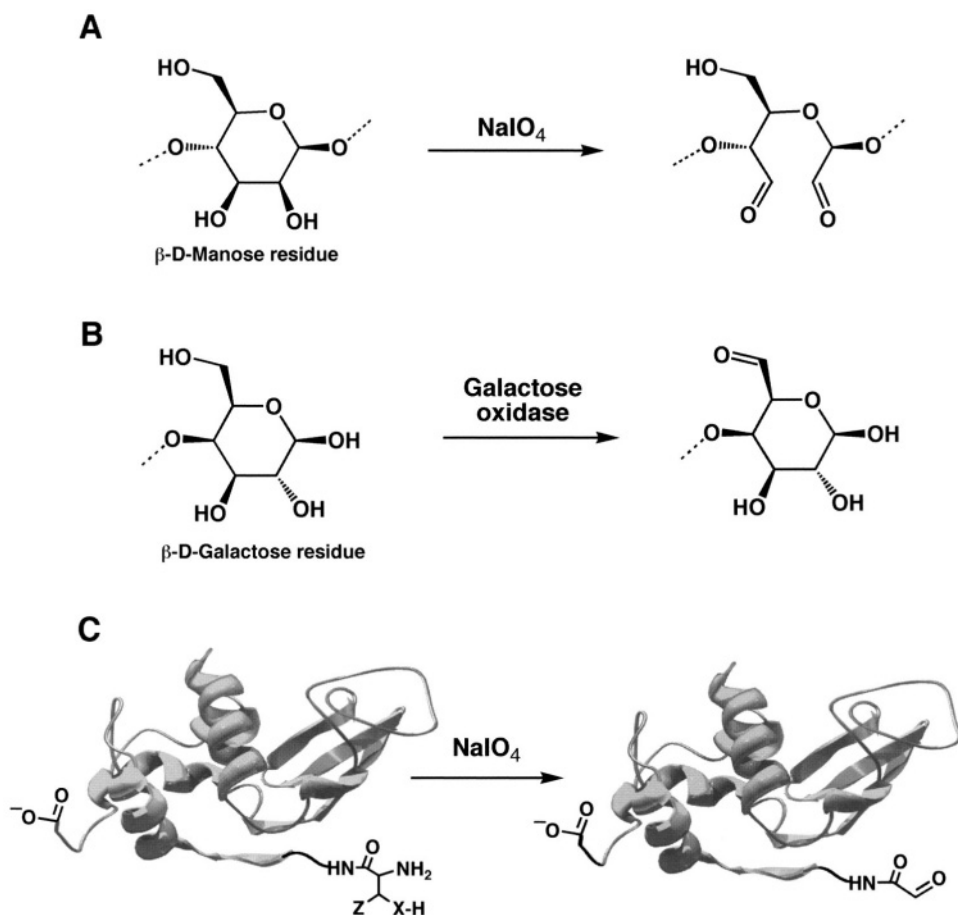
FIGURE 7.11. Introduction of the carbonyl group into proteins by mild oxidation. (A) Oxidation with sodium periodate of glycoproteins introduces carbonyl groups at the glycosylation site of the protein. (B) Galactose oxidase selectively oxidizes the C-6 hydroxyl group of galactose residues into an aldehyde. (C) Oxidation with sodium periodate of a protein containing a Cys (X = S, Z = H), Ser (X = O, Z = H) or Thr ($X = O, Z = CH_3$) residue at the N-terminal position yields an aldehyde function in this position.

Met–Ile–Glu–Gly–Arg–Ser was introduced by using PCR-driven mutagenesis techniques at the N-terminus of the original protein. This added extra sequence contains a factor Xa proteolysis site which can be selectively cleaved after the Arg residue to yield the corresponding protein containing a N-terminal Ser residue.

A more general approach for the introduction of N-terminal carbonyl groups is has been developed by Dixon and co-workers [61,62]. This approach can be used with any N-terminal residue and does not involve an oxidation step but rather a transamination reaction. This reaction is usually carried out at pH 5–7 in presence of glyoxylic acid and transition metals that act as catalysts (Figure 7.12). Note that this approach will only yield an aldehyde function when the N-terminal residue is Gly, in all the other N-terminal amino acids the result will be the corresponding ketone.
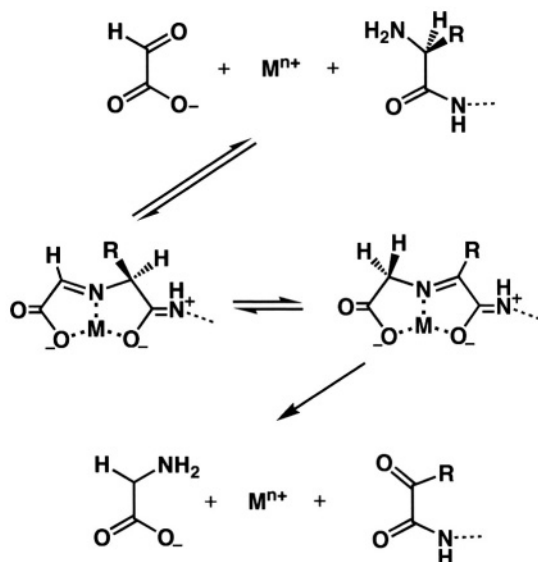
FIGURE 7.12. Mechanism for the metal-catalized transamination reaction of the N-terminal residue of a peptide or protein.

The chemoselective attachment of a protein through a carbonyl function is the method most commonly used for the attachment of antibodies to solid surfaces. Antibodies are glycosylated symmetrically at the Fc fragment and can be mildy oxidized with sodium periodate or the corresponding glyco-oxidase to yield an aldehyde function at the glycosylation site. Huang *et al.* [63] carried out site-directed coupling of antibodies using an aminated silica surface as substrate. They first introduced a difunctionalized hydrazide–polyethylenglycol moiety into the amine-containing surface via glutaraldehyde coupling. The available hydrazide moiety was then selectively reacted with an anti-fluorescein antibody previously oxidized with sodium periodate. As stated before, the poly-ethylenglycol moiety helped to reduce the non-specific absorption of proteins to the surface. They also found that site-directed chemisorption of antibodies yielded higher activity densities that random coupling techniques. Routh *et al.* [55] have also used glass slides for the oriented immobilization of the anti-neuropeptide P antibody. The functionalized surfaces were used as microprobes for measuring the neuropeptide P release in the central nervous system. In this case the authors used a thiol-terminal silane and the MPBH hetero-functional crosslinker to immobilize the oxidized antibody on a glass surface (Figure 7.10). More recently, Muchova *et al.* [64] have been able to immobilize a monoclonal antibody directed against the carcinoembryonic cell adhesion molecule I (CECAM 1) on a hydrazide-activated cellulose. This support was obtained by treating partially oxidized cellulose with adipic acid dihydrazide. The monoclonal antibody was first oxidized with periodate and then bound to the hydrazide-activated matrix through its glycosylation site. This functionalized cellulose substrate was then used for the purification of CECAM1 protein by affinity chromatography. Using a similar approach, Bilkova *et al.* [65] have been able to immobilize galacto oxidase orientedly through its carbohydrate chain to hydrazide-activated cellulose beads. As stated

before, the sugar moiety of the enzyme was oxidized with periodate to yield the reactive aldehyde function.

Some other authors have used the amine function instead the hydrazide function for attaching carbonyl-containing proteins to surfaces [66,67]. It is important to remark, however, that in this case the linkage between the protein and the surface (i.e., an imine function) is not stable unless is reduced with mild reductive agents such as $NaBH_3CN$. Reductive treatments of proteins may sometimes reduce the disulfide bonds of the protein, which may result in its biological inactivation. Note that antibodies contain several disulfide bonds which are essential for the stabilization of their tertiary and quaternary structure (see Section 7.2).

7.4.2.3. Attachment through the C-terminal α-thioester group   The thioester function behaves like a mild electrophile and therefore can react with high chemoselectivity with different nucleophiles. One of the most important reactions involving thioesters is the so called native chemical ligation developed independently by Kent [68] and Tarn [69]. In this reaction, two fully unprotected polypeptides, one containing an C-terminal α-thioester group and the other an N-terminal Cys residue, react chemoselectively under neutral aqueous conditions with the formation of a native peptide bond at the ligation site (Figure 7.13). The initial step in this ligation involves the formation of a thioester-linked intermediate, which is generated by a transthioesterification reaction involving the C-terminal thioester moiety of one fragment and the N-terminal Cys thiol group of the other. This intermediate then spontaneously rearranges to produce a native peptide bond at the ligation site. This type of thioester-based chemistry was first pioneered by Wieland in 1950's for the synthesis of small Cys-containing peptides [70,71]. Blake [72] and Yamashiro [73] also have used the acylating power of the α-thioester function for ligating peptides through the α-amino group. This approach, however, required the temporary protection of all of the remaining amino groups present in both peptide fragments. In contrast, native chemical ligation is compatible with all the naturally occurring side-chain groups including the thiol group of the Cys residue. Note that only N-terminal Cys residues thioester-intermediates can rearrange to the final amide bond. The non N-terminal Cys thioesters are non-productive and can be simply converted back to starting materials by including small amounts of a thiol cofactor in the reaction mixture. Tam and co-workers [74] have also shown that the C-treminal thioester function of a polypeptide can also react with polypeptides containing some other N-terminal residues like histidine and homocysteine. However in both cases the final step involves a six rather than a five member ring transition state (as occurs with the N-terminal cysteine residue) hence reducing the efficiency of the ligation. We have also shown that C-terminal thioesters can react very efficiently with other N-nucleophiles such as hydrazino and aminoxy functions (Figure 7.14) [75]. These reactions can be performed at pH 6–7 in the presence of the functional groups normally present in a protein (see Table 7.1) without any kind of interference.

The highly chemoselective reactivity of the thioester group provides a good opportunity for the selective attachment of a protein to a surface through its C-terminus. The only two requirements are introducing a thioester function at the C-terminus of the protein and complementary chemical groups on the surface (Figure 7.14).

Most of the naturally occurring proteins do not contain the thioester function, although this function can be found as a reactive intermediate in some biochemical processes such as the blood coagulation cascade [76], non-ribosomal peptide synthesis [77,78] and protein-splicing [79–81].
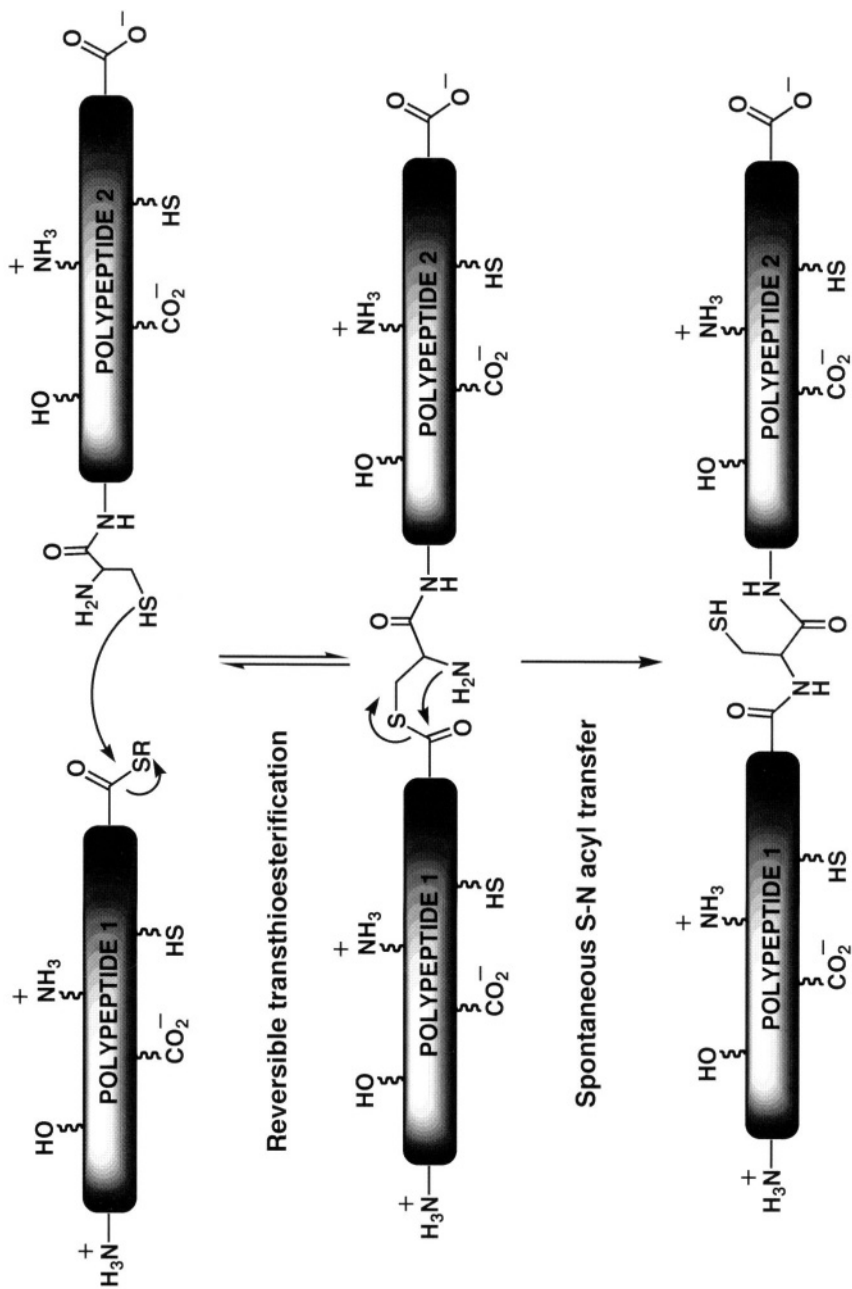
FIGURE 7.13. The principle of native chemical ligation. The two unprotected polypeptides, one containing an α-thioester function and the other an N-terminal Cys residue, react chemoselectively to form a natural peptide (amide) bond at the ligation site.
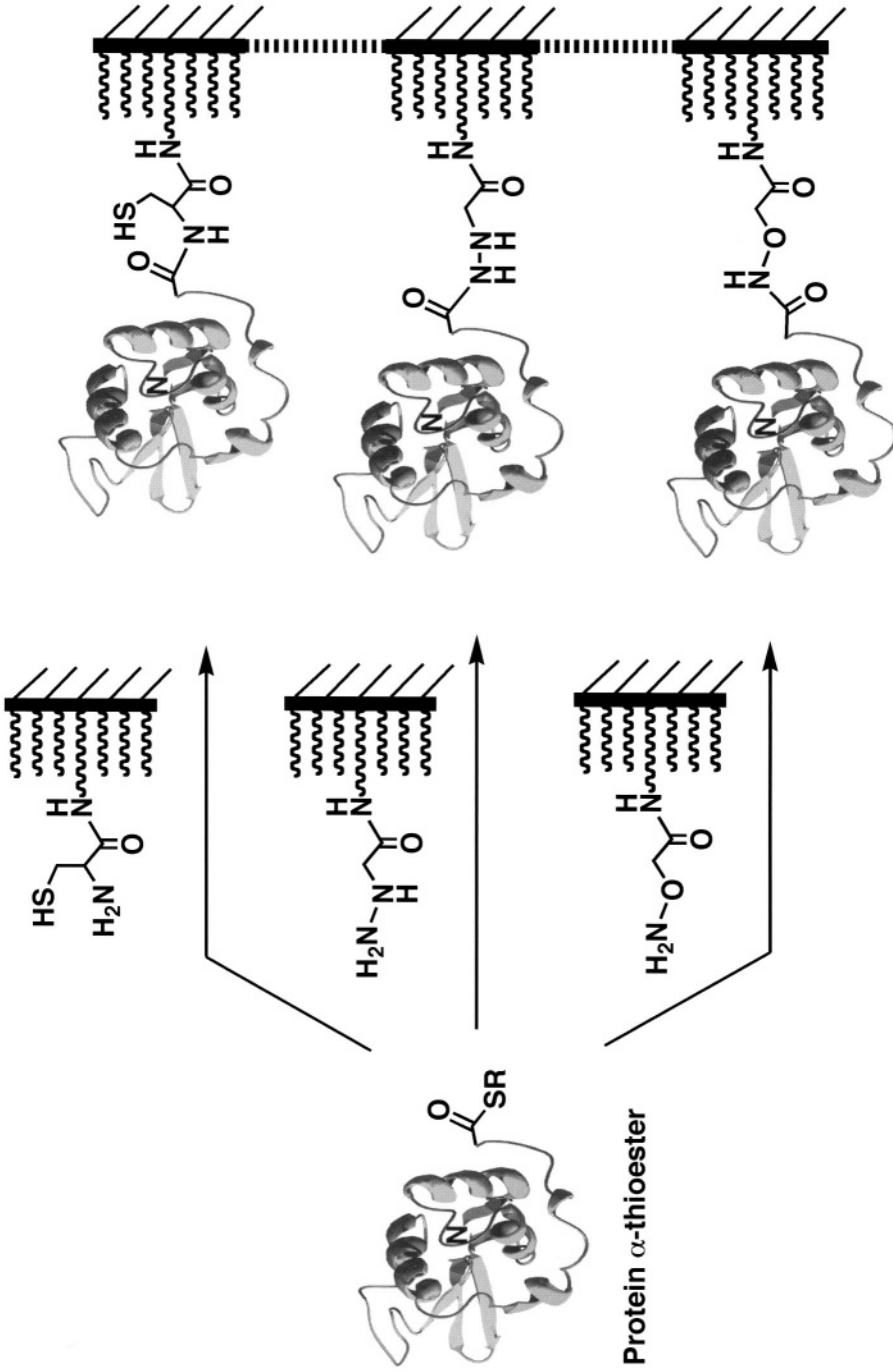
FIGURE 7.14. Reactivity of the α-thioester function versus different nucleophiles. Application to the chemoselective attachment of α-thioester proteins to appropriately chemically modified surfaces.

The elucidation of the protein splicing mechanism by Perler and co-workers [80] (Figure 7.15 A) has made the production of recombinant C-terminal α-thioester proteins possible by a modification of the naturally occurring splicing process [21,82–84]. Protein splicing is a cellular processing event that occurs post-translationally at the polypeptide level. In this multistep process an internal polypeptide fragment, called intein (by analogy with the RNA splicing terms intron and exon), is self-excised from a precursor protein which allows the ligation of the flanking protein sequences (N- and C-exteins) to give a different protein (Figure 7.15A). The current understanding of the mechanism is summarized in Figure 7.15A and involves in the formation of thioester/ester intermediates [80]. The first step in the splicing process involves an $N \rightarrow S$ or $N \rightarrow O$ acyl shift in which the N-extein is transferred to the thiol/alcohol group of the first residue of the intein (note that in all the inteins known so far, the first residue is always a Cys, Ser or Thr residue). It has been speculated that the driving force for this rather unfavorable acyl shift could be found in the recently solved crystal structure of the PI-SceI intein [85] where the amide bond between the last residue in the N-extein and first residue in the intein to be in a distorted trans conformation (i.e., non-planar) [86]. The adoption of this high energy conformation is forced by the folded structure of the intein-containing protein.

After the initial $N \rightarrow (S/O)$ acyl shift, a trans esterification step follows in which the N-extein is transferred to the side-chain of a second conserved Cys, Ser or Thr residue located at the junction between the intein and the C-extein. The amide bond at this junction is then broken as a result of succinimide formation involving a conserved Asn residue within the intein. In the final step of the process, a peptide bond is formed between the N-extein and C-extein following an $(S/O) \rightarrow N$ acyl shift (in a similar way that the last step of Native Chemical Ligation, see Figure 7.13).

Mutation of the conserved Asn residue within the intein to Ala blocks the splicing process in midstream thus resulting in the formation of an α-thioester linkage between N-extein and the intein [80] (Figure 7.15B). This thioester bond can be cleaved using an appropriate thiol to give the corresponding α-thioester N-extein through a transthioesterfication reaction. The IMPACT expression system, commercially available from New England Biolabs (www.neb.com) [87,88], allows the generation of recombinant α-thioester proteins by making use of such modified inteins in conjunction with a chitin binding domain (CBD) for easy purification by affinity chromatography (see Figure 7.15B).

Modification of the surface with the appropriate chemical reactive groups for chemoselective reaction with α-thioester can be easily achieved by using aminated surfaces. Hydrazinoacetic and aminooxyacetic acid derivatives can be easily introduced onto these surfaces, as shown in Figure 7.9, and Cys residues can also be introduced by using the activated Boc–Cys(Trt)–OH, instead (Trt stands for trityl group and acts as a temporary acid-labile protecting group for the thiol function).

We have used the approach depicted in Figure 7.7 for the synthesis of long alkylthiols containing the above chemical functionalities. This modified thiols are being used for the creation of ordered protein arrays onto gold surfaces [45].

7.4.2.4. Attachment through the C-terminal α-hydrazide group   As we saw in Section 7.4.2.2, hydrazine derivatives can react very selectively with carbonyl compounds around pH 5–6 yielding the corresponding and relatively stable hydrazones [89]. We have also seen that this reaction can be successfully used for the attachment of carbonyl-containing proteins to surfaces containing a hydrazine derivative. Therefore the same reac-
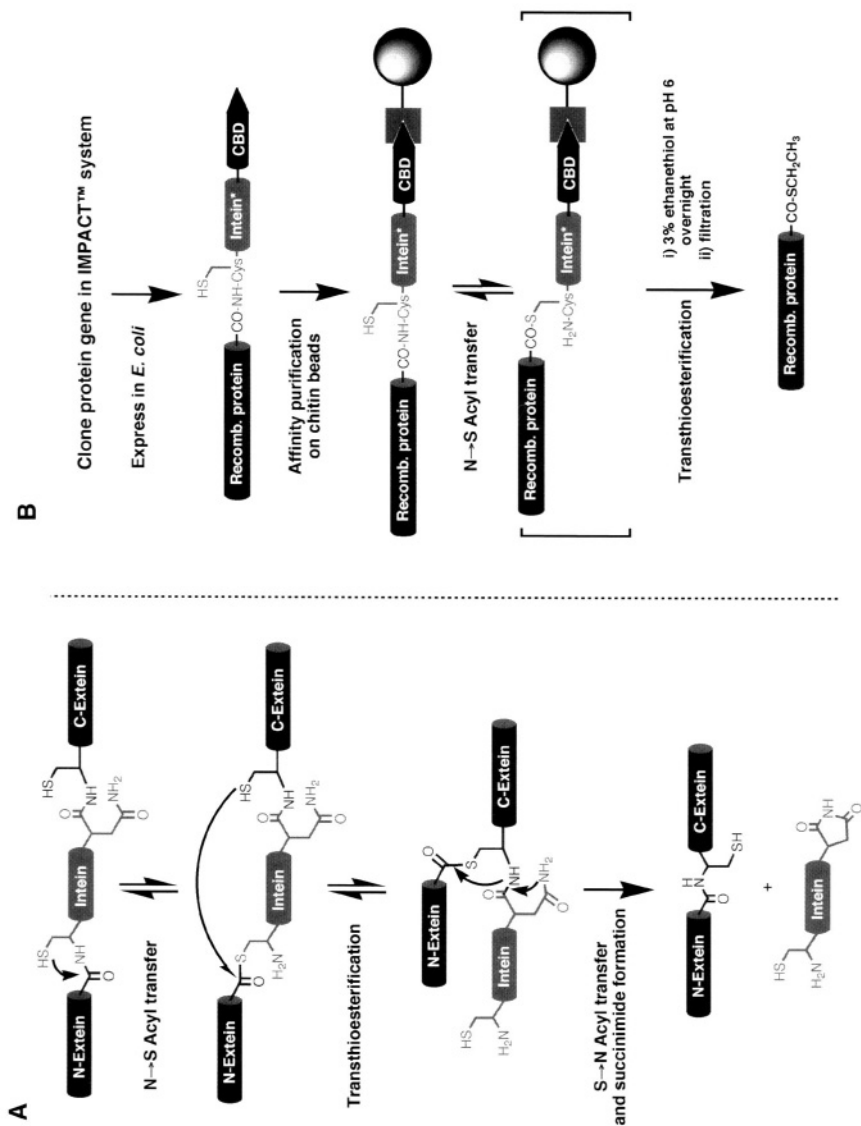
FIGURE 7.15. Principles of the biosynthetic preparation of α-thioester proteins by recombinant techniques. (A) Scheme representing the proposed mechanism of protein splicing [80]. (B) Expression, purification and cleavage of a protein-intein*-CBD fusion protein (where the asterisk refers to the mutation of the conserved Asn residue to Ala) with an appropriate thiol to yield the corresponding α-thioester protein.
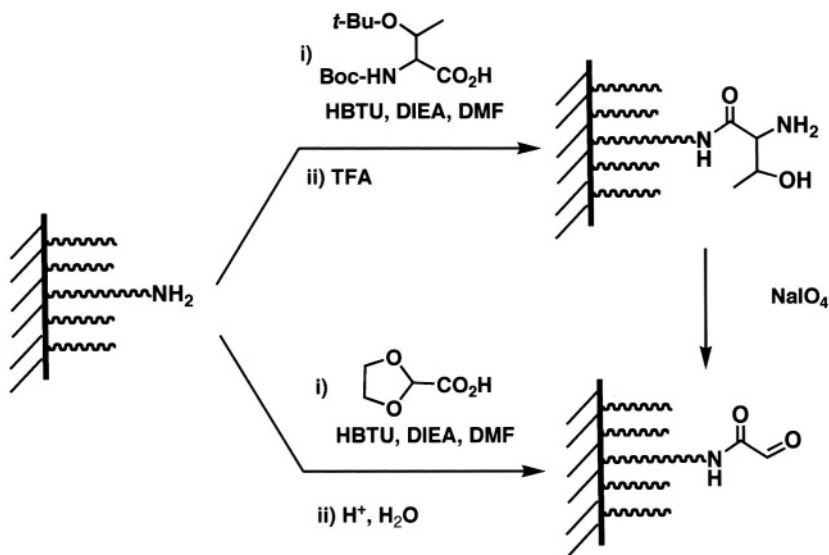
FIGURE 7.16. Introduction of the aldehyde functionality on an aminated surface. (A) In this approach the first step involves the acylation of the amino group with the activated Boc–Ser(t-Bu)–OH amino acid derivative. Once the coupling has been completed, the Boc- and t-butyl protecting groups are removed by treatment with tri-fluoroacetic acid (TEA) and then oxidized with $NaIO_4$ to yield the corresponding aldehyde. (B) An alternative approach involves the acylation of the amine-containing surface with the ethylenglycol acetal of the glyoxylic acid (note that in this case the aldehyde function is protected as an acetal). Once the coupling step has been carried out the acetal protecting group is removed by acidic hydrolysis yielding back the aldehyde function.

tion could be also used for attaching proteins containing a unique hydrazine derivative to a carbonyl-modified surface.

The aldehyde function can be directly introduced into a silicon-based surface by using the commercially available aldehyde-containing 4-oxo-butyltrialkylsilane [9] or by indirect means using an aminated-silicon surface (see Figure 7.16) [90].

On the other hand, C-terminal α-hydrazide proteins can be obtained from their corresponding C-terminal α-thioesters (see previous section) by treatment with hydrazine under neutral or slightly acidic pH [75,80]. An alternative method for the introduction of the α-hydrazide function involving reverse proteolysis in the presence of hydrazine can also be used [56], however this method involves the use of organic solvents (50% DMSO in acetate buffer pH 5.5), which in some cases may denature and/or inactivate the protein.

7.4.2.5. *Attachment through the C-terminal α-thioacid* The α-thioacid function is not normally present in naturally occurring proteins, it only can be found as a reactive interme-diate in some biosynthetic pathways [91]. However, it can be easily introduced in proteins by treating the corresponding α-thioester protein with $(NH_4)_2S$ or NaHS under neutral or slightly alkaline conditions [75,92]. The α-thioacid function is strongly nucleophilic and can react very efficiently with different electrophiles under slightly acidic conditions (pH $\approx$ 3–5, Figure 7.17). Under these conditions the other naturally occurring side-chain nucleophiles (i.e., mainly –SH and –NH₂ groups) are protonated and therefore their nucle-ophilic character is virtually eliminated. Hence, there is a well defined pH window (3–5) where the reaction of the α-thioacid function will be completely chemoselective thus al-
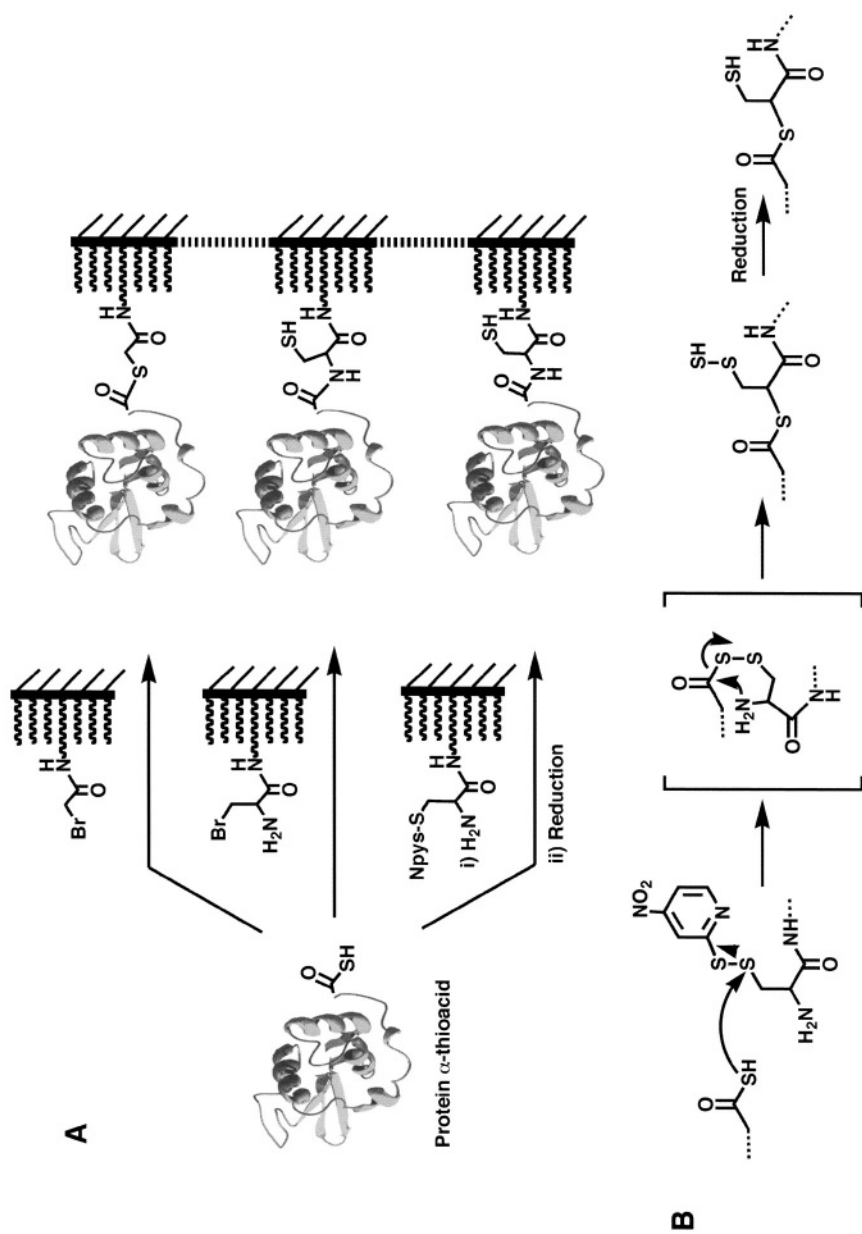
FIGURE 7.17. Reactivity of the α-thioacid function versus different electrophilic functions covalently attached to an amine-containing surface. (A) Application for the chemoselective attachment of a α-thioacid protein to a surface through its C-terminus. (B) Mechanism for the acyl disulfide-mediated intramolecular acylation reaction (third reaction in panel A).

lowing to have total control over the orientation of how the protein that will be attached to the chemically modified surface.

As depicted in Figure 7.17A, α-thioacid proteins can react very efficiently with the α-bromoacetyl group. This results in the protein being attached to the surface through its C-terminus by a thioester bond. The alkylbromide group can be easily introduced on aminated surface by acylation with the corresponding symmetrical anhydride. It is worth to note that this reaction was used by Kent and co-workers [93] for the total chemical synthesis of a backbone-engineered HIV proteases by chemoselective ligating two HIV-derived polypeptides containing the α-thioacid and bromoacetyl groups, respectively. The only inconvenience of this chemoselective ligation approach, however, is that yields a rather unstable thioester linkage between the surface and the protein. The thioester function is slowly hydrolyzed at $pH \geqslant 7$ and can also be cleaved by the presence of soluble thiols through a trans-thioesterification process. This problem can be solved, by using a bromoalanyl group instead the bromoacetyl group (see second reaction in Figure 7.17A). As described by Tam and coworkers [69] the α-thioacid function reacts very efficiently with the bromoalanyl group under slightly acidic conditions ($pH \approx 5$) in a two step reaction yielding at the end of the process a stable amide linkage. The first step of the reaction involves a nucleophilic attack of the α-thiolate onto the alkylbromide moiety to yield an alkylthioester. This thioester then rearranges spontaneously, through an $S \rightarrow N$ acyl shift, to finally yield an amide bond linkage (note that the generated thioester intermediate in this case is the same that is obtained during the native chemical ligation process, see Figure 7.13). As in the case of the α-bromoacetyl group, the bromoalanyl moiety can be also easily introduced into an amine-containing surface by acylation using the symmetrical anhydride of the commercially available non-natural amino acid bromoalanine.

Liu *et al.* [94] have also shown that α-thioacids can react very selectively with S-Npys (2-thio-4-nitropyridine) activated cysteinyl groups to form amide bond linkages (see third reaction in Figure 7.17A). The mechanism of this reaction, depicted in Figure 7.17B, involves two different steps and resembles the two-step thiol capture approach originally devised by Kemp and co-workers [95]. In the first step, the α-thiolate function captures (reacts) the activated thiol side-chain of the cysteinyl group thus forming a mixed acyl disulfide (also called perthioester) intermediate. This unstable intermediate undergoes rapid intramolecular $S \rightarrow N$ acyl shift through a six-member ring intermediate to yield the final amide bond. The final resulting hydrodisulfide (–S–SH) group on the cysteinyl moiety can be optionally reduced with DTT (1,4-dithio-DL-threitol) to the corresponding thiol group. Note that in this case the transition state for the rearrangement involves a six-member ring in contrast with the previous case where a five-member ring transition state was involved, and therefore the reaction is expected to be slightly less favorable.

As shown earlier, the S-Npys activated cysteinyl group can be introduced on aminated surface by using the symmetrical anhydride of the commercial available Boc–Cys(Npys)–OH amino acid derivative. Once the acylation reaction is complete, the Boc group can be easily removed by acidic treatment thus yielding the reactive cysteinyl group.

7.4.2.6. Attachment through the N-terminal amino group   The α-amino group of a protein (see Figure 7.1) can react with a carbonyl group under slightly acidic pH (≈ 4–5) to yield the corresponding imine. However, as we have seen in Section 7.4.2.2, the imine function is rather unstable and can not be used as a stable linkage for attaching proteins onto surfaces. One exception to this rule, however, is when the N-terminal amino acid of a protein is either

Cys, Ser or Thr (note that all these amino acids contain an heteroatom, either oxygen or sulfur, in β position to the α-amino group). In these cases the initially formed imine reacts intramolecularly with the heteroatom through a favorable 5-member ring transition state to give the relatively stable thiazolidine or oxazolidine ring (see Figure 7.18A). Tam and co-workers [96,97] have further developed this reaction by using a glycol aldehyde ester (see Figure 7.18A). In this case the nitrogen on the thiazolidine (or oxazolidine) ring attacks the ester function through a favorable 5-member ring transition state to finally give a very stable pseudo-proline linkage. This final step is usually carried out by increasing slightly the pH to 6 in order to increase the nucleophilic character of the nitrogen.

These two reactions are extremely chemoselective and therefore can be used for the attachment of proteins to an aldehyde-containing surface through its N-terminus under relatively mild conditions. As described in Section 7.4.2.2 (see Figure 7.16), the aldehyde function can easily be introduced into amine-containing surfaces. The glycol aldehyde ester moiety can also be introduced in surfaces containing the carboxylic function (see Section 7.4.1) using the synthetic approached depicted in Figure 7.18B [96].

On the other hand, recombinant proteins containing N-terminal Ser, Thr or Cys residues can be easily obtained by using different specific proteolytic approaches as described earlier in Section 7.4.2.2.

7.4.2.7. Attachment based on the Staudinger ligation reaction   A new exciting chemoselective peptide ligation method has been recently developed by two groups independently [98–100]. This reaction is a modification of the so-called Staudinger reaction and allows the chemoselective formation of an amide bond between an arylphosphine moiety and azide group (see Figure 7.19A). The reaction proceeds by the nucleophilic attack of an arylphosphine on the azide group to form a reactive aza-ylide intermediate. The acyl group then traps the ylide intermediate in an intramolecular fashion, resulting in an amide-linked phosphine oxide after hydrolysis. In the modified version of this reaction the attack of the ylide on the acyl group cleaves also at the same time the arylphosphine moiety yielding at the end a neat amide bond formation as shown in Figure 7.19B. This reaction is highly chemoselective and works with better yields when Z is $-CH_2-$ (note that in this case the transition state during the intramolecular rearrangement is again a favorable 5-membered ring) and X is sulfur (i.e. a thioester function).

Therefore if we are able to selectively introduce a unique azide on a protein and modify a surface to contain the corresponding arylphosphine, we should be able to immobilize on the surface the corresponding protein with total control over the orientation.

The introduction of the arylphosphine derivative in carboxylic-containing surface can be conveniently carried out as depicted in Figure 7.19C by using an activated carboxylic surface and the diphenylphosphinomethanethiol which synthesis has been recently reported by Raines and co-workers [100].

The azide function is not present in any naturally occurring protein. However, Bertozzi and co-workers [101], have recently reported a novel method for incorporation of azide groups into recombinant proteins. They have showed the unnatural azidohomoalanine amino acid, a surrogate of methionine, can be loaded into the methionyl-tRNA synthetase of *Escherichi coli* and incorporated in recombinant proteins expressed in methionine-depleted bacterial cultures by using a methionine auxotroph *E. coli* strain (i.e., a strain unable to biosynthesize methionine). It is important to note, however, that this approach would only work if the protein only contains a unique solvent accessible (i.e., reactive)
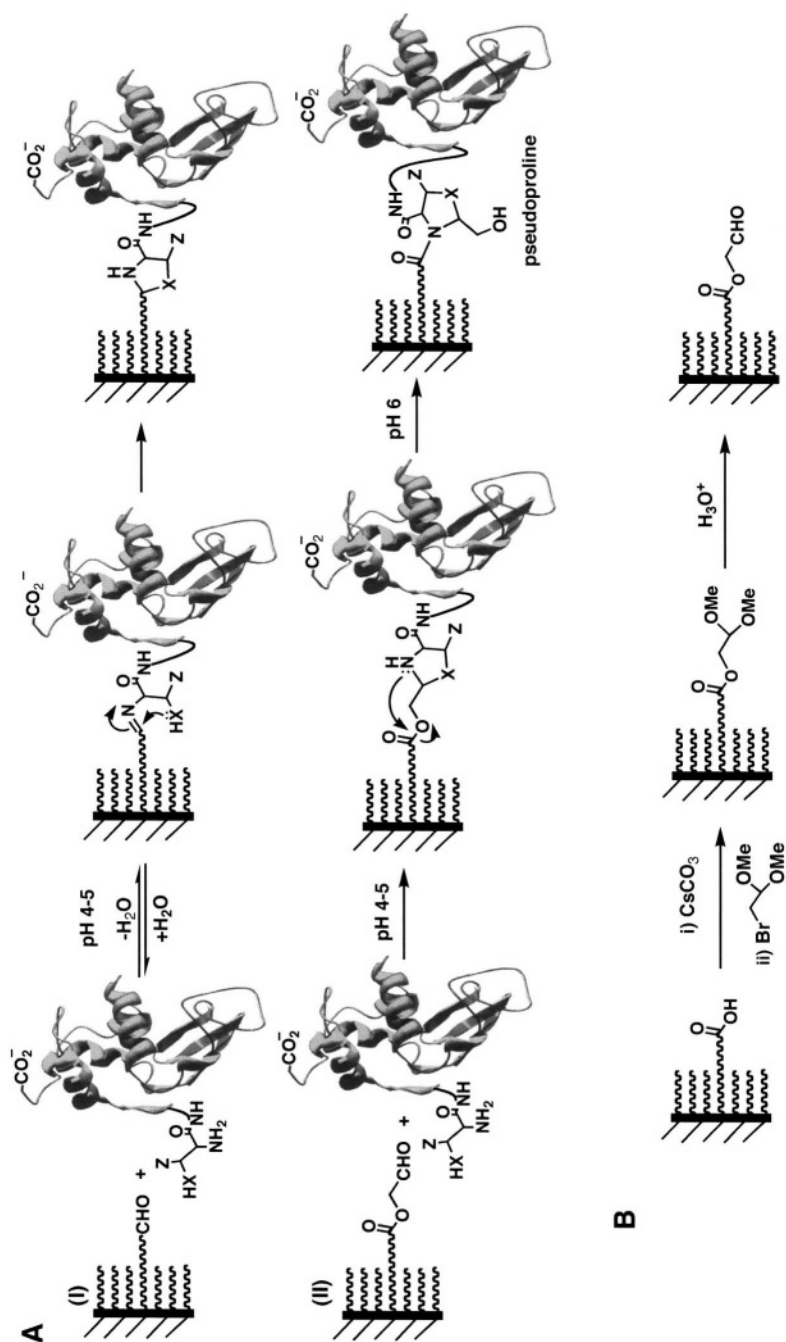
FIGURE 7.18. Attachment of a protein through its N-terminal amino group to a carbonyl-containing surface. (A) Chemoselective reaction between an N-terminal Ser (X = O and Z = H), Thr (X = O and Z = CH$_3$) or Cys (X = S and Z = H) protein and a surface containing the aldehyde (I) or a glycol aldehyde ester (II) functionalities. (B) Introduction of a glycol aldehyde ester on a surface containing a carboxylic acid functionality. The glycoaldehyde group was introduced on the carboxylic group by alkylation of the carboxylate cesium salt with bromoacetaldehyde dimethyl acetal. The free aldehyde was then released by brief treatment with aqueous trifluoroacetic acid (TFA).
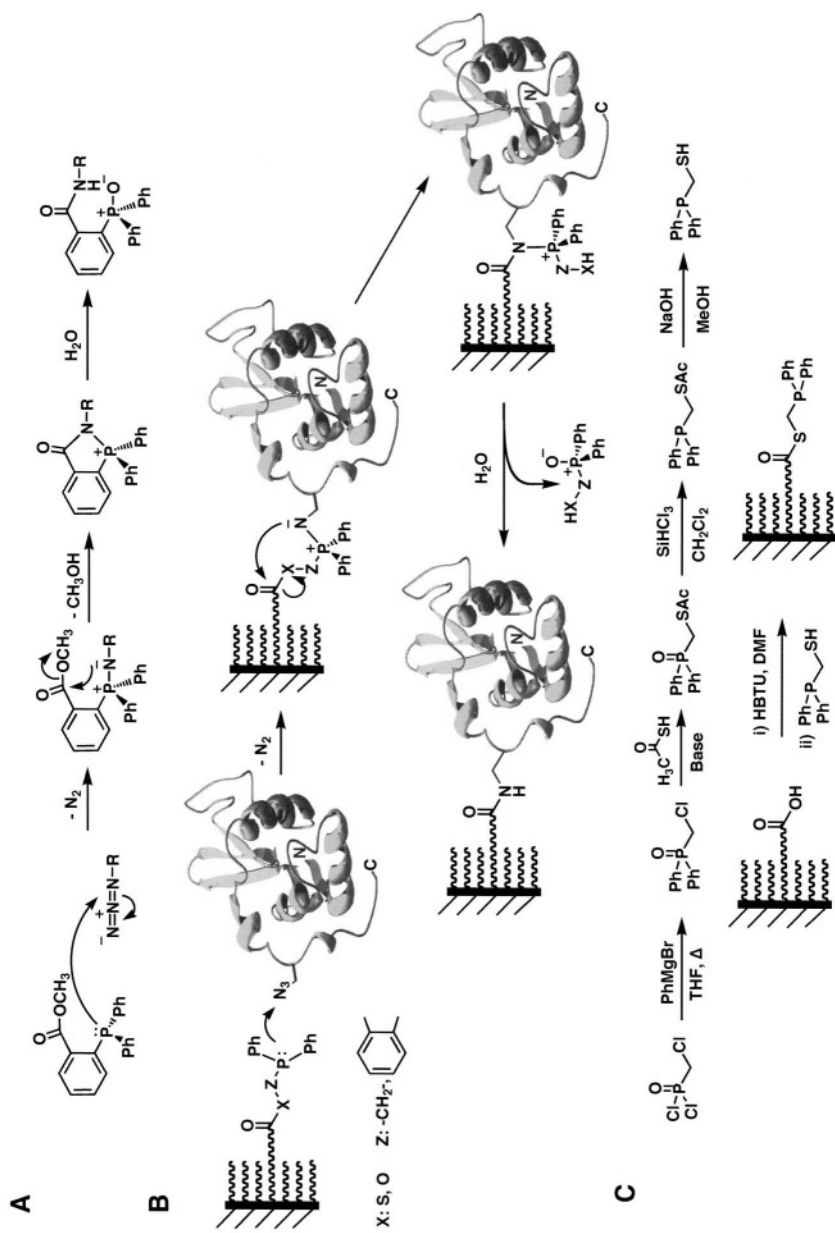
FIGURE 7.19. Chemoselective attachment of proteins to surfaces by using a modification of the Staudinger reaction. (A) Proposed mechanism for the Staudinger reaction. (B) Attachment of a protein to a solid surface by using a modified version of the Staudinger reaction. (C) Synthetic scheme for modifying a carboxylic surface with a suitable phosphinothiol for the Staudinger ligation reaction.

methionine residue. Otherwise, multiple solvent accessible azide groups would be incorporated in the corresponding protein and therefore the control over the orientation during the attachment would be lost. It is also important to remember that the first amino acid to be translated by the ribosome during the biosysthesis of any protein is always a methionine residue and this residue is efficiently removed by the endogenous methionine aminopeptidase only when the second residue is Gly, Ala, Pro, Ser, Thr, Val or Cys [59]. In all the remaining cases the N-terminal methionine will not be cleaved thus providing a unique methionine residue in proteins where no additional Met residues are exposed.

7.5. CHEMOENZYMATIC-LIKE METHODS FOR ATTACHMENT OF PROTEINS TO SURFACES

All the methods described so far rely on chemoselective reactions that are mostly uncatalyzed bimolecular-like reactions with little or not entropic activation at all. This lack of entropic activation means that the efficiency of these bimolecular-like reactions will depend strongly on the concentration of the reagents (i.e. on the concentration of the protein to be attached to the corresponding surface). This is basically due to the loss of entropy associated with two reacting groups brought together in the right orientation prior to the reaction. A way to overcome this intrinsic entropic barrier and make ligation reactions more efficient, even under high dilution conditions (high dilution means less protein is used), is through specific non-covalent interactions that bring both reactive groups in close proximity (Figure 7.20). In nature, this is carried out very efficiently by enzymes. Enzymes work mainly, although not exclusively (note that enthalpic contributions are also responsible for stabilizing the transition state) by binding the substrate and placing it in the right orientation to react with the chemically reactive groups at the enzyme's active site [102]. This exquisite network of non-covalent and very specific interactions between the enzyme and the substrate requires a folded structure in the enzyme (i.e., its tertiary structure). Consequently, if the enzyme is denatured, the network of specific interactions is lost and the catalysis gone.

Entropic activation can also be used for improving the rate of bimolecular protein chemical ligation reactions even under high dilution conditions (the rate of a bimolecular reaction should be very slow under high dilution conditions). It has been recently shown that the native chemical ligation (see Section 7.4.2.3) of two fragments of the subunit σ of the bacterial RNA polymerase proceeds very fast and efficiently, even under high dilution conditions [103]. Under these conditions the two protein fragments are able to form a specific non-covalent complex, which places both reacting groups in close proximity allowing them to react very efficiently even under unfavorable conditions for a bimolecular reaction. This effect was first reported by Sheppard and co-workers [104] who noticed that pancreatic trypsin inhibitor fragments obtained by CNBr cleavage were able to spontaneously religate forming the original native peptide bond between them. The same effect was also observed with cytochrome c [105]. In both cases, the two protein fragments produced after the CNBr cleavage, were able to cooperatively refold thus bringing the homoserine lactone at the C-terminus of one of the fragments in close proximity of the α-amino group of the other fragment. As before, the high local concentration effect of these groups and the mild activation of the homoserine lactone functionality resulted in spontaneous amide bond
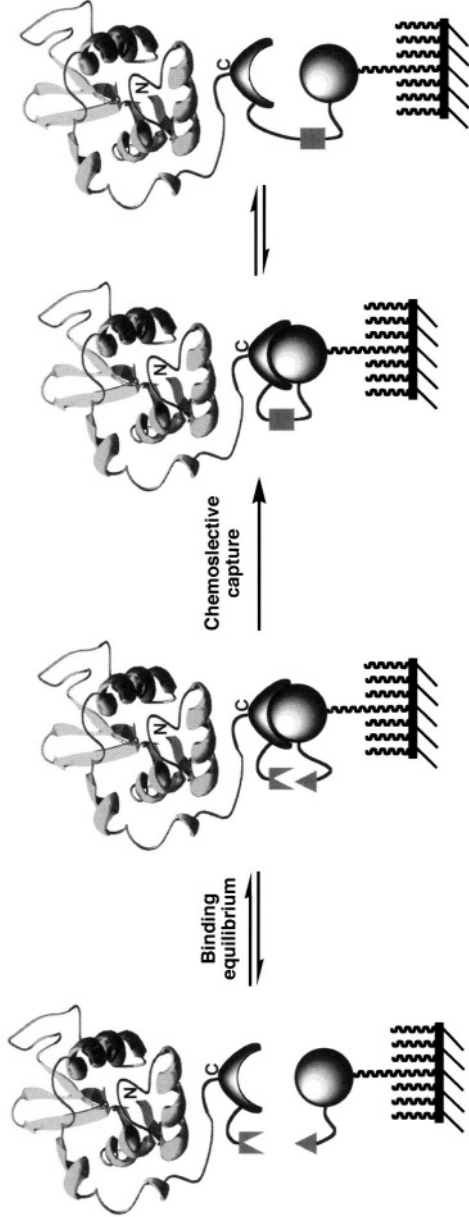
FIGURE 7.20. Principle for the attachment of a protein to a surface by using an entropically activated chemoselective reaction.

formation. Since then, several groups have reported the use of this entropically activated re-
actions in both intramolecular [106,107] and intermolecular chemoselective ligations [103,
108].

This entropic activation approach could be also used for improving the efficiency and
rate for the attachment of proteins to surfaces with total control over the orientation of
attachment (see Figure 7.20). The main advantages would be: (1) the requirement of con-
siderable less protein since the ligation reaction works very efficiently even under high
dilution conditions; and (2) no need for purification since at high dilution the only pro-
tein that will react with the surface will be the one having the complementary affinity and
reactive tag (Figure 7.20). The success of this approach depends on the introduction of
complementary moieties in the protein and the surface, which can form a stable and spe-
cific intermolecular complex. Once formed, this complex should permit a selective reaction
of the complementary chemical groups leading to the covalent attachment of the protein to
the surface.

In the next two sections, two different approaches using this concept will be discussed.

7.5.1. Attachment of proteins by using active site-directed capture ligands

This approach relies on producing a recombinant fusion protein which contains a cap-
ture protein (usually an enzyme) as well as the protein of interest to be immobilized at the
surface. The surface is modified to contain a ligand (usually a substrate for the enzyme) that
would be specifically recognized by the capture protein. This ligand is designed to contain
a reactive group which, once the complex is formed, will react covalently with the capture
protein thus leading to the immobilization of the fusion protein.

The idea of using reactive ligands to capture proteins has been recently used by Meares
and co-workers [109] for creating antibodies with infinite affinity. In this interesting work,
the authors created an antibody against a metal-complex ligand which contained a reactive
electrophile close to the binding site. When the antibody and the ligand are apart, their
complementary groups do not react (mainly due to the dilution effect). However, when
the antibody specifically binds the ligand, the effective concentration of their complemen-
tary groups is greatly increased thus leading to the irreversible formation of a covalent
bond.

More recently, Mrksich and co-workers [110] used this same principle for the selective
attachment of protein onto surfaces with total control over the orientation (Figure 7.21 A).
In this approach, they used the protein calmodulin fused with the enzyme cutinase as a
capture protein. Cutinase is a 22 kDa serine esterase that is able to form a site-specific co-
valent adducts with chorophosphonate ligands [111]. The chlorophosphonate group mimics
the tetrahedral transition state of an ester hydrolysis. When it binds specifically to the ac-
tive site of the enzyme, the hydroxyl group of the catalytic serine residue reacts covalently
with the chlorophosphonate to yield a stable covalent adduct that is resistant to hydrolysis
(Figure 7.21B). In this case the authors used a gold surface to immobilize the cutinase in-
hibitor. The synthesis of this modified phophonate is depicted in Figure 7.21C. Note that in
this case the *p*-nitrophenyl group has the same role that the chorine atom, i.e. transform the
phosphonate group in a good electrophile to react with the hydroxyl group of the catalytic
Ser residue [110]. The final result of the process is the selective attachment of the protein to
the surface through the capture protein that acts as a linker. The attachment is so selective

A

B

C

FIGURE 7.21. Attaching proteins to a surface by using an active-site directed capture ligand approach. (A) Principle of the active-site directed capture ligand approach. (B) Structure of *F. solani* cutinase enzyme free and bound to the inhibitor N-undecyl-O-methyl phosphonate chloride. The inhibitor is covalently bound through the side-chain hydroxyl group of the Ser120 residue which is located at the active site of the enzyme. (C) Synthetic scheme for the preparation of the phosphonate irreversible inhibitor and its attachment to an aminated surface.

that even the whole crude *E. coli* periplasmic lysate containing the cutinase can be used for the specific attachment of the enzyme thus demonstrating that the protein does not need to be purified before the immobilization step [110].

7.5.2. Attachment of proteins by using a protein trans-splicing technique

The main limitation of the previous method, however, is that the linker between the protein of interest and the surface is always another protein (note that in the previous case a 20 kDa enzyme was used as a linker for attaching the smaller 16 kDa calmodulin). The presence of such a big linker could potentially give rise to some problems, specially in those applications where the attached protein will be involved in studying protein/protein interactions with complex protein mixtures [4,5], mainly due to potential cross-reactivity issues.

In order to solve this problem, our group is developing a new method for the chemoenzymatic-like attachment of proteins to surfaces based on the protein trans-splicing process (Figure 7.22A). This process is similar to the protein splicing described earlier in Section 7.4.2.3 with the only difference that the intein self-processing domain is split in two fragments (called N-intein and C-intein, respectively) [112–116]. These two intein fragments alone are inactive, however, when they are put together under the appropriate conditions they bind specifically each other yielding a totally functional splicing domain, which it splices itself out at the same time both extein sequences are ligated. In our approach, one of the fragments (C-intein) will be covalently attached to the surface through a small peptide-linker while the other fragment (N-intein) will be fused to the C-terminus of the protein to be attached to surface. When both intein fragments interact, they will form the active intein which ligates the protein of interest to the surface at the same time the split intein is spliced out into solution (see Figure 7.22A).

Key to our approach is the use of the split DnaE intein from Synechocystis sp. PCC6803. This naturally occurring split intein was first discovered by Liu and co-workers [114] and also predicted through sequence analysis in a independent study by Gorbalenya [115]. In contrast with other inteins engineered to act as trans-splicing elements [112,113], which only work after a refolding step, the C- and N-intein fragments of the DnaE intein are able to self-assemble spontaneously without any refolding step [117,118]. The DnaE split intein consists of a N-intein fragment comprising 123 residues and a C-intein fragment of only 37 residues in length. Our approach consists in expressing a recombinant fusion protein where the DnaE C-intein fragment will be fused to the C-terminus of the protein to be attached to the surface (Figure 7.22A). The C-intein fragment will be synthesized as a synthetic peptide by using a Solid-Phase Peptide Synthesis (SPPS) approach. This will allow us to introduce an alkylthiol moiety at the C-terminus of the C-intein peptide which will be used for attachment to a gold surface (see Section 7.4.1).

Another key aspect in our approach is the potential to create spatially addressable protein arrays with multiple protein components. This can be easily accomplished by creating a C-intein fragment where some of the functional side-chains key for the interaction with the N-intein have been caged with a protecting group removable by UV-light (i.e. photocaged). This protected C-intein fragment will be unable to assemble with the N-intein fused protein and therefore no attachment of the protein to the surface will occur. However, when this photo-labile protecting group is removed by the action of UV-light, the two intein fragments will assemble in functional intein domain thus allowing the attachment of the corresponding protein to the surface through protein splicing (see Figure 7.22B). This approach opens the possibility of creating spatially addressable protein arrays with multiple components.
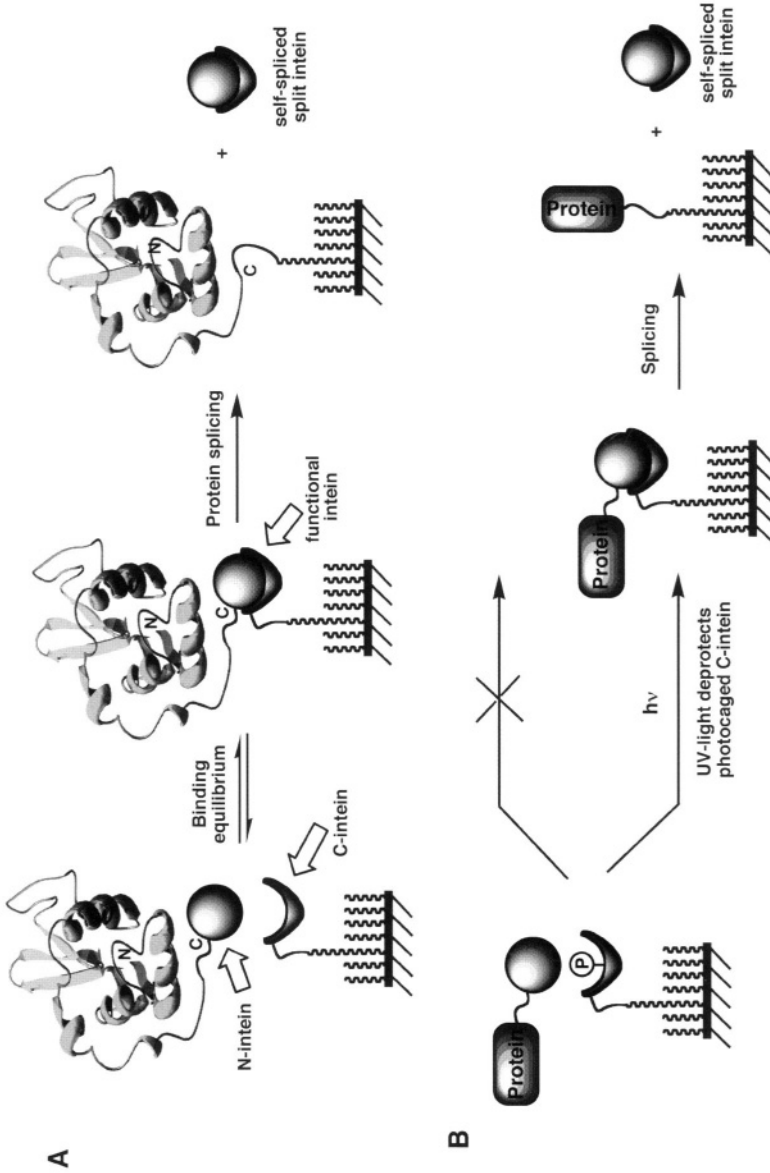
FIGURE 7.22. Attaching proteins to solid surfaces by using a protein trans-splicing technique. (A) Principle of the protein trans-splicing approach for the immobilization of proteins. The C-intein fragment is attached to the surface and the N-intein fragment is fused to the C-terminus of the protein to be attached. When this fusion protein is exposed to C-intein-containing surface, the two intein fragments associate yielding a fully operational intein domain that then splices out attaching at the same time the protein to the surface. (B) The attachment of proteins using this technique can be easily controlled by photo-caging the C-intein fragment. Under this conditions the intein complex can not be formed and consequently the protein is not attached. Only when the photo-labile group is removed by action of UV light the C-intein can yield the active intein domain which then attaches the protein to the surface.

7.6. REMARKS AND CONCLUSIONS

In this review, we have summarized the chemoselective methods available for the controlled attachment and orientation of proteins onto solid surfaces. As mentioned earlier, the ability to attach proteins to a solid support in an ordered fashion will play a critical role in biology and biophysics. For example, the creation of functional protein microarrays is critical for the progress in proteomics research. Like DNA chips, protein chips will allow the analysis and screening of thousand of proteins simultaneously, which will promote the discovery of new drug targets. Moreover, it should be relatively easy to employ protein chips to screen potential drug candidates for unwanted side-effects in all the metabolic pathways. Protein chips can also be also used as a diagnosis tool for profiling protein expression in order to find potential potentially relevant biomarkers. Another potential application for ordered protein films on surfaces will be the production of optimized biosensors [119]. An ordered protein film has a higher activity density than a random protein film, where a significant percentage of the protein molecules bound to the surface are potentially inactive conformations. This will allow biosensor miniaturization without losing sensitivity. Also, the combination of recent nano-lithography techniques combined with the ability to bind proteins in extremely ordered fashion will allow the creation of protein nanopatterns which could be used as templates for the crystallization of biomolecules. This emerging technology is expected to have a significant impact in structural biology field as the main bottleneck in this field is obtaining suitable crystals for physical studies.

In summary, protein biochips furnish us with very powerful tools that will shape the future of biology and biophysics.

ACNOWLEDGMENTS

REFERENCES

1. S. Fields, Proteomics. Proteomics in genomeland, *Science* **291**(5507), 1221–1224 (2001).
2. H. Zhu and M. Snyder, Protein arrays and microarrays, *Curr. Opin. Chem. Biol.* **5**(1), 40–45 (2001).
3. G. Wu, R.H. Datar, K.M. Hansen, T. Thundat, R.J. Cote and A. Majumdar, Bioassay of prostate-specific antigen (PSA) using microcantilevers, *Nat. Biotechnol.* **19**(9), 856–860 (2001).
4. H. Zhu, J.F. Klemic, S. Chang, P. Bertone, A. Casamayor, K.G. Klemic, D. Smith, M. Gerstein, M.A. Reed and M. Snyder, Analysis of yeast protein kinases using protein chips, *Nat. Genet.* **26**(3), 283–289 (2000).
5. H. Zhu, M. Bilgin, R. Bangham, D. Hall, A. Casamayor, P. Bertone, N. Lan, R. Jansen, S. Bidlingmaier, T. Houfek, T. Mitchell, P. Miller, R.A. Dean, M. Gerstein and M. Snyder, Global analysis of protein activities using proteome chips, *Science* **293**(5537), 2101–2105 (2001).
6. D.L. Wilson, R. Martin, S. Hong, M. Cronin-Golomb, C.A. Mirkin and D. L. Kaplan, Surface organization and nanopatterning of collagen by dip-pen nanolithography, *Proc. Natl. Acad. Sci. USA* **98**(24), 13660–13664 (2001).

7. K.B. Lee, S.J. Park, C.A. Mirkin, J.C. Smith and M. Mrksich, Protein nanoarrays generated by dip-pen nanolithography, *Science* **295**(5560), 1702–1705 (2002).

8. P. Arenkov, A. Kukhtin, A. Gemmell, S. Voloshchuk, V. Chupeeva and A. Mirzabekov, Protein microchips: use for immunoassay and enzymatic reactions, *Anal. Biochem.* **278**(2), 123–131 (2000).

9. G. MacBeath and S.L. Schreiber, Printing proteins as microarrays for high-throughput function determination, *Science* **289**(5485), 1760–1763 (2000).

10. G.Y. Liu and N.A. Amro, Positioning protein molecules on surfaces: a nanoengineering approach to supramolecular chemistry, *Proc. Natl. Acad. Sci. USA* **99**(8), 5165–5170 (2002).

11. G.B. Sigal, C. Bamdad, A. Barberis, J. Strominger and G.M. Whitesides, A self-assembled monolayer for the binding and study of histideine-tagged proteins by surface plasmon resonance, *Anal. Chem.* **68**, 490–497 (1996).

12. N.H. Thomson, B.L. Smith, N. Almqvist, L. Schmitt, M. Kashlev, E.T. Kool and P.K. Hansma, Oriented, active Escherichia coli RNA polymerase: an atomic force microscope study, *Biophys. J.* **76**(2), 1024–1033 (1999).

13. M. Saleemuddin, Bioaffinity based immobilization of enzymes, *Adv. Biochem. Eng. Biotechnol.* **64**, 203–226 (1999).

14. L.J. Holt, C. Enever, R.M. de Wildt and I.M. Tomlinson, The use of recombinant antibodies in proteomics, *Curr. Opin. Biotechnol.* **11**(5), 445–449 (2000).

15. W.R. Taylor, The classification of amino-acid conservation, *J. Theor: Biol.* **119**, 205–218(1986).

16. C.B. Anfinsen, Principles that govern the folding of protein chains, *Science* **181**(96), 223–230 (1973).

17. J.P. Tam, J. Xu and K.D. Eom, Methods and strategies of peptide ligation, *Biopolymerx* **60**(3), 194–205 (2001).

18. S. Aimoto, Contemporary methods for peptide and protein synthesis, *Curr. Org. Chem.* **5**(1), 45–87 (2001).

19. RE. Dawson and S.B. Kent, Synthesis of native proteins by chemical ligation, *Annu. Rev. Biochem.* 69, 923–960 (2000).

20. G.J. Cotton and T.W. Muir, Peptide ligation and its application to protein engineering, *Chem. Biol.* **6**(9), R247–R256 (1999).

21. J.A. Camarero and T.W. Muir, Native chemical ligation of polypeptides, *Current Protocols in Protein Science* (18.4), 1–21 (1999).

22. J.P. Tam, Q. Yu and Z. Miao, Orthogonal ligation strategies for peptide and protein, *Biopolymers* **51**(5), 311–332 (1999).

23. M.A. Walker, Protein synthesis by chemical ligation of unprotected peptides in aqueous solution, *Angew. Chem. Int. Ed.* **36**(10), 1069–1071 (1997).

24. C.J.A. Wallace, Peptide ligation and semisynthesis, *Curr: Opin. Biotech.* **6**, 403–410 (1995).

25. H.-G. Hong, M. Jiang, S.G. Sligar and P.W. Bohn, Cysteine-speciric surface tethering of genetically engineered cytochromes for fabrication of metalloprotein nanostructures, *Langmuir* **10**(1), 153–158 (1994).

26. D.G. Kurth and T. Bein, Thin films of (3-aminopropyl)triethoxysilane on aluminum oxide and gold substrates, *Langmuir* **11**, 3061-3067 (1995).

27. G. MacBeath, A.N. Koehler and S.L. Schreiber, Printing small molecules as microarrays and detecting protein–ligand interactions en masse, *J. Am. Chem. Soc.* **121**, 7967–7968 (1999).

28. P.A. Heiney, K. Gruneberg and J. Fang, Structure and growth of chromophore-funtionalized (3-aminopropyl)triethoxysilane self-assembled on silicon, *Langmuir* **16**, 2651–2657 (2000).

29. H.-G. Hong, M. Jiang, S.G. Sligar and P.W. Bohn, Cysteine-speciric surface tethering of genetically engineered cytochromes for fabrication of metallopotein nanostructures, *Langmuir* **10**, 153–158 (1994).

30. F.J. Boerio, L. Armogan and S.Y. Cheng, Structure of gamma-aminopropyltriethoxysilane films on iron mirrors, *J. Colloid Interface Sci.* **1980**(73), 416–424 (1980).

31. M. Pomerantz, A. Segmuller, L. Netzer and J. Sagiv, Coverage of Si substrates by self-assembling monolayers and multilayers as measured by IR, wettability and X-ray-diffraction, *Thin Solid Films* **132**(1–4), 153–162(1985).

32. K. Bierbaum, M. Kinzler, C. Woll, M. Grunze, G. Hahner, S. Heid and F. Effenberger, A near-edge X-ray-absortion fine structure spectroscopy and X-ray photoelectron-speetroscopy study of the film properties of self-assembled monolayers of organosilanes on oxidized Si(100), *Langmuir* **11**(2), 512–518 (1995).

33. N. Balachander and C.N. Sukenik, Monolayer transformation by nucleophilic-substitution. Applications to the creation of new monolayer assemblies, *Langmuir* **6**(11), 1621–1627 (1990).

34. A. Heise, H. Menzel, H. Yim, M.D. Foster, R.H. Wieringa, A.J. Schouten, V. Erb and M. Stamm, Grafting of polypeptides on solid substrates by initiation of N-carboxyanhydride polymerization bu amino-terminated self-assembled monolayers, *Langmuir* **13**(4), 723–728 (1997).

35. A. Ulman, Formation and structure of self-assembled monolayers, *Chem. Rev.* **96**, 1533–1554 (1996).

36. H.A. Biebuyck, C.D. Bian and G.M. Whitesides, Comparison of organic monolayers on polycrystalline gold spontaneously, *Langmuir* **10**(6), 1825–1831 (1994).

37. L.H. Dubois and R.G. Nuzzo, Synthesis, structure and protperties of model organic-surfaces, *Ann. Phys. Chem.* **43**, 437–463(1992).

38. P. Wagner, M. Hegner, H.-J. Guntherodt and G. Semenza, Formation and in situ modification of monolayers chemisorbed on ultraflat template-stripped gold surfaces, *Langmuir* **11**, 3867–3875 (1995).

39. C.-M. Yam, C.M. Pradier, M. Salmain, P. Marcus and G. Jaouen, Binding of biotin to gold surfaces funtionalized by self-assembled monolayers of cystamine and cysteamine: combined FT-IRRAS and XPS characterization, *J. Colloid Interface Sci.* **235**(1), 183–189 (2001).

40. K. Uvdal and T.P. Vikinge, Chemisorption of the dipeptide Arg-Cys on a gold surface and the selectivity of G-protein adsorption, *Langmuir* **17**(6), 2008–2012 (2001).

41. Y.C. Liu, C.M. Wang and K.P. Hsiung, Comparison of different protein immobilization methods on quartz crystal microbalance surface in flow injection immunoassay, *Anal. Biochem.* **299**(2), 130–135 (2001).

42. C. Pale-Grosdemange, E. Simon, K.L. Prime and G.M. Whitesides, Formation of self-assembled monolayers by Chemisorption of derivatives of oligo(ethylene glycol) of structure $HS(CH_2)_{11}(OCH_2CH_2)_m OH$ on gold, *J. Am. Chem. Soc.* **113**, 12–20 (1991).

43. E. Ostuni, R.G. Chapman, R.E. Holmlin, S. Takayama and G.M. Whitesides, A survey of structure–property realtionships of surfaces that resist the adsorption of protein, *Langmuir* **17**, 5605–5620 (2001).

44. E. Ostuni, R.C. Chapman, M.N. Liang, G. Meluleni, G. Pier, D.E. Ingber and G.M. Whitesides, Self-assembled monolayers that resist the adsorption of proteins and the adhesion of bacterial and mammalian cells, *Langmuir* **17**, 6336–6343 (2001).

45. C.L. Cheung, J.A. Camarero, B. Woods, T. Lin, J.E. Johnson and J.J. De Yoreo, Fabrication of assembled virus nanostructures on templates of chemoselective linkers formed by scanning probe nanolithography, *J. Am. Chem. Soc.* **125**, 6848–6849 (2003).

46. J.A. Camarero, G.J. Cotton, A. Adeva and T.W. Muir, Chemical ligation of unprotected peptides directly form a solid support, *J. Pept. Res.* **51**, 303–316 (1998).

47. M.D. Partis, D.G. Griffiths, G.C. Roberts and R.B. Beechey, Cross-linking of protein by maleimido alkanoyl N-hyroxysuccinimido esters, *J. Protein Chem.* **2**, 263–277 (1983).

48. M.A. Firestone, M.L. Shank, S.G. Sligar and P.W. Bohn, Film architecture in biomolecular assemblies. Effect of linker on the orientation of genetically engineered surface-bound protein, *J. Am. Chem. Soc.* **118**(38), 9033–9041 (1996).

49. A.M. Edwards, J.K. Blasie and J.C. Bean, Vectorially ordered monolayers of the cytochrome c/cytochrome oxidase bimolecular complex, *Biophys. J.* **74**(3), 1346–1357 (1998).

50. S.J. Xiao, M. Textor, N.D. Spencer and H. Sigrist, Covalent attachment of cell-adhesive, (Arg–Gly–Asp)-containing peptides to titanium surfaces, *Langmuir* **14**(19), 5507–5516 (1998).

51. L.L. Wood, S.S. Cheng, P.L. Edmiston and S.S. Saavedra, Moleculr orientation distributions in proteins films. 2. Site-directed immobilization of yeast cytochrome c on thiol-capped, self-assembled monolayers, *J. Am. Chem. Soc.* **119**(3), 571–576 (1997).

52. S. Kanno, Y. Yanagida, T. Haruyama, E. Kobatake and M. Aizawa, Assembling of engineered IgG-binding protein on gold surface for highly oriented antibody immobilization, *J. Biotechnol.* **76**(2–3), 207–214 (2000).

53. Q. Wang, L. Tianwei, T. Liang, J.E. Johnson and M.G. Finn, Icosahedral virus particles as addressable nanoscale building blocks, *Angew. Chem. Int. Ed.* **41**(3), 459–462 (2002).

54. O. Cavalleri, C. Natale, M. E. Stroppolo, A. Relini, E. Cosulich, S. Thea, M. Novi and A. Gliozzi, Azurin immobilization on thiol covered Au(111), *Phys. Chem. Chem. Phys.* **2000**(2), 4630–4635 (2000).

55. V.H. Routh and C.J. Helke, A novel technique for producing antibody-coated microprobes using a thiol-terminal silane and a heterobifunctional crosslinker, *J. Neurosci. Methods* **71**(2), 163–168 (1997).

56. H.F. Gaertner, K. Rose, R. Cotton, D. Timms, R. Camble and R.E. Offord, Construction of protein analogues by site-specific sondensation of unprotected Peptides, *Bioconjugate Chem.* **3**, 262–268 (1992).

57. H.F. Gaertner, R.E. Offord, R. Cotton, D. Timms, R. Camble and K. Rose, Chemo-enzymic backbone engineering of proteins. Site-specific incorporation of synthetic peptides that mimic the 64–74 disulfide loop of granulocyte colony-stimulating factor, *J. Biol. Chem.* **269**(10), 7224–7230 (1994).

58. H.F. Gaertner and R.E. Offord, Site-specific attachment of functionalized poly(ethylene glycol) to the amino terminus of proteins, *Bioconjug. Chem.* **7**(1), 38–44 (1996).

59. P.H. Hirel, M.J. Schmitter, P. Dessen, G. Fayat and S. Blanquet, Extent of N-terminal methionine excision from *Escherichia coli* proteins is governed by the side-chain length of the penultimate amino acid, *Proc. Natl. Acad. Sci. USA* **86**(21), 8247–8251 (1989).

60. D.A. Erlandson, M. Chytil and G.L. Verdine, The leucine zipper domain controls the orientation of AP-1 in the NFAT·AP-1·DNA complex, *Chem. Biol.* **3**, 981–991 (1996).

61. H.B.F. Dixon and R. Fields, Specific modification of the NH_2-terminal residues by transamination, *Methods Enzymol.* **25**, 409–419 (1972).

62. H.B.F. Dixon, N-terminal modification of proteins. A review, *J. Protein Chem.* **3**, 99–108 (1984).

63. S.-C. Huang, K.D. Caldwell, J.-N. Lin, H.-K. Wang and J.N. Herron, Site-specific immobilization of monoclonal antibodies using a spacer-mediated antibody attachment, *Langmuir* **12**, 4292–4298 (1996).

64. L. Muchova, M. Jirsa, M. Kuroki, L. Dudkova, M.J. Benes, Z. Marecek and F. Smid, Immunoaffinity isolation of CECAM1 on hydrazide-derivatized cellulose with immobilized monoclonal anti-CEA antibody, *Biomed. Chromatogr.* **15**(6), 418–422 (2001).

65. Z. Bilkova, M. Slovakova, A. Lycka, D. Horak, J. Lenfeld, J. Turkova and J. Churacek, Oriented immobilization of galactose oxidase to bead magnetic bead cellulose and poly(HEMA-co-EDMA) and magnetic poly(HEMA-co-EDMA) microspheres, *J. Chromatogr. B* **770**(1–2), 25–34 (2002).

66. W.P. Quian, B. Xu, L. Wu, C.X. Wang, D.F. Yao, F. Yu, C.W. Yuan and Y. Wei, Controlled site-directed assembly of antibodies by their oligosaccharide moieties onto APTES derivatized surfaces, *J. Colloid Interface Sci.* **214**(1), 16–19 (1999).

67. W.P. Quian, D. Yao, B. Xu, F. Yu, Z. Lu and W. Knoll, Atomic force microscopic studies of site-directed immobilization of antibodies using their carbohydrate residues, *Chem. Mater.* **11**(6), 1399–1410 (1999).

68. P.E. Dawson, T.W. Muir, I. Clark-Lewis and S.B.H. Kent, Synthesis of proteins by native chemical ligation, *Science* **266**, 776–779 (1994).

69. J.P. Tam, Y.A. Lu, C.F. Liu and J. Shao, Peptide synthesis using unprotected peptides through orthogonal coupling methods, *Proc. Natl. Acad. Sci. USA* **92**(26), 12485–12489 (1995).

70. T. Wieland, E. Bokelmann, L. Bauer, H.U. Lang and H. Lau, Polypeptide synthesis. VIII. Formation of sulfur containing peptides by intramolecular migration of aminoacyl groups, *Liebigs Ann. Chem.* **583**, 129–135 (1953).

71. T. Wieland, Sulfur in Biomimetic Peptide Synthesis, in: *The Roots of Modern Biochemistry,* Ed. J.v.D. Kleinkauf (Walter de Gruyter & Co., Berlin, New York, 1988) pp. 213–221.

72. J. Blake, Peptide segment coupling in aqueous medium: silver ion activation of the thiolcarboxyl group, *Int. J. Pept. Protein Res.* **17**(2), 273–274 (1981).

73. D. Yamashiro and C.H. Li, New segment synthesis of *α*-inhibin-92 by the acyl disulphide method, *Int. J. Pept. Protein Res.* **31**, 322–334 (1988).

74. J.P. Tam and Q.T. Yu, Methionine ligation strategy in the biomimetic synthesis of parathyroid hormones, *Biopolymers* **46**(5), 319–327 (1998).

75. J.A. Camarero, A. Adeva and T.W, Muir, 3-Thiopropionic acid as a highly versatile multidetachable thioester resin linker, *Lett. Pept. Sci.* **7**(1), 17–21 (2000).

76. R. Micanovic, R. Procyk, W. Lin and G.R. Matsueda, Role of histidine 373 in the catalytic activity of coagulation factor XIII, *J. Biol. Chem.* **269**(12), 9190–9194 (1994).

77. J.W. Trauger, R.M. Kohli, H.D. Mootz, M.A. Marahiel and C.T. Walsh, Peptide cyclization catalysed by the thioesterase domain of tyrocidine synthetase, *Nature* **407**(6801), 215–218 (2000).

78. C.T. Walsh, H. Chen, T.A. Keating, B.K. Hubbard, H.C. Losey, L. Luo, C.G. Marshall, D.A. Miller and H.M. Patel, Tailoring enzymes that modify nonribosomal peptides during and after chain elongaion on NRPS assembly lines, *Curr. Opin. Chem. Biol.* **5**(5), 525–534 (2001).

79. P.M. Kane, C.T. Yamashiro, D.F. Wolczyk, N. Neff, M. Goebl and T.H. Stevens, Protein splicing converts the yeast TFP1 gene product to the 69-kD subunit of the vacuolar H(+)-adenosine triphosphatase, *Science* **250**(4981), 651–657(1990).

80. M.-Q. Xu and F.B. Perler, The mechanism of protein splicing and its modulation by mutation, *EMBO J.* **15**(19), 5146–5153 (1996).

81. C.J. Noren, J.M. Wang and F.B. Perler, Dissecting the chemistry of protein splicing and its applications, *Angew. Chem. Int. Ed.* **39**(3), 451–456 (2000).

82. T.W. Muir, D. Sondhi and P.A. Cole, Expressed protein ligation: a general method for protein engineering, *Proc. Natl. Acad. Sci. USA* **95**(12), 6705–6710 (1998).

83. K. Severinov and T.W. Muir, Expressed protein ligation, a novel method for studying protein–protein interactions in transcription, *J. Biol. Chem.* **273**(26), 16205–16209 (1998).

84. T.C. Evans, J. Benner and M.-Q. Xu, Semisynthesis of cytotoxic proteins using a modified protein splicing element, *Protein Sci.* **7**, 2256–2264 (1998).

85. X. Duan, F.S. Gimble and F.A. Quiocho, Crystal structure of PI-SceI, a homing endonuclease with protein splicing activity, *Cell* **89**, 555–564 (1997).

86. B.W. Poland, M.Q. Xu and F.A. Quiocho, Structural insights into the protein splicing mechanism of PI-SceI, *J. Biol. Chem.* **275**(22), 16408–16413 (2000).

87. S. Chong, F.B. Mersha, D.G. Comb, M.E. Scott, D. Landry, L.M. Vence, F.B. Perler, J. Benner, R.B. Kucera, C.A. Hirvonen, J.J. Pelletier, H. Paulus and M.Q. Xu, Single-column purification of free recombinant proteins using a self-cleavable affinity tag derived from a protein splicing element, *Gene* **192**(2), 271–281 (1997).

88. S. Chong, G.E. Montenello, A. Zhang, E.J. Cantor, W. Liao, M.-Q. Xu and J. Benner, Utilizing the C-terminal cleavage activity of a protein splicing element to purify recombinant proteins in a single chromatographic step, *Nucleic Acid Res.* **26**(22), 5109–5115 (1998).

89. T.P. King, S.W. Zhao and T. Lam, Preparation of protein conjugates via intermolecular hydrazone linkage, *Biochemistry* **25**(19), 5774–5779 (1986).

90. J.R. Falsey, M. Renil, S. Park, S. Li and K.S. Lam, Peptide and small molecule microarray for high throughput cell adhesion and functional assays, *Bioconjug. Chem.* **12**(3), 346–353 (2001).

91. S.V. Taylor, N.L. Kelleher, C. Kinsland, H.J. Chiu, C.A. Costello, A.D. Backstrom, F.W. McLafferty and T.P. Begley, Thiamin biosynthesis in Escherichia coli. Identification of this thiocarboxylate as the immediate sulfur donor in the thiazole formation, *J. Biol. Chem.* **273**(26), 16555–16560 (1998).

92. C. Kinsland, S.V. Taylor, N.L. Kelleher, F.W. McLafferty and T.P. Begley, Overexpression of recombinant proteins with a C-terminal thiocarboxylate: implications for protein semisynthesis and thiamin biosynthesis, *Protein Sci.* **7**(8), 1839–1842 (1998).

93. M. Schnolzer and S.B. Kent, Constructing proteins by dovetailing unprotected synthetic peptides: backbone-engineered HIV protease, *Science* **256**(5054), 221–225 (1992).

94. C.-F. Liu, C. Rao and J.P. Tam, Acyl disulfide-mediated intramolecular acylation for orthogonal coupling between unprotected peptide segments. Mechanism and application, *Tetrahedron Lett.* **37**(7), 933–936 (1996).

95. D.S. Kemp and R.I. Carey, Synthesis of a 39-peptide and a 25-peptide by thiol-capture ligations: observation of a 40-fold rate acceleration of the intramolecular O,N-acyl transfer reaction between peptide fragments bearing only cysteine protecting groups, *J. Org. Chem.* **58**, 2216–2222 (1993).

96. C.-F. Liu and J.P. Tam, Peptide segment ligation strategy without use of protecting groups, *Proc. Natl. Acad. Sci. USA* **91**, 6584–6588 (1994).

97. C.-F. Liu, C. Rao and J.P. Tam, Orthogonal ligation of unprotected peptide segments through pseudoproline formation for the synthesis of HIV-1 protease analogs, *J. Am. Chem. Soc.* **118**, 307–312 (1996).

98. E. Saxon, J.I. Armstrong and C.R. Bertozzi, A "traceless" Staudinger ligation for the chemoselective synthesis of amide bonds, *Org. Lett.* **2**(14), 2141–2143 (2000).

99. E. Saxon and C.R. Bertozzi, Cell surface engineering by a modified Staudinger reaction, *Science* **287**(5460), 2007–2010 (2000).

100. B.L. Nilsson, L.L. Kiessling and R.T. Raines, High-yielding Staudinger ligation of a phosphinothioester and azide to form a peptide, *Org. Lett.* **3**(1), 9–12 (2001).

101. K.L. Kiick, E. Saxon, D.A. Tirrell and C.R. Bertozzi, Incorporation of azides into recombinant proteins for chemoselective modification by the Staudinger ligation, *Proc. Natl. Acad. Sci. USA* **99**(1), 19–24 (2002).

102. J. Villa, M. Strajbl, T.M. Glennon, Y.Y. Sham, Z.T. Chu and A. Warshel, How important are entropic contributions to enzyme catalysis?, *Proc. Natl. Acad. Sci. USA* **97**(22), 11899–11904 (2000).

103. J.A. Camarero, A. Shektman, E. Campbell, M. Chlenov, T.M. Gruber, D.A. Bryant, S.A. Darst, D. Cowburn and T.W. Muir, Autoregulation of a bacterial sigma factor explored using segmental isotopic labeling and NMR, *Proc. Natl. Acad. Sci. USA* **99**(13), 8536–8541 (2002).

104. D.F. Dyckes, T. Creighton and R.C. Sheppard, Spontaneous re-formation of a broken peptide chain, *Nature* **247**(438), 202–204 (1974).

105. C.J. Wallace and I. Clark-Lewis, Functional role of heme ligation in cytochrome c. Effects of replacement of methionine 80 with natural and non-natural residues by semisynthesis, *J. Biol. Chem.* **267**(6), 3852–3861 (1992).

106. J.A. Camarero, J. Pavel and T.W. Muir, Chemical synthesis of a circular protein domain: evidence for folding-assisted cyclization, *Angew. Chem. Int. Ed.* **37**(3), 347–349 (1998).

107. J.A. Camarero and T.W. Muir, Biosynthesis of a head-to-tail cyclized protein with improved biological activity, *J. Am. Chem. Soc.* **121**, 5597–5598 (1999).

108. G.S. Beligere and P.E. Dawson, Conformationally assisted ligation using C-terminal thioester peptides, *J. Am. Chem. Soc.* **121**, 6332–6333 (1999).

109. A.J. Chmura, M.S. Orton and C.F. Meares, Antibodies with infinite affinity, *Proc. Natl. Acad. Sci. USA* **98**(15), 8480–8484 (2001).

110. C.D. Hodneland, Y.S. Lee, D.H. Min and M. Mrksich, Supramolecular chemistry and self-assembly special feature: selective immobilization of proteins to self-assembled monolayers presenting active site-directed capture ligands, *Proc. Natl. Acad. Sci. USA* **99**(8), 5048–5052 (2002).

111. M.L. Mannesse, J.W. Boots, R. Dijkman, A.J. Slotboom, H.T. van der Hijden, M.R. Egmond, H.M. Verheij and G.H. de Haas, Phosphonate analogues of triacylglycerols are potent inhibitors of lipase, *Biochem. Biophys. Acta* **1259**(1), 56–64 (1995).

112. B.M. Lew, K.V. Mills and H. Paulus, Protein splicing in vitro with a semisynthetic two-component minimal intein, *J. Biol. Chem.* **273**(26), 15887–15890 (1998).

113. K.V. Mills, B.M. Lew, S. Jiang and H. Paulus, Protein splicing in trans by purified N- and C-terminal fragments of the Mycobacterium tuberculosis RecA intein, *Proc. Natl. Acad. Sci. USA* **95**(7), 3543–3548 (1998).

114. H. Wu, Z. Hu and X.Q. Liu, Protein *trans*-splicing by a split intein encoded in a split DnaE gene of *Synechocystis* sp. PCC6803, *Proc. Natl. Acad. Sci. USA* **95**, 9226–9231 (1998).

115. A.E. Gorbalenya, Non-canonical inteins, *Nucleic Acids Res.* **26**(7), 1741–1748 (1998).

116. F.B. Perler, A natural example of protein trans-splicing, *Trends Biochem. Sci.* **24**(6), 209–211 (1999).

117. T.C. Evans, Jr., D. Martin, R. Kolly, D. Panne, L. Sun, I. Ghosh, L. Chen, J. Benner, X.Q. Liu and M.Q. Xu, Protein trans-splicing and cyclization by a naturally split intein from the dnaE gene of Synechocystis species PCC6803, *J. Biol. Chem.* **275**(13), 9091–9094 (2000).

118. D.D. Martin, M.Q. Xu and T.C. Evans, Jr., Characterization of a naturally occurring trans-splicing intein from Synechocystis sp. PCC6803, *Biochemistry* **40**(5), 1393–1402 (2001).

119. G. Wu, H. Ji, K. Hansen, T. Thundat, R. Datar, R. Cote, M.F. Hagan, A.K. Chakraborty and A. Majumdar, Origin of nanomechanical cantilever motion generated from biomolecular interactions, *Proc. Natl. Acad. Sci. USA* **98**(4), 1560–1564 (2001).

8

The creation of organic and biological nanostructures at surfaces using scanning probe nanolithography

B.L. Weeks, C.L. Cheung, J.J. De Yoreo*

Biosecurity and Nanosciences Laboratory, Chemistry and Materials Science Directorate, Lawrence Livermore National Laboratory, Livermore, CA 94551, USA

8.1. INTRODUCTION

As the size of microelectronic devices continues to shrink and the desire to build in hierarchical structures of organic and biological materials grows, control of the chemistry and structure of materials at the molecular level will become increasingly important. Conventional lithographic techniques to pattern polymeric thin films are beginning to reach their resolution limit and several alternative "bottom-up" strategies have emerged that use the scanning probe microscope to manipulate matter at the atomic or molecular scale. Of these new scanning probe nanolithography (SPN) techniques, dip-pen nanolithography (DPN) [1] and scanning probe nanografting (SNG) [2] are particularly promising.

The DPN methodology utilizes the tip of an atomic force microscope (AFM) as a "nanopen" to transport an "ink" containing organic molecules onto a solid support as illustrated in Figure 8.1. Using the same tip to "write" and subsequently "read" patterns, it is possible to create nanoscale patterns of alkyl thiols with remarkable resolution (~10 nm) and simultaneously control the chemical functionality of the written areas. Examples of patterns created using a variety of inks are shown in Figure 8.2.

The SNG methodology also relies on an AFM tip to pattern the surface, but in this case the substrate is first uniformly functionalized with a layer of one kind of ink, and the tip is used to remove portions of that layer, which are then filled in by a second ink to create patterns with multiple functionality. Removal and re-deposition are done either in a single step by operating in the presence of a solution containing the second ink, which fills in

---

*Corresponding author. E-mail address: deyoreo1@llnl.gov
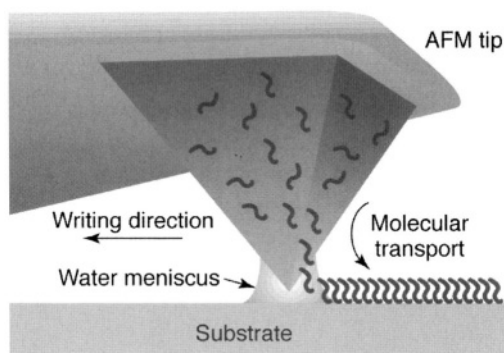
FIGURE 8.1. Schematic of the dip pen nanolithography process. Ink molecules coated onto an AFM tip are deposited as the tip moves across a substrate.

behind the tip, or they are performed in a two-step process in which removal is done in air and followed by subsequent exposure of the substrate to a solution of the second ink. Both methods also give feature sizes down to ~10 nm. The two-step nanografting process is illustrated in Figure 8.3, and an example of a two-ink SNG pattern is given in Figure 8.4.

This technology provides a particularly attractive tool for nanostructural engineering because it immediately lends itself to construction of an inorganic–organic interface that is controlled at the atomic scale by the nature of the intermolecular interactions between the ink molecules, as well as at the nanoscale by the inherent size of the tip–surface contact. Moreover, because alkyl chains can readily be synthesized with a variety of functionalities in the head group, SPN provides a route towards constructing hierarchical nanostructures comprised of inorganic substrates, organic linkers, and biological molecules such as proteins, DNA, and even whole organisms. Indeed, as this chapter will show, patterning of all three at length scales of 100 nm or less have already been achieved.

8.2. DEVELOPMENT OF SCANNING PROBE NANOLITHOGRAPHY

The break-through that has allowed for the formation of these soft structures is scanning probe microscopy. The grandfather of all scanning probe techniques is the scanning tunneling microscope (STM) [3]. Scanning tunneling microscopy is an analytical technique based on the detection of a quantum mechanical tunneling current between a tip and a sample. When the tip is brought within about 10 Å of the sample, electrons begin to "tunnel" across the gap. Because the resulting tunneling current varies strongly with tip-to-sample spacing, the variations in this current can be used to create an image of the surface. Changes in surface features of about 1 Å cause the tunneling current to change by almost an order of magnitude. It is this relationship that gives STM the ability to obtain true atomic resolution on conducting and semi-conducting surfaces. Unfortunately, there are some limitations with STM. The most significant is that both the surfaces of the tip and sample must be conducting, limiting the types of materials that can be studied. This limitation helped to drive the invention of the first atomic force microscope in 1986.

Like STM, AFM also uses a very sharp tip to probe the surface. However, in AFM there is no requirement to measure a current flowing between the tip and sample, which allows
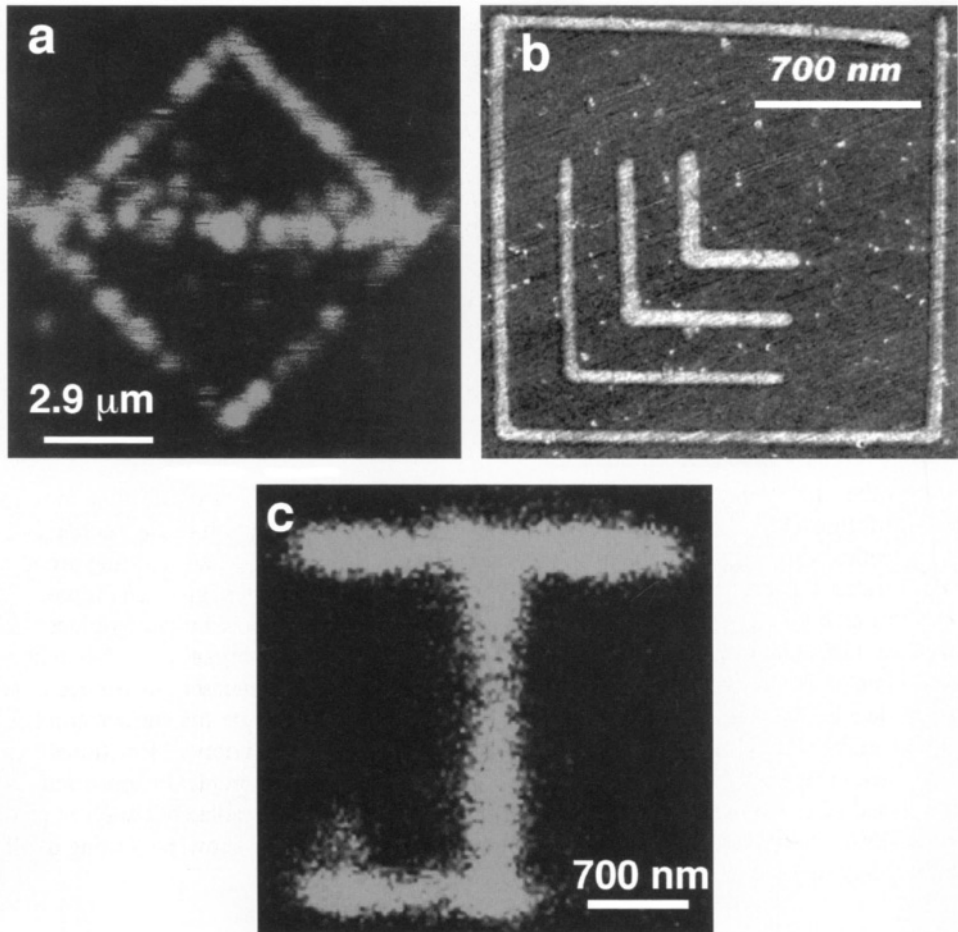
FIGURE 8.2. Examples of structures created with dip pen nanolithography: (a) scanning confocal image of Rhodamine 6G patterned with DPN on a glass substrate; (b) friction force image of 16-mercaptohexadecanoic acid on a gold substrate; (c) scanning confocal microscopy image of a HCG antibody pattern fabricated on glass. Probe translation speed was $0.2~\mu m\,s^{-1}$. Each line in the pattern was overwritten ten times to maximize the protein surface density. Note that in the confocal images, the apparent line-width is determined by the resolution of the confocal system which is about 500 nm. In the case of Rhodamine 6G, fluorescent signals from single molecules are observed.

one to image both conducting and non-conducting samples. The first AFM was made by meticulously gluing a tiny sliver of diamond onto one end of a strip of foil to form a micro cantilever, which was then used to examine insulating surfaces [4]. The results were staggering, demonstrating lateral resolution at insulating surfaces on the order of 300 Å. However, without a breakthrough in tip manufacturing, the AFM probably would have remained a curiosity in many research groups. It was Albrecht *et al.* who fabricated the first silicon microcantilever and measured the atomic structure of boron nitride [5]. Today, most commercial cantilevers are mass-produced with optical lithographic techniques and are constructed from Si or Si_3N_4. Figure 8.5 shows an SEM micrograph of a silicon cantilever.
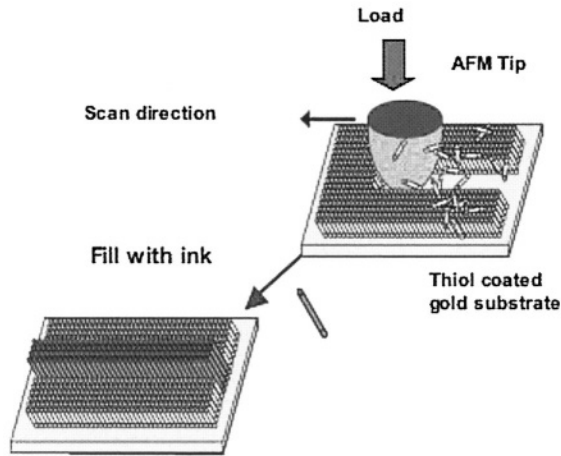
FIGURE 8.3. Schematic of the two-step nanografting process. A substrate is initially coated with a self-assembly monolayer (SAM), which is then locally removed by the AFM tip. Subsequent exposure to a solution containing a second ink results in a two-phase SAM.
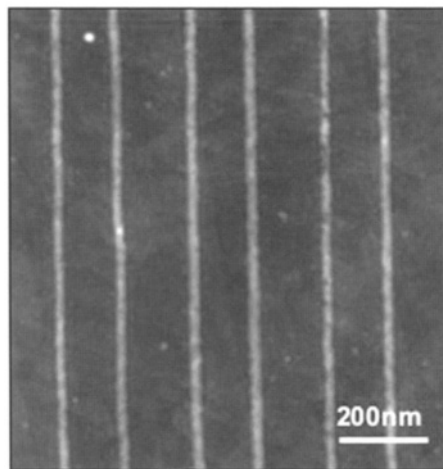
FIGURE 8.4. AFM image of alkyl thiols patterned on a gold substrate. Darker regions are coated with a self-assembly monolayer of polyethylene glycol terminated alkyl thiol. The lines are regions containing longer chain, amino terminated alkyl thiols.

The force between an AFM tip and sample surface during imaging is very small, usually less than 10^{-9} N. But the detection system does not measure this force directly. Instead it senses the deflection of the microcantilever, which follows Hook's law. The detecting systems for monitoring the deflection fall into several categories. The first device introduced by Binnig was a tunneling tip placed above the surface of a cantilever that had been metallized. As with the STM, a change in spacing of 1 Å between tip and cantilever changed the tunneling current by an order of magnitude. Thus, it was straightforward to measure deflections smaller than 0.01 Å. Subsequent systems were based on optical techniques. The interferometer is the most sensitive of the optical methods, but it is somewhat more
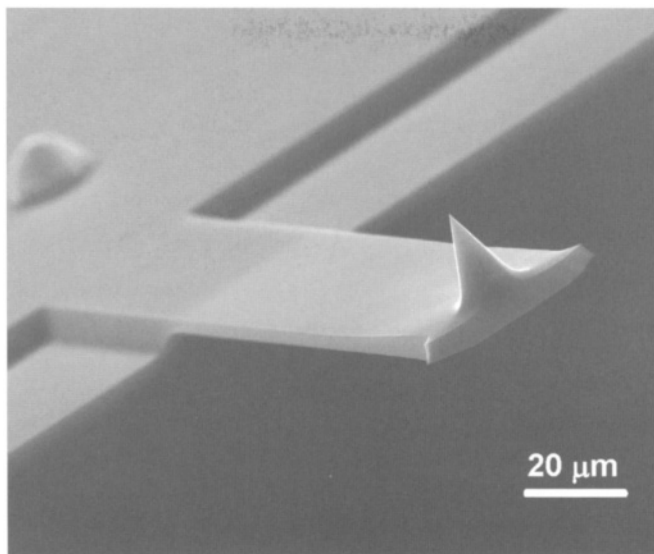
FIGURE 8.5. A scanning electron microscopy image of a silicon cantilever.

complicated than the optical lever, which was introduced by Meyer and Amer [6]. In the latter, visible light from a low power laser diode is focused on the apex of a cantilever. The light is then reflected from the mirrored surface on the backside of the cantilever onto a position-sensitive photodetector. The distance traveled by the laser beam is proportional to the cantilever deflection and magnified by the cantilever-photodetector distance as the arm of a lever. By far the most common method of detection used by commercial AFMs is the optical lever with a four-quadrant photo detector [7] as shown in Figure 8.6. By using a four-quadrant photo detector both cantilever deflection (which reflects the sample topography) and cantilever twisting (which occurs in response to friction forces between tip and surface) can be measured simultaneously.

Early in the development of the STM, scientists began to use it as a tool for creating topographical structures on various surfaces. Methods included localized chemical vapor deposition [8], electrodeposition [9], mechanical contact of the tip with the surface [10], and deformation of the surface by electrical pulses in both vacuum and elevated pressures [11,12]. The majority of STM lithography experiments focused on producing the smallest possible structures. Perhaps the most delicate examples of nanofabrication to date are the atomic structures formed by using the STM to deposit individual xenon atoms on nickel [13].

AFM-based lithography affords somewhat less precision and resolution than that obtained with STM lithographic techniques, but opens the door to manipulation of non-conducting surfaces. The AFM can also be used to modify surfaces locally via electrodeposition or catalytic chemical reactions [9,10]. However, one of the main advantages of AFM-based lithography results from the contact between tip and surface, which enables one to produce physical deformation of surfaces at a local scale. In typical AFM contact imaging the forces exerted on the surface are on the order of 0.05 nN. But increasing the local pressure will eventually lead to a surface deformation. In the case of an alkyl thiol
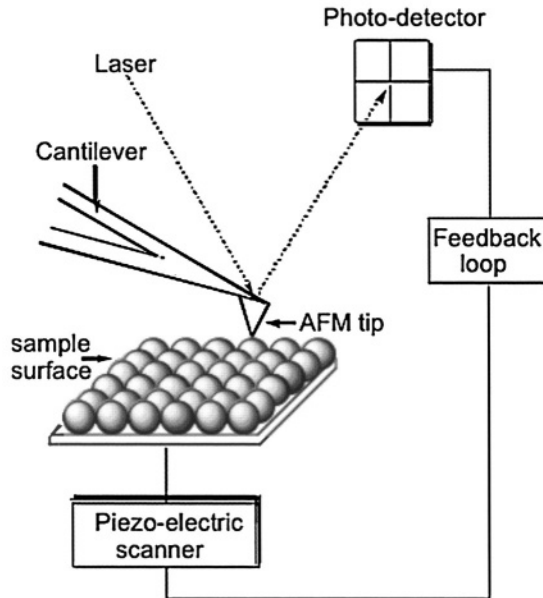
FIGURE 8.6. Diagram of an atomic force microscope with optical lever detection and a four-quadrant photodetector.

coated gold surfaces, the tip can be used like a "snowplow" to locally remove a monolayer of the self-assembled monolayer (SAM), which is the basis of SNG. With increasing pressure, the tip first causes deformation, then disrupts the alkyl thiol packing, and eventually displaces the alkyl thiol molecules at the adsorption site because the Au–S bond is the weakest one at the interface. (The binding energies for S–Au, C–C, C–H, and C–S are 40, 145, 81, and 171 kcal/mol, respectively. In addition, the lateral movement of thiols on gold requires less activation energy than does desorption.) Increasing the load still further causes the underlying gold substrate to deform.

8.3. DIP PEN NANOLITHOGRAPHY

The other advantage of the tip surface contact that the AFM provides, is the ability to directly transfer molecules from tip to surface, which is the basis of DPN. The discovery of DPN came from studies of the dynamics of the capillary effect and water transport from an AFM tip in air [14]. From that work, Piner and Mirkin were able to demonstrate that by bringing the tip of an AFM in contact with a surface would cause depletion or an increase in the amount of water on the surface dependent on the surface energy, contact time, and initial humidity. The structures formed were only observable for approximately a day depending on humidity, temperature, size of feature, etc. Using the meniscus that naturally forms in air between the tip and sample as a transport medium provided a way of controlling molecular deposition from a coated AFM tip onto the substrate. By carefully choosing molecules that were designed to react with the surface to be patterned, they created a chemical driving force favoring the transfer of such molecules to the substrate. Chemisorption of the ink

molecules onto the substrate led to stable nanostructures, which would not degrade over time as was the case in the experiments using water condensation.

The first demonstration of DPN showed that alkyl thiols could be patterned onto gold surfaces and that regulating humidity and temperature led to control over the feature size. Hydrophilic and hydrophobic molecules—including biomolecules such as DNA and proteins—have now been patterned via the DPN process [15,16]. Moreover, through the development of controlled-environmental chambers, which allow one to replace the water meniscus with other solvents, it seems likely that it will be possible to extend DPN to a wide range of molecular species and substrates.

One feature that sets DPN apart from other high resolution nanolithographic techniques is its registration capabilities. Since one uses the same AFM cantilever to write the pattern and subsequently read the image, one can generate multiple nanostructures, made of the same or different inks, and align them with respect to one another with nanometer-scale precision. This capability makes DPN an excellent tool for generating multifunctional nanostructures and for making chips with integrated soft lithographic molecules comprised of different chemical components. For this reason, DPN could have a major impact in molecular electronics, bioinformatics, catalysis, and sensor design. With commercially available cantilevers, DPN currently offers 15 nm line-width and 5 nm spatial resolution and, therefore, rivals other techniques such as e-beam lithography for patterning solid substrates while having the advantage of not requiring a vacuum to operate.

One of the largest drawbacks of DPN is that it is an inherently a serial process. Most researchers use a single cantilever, which limits the size of the lithographic pattern being formed to that of the scan range of the AFM. Recently, DPN has been partially transformed from a serial to parallel process through the use of eight cantilevers, and arrays of 10,000 cantilevers have now been produced for the next generation of DPN machines. Because the feature dimensions in a DPN experiment are almost independent of the tip/sample contact force over a range of two orders of magnitude, an array of tips can be used in a parallel writing fashion by engaging all of the tips in the array with the substrate to be patterned. Through careful design, it seems likely that each of these tips can be engaged individually to allow the multiple pen system to be used in serial fashion like a nanoplotter, where each of the tips has a different ink.

Although DPN is particularly well suited for patterning flat solid substrates with soft matter, it has been combined with wet chemical etching procedures to fabricate silicon structures, thus far on a length scale greater than 40 nm. Recently, silicon nanostructures were generated via a multi-step process that utilizes DPN to generate soft resist structures comprised of octadecane thiol (ODT) on gold /titanium/silicon layered structures [17]. The areas that were coated with the ODT layers were resistant to the etchant (ferrocyanide-based solution) while the unmodified gold could be selectively etched, to leave behind an alkyl thiol-capped gold surface. The exposed titanium-coated silicon were subsequently etched with KOH. Removing the Au and Ti layers with *aqua regia* yielded a 3D modified bare silicon surface. This approach, in principle, could be extended to other metal-coated substrates or doped silicon to produces conducting circuits with features much smaller than currently available through commercial photolithography.

DPN can also be used for combinatorial chemistry experiments at the nanoscale [18]. Essentially, the instrument can be programmed to generate a series of monolayer patterns that vary with respect to composition, feature size, and feature spacing. These patterns

subsequently can be used to study a wide range of chemical or physical processes. These include crystallization, catalysis, chemical and biochemical recognition, etching behavior, surface molecular transport, and many others. One can determine the type of pattern appropriate for a given application and then, because of the dimensions associated with these patterns, the same scanning probe instrument used to generate them can be used to screen thousands on a relatively fast time scale. This combinatorial-nanotechnology approach has the potential to change the way we explore many nanoscale phenomena and, therefore, have a major impact on the development of new technologies based on materials with sub- 100 nm dimensions.

Although DPN is still in its infancy, its development already has led to the accomplishment of several important milestones in nanotechnology and in scanning probe nanolithographies in particular. First, it is now a user-friendly form of lithography accessible to any group with a conventional AFM. This alone should accelerate its use throughout the scientific community at large and especially within the chemical and biochemical communities. Second, its direct-write nature sets it apart from other scanning probe lithography alternatives and provides some unique capabilities with respect to nanostructure registration and the chemical complexity one can incorporate into soft nanostructures. Third, it offers comparable resolution to optical lithography, but it is substantially more general with respect to the types of structures (hard and soft) one can pattern. With the incorporation of multiple probes, it offers parallel writing capabilities with minimal increase in the complexity of the patterning instrumentation. The challenge facing future development of DPN is its advancement from an academic curiosity to a highly-automated, massively-parallel workhorse for industry.

8.4. SCANNING PROBE NANOGRAFTING

Due to the similarity of the two methods, much of the discussion about DPN also applies to SNG, which was also developed at about the same time as DPN. The resolution limit is quite similar. However, Liu *et al.* used SNG, to create nano-islands with dimensions of 3 nm by 5 nm, making these the smallest AFM-based SPN structures yet reported [2]. Moreover, they have shown that SNG features can be erased and recreated simply by performing a second SNG experiment on the feature to be erased while using the original ink to fill in behind the tip. Using both one and two-step nanografting methods, patterns of alkane thiols, proteins, and DNA have all been formed [19,20].

Because SNG is performed by first covering the entire substrate with an initial SAM, DPN affords somewhat greater flexibility than nanografting. However, the fidelity and reproducibility of DPN is inherently worse than in SNG. This is because both the coverage of ink on the tip as well as the ink transfer rate are sensitive to a myriad of factors including ink composition, coating methodology, humidity, temperature, and deposition time or writing speed. (The reasons for these dependencies will be discussed below.) In SNG, while ink deformation and removal is done locally by the tip (and can be well controlled by maintaining constant force), ink deposition is actually a bulk chemical process that ensures high uniformity. For this reason, SNG offers some advantages when developing inks or methods for using those inks as templates to create hierarchical structures. But inks that are successful with one method are generally transferable to the other.

8.5. PHYSICAL MODELS OF INK TRANSFER DURING DPN

A variety of factors could determine the feature size achieved during DPN. These factors include dwell time, writing speed, temperature, tip coverage, interfacial tension, and humidity. Recently, a number of researchers have used measurements of feature size in an attempt to both assess some of these factors and create a physical model of ink transfer from tip to substrate. Nonetheless, a complete picture of the physical processes and materials parameters that control transfer and deposition has yet to emerge. For example, there is a controversy over whether a water meniscus is needed for this transfer. DPN patterns of ODT have been fabricated in 0% relative humidity and show little or no dependence of feature size on humidity. In contrast, measurements of the dependence of feature size on humidity for 16-mercaptohexadecanoic acid (MHA) exhibit significant humidity effects. Indeed, many capillarity-related phenomena originate from the well-documented formation of water films on surfaces [21]. Thin water films have been studied by a variety of techniques including ellipsometry [22], NMR [23], adsorption isotherms [24], and atomic force microscopy [25]. These investigations have shown that the films are often just a few monolayers in thickness. When a water meniscus forms between an AFM tip and a surface, it has a profound effect on tip–sample interactions, both degrading image quality and interfering with force measurements [26]. Consequently, the meniscus formed between the tip and surface has often been assumed to be a crucial feature DPN [27,28]. However, even in the case of MHA, where the importance of the meniscus is now widely accepted, there is still debate over the ink transfer mechanisms.

Some researchers have modeled the dependence of feature size on dwell time using a diffusion-controlled mechanism through the meniscus [29,30]. But these models have ignored the dynamics of ink dissolution into the meniscus, a process which must be considered for soluble inks. Weeks *et al.* recently presented a model for MHA transfer that takes into account the ink dissolution kinetics [31]. Arrays of dots were fabricated by bringing an inked cantilever into contact with a freshly prepared gold surface. To minimize the transfer of MHA from the tip to the substrate, the sample was rastered at speeds greater than 4 Hz. To make a dot, the rastering was stopped and the tip was allowed to dwell at a specific location for a given time. The tip was then moved quickly to the next position and the process was repeated. In order to image the resulting pattern, the sample was rastered while recording the friction (lateral force) signal from the AFM. Figure 8.7 shows a typical friction image for an array of MHA dots deposited on gold. Experiments were repeated by varying the humidity from 0–55%. At a relative humidity at or below 15%, reproducible features were not observed for the shortest contact times (0.5 seconds and below) while for longer contact times we were able to produce features systematically at all contact times. Weeks *et al.* proposed that at that humidity the meniscus does not form between the tip and the sample, thus the ink transport to the surface is inhibited. However, subsequent experiments (by us) have shown that the meniscus takes time to form and that a meniscus can form even at low humidity. (Another possible explanation for the earlier result is that the gold used in these experiments was sputtered making grains that are larger than the smallest patterned features, making the features indistinguishable from the grains.)

Figure 8.8a shows the dependence of the dot area on dwell time for times between 0.5 s and 60 s and humidity ranging from 20% to 54%. Figure 8.8b shows the dependence of dot size on humidity for three different dwell times. Three features are evident. First, the
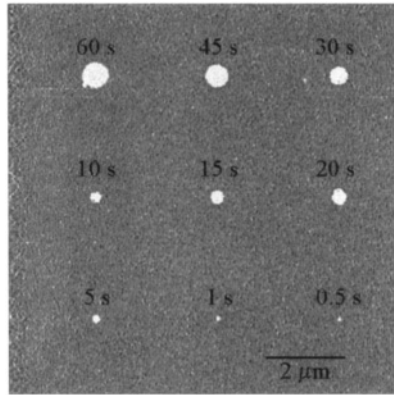
FIGURE 8.7. Friction-force image of MHA dots on gold fabricated with the indicated dwell times.
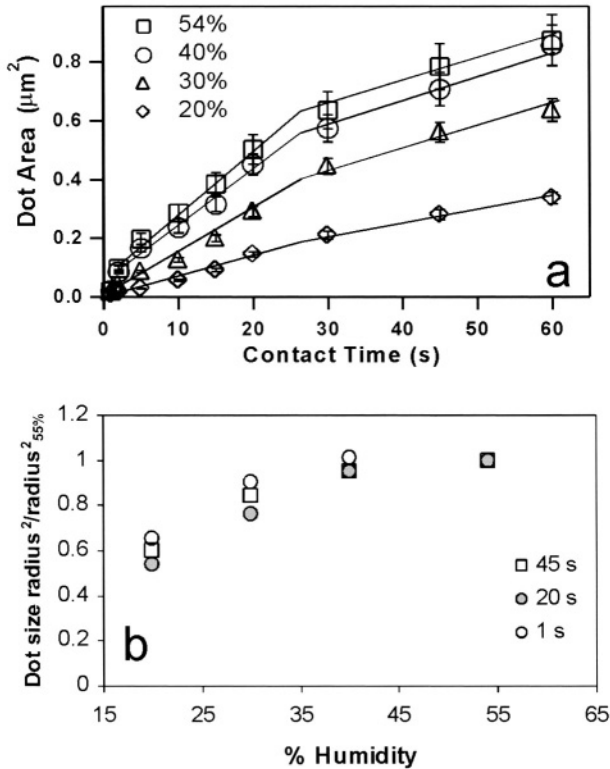
FIGURE 8.8. (a) Dependence of radius squared on dwell time as a function of relative humidity (H); (h) dependence of dot radius squared on humidity for three different dwell times normalized by the maximum radius squared at $H = 55\%$.

dependence of the square of the dot radius on dwell time is well fitted by two linear regions separated by a sharp transition zone which occurs over the same range of dwell times for all humidities. Second, from humidity of 20% to 45%, the spot size increases; while above
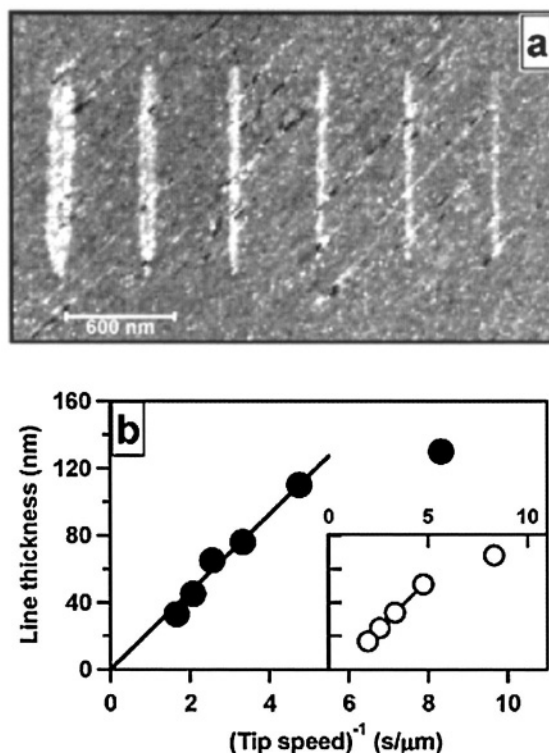
FIGURE 8.9. (a) Friction-force image of MHA lines on gold fabricated at tip speeds between 0.1 and 1 $\mu m s^{-1}$; (b) dependence of line width on inverse tip speed for both MHA and MEH-PPV (inset).

45% there is little change in the diameter of the spot. Third, the dependence of feature size on humidity is the same for all dwell times. At the highest humidity, the precision of the measurements decreased and the edges of the dots became less well defined. These results are consistent with lateral force microscopy and force spectroscopy studies [32,33].

In addition to dot fabrication, DPN can be used to write lines. In contrast to the case of dot generation where the tip is held stationary for the deposition time, during the fabrication of lines the tip continuously moves along the sample. In order to make a comparison between the controls on dot size and line width, lines were fabricated at tip speed, v, ranging from about 0.1 to 1 $\mu m/s$. The dependence of line width, W, on inverse speed, $1/v$, is presented in Figure 8.9. The data show a linear increase down to a speed of about 0.2 $\mu m/s$ where the dependence weakens significantly. Data on line widths for the lines of poly[2-methoxy-5-($2'$-ethyl-hexyloxy)-p-phenylene-vinylene] (MEH-PPV), a luminescent polymer, drawn on a SiO_2 surface are also given in the inset to show that this behavior is not peculiar to MHA.

To understand these experimental results Weeks *et al.* proposed the following model for ink transfer to the surface (Figure 8.10). The tip moves at constant speed, v,—which is zero for fabrication of dots—through a water film of thickness, δ, on the surface. Due to a non-zero contact angle at the tip, the height, h, of the meniscus at the tip, is different from δ. Thiol molecules dissolve from the tip into the meniscus, diffuse through the meniscus and
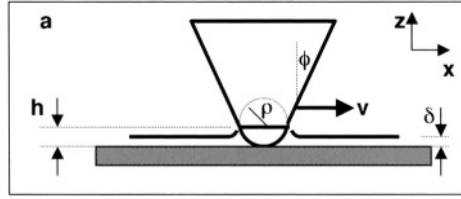
FIGURE 8.10. Schematic of the physical model for molecular transfer from AFM tip to substrate through meniscus of height h.

attach to the surface making a continuous self-assembled monolayer. After a time, τ, the tip is removed from the water film. At this time, thiol molecules are both attached to the surface and dissolved in the meniscus. Through diffusion, the dissolved thiols will eventually reach the edge of the SAM and attach to the substrate, contributing to the final feature size. Regardless of the tip-meniscus geometry, the magnitude of the diffusion constant, or the dissolution rate, the total number of molecules, N, transferred to the surface will be given by the integral of the transfer rate dN/dt over the total tip–surface contact time τ.

For dot fabrication, two terms contribute to dN/dt: first, molecules dissolve from the tip through thermal activated detachment at a rate:

$$\left(\frac{dN}{dt}\right)_{+} = \frac{A}{\pi a^2}\beta_{+} = \frac{A}{\pi a^2}\nu e^{-E_D/kT}, \tag{1}$$

where A is the contact area between the tip and the meniscus, πa^2 is the average area per thiol ink molecule, E_D is the activation energy for ink detachment, k is Boltzmann's constant, T is the temperature, and ν is an attempt frequency. In this case, the ink molecules are not detaching from the surface of a silicon nitride tip, rather they are detaching from the surface of a bulk alkane thiol solid that has precipitated onto the tip during the inking process. Second, molecules return to the tip simply due to impingement and attachment at a rate given by:

$$\left(\frac{dN}{dt}\right)_{-} = A\beta_{-}C_0 \approx A\left(\frac{kT}{2\pi m}\right)^{1/2} e^{-E_A/kT}C_0, \tag{2}$$

where m is the mass of a thiol, E_A is the activation energy for attachment, and C_0 is the concentration of thiols in solution adjacent to the tip. The right hand side of eq. (2) assumes a gas kinetic expression for the impinging flux. A more complicated description would modify the factors in β_{-}, but will not change the dependence on C_0. (Note that in the absence of diffusion, C_0 will simply increase until it reaches the equilibrium solubility, C_e, at which time, $(dN/dt)_{+} = (dN/dt)_{-}$.)

The dot radius is related to N through $\pi R^2 = N\pi a^2$. Combining this relationship with eqs (1) and (2) and integrating gives:

$$R^2 = A\left(\beta_{+}\tau - \pi a^2\beta_{-}\int_0^{\tau} C_0(t)dt\right). \tag{3}$$

Similar arguments lead to an expression for the dependence of line-width on tip speed. Assuming the tip moves over a distance l at a speed v, we write:

$$N = \int_0^l \left(\frac{dN}{dt}\right)\left(\frac{dt}{dx}\right)dx = \frac{1}{v}\int_0^l \left(\frac{dN}{dt}\right)dx. \tag{4}$$

The expressions for $(dN/dt)_+$ and $(dN/dt)_-$ remain the same as for dots, except that C_0 is now expressed as a function of v instead of t. Recognizing that $C_0(v)$ and β_- are both independent of x and that the line width $W = N\pi a^2/l$, eq. (4) becomes:

$$W = \left(\frac{A}{v}\right)\left(\beta_+ - \pi a^2\beta_-C_0(v)\right). \tag{5}$$

For both dots and lines, the exact form of C_0 depends on a number of factors including the tip–meniscus geometry, surface attachment probability and the diffusivity, but because C_0 is small at short contact times or high tip speeds, two regimes emerge. For small τ (high v), $C_0 \approx 0$ and the dot size [(line-width)] is given by the first term in eq. (3) [(5)]. That is $R^2 \sim A\tau$ and $W \sim A/v$. This is the regime in which surface kinetics dominates the transfer process. For long contact times/slow tip speeds, C_0 reaches a limiting value C_0 that is less than C_e. Once again, $R^2 \sim A\tau$ and $W \sim A/v$, but the slopes of these linear relationships are reduced. In this regime the transfer process is controlled by diffusion. The predicted dependencies are similar to those observed for both dot and line fabrication (Figures 8.8 and 8.9).

The effect of humidity comes into this model through the impact of meniscus height, h, on contact area, A. The tip can be approximated by a cone terminated by a hemisphere of radius ρ. If $h \gg \rho$, A is approximately equal to that of a conical tip with half-cone angle ϕ, and height h, which is $\pi h^2 \sin\phi$. In contrast, for $h < \rho$, $A = 4\rho^2 \cos^{-1}(1 - h/\rho)$. For $h \ll \rho$, this has an $h^{0.5}$ dependence, while for $h \approx \rho$, it is linear in h. Consequently, as the humidity is increased from 15% to 50%, we expect the dot size to increase with a dependence that ranges from $h^{0.5}$ to h^2. Furthermore, because A is a multiplicative factor for both terms in eqs (3) and (5), in agreement with the measurements, the transition from dissolution-dominated to diffusion-dominated deposition should be independent of the humidity and the functional form of the dependence of dot radius on humidity should be the same for all dwell times (Figure 8.8).

An investigation of water film thickness performed on gold surfaces using scanning tunneling microscopy concluded that the film consisted of 30–50 nm islands that increased in thickness from about 2 nm at $H = 20\%$ to 10 nm at $H = 45\%$ [34]. Coincidentally, the increases in film thickness from that study, which are about a factor of four between H of 20% and 30% and about 1.4 between H of 30% and 40%, match the measured increases in dot size with humidity assuming an $h^{0.5}$ dependence in the low range, and an h^2 dependence in the high range.

One can quantitatively test the sensibility of this model to some degree by examining the low τ/ high v dependence of dot size and line width. In this regime, the slopes of R^2 vs. τ and W vs. $1/v$ are both given by $A\beta_+$. An upper limit for the attempt frequency, ν, is given by kT/h_p, where h_p is Planck's constant. This value is appropriate for simple atomic
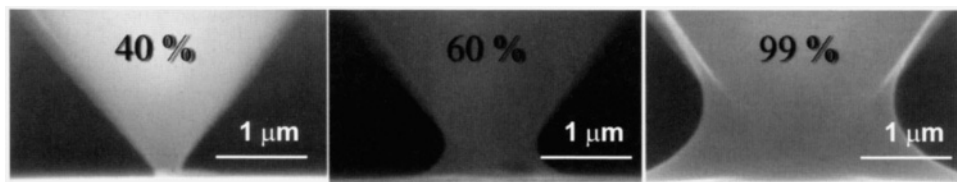
FIGURE 8.11. Environmental scanning electron microscopy (ESEM) images of an AFM tip in contact with a gold substrate. The relative humidity is noted in each image. The same tip was used for all images. The meniscus formed at 60% is approximately 400 nm in height while at 100% is nearly 2 μm. We cannot verify whether a meniscus forms at the low humidity range due to the resolution limit of the ESEM (approximately 75 nm under these conditions).

solids. In the case of chain-like molecules such as alkyl thiols, the attempt frequency is smaller. Although no detailed calculations of the appropriate frequency factor for these systems exist, models of idealized chain-like molecules lead to an estimate for ν, which is one to two orders of magnitude smaller. Taking the data for 20% to 54% relative humidity, using a range for n of 10^{10} to 6×10^{12} s^{-1}, and assuming the film thickness of 2 to 10 nm from Freund *et al.* [34] gives $E_D = 45$ to 60 kJ/mole for both the dots and the lines. This number should be greater than or equal to the heat of solution for MHA in water. Literature values for the heat of solution of a number of alkanes range from 25 to 40 kJ/mole [35,36].

As mentioned above, a number of researchers have found that a meniscus is not needed for creating features by DPN. Patterning of a number of molecules including MHA have been performed at relative humidity around 0%. In addition, experiments performed with octadecane thiol have shown little or no change on the patterning characteristics over a large range of relative humidity (~0 to 100%). One of the arguments against a role for the meniscus is that the Kelvin equation, which gives the size of the meniscus formed due to capillary condensation, predicts that the height of the meniscus should only be on the order of a few nanometers making it insufficient to account for the large feature sizes observed experimentally. However, environmental scanning electron microscopy images of a cantilever in contact with a surface show conclusively that the meniscus formed even at moderate humidity (40%) can be hundreds of nanometers to even many microns in height (Figure 8.11). Nonetheless, patterning at 0% can not be explained by transport through a meniscus (note that many molecules cannot be patterned at 0% including: DNA, dendrimers, and metal salts).

The obvious mechanism to explain patterning without a meniscus is that the molecules travel from the tip to the surface via surface diffusion as proposed by Sheehan *et al.* [37] and Schwartz [38] (see Figure 8.12a). In the case of ODT, it has been observed that there is no dependence of patterning rate on relative humidity. Moreover, the diffusion-based models appear to fit the data quite well. These data even predict a reasonable surface diffusion constant. In fact, Schwartz has proposed that humidity can actually impede the patterning rate of ODT. This "surface protection" effect provides a measurement of the special extent of the capillary meniscus as a function of relative humidity. In that work, Schwartz concluded that because ODT is not soluble in water, the lowest energy state would be for the ODT molecules to be at the air/water interface of the water meniscus. This effect has been proposed as the reason why a double line is produced by ODT under high humidity as seen in Figure 8.12b. By changing the vapor composition to ethanol, the molecules appear to
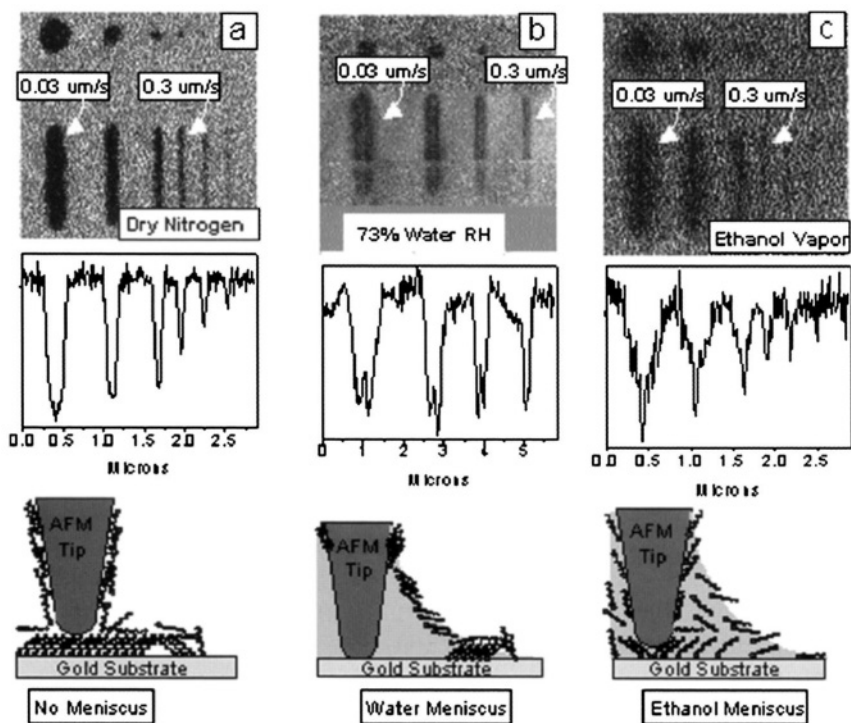
FIGURE 8.12. Effect of vapors on line profile. (a) Lines of ODT were DPN-generated and LFM imaged in a dry nitrogen environment; (b) lines of ODT were DPN-generated and LFM imaged in an environment high in water vapor; (c) lines of ODT were DPN-generated and LFM imaged in an environment of ethanol vapors. All experiments were done at room temperature. Below each LFM profile is a representation of the corresponding ODT molecular distribution that is consistent with both of the corresponding LFM profile as well as the bulk behavior of ODT.

readily diffuse through the meniscus as illustrated in Figure 8.12c. A very elegant model was presented by Schwartz in which the diffusion rate can be calculated by treating the patterning rate as a concentration gradient throughout the features being patterned.

8.6. USING SPN TEMPLATES TO CREATE HIERARCHICAL STRUCTURES

Methods for fabricating nanometric bio-molecular arrays are attracting intense interest due to their great potential in numerous applications including protein and DNA chips for proteomic and genomic analysis, biological sensors for pathogen detection, and 2D or 3D crystalline arrays for determination of protein structure. Because SPN naturally lends itself to forming nanometric arrays of functional molecules, a number of researchers have recently explored it as a means for either directly patterning or templating subsequent deposition of biomolecules [16,39–43]. For example, Demers *et al.* fabricated arrays of DNA using DPN [15]. Similarly, Liu *et al.* used SNG to create DNA arrays by performing the grafting step in a solution containing thiolated single stranded DNA which filled in behind

AFM tip to form an array with the DNA at the free end [40]. Liu *et al.* also used bioti-
nated thiols as an ink to template the subsequent deposition of streptavidin on 50 nm spots
and both DPN and NG have been used to create protein arrays by first generating patterns
of hydrophillic regions (e.g., MHA) in a hydrophobic background (e.g., PEG) [41]. The
patterned substrates were subsequently exposed to a solution containing proteins such as
lysozyme or BSA, which only adsorbed to the hydrophobic regions. Using a similar ap-
proach, Wilson *et al.* created arrays of collagen proteins [42].

   All of these systems represent a miniaturization of more conventional biomolecular
arrays produced through other techniques of patterning such as micro-stamping. Although
there are many important applications of sub-100 nm scale patterns, such as ultra-dense
protein chips, they generally do not involve systems in which the feature sizes are com-
mensurate with the dimensions of the biomolecules. Systems in which this is the case offer
the possibility of controlled molecule-by-molecule assembly of macromolecular architec-
tures, one that becomes all the more attractive if the both the position *and* orientation of
the biomolecules can be controlled.

   Viruses, which are supramolecular assemblies of macromolecules, are typically on the
order of tens of nanometers in size and have a wide range of functional groups present on
their surfaces that can be targeted as sites for attachment. In fact, by genetically modify-
ing viruses, it is possible to express unique chemical groups at a small number of surface
sites [44]. In the case of icosahedral viruses, these sites can be chosen to be symmetrically
equivalent. Moreover, because viruses are produced biologically according to a genetic
code, they are atomically precise and monodisperse. Hence viruses provide ideal nanomet-
ric building blocks for the investigating molecularly directed assembly of bio-molecular
arrays using SPN templates. Cheung *et al.* demonstrated a generic, multi-step approach to
assembling arrays of viruses on SPN templates [45]. First they introduced unique chemical
groups on the virus surface. Then they designed a long-chain linker that would form a cova-
lently bound SAM at a gold surface while present a functional head group that would react
chemoselectively with the engineered chemical groups on the virus surface. Afterwards,
they grafted that linker into a background SAM that resisted virus binding.

   Cheung *et al.* used a system that consisted of gold coated mica for the substrate,
functionalized alkyl thiols as the linkers, and genetically modified cow pea mosaic virus
(Cys-CPMV) [44] as the adsorbate as shown schematically in Figure 8.13. Smith *et al.*
had also used a similar scheme to template virus deposition [46]. The virus was genet-
ically engineered to present cysteine residues (Cys) at geometrically equivalent positions
on the viral capsomer as shown in Figure 8.14. Because the reaction between the sulfhydryl
groups on the virus and maleimides is highly chemoselective [47], a sulfhydryl–maleimide
chemoselective reaction scheme was utilized. Functional thiols produced through a novel
solid-phase synthesis process (Figure 8.17) and applied by two-step nanografting linked
the mutated virus onto the substrate while triethylene glycol (TEG) terminated thiols (Fig-
ure 8.15) were applied as the resist to the surrounding regions for prevention of non-specific
adsorption [48]. Figure 8.4 shows a pattern of ca. 30-nm-width lines filled with the amine
terminated thiol that extend 0.5–2.0 nm above the background TEG terminated layer.

   Using the highly selective thiol–maleimide reaction, Cys-CPMV virus was chemos-
electively attached on chemical templates containing the maleimido functionality. To
demonstrate a proof of principle for the virus assembly scheme, Cheung *et al.* first fab-
ricated a micron-scale chemical template by micro-contact printing 10 μm squares of the
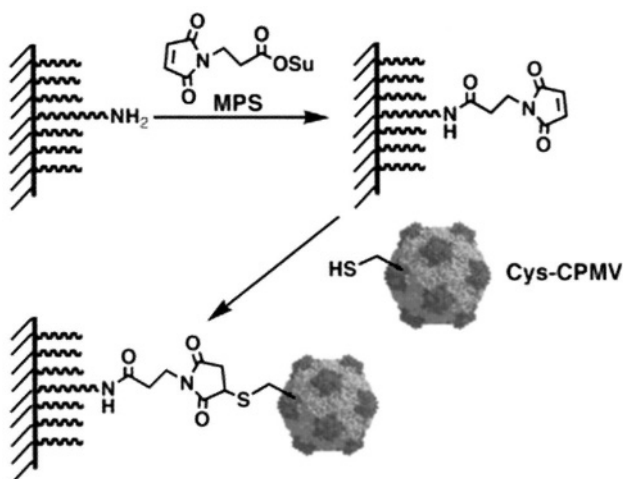
FIGURE 8.13. Scheme for attaching genetically modified virus (Cys-CPMV) to SPN templates on gold.
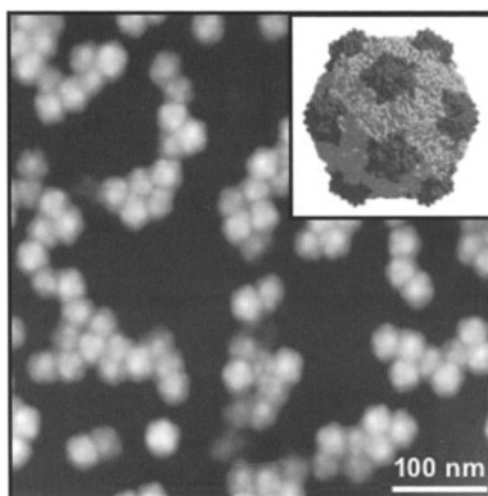
FIGURE 8.14. AFM height image of cow pea mosaic virus (CPMV). (Inset) Model of genetically modified CPMV virus with unique cysteine residues (Cys-CPMV). Red dots indicate the locations of mutated cysteine residues.

amino linker thiol on gold substrates and subsequently filling in the background with the TEG thiol. The maleimido function was then introduced by acylating the patterned amino groups with 3-maleimidopropionate N-hydroxysuccinimide ester (MPS). The chemical template was then treated with freshly reduced Cys-mutated CPMV in phosphate buffer at pH = 7.0 for 2 h, and the unbound virus was then washed away. As shown in Figure 8.16, the Cys-CPMV preferentially attached to the squares containing the maleimido function. Few virions were found in the background area. However, neither spatial correla-
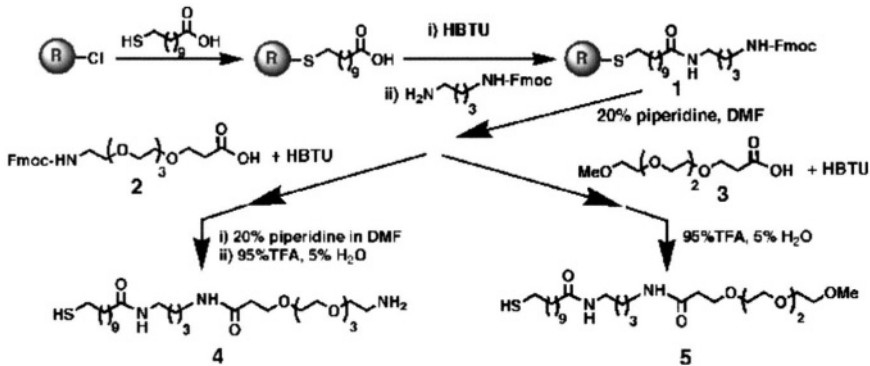
FIGURE 8.15. Scheme for synthesizing amino terminated and polyethylene glycol terminated inks. The former serves the virus linker and the latter functions as resist to virus binding.
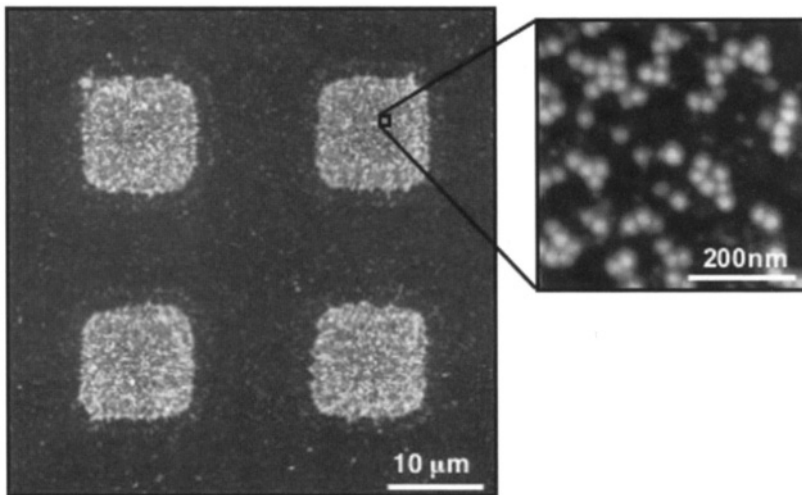
FIGURE 8.16. AFM height image of Cys-CPMV virus assembled on micrometer-sized template. (Inset) Magnified section of functionalized square.

tion, short-range order, nor long-range order between the viruses was observed within the squares.

When the dimension of the chemical template were reduced from the micron-scale to a size comparable to that of a CPMV, the morphology of virus assembly changed dramatically. Figure 8.17 shows an assembly of a dense population of the Cys-CPMV virions on most of the 30-nm-wide patterned lines made by nanografting and processed as the micron-sized templates. Probably due to size exclusion, a significant inter-virion attractive interaction, and the lack of an attractive virion-TEG interaction, the virions started to pack together into a close-packed morphology (Inset to Figure 8.17b). Not only did the lines themselves act as templates for attachment of the virions, but the lines of assembled virions then acted as templates for lateral growth of the viral assembly. As other virions
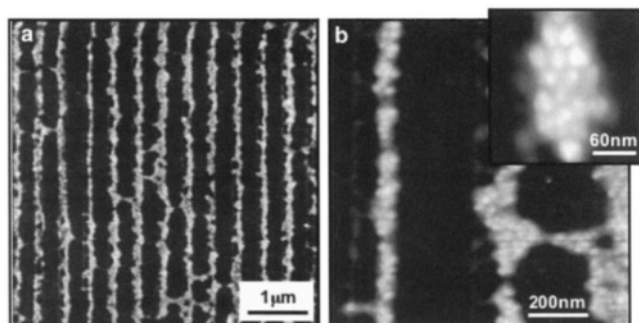
FIGURE 8.17. (a) AFM height image of a monolayer-thick virions assembled on a parallel line pattern created by nanografting with the chemoselective linkers. (b) Magnified section of Figure 8.17a. (Inset) Magnified image of another section of the same sample as in (b).
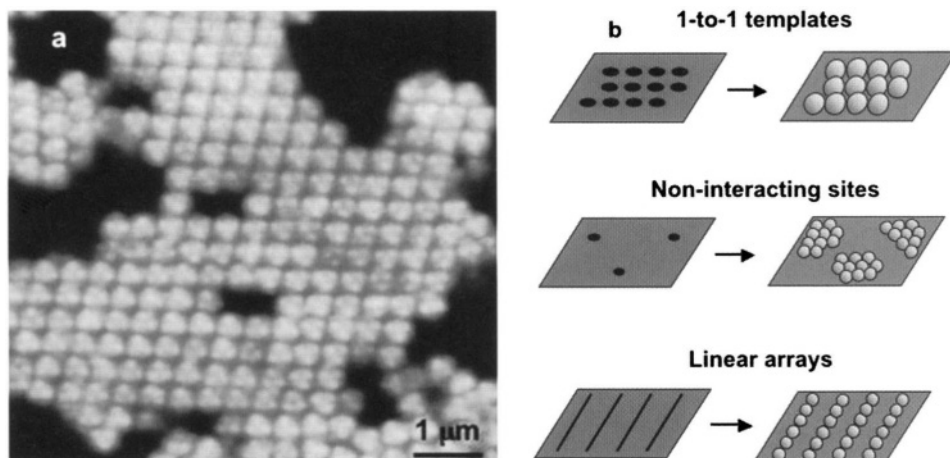
FIGURE 8.18. (a) Ordered islands of CPMV virus deposited on mica indicating tendency of virions to order under appropriate solution conditions, (b) Three potential methods to induce ordering at SPN patterns of linkers.

"stuck" to these lines, the lines "grew" laterally at the resulting step-edge and, in some cases, contacted adjacent lines of virions to form a pseudo-2D assembly (Figure 8.17b). Nevertheless, presumably because the attractive inter-virion interaction was too large, the lateral expansion did not proceed in a smooth and well-ordered manner.

Taking a lesson from the science of bulk crystallization of macromolecules, modulation of this strong inter-virion interaction by altering solution conditions such as pH and ionic strength could assist the creation of 1D nucleation templates for growth of ordered 2D crystalline films. Moreover, by varying these factors, as well as the concentration of virus in the solution during deposition, these templates can serve as platforms for investigating the physics of bio-molecular aggregation. As illustrated in Figure 8.19, by comparing the morphology and kinetics of assembly seen with *in situ* AFM with simulations of assembly using kinetic Monte Carlo methods, the strength of the virus–template and inter-virion

**Roughness
of virus islands**

$$\frac{\text{Virus Flux}}{\text{Virus Mobility}}$$
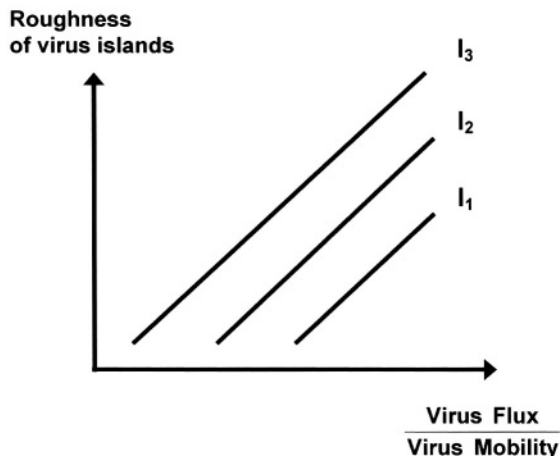
FIGURE 8.19. Schematic showing expected dependence of island roughness on virus flux and mobility. The flux is determined by the concentration and the mobility by the solution composition. I_x's, where $x = 1, 2$ and 3, represent the amount of precipitant in the virus solution with $I_3 > I_2 > I_1$. Analysis of nucleation and growth kinetics, as well as island morphology provides a means of probing the inter-virion and virus–template interactions through kinetic Monte Carlo modeling.

interactions can be estimated, and the importance of diffusion and attachment/detachment events evaluated.

8.7. CONCLUSION

In summary, scanning probe nanolithography has emerged as a versatile method for both direct patterning of soft structures and indirect templating of hierarchical structures at the nanoscale. It has been used to pattern a wide variety of compounds and biomolecules including alky thiols, organic dyes, proteins, antibodies, DNA, and viruses. In addition to providing a means of creating features at 10 to 100 nm length scales, this approach allows for generation of patterns with multiple functionalities opening up the possibility of producing ultra-dense DNA and protein chips, as well as platforms for combinatorial chemistry and protein crystallization using minute quantities of material.

While the physical mechanisms by which ink transfer proceeds during DPN remains an area for future research, for soluble compounds, the aqueous meniscus formed between the tip and substrate clearly plays an important role. Indeed, DNA patterning cannot be done without it. More work is needed to sort out the relative importance of thermal desorption and surface diffusion versus dissolution and bulk diffusion. Experiments that investigate meniscus formation directly through environmental electron microscopy will be critical to this effort.

SPN templates for biomolecular adsorption present excellent platforms both for technological applications as well as fundamental studies of macromolecular aggregation. The role of interactions between the adsorbate and the solvent, the template, and other adsorbates, as well as the impact of flux and adsorbate mobility can all be explored. Perhaps the most far-reaching outcome of this work, would be an ability to define a generic route

to ordering macromolecules at surfaces. Such ordered patterns could take the place of 3D crystals in the field of protein structure determination, especially when the 4th generation light sources become available later this decade.

ACKNOWLEDGEMENTS

REFERENCES

1. D.S. Ginger, H. Zhang and C.A. Mirkin, *Angew. Chem.* **43**, 30 (2004).
2. G.Y. Liu, S. Xu and Y.L. Qian, *Accounts of Chem. Res.* **33**, 457 (2000).
3. G. Binnig, H. Rohrer, C. Gerber and E. Weibel, *Appl. Phys. Lett.* **49**, 178 (1982).
4. G. Binnig, C.F. Quate and C. Gerber, *Phys. Rev. Lett.* **56**, 930 (1986).
5. T.R. Albrecht, S. Akamine, T.E. Carver and C.F. Quate, *J. Vac. Sci. Technol. A* **8**, 3386 (1990).
6. G. Meyer and N.M. Amer, *Appl. Phys. Lett.* **53**, 1045 (1988).
7. G. Meyer and N.M. Amer, *Appl. Phys. Lett.* **57**, 2089 (1990).
8. E.E. Ehrichs, S. Yoon and A.L. de Lozanne, *Appl. Phys. Lett.* **53**, 2287 (1988).
9. F.R.F. Fan and A.J. Bard, *J. Electrochem. Soc.* **136**, 3216 (1989).
10. R.C. Jaklevic and L. Ellie, *Phys. Rev. Lett.* **60**, 120 (1988).
11. B.L. Weeks, T. Rayment and M.E. Welland, *Nanotechnology* **13**, 38 (2002).
12. J.P. Rabe and S. Buchholz, *Appl. Phys. Lett.* **58**, 702 (1991).
13. D.M. Eigler and E.K. Schweizer, *Nature* **344**, 524 (1990).
14. R.D. Piner and C.A. Mirkin, *Langmuir* **13**, 6864 (1997).
15. L.M. Demers, D.S. Ginger, S.J. Park, Z.X. Li, S.W. Chung and C.A. Mirkin, *Science* **296**, 1836 (2002).
16. A. Noy, A.E. Miller, J.E. Klare, B.L. Weeks, B.W. Woods and J.J. De Yoreo, *Nano Lett.* **2**, 109 (2002).
17. H. Zhang, S.W. Chung and C.A. Mirkin, *Nano Lett.* **3**, 43 (2003).
18. A. Ivanisevic, K.V. McCumber and C.A. Mirkin, *J. Am. Chem. Soc.* **124**, 11997 (2002).
19. J.F. Liu, S. Cruchon-Dupeyrat, J.C. Garno, J. Frommer and G.Y. Liu, *Nano Lett.* **2**, 937 (2002).
20. P.V. Schwartz, *Langmuir* **17**, 5971 (2001).
21. P.A. Thiel and T.E. Madey, *Surf. Sci. Rep.* **7**, 211 (1987).
22. D. Beaglehole and H.K. Christenson, *J. Phys. Chem.* **96**, 3395 (1992).
23. J.R. Zimmerman and J.A. Lasater, *J. Phys. Chem.* **62**, 1157 (1958).
24. R.M. Pashley, *J. Colloid Interface Sci.* **78**, 246 (1980).
25. L. Xu, A. Lio, D.F. Ogletree and M. Salmeron, *J. Phys. Chem.* **102**, 540 (1998).
26. D.A. Grigg, P.E. Russell and J.E. Griffith, *J. Vac. Sci. Technol. A* **10**, 680 (1992).
27. R.D. Piner, J. Zhu, F. Xu, S. Hong and C.A. Mirkin, *Science* **283**, 661 (1999).
28. C.A. Mirkin, S. Hong and L. Demers, *Chemphyschem* **2**, 37 (2001).
29. J. Jang, S. Hong, G.C. Schatz and M.A. Ratner, *J. Chem. Phys.* **115**, 2721 (2001).
30. S. Rozhok, R. Piner and C.A. Mirkin, *J. Phys. Chem. B.* **107**, 751 (2003).
31. B.L. Weeks, A. Noy, A.E. Miller and J.J. De Yoreo, *Phys. Rev. Lett.* **88**, 255505 (2002).
32. R.D. Piner and C.A. Mirkin, *Langmuir* **13**, 6864 (1997).
33. L. Xu, A. Lio, D.F. Ogletree and M. Salmeron, *J. Phys. Chem.* **102**, 540 (1998).
34. J. Freund, J. Halbritter and J.K.H. Horber, *Microscopy Research and Technique* **44**, 327 (1999).
35. C. Tsonopoulos, *Fluid Phase Equilibria* **156**, 21 (1999).
36. C. Tsonopoulos, *Fluid Phase Equilibria* **186**, 185 (2001).
37. P.E. Sheehan and L.J. Whitman, *Phys. Rev. Lett.* **88**, 156104 (2002).
38. P.V. Schwartz, *Langmuir* **18**, 4041 (2002).
39. G.Y. Liu and N.A. Amro, *Proc. Natl. Acad. Sci. USA* **99**, 5165 (2002).

40. M.Z. Liu, N.A. Amro, C.S. Chow and G.Y. Liu, *Nano Lett.* **2**, 863 (2002).

41. K. Wadu-Mesthrige, N.A. Amro, J.C. Garno, S. Xu and G.Y. Liu, *Biophys. J.* **80**, 1891 (2001).

42. D.L. Wilson, R. Martin, S. Hong, Cronin-Golomb, C.A. Mirkin and D.L. Kaplan, *Proc. Natl. Acad. Sci. USA* **98**, 13660 (2001).

43. K.B. Lee, S.J. Park, C.A. Mirkin, J.C. Smith and M. Mrksich, *Science* **295**, 1702 (2002).

44. Q. Wang, T. Lin, L. Tang, J.E. Johnson and M.G. Finn, *Angew. Chem. Int. Ed.* **41**, 459 (2002).

45. C.L. Cheung, J.A. Camarero, B.W. Woods, T. Lin, J.E. Johnson and J.J. De Yoreo, *J. Am. Chem. Soc.* **125**, 6849 (2003).

46. J.C. Smith, K.B. Lee, Q. Wang, M.G. Finn, J.E. Johnson, M. Mrksich and C.A. Mirkin, *Nano Lett.* **3**, 883 (2003).

47. J.A. Camarero, in: *From Solid–Fluid Interfaces to Nanostructural Engineering,* Vol. II (Plenum/Kluwer Academic Publisher, New York, 2003) in press.

48. K. Prime and G.M. Whitesides, *J. Am. Chem. Soc.* **115**, 10714 (1993).

Index to Volume I

Index to Volume II